Small- signal stability analysis of Modular Multilevel Converters and application to MMC –based Multi-Terminal DC grids

Julian Freytes

N° d'ordre : 332

CENTRALE LILLE

THESE

Présentée en vue
d'obtenir le grade de

DOCTEUR

En

Spécialité : Génie Électrique

Par

Julian FREYTES

DOCTORAT DELIVRE PAR CENTRALE LILLE

Titre de la thèse :

Analyse de stabilité en petit signaux des Convertisseurs Modulaires Multiniveaux et application à l'étude des MMC dans des Réseaux HVDC

Small-signal stability analysis of Modular Multilevel Converters and application to MMC-based Multi-Terminal DC grids

---

Soutenue le 07 Décembre 2017 devant le jury d'examen :

Président	*Seddik BACHA, Professeur, G2Elab – Grenoble INP*
Rapporteur	*Sibylle DIECKERHOFF, Professeur, T. University of Berlin*
Rapporteur	*Dragan JOVCIC, Professeur, University of Aberdeen*
Examinateur	*Olav B. FOSSO, Professeur, NTNU*
Examinateur	*Olivier DESPOUYS, Docteur-Ingénieur, RTE*
Directeur de thèse	*Xavier GUILLAUD, Professeur, Centrale Lille*
Invité	*Guillaume DE PREVILLE, Ingénieur, General Electric*

Encadrant	*Frédéric COLAS, Ingénieur de recherche, A&M ParisTech*
Encadrant	*François GRUSON, Maitre de conférences, A&M ParisTech*
Encadrant	*Pierre RAULT, Docteur-Ingénieur, RTE*
Encadrant	*Hani SAAD, Docteur-Ingénieur, RTE*

Thèse préparée dans le Laboratoire L2EP
Ecole Doctorale SPI 072 (Lille I, Lille III, Artois, ULCO, UVHC, Centrale Lille)

Abstract

The attempt to massively integrate renewable energy sources in the electric power system has encouraged major interest in High Voltage DC systems (HVDC). Furthermore, Multi-Terminal DC grids (MTDC) appear as an attractive solution for the connection of offshore energy sources. Among different types of Voltage Source Converter (VSC), one of the most promising topologies for future MTDC grids is the Modular Multilevel Converter (MMC), which are proposed by the main European vendors. Up to now in Europe, a single vendor is in charge of the converter stations for each HVDC project, but future DC grids are likely to be multivendor schemes, where different control strategies may be applied to each converter station depending on its provider. However, due to intellectual property, manufacturers do not provide the complete control structure in open source but rather as a black-box models or control cubicles replicas. For this reason, it is impossible to use a formal mathematical approach to perform interoperability analysis. Hence, a more formal approach is needed to cope with the different issues that may arise due to the impact of the MMC controllers on the MTDC grids.

This thesis deals with the modeling and control of MMCs in the context of MTDC. The first objective is to obtain an MMC model in *dq* frame which can reproduce accurately the AC- and DC- interactions, while representing at the same time the internal dynamics which may interact with the rest of the system. This model is suitable for linearization and stability studies, among other linear techniques. Then, based on the developed *dq* model, different control strategies are developed based on state-of-the-art MMC controllers. Since the dimension of the system is a limiting factor for studying MTDC grids with many MMCs, different reduced-order models are presented and compared with the detailed *dq* model. Finally, the developed MMC models with different controllers are used for the MTDC studies. The impact of the selected controllers for each MMC is evaluated to highlight the potential issues that may occur in multivendor schemes.

Keywords

«HVDC transmission», «Modular multilevel converter», «State-Space modeling», «Small-Signal stability analysis», «Interoperability in MTDC grids».

Résumé étendu en français

Contexte de l'étude

Les développements technologiques, économiques et industriels ont conduits à l'utilisation massive de l'énergie électrique, où les combustibles fossiles, le charbon, le gaz naturel et le pétrole étaient toujours les sources d'énergies dominantes. L'exploitation des énergies fossiles provoque l'émission de gaz à effet de serre, et plus particulièrement de dioxyde de carbone CO_2. Par conséquent, l'écran qui retient la chaleur se densifie, ce qui conduit à l'augmentation de la température de la planète et le réchauffement climatique. Comme réaction face à ce danger environnemental qui découle d'une prise de conscience mondiale, des consensus et protocoles ont été signés et des démarches ont été mises en œuvre pour limiter les dégâts. L'une des principales actions consiste à transformer progressivement les sources d'énergies fossiles vers des sources d'énergies naturelles ou vertes, telles que l'énergie solaire et/ou éolienne.

En Europe, les sources d'énergies renouvelables sont disponibles sur des sites éloignés, en général au large ou à proximité de la mer. Cependant, les investissements dans les systèmes de transport de l'énergie électrique, en particulier sur de nouvelles lignes, ont été limités en Europe, à cause de l'opposition de la société civile contre les lignes aériennes pour des raisons environnementales ou décisions politiques. En outre, la transmission en masse de l'énergie électrique moyennant des câbles enterrés sous terre (ou sous-marins) en utilisant le courant alternatif (AC) est non faisable au point de vue technique. De ce fait, l'immigration vers le transport en courant continu (DC) pour les réseaux électriques en haute tension, été une nécessité face aux défis actuels où certaines limites des réseaux alternatifs apparaissent. Les réseaux à courant continu haute tension (HVDC) multi-terminaux peuvent être une alternative sous réserve de trouver des solutions aux barrières scientifiques et technologiques existantes.

Le débat entre les systèmes électriques à courant continu et à courant alternatif date de plusieurs décennies, depuis la première ère de l'électrification. Dans les premiers temps, les systèmes AC ont pris de l'avance, précisément dans les années 1880, à cause de la facilité de la transformation de la tension qui peut atteindre des niveaux relativement élevés, du champ tournant (pour les machines électriques) et de la difficulté pour interrompre les courants DC. Néanmoins, dans les années 1950, la première reprise des systèmes HVDC s'est produite avec le développement de la technologie à thyristors pour des niveaux d'intensité assez élevés. Cette technologie de l'électronique de puissance a été principalement utilisé pour la transmission de puissance sur de longues distances, du transport via des câbles sous-marins et également pour l'interconnexion de réseaux asynchrones. Au début des années 90, un retour en force aux applications de type HVDC a été identifié avec l'apparition sur le marché, de nouveaux composants à base de transistor (IGBT). Avec cette nouvelle technologie d'électronique de puissance, les systèmes HVDC ont commencés à s'imposer en attirant de plus en plus l'attention de la communauté scientifique ainsi que les décideurs politiques. Ainsi, la multiplication des projets HVDC de par le monde prouve l'engouement toujours croissant pour cette technologie de transport de l'électricité.

L'histoire de systèmes de transport à courant continu (HVDC) a été remarquée par les convertisseurs de puissance de type LCC (convertisseurs commutés par la ligne). En revanche, suite aux développements technologiques et afin de répondre aux exigences du cahier des charges, l'émergence de convertisseurs source de tension (Voltage Source Converter, VSC) a changé la donne par rapport aux nouvelles tendances. Le recours à cette technologie se justifie par le fait que moyennant les stations de conversion VSC, nous pouvons accueillir plus de sources d'énergies renouvelables et d'équilibrer les puissances sur des grandes étendues. En

outre, les flux de puissance peuvent être commandés dans les deux sens sans changer la polarité de la tension continue.

Dans la littérature, il existe de nombreuses topologies pour les convertisseurs de type VSC. Néanmoins, trois topologies sont les plus étudiées par les scientifiques et les spécialistes du domaine, à savoir : *2-level*, *3-level* (par exemple, Neutral Point Clamped (NPC) ou Flying Capacitor) et *Multi-level* VSC. Les VSC *2-level* et *3-level* fonctionnent avec une fréquence de commutation élevée (1–2 kHz) afin de minimiser le taux de distorsion harmonique (THD), ce qui peut engendrer des pertes par commutation plus élevées ainsi que des contraintes de haute tension. Dans les applications à haute puissance, les pertes de conversion entraînent un coût élevé pour les opérateurs du réseau. Pour cette raison, une nouvelle technologie de VSC à plusieurs niveaux a été développée, connue par les intervenants dans le domaine, sous le nom de Convertisseur Modulaire Multi-niveaux (MMC, Modular Multilevel Converter), qui a été largement présentée dans la littérature, avec beaucoup de succès, par Dr. Lesnicar et Prof. Marquardt. L'avantage majeur de cette topologie est la possibilité de travailler avec des fréquences de commutation plus faibles (un ordre de grandeur inférieur que celui du VSC classique), tout en garantissant une meilleure performance harmonique par rapport aux VSC *2-level* et *3-level*.

Développement de l'exploitation de l'énergie offshore

La Figure 1 montre la vision de développement offshore dans le nord de la mer par Wind Europe (ex. European Wind Energy Association), où l'idée d'acheminer de l'énergie éolienne à partir des sources offshore est clairement mise en avant. Par conséquent, un plan de développement ambitieux analogue à celui proposé par Wind Europe pourrait apporter beaucoup d'avantages aux réseaux électriques européens, outre l'exploitation des sources de l'énergie verte. Pour aboutir à ce niveau d'innovation et de performance pour le réseau électrique européen, des investissements importants sont nécessaires pour répondre aux objectifs soulignés à travers la nouvelle politique énergétique européenne. Cette nouvelle vision pour les réseaux électriques de demain est bien exprimée à travers les démarches adoptées par ENTSO-E (European Network of Transmission System Operators).

Systèmes HVDC "Multivendor"

Comme il est illustré par la Figure 1, toutes les liaisons HVDC opérationnels actuellement sont des liaisons *point-to-point*. Cependant, vu le besoin que les réseaux électriques à haute tension ont un intérêt à être plus renforcés pour faciliter les échanges, maintenir la sécurité de fonctionnement, et raccorder des sources offshore, il est important de passer à une configuration HVDC multi-terminaux (MTDC). Le VSC est la technologie la plus appropriée pour les applications MTDC, car elle utilise une tension continue commune, ce qui facilite la construction et la commande des interconnexions. Cependant, avec l'apparition du MMC sur le marché et sa capacité d'atteindre des niveaux de tensions très élevés sans le recours au filtrage côté AC, la technologie MMC-VSC est considérée comme la solution la plus adéquate pour les réseaux du futur à très haute tension, appelés "Supergrids". Le développement et les avancés scientifiques qui ont été réalisées sur les réseaux HVDC a permis d'accueillir de l'expérience dans le domaine, ce qui a été traduit par la création de nombreuses normes. Cependant, ces normes traitent plus le comportement des convertisseurs côté AC, mais jusqu'à présent, aucune norme n'a vu le jour pour le comportement côté DC ("DC Grid Code"). Ainsi, de nombreuses questions techniques sont en attente de réponses. En considérant les liaisons *point-to-point*,

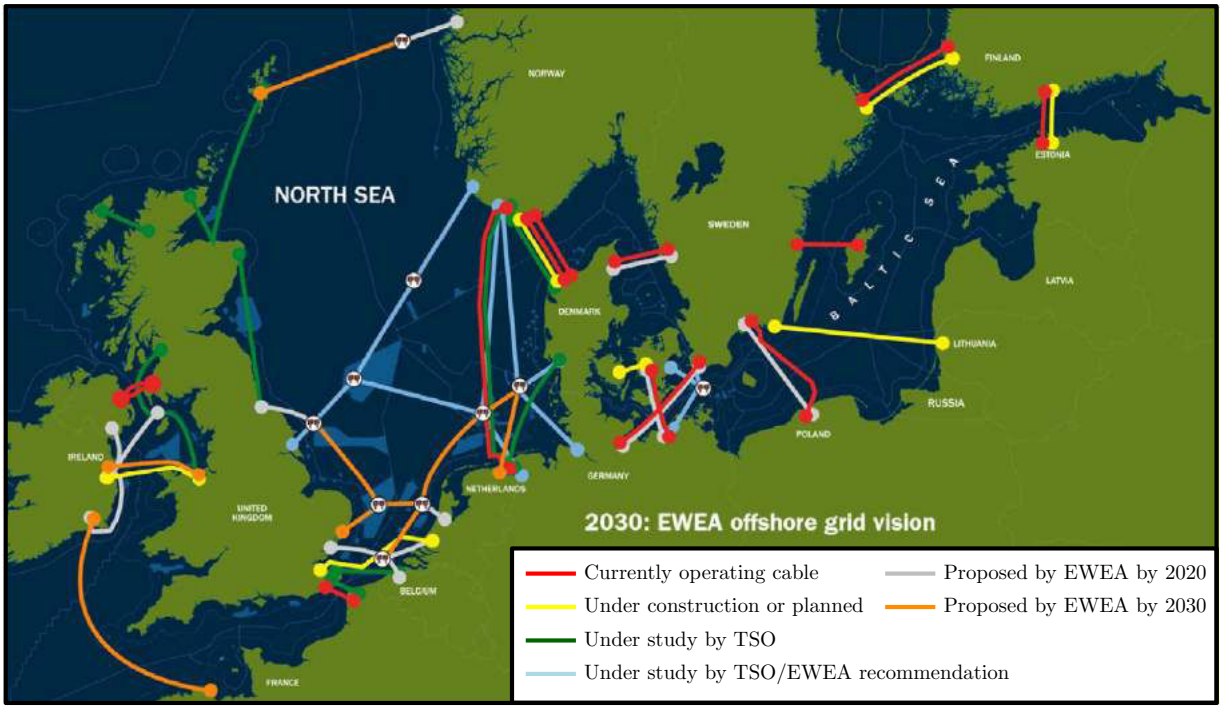

Figure 1 – Développement de l'exploitation de l'énergie offshore — Vision par Wind Europe

les convertisseurs sont fournis généralement par le même constructeur. Le comportement dynamique côté DC incombe à chaque fabricant car il est responsable du bon fonctionnement du système complet. En revanche, les réseaux MTDC ont plus tendance à être des systèmes avec différents constructeurs contribuant ensemble pour la mise en place du réseau maillé. Ainsi, nous nous retrouvons devant une configuration d'un réseau DC où les convertisseurs fournis par les différents constructeurs doivent fonctionner ensemble d'une manière fiable tout en assurant le cahier des charges imposé par le TSO. À ce stade, l'absence de normes qui unifient le comportement côté DC, pourra engendrer des problèmes et des nuances qui peuvent impacter le bon fonctionnement du système global (e.g., les valeurs de tension et de courant continu ne sont pas normalisées). En outre, le comportement dynamique de ces futurs réseaux DC sera fortement influencé par les stratégies de commandes associées aux convertisseurs pour chaque constructeur. Dans ce sens, il est important que le contrôleur mis en œuvre doit amortir le comportement oscillatoire qui peut impacter les caractéristiques du câble côté DC et éviter les problèmes d'instabilité qui peuvent surgir suite aux interactions dynamiques avec le reste du système.

Le projet européen *Best Paths* a réuni des partenaires experts du milieu académique et également de l'industrie autour de cinq démonstrations à grande échelle pour valider la faisabilité technique, les coûts, les impacts et les avantages des technologies HVDC. L'objectif des démonstrations est de fournir des solutions permettant de passer des lignes HVDC aux réseaux MTDC, de mettre à niveau et de réalimenter les lignes AC existants du réseau et d'intégrer des liaisons supraconductrices à haute puissance dans un réseau maillé AC. Le démonstrateur # 2 of *Best Paths* traite des problèmes d'interopérabilité possibles qui peuvent apparaître entre les MMCs connectés au même réseau DC fournis par différents constructeurs. Cette problématique pourrait être abordée en fonctionnement normal où la stabilité du réseau DC est assurée, mais également dans des conditions de fonctionnement anormales, telles que le décrochage d'une station de conversion, la reconfiguration du réseau et les évènements indésirables qui peuvent survenir. Les résultats de ce démonstrateur comprennent des recommandations pour les spéci-

fications et la mise en œuvre du contrôle matériel qui assurera une interopérabilité maximale pour la configuration en multi-constructeurs. Les lignes directrices proposées ainsi que les principales conclusions seront fournis comme des recommandations aux équipes de développement du "DC-Grid Code" de l'ENTSO-E et formeront une base solide pour faire des avancées significatives vers les exigences d'interopérabilité pour les réseaux HVDC multi-constructeurs, actuellement ciblés par les groupes de normalisation (CENELEC, CEI, ...).

Néanmoins, la notion d'interopérabilité peut être assez large pour explorer tous les domaines d'application. Ce travail a pour objectif de mettre en place une démarche systématique et rigoureuse pour l'étude des réseaux MTDC à base de convertisseurs modulaires multiniveaux tout en identifiant d'une manière formelle les principaux facteurs qui pourraient engendrer les phénomènes d'interopérabilité. Par conséquent, l'objectif majeur de ce travail résulte dans le développement de méthodologies appropriées permettant de synthétiser de lois de commandes locales basées sur les différentes approches de modélisation du convertisseur MMC et qui répondent convenablement aux performances désirées. Outre cela, des études d'analyse de stabilité en petits signaux et de sensibilité sont établies sur des modèles linéarisés du réseau MTDC permettant d'évaluer l'impact de différentes stratégies de contrôle proposées sur la dynamique du réseau. Cette étude aidera à formuler une idée sur l'interaction entre les différentes stratégies de commande des MMCs intégrés dans le réseau DC et élaborer éventuellement un schéma de recommandations, actuellement inexistant, pour les réseaux MTDC.

Plan de la thèse

Le plan de la thèse s'articule en cinq chapitres, comme il est indiqué par la Figure 2 :

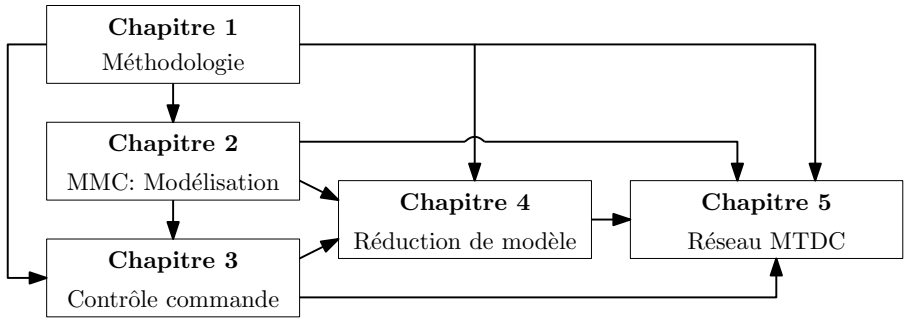

Figure 2 – Plan de la thèse

- Le **Chapitre 1** introduit la méthodologie appliquée tout au long de cette thèse pour l'étude des convertisseurs d'électroniques de puissance avec un intérêt particulier pour l'intégration dans les réseaux DC. Ce chapitre traite principalement de *2-level* VSC, où les principaux niveaux de modélisation sont bien détaillés : du modèle moyen classique dans le repère *abc* au modèle *dq*, jusqu'à son intégration dans une liaison HVDC point à point ainsi qu'un réseau MTDC. La technique de linéarisation relative à l'étude de stabilité en petits signaux est présentée pour assurer par la suite une étude fréquentielle basée sur les valeurs propres du système. Ce premier chapitre expose également les principaux concepts qui seront appliqués, tout au long de la thèse, au réseau DC à base de convertisseurs MMCs.

- Le **Chapitre 2** présente la démarche de modélisation en *dq* dans le domaine continu du convertisseur MMC. Le modèle non linéaire résultant est valable en régime stationnaire

dont les variables d'état sont constantes en régime permanent. Cette caractéristique nous offre la possibilité de linéariser le modèle autour d'un point de fonctionnement et d'étudier par la suite, la stabilité en se basant sur l'approche d'analyse modale. Sachant que le modèle à temps invariant exprimé dans l'espace d'état est validé par rapport à un modèle non linéaire de simulation en EMT (un modèle détaillé du MMC à 401 niveaux) implanté sous EMTP-RV.

- Dans le **Chapitre 3**, les stratégies de commande classiques basés sur l'inversion de modèle sont développées pour un MMC en vue de l'intégrer dans un réseau MTDC. Pour cela, un bus DC équivalent est pris en considération pour la modélisation du convertisseur MMC. L'objectif est d'analyser les interactions dynamiques du convertisseur avec le réseau DC en considérant les différents schémas de contrôle. Pour évaluer l'influence des stratégies de commande étudiées, nous nous basons sur le modèle MMC du Chapitre 2. Deux stratégies de commande découlent de ce chapitre, à savoir : le *commande pour la suppression du courant circulaire* (*Classical CCSC*) et la commande en énergie (*Energy-Based*). La première stratégie est la plus évoquée dans la littérature en raison de sa simplicité et sa performance même si nous ne maitrisons pas toutes les variables du système. Cependant, le principal inconvénient de cette méthode résulte dans les oscillations qui sont faiblement amorties par la commande dues aux courant DC ainsi que les variables en énergies qui sont en régime libre. Cependant, en ce qui concerne la deuxième stratégie de commande en énergie *Energy-based*, toutes les variables en énergies ainsi que le courant côté DC sont parfaitement contrôlées. Néanmoins, si nous nous tenons en compte des modèles détaillés des systèmes de commande et de puissance du MMC, le développement dans l'espace d'état du modèle augmenté nous conduit à un ordre très élevé du système global. Vu l'ordre du système, l'utilisation de ce modèle pour l'analyse modale en domaine fréquentiel, demeure difficile, principalement par rapport à l'interprétation des modes du système dans le plan complexe.

- Dans le **Chapitre 4**, un modèle d'ordre réduit du MMC est proposé pour faciliter l'étude de l'interaction AC-DC. Pour évaluer la validité du modèle réduit, un plan de test est appliqué en domaines temporel et fréquentiel. Les deux stratégies de commande basées sur le modèle complet, présentées dans le chapitre précédent, sont considérées où une étude comparative est menée avec le modèle réduit. D'après les résultats obtenus, nous confirmons l'utilisation du modèle réduit du MMC pour l'étude d'interopérabilité dans les réseaux MTDC avec MMC.

- Dans le **Chapitre 5**, l'analyse dynamique des réseaux MTDC à base de convertisseurs MMC est détaillée pour les études d'interopérabilité. Sur la base d'un réseau MTDC à quatre stations, plusieurs variantes d'études sont présentées pour évaluer l'influence de chaque stratégie de commande du MMC sur la dynamique globale du réseau MTDC. Par ailleurs, nous proposons également le développement de commande haut niveau permettant la régulation du niveau de l'énergie stockée (l'énergie interne du MMC) et la mettre, via la commande, à la disposition du bus DC afin d'améliorer le comportement de la tension continue. Les résultats obtenus illustrent clairement l'intérêt d'un convertisseur MMC par rapport à un VSC classique en termes de gestion de l'énergie et la possibilité de supporter le réseau DC en cas de perturbation. La route pour de nouvelles stratégies de contrôle pour l'amélioration des réseaux MTDC est pavée dans ce chapitre.

Les conclusions de la thèse

L'intégration des réseaux HVDC Multi-Terminaux dans les réseaux électriques existants a mis en défi de nombreux aspects et théories associées au domaine de l'électrotechnique et l'électronique de puissance. Grâce aux avancés technologiques, nous disposons aujourd'hui tous les moyens pour mettre en place des réseaux de type HVDC qui peuvent atteindre des niveaux de puissances élevées. Le convertisseur modulaire multi-niveaux est la topologie la plus appropriée pour faire face aux objectifs envisagés en misant sur la technologie HVDC. De plus, il est fort probable que cette topologie de convertisseurs de puissance multiniveaux, sera la topologie la plus utilisée pour les projets futurs. L'immigration vers les réseaux MTDC est fortement envisageable pour des configurations basées sur des multi-constructeurs, où le développement des algorithmes de contrôle et de protection pour chaque station de convertisseur sera géré d'une manière locale par chaque constructeur impliqué dans le projet. Cependant, ces algorithmes doivent garantir l'interopérabilité pour chaque convertisseur dans les réseaux DC et AC. Comme il a été démontré à travers les résultats obtenus dans ces travaux de thèse, la dynamique globale du réseau DC est très sensible au choix de stratégies de commande pour chaque station de conversion.

Cette thèse vise à évaluer certains des éléments clés de l'analyse dynamique des réseaux MTDC basés sur MMC afin d'étudier les problèmes d'interopérabilité éventuels qui peuvent survenir. Dans ce qui suit, les principales conclusions issues de chaque chapitre sont présentées :

1. Une méthodologie pour l'analyse dynamique des systèmes HVDC à base de convertisseurs de puissance a été détaillée dans le Chapitre 1. Les principaux niveaux de modélisation des systèmes HVDC à base de VSC deux niveaux ont été détaillés. Nous précisons, que les *modèles de simulation* se distinguent des *modèles pour l'analyse*. Les modèles *modèles de simulation* sont des modèles non linéaires détaillés, développés dans un environnement en EMT (généralement utilisées dans l'industrie). Ces modèles représentent, avec une grande précision, le comportement réel des convertisseurs, mais dans de nombreux cas, ils sont fournis sous forme de modèles de boîtes noires (e.g., projet *Best Paths* DEMO # 2) qui font l'étude et la catégorisation dès les convertisseurs et les contrôleurs sont une tâche impossible (sans parler des conséquences juridiques). Par contre, les modèles *modèles pour l'analyse*, qui sont généralement des modèles dynamiques exprimés par des équations différentielles de premier ordre à temps continu, sont fournis pour l'analyse de stabilité des convertisseurs AC/DC et leur intégration dans les réseaux. Nous distinguons, deux familles de modèles mathématiques, à savoir : les modèles périodiques en régime permanent "Steady-State Time Periodic" (SSTP), où les variables d'état au point d'équilibre stable admettent un comportement sinusoïdal. Ce modèle n'est pas adapté à la linéarisation classique pour l'analyse en se basant sur les valeurs propres du système. Pour la deuxième classe de systèmes dynamiques, appelée "Steady-State Time Invariant" (SSTI), toutes les variables d'état convergent vers un état constant lorsque le convertisseur atteint un point de fonctionnement donné. Ce modèle mathématique peut être linéarisé autour d'un point de fonctionnement, de telle sorte que les outils mathématiques linéaires dont nous y disposons, peuvent être appliqués facilement pour l'étude de stabilité et l'analyse dynamique des systèmes complets. En outre, les principes fondamentaux respectifs aux réseaux MTDC ainsi que le principe de contrôle coordonné sont largement discutés.

2. Pour appliquer la méthodologie susmentionnée avec les MMC, un modèle mathématique continu non linéaire approprié est nécessaire, capable de représenter toutes les

dynamiques internes avec une grande précision, c'est-à-dire un *modèle pour analyse* avec la représentation SSTI. Dans le Chapitre 2, une analyse approfondie des équations mathématiques de la MMC dans des repères référence rotatif synchrone est fournie pour déduire le modèle SSTI du MMC de façon complète. Une validation détaillée en domaine temporel est fournie, ce qui prouve une excellente correspondance avec le *modèle de simulation* détaillé du MMC.

3. Une fois que le *modèle pour l'analyse* du MMC est obtenu (SSTI), les stratégies de contrôle les plus courantes et disponibles dans la littérature ont été discutées à travers ce Chapitre 3 en vue de l'intégration des convertisseurs dans les réseaux AC et DC. Dans ce chapitre, deux stratégies de modulation ont été distinguées : "Un-Compensated" ou "Compensated" Modulation, UCM ou CM, respectivement. De plus, deux méthodes principales de contrôle, issues des travaux de cette thèse, se posent: *Classical CCSC* et *Energy-based*. Le premier est un contrôle typique largement discuté dans la littérature, qui repose sur l'élimination des courants circulaires au sein du convertisseur. Étant donné que le courant côte DC est non contrôlé, il a été démontré que des interactions dynamiques de ce courant avec les autres variables du réseau DC peuvent se produire et déstabiliser l'ensemble du système en tenant en compte de plusieurs paramètres tels que la capacité du réseau DC, les inductances de bras ou même les réglages des régulateurs. Pour améliorer la stabilité, les contrôleurs en énergie *Energy-based* ont été largement présentés et discutés. Cette stratégie repose sur le contrôle de toutes les variables internes du MMC (courants AC et DC, et variables en énergies stockées). Cependant, il est nécessaire d'adapter les contrôleurs pour leur propre interface avec le modèle SSTI précédemment développé. Certaines des boucles de contrôle sont déjà développées dans le repère *dq* (par exemple, les boucles de contrôle du courant alternatif en *dq* ou le contrôleur de suppression de courant circulaire classique) tandis que les autres sont exprimés dans le repère fixe en (*abc*). La somme et la différence d'énergies par bras sont contrôlés également dans le repère *abc*. Toute la démarche mathématique pour aboutir au modèle SSTI a été exposée. Des tests de validation par simulation en domaine temporel ont été proposés pour confirmer les approches proposées.

4. Pour étudier les grands systèmes à l'instar des réseaux MTDC, la complexité de chaque convertisseur et de son système de contrôle rend difficile l'analyse en petits signaux moyennant les outils linéaires que nous disposons pour les études d'interopérabilité. A ce titre, dans le Chapitre 4 nous nous sommes intéressé au développement de modèles réduits SSTI-MMC en vue de l'étude de l'interaction des réseaux AC-DC. Dans ce chapitre, un modèle d'ordre réduit qui peut représenter fidèlement le comportement du MMC a été développé. Plusieurs études ont été effectuées pour démontrer la validité du modèle lorsque le MMC *modèle de simulation* est contrôlé en *Classical CCSC* d'une part, ou par les commandes en *Energy-based* d'autre part . Il est prouvé que le modèle d'ordre réduit peut traduire avec précision le comportement du MMC en présence d'un contrôleur en *Energy-Based* vu que la technique de modulation découple parfaitement la dynamique interne du convertisseur. De ce fait, il est clair que la dynamique non représentée à travers le modèle réduit ne participe pas au comportement du terminal des côtés AC et DC dans les cas étudiés (les MMC sont connectes aux réseaux AC équilibrées et en mode de fonctionnement normal). En outre, il a été démontré que le modèle à ordre réduit ne représente pas exactement le MMC lorsque la commande en *Classical CCSC* est considérée. Cette conclusion est antonyme avec plusieurs études déjà publiées où l'utilisation du modèle de commande réduit a été effectuée sans le recours à une validation

appropriée du modèle. En conséquence, le modèle SSTI-MMC complet du Chapitre 2 représente la solution adéquate lorsque le système est muni de la stratégie de contrôle mentionnée ci-dessus. D'autres variantes de commande ont été investiguées, à l'instar d'une combinaison de contrôleurs en *Energy-based* et *CCSC*. Dans ce cas, l'utilisation du modèle réduit a conduit à une précision limitée, puisque le choix de la modulation peut provoquer des dynamiques internes qui ne sont pas modélisées via le modèle réduit.

5. Dans le Chapitre 5, l'étude d'un réseau MMC-MTDC en présence d'un parc éolien offshore est réalisée afin d'étudier l'interopérabilité entre les différents convertisseurs. Un accent particulier a été accordé au comportement dynamique de la tension continue associée à chaque convertisseur. En se basant sur les résultats des chapitres précédents, il a été démontré que la principale caractéristique des réseaux MMC-MTDC est la sensibilité de la tension du bus qui pourra provoquer un comportement fortement oscillatoire, observée sur la tension DC. En conséquence, pour contourner ce problème, il serait intéressant d'exploiter l'énergie interne du convertisseur MMC pour supporter la tension du bus DC. Dans ce sens, des études ont été menées courant ce chapitre pour évaluer les différentes stratégies de commandes en énergie afin d'offrir au réseau DC, des degrés de liberté supplémentaires pour améliorer la dynamique globale du système. Ainsi, nous avons démontré qu'une gestion optimale de l'énergie interne de chaque convertisseur MMC à travers les méthodes de commande proposées, permettra d'améliorer le comportement des variables coté DC. En effet, nous précisons que même la dynamique globale du réseau DC peut être ajustée correctement à travers les approches de contrôle proposées. D'ailleurs, en se basant sur ces techniques de commande en énergie, nous avons conclu que l'amélioration du comportement de la tension continue au point de raccordement DC de chaque convertisseur, contribue à la minimisation de problèmes d'interopérabilité qui peuvent apparaître entre les convertisseurs MMC.

Preface

This Thesis summarizes the main results obtained from my time as a PhD student at Centrale Lille, within the Laboratory of Electrical Engineering and Power Electronics (*L2EP*). This work was funded: two thirds by Réseau de Transport d'Éelectricité de France (RTE; French transmission system operator) and the rest by the European project *Best Paths*. My main supervisor at Centrale Lille during this period has been Prof. Xavier Guillaud. This Thesis was strongly based on several collaborations during the three years of work, which are detailed in the following.

My participation on the Demonstrator # 2 of the *Best Paths* project in representation of Centrale Lille was concentrated in the offline simulations with detailed Modular Multilevel Converter models provided by the main European vendors: ABB, General Electric and Siemens. Also, in this Demonstrator, the work was performed with the TSOs RTE, Elia and REE; and the University of Strathclyde. More or less, one year of actively participation in this project gave me the possibility to encounter the main actors on the High-Voltage DC transmission and to discuss about numerous topics related to DC networks in several meetings and different cities across Europe (such as Erlangen, Glasgow, Madrid, Paris, Stafford and Västerås). Even if the amount of time dedicated to this project was very important, results obtained from the project are not directly incorporated in this Thesis due to non-disclosure agreements signed prior the project. However, the invaluable experience gained within this project gave me the possibility to learn about the simulation tools such as EMTP-RV, and to gain experience within the industrial environment of real projects.

During the three years of studies, I've had the possibility to work and collaborate with several experts in electrical engineering. I've been working with Dr. Frédéric Colas, Dr. François Gruson, Dr. Shabab Samimi and Dr. Moez Belhaouane at ENSAM-Lille, where I've passed all my normal workdays (when I wasn't absent because of travels). I've been closely working in collaboration with RTE, particularly with Dr. Pierre Rault, Dr. Hani Saad, Dr. Olivier Despouys and Dr. Samuel Nguefeu; which all have been present on different degrees across this journey. During my first period as a PhD student, I've worked with (soon Dr.) Lampros Papangelis and Prof. Thierry Van Cutsem from the University of Liège on the modeling of modular multilevel converters for large scale studies. Then, a very fruitful collaboration with Dr. Samy Akkari on the small-signal stability studies opened many undiscovered roads for this Thesis. With Dr. Noe Barrera-Gallegos, we have been working on the implementation of linear analysis tools for HVDC studies. Finally, I've been pleased to collaborate with Dr. Gilbert Bergna-Díaz from NTNU, who introduced myself on the modeling of modular multilevel converters with steady-state time invariant solutions. Also, this last collaboration was completed with Dr. Salvatore D'Arco and Dr. Jon Are Suul from SINTEF. From this last collaboration, I've been invited to spend one week in Trondheim, Norway during 2016. Several contents of this Thesis are based on all the aforementioned collaborations and all of them helped on the completion of this work.

I'm deeply grateful to everyone who accompanied me on this journey of three magnificent years.

Julian Freytes

Table of Contents

Introduction to HVDC Systems

1 Context and motivations

Since the massive utilization of electrical energy in the world, fossil fuels — coal, natural gas, and oil — were always the predominant energy sources. This choice had a very important impact on the world's climate change due to carbon dioxide (CO_2) emissions [1,2]. Fortunately, most countries in the world have agreed to limit CO_2 production to slow down the global warming [3]. One of the main actions is to transform gradually the energy sources: from fossil fuels to natural and *greener* energy sources such as solar and wind power.

In Europe, large amounts of renewable energy are available on remote locations, often offshore or near the sea [4, 5]. However, transmission system investments, especially on new lines, have been limited in densely populated Europe, mainly because of opposition against overhead lines for environmental or political reasons [6]. Furthermore, the transmission of large quantities of electric power underground (or undersea) is virtually impossible using the commonly adopted Alternating Current (AC) because of the capacitance of the cable systems [7]. For these reasons (among others), High Voltage Direct Current transmission schemes (HVDC) are now becoming more and more relevant [8].

The struggle between DC or AC electrical systems is not a modern concern; in fact, it occurred in the beginnings of the electrification era [9]. In those early ages, the AC systems won the *war of currents* in the 1880s, mainly because of the ease of voltage transformation up to higher voltages, the rotating field (for electrical machines) and the difficulty for breaking DC currents in HVDC systems [10]. Nevertheless in the 1950s the first revival of HVDC systems occurred with the development of the thyristors with high rating capabilities. It was mainly used for bulk power transmission over long distances, undersea (cable) connections and also for the interconnection of non-synchronous networks (e.g. asynchronous AC networks as France - UK; or 50 to 60 Hz back-to-back as Japan; or Argentina - Brazil). The second revival was due to the development of transistor based components (IGBT) for HVDC, which started in the 90s [11]. From that moment, the HVDC technology continued to grow with a great success.

The most common and oldest technology in HVDC is the Line Commutated Converter (LCC) technology, but the Voltage Source Converter (VSC) technology is now well established in HVDC and is, in many respects, complementary to the older structures. There are many topologies for the VSC, but three of them are the most widely studied: *2-level*, *3-level* (e.g. Neutral Point Clamped (NPC) or Flying Capacitor) and *Multi-level* VSC [12–14]. The *2-level* and *3-level* VSC have a high switching frequency (1–2 kHz) for obtaining a low harmonic distortion, leading to higher switching losses as well as high voltage stresses. In high power applications, the conversion losses result in high cost for the grid operators [15]. For this reason, a new *Multi-level* VSC technology has been developed called Modular Multilevel Converters (MMC), which was introduced with great success by Dr. Lesnicar and Prof. Marquardt in [16]. The main advantage for these converters is the possibility of working with lower

switching frequencies (one order of magnitude less), while simultaneously achieving better harmonic performance compared to *2-level* and *3-level* VSCs [17–19].

Development of offshore energy harvesting

Figure 3 shows the offshore development vision in the North-Sea by Wind Europe (ex European Wind Energy Association), where the tendency of harvesting the wind energy from the sea is clearly highlighted. Consequently, an ambitious development plan as imagined by Wind Europe could bring many other benefits to the European electrical grids, in addition to the improvement of the green energy portfolio. For the achievement of this modernization of European power grid, significant investments are needed in order to reach European energy policy goals as pointed out by the European Network of Transmission System Operators for Electricity (ENTSO-E) [20].

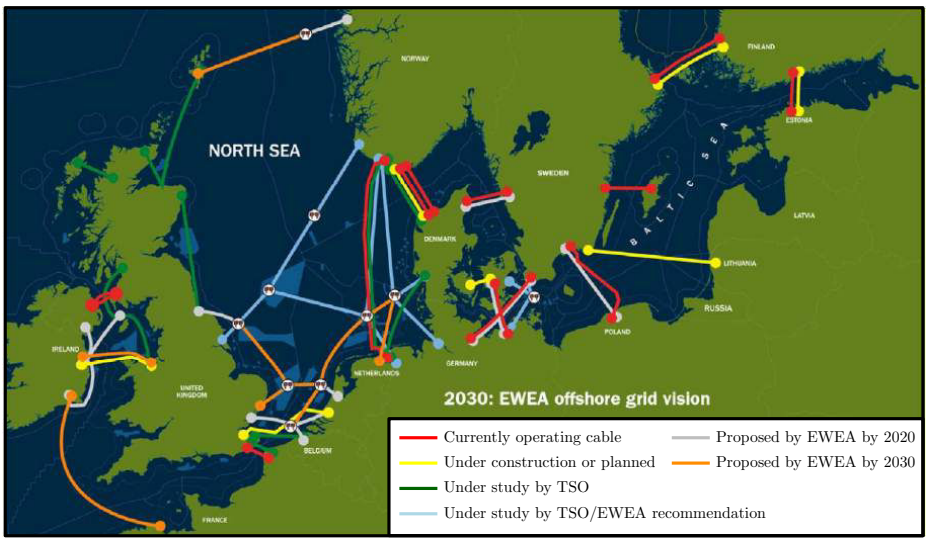

Figure 3 – Offshore development vision in the North-Sea by Wind Europe [21]

Multivendor HVDC systems

As seen in Fig. 3, all the current operating cables with HVDC technology are *point-to-point* schemes. However, these schemes may develop into Multi-Terminal DC systems (MTDC). The VSC HVDC is the most appropriate technology for MTDC applications as it uses a common DC voltage, making parallel connections easy to build and control [22]. Moreover, the MMC-VSC technology is aimed to be the preferred option for these future supergrids [23]. The development of HVDC systems brought a lot of experience in the field, bringing to light numerous standards. However, these standards address the converters behavior on the AC side, but none exist for the DC side connections and many technical issues remain unsolved [24]. On the one hand, when dealing with *point-to-point* connections, the converters are always provided by a single vendor. The dynamic behavior on the DC side is responsibility of each manufacturer since they are in charge of the proper functioning of the complete system. On the other hand, MTDC systems are likely to be multivendor systems, where converters provided from different manufacturers coexist in the same DC grid [25]. At this point, the lack of requirements with respect to the DC side connections will become an issue to be solved since, for instance, even the DC voltage and current ratings are not normalized [26]. Furthermore, since the dynamic behavior of these

future DC grids will be greatly influenced by the control strategies adopted for each vendors, the converter controller should have the ability to damp potentially hazardous oscillations and avoid undesired interactions with the rest of the DC grid component [27].

The European project *Best Paths*[1] gathers expert partners from academia and the industry around five large-scale demonstrations to validate the technical feasibility, costs, impacts and benefits of the tested HVDC technologies [28]. The focus of the demonstrations is to deliver solutions to allow for transition from HVDC lines to MTDC grids, to upgrade and re-power existing AC parts of the network, and to integrate superconducting high power DC links within AC meshed network. Demonstrator # 2 of *Best Paths* deals with the possible interoperability issues that may appear between MMCs connected to the same DC grid from different manufacturers [29]. This problematic could be addressed in normal operation where the stability of the DC grid must be assured, but also in different operations such as the abrupt disconnection of a converter station, grid reconfiguration, or as many possible cases that may occur. Results from this Demonstrator will include recommendations for both specifications and hardware control implementation which would ensure maximum interoperability for multivendor solutions [30]. The proposed guidelines will provide feedback to the Network Code drafting teams of ENTSO-E, and form a solid basis to make significant advances towards interoperability requirements for multi-vendor HVDC grids as currently targeted by standardization groups (CENELEC, IEC, etc.).

The most appropriate definition of "interoperability" for this context may be [31]:

- ***Interoperability*** *is a characteristic of a product or system, whose interfaces are completely understood, to work with other products or systems, present or future, in either implementation or access, without any restrictions.*

Nevertheless, the concept of "interoperability" may be very broad to explore all the possibilities. This Thesis intends to provide an elementary block for the understanding of MTDC grids with Modular Multilevel Converters where the main key factors that could provoke interoperability issues are addressed. For this reason, the development of a proper methodology in conjunction with the converter models and different controls strategies establishes the main objectives of this work. Studies on generic MTDC grids are carried out to evaluate the impact of different available control strategies on the grid dynamics. This task helps to evaluate the interoperability of the resulting converter with different control strategies in DC grids and eventually help in the development of the nonexistent recommendations for MTDC grids.

2 HVDC Systems — Generalities

Numerous technological advances in terms of hardware (e.g. semiconductors with lower losses and higher capabilities) and software (e.g. faster and sophisticated control algorithms) allowed to consider HVDC systems as a reliable solution for the transmission of electrical energy with competitive costs and a large number of advantages [32, 33]. Each new HVDC project challenges thee major electrical engineering disciplines: *power transmission engineering* since the penetration of HVDC systems in the existent AC grids is of primary importance; *Power electronics* due to the technology involved on each converter station and *Control engineering* since the modeling and control design for HVDC systems is the primary responsible for the proper functioning of the systems [34].

[1] Best Paths stands for **BE**yond **S**tate-of-the-art **T**echnologies for **P**ower **A**C corridors and Multi-**T**erminal **H**VDC **S**ystems.

Even if the list of HVDC projects in the world is very extensive nowadays [35], the modern history of VSC-based HVDC systems is remarked by four main disruptive events:

1. **2009**: ABB commissioned the first offshore HVDC system *BorWin1* which was the first one to use VSC for the converter stations [36, 37].
2. **2011**: The first HVDC system using Modular Multilevel Converters; *Trans Bay Cable* commissioned by Siemens [38, 39].
3. **2013**: First three-terminal "multivendor" MTDC grid with MMCs commissioned by the State Grid Corporation of China (SGCC) [40].
4. **2015**: First HVDC link with MMCs for transmitting power in the GW range called *Inelfe*, which was commissioned by Siemens [41]. Up to date, it has the biggest HVDC power capacity in the world.

In HVDC systems, one of the principal and most expensive components of the DC grids are the cables: the cost of installation and eventual reparation exceeds the cost of converters and associated hardware. In fact, as a rule of thumb, the cost of the cable itself and its installation may surpass the price of the converters at each endpoint (when considering point-to-point connections) [42]. For this reason, the dynamics in the cable should be carefully studied for assuring that the voltage limits are not surpassed in normal or abnormal operation.

2.1 Voltage Source Converters for HVDC applications

Voltage Source Converters in HVDC applications make use of self-commutated semiconductor devices such as Insulated Gate Bipolar Transistors (IGBT) which allow the full controllability of the converter [43]. The main characteristic of this type of HVDC converter is that it can synthesize an AC voltage output with high accuracy regarding its amplitude and phase. This way, active and reactive power can be independently controlled. There are mainly three Voltage Source Converters topologies available in operation for HVDC systems [12]:

1. *2-level* topology.
2. *3-level* diode-clamped topology.
3. Modular Multilevel topology.

In the following, the *2-level* and multilevel floating-capacitor topologies are introduced. The multilevel diode-clamped topology is out of the scope of this Thesis; however, many of the studies performed with the *2-level* topology apply to this category as well.

2-level VSC

A typical three-phase *2-level* topology interfacing an AC and DC grid is shown in Fig. 4a. It is composed by three phase legs and each one has a series array of semiconductor switches that in turn, inserts or bypasses each leg thus chopping the DC voltage to form the desired AC voltage output. The number of switches in series depends on the voltage ratings. On the DC side, there is a capacitor C_S acting as a filter. The typical Pulse-Width Modulation (PWM) AC output voltage is shown in Fig. 4b. More details on the modeling and control of the *2-level* VSC are given in Chapter 1.

The main disadvantages of the *2-level* VSC is the need to switch a large array of IGBT on each leg simultaneously causing high voltage stresses on the valves, which can be very challenging. Also, to reduce the harmonic components on the synthesized AC output voltage, the PWM frequency may be augmented, compromising the switching losses. In HVDC systems,

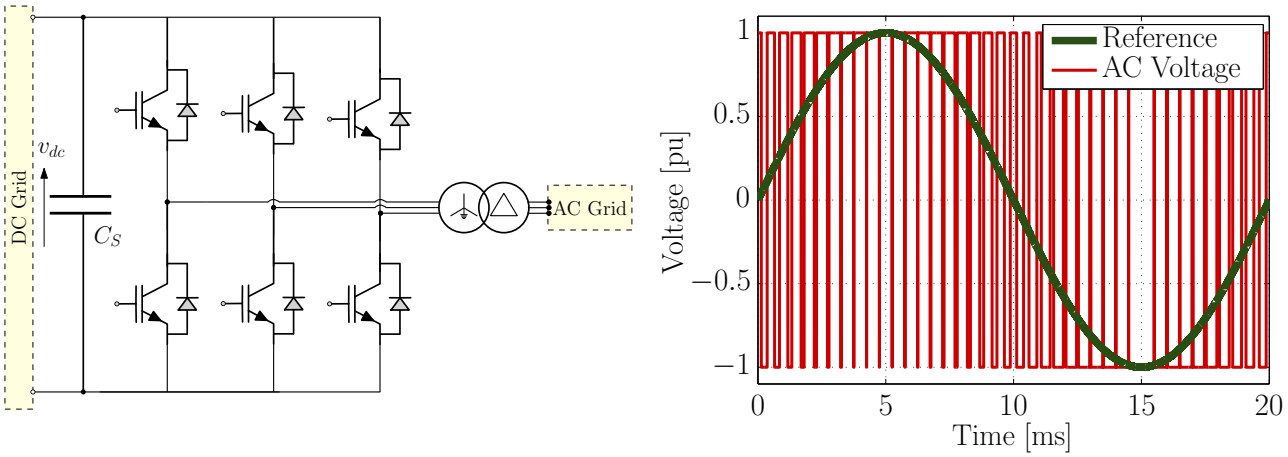

(a) *2-level* VSC Topology

(b) AC Voltage waveform

Figure 4 – *2-level* VSC: Topology and output voltage waveform

these losses are conditioned by the cost of the energy lost, which is a significant issue for transmission at the MW or GW level [44]. Furthermore, in conjunction with an elevated switching frequency, the AC filters may be bulky and costly. These factors limit the power ratings of the whole HVDC project with *2-level* VSC.

Modular Multilevel Converter

The most promising topology of multilevel converter is the so-called "Modular Multilevel Converter" (MMC) [16]. The three-phase MMC topology, shown in Fig. 5a, is composed by three phase legs, each one formed by an Upper and Lower arm. The arms are constituted by a stack of Sub-Modules (SM), whose topology may vary from a Half-Bridge, Full-bridge or other topologies [45]. In this Thesis, the Half-Bridge (HB) is assumed for the SMs due to the reduced number of semiconductor devices in the converter, as illustrated in the upper-right corner of Fig. 5a. Moreover, each arm has a series inductance which is used to filter the arm currents and to limit the inrush currents in case of faults. In the MMC, there is no capacitor directly connected in the DC bus as it is the case for the *2-level* VSC; instead, each SM has a smaller capacitor which is inserted or bypassed in the circuit to form the desired voltages, as illustrated in Fig. 5b. More details on the modeling of the MMC are given in Chapter 2.

One of main drawback of the MMC is the high complexity of the control system [46]. On the one hand, a dedicated controller is in charge of the complex balancing of the voltage on the submodules capacitors, while guaranteeing at the same time that the output voltages are as expected from the current controllers. On the other hand, as can be seen by comparing the MMC topology in Figs. 5a and the *2-level* predecessor in Fig. 4a, many currents and voltages inside the converters should be monitored to avoid any possible misbehavior [47]. For this reason, it is understood that the control system of the MMC is more challenging than for the *2-level* VSC. More details on the control of the MMC are given in Chapter 3.

2.2 Point-to-point MMC-Based schemes

The most common configuration for HVDC projects is the so-called "point-to-point" scheme, which is exemplified in Fig. 6. In this configuration, there are two AC-DC converters connected

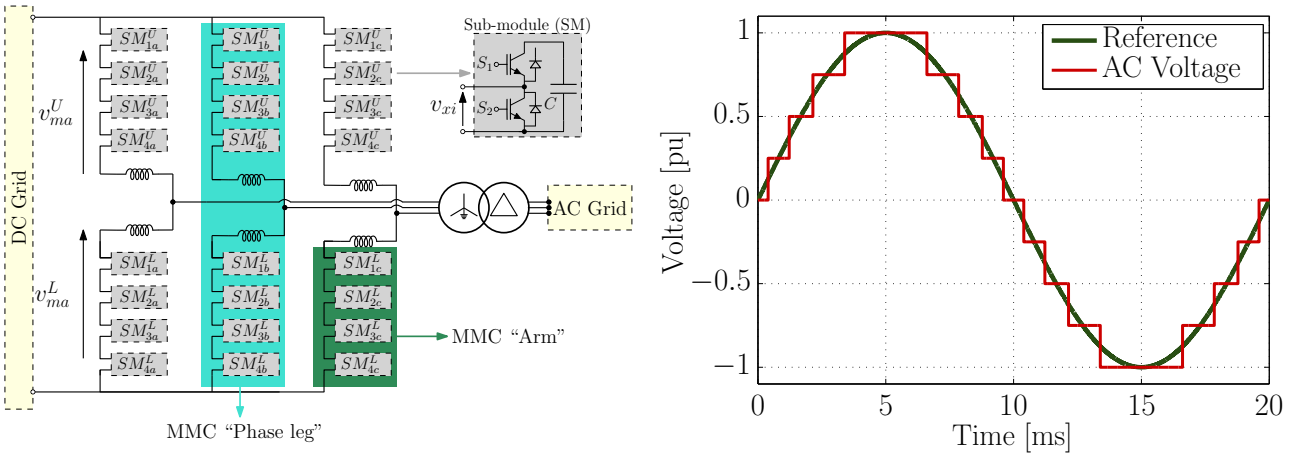

(a) MMC Topology

(b) AC Voltage waveform

Figure 5 – Modular Multilevel Converter: Topology and output voltage waveform

with a DC conductor which may be a cable or an Over-Head Line (OHL). Even if the OHL technology is very interesting since normal AC corridors may be re-developed into DC grids, this Thesis only focuses on cable configurations. One of each converter in Fig. 6 has a specific role in terms of control. One converter is in charge of the power flow in the DC link, while the other fixes the DC voltage to a certain level (the details on the control configurations are given in Section 1.3). The advantage of this configuration with respect to the classical AC lines is the ability to control the power flow in the system [44].

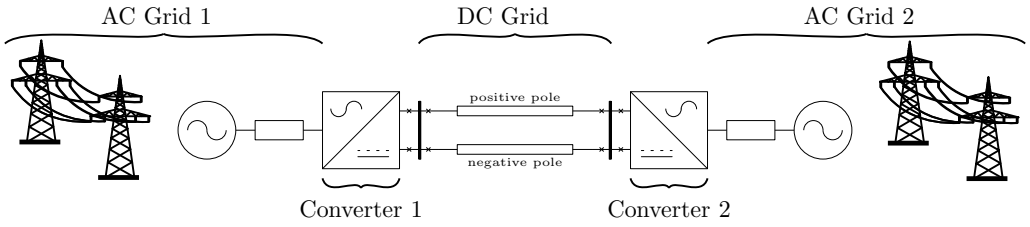

Figure 6 – HVDC point-to-point: Example of typical schematic diagram

As an example of a point-to-point real project, let us consider the INELFE project [48]. This project is made by a joint venture from RTE and "Red Eléctrica de España" (Spanish TSO). The configuration is given in Fig. 7. This project was carried out for improving the electric network capacity between Spain and France and hence, with the rest of Europe.

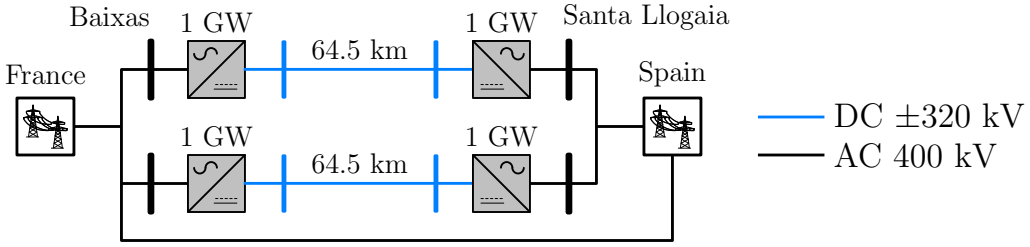

Figure 7 – INELFE project — HVDC point-to-point scheme

The INELFE point-to-point scheme is composed by two 1 GW MMC-based HVDC links. As seen in Fig. 7, the AC grid from Spain and France are also connected in AC, in particular

by a 400kV AC line in parallel to the two HVDC links, which is partly relieved thanks to the DC line. From an electrical point of view, both converters are electrically close to each other which makes the project very challenging from a engineering perspective. For studying the system, RTE acquired a real-time mock-up of the complete link, where the actual MMC control replicas are installed and evaluated [49].

In Fig. 8, the footprint of a *2-level* VSC station from the *BorWin1* project and the MMC station from INELFE is compared . As it can be seen, in a similar footprint, the MMC of INELFE project have five times more power than in *BorWin1*.

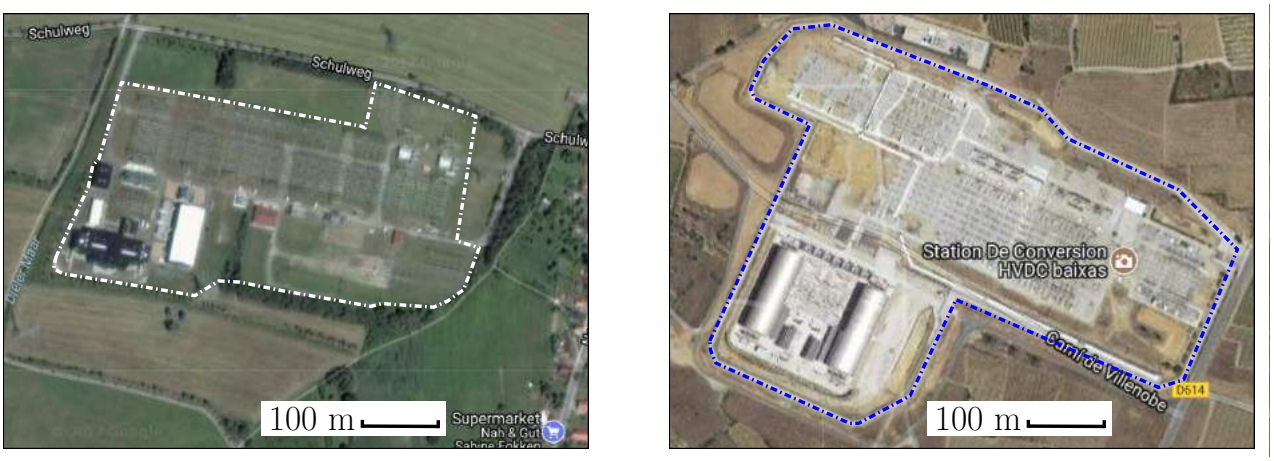

(a) **BorWin1**: *2-level* VSC, 400 MW, ±150 kV

(b) **INELFE**: MMC, 2 × 1000 MW, ±320 kV

Figure 8 – **BorWind1** VSC station in Diele, Germany. **INELFE**, 2 MMC stations in Baixas, France. — Source: `https://maps.google.com/`

3 Multi-Terminal DC schemes

When more than two converter stations are connected to the same DC grid, the configuration is referred as a "Multi-Terminal DC" system (MTDC). These schemes are expected to provide additional features compared to *point-to-point* HVDC links, such as:

- More flexibility in power dispatch [8]
- Optimized assets for offshore wind farm connection to shore and power transmission capability [50]
- Smoothing wind power fluctuations (mitigation of wind power which is produced from different area) [51]
- Frequency support to onshore grids [52, 53]
- More reliability (can operate or at least partially operate even if one element is out of service) [54]

From an operational point of view, power flows in HVDC grids would be decided on the electricity markets in advance according to the supply and the demand. In real time, power flows must correspond to the schedule and deviations should be regulated according to predefined rules. As for AC system, TSOs are likely to be in charge of managing HVDC grids to assess their stability and comply with the market schedule. To control the power flows in the DC grid, two layers of controllers are likely to be used [55]. The first control layer is

constituted by the coordinated controllers managed by TSOs to dispatch suitable converter set-points in order to achieve a precise power flow control [56]. Also, in case of a contingency, it would automatically adapt set-points to find a new stable operating point [57]. Second, local controls in the VSC stations such as DC voltage droop control are used to the adjustments of set-points in real-time [58].

Multivendor MTDC real projects

There is little experience worldwide in multivendor VSC-based MTDC schemes. The only two relevant examples are Nan'ao and Zhoushan projects in China, whose layouts are depicted in Fig. 9 [59,60]. Both projects, which are operating nowadays, prove that the MTDC schemes are a feasible solution for high-power transmission systems.

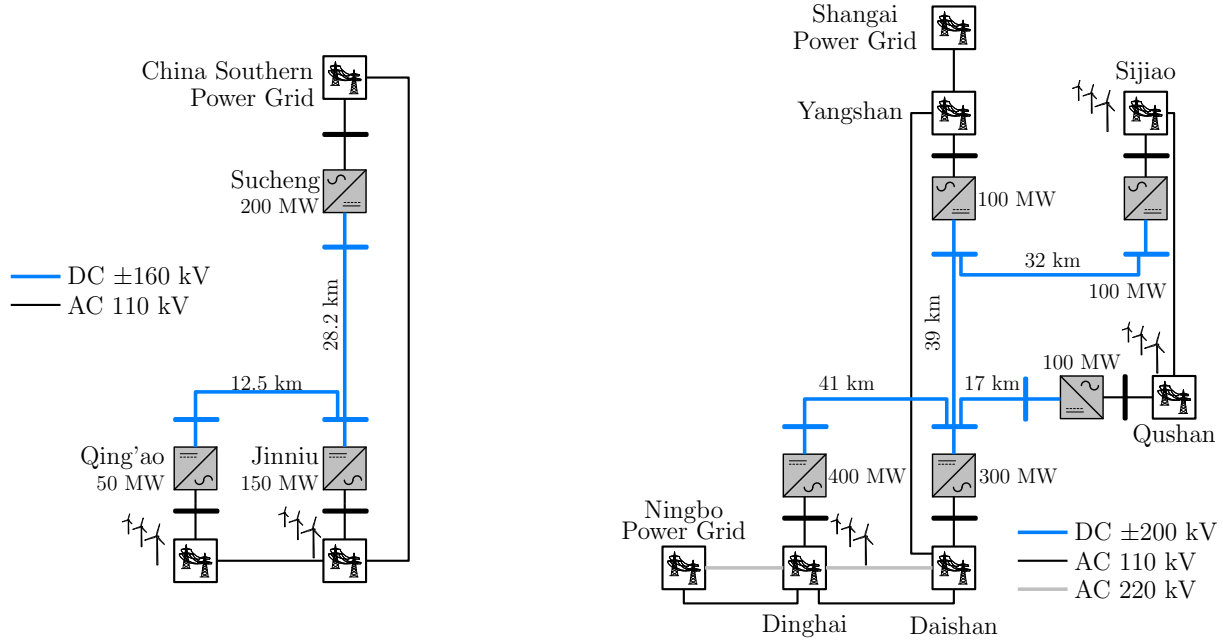

(a) **Nan'ao project** [61]

(b) **Zhoushan project** [62,63]

Figure 9 – VSC-based MTDC schemes in China

The aforementioned MTDC projects in China are multivendor schemes, where different vendors were in charge of the deployment of the hardware of each converter station. However, control and protection of each station was fully designed by a single vendor [40]. In the western market, this scenario is most unlikely since western manufacturers mostly valor their *know-how* related to the specific control and protection design adapted for their high-voltage equipment. For this reason, in the *Best Paths* project the idea was to evaluate interoperability for HVDC converters from different vendors whereas the control and protection algorithms are specific to each company.

4 Objectives of the Thesis and Main Contributions

The main research questions of this Thesis are the following:

1. What are the main tools to study the stability of HVDC systems?

2. How to model the MMC for being able to use it for small-signal stability analysis?
3. What is the impact of the MMC controllers on MTDC grids dynamics?
4. Are the reduced order MMC models valid and representative for large-scale studies such as MTDC grids?
5. What are the main key factors influencing the DC dynamics and how to improve them?

This Thesis, which aims to answer the aforementioned questions, deals with the dynamic analysis of MMC-based MTDC grids for interoperability studies, in the same spirit as the *Best Paths* project; even if the presented studies were **not** conducted with the vendors models. Instead, the idea is to detail the modeling and control of MMCs first, before introducing the converter in a multi-terminal environment. A step-by-step approach is followed to highlight each relevant and particular aspect of MMCs for interoperability analysis with special focus on the overall stability.

The main contributions of this work are listed below:

1. A methodology for the dynamic analysis of HVDC systems with Power Electronics Converters is given. This methodology implies the different modeling degrees and control strategies for the converters. Mathematical tools that can be applied to each model representation are defined.
2. Documentation of a novel MMC mathematical model that takes into account all internal dynamics. This model, which can be easily linearized, is one of the pillars of this Thesis, since the small-signal dynamics can be studied from the developed model. This model was firstly developed by NTNU and SINTEF, and later generalized within a collaboration.
3. Different controls strategies for the MMC are described. The impact of each control in terms of small-signal dynamics is analyzed. Improvements on the system stability are proposed, which conduces to a promising family of control strategies in term of interoperability.
4. Demonstration of the applicability of reduced order MMC models: the limitations of the usage of simplified models is highlighted with respect to the MMC control strategies.
5. Simulations and analysis of MMC-based MTDC grids and the application of linear mathematical tools for the deep understanding of dynamic behavior of the DC grid. The main variables governing the dynamics, and the impact of the converter controllers on the DC voltage dynamics are explored.

5 Layout of the Thesis

The Thesis is organized as shown in Fig. 10 and detailed in the following.

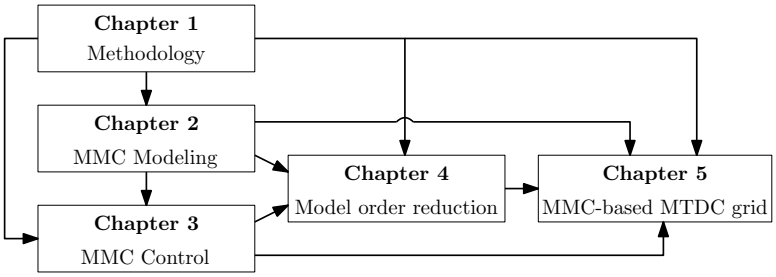

Figure 10 – Thesis Road-map

Chapter 1 introduces the methodology applied throughout this Thesis for the study of power electronic converters with particular interest on the integration to DC grids. This

Chapter deals mainly with *2-level* VSC, where the main modeling degrees are clearly shown: from the classical averaged model in *abc* frame to the *dq* model, up to its integration in HVDC point-to-point schemes and MTDC grids. The linearization technique used for eigenvalue-based stability and dynamic analysis for DC systems is presented. This Chapter stands out the main concepts that are applied to DC systems with MMC through the Thesis.

Chapter 2 presents the most up-to-date MMC non-linear continuous model in *dq* frame, which has the main property that the steady-state operation is represented by constant state variables. This characteristic makes it possible to linearize the model and to study its stability with eigenvalue-based techniques. The model is compared against a very detailed EMT MMC model[2] with 401 levels implemented in EMTP-RV.

In **Chapter 3** the classical control strategies for the MMC are developed in views of its integration in MTDC systems. For this reason, an equivalent DC bus is considered with the MMC. The objective is to analyze the interactions of the MMC with the DC grid when considering different controllers. For evaluating the degree of impact of the analyzed controllers, the MMC model with steady-state time-invariant solution from Chapter 2 is used. Two main control strategies arise from this Chapter: the *Classical Circulating Current Suppressing Controller* (CCSC) and the *Energy-Based* controller. The first one is the most used in the literature due to its simplicity. However, the main drawback of this strategy is the poorly damped oscillations that can be caused by the uncontrolled DC output current and internal energy. The *Energy-Based* controller, in turn, considers closed-loop controllers for all the energies and currents of the MMC. Nevertheless, when considering full detailed controllers and the MMC, the state-space model results with a high number of state variables. This results in a difficult task for the dynamic and stability analysis based on eigenvalues.

In **Chapter 4**, a reduced order model of the MMC for interfacing AC and DC grids is presented. For evaluating the validity of the introduced model, several tests based on eigen-analysis, time domain simulations and frequency analysis are carried out to delimit the boundaries and highlight its usage. Two control options detailed in previous Chapter are considered for the MMC and compared with the analogous reduced order model. Results from this Chapter are fundamental for the application of reduced order models in MTDC grids for interoperability studies.

In **Chapter 5**, the dynamic analysis of MMC-based MTDC grids is presented for interoperability studies. Based on a benchmark four-terminal MTDC model, several studies are developed for evaluating the impact of different MMC control strategies on the MTDC dynamics. The use of dedicated controllers for regulating the internal energy of the MMC in views of the collaboration of each converter on the DC voltage dynamics is explored. Results highlight the main differences with MTDC grids with *2-level* VSCs in terms of the DC grid energy allocation. The road for new control strategies for improvement of MTDC grids is paved in this Chapter.

6 List of publications derived from this work

The publications resulting from this Thesis project are listed below. The main contributions presented in this manuscript are based on the journal papers **Journal I** and **Journal II**, and also the conference papers **Conference I** to **Conference VII**. The results of the remaining publications are not directly embedded in this Thesis, although they helped in the development of the whole work. For the ease of reading this Thesis, self-citations are given with **bold**

[2]EMT: Electro-Magnetic Transient

brackets, e.g. [**00**].

- **Journal I**: "*Improving Small-Signal Stability of an MMC With CCSC by Control of the Internally Stored Energy*". **J. Freytes**, G. Bergna, J. A. Suul, S. D'Arco, F. Gruson, F. Colas, H. Saad, X. Guillaud. IEEE Transactions on Power Delivery, 2017.
- **Journal II**: "*Generalized Voltage-based State-Space Modelling of Modular Multilevel Converters with Constant Equilibrium in Steady-State*". G. Bergna, **J. Freytes**, X. Guillaud, S. D'Arco, J. A. Suul. IEEE Journal of Emerging and Selected Topics in Power Electronics, 2018.
- **Journal III**: "*Dynamic Analysis of MMC-Based MTDC Grids: Use of MMC Energy to Improve Voltage Behavior*". **J. Freytes**, S. Akkari, P. Rault, M. M. Belhaouane, F. Gruson, F. Colas, X. Guillaud. IEEE Transactions on Power Delivery, 2018. UNDER REVIEW

- **Conference I**: "*On the modeling of MMC for use in large scale dynamic simulations*". **J. Freytes**, L. Papangelis, H. Saad, P. Rault, T. V. Cutsem, X. Guillaud. Power Systems Computation Conference (PSCC), Genoa, Italy; 06/2016.
- **Conference II**: "*Small-Signal State-Space Modeling of an HVDC Link with Modular Multilevel Converters*". **J. Freytes**, S. Akkari, J. Dai, F. Gruson, P. Rault, X. Guillaud. COMPEL 2016, Trondheim, Norway; 06/2016.
- **Conference III**: "*Dynamic impact of MMC controllers on DC voltage droop controlled MTDC grids*". **J. Freytes**, P. Rault, F. Gruson, F. Colas, X. Guillaud. EPE 2016; 09/2016.
- **Conference IV**: "*Energy Difference Controllers for MMC without DC Current Perturbations*". K. Shinoda, **J. Freytes**, A. Benchaib, J. Dai, H. Saad, X. Guillaud. CIGRE HVDC2016.
- **Conference V**: "*Small-Signal Model Analysis of Droop-controlled Modular Multilevel Converters with Circulating Current Suppressing Controller*". **J. Freytes**, G. Bergna, J. A. Suul, S. D'Arco, H. Saad, X. Guillaud. 13th IET International Conference on AC and DC Power Transmission, 2017 (ACDC); Manchester; 02/2017.
- **Conference VI**: "*State-space modelling with Steady-State Time Invariant Representation of Energy Based Controllers for Modular Multilevel Converters*". **J. Freytes**, G. Bergna, J. A. Suul, S. D'Arco, H. Saad, X. Guillaud. 12th IEEE PES PowerTech Conference, 2017, Manchester.
- **Conference VII**: "*Simplified model of droop-controlled MTDC grid — Influence of MMC energy management on DC system dynamics*". **J. Freytes**, F. Gruson, F. Colas, P. Rault, H. Saad, X. Guillaud. Power Systems Computation Conference (PSCC), 2018, Dublin. UNDER REVIEW

- **Conference VIII**: "*Impact of control algorithm solutions on Modular Multilevel Converters electrical waveforms and losses*". F. Gruson, **J. Freytes**, S. Samimi, P. Delarue, X. Guillaud, F. Colas, M. M. Belhaouane. EPE 2015, Geneva; 09/2015.
- **Conference IX**: "*Losses Estimation Method by Simulation for the Modular Multilevel Converter*" **J. Freytes**, F. Gruson, P. Delarue, F. Colas, X. Guillaud. EPEC, London, Ontario; 10/2015.
- **Conference X**: "*Coordinated control for multi terminal DC grids connected to offshore wind farms*" Pierre Rault, **J. Freytes**, X. Guillaud, F. Colas, H. Saad, O. Despouys, S. Nguefeu. COMPEL 2016, Trondheim, Norway; 06/2016.
- **Conference XI**: "*Optimal Control Design for Modular Multilevel Converters Operating on Multi-Terminal DC Grid*". M. M. Belhaouane, **J. Freytes**, M. Ayari, F. Colas, F. Gruson, N. B. Braiek, X. Guillaud. PSCC 2016; 06/2016.

Chapter 1

Methodology for dynamic analysis of HVDC systems with Power Electronics Converters

1.1 Introduction

One of the major concerns in power systems is the assurance of reliability: the system must operate in an non-interrupted way. This means that the system must be able to cope with different events in normal or abnormal operation, such as changes in the power flows, faults, etc [64]. When the system is operating in a given initial point and it is perturbed (e.g. with a change on the set-points), it must keep working smoothly and it should be able to stabilize itself in any possible operating point [65]. This means that a formal study of the *dynamics* and *stability* should be addressed [66]. This aspect is even more relevant when considering the inclusion of HVDC systems to the grid: the nature of this new equipment is different by working principle than the existent devices. Hence, the modeling, control and analysis of the HVDC systems with power electronics becomes crucial [67]. For this reason, this Chapter deals firstly with the different modeling degrees of a single Voltage Source Converters and HVDC systems, highlighting the followed methodology for stability and dynamic analysis.

For studying the dynamics and stability of Multi-Terminal DC grids with static Voltage Source Converters (VSC), the first step is focused on the modeling of the different elements that compose the system. There are different degrees of modeling depending on the phenomenon considered, as shown in Fig. 1.1. The most detailed models of the MTDC with VSC consider all the components of each converters separately, and they are directly assembled to form the complete system, typically in Electro-Magnetic Transient software such as EMTP-RV [68] or PSCAD. This degree of modeling is often referred as "Simulation models" or "EMT-type models". With these models, parametric and statistical studies techniques are often used. For this reason (among others) simpler yet representative models are needed to be able to apply the vast theory on control and stability analysis of dynamic systems. It should be always borne in mind that all the mathematical models and analysis are meant to be useful for a better understanding of the "Real system". For this reason, the "Simulation models" and the mathematically derived models for analysis are both needed to perform a complete study of the MTDC system.

In Fig. 1.1, the different levels of modeling for the MTDC grids with VSCs are shown. After applying fundamental physical relations to model the converters and the other components, dynamic models of each sub-systems are obtained. Due to the nature of the system, the

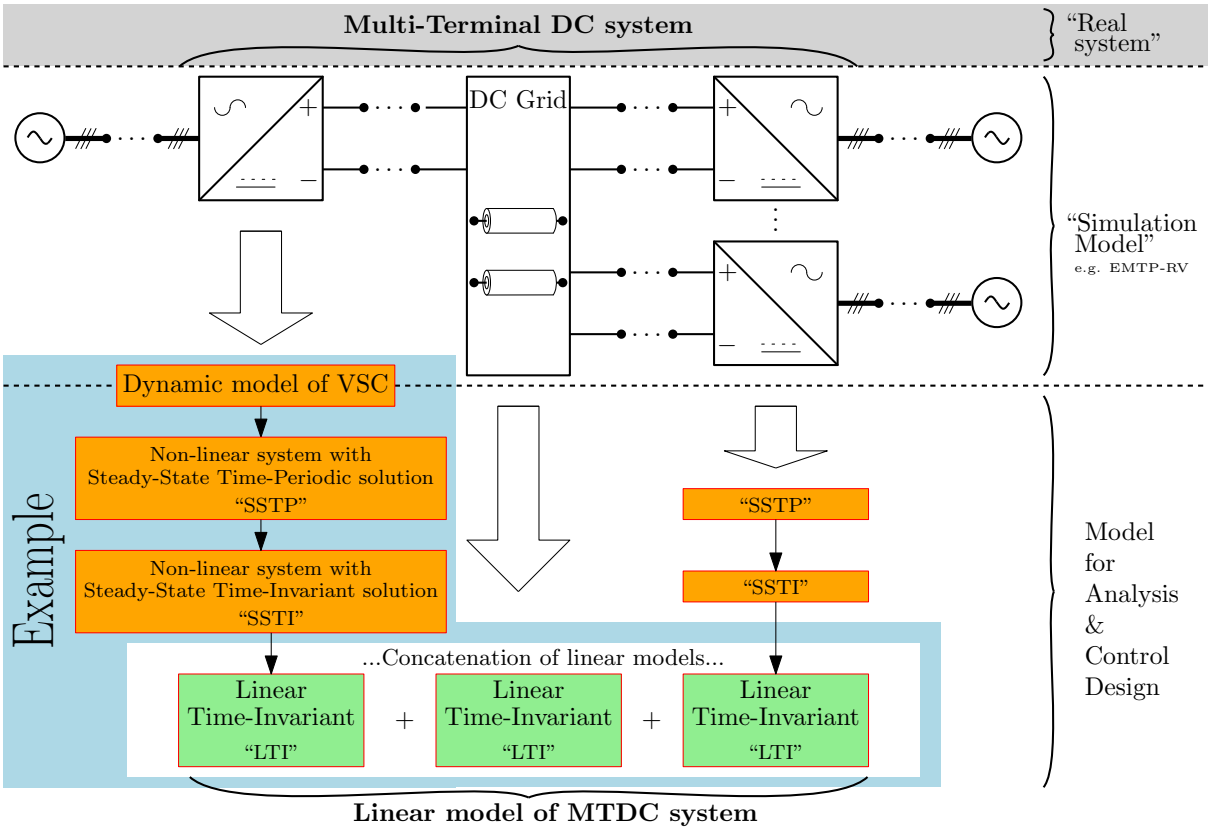

Figure 1.1 – Different models of MTDC grids with VSC for stability and dynamic studies

resultant model may be linear or non-linear, and depends on the absolute time or not. The models for VSC power electronic devices are usually non-linear. It is of interest to consider the way that the states of the system (such as currents, voltages or controller state variables) behave in steady state, i.e. if they are oscillating variables or constant. This is important since the subset of system variables may represent a fixed point in the state-space when they don't depend on the absolute time (usually dqz variables), or an orbit if their are oscillatory (abc, or $\alpha\beta z$). In case that the system presents periodically oscillating variables in steady state, it will be referred as a system with "Steady-State Time Periodical" solution, or simply "SSTP". In the other hand, if the state-variables of the system in steady-state are constant, it will be referred as a system with "Steady-State Time Invariant" solution, or simply "SSTI". This last kind of models can be linearized around an operating point, deriving in the "Linear Time-Invariant" (LTI) models. With the LTI models, the stability and dynamic analysis based on eigenvalues can be applied, which is very well established in the power system domain [69–72]. The LTP models can also be linearized; however, the models cannot be utilized for conventional eigenvalue-based analysis of small-signal dynamics. Instead, the lack of a constant equilibrium in steady state implies that time periodic theory must be applied [73].

This Chapter is organized as follows. In Section 1.2, and based on a simple *2-level* VSC, the methodology to build the elementary LTI blocks of an HVDC system from Fig. 1.1 is presented. Once the LTI models of each converter are obtained, they can be used as "building blocks" for the analysis of HVDC systems. As shown in Fig. 1.1, the "LTI" models can be assembled to form a complete linear model of the MTDC system. In Section 1.3, an HVDC point-to-point scheme is modeled and analyzed. Finally, in Section 1.4, a simplified analysis on MTDC grids is performed to highlight the main results from [74], which serve as a starting point of analysis for the rest of this Thesis.

1.2 Modeling of a *2-level* Voltage Source Converter

Let us consider a simplified *2-level* VSC interfaced between AC and DC sides as depicted in Fig. 1.2. In this schematic, the AC grid is considered to be a balanced voltage source providing the voltages $\boldsymbol{v}^{\boldsymbol{G}}_{\boldsymbol{abc}} = [v^G_a\ v^G_b\ v^G_c]^\top$. The AC grid currents are denoted by $\boldsymbol{i}^{\boldsymbol{G}}_{\boldsymbol{abc}} = [i^G_a\ i^G_b\ i^G_c]^\top$, and the active and reactive power at the AC-side Point of Common Coupling (PCC-AC) are given by P_{ac} and Q_{ac}, respectively. The resistance and inductor given by R^{ac}_{eq} and L^{ac}_{eq} are modeling the AC-side impedance of the converter (such as transformer, etc.).

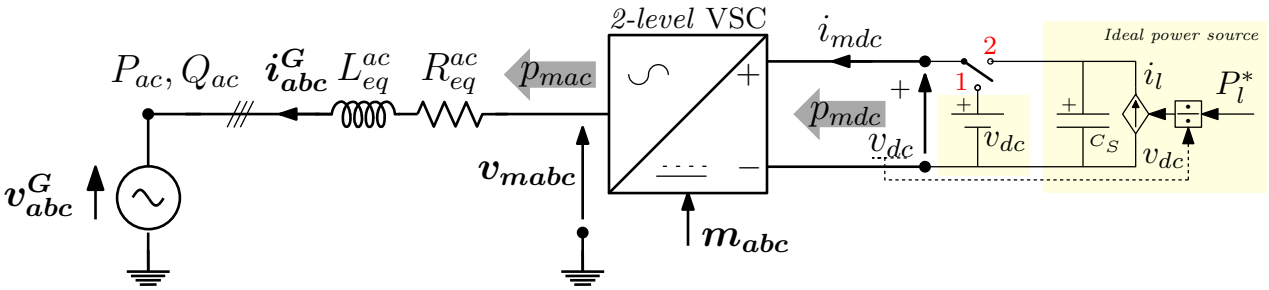

Figure 1.2 – Simplified *2-level* VSC — Selector 1: Constant DC bus voltage; Selector 2: Variable DC bus voltage and ideal power source

In the rest of this Chapter, the DC side is considered to be either a stiff DC source with voltage v_{dc} (Selector in lower position), or a variable DC voltage with an ideal power source where the DC voltage v_{dc} would be represented by the dynamic state of the DC-side capacitor C_S (Selector in upper position). The "DC-side Selector" doesn't have a physical meaning: it is only intended to highlight the different configurations that are exploited in this Chapter.

Even though the power converters models are discontinuous due to the switching events, the average value model is commonly considered by power electronic engineers as the *real system* since it provides an insight on the general behavior of the converter [75]. The considered averaged value *2-level* VSC model is based on a AC and DC modulated powers balance, i.e. $p_{mdc} = p_{mac}$, where the semiconductor losses are neglected. The working principle consist in chopping the DC voltage to form the desired AC modulated voltages $\boldsymbol{v}_{\boldsymbol{mabc}} = [v_{ma}\ v_{mb}\ v_{mc}]^\top$ by means of the modulation indices $\boldsymbol{m}_{\boldsymbol{abc}} = [m_a\ m_b\ m_c]^\top$.

Even if the model from Fig. 1.2 is overly simplified, it is exploited in this Section for introducing the different levels of modeling for VSCs used along this Thesis.

1.2.1 Non-linear state-space model with steady-state time-periodic solution

The first type of VSC model consists in the non-linear state-space model with steady-state time-periodic solution. A dynamic system can be modeled with a set of n first order differential equations with m inputs and p algebraic output equation [76, 77] as show in (1.1)[1].

$$\dot{\boldsymbol{x}}(t) = \boldsymbol{f}\left(\boldsymbol{x}(t), \boldsymbol{u}(t), t\right) \tag{1.1a}$$
$$\boldsymbol{y}(t) = \boldsymbol{h}\left(\boldsymbol{x}(t), \boldsymbol{u}(t), t\right) \tag{1.1b}$$

[1]Note that $\dot{\boldsymbol{x}}(t) = d\boldsymbol{x}(t)/dt$. Both notations are used indistinctly during this Chapter

where,

$$\boldsymbol{x} = [x_1(t), x_2(t), ..., x_n(t)]^\top \in \mathbb{R}^n \tag{1.2a}$$

$$\boldsymbol{u} = [u_1(t), u_2(t), ..., u_m(t)]^\top \in \mathbb{R}^m \tag{1.2b}$$

$$\boldsymbol{y} = [y_1(t), y_2(t), ..., y_p(t)]^\top \in \mathbb{R}^p \tag{1.2c}$$

$$\boldsymbol{f} = [f_1(\boldsymbol{x}(t), \boldsymbol{u}(t), t),\ f_2(\boldsymbol{x}(t), \boldsymbol{u}(t), t),\ ...,\ f_n(\boldsymbol{x}(t), \boldsymbol{u}(t), t)]^\top \tag{1.2d}$$

$$\boldsymbol{h} = [h_1(\boldsymbol{x}(t), \boldsymbol{u}(t), t),\ h_2(\boldsymbol{x}(t), \boldsymbol{u}(t), t),\ ...,\ h_p(\boldsymbol{x}(t), \boldsymbol{u}(t), t)]^\top \tag{1.2e}$$

The vector $\boldsymbol{x}$ groups the dynamic states of the systems, $\boldsymbol{u}$ the inputs and $\boldsymbol{y}$ the outputs. The functions $\boldsymbol{f}$ relate the inputs and states of the system with their derivatives, while $\boldsymbol{h}$ relate the inputs and states of the system with the outputs. When $\boldsymbol{f}$ and $\boldsymbol{h}$ represents non-linear functions of $\boldsymbol{x}$ and $\boldsymbol{u}$, the dynamic equations described by (1.1) are non-linear.

Following the example of the *2-level* VSC from Fig. 1.2, the balanced inputs $\boldsymbol{v^G_{abc}}$ and control inputs $\boldsymbol{m_{abc}}$ are given by the following equations:

$$\boldsymbol{v^G_{abc}} = \begin{bmatrix} v_a^G \\ v_b^G \\ v_c^G \end{bmatrix} = \begin{bmatrix} \hat{v}^G \cos(\omega t) \\ \hat{v}^G \cos(\omega t - 2\pi/3) \\ \hat{v}^G \cos(\omega t - 4\pi/3) \end{bmatrix}; \quad \boldsymbol{m_{abc}} = \begin{bmatrix} m_a \\ m_b \\ m_c \end{bmatrix} = \begin{bmatrix} \hat{m} \cos(\omega t + \phi) \\ \hat{m} \cos(\omega t - 2\pi/3 + \phi) \\ \hat{m} \cos(\omega t - 4\pi/3 + \phi) \end{bmatrix} \tag{1.3}$$

where $\hat{v}^G$ and $\hat{m}$ are the amplitudes of the AC voltage and modulation indices, respectively. The variable ϕ represents the phase of the modulation index vector.

The dynamics of the currents $\boldsymbol{i^G_{abc}} = [i_a^G, i_b^G, i_c^G]^\top$ are given by,

$$\frac{di_a^G}{dt} = \frac{1}{L_{eq}^{ac}} \left(v_{ma} - v_a^G - R_{eq}^{ac}\, i_a^G \right) \tag{1.4a}$$

$$\frac{di_b^G}{dt} = \frac{1}{L_{eq}^{ac}} \left(v_{mb} - v_b^G - R_{eq}^{ac}\, i_b^G \right) \tag{1.4b}$$

$$\frac{di_c^G}{dt} = \frac{1}{L_{eq}^{ac}} \left(v_{mb} - v_c^G - R_{eq}^{ac}\, i_c^G \right) \tag{1.4c}$$

$$i_a^G + i_b^G + i_c^G = 0 \tag{1.4d}$$

Since in this Section it is considered a perfectly balanced AC system, the sum of the currents is equal to zero, so the third current (i.e. i_c^G) is the difference between the two states. The modulated voltages $\boldsymbol{v_{mabc}}$ are given by (1.5).

$$\boldsymbol{v_{mabc}} = \begin{bmatrix} v_{ma} \\ v_{mb} \\ v_{mc} \end{bmatrix} = \begin{bmatrix} m_a\ v_{dc} \\ m_b\ v_{dc} \\ m_c\ v_{dc} \end{bmatrix} \tag{1.5}$$

Finally, the modulated DC current i_{mdc} is given in (1.6).

$$i_{mdc} = m_a i_a^G + m_b i_b^G + m_c i_c^G \tag{1.6}$$

The equations from (1.4) can be represented in a state space form of (1.1) as follows:

$$\frac{d}{dt} \begin{bmatrix} i_a^G \\ i_b^G \\ i_c^G \end{bmatrix} = \begin{bmatrix} -\frac{R_{eq}^{ac}}{L_{eq}^{ac}} & 0 & 0 \\ 0 & -\frac{R_{eq}^{ac}}{L_{eq}^{ac}} & 0 \\ 0 & 0 & -\frac{R_{eq}^{ac}}{L_{eq}^{ac}} \end{bmatrix} \begin{bmatrix} i_a^G \\ i_b^G \\ i_c^G \end{bmatrix} + \frac{1}{L_{eq}^{ac}} \begin{bmatrix} v_{dc}\hat{m} \cos(\omega t + \phi) \\ v_{dc}\hat{m} \cos(\omega t - 2\pi/3 + \phi) \\ v_{dc}\hat{m} \cos(\omega t - 4\pi/3 + \phi) \end{bmatrix} - \frac{1}{L_{eq}^{ac}} \begin{bmatrix} \hat{v}^G \cos(\omega t) \\ \hat{v}^G \cos(\omega t - 2\pi/3) \\ \hat{v}^G \cos(\omega t - 4\pi/3) \end{bmatrix} \tag{1.7}$$

The vector of independent states (it is considered that $i_c^G = -i_a^G - i_b^G$) and inputs are:

$$\boldsymbol{x} = \left[i_a^G, i_b^G\right]^\top \in \mathbb{R}^2, \quad \boldsymbol{u} = [\underbrace{\hat{v}^G, v_{dc}}_{\textbf{Physical}}, \underbrace{\hat{m}, \phi}_{\textbf{Control}}]^\top \in \mathbb{R}^4 \tag{1.8}$$

For this example, the number of independent states is $n = 2$, the number of inputs is $m = 4$ and the number of outputs p will depend on the desired outputs of the system.

In case that the Selector from Fig. 1.2 is in lower position, i.e. it is considered a stiff DC source, the model is linear. However, if the Selector is in upper position, i.e. the DC bus is a variable source, the model is bilinear (i.e. a dynamic system where there is a multiplication of state variables with control input variables). Also, due to the fact that (1.7) depends explicitly on the time t (with the $\cos(\omega t)$ functions), the solution of the system equations in steady state are time-variant. Due to the periodical solution of the sinusoidal functions, the model from (1.7) have a Steady-State with Time Periodic solution (SSTP)[2].

Open loop control in *abc* frame

The control system of the VSC adapts dynamically the modulated voltages $\boldsymbol{v_{mabc}}$ by changing the modulation indices according to the desired operating point in terms of different control strategies that can be adopted [58]. As an example, the Open-loop control for the VSC is depicted in Fig. 1.3 where the active and reactive power references are controlled.

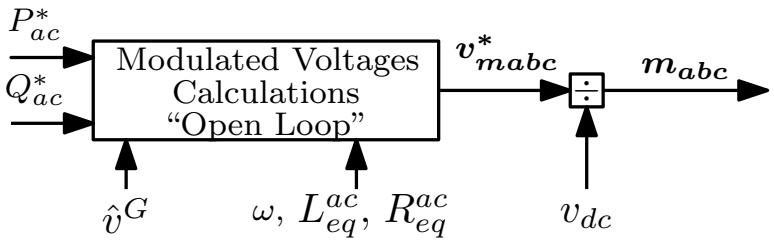

Figure 1.3 – Open-loop control for *2-level* VSC

Given the active and reactive power references at the PCC-AC, P^*_{ac} and Q^*_{ac} respectively, it is possible to calculate the functions of the modulated voltages $\boldsymbol{v_{mabc}}$ for the desired operating point as shown in (1.9). The mathematical deduction of (1.9) is given in the Appendix B. Note that the frequency ω is given as a parameter. This basic control fails to control the transient behavior in an acceptable way. Moreover, it is highly sensitive to the parameter variations. For these reasons, the Open-loop control strategies are not preferred. Nevertheless, it is used at this stage for exemplifying the modeling steps.

$$v^*_{ma} = \hat{v}^G \cos(\omega t) + \frac{2}{3\hat{v}^G}\left(\omega L^{ac}_{eq}\left(Q^* \cos(\omega t) - P^* \sin(\omega t)\right)\right) + ... \tag{1.9a}$$

$$... + \frac{2}{3\hat{v}^G}\left(R^{ac}_{eq}\left(P^* \cos(\omega t) + Q^* \sin(\omega t)\right)\right)$$

$$v^*_{mb} = \hat{v}^G \cos(\omega t - 2\pi/3) + \frac{2}{3\hat{v}^G}\left(\omega L^{ac}_{eq}\left(Q^* \cos(\omega t - 2\pi/3) - P^* \sin(\omega t - 2\pi/3)\right)\right) + ... \tag{1.9b}$$

$$... + \frac{2}{3\hat{v}^G}\left(R^{ac}_{eq}\left(P^* \cos(\omega t - 2\pi/3) + Q^* \sin(\omega t - 2\pi/3)\right)\right)$$

$$v^*_{mc} = -v^*_{ma} - v^*_{mb} \tag{1.9c}$$

[2]The double "SS" for SSTP stands for Steady-State, do not mix it with State-Space

The system from (1.7) with the Open-loop control in (1.9) is simulated considering the average value model of the VSC implemented in Matlab/Simulink. The scenario considers an active power reference change from $P^*_{ac} = 1$ pu to 0.5 pu at 50 ms, while maintaining the reactive power reference Q^*_{ac} at 0 pu. The simulation parameters are given in the Appendix A. Simulation results are gathered in Fig. 1.4. The DC voltage is considered to be a stiff DC voltage source (Selector from Fig. 1.2 in lower position).

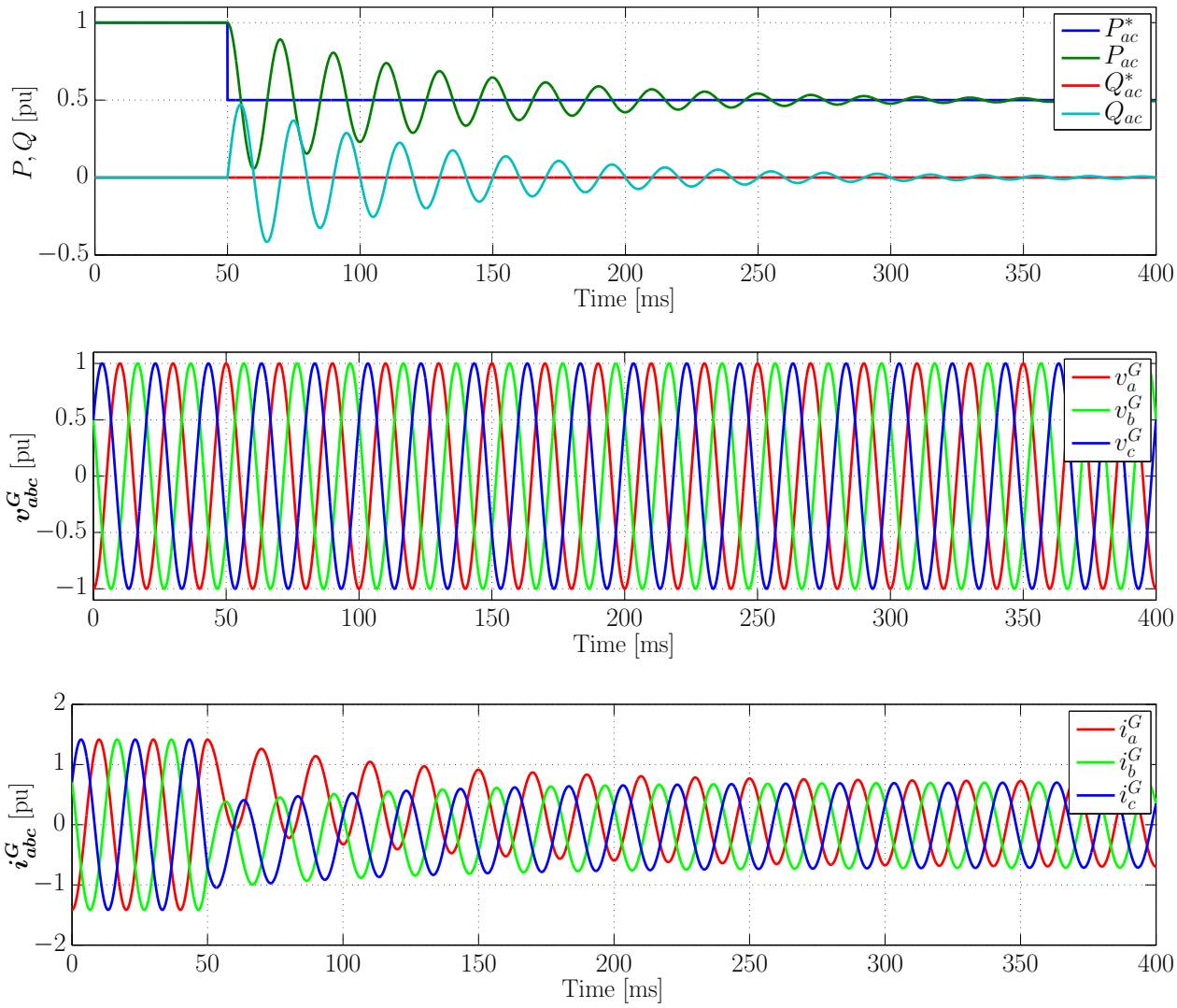

Figure 1.4 – SSTP Model: Simulation results of a *2-level* VSC with Open-loop control

As it can be seen in Fig. 1.4, the active and reactive powers are highly coupled with the considered Open-loop control. Moreover, the dynamics of the system are completely unacceptable, due to severe oscillations and a slow response time (more than 200 ms) [23]. However, the interest of this simulation is to highlight that the state variables of the system are periodic in steady state. If it is desired to study the system stability as it is, complicated mathematical theories should be applied. The main complexity resides in the fact that, in steady-state, the solution of the equations given by (1.7) is given by a periodic point on the state-space from $\boldsymbol{x}$ (i.e. a point which the system returns to after a certain number of time [78]), and not a fixed point independent of the absolute time. For these two reasons, highly coupled active and reactive powers and the periodicity of the solutions, the *dq* theory is commonly applied for obtaining an equivalent system where the state variables are constant in steady state.

1.2.2 Non-linear model with time-invariant solution in steady state

Continuing with the example from Fig. 1.2, a state-space model with time invariant solution is obtained by applying the Park transformation $\boldsymbol{P_\omega}$ defined in the Appendix A to (1.7) [74]:

$$\frac{di_d^G}{dt} = \frac{1}{L_{eq}^{ac}} \underbrace{m_d v_{dc}}_{v_{md}} - \frac{1}{L_{eq}^{ac}} v_d^G - \frac{R_{eq}^{ac}}{L_{eq}^{ac}} i_d^G - \omega i_q^G \tag{1.10a}$$

$$\frac{di_q^G}{dt} = \frac{1}{L_{eq}^{ac}} \underbrace{m_q v_{dc}}_{v_{mq}} - \frac{1}{L_{eq}^{ac}} v_q^G - \frac{R_{eq}^{ac}}{L_{eq}^{ac}} i_q^G + \omega i_d^G \tag{1.10b}$$

$$i_{mdc} = \frac{3}{2} \left(\underbrace{m_d i_d^G}_{i_{md}} + \underbrace{m_q i_q^G}_{i_{mq}} \right) \tag{1.10c}$$

As it can be seen in (1.10) the equations do not depend explicitly on time, so the solution of the system equations in steady state becomes time-invariant. This is advantageous since the steady-state condition can be easily calculated by non-linear numerical methods. Also, dealing with constant state variables in steady state is more favorable for control purposes, since simple Proportional-Integral-Derivatives (PID) controllers can be used for achieving acceptable dynamic responses. These types of models are called in this Thesis as state-space models with "Steady-State Time Invariant solution" (SSTI).

Calculation of operating point

As it was stated before, one interesting property of SSTI systems is that the operating point is defined by constant values of the state variables and inputs in steady state. For the VSC example with fixed DC bus, the operating point is defined by the set of values $\boldsymbol{x_0}$ and $\boldsymbol{u_0}$:

$$\boldsymbol{x_0} = \left[i_{d0}^G, i_{q0}^G \right]^\top \in \mathbb{R}^2, \quad \boldsymbol{u_0} = \left[v_{d0}^G, v_{dc0}, m_{d0}, m_{q0} \right]^\top \in \mathbb{R}^4 \tag{1.11}$$

which verifies:

$$\frac{d}{dt} \begin{bmatrix} i_d^G \\ i_q^G \end{bmatrix} = \begin{bmatrix} 0 \\ 0 \end{bmatrix} = \begin{bmatrix} -\frac{R_{eq}^{ac}}{L_{eq}^{ac}} & \omega \\ -\omega & -\frac{R_{eq}^{ac}}{L_{eq}^{ac}} \end{bmatrix} \begin{bmatrix} i_{d0}^G \\ i_{q0}^G \end{bmatrix} + \frac{1}{L_{eq}^{ac}} \begin{bmatrix} v_{dc0} m_{d0} \\ v_{dc0} m_{q0} \end{bmatrix} - \frac{v_{d0}^G}{L_{eq}^{ac}} \begin{bmatrix} 1 \\ 0 \end{bmatrix} \tag{1.12}$$

The system of equations given in (1.12) have 6 unknowns (2 state variables, and 4 inputs). For this reason, the expressions of the active and reactive power given in (1.13) are also considered, where it is assumed that $v_q^G = 0$[3].

$$P_{ac0} = \frac{3}{2} v_{d0}^G i_{d0}^G; \quad Q_{ac0} = \frac{3}{2} v_{d0}^G i_{q0}^G \tag{1.13}$$

Taking into account (1.12) and (1.13), it is needed to know *a priori* 2 out of 6 unknowns so the system may have a solution. In the example followed in this Chapter, the AC and DC voltages are known at the steady-state condition since they are given by their respective sources. Moreover, the active and reactive power references are imposed. In this way, the 4 unknowns to be found are i_{d0}^G, i_{q0}^G, m_{d0} and m_{q0}. However, different combinations can be used; for instance, if the AC or DC voltage are not known, the values m_{d0} and m_{q0} can be imposed to solve the system.

[3]The VSC is considered to be perfectly synchronized with the AC-grid

Generalization

The non-linear time-invariant models can be expressed as follows:

$$\begin{aligned} \dot{\boldsymbol{x}}(t) &= \boldsymbol{f}\left(\boldsymbol{x}(t), \boldsymbol{u}(t)\right) \\ \boldsymbol{y}(t) &= \boldsymbol{h}\left(\boldsymbol{x}(t), \boldsymbol{u}(t)\right) \end{aligned} \tag{1.14}$$

where,

$$\boldsymbol{f} = \left[f_1(\boldsymbol{x}(t), \boldsymbol{u}(t)),\ f_2(\boldsymbol{x}(t), \boldsymbol{u}(t)),\ ...,\ f_n(\boldsymbol{x}(t), \boldsymbol{u}(t))\right]^\top \tag{1.15a}$$

$$\boldsymbol{h} = \left[h_1(\boldsymbol{x}(t), \boldsymbol{u}(t)),\ h_2(\boldsymbol{x}(t), \boldsymbol{u}(t)),\ ...,\ h_p(\boldsymbol{x}(t), \boldsymbol{u}(t))\right]^\top \tag{1.15b}$$

Note that $\boldsymbol{f}$ and $\boldsymbol{h}$ in (1.14) and (1.15) (time-invariant) are **not** the same system functions as in (1.1) (time-variant). This is due to the fact that the absolute time t does not appear as an explicit parameter on the right side equations of $\boldsymbol{f}$ and $\boldsymbol{h}$ given in (1.15).

The operating point is defined by:

$$\boldsymbol{x_0} = \left[x_{1_0}, x_{2_0}, ..., x_{n_0}\right]^\top \in \mathbb{R}^n \tag{1.16a}$$

$$\boldsymbol{u_0} = \left[u_{1_0}, u_{2_0}, ..., u_{m_0}\right]^\top \in \mathbb{R}^m \tag{1.16b}$$

which verifies:

$$\boldsymbol{0} = \boldsymbol{f}\left(\boldsymbol{x_0}, \boldsymbol{u_0}\right) \tag{1.17}$$

The outputs in the steady state condition can be obtained by evaluating the output functions $\boldsymbol{h}$ with $(\boldsymbol{x_0}, \boldsymbol{u_0})$ as shown in (1.18).

$$\boldsymbol{y_0} = \boldsymbol{h}\left(\boldsymbol{x_0}, \boldsymbol{u_0}\right) \tag{1.18}$$

Open loop control in *dq* frame

The Open-loop control presented in previous section in *abc* frame is referred to the *dq* axes applying the Park transformation to (1.9) as follows:

$$v_{md}^* = \frac{2}{3}\frac{P_{ac}^* R_{eq}^{ac}}{v_d^G} + \frac{2}{3}\frac{Q_{ac}^* \omega L_{eq}^{ac}}{v_d^G} + v_d^G \tag{1.19a}$$

$$v_{mq}^* = \frac{2}{3}\frac{Q_{ac}^* R_{eq}^{ac}}{v_d^G} - \frac{2}{3}\frac{P_{ac}^* \omega L_{eq}^{ac}}{v_d^G} + v_q^G \tag{1.19b}$$

The same simulation as for the SSTP model is performed, and results are shown in Fig. 1.5. As it can be seen, the AC grid voltage is now constant and not a sinusoidal function as in Fig. 1.4. The AC currents in the *dq* axis are also constant in steady state. During the transient, a similar behavior as the active and reactive power as in Fig. 1.4 can be noticed.

As it was already pointed out, the Open loop control approach cannot guarantee an acceptable transient behavior. For this reason, in the following section the classical grid current controllers in Synchronous Rotating Reference Frames (SRRF) based on feedback control and Proportional-Integral (PI) controllers are introduced.

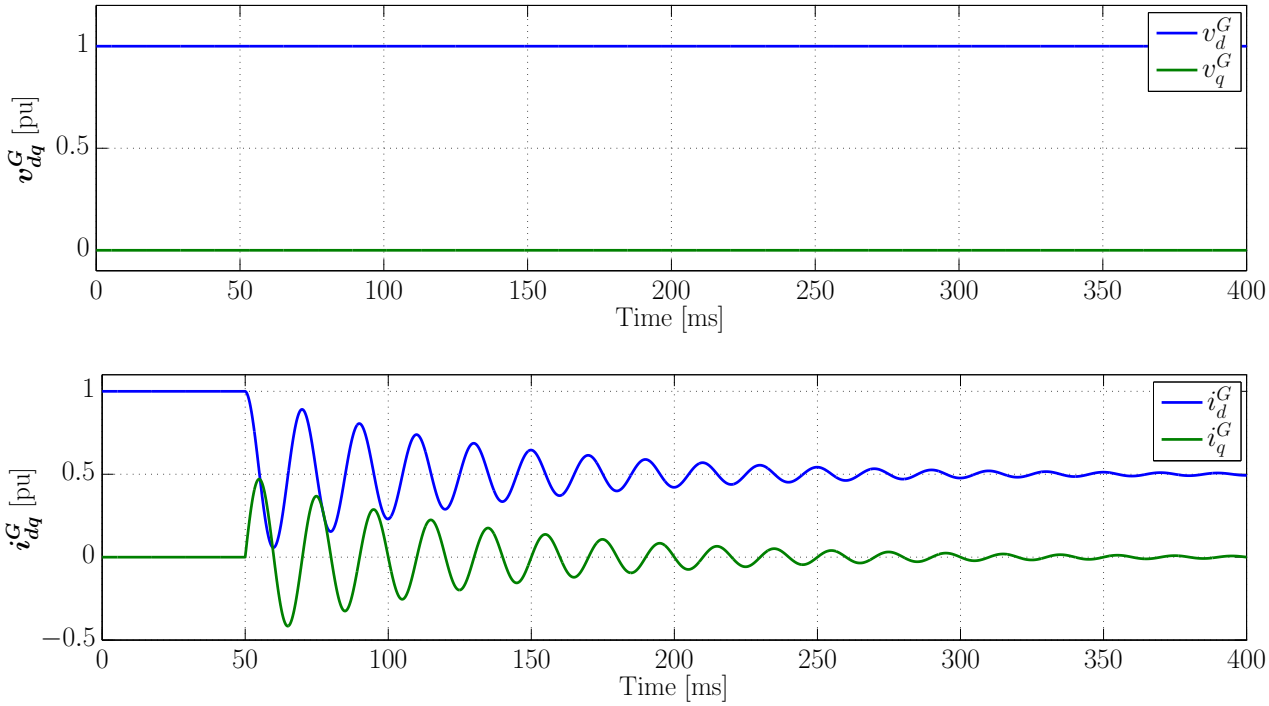

Figure 1.5 – SSTI Model: Simulation results of a *2-level* VSC with Open-loop control in *dq* frame

VSC Classical control

The VSC classical control strategy is based on two cascaded loops (namely inner and outer loops). The inner loops control the AC currents in *dq* frame, while the outer loops generate their references [74].

Since the *dq* variables are DC values in steady state, the widely adopted Proportional-Integral (PI) controllers can be used in Synchronous Rotating Reference Frame for achieving an acceptable dynamic behavior while guaranteeing zero steady-state errors at the same time. The block diagram of (1.10) and the AC current controllers are depicted in Fig. 1.6.

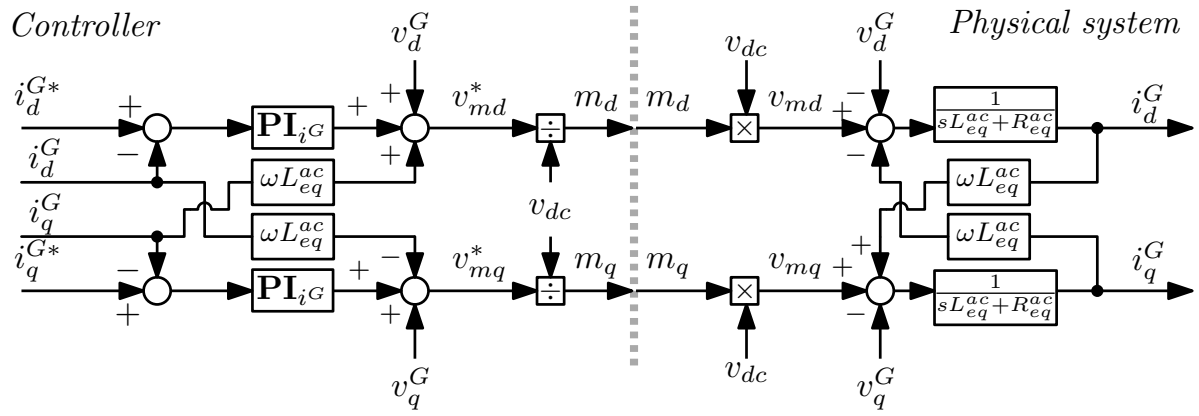

(a) Current controllers (b) Physical system

Figure 1.6 – VSC AC Inner current controller in SRRF

Feed-forward decoupling terms are added in the controller structure for allowing an indepen-

dent control of the dq currents (and in this way, independent control of active and reactive powers). The response time of these controllers is usually in the order of a few milliseconds. In this Thesis, the grid current controllers are set to obtain a theoretical time response of 10 ms. Note that the control structure is derived from an exact inversion of the equations of the physical system [79]. The controller tuning methodology is explained in Appendix C.

It has to be noted that the dq reference frame to which all AC currents and voltages are referred to, has to be provided by a Phase-Lock-Loop (PLL), which aims at aligning the grid voltage phasor v^G with the d axis[4]. However, a perfect PLL is considered in this Chapter.

The current references in Fig. 1.6 are generated by the outer controllers shown in Fig. 1.7. Different control strategies can be implemented for the components i_d^{G*} and i_q^{G*} [80].

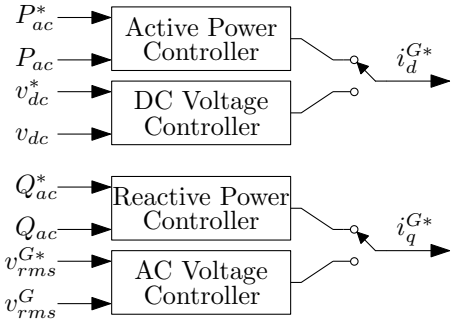

Figure 1.7 – VSC Outer controllers

The design of the active and reactive power controllers are based on the following expressions of the AC powers in dq frame:

$$P_{ac} = \frac{3}{2}\left(v_d^G i_d^G + \underbrace{v_q^G}_{=0} i_q^G\right) \tag{1.20a}$$

$$Q_{ac} = \frac{3}{2}\left(v_d^G i_q^G - \underbrace{v_q^G}_{=0} i_d^G\right) \tag{1.20b}$$

Several types of controllers can be considered for the AC active and reactive powers [9, 81], however in this Chapter it is considered a perfect PLL, so the reference frame used for the controlled is always aligned with v_d^G. This simplification allows to consider that $v_q^G = 0$. In this way, simple controllers can be deduced by inversion and shown in Fig. 1.8.

(a) Active power control

(b) Reactive power control

Figure 1.8 – VSC Outer controllers: Active and reactive power controllers

The VSC controller is demonstrated through time-domain simulations. Starting with an AC power transfer of $P_{ac} = 1$ pu and $Q_{ac} = 0$ pu, a step on P_{ac}^* of -0.2 pu is applied at 50

[4]In case that v^G is not constant, this variable varies due to the AC-side impedance. In such case, the AC grid model can be modeled using a Thévenin model with the Short-Circuit Ratio, as detailed in Chapter 4.

ms. Then, a step on Q_{ac}^* of 0.1 pu is applied at 250 ms. Results of the AC active and reactive powers for the VSC are gathered in Fig. 1.9.

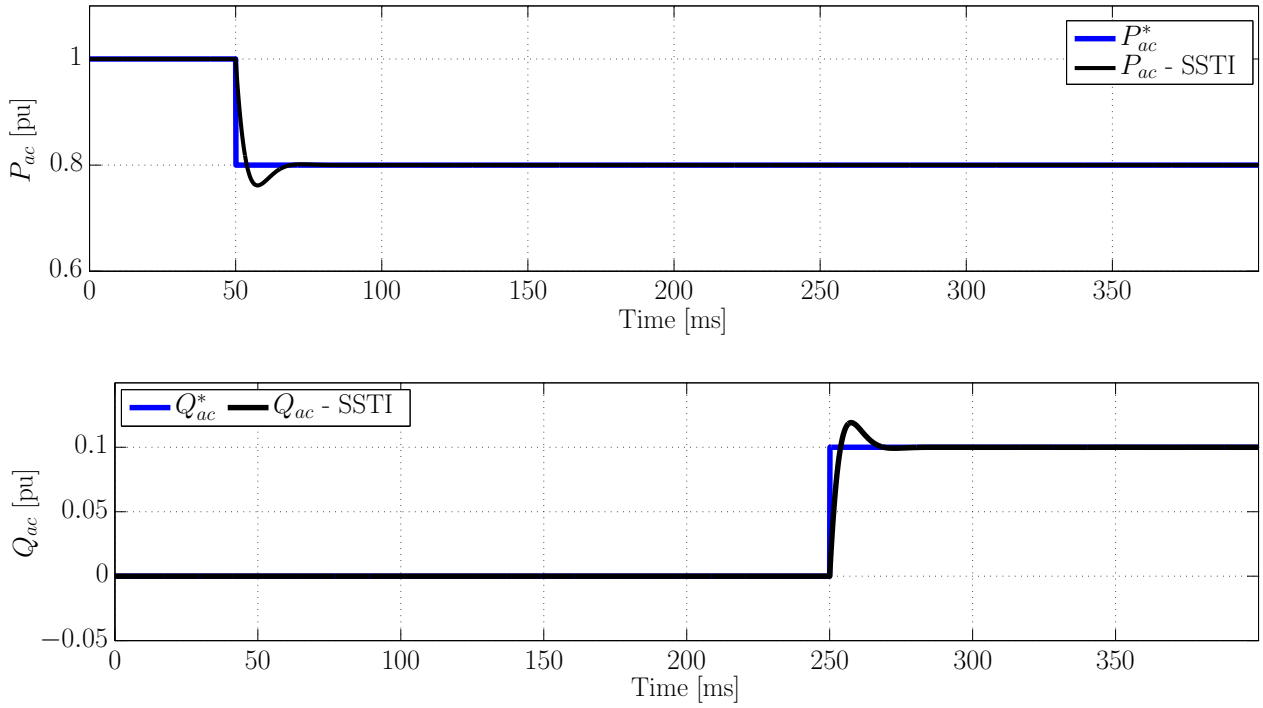

Figure 1.9 – Time domain verification of grid current controllers *2-level* VSC

Note that the dynamic responses are highly improved with respect to the results from Section 1.2, i.e. with the *Open-loop* strategy. Moreover, a perfect decoupling between the currents in the d and q axes can be achieved.

1.2.3 VSC with variable DC bus voltage: Energetic modeling

Until now, the Selector in Fig. 1.2 was considered in the lower position, where the DC voltage is imposed by the DC source. In this subsection, the DC bus is represented by a capacitor C_S. The dynamics of the DC bus are given in (1.21):

$$\frac{dv_{dc}}{dt} = \frac{1}{C_S}\left(i_l - \underbrace{\frac{3}{2}\left(m_d i_d^G + m_q i_q^G\right)}_{i_{mdc}}\right) \tag{1.21}$$

The block diagram of the VSC model associated with the DC capacitor C_S is drawn in Fig. 1.10. This model highlights the bilinear characteristic of the VSC, where the inputs $\boldsymbol{m_{dq}} = [m_d\ m_q]^\top$ modulates at the same time the AC voltages $\boldsymbol{v_{mdq}} = [v_{md}\ v_{mq}]^\top$ and the AC currents to form i_{mdc}. This property is inherent to static converters [82].

For designing a DC bus voltage controller, a simplified model linking the active power P_{ac} and v_{dc} is needed. Multiplying (1.21) by v_{dc} it results in:

$$\frac{dv_{dc}^2}{dt} = \frac{2}{C_S}\left(\underbrace{v_{dc} i_l}_{P_l^*} - \underbrace{v_{dc} i_{mdc}}_{p_{mdc}}\right) \tag{1.22}$$

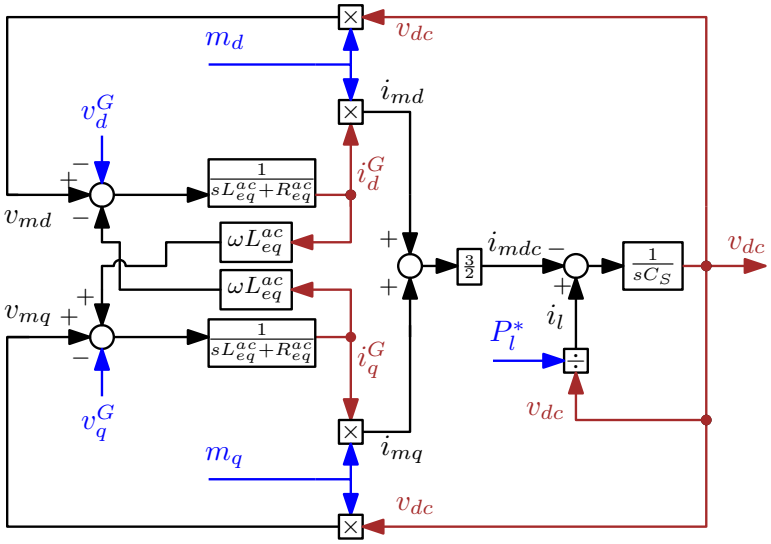

Figure 1.10 – Block diagram of *2-level* VSC connected to a DC capacitor C_S

Assuming no losses, i.e. $p_{mdc} \approx P_{ac}$, the following block diagram can be drawn for (1.22) in Fig. 1.11, where the deduced controller for v_{dc}^2 by inversion is also shown. The DC voltage controller is set to obtain a theoretical time response of 100 ms, i.e. 10 times slower than the current controllers to avoid undesired interactions [58].

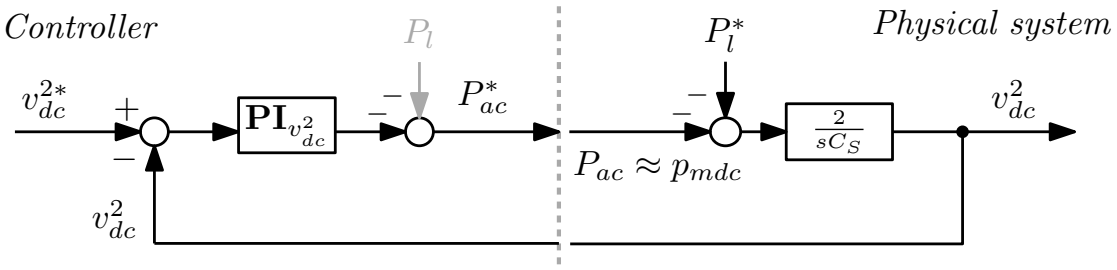

(a) DC Voltage controller (b) Simplified physical system

Figure 1.11 – DC Voltage controller and simplified physical system

It is important to note that a compensation term of P_l (marked in gray) is added in the v_{dc}^2 controller. In real projects, this compensation is likely to be present but with the power reference (i.e. P_l^*) synchronized in the DC grid by means of a communication system. This allows to help the v_{dc}^2 controller to anticipate actions from the other converter, and in this way, the DC voltage excursion is limited in normal operation. This communication is useful (and maybe mandatory) for fast power inversions in HVDC links (for example, a complete power reversal from 1 pu to -1 pu in less than 200 ms, or vice-versa), and coordinated actions in MTDC grids. Nevertheless, in the following no communication is considered, as it is the possible worst case scenario.

1.2.4 Linear time invariant model and linear analysis

Although almost every physical system contains nonlinearities, most of their behavior can be reasonably approximated around a certain operating point by a linear model [77]. The

linearized model is commonly referred as linear time-invariant (LTI). In this subsection, a linearized model of the VSC is obtained and validated through time-domain simulations.

Linearizing a non-linear model with Jacobian

Suppose $(\boldsymbol{x_0}; \boldsymbol{u_0})$ is an equilibrium point defined by the steady state conditions of the variables and inputs (i.e. it verifies (1.17)). It is known that if the system is in equilibrium at the point defined by $\boldsymbol{x}(t_0) = \boldsymbol{x_0}$ with a constant input $\boldsymbol{u}(t_0) = \boldsymbol{u_0}$, then the states of the system will remain fixed at $\boldsymbol{x}(t) = \boldsymbol{x_0}$ for all time t (time-invariant steady-state solution). When the system is then perturbed and moves a bit away from $\boldsymbol{x_0}$ by applying a slightly different input from $\boldsymbol{u_0}$ it is used the deviation (or small-signal) variables to study its behavior [83]. The deviation variables are expressed as:

$$\Delta \boldsymbol{x} = \boldsymbol{x} - \boldsymbol{x_0} \quad \rightarrow \quad \boldsymbol{x} = \Delta \boldsymbol{x} + \boldsymbol{x_0} \tag{1.23a}$$

$$\Delta \boldsymbol{u} = \boldsymbol{u} - \boldsymbol{u_0} \quad \rightarrow \quad \boldsymbol{u} = \Delta \boldsymbol{u} + \boldsymbol{u_0} \tag{1.23b}$$

$$\Delta \boldsymbol{y} = \boldsymbol{y} - \boldsymbol{y_0} \quad \rightarrow \quad \boldsymbol{y} = \Delta \boldsymbol{y} + \boldsymbol{y_0} \tag{1.23c}$$

Equation (1.23) refers to a translation of the origin. Substituting (1.23) into (1.14) it is obtained:

$$\frac{d(\Delta \boldsymbol{x} + \boldsymbol{x_0})}{dt} = \Delta \dot{\boldsymbol{x}} + \underbrace{\dot{\boldsymbol{x_0}}}_{=0} = \boldsymbol{f}\left(\Delta \boldsymbol{x} + \boldsymbol{x_0}, \Delta \boldsymbol{u} + \boldsymbol{u_0}\right) \tag{1.24a}$$

$$\Delta \boldsymbol{y} + \boldsymbol{y_0} = \boldsymbol{h}\left(\Delta \boldsymbol{x} + \boldsymbol{x_0}, \Delta \boldsymbol{u} + \boldsymbol{u_0}\right) \tag{1.24b}$$

Equations (1.14) and (1.24) are strictly the same up to this point. The next step is to perform a Taylor expansion of the right hand side of (1.24), and neglect all higher order terms:

$$\Delta \dot{\boldsymbol{x}} \approx \underbrace{\boldsymbol{f}(\boldsymbol{x_0}, \boldsymbol{u_0})}_{=0} + \left[\frac{\partial \boldsymbol{f}(\boldsymbol{x},\boldsymbol{u})}{\partial x_1}, \ldots, \frac{\partial \boldsymbol{f}(\boldsymbol{x},\boldsymbol{u})}{\partial x_n}\right]\Big|_{(\boldsymbol{x_0};\boldsymbol{u_0})} \Delta \boldsymbol{x} + \left[\frac{\partial \boldsymbol{f}(\boldsymbol{x},\boldsymbol{u})}{\partial u_1}, \ldots, \frac{\partial \boldsymbol{f}(\boldsymbol{x},\boldsymbol{u})}{\partial u_m}\right]\Big|_{(\boldsymbol{x_0};\boldsymbol{u_0})} \Delta \boldsymbol{u} \tag{1.25a}$$

$$\Delta \boldsymbol{y} + \boldsymbol{y_0} \approx \underbrace{\boldsymbol{h}(\boldsymbol{x_0}, \boldsymbol{u_0})}_{=\boldsymbol{y_0}} + \left[\frac{\partial \boldsymbol{h}(\boldsymbol{x},\boldsymbol{u})}{\partial x_1}, \ldots, \frac{\partial \boldsymbol{h}(\boldsymbol{x},\boldsymbol{u})}{\partial x_n}\right]\Big|_{(\boldsymbol{x_0};\boldsymbol{u_0})} \Delta \boldsymbol{x} + \left[\frac{\partial \boldsymbol{h}(\boldsymbol{x},\boldsymbol{u})}{\partial u_1}, \ldots, \frac{\partial \boldsymbol{h}(\boldsymbol{x},\boldsymbol{u})}{\partial u_m}\right]\Big|_{(\boldsymbol{x_0};\boldsymbol{u_0})} \Delta \boldsymbol{u} \tag{1.25b}$$

Since $\dot{\boldsymbol{x}} = \Delta \dot{\boldsymbol{x}}$ and $\boldsymbol{f}(\boldsymbol{x_0}, \boldsymbol{u_0}) = 0$, the linear time-invariant (LTI) approximation of (1.14) takes the State-Space form as:

$$\Delta \dot{\boldsymbol{x}} = \boldsymbol{A} \Delta \boldsymbol{x} + \boldsymbol{B} \Delta \boldsymbol{u} \tag{1.26a}$$

$$\Delta \boldsymbol{y} = \boldsymbol{C} \Delta \boldsymbol{x} + \boldsymbol{D} \Delta \boldsymbol{u} \tag{1.26b}$$

where,

$$\boldsymbol{A}_{n\times n} = \begin{bmatrix} \frac{\partial f_1(\boldsymbol{x},\boldsymbol{u})}{\partial x_1} & \cdots & \frac{\partial f_1(\boldsymbol{x},\boldsymbol{u})}{\partial x_n} \\ \vdots & \ddots & \vdots \\ \frac{\partial f_n(\boldsymbol{x},\boldsymbol{u})}{\partial x_1} & \cdots & \frac{\partial f_n(\boldsymbol{x},\boldsymbol{u})}{\partial x_n} \end{bmatrix}\Bigg|_{(\boldsymbol{x_0};\boldsymbol{u_0})}, \quad \boldsymbol{B}_{n\times m} = \begin{bmatrix} \frac{\partial f_1(\boldsymbol{x},\boldsymbol{u})}{\partial u_1} & \cdots & \frac{\partial f_1(\boldsymbol{x},\boldsymbol{u})}{\partial u_m} \\ \vdots & \ddots & \vdots \\ \frac{\partial f_n(\boldsymbol{x},\boldsymbol{u})}{\partial u_1} & \cdots & \frac{\partial f_n(\boldsymbol{x},\boldsymbol{u})}{\partial u_m} \end{bmatrix}\Bigg|_{(\boldsymbol{x_0};\boldsymbol{u_0})} \tag{1.27a}$$

$$\boldsymbol{C}_{p\times n} = \begin{bmatrix} \frac{\partial h_1(\boldsymbol{x},\boldsymbol{u})}{\partial x_1} & \cdots & \frac{\partial h_1(\boldsymbol{x},\boldsymbol{u})}{\partial x_n} \\ \vdots & \ddots & \vdots \\ \frac{\partial h_p(\boldsymbol{x},\boldsymbol{u})}{\partial x_1} & \cdots & \frac{\partial h_p(\boldsymbol{x},\boldsymbol{u})}{\partial x_n} \end{bmatrix}\Bigg|_{(\boldsymbol{x_0};\boldsymbol{u_0})}, \quad \boldsymbol{D}_{p\times m} = \begin{bmatrix} \frac{\partial h_1(\boldsymbol{x},\boldsymbol{u})}{\partial u_1} & \cdots & \frac{\partial h_1(\boldsymbol{x},\boldsymbol{u})}{\partial u_m} \\ \vdots & \ddots & \vdots \\ \frac{\partial h_p(\boldsymbol{x},\boldsymbol{u})}{\partial u_1} & \cdots & \frac{\partial h_p(\boldsymbol{x},\boldsymbol{u})}{\partial u_m} \end{bmatrix}\Bigg|_{(\boldsymbol{x_0};\boldsymbol{u_0})} \tag{1.27b}$$

Note that the $\boldsymbol{A}_{n\times n}$ and $\boldsymbol{B}_{n\times m}$ matrices are obtained by applying the Jacobian of the system equations $\boldsymbol{f}$ with regards to the n states $\boldsymbol{x}$ and the m inputs $\boldsymbol{u}$ respectively, evaluated at the operating point $(\boldsymbol{x_0}; \boldsymbol{u_0})$. The $\boldsymbol{C}_{p\times n}$ and $\boldsymbol{D}_{p\times m}$ matrices are obtained with the Jacobian of the output equations $\boldsymbol{y}$ with regards to the n states $\boldsymbol{x}$ and the m inputs $\boldsymbol{u}$ respectively, evaluated at the operating point $(\boldsymbol{x_0}; \boldsymbol{u_0})$.

Linearization of the 2-level VSC model with variable DC bus

Continuing with the VSC example from Fig. 1.2, it is recalled what it was already obtained:

- The non-linear model with time invariant solution (SSTI) from (1.10) and (1.21).
- The operating point given by $(\boldsymbol{x_0}, \boldsymbol{u_0})$ from the solution of the system equations obtained by setting the derivatives to zero as in (1.17).

For obtaining a linearized model of the *2-level* VSC considering the DC bus connection, the complete system (physical part and controllers) in a "SSTI" representation is needed: this was already developed in this Chapter. The summary of the different parts of the system and their relations is shown in Fig. 1.12.

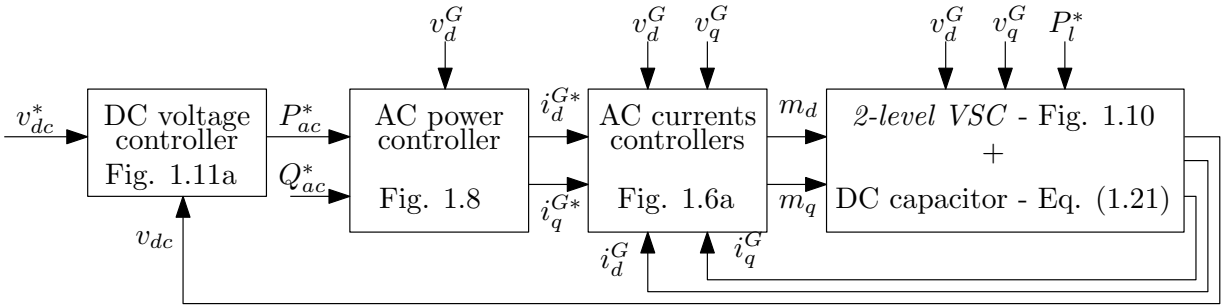

Figure 1.12 – *2-level* VSC with DC bus connection - SSTI equations

This kind of block diagrams is exploited in this Thesis for highlighting the SSTI model (converter and controller, for instance) which is considered prior the linearization process. The SSTI model from Fig. 1.12 is developed in per-unit[5] for each dynamic state in (1.28) and the algebraic equations in (1.29). The state-variables named as "ξ_X" correspond to the state of controller of the variable "X". Moreover, I_{dcb} and V_{dcb} are the nominal current and voltage for the DC side, I_{bdq} and V_{bdq} the nominal current and voltage for the AC side in dq frame (See Appendix A). Note that the DC voltage (square) controller structure corresponds to an **IP** controller, to avoid overshoots for reference steps (See Appendix C).

$$f_1 = \frac{d\xi_{v_{dc}^2}}{dt} = \frac{1}{T_{i,v_{dc}^2}} \left((v_{dc}^*)^2 - (v_{dc})^2 \right) \tag{1.28a}$$

$$f_2 = \frac{d\xi_{i_d^G}}{dt} = \frac{1}{T_{i,i^G}} \underbrace{(i_d^{G*}}_{(1.29a)} - i_d^G) \tag{1.28b}$$

$$f_3 = \frac{d\xi_{i_q^G}}{dt} = \frac{1}{T_{i,i^G}} \underbrace{(i_q^{G*}}_{(1.29a)} - i_q^G) \tag{1.28c}$$

$$f_4 = \frac{di_d^G}{dt} = \frac{\omega_b}{L_{eq}^{ac}} \left(\underbrace{v_{md}}_{(1.29b)} - v_d^G - \omega L_{eq}^{ac} i_q^G - R_{eq}^{ac} i_d^G \right) \tag{1.28d}$$

[5]No indication in the variables in the notation to identify per-unit variables for simplicity

$$f_5 = \frac{di_q^G}{dt} = \frac{\omega_b}{L_{eq}^{ac}} \left(\underbrace{v_{mq}}_{(1.29c)} - v_q^G + \omega L_{eq}^{ac} i_d^G - R_{eq}^{ac} i_d^G \right) \tag{1.28e}$$

$$f_6 = \frac{dv_{dc}}{dt} = \frac{1}{2\left(\frac{1}{2} C_S \frac{v_{dc}^2}{P_n}\right)} \left(\frac{P_l^*}{v_{dc}} - \frac{I_{bdq}}{I_{dcb}} \frac{3}{2} \left(m_d i_d^G + m_q i_q^G \right) \right) \tag{1.28f}$$

$$P_{ac}^* = -\left(\xi_{v_{dc}^2} - K_{p,v_{dc}^2} (v_{dc})^2 \right); \quad i_d^{G*} = \frac{2}{3} \frac{P_{ac}^*}{v_d^G}; \quad i_q^{G*} = \frac{2}{3} \frac{Q_{ac}^*}{v_d^G} \tag{1.29a}$$

$$v_{md}^* = K_{p,i^G} \left(i_d^{G*} - i_d^G \right) + \xi_{i_d^G} + \omega L_{eq}^{ac} i_q^G + v_d^G; \quad m_d = \frac{V_{bdq}}{V_{dcb}} \frac{v_{md}^*}{v_{dc}}; \quad v_{md} = \frac{V_{dcb}}{V_{bdq}} m_d v_{dc} \tag{1.29b}$$

$$v_{mq}^* = K_{p,i^G} \left(i_q^{G*} - i_q^G \right) + \xi_{i_q^G} - \omega L_{eq}^{ac} i_d^G + v_q^G; \quad m_q = \frac{V_{bdq}}{V_{dcb}} \frac{v_{mq}^*}{v_{dc}}; \quad v_{mq} = \frac{V_{dcb}}{V_{bdq}} m_q v_{dc} \tag{1.29c}$$

The states $\boldsymbol{x}$ and inputs $\boldsymbol{u}$ are listed below (the "$*$" in P_l^* denotes that this power is imposed externally):

$$\boldsymbol{x} = \left[\xi_{v_{dc}^2} \; \xi_{i_d^G} \; \xi_{i_q^G} \; i_d^G \; i_q^G \; v_{dc} \right]^\top \in \mathbb{R}^6 \tag{1.30}$$

$$\boldsymbol{u} = \left[\underbrace{v_d^G \; v_q^G \; P_l^*}_{\textbf{Phys.}} \underbrace{v_{dc}^* \; Q_{ac}^*}_{\textbf{Control}} \right]^\top \in \mathbb{R}^5 \tag{1.31}$$

The operation point in steady-state is given by the point $(\boldsymbol{x_0}, \boldsymbol{u_0})$, where:

$$\boldsymbol{x_0} = \left[\xi_{v_{dc0}^2} \; \xi_{i_{d0}^G} \; \xi_{i_{q0}^G} \; i_{d0}^G \; i_{q0}^G \; v_{dc0} \right]^\top \in \mathbb{R}^6 \tag{1.32}$$

$$\boldsymbol{u_0} = \left[\underbrace{v_{d0}^G \; v_{q0}^G \; P_{l0}^*}_{\textbf{Phys.}} \underbrace{v_{dc0}^* \; Q_{ac0}^*}_{\textbf{Control}} \right]^\top \in \mathbb{R}^5 \tag{1.33}$$

For simplicity, let us consider the following output functions:

$$h_1 = i_d^G \quad h_2 = i_q^G \quad h_3 = v_{dc} \tag{1.34}$$

The matrices $\boldsymbol{A}$, $\boldsymbol{B}$, $\boldsymbol{C}$ and $\boldsymbol{D}$ are computed taking into account (1.27) as follows:

$$\boldsymbol{A}_{6\times6} = \left[\begin{matrix} \frac{\partial f_1}{\partial \xi_{v_{dc}^2}} & \frac{\partial f_1}{\partial \xi_{i_d^G}} & \frac{\partial f_1}{\partial \xi_{i_q^G}} & \frac{\partial f_1}{\partial i_d^G} & \frac{\partial f_1}{\partial i_q^G} & \frac{\partial f_1}{\partial v_{dc}} \\ \frac{\partial f_2}{\partial \xi_{v_{dc}^2}} & \frac{\partial f_2}{\partial \xi_{i_d^G}} & \frac{\partial f_2}{\partial \xi_{i_q^G}} & \frac{\partial f_2}{\partial i_d^G} & \frac{\partial f_2}{\partial i_q^G} & \frac{\partial f_2}{\partial v_{dc}} \\ \frac{\partial f_3}{\partial \xi_{v_{dc}^2}} & \frac{\partial f_3}{\partial \xi_{i_d^G}} & \frac{\partial f_3}{\partial \xi_{i_q^G}} & \frac{\partial f_3}{\partial i_d^G} & \frac{\partial f_3}{\partial i_q^G} & \frac{\partial f_3}{\partial v_{dc}} \\ \frac{\partial f_4}{\partial \xi_{v_{dc}^2}} & \frac{\partial f_4}{\partial \xi_{i_d^G}} & \frac{\partial f_4}{\partial \xi_{i_q^G}} & \frac{\partial f_4}{\partial i_d^G} & \frac{\partial f_4}{\partial i_q^G} & \frac{\partial f_4}{\partial v_{dc}} \\ \frac{\partial f_5}{\partial \xi_{v_{dc}^2}} & \frac{\partial f_5}{\partial \xi_{i_d^G}} & \frac{\partial f_5}{\partial \xi_{i_q^G}} & \frac{\partial f_5}{\partial i_d^G} & \frac{\partial f_5}{\partial i_q^G} & \frac{\partial f_5}{\partial v_{dc}} \\ \frac{\partial f_6}{\partial \xi_{v_{dc}^2}} & \frac{\partial f_6}{\partial \xi_{i_d^G}} & \frac{\partial f_6}{\partial \xi_{i_q^G}} & \frac{\partial f_6}{\partial i_d^G} & \frac{\partial f_6}{\partial i_q^G} & \frac{\partial f_6}{\partial v_{dc}} \end{matrix} \right]_{(\boldsymbol{x_0};\boldsymbol{u_0})} \quad \boldsymbol{B}_{6\times5} = \left[\begin{matrix} \frac{\partial f_1}{\partial v_d^G} & \frac{\partial f_1}{\partial v_q^G} & \frac{\partial f_1}{\partial P_l^*} & \frac{\partial f_1}{\partial v_{dc}^*} & \frac{\partial f_1}{\partial Q_{ac}^*} \\ \frac{\partial f_2}{\partial v_d^G} & \frac{\partial f_2}{\partial v_q^G} & \frac{\partial f_2}{\partial P_l^*} & \frac{\partial f_2}{\partial v_{dc}^*} & \frac{\partial f_2}{\partial Q_{ac}^*} \\ \frac{\partial f_3}{\partial v_d^G} & \frac{\partial f_3}{\partial v_q^G} & \frac{\partial f_3}{\partial P_l^*} & \frac{\partial f_3}{\partial v_{dc}^*} & \frac{\partial f_3}{\partial Q_{ac}^*} \\ \frac{\partial f_4}{\partial v_d^G} & \frac{\partial f_4}{\partial v_q^G} & \frac{\partial f_4}{\partial P_l^*} & \frac{\partial f_4}{\partial v_{dc}^*} & \frac{\partial f_4}{\partial Q_{ac}^*} \\ \frac{\partial f_5}{\partial v_d^G} & \frac{\partial f_5}{\partial v_q^G} & \frac{\partial f_5}{\partial P_l^*} & \frac{\partial f_5}{\partial v_{dc}^*} & \frac{\partial f_5}{\partial Q_{ac}^*} \\ \frac{\partial f_6}{\partial v_d^G} & \frac{\partial f_6}{\partial v_q^G} & \frac{\partial f_6}{\partial P_l^*} & \frac{\partial f_6}{\partial v_{dc}^*} & \frac{\partial f_6}{\partial Q_{ac}^*} \end{matrix} \right]_{(\boldsymbol{x_0};\boldsymbol{u_0})} \tag{1.35a}$$

$$\boldsymbol{C}_{6\times3} = \left[\begin{matrix} \frac{\partial h_1}{\partial \xi_{v_{dc}^2}} & \frac{\partial h_1}{\partial \xi_{i_d^G}} & \frac{\partial h_1}{\partial \xi_{i_q^G}} & \frac{\partial h_1}{\partial i_d^G} & \frac{\partial h_1}{\partial i_q^G} & \frac{\partial h_1}{\partial v_{dc}} \\ \frac{\partial h_2}{\partial \xi_{v_{dc}^2}} & \frac{\partial h_2}{\partial \xi_{i_d^G}} & \frac{\partial h_2}{\partial \xi_{i_q^G}} & \frac{\partial h_2}{\partial i_d^G} & \frac{\partial h_2}{\partial i_q^G} & \frac{\partial h_2}{\partial v_{dc}} \\ \frac{\partial h_3}{\partial \xi_{v_{dc}^2}} & \frac{\partial h_2}{\partial \xi_{i_d^G}} & \frac{\partial h_2}{\partial \xi_{i_q^G}} & \frac{\partial h_2}{\partial i_d^G} & \frac{\partial h_2}{\partial i_q^G} & \frac{\partial h_2}{\partial v_{dc}} \end{matrix} \right]_{(\boldsymbol{x_0};\boldsymbol{u_0})} \quad \boldsymbol{D}_{3\times5} = \left[\begin{matrix} \frac{\partial h_1}{\partial v_d^G} & \frac{\partial h_1}{\partial v_q^G} & \frac{\partial h_1}{\partial P_l^*} & \frac{\partial h_1}{\partial v_{dc}^*} & \frac{\partial h_1}{\partial Q_{ac}^*} \\ \frac{\partial h_2}{\partial v_d^G} & \frac{\partial h_2}{\partial v_q^G} & \frac{\partial h_2}{\partial P_l^*} & \frac{\partial h_2}{\partial v_{dc}^*} & \frac{\partial h_2}{\partial Q_{ac}^*} \\ \frac{\partial h_3}{\partial v_d^G} & \frac{\partial h_3}{\partial v_q^G} & \frac{\partial h_3}{\partial P_l^*} & \frac{\partial h_3}{\partial v_{dc}^*} & \frac{\partial h_3}{\partial Q_{ac}^*} \end{matrix} \right]_{(\boldsymbol{x_0};\boldsymbol{u_0})} \tag{1.35b}$$

The computation of $\boldsymbol{A}$, $\boldsymbol{B}$, $\boldsymbol{C}$ and $\boldsymbol{D}$ is performed in Matlab by means of the *Jacobian* function. Then, after the operating point $(\boldsymbol{x_0}; \boldsymbol{u_0})$ is obtained numerically, the matrices from (1.35) are evaluated (becoming full numerical). Finally, the state-space representation of the LTI model is obtained as follows:

$$\frac{d}{dt}\begin{bmatrix}\Delta\xi_{v_{dc}^2}\\ \Delta\xi_{i_d^G}\\ \Delta\xi_{i_q^G}\\ \Delta i_d^G\\ \Delta i_q^G\\ \Delta v_{dc}\end{bmatrix} = \boldsymbol{A}_{6\times6}\begin{bmatrix}\Delta\xi_{v_{dc}^2}\\ \Delta\xi_{i_d^G}\\ \Delta\xi_{i_q^G}\\ \Delta i_d^G\\ \Delta i_q^G\\ \Delta v_{dc}\end{bmatrix} + \boldsymbol{B}_{6\times5}\begin{bmatrix}\Delta v_d^G\\ \Delta v_q^G\\ \Delta P_l^*\\ \Delta v_{dc}^*\\ \Delta Q_{ac}^*\end{bmatrix} \tag{1.36a}$$

$$\begin{bmatrix}\Delta i_d^G\\ \Delta i_q^G\\ \Delta v_{dc}\end{bmatrix} = \boldsymbol{C}_{6\times3}\begin{bmatrix}\Delta\xi_{v_{dc}^2}\\ \Delta\xi_{i_d^G}\\ \Delta\xi_{i_q^G}\\ \Delta i_d^G\\ \Delta i_q^G\\ \Delta v_{dc}\end{bmatrix} + \boldsymbol{D}_{3\times5}\begin{bmatrix}\Delta v_d^G\\ \Delta v_q^G\\ \Delta P_l^*\\ \Delta v_{dc}^*\\ \Delta Q_{ac}^*\end{bmatrix} \tag{1.36b}$$

Note that for being allowed to linearize the dynamic model expressed generically in (1.14) in the classical state-space form of LTI models in (1.26) it is mandatory to know the steady-state condition given by $(\boldsymbol{x_0}; \boldsymbol{u_0})$. Moreover, the LTI model from (1.26) is an *approximation* of the non-linear model around the operating point $(\boldsymbol{x_0}; \boldsymbol{u_0})$. The range of validity of the LTI model depends on the degrees of non-linearity of the studied non-linear system. To assess the validity of the LTI model on a range of operating points, time domain simulations and comparisons of the LTI and Simulation models are needed (See Fig. 1.1).

LTI time-domain model validation

The resulting LTI model of the single-terminal *2-level* VSC with the DC capacitor C_S from (1.36) is compared against the non-linear model with SSTI solution from Fig. 1.12 in time-domain simulation. A DC power reference change from $P_l^* = 1$ pu to 0.8 pu at 50 ms is simulated, while maintaining the reactive power reference Q_{ac}^* at 0 pu. At $t = 350$ ms, a change on DC voltage reference v_{dc}^* is applied from 1 pu to 1.05 pu at $t = 350$ ms. The comparison results are shown in Fig. 1.13. Note that the operating point is added to the dynamic simulation of the LTI model, since this one deals only with the variable deviations [58].

As observed in the comparison, results from both models are acceptably similar. As long as the perturbation is small (i.e. the system remains in the proximity of the starting point defined by $\boldsymbol{x_0}$ and $\boldsymbol{y_0}$), the LTI model replicates accurately the dynamics of the non-linear SSTI model.

Linear analysis of LTI models

One of the main purposes of obtaining the LTI model is that the vast theory available for dynamic linear systems can now be applied. For instance, it is possible to calculate the eigenvalues of the $\boldsymbol{A}$ matrix (also called "modes") which provide valorous information about the system dynamics [64]. The most important feature is that they provide a quick information about the stability of the system. If all the eigenvalues are placed in the Left-Hand Plane (LHP) of the "Real-Imaginary" plane (i.e. all the real parts of the eigenvalues are negative), the linear system is asymptotically stable. If at least one eigenvalue is placed in the Right-Hand Plane

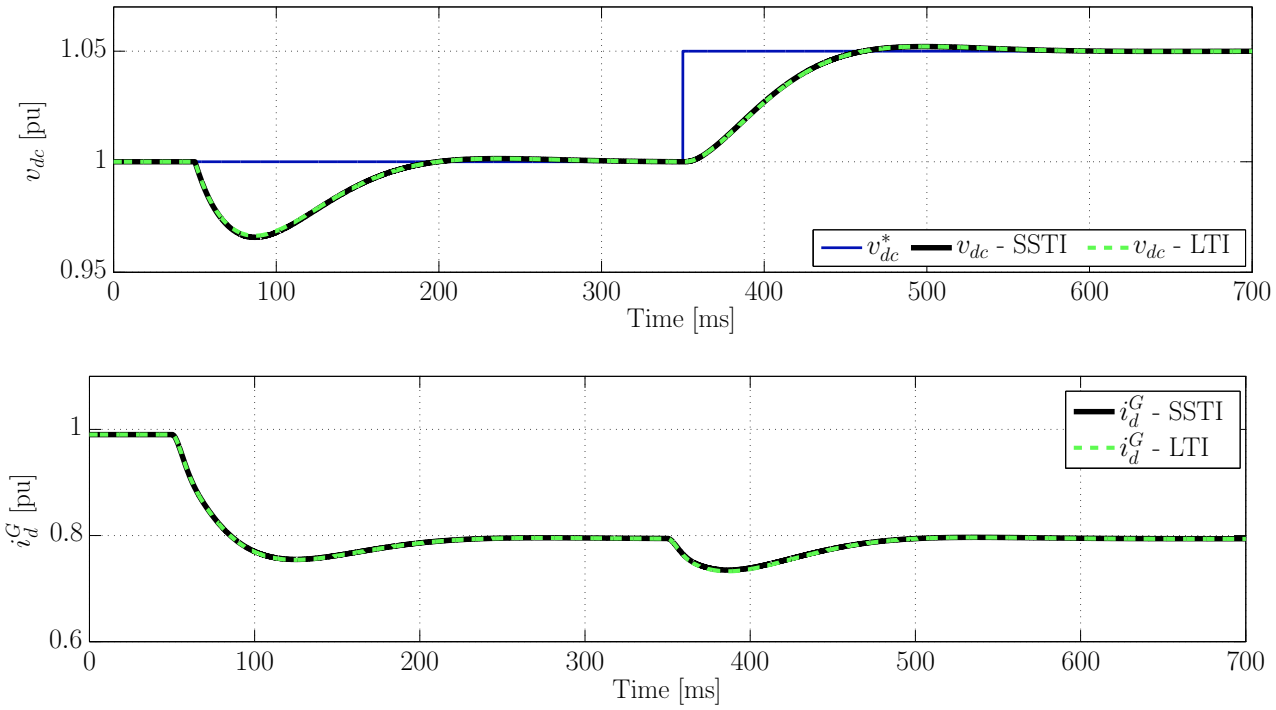

Figure 1.13 – Time domain validation of the LTI model of a *2-level* VSC with Open-loop control in *dq* frame – Small signal perturbation

(RHP), the system is unstable [84]. If the non-linear SSTI and the LTI model are close enough in terms of dynamic behavior, the stability properties of both systems are the same.

The eigenvalues λ of the $\boldsymbol{A}$ matrix from (1.35) are shown in Table 1.1 and plotted in Fig. 1.14 for gaining a faster representation of the system dynamics. In this figure, a gray triangle is marked which corresponds to the area where the eigenvalues have a damping equal or less to $\zeta = 0.7$. The dashed gray zone (positive real part) represents the unstable zone. Also, the figure highlights the reference eigenvalues obtained with the theoretical closed-loops simplified systems used for tuning the PI controllers (Fig. 1.6 for the inner current i^G controller, and Fig. 1.11 for the DC voltage (square) v_{dc}^2 controller).

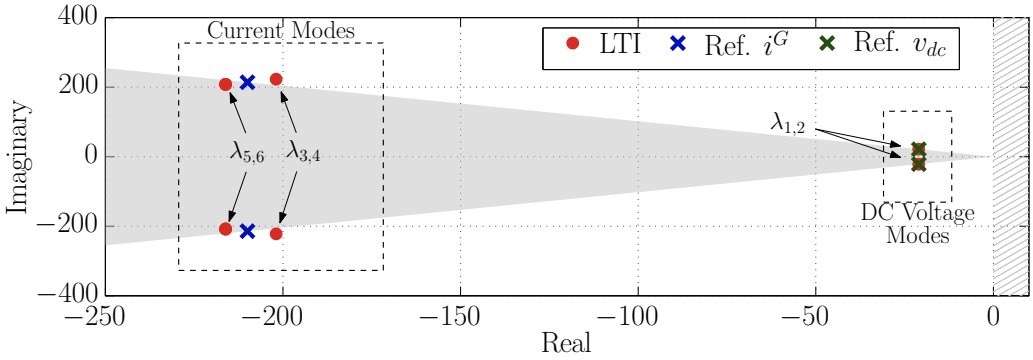

Figure 1.14 – Eigenvalues of LTI model of HVDC Link with *2-level* VSC

As seen in Fig. 1.14, the eigenvalues λ are grouped into two squares, denoting the modes associated with the current loops, and also the DC voltage modes. Due to the simplicity of the current example, the eigenvalues can be directly associated to the currents or voltages by visual inspection with respect to the reference eigenvalues. It is clear that the eigenvalues

Table 1.1 – Eigenvalues of $\boldsymbol{A}$ matrix from (1.35) - VSC connected to variable DC voltage

	Eigenvalue	Frequency ω_n	Damping ζ
$\lambda_{1,2}$	$-21.1444 \pm j20.923$	3.33	0.71082
$\lambda_{3,4}$	$-202.1045 \pm j229.1433$	36.4693	0.66147
$\lambda_{5,6}$	$-216.16 \pm j208.0261$	33.1084	0.72053

$\lambda_{1,2}$ are linked with the DC voltage since those eigenvalues overlap with the reference modes. The reference eigenvalues from the DC voltage controller are given in (1.37) (see (C.6) from Appendix C).

$$\lambda^{\text{Ref.}}_{\text{DC Voltage}} = \omega_n \left(-\zeta \pm \sqrt{\zeta^2 - 1}\right) = \underbrace{\frac{3}{\tau_{v_{dc}^2}}}_{100ms} \left(-0.7 \pm \sqrt{0.7^2 - 1}\right) = -21 + \pm j21.4243 \quad (1.37)$$

For verifying that $\lambda_{1,2}$ corresponds to the DC voltage, the participation factors can be calculated as detailed in [64,85], and the results are shown in Fig. 1.15. The participation factors technique relates each mode with the associated state variables. When the $\boldsymbol{A}$ matrix from the LTI system is diagonal-dominant (i.e. the states are mostly decoupled between them), the participation factors provide precise information about the system. For very coupled systems the information that can be obtained with these technique for certain eigenvalues is limited [85]. Nevertheless, this technique will be exploited in this Thesis for different LTI systems.

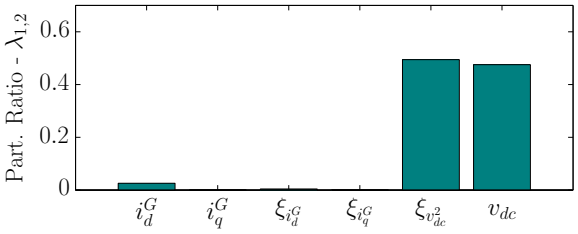

Figure 1.15 – Participation factors of eigenvalues $\lambda_{1,2}$ of LTI model of HVDC Link

Finally, the participation factors are calculated and shown in Fig. 1.16 for the rest of the eigenvalues. This figure verifies the eigenvalues inside the square with "Current modes" from Fig. 1.14. The reference eigenvalues from the current controllers are given in (1.38).

$$\lambda^{\text{Ref.}}_{\text{Currents}} = \omega_n \left(-\zeta \pm \sqrt{\zeta^2 - 1}\right) = \underbrace{\frac{3}{\tau_{iG^2}}}_{10ms} \left(-0.7 \pm \sqrt{0.7^2 - 1}\right) = -210 + \pm j214.243 \quad (1.38)$$

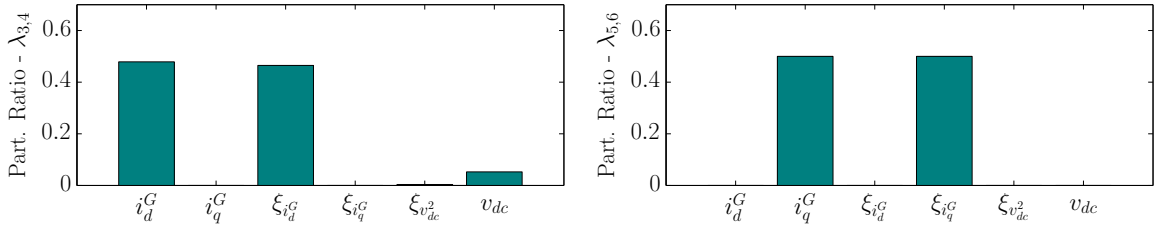

Figure 1.16 – Participation factors of eigenvalues λ_3 — λ_6 of LTI model of HVDC Link

1.3 Modeling, control and dynamic analysis of HVDC links with *2-level* VSC

In this section, an HVDC point-to-point connection with *2-level* VSC as depicted in Fig. 1.17 is considered. In this configuration, one converter is in charge of the power flow in the DC link (P-mode converter) and the other has the task of maintaining the DC voltage to the desired level (DC Voltage mode) [9]. This arrangement of control tasks between both converters is usually called "Master-Slave". For the sake of simplicity, the DC cable is considered as a pure capacitor C_{dc} in this section[6].

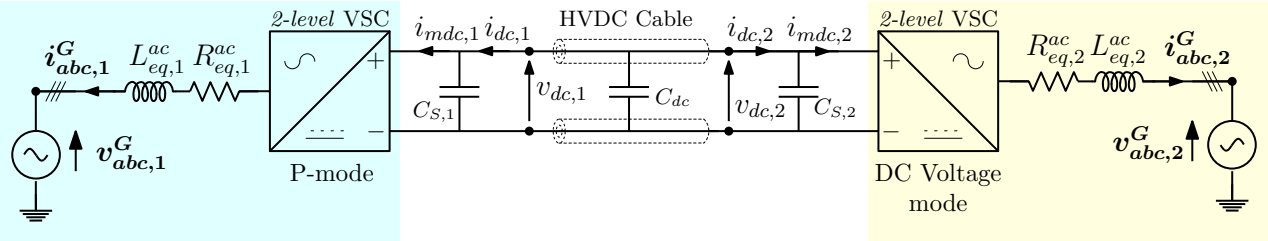

Figure 1.17 – Configuration of a VSC-based HVDC link

The mathematical model of each VSC in dq frame is given in (1.10) and for the sake of simplicity, the parameters of both converters are identical. Also, the dynamics of the simplified DC bus are given in (1.39):

$$\frac{dv_{dc}}{dt} = \frac{1}{C^{dc}_{eq}} \left(-i_{mdc,1} - i_{mdc,2}\right), \tag{1.39}$$

where,

$$C^{dc}_{eq} = C_{S,1} + C_{dc} + C_{S,2} \tag{1.40}$$

Note that the DC voltage dynamics are governed by a power balance in the DC grid, and the parameter associated to these dynamics is the equivalent capacitor C^{dc}_{eq}. The tuning of the DC voltage controller relies heavily on this parameter for having a good voltage regulation. As it will be discussed in Chapter 5, the equivalent capacitor C^{dc}_{eq} would have a great impact in MTDC grid dynamics and its determination is becoming challenging when converter are MMCs instead of *2-level* VSCs. In the next section, the discussion of the equivalent capacitor value is treated on a simplified HVDC point-to-point configuration to introduce this concept.

1.3.1 LTI model of the HVDC link: Concatenation of linear models

The HVDC link from Fig. 1.17 with the respective controllers can be expressed as a general block diagram as in Fig. 1.18. This figure highlights the relations "inputs-outputs" for the different sub-systems composing the non-linear HVDC link model with SSTI solution [9, 86]. This figure also shows how the complete LTI model is built from the concatenation of the linearized models of each VSC with the DC bus equation. The applied methodology is described in the Appendix B.2.

The different LTI models defined by Fig. 1.18 are linearized around an operating point defined by an active power transfer of 1 pu and a DC voltage level of 1 pu as well. The information on the operating point condition is listed in Table 1.2. It has to be noted that the model obtained from the aggregation of linear models is not strictly the same as the linearization

[6] In Chapter 5, more detailed cable models are used.

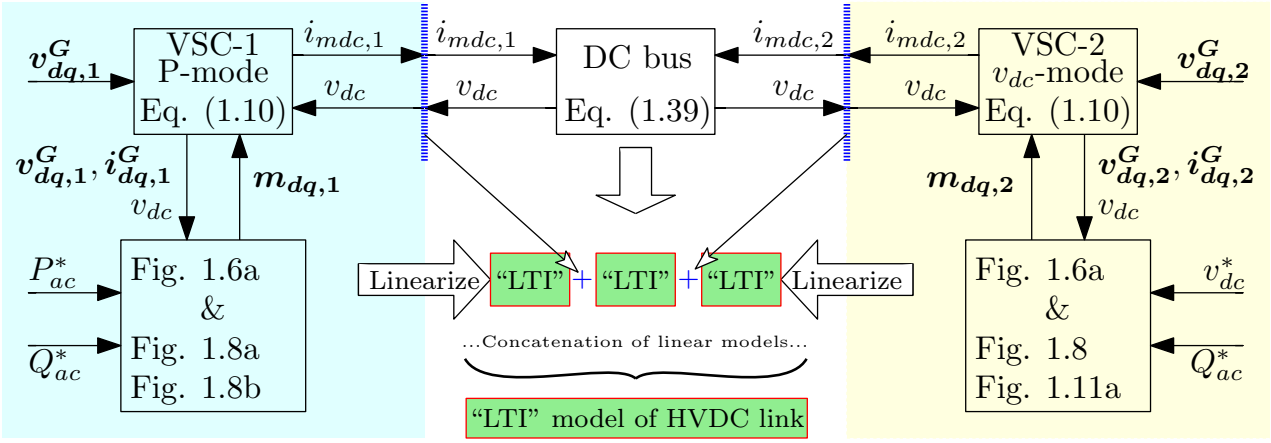

Figure 1.18 – Block diagram of non-linear model of an HVDC link with SSTI solution

of the complete non-linear model: the main difference is due to the degree of non-linearity of the SSTI system. In this case, since the non-linearity is not so important, the concatenation method is acceptable.

Table 1.2 – Operating point of HVDC link for linearization

Variable	Value	Variable	Value
$P_{ac,1}$	1 pu	$Q_{ac,1}$	0 pu
v_{dc}	1 pu	$Q_{ac,2}$	0 pu

The remaining variables defining the operating point of the system are obtained by solving the non-linear equations that results from setting the derivatives of the equations to zero in Fig. 1.18. The states of the complete HVDC link LTI model are listed in (1.41).

$$\boldsymbol{x_{hvdc}} = \left[i^G_{d,1}\ i^G_{q,1}\ \xi_{i^G_{d,1}}\ \xi_{i^G_{q,1}}\ i^G_{d,2}\ i^G_{q,2}\ \xi_{i^G_{d,2}}\ \xi_{i^G_{q,2}}\ \xi_{v^2_{dc}}\ v_{dc}\right]^\top \in \mathbb{R}^{10} \tag{1.41}$$

Time Domain Validation of LTI model

The LTI model is validated through time-domain simulations. Starting with the operating point defined in Table 1.2, a step on $P^*_{ac,1}$ of -0.2 pu is applied at 50 ms. Then, a step on $Q^*_{ac,1}$ of 0.1 pu is applied at 250 ms. Finally, the DC voltage reference v^*_{dc} is changed from 1 pu to 1.05 pu at 300 ms. In this simulation, two models are compared: the non-linear model (with VSCs average value models), which is denoted with "SSTI" in the legend; and the LTI model from the complete system, denoted as "LTI".

Results of the currents in dq frame for the VSC-1 (P-mode) are gathered in Fig. 1.19 where it can be noticed that the LTI model reproduces accurately the dynamics of the SSTI system. Moreover, a perfect decoupling between the currents in the d and q axes can be achieved.

The results of the DC bus voltage is shown in Fig. 1.20, where both models give similar results. At the moment of the AC power step on the VSC-1, a power imbalance in the DC capacitor C^{dc}_{eq} occurs, so the voltage tends to vary. The DC voltage controller adapts the AC power of VSC-2 for reestablishing the power balance in the DC bus. At $t = 300$ ms, the voltage follows the reference step applied with the 100 ms of response time.

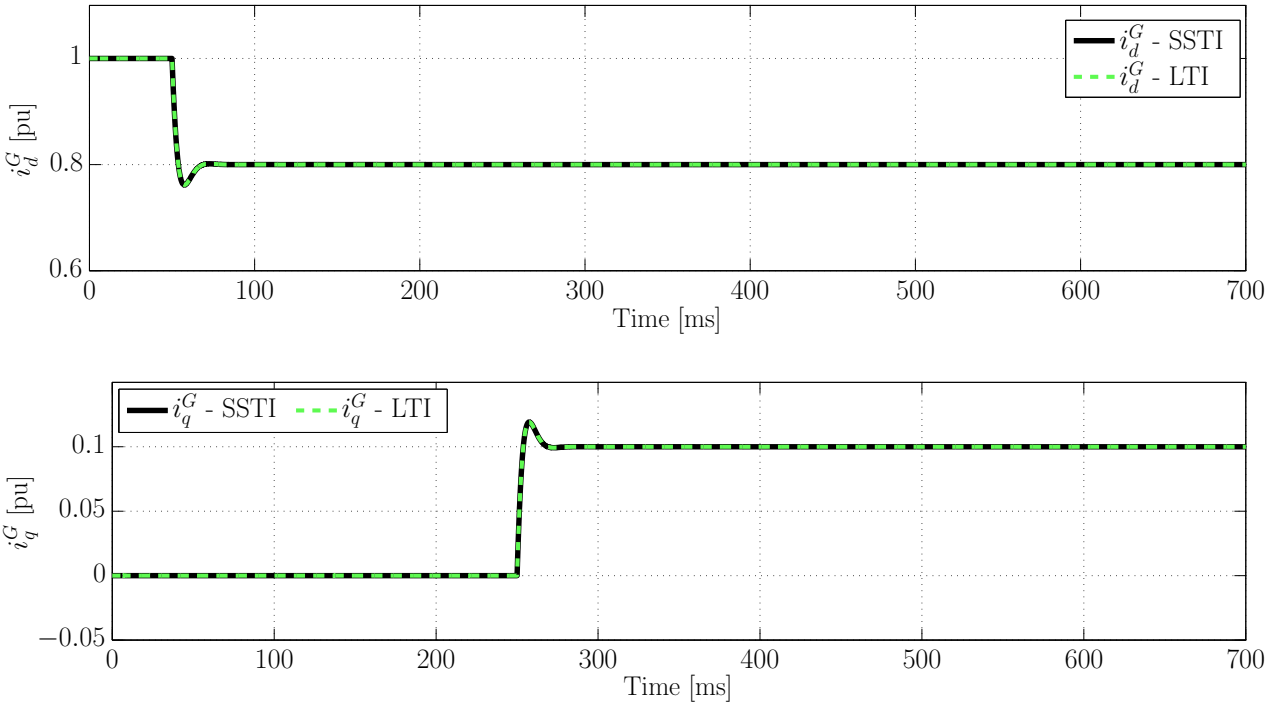

Figure 1.19 – Time domain validation of the LTI model of HVDC Link with *2-level* VSC — Grid currents of VSC-1 (P-mode)

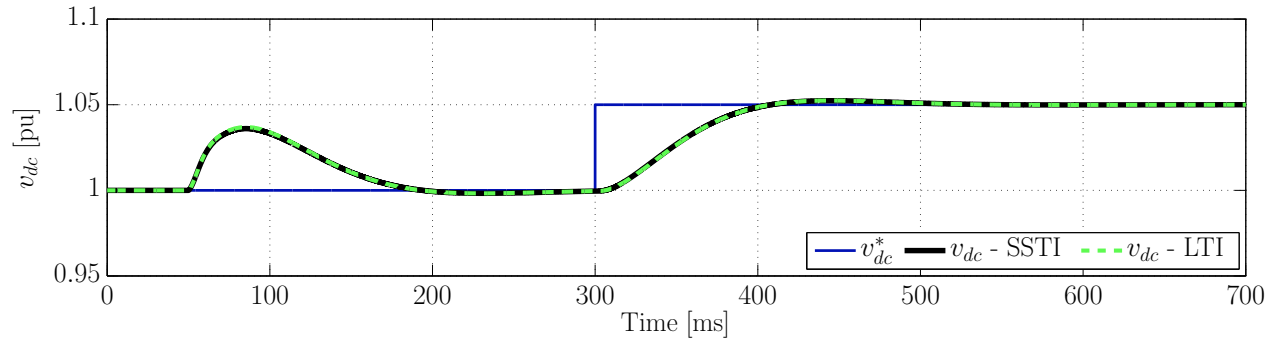

Figure 1.20 – Time domain validation of the LTI model of HVDC Link with *2-level* VSC — DC Voltage

As it was shown in Figs. 1.19 and 1.20, the LTI model reproduces accurately the dynamics of the non-linear model. It is recalled that the intention of this Chapter is to highlight the methodology followed in this Thesis, without too much attention on the analysis of the results.

1.3.2 Linear analysis of HVDC link LTI model

Once the LTI model is validated, the eigenvalues are calculated for studying the dynamics of the system and, most importantly, its stability. The eigenvalues for the HVDC link example of this section are shown in Fig. 1.21. Also, the figure highlights the reference eigenvalues obtained with the theoretical closed-loops simplified systems used for tuning the PI controllers as the approach followed in the single-terminal VSC station in Fig. 1.14.

Due to the simplicity of the current example, the eigenvalues can be related to the system states by simple inspection of Fig. 1.21, however, the participation factor analysis is used as

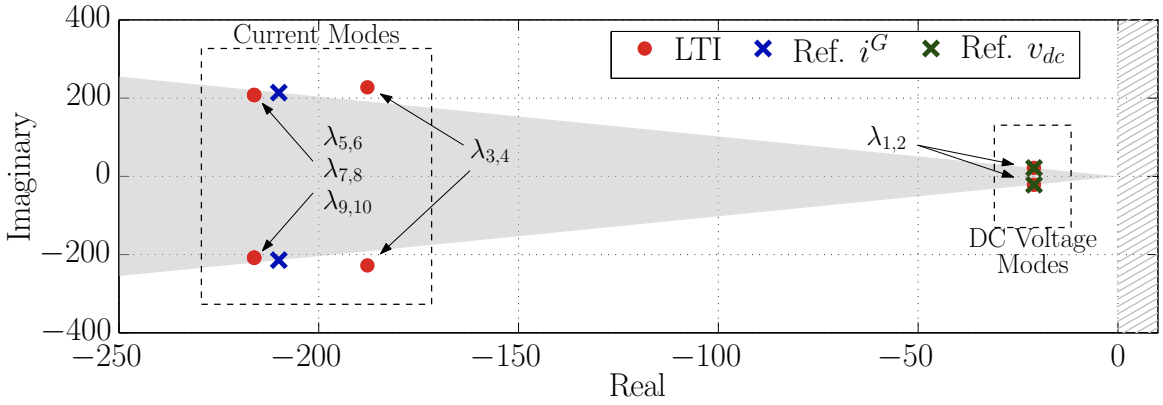

Figure 1.21 – Eigenvalues of LTI model of HVDC Link with *2-level* VSC

in Section 1.2.4 for validating the intuitive deductions. At the top of Fig. 1.22, results of the participation factors for the eigenvalues $\lambda_{1,2}$ are shown, which are related to the DC voltage closed loop control and its controlled state, as it was suspected from Fig. 1.21. Finally, the participation factors are calculated and shown in Fig. 1.22 for the rest of the eigenvalues. This figure verifies the eigenvalues inside the square with "Current modes" from Fig. 1.21.

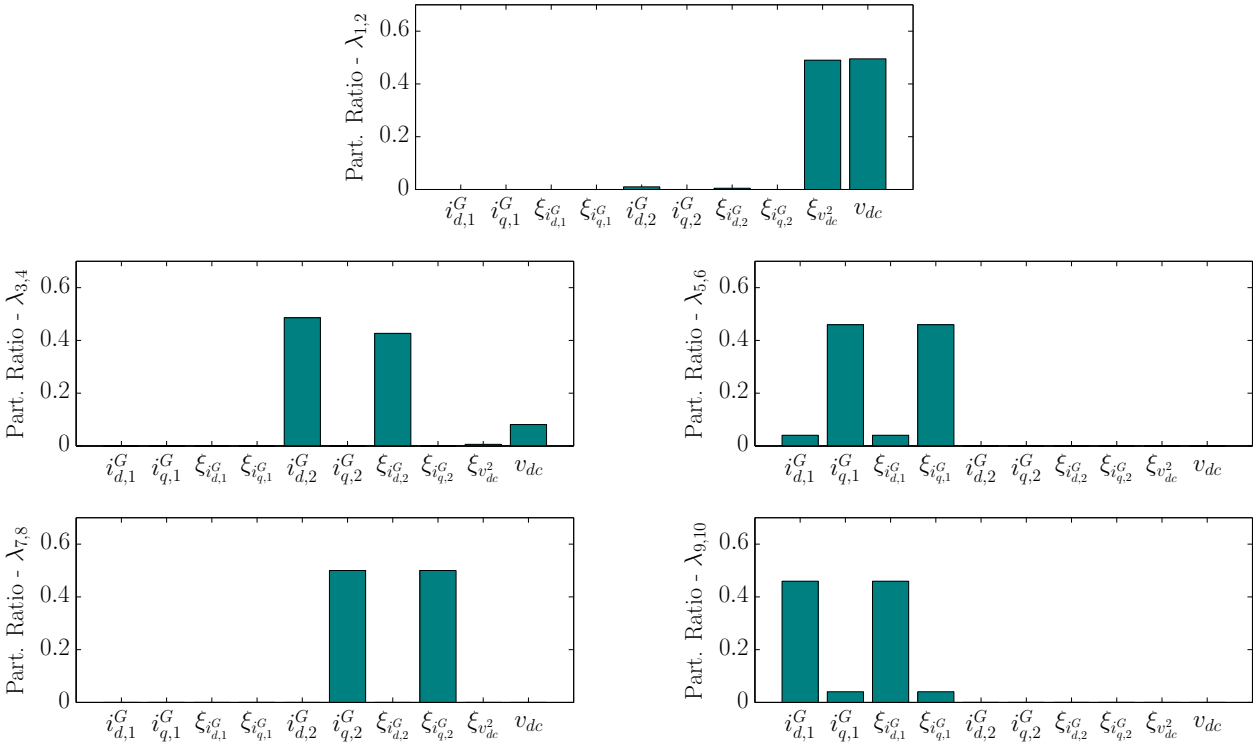

Figure 1.22 – Participation factors of eigenvalues λ_1 — λ_{10} of LTI model of HVDC Link

In this section the HVDC link with *2-level* VSC was presented and linearized for obtaining the LTI model of the overall system. Once that the LTI model was verified, the dynamics are analyzed with the eigenvalues and the participation factors. The system considered is relatively simple, but it allows to highlight the main key points of the system: the equivalent DC capacitor C^{dc}_{eq}, which governs the DC voltage dynamics in conjunction with the DC voltage controller.

1.4 Modeling, control and dynamic analysis of MTDC grids with *2-level* VSC

As it was stated in the Introduction, the MTDC grids are composed by at least three converters connected to the same HVDC grid. With VSC converters, the studies of MTDC grids become very popular and many publications can be found on this topic [67]. The aim of this section is to summarize the main key elements of the MTDC grids with VSCs [74].

For understanding the main phenomenons in DC grids, an analogy with classical AC grids is fruitful [58, 87]. AC system dynamics are characterized by the kinetic energy stored in synchronous rotating machines connected to it. For DC systems, the energy is stored under an electrostatic form since it corresponds mainly to the energy stored in converter station capacitors (and in the core-to-screen capacitor of DC cables, to a certain extent), as expressed in (1.42).

$$E_c = \frac{1}{2} C_s {v_{dc}}^2, \tag{1.42}$$

where C_s is the converter station capacitor value (in F) and E_c is the energy stored in a converter station capacitor (in J). In DC systems; the electrostatic energy stored in the substations capacitor can be weighted by the substation base power P_n. This leads to an electrostatic constant H_c which is homogeneous to a time as shown in (1.43).

$$H_c = \frac{1}{2} C_s \frac{{v_{dc}}^2}{P_n}, \tag{1.43}$$

where P_n is the nominal power of the converter station (in W) and H_c is the electrostatic constant (in s). For HVDC converters stations H_c is in the order of 30 ms to 40 ms, which is a very small value compared to conventional unit inertia constant (3 s up to 10 s) [64]. This means that the dynamics involved in DC systems are much faster than the ones in classical AC systems.

One of the main concerns in MTDC systems is the control of the DC bus voltage and the power flows inside the grid. Several works were focused on the coordinated control of the power dispatch of MTDC grids [**88**], basically oriented in power flow calculations for generating the DC power and voltage references for each converters. These controllers rely heavily on the communication between the converters and a master control unit which calculates the appropriated references [89]. This aspect of the MTDC grids is not covered in this Thesis. Nevertheless, the control and dynamics of the DC bus voltage is of interest.

For improving the reliability of MTDC grids, the control of the DC voltage should be performed without relying on external communications. Therefore, the converters involved on this task should only utilize the local measures at its Point of Common Coupling on its DC side (PCC-DC). As for HVDC links, the "Master-Slave" strategy can be used, where only one converter is in charge of fixing the voltage level at its DC endpoint. However, if this converter is lost (e.g. due to an external AC fault), the DC voltage is no more controlled. In this way, MTDC system has a high risk of collapsing if no other action is taken. To avoid this drawback, it is expected that several converters will share the DC voltage control efforts. In the following section, the most typical controller of the DC voltage on MTDC grids is introduced: the DC voltage droop method.

1.4.1 DC Voltage distributed control: DC Droop Control

The voltage droop method is inspired by the primary frequency control [87]. In AC systems, to maintain the balance between production and demand, some production units are equipped by a controller which regulates their output power according to the frequency by following a power-frequency characteristic which is commonly called droop control [90]. As said in the previous section, the frequency counterpart in the DC system is the DC voltage level, hence following the same principle the power flow can be controlled by a Power-Voltage droop as:

$$\Delta p_{dc} = -\frac{1}{k_{dr}} \left(v_{dc}^{*} - v_{dc}\right) \tag{1.44}$$

where k_{dr} is the droop value (in V/W or pu/pu), Δp_{dc} is the deviation power injected into the DC grid (in W or pu) and Δv_{dc} is the deviation of the DC voltage (in V or pu). This controller, shown in Fig. 1.23, is adopted in conjunction with the AC active power controller from Fig. 1.8a, where it is assumed that $P_{ac} \approx P_{dc}$.

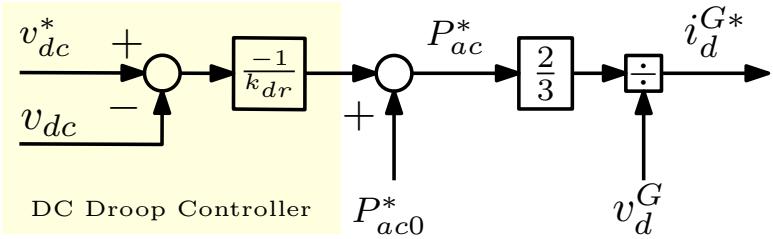

Figure 1.23 – DC Voltage droop controller

This method increases the reliability and reduces the stress on the DC system [91], however, due to the proportional controller; the DC voltage level is not strictly maintained at the reference value if a transient behavior occurs. Nevertheless, this can be amended by an external master controller to re-adapt the converter set-points [58, 74]. It should be noted that in this Thesis it is preferred the droop controllers which generate a new power reference, instead of a DC current reference [57, 92, 93]. The reason is that with the DC current approach there is a risk of multiple operating points in the DC grid when a disturbance occurs, and some of them may be unstable as described in [94].

The choice of the droop gain k_{dr} requires special attention. The most common-practice is to set the droop-gain following steady-state considerations (i.e. setting a maximum steady-state possible deviation of DC voltages and power injections, and then calculate the droop parameters as it will be demonstrated in the following section). This choice may conduct to undesired oscillations and interactions in the DC grid during transients. For this reason, in [95] and [69] it is proposed to study the linear models of the MTDC grids for sizing the droops taking into account the systems dynamics. The dynamic impact of the droop gains will be exploited along this Thesis.

There is a wide range of other techniques for achieving the same distributed voltage control in the literature [96]. In the following, a short description on the main methods is given:

- *Voltage margin method:* This method can be considered as an extension of the master-slave method: the master role may be successively devoted to different substations depending on the level of power in each station [74, 97].
- *Dead-band droop method:* The dead-band droop control is a mix between the voltage margin method and the droop voltage method [98, 99]. With low power deviations the

balance role is assumed by the stations which are classically droop controlled, but for severe deviations, when the DC voltage reaches a first critical limit, stations which were initially constant power controlled switch to droop control to support the DC voltage and contribute to the balance effort [100]. This method is well adapted for wind farms, in this way the wind farms produce power delivered by wind in normal operation and help to the power balance when the DC voltage is outside the bounds.

- *Piece-wise droop method:* The piece-wise droop method is also called undead-band droop control and has firstly been presented in [101]. This method is based on piecewise droop characteristics; it enables to define different droop values according to the voltage level, i.e. for small and large power deviations. This method seems interesting for on-shore converters, since the DC voltage operating range can be limited [102].
- *Advanced droop methods:* In [103] it is proposed an advanced controller with droop mechanism for linear relation between power and square of the DC voltage. In this way, the energy of the converter is taken into account in the control design. For improving the DC voltage dynamics, in [104] it is proposed to add lead-lag compensations in addition to the proportional droop controller. The authors of [105] propose a novel scheme for adapting the droop coefficients to share the burden according to the available headroom of each converter station. Finally, in [106] it is proposed a continuous non-linear P-v_{dc} relation instead of a simple linear correlation. However, this kind of advanced droop techniques requires a perfect knowledge of the HVDC system and parameters for a proper tuning, which is not always the case.

In this Thesis, only the droop controller shown in Fig. 1.23 is considered since advanced droop methods may be not being considered by TSO and market players because it is difficult to determine the power flows in advance. However, the other methods can be treated similarly with the methodology presented in this Thesis providing small adaptations.

1.4.2 Simplified dynamic analysis of droop-controlled MTDC grids

In this section, a simplified analysis of an MTDC grid is performed with the objective of highlighting the main key parameters of the system. For this task, let us first consider the MTDC system with N_c VSCs from Fig. 1.24. The first N_d converters are in DC voltage droop control mode (left side converters in Fig. 1.24), while the rest $(N_c - N_d)$ are controlling the power into the DC grid (right side converters in Fig. 1.24). A strong assumption is made on the DC grid at this point: all DC cables are represented by a single equivalent capacitor C_{dc}. Even though the lossless DC grid assumption may conduct to different results from the detailed models [107], the intention is to deduce simple formulations for understanding the key elements governing the MTDC grid dynamics.

The general model of the VSCs has been simplified as follows [74]:

- Suppression of all parts related to reactive power control.
- The dynamics of the current loops are neglected, set at unitary gain.
- The active power at the AC side becomes equal to the active power at the DC side for each converter, as expressed in (1.45).

$$P_{mdc,j} = P^*_{ac,j} = v_{dc} i_{mdc,j}. \tag{1.45}$$

Due to the non-linearity of (1.45), a deviation model is derived as follows:

$$\Delta P_{mdc,j} = \Delta v_{dc} i_{mdc,j0} + v_{dc0} \Delta i_{mdc,j}, \tag{1.46}$$

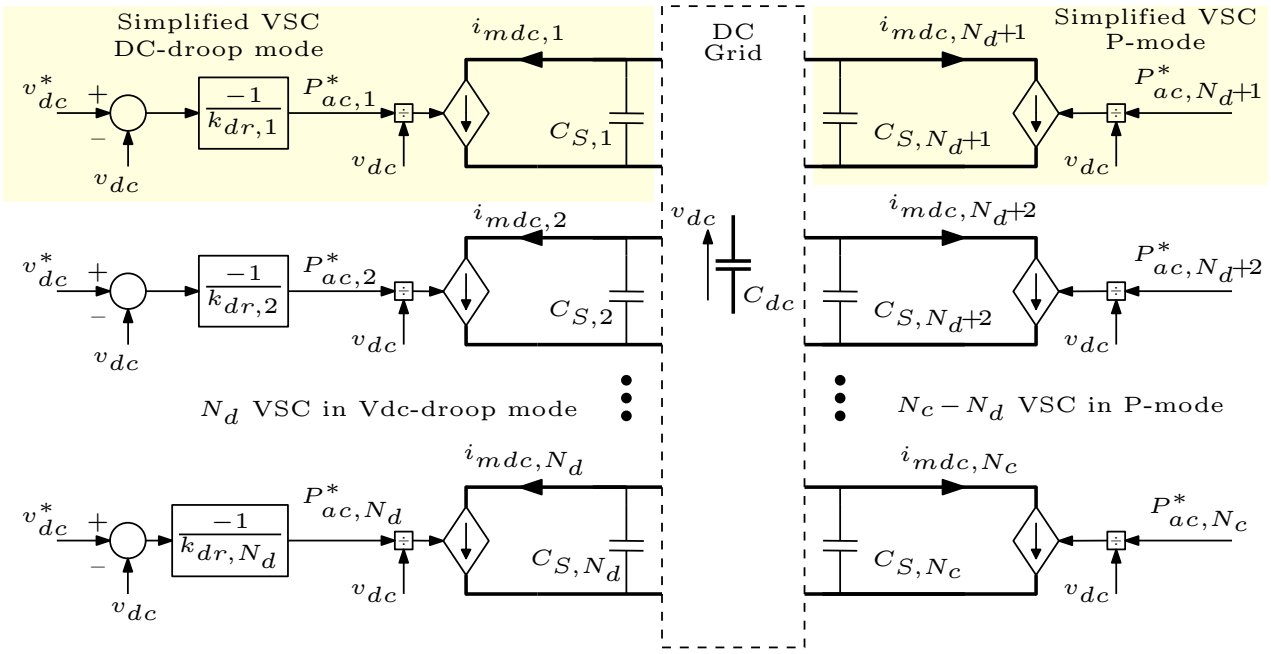

Figure 1.24 – Simplified MTDC grid with droop controlled VSCs

where the variables with Δ denote small deviations, the variables with subscript $_0$ represent the operating point and j corresponds to the index of each VSC.

From (1.46), the linear VSC model can be obtained as shown in Fig. 1.25, where P_n and v_{dcn} are the power and DC voltage base of the converter. Note that the quantities outside the dashed box are in per-unit system (pu) and the droop parameter k_d has no units.

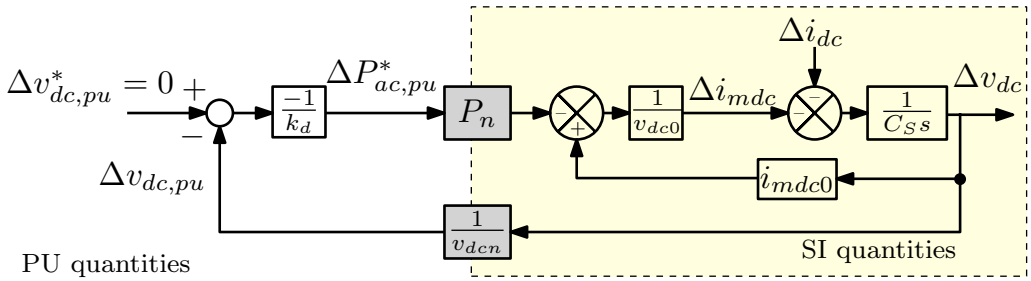

Figure 1.25 – Linearized VSC-MMC model – SI quantities inside the dashed box and PU quantities outside the dashed box

Applying the same concept of equivalent DC capacitance C_{eq}^{dc} from the previous section, the equivalent DC grid capacitance of the MTDC grid C_{mtdc} can be represented by (1.47).

$$C_{mtdc} = C_{dc} + \sum_{j=1}^{N_c} C_{S,j}, \tag{1.47}$$

As the grid is simplified, the DC voltage is the same for all the converters, and considering (1.45) for each VSC; the DC bus dynamics are given by (1.48).

$$C_{mtdc}\frac{dv_{dc}}{dt} = \sum_{j=1}^{N_c} i_{mdc,j} \approx -\frac{1}{v_{dc}}\sum_{j=1}^{N_c} P_{ac,j}^{*}. \tag{1.48}$$

Considering (1.46), the linearization of (1.48) yields:

$$C_{mtdc}\frac{d\Delta v_{dc}}{dt} = -\frac{1}{v_{dc0}}\sum_{j=1}^{N_c}\left(\Delta P^*_{ac,j} - \Delta v_{dc} i_{mdc0,j}\right). \tag{1.49}$$

The power balance is expressed by the sum of substations output power. At an equilibrium point this sum must be null if the losses are neglected. Moreover, since the voltage drops are also neglected, the sum of out-coming currents into the simplified DC grid is null. This leads to considerably simplify the model with:

$$\sum_{j=1}^{N_c} i_{mdc0,j} = 0. \tag{1.50}$$

Using the simplified model of droop controlled station from Fig. 1.25, the linearized model of the MTDC grid is represented in Fig. 1.26. The voltage deviation reference Δv^*_{dc} is equal to zero for the droop controlled converters.

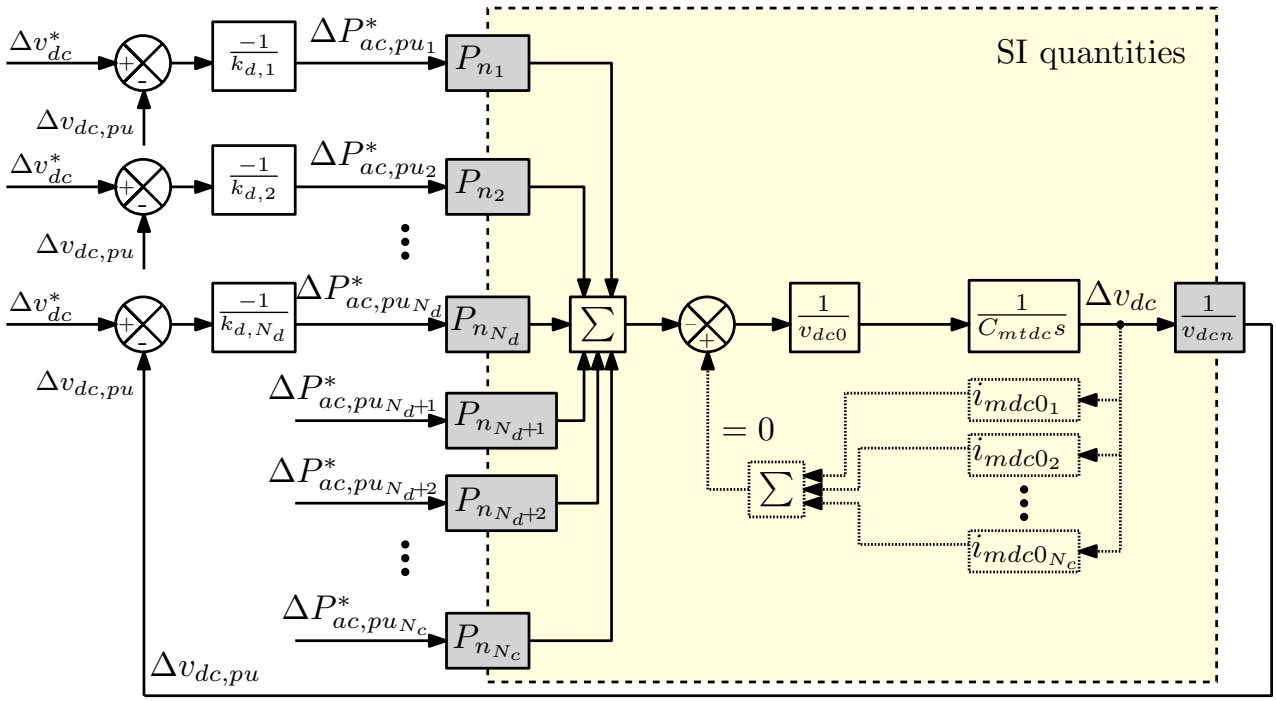

Figure 1.26 – Simplified model of the N_c-terminal MTDC grid – SI quantities inside the dashed square; PU quantities outside the dashed square

From the block diagram of Fig. 1.26, the DC voltage deviation which occurs after a power change in the VSC j can be defined by the following first order transfer function:

$$\Delta v_{dc,pu} = -\frac{\frac{1}{\left(\sum_{j=1}^{N_d}\frac{P_{n,j}}{k_{d,j}}\right)}}{1 + \frac{v_{dc0}v_{dcn}C_{mtdc}}{\left(\sum_{j=1}^{N_d}\frac{P_{n,j}}{k_{d,j}}\right)}s}\frac{P_{n,j}}{v_{dcn}}\Delta P^*_{ac,j_{pu}}. \tag{1.51}$$

Simplification with equally rated converters

For the sake of understanding, it is now assumed that power ratings are the same for each converter. Moreover, all droop parameters are set to an equal value k_d, and the initial value of v_{dc} is equal to its nominal value (i.e. $v_{dc0} = v_{dcn}$). Taking into account the aforementioned considerations, (1.51) is simplified as follows:

$$\Delta v_{dc,pu} = -\frac{\frac{k_d}{N_d}}{1 + \frac{k_d}{N_d}\frac{C_{mtdc}v_{dcn}^2}{P_n}s}\Delta P^*_{ac,pu_j}. \tag{1.52}$$

The time for $\Delta v_{dc,pu}$ to reach 95% of the final value for a step in $\Delta P^*_{ac,pu_j}$ is given by (1.53).

$$\tau_{v_{dc,mtdc}} = 3 \times \frac{k_d}{N_d} C_{mtdc}\frac{v_{dcn}^2}{P_n}. \tag{1.53}$$

Thus, for a given number of droop controlled stations N_d, the final value of the DC voltage with respect to a power variation in the grid is directly provided by the numerator of (1.52), which is function of the droop value k_d and the number of converters N_d which participate to the voltage control [74]. Moreover, the voltage dynamics depends not only on k_d, but also on the equivalent capacitance of the DC grid (C_{mtdc}). This capacitance does not affect the steady state voltage deviation.

1.4.3 LTI Model of a simplified MTDC grid

In this section, the LTI model of a four terminal MTDC grid with *2-level* VSC (i.e. $N_c = 4$) as shown in Fig. 1.27 is evaluated. It is considered that the converters VSC-1, VSC-2 and VSC-3 are droop controlled (i.e. $N_d = 3$). The droop gain is set equally for the three converters, with value k_d (in pu). The converter VSC-4 is attached to a Wind-Farm and it is modeled as a simple power-injector to the MTDC grid [95].

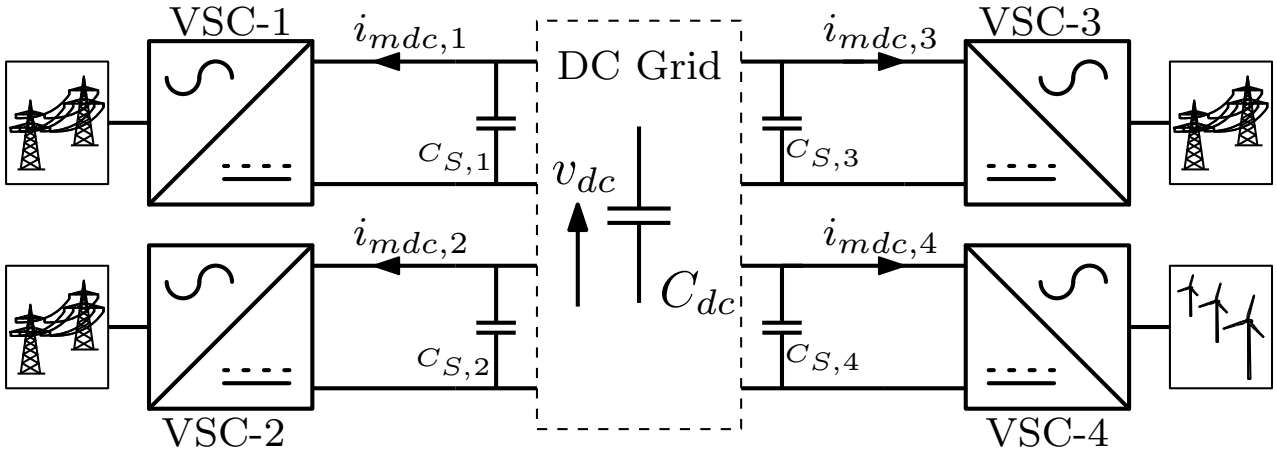

Figure 1.27 – Four terminal MTDC grid with *2-level* VSC

The MTDC grid from Fig. 1.27 is expressed as a block diagram in Fig. 1.28. This figure highlights the connections of the different models considered at this point.

Considering the state-equations from Fig. 1.28, it is possible to apply the Jacobian linearization explained in Section 1.2.4 to obtain the general state-space system of the MTDC grid as expressed in (1.54), where the vector of states is given in (1.55) and the inputs in (1.56). The

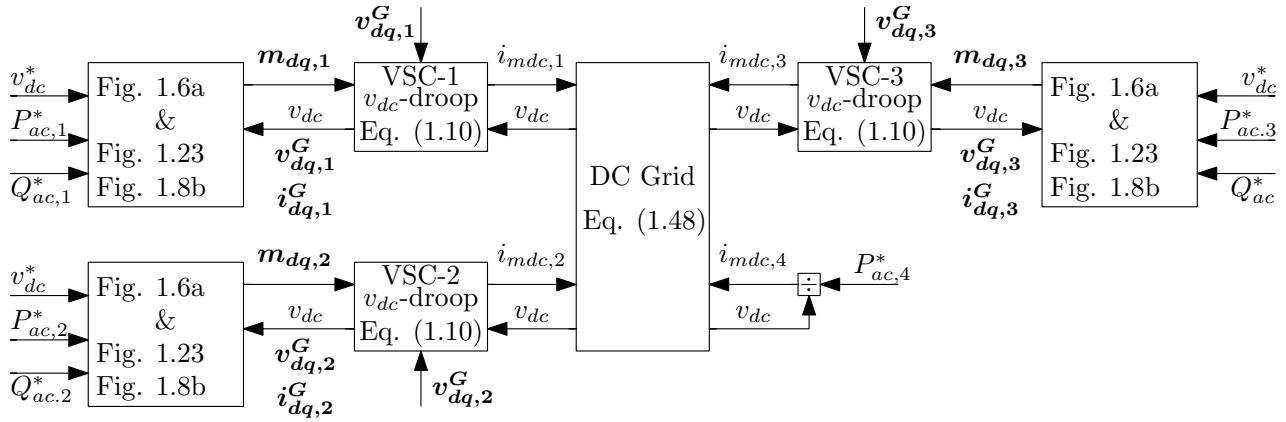

Figure 1.28 – Mathematical model of four terminal MTDC grid with *2-level* VSC from Fig. 1.27

matrices $\boldsymbol{A_{mtdc}}$, $\boldsymbol{B_{mtdc}}$, $\boldsymbol{C_{mtdc}}$ and $\boldsymbol{D_{mtdc}}$ are obtained with the same approach followed for the HVDC point-to-point scheme from previous Section, i.e. the complete LTI model of the MTDC grid is obtained by the concatenation of the linearized models of each VSC with the routine detailed in [9].

$$\Delta\dot{\boldsymbol{x}}_{\boldsymbol{mtdc}} = \boldsymbol{A_{mtdc}}\Delta\boldsymbol{x_{mtdc}} + \boldsymbol{B_{mtdc}}\Delta\boldsymbol{u_{mtdc}} \tag{1.54}$$

$$\boldsymbol{x_{mtdc}} = \left[\boldsymbol{i_{dq,1}^G}\ \boldsymbol{\xi}_{\boldsymbol{i_{dq,1}^G}}\ \boldsymbol{i_{dq,2}^G}\ \boldsymbol{\xi}_{\boldsymbol{i_{dq,2}^G}}\ \boldsymbol{i_{dq,3}^G}\ \boldsymbol{\xi}_{\boldsymbol{i_{dq,3}^G}}\ v_{dc}\right]^\top \in \mathbb{R}^{13} \tag{1.55}$$

$$\boldsymbol{u_{mtdc}} = \left[P_{ac,1}^*\ Q_{ac,1}^*\ P_{ac,2}^*\ Q_{ac,2}^*\ P_{ac,3}^*\ Q_{ac,3}^*\ P_{ac,4}^*\ v_{dc}^*\ \right]^\top \in \mathbb{R}^8 \tag{1.56}$$

In the following sub-section the linearized model of the four-terminal MTDC grid is validated via time-domain simulations.

Time domain validation of MTDC LTI model

The linear model from (1.54) is compared with the non-linear model from Fig. 1.28 via a time domain simulation. The response times for the current controllers τ_{iG} are set to 10 ms for the converters VSC-1, VSC-3 and VSC-3. The initial operating point is given in Table 1.3, where the nominal power P_n is 1GW.

Table 1.3 – Operating point of the four-terminal MTDC grid with *2-level* VSCs

Variable	Value	Variable	Value	Variable	Value	Variable	Value
$P_{ac,1}$	-0.3 pu	$P_{ac,2}$	0.49 pu	$P_{ac,3}$	0.8 pu	$P_{ac,4}$	-1 pu
$Q_{ac,1}$	0 pu	$Q_{ac,2}$	0 pu	$Q_{ac,3}$	0 pu	v_{dc}	1 pu

The value of droop parameter k_d is calculated based on the numerator of (1.52), which is shown in (1.57). The gain k_d is calculated based on a $N-1$ condition, where it is admitted that one converter may be suddenly lost, causing a deficit of power in the DC grid of 1 pu (i.e. 1 GW).

$$\Delta v_{dc} = \pm 0.05 \text{ pu} = -\frac{k_d}{3}\underbrace{\Delta P_{ac,pu_j}^*}_{=1 \text{ pu}} \rightarrow k_d = 0.05 \times 3 = 0.15 \text{ pu}. \tag{1.57}$$

The values of the DC capacitance for each VSC is considered to be the same for simplicity, and their values are listed in Table 1.4, where the value of the considered C_{dc} is also given.

The value of C_S of each converter corresponds to an electrostatic constant of $H_C = 40$ ms, which is a typical value for HVDC converters [74].

Table 1.4 – DC Capacitor values of *2-level* VSCs and DC grid

Variable	Value	Variable	Value
$C_{S,1} = C_{S,2} = C_{S,3} = C_{S,4}$	195.31 μF	C_{dc}	32.55 μF

The theoretical response time $\tau_{v_{dc,mtdc}}$ of the four-terminal MTDC grid can be calculated based on (1.53), with the parameters from Table 1.4, and considering that $v_{dcn} = 640$ kV, and $P_n = 1$ GW. The calculation of $\tau_{v_{dc,mtdc}}$ is then given as:

$$\tau_{v_{dc,mtdc}} = 3 \times \frac{k_d}{N_d} C_{mtdc} \frac{v_{dcn}^2}{P_n} = 3 \times \frac{0.15\text{pu}}{3} 813.80\ \mu\text{F} \frac{(640\ \text{kV})^2}{1\ \text{GW}} = 50\ \text{ms} \tag{1.58}$$

Starting with a power flow as shown in Table 1.3, a step on $P^*_{ac,4}$ of 0.8 pu is applied at $t = 50$ ms. The final voltage can be easily calculated from (1.57), as $\Delta v_{dc} = -(0.15/3) \times 0.8 = -0.04$ pu. The steady state error on the DC voltage is directly related to the droop gain k_d and the amplitude of the perturbation $P_{ac,4}$. Results are shown in Fig. 1.29. In Fig. 1.29a the response of the DC voltage v_{dc} is given, where the legend "SSTI" corresponds to the non-linear model from Fig. 1.28, "LTI" is the model from (1.54) and "Simp." is the simplified model from (1.52). As it can be observed, it is not possible to distinguish any difference between the three models, validating the 50 ms of response time as predicted in (1.58).

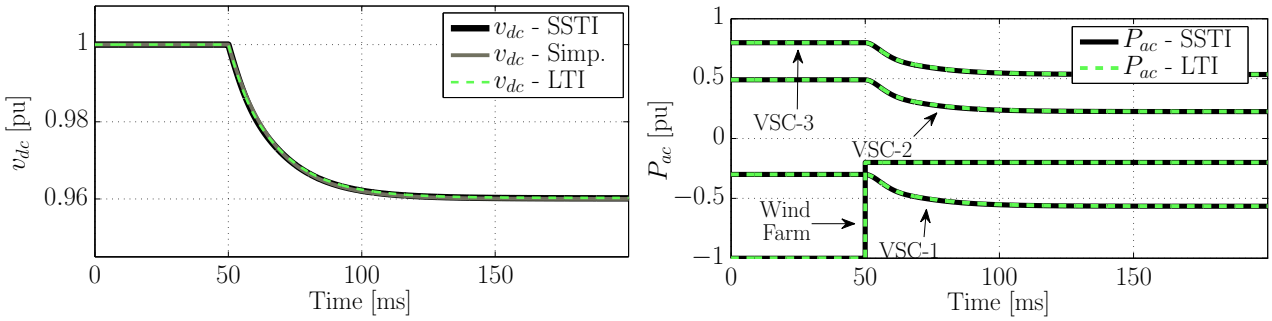

(a) DC Voltage (b) AC Powers

Figure 1.29 – Simulation results of a four-terminal MTDC grid with *2-level* VSC

In Fig. 1.29b, the results for the active power are shown. The three converters equipped with the droop controller change their active power in the same amount since their droop values are equal.

Dynamic analysis of MTDC LTI model

After the time-domain validation of the LTI model, the eigenvalues of the system are calculated and shown in Fig. 1.30. The reference eigenvalues of the closed-loop for the current controllers are close to the predicted eigenvalues (blue crosses). The pole from the simplified formulation from (1.52) (with the legend "Simp.") is also shown in this figure. As it can be seen, there is one real pole from the "LTI" system which is very close to the predicted pole with the simplified formulation, as it was expected due to the close match of the time-domain results.

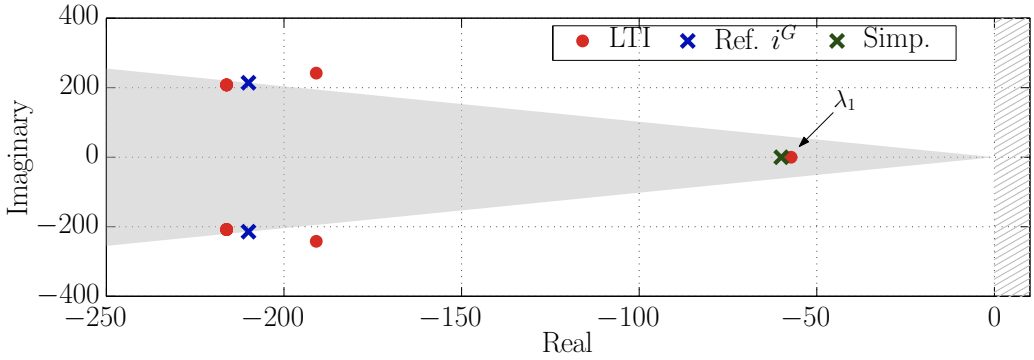

Figure 1.30 – Eigenvalues of LTI model of HVDC Link with *2-level* VSC

The participation factors for the real eigenvalue λ_1 is shown in Fig. 1.31. As it was expected, the graphic shows that the state with more participation on this mode corresponds to the DC voltage v_{dc}.

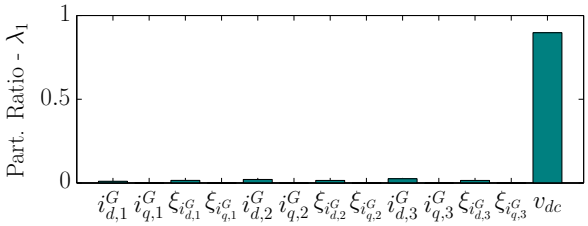

Figure 1.31 – Participation factors of LTI model of four-terminal MTDC grid - λ_1

To evaluate the range of validity of the simplified model, three different parametric variations are performed to the LTI system. First, in Fig. 1.32a, the droop gain k_d is varied from 0.2 pu down to 0.05 pu (this last value corresponds to a voltage deviation of 0.0167 pu for a DC power mismatch of 1 pu). Second, in Fig. 1.32b the electrostatic constant H_{mtdc}, which is defined in (1.59), is varied from 166.66 ms down to 16.66 ms. The value of $H_{mtdc} = 166.66$ ms corresponds to the capacitance values from Table 1.4. Finally, in Fig. 1.32c, the response times for VSC-1, VSC-2 and VSC-3 are varied from $\tau_{i^G} = 5$ ms up to 20 ms.

$$H_{mtdc} = \frac{1}{2} C_{mtdc} \frac{v_{dcn}^2}{P_n}. \tag{1.59}$$

As shown in Fig. 1.32, when the droop gain k_d or the electrostatic constant H_{mtdc} decrease, the real pole from the simplified model and the complete LTI systems start to diverge from each other. Moreover, when the current controllers are slower (higher values of τ_{i^G}), the simplified model does not represent accurately the LTI model. The reason is that the assumption of infinite wideband of current controllers (without interactions with the DC voltage droop) during the development of the simplified model is violated [74].

For highlighting the limit of the models validity, an example with $k_d = 0.05$ pu, $H_{mtdc} = 16.66$ ms ($C_{S,j} = 48.82$ μ F) and $\tau_{i^G} = 10$ ms is evaluated via time-domain simulations. With these parameters, the theoretical response time of the MTDC grid is given by (1.60). Results are shown in Fig. 1.33. As it can be seen, the simplified model cannot reproduce the oscillations on the DC voltage. In the other hand, the LTI model does reproduce the oscillations on the DC voltage and AC powers. However, the validity of the simplified model can be questioned directly from (1.60). The theoretical response time is slower than the grid current controllers.

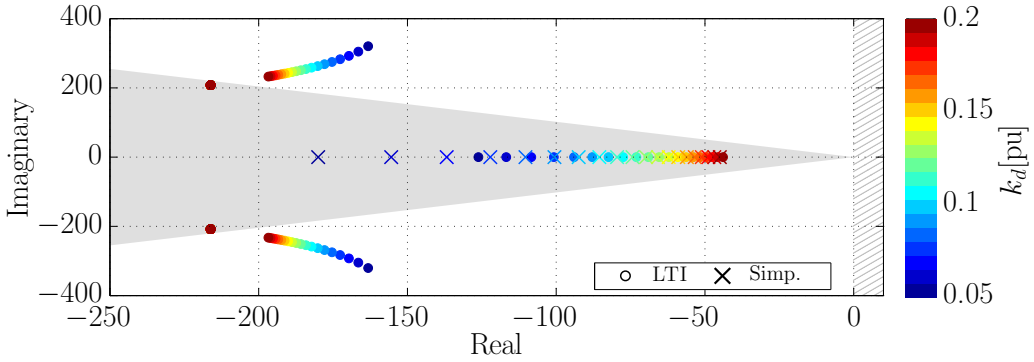

(a) DC Droop gain k_d parametric variation

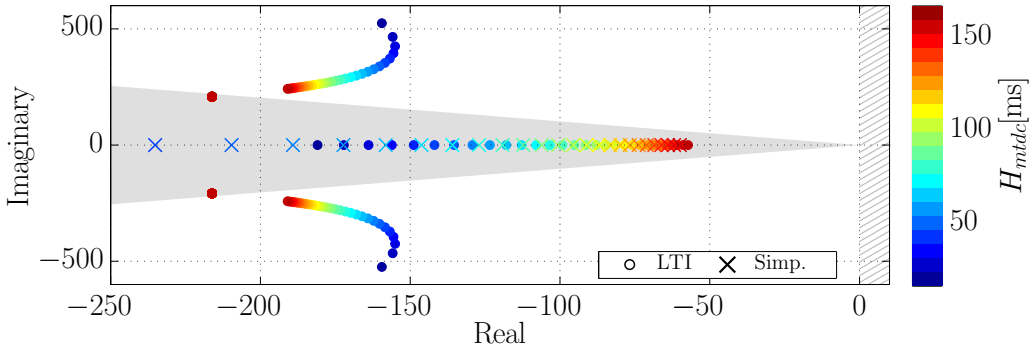

(b) DC electrostatic constant H_{mtdc} parametric variation

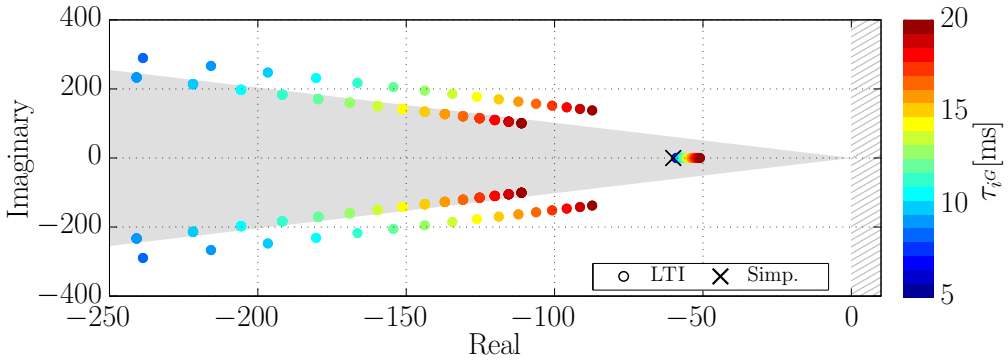

(c) Grid current controllers response time τ_{iG} parametric variation

Figure 1.32 – Parametric variations of k_d, H_{mtdc} or τ_{iG} of the LTI model of a four-terminal MTDC grid with *2-level* VSCs

Since the DC voltage droop control is an "outer" loop, for avoiding interactions with the current controllers, the response times for both loops should be separated in the time frames.

$$\tau_{v_{dc,mtdc}} = 3 \times \frac{k_d}{N_d} C_{mtdc} \frac{v_{dcn}^2}{P_n} = 3 \times \frac{0.05\text{pu}}{3} 48.82\mu\text{F} \frac{(640\text{kV})^2}{1\text{GW}} = 4.66\text{ms} \tag{1.60}$$

In this section, a linearized model of an MTDC grid is presented. Also, a simplified model is recalled from [74], which yields a simple equation relating the power deviation and the DC voltage which highlights the influence of the droop parameter and the stored energy on the DC grid on the overall dynamics of the system. Even though strong assumption has been made to lead to this simplified, for realistic values the model is accurate enough for a good indication on the systems response.

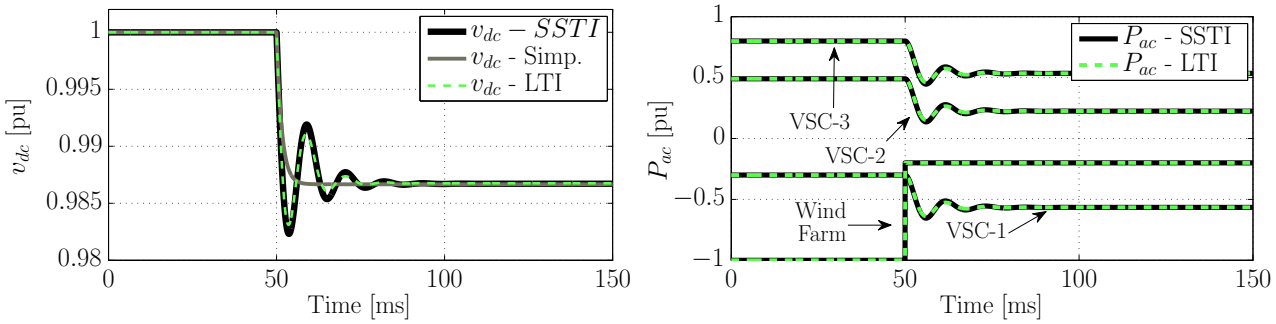

(a) DC Voltage (b) AC Powers

Figure 1.33 – Simulation results of a four-terminal MTDC grid with *2-level* VSC – $k_d = 0.05$ pu, $H_{mtdc} = 16.66$ ms, $\tau_{iG} = 10$ ms

1.5 Chapter Conclusions

This Chapter introduces the methodological principles in the modeling and dynamic analysis of HVDC systems with power electronics converters used through this Thesis. The used examples are based on simple DC systems considering classical *2-level* VSCs in order to highlight the modeling steps. The different models and nomenclature used in this Chapter are summarized as follows:

- **SSTP:** Dynamic model (usually non-linear) whose state variables oscillate periodically in steady state. This model is usually expressed in *abc* frame.
- **SSTI:** Dynamic model (usually non-linear) whose state variables are constant in steady state. It may be obtained directly from mathematical manipulations of the SSTP model without losing generality. This model is usually expressed in *dqz* frame.
- **LTI:** The linearized version around an operating point of the SSTI model and its associated controller (also in SSTI representation). The LTI models are very convenient since there is a lot of mathematical theory readily available to be applied, such as stability studies based on eigenvalues.

Once the different models of the single converter are well established, they may be easily used to build up bigger systems such as HVDC links or MTDC grids. This Chapter presented a point-to-point scheme, where the classical controllers (current and voltage) based on cascaded control loops are introduced. Also, an MTDC case study is presented. The most common distributed control strategy for the DC voltage, namely droop-control, is presented. Moreover, a simplified model (first order transfer function) is developed which highlights the main key components governing the droop-controlled MTDC grid dynamics: the droop parameter, and the stored energy on the DC grid. Even though the model is very simplified, it us exploited for the analysis of MTDC grids along this Thesis, mostly when considering the MMC-based MTDC grids in Chapter 5.

The concepts in this Chapter serve as a prelude for the following in this Thesis. The following Chapter is focused on the modeling MMC with Steady-State Time Invariant Solution.

Chapter 2

Modeling of Modular Multilevel Converters with Steady-State Time Invariant Solution

2.1 Introduction

As a prerequisite for performing small-signal stability analysis of MMC-based HVDC systems, it is needed a suitable MMC model that can be linearized. In Chapter 1, the non-linear model of the *2-level* VSC was expressed in *dq* frame to achieve a Steady-State Time-Invariant solution (SSTI) in a straightforward manner, obtaining a linearizable model. Obtaining a linearized small-signal model of an MMC that can be analyzed by traditional techniques for eigenvalue-based stability techniques requires a model formulation with a uniquely defined equilibrium point for each operating condition, which corresponds to all state variables settling to constant values in steady-state [64]. Thus, it is necessary to derive a state-space model with a SSTI solution in a set of suitably defined Synchronously Rotating Reference Frames.

This Chapter presents a MMC model with SSTI solution which can be linearized involving as few simplifications as possible in the derivation of the model. Indeed, the presented approach is intended for preserving the fundamental non-linearity of the stationary frame average model of the MMC that is used as starting point for the presented derivations. This is achieved by utilizing the information about how the different variables of the MMC contain mainly combinations of DC-components, fundamental frequency components (ω), double frequency oscillations (2ω) and third harmonics (3ω) in steady-state operation. By manipulating the MMC natural variables corresponding to physical quantities of the upper and lower arms by using the sum (Σ) and difference (Δ) between those quantities as MMC state variables, a natural frequency separation can be obtained where the Δ variables contain only a fundamental frequency and third harmonic component, while Σ variables contain DC and double-frequency components. Since the DC- and third harmonic components will be equal in all three phases, they appear only as zero sequence components, and this frequency separation allows for applying appropriate Park transformations to each set of variables, resulting in an SRRF model where all state variables settle to a constant equilibrium point in steady-state operation. The derived model is validated by time-domain simulations in comparison to the average model used as a starting point for the derivations and then confirmed by EMT detailed simulation of an MMC with 400 sub-modules per arm.

The content of this Chapter was developed in collaboration with SINTEF and NTNU (Gilbert Bergna, Jon Are Suul and Salvatore D'Arco) and is part of **Journal II**.

2.2 Literature review on the MMC modeling approaches

Different types of studies are necessary for design and analysis of MMC-based HVDC transmission systems, requiring various detail levels in the modeling [108]. A general overview of MMC modeling approaches suitable for different types of studies is shown in Fig. 2.1. The most detailed models allow for simulating the switching operations of the individual sub-modules of the MMC, as shown to the left of the figure. Such models can be used for studying all modes of operation and all MMC control loops, including algorithms for balancing the sub-module voltages [109, 110]. Two main models are found in this category with respect to [111]: "Model # 1: Detailed IGBT-Based Model", where each IGBT and diodes are modeled in detail; and "Model # 2: Equivalent Circuit-Based Model", which each sub-module switch is replaced by a resistance with high value if the switch is off or low value if the switch is on. This last model was first presented in [112], proving that the computation time can be reduced and is used as the *simulation EMT model* in this Thesis as a reference for the rest of the developed models (more details in Appendix F).

If equal voltage distribution among the sub-modules in each arm of an MMC can be assumed, Average Arm Models (AAM) can be introduced, or also referred as "Model # 3: MMC Arm Switching Function" in [111]. The AAM modeling approach allows for representing each arm of the MMC by a controllable voltage source associated with a corresponding equivalent capacitance, and introduces a significant reduction in complexity while still maintaining an accurate representation of the internal dynamics [113].

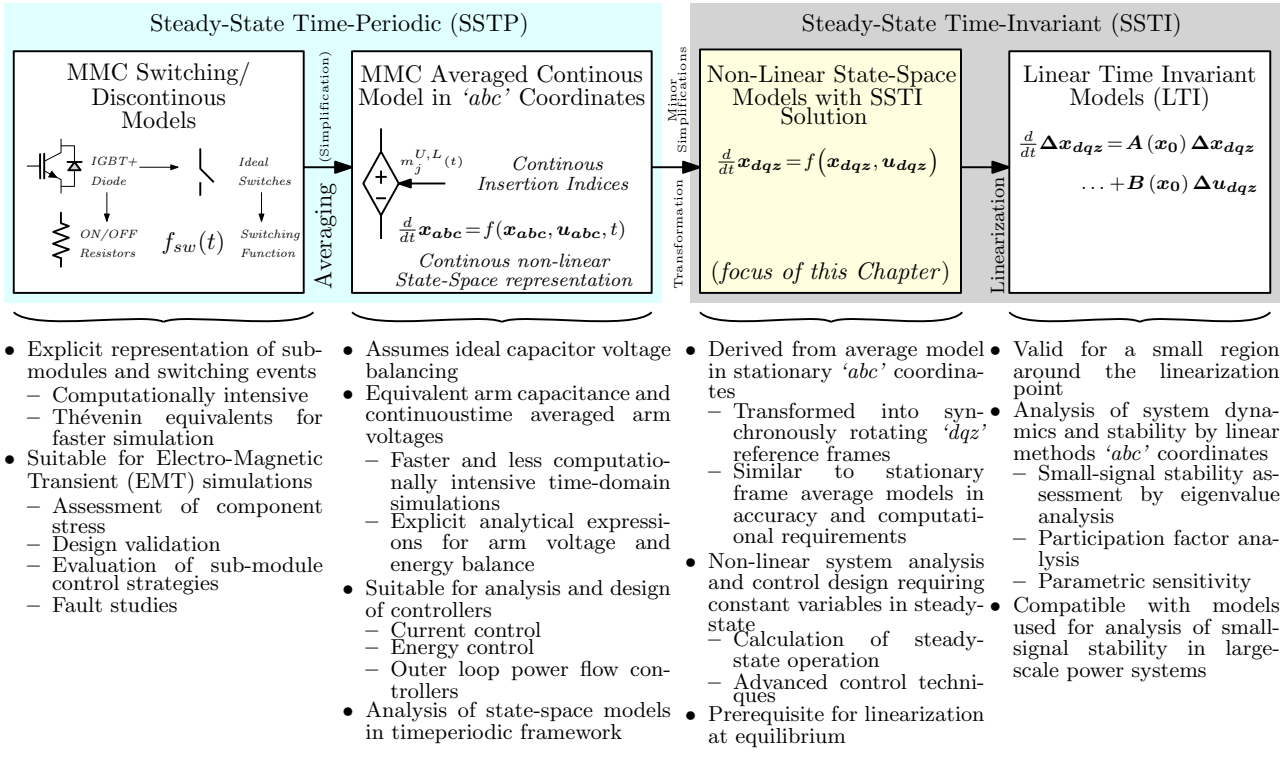

Figure 2.1 – Overview of MMC modeling approaches and their areas of application

Average modeling by the AAM representation, or by equivalent energy-based models, are suitable for simplified simulations and analysis, and have been widely used as basis for control system design [114–117]. However, the variables of such models are Steady-State Time Periodic (SSTP), but most importantly, the currents and capacitor voltages in each arm of the MMC contain multiple frequency components [118]. This prevents a straightforward application of

the Park transformation for obtaining state-space models of three-phase MMCs represented in a single SRRF, as already performed for the *2-level* VSC in Chapter 1. As indicated in Fig. 2.1, such a SRRF dqz model must be derived from an equivalent average model in the stationary abc coordinates. If a non-linear model with a SSTI solution, corresponding to defined equilibrium point, can be formulated, a Linear Time Invariant (LTI) model suitable for eigenvalue analysis can be directly obtained by the Jacobian linearization detailed in Section 1.2.4.

Several approaches for obtaining LTI state-space models of MMCs have been recently proposed in the literature, motivated by the need for representing MMC HVDC transmission systems in eigenvalue-based small-signal stability studies. The simplest approach has been to neglect parts of the internal dynamics of the MMC, and to model mainly the AC-side dynamics in a SRRF together with a simplified DC-side representation, as in the models proposed in [119–121]. However, if the dynamics associated with the internal equivalent capacitor voltages of the MMC and the interaction with the internal currents are ignored, such models may imply significant inaccuracies. Especially if the MMC equivalent capacitor is directly connected to the DC bus similarly as a *2-level* VSC, like in [119, 121]; in this case the model will only be suitable for representing very slow transients. Therefore, more detailed dynamic state-space models have been proposed in [122–128]. These available models have been developed for representing two different cases as discussed in the following.

The approaches presented in [122] and **[123]** are based on the assumption that the modulation indices for the MMC arms are calculated to compensate for the voltage oscillations in the internal equivalent arm capacitor voltages, referred to as Compensated Modulation (CM) (more details on the modulation indices calculations for the MMC are found in Appendix F). This strategy for control system implementation limits the coupling between the internal variables of the MMC and the AC- and DC-side variables. Thus, CM-based control allows for simplified modeling of the MMC, where only the aggregated dynamics of the DC-side current and the total energy stored in the capacitors of the MMC are represented. As a result, these models can provide accurate representation of the AC- and DC-side terminal behavior of MMCs, but imply that the dynamics of many internal variables cannot be analyzed. Nevertheless, these modeling approaches are very useful for HVDC involving many converters and they are evoked again in Chapter 4.

The approaches proposed in [124–126, 128] consider all the internal variables of the MMC, under the assumption of a control system with a Circulating Current Suppression Controller (CCSC) implemented in a negative sequence double frequency SRRF [109]. Indeed, the methods proposed in [124, 125, 128] model the MMC by representing the internal second harmonic circulating currents and the corresponding second harmonic arm voltage components in a SRRF rotating at twice the fundamental frequency. The same approach was followed in [129] and further linearized in [130]. However, since the initial formulation of the MMC is performed with respect to the arm quantities (i.e. "Upper-Lower" variables), where the ω and 2ω components coexist in the same state variables, the harmonic superposition principles has to be assumed in the modeling. This approach corresponds to the phasor-based representation and this could affect the information about the non-linear characteristics of the MMC, and correspondingly limit the applicability of the models in non-linear techniques for analysis and control system design. A similar approximation was also made when separately modeling the fundamental frequency and the second harmonic frequency dynamics of the upper and lower arm capacitor voltages in [126].

The first contribution to the modeling approach from this Chapter was presented in [127], but this Chapter extends the derivations from [127] to obtain a model that is applicable independently from the applied approach for calculating the modulation indices of the MMC.

Furthermore, the model derivation has been expanded to include the effect of the zero-sequence of the difference between upper and lower modulation indices m_z in the MMC dynamics, which was neglected in [127]. This extension of the model can be useful when third harmonic injection is used for increasing the voltage utilization [131, 132], and in case a zero sequence component in the output voltage is utilized to control the energy distribution within the MMC. Also, it is fundamental for having the possibility of considering different modulation approaches as it will be explored in the following Chapter.

2.3 MMC Modeling in the stationary reference frame: Topology, $\Sigma-\Delta$ vector representation and frequency analysis

2.3.1 Arm Averaged Model representation of the MMC topology

The basic topology of a three-phase MMC is synthesized by the series connection of N sub-modules (SMs) with independent capacitors C to constitute one arm of the converter as indicated by Fig. 2.2. The sub-modules in one arm are connected to a filter inductor with equivalent inductance L_{arm} and resistance R_{arm} to form the connection between the DC terminal and the AC-side output. Two identical arms are connected to the upper and lower DC-terminals respectively to form one leg for each phase j ($j=a,b,c$). The AC-side is modeled with an equivalent resistance and inductance R_f and L_f respectively [108]. On the DC-side, the smoothing reactors L_{dc} may be present or not depending on the vendor. In this Thesis, these inductors are neglected, but the way of taking them into account is highlighted.

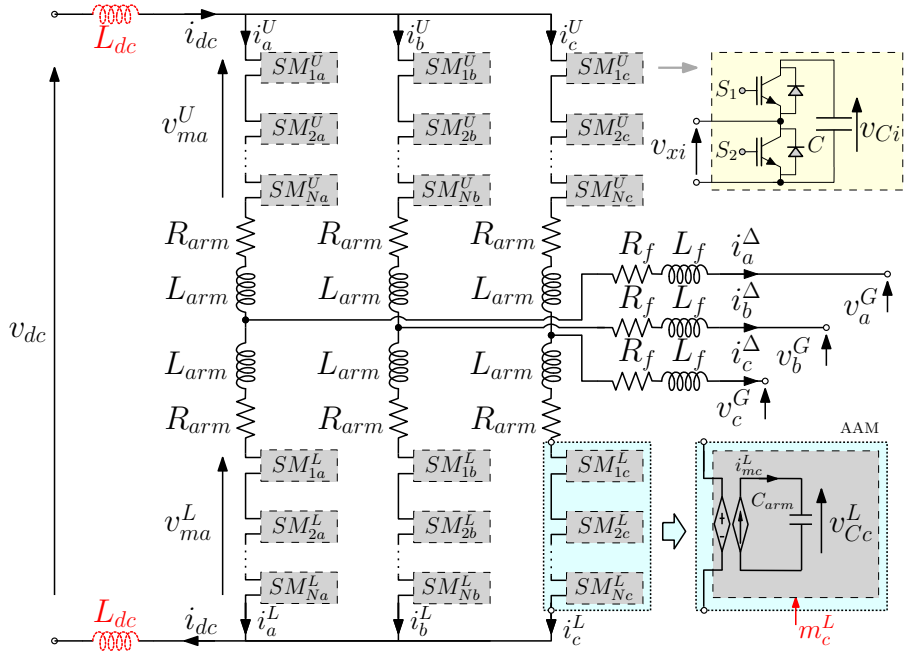

Figure 2.2 – MMC Topology and AAM for the lower arm (phase C)

Assuming that all the SMs capacitors voltages are maintained in a close range, the series connection of submodules in each arm can be replaced by a circuit-based average model, corresponding to the so-called Arm Averaged Model (AAM) as indicated in Fig. 2.2 for the lower arm of phase c [115, 133]. With the AAM representation, each arm appears as a controlled

voltage source, while a power balance is established between the arm and its equivalent capacitance [134]. Thus, each arm can be represented by a conventional power-balance-based average model of a VSC, with a modulated voltage source in series with the arm inductor L_{arm}, and a modulated current source interfacing the arm equivalent capacitor C_{arm}.

The output of the controlled voltage and current sources of the AAM are here referred as the modulated voltages v^U_{mj} and v^L_{mj} and modulated currents i^U_{mj} and i^L_{mj}, for the upper (U) and lower (L) arms of a generic phase j, and are described by the following equations[1]:

$$v^U_{mj} = m^U_j v^U_{Cj},\ v^L_{mj} = m^L_j v^L_{Cj} \tag{2.1a}$$

$$i^U_{mj} = m^U_j i^U_j,\ i^L_{mj} = m^L_j i^L_j \tag{2.1b}$$

where v^U_{Cj} and v^L_{Cj} are respectively the voltages across the upper and lower arm equivalent capacitors; m^U_j and m^L_j are the corresponding modulation indices for the upper and lower arms, and i^U_j and i^L_j are the currents in the upper and lower arms. The voltages and currents of the equivalent capacitor are related through the following equations:

$$C_{arm}\frac{dv^U_{Cj}}{dt} = i^U_{mj} \tag{2.2}$$

$$C_{arm}\frac{dv^L_{Cj}}{dt} = i^L_{mj} \tag{2.3}$$

It is important to mention that the variables v^U_{Cj} and v^L_{Cj} present multiple frequencies at the same time in steady-state [118] in addition to the DC value which is usually around v_{dc}, as exemplified in Fig. 2.3, where $\boldsymbol{v^U_{Cabc}}$ and $\boldsymbol{v^L_{Cabc}}$ are the vectors defined as $[v^U_{Ca}\ v^U_{Cb}\ v^U_{Cc}]^\top$ and $[v^L_{Ca}\ v^L_{Cb}\ v^L_{Cc}]^\top$, respectively. This property makes it impossible to obtain a SSTI version of the MMC model without further mathematical manipulations. For instance, these variables cannot be referred to single Synchronous Rotating Frame with the Park transformation. For this reason, more modeling efforts are needed to isolate different frequency components and then apply the corresponding transformations.

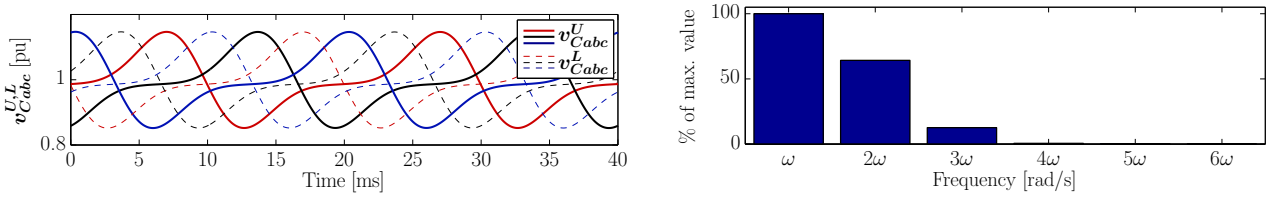

(a) $\boldsymbol{v^U_{Cabc}}$, $\boldsymbol{v^L_{Cabc}}$ (b) FFT - $\boldsymbol{v^U_{Cabc}}$, $\boldsymbol{v^L_{Cabc}}$

Figure 2.3 – MMC Steady-State Analysis - Arm capacitor voltages *Upper-Lower*

2.3.2 Modeling of the MMC with $\Sigma - \Delta$ variables in the stationary *abc* frame

As mentioned in the introduction of this Chapter, the proposed approach adopts the Σ-Δ representation as opposed to the more common one based on the *Upper-Lower* (U-L) arm notation, to ease the derivation of an MMC model with SSTI solution. More precisely, under this Σ-Δ representation, it is possible to initially classify the 11 states and 6 control variables of the Arm Averaged Model of the MMC into two frequency groups; i.e., the Δ variables which

[1]The limits on the modulated voltages v^U_{mj} and v^L_{mj} are studied in Appendix E.

are associated to the fundamental frequency ω and 3ω, and the Σ variables which are in turn associated to DC and -2ω, and will be further discussed in Section 2.3.3.

It is therefore useful to redefine the voltages and currents that are defined in Fig. 2.2 using this nomenclature, resulting in (2.4). Indeed, i_j^{Δ} is the current flowing through the AC-side grid, whereas i_j^{Σ} is the common-mode current of the MMC. The current i_j^{Σ} is commonly referred as "circulating current" or "differential current" [108, 114]; however, the more general term "common-mode current" is preferred in this Thesis, since i^{Σ} is calculated as a *sum* of two currents[2]. Also, the author considers that the term "circulating current" should be reserved to the dq (or $\alpha\beta$) components of the three-phase i_j^{Σ} currents [135]. Moreover, v_{Cj}^{Δ} and v_{Cj}^{Σ} are respectively the difference and the sum of voltages across the upper and lower arm equivalent capacitors.

$$i_j^{\Delta} \stackrel{\text{def}}{=} i_j^U - i_j^L, \qquad i_j^{\Sigma} \stackrel{\text{def}}{=} \left(i_j^U + i_j^L\right)/2, \qquad v_{Cj}^{\Delta} \stackrel{\text{def}}{=} (v_{Cj}^U - v_{Cj}^L)/2, \qquad v_{Cj}^{\Sigma} \stackrel{\text{def}}{=} (v_{Cj}^U + v_{Cj}^L)/2, \tag{2.4}$$

In addition, it is also useful to define the modulated voltages given in (2.1) in the Σ-Δ representation as in (2.5)[3] [117], as well as modulation indices as in (2.6).

$$v_{mj}^{\Delta} \stackrel{\text{def}}{=} \frac{-v_{mj}^U + v_{mj}^L}{2}, \qquad v_{mj}^{\Sigma} \stackrel{\text{def}}{=} \frac{v_{mj}^U + v_{mj}^L}{2} \tag{2.5}$$

$$m_j^{\Delta} \stackrel{\text{def}}{=} m_j^U - m_j^L, \qquad m_j^{\Sigma} \stackrel{\text{def}}{=} m_j^U + m_j^L \tag{2.6}$$

Equations (2.5), (2.6) and the voltages from (2.4) can be gathered in a matrix relating the "Upper-Lower" modulation indices (which in turn, are the physical inputs of the MMC), with the internal modulated voltages "Σ-Δ", as shown in (2.7). This equation highlights one of the main differences between the *2-level* VSC with the MMC, since in the first, the modulated voltage on the AC-side is a product with the actual DC bus voltage v_{dc}. In turn, the AC modulated voltage on the MMC depends on the arm capacitor voltages v_C^{Δ} and v_C^{Σ} (marked in blue for highlighting the fact that $v_C^{\Sigma} >> v_C^{\Delta}$).

$$\left[\begin{array}{c} v_{ma}^{\Sigma} \\ v_{mb}^{\Sigma} \\ v_{mc}^{\Sigma} \\ \hline v_{ma}^{\Delta} \\ v_{mb}^{\Delta} \\ v_{mc}^{\Delta} \end{array}\right] = \underbrace{\frac{1}{2}\left[\begin{array}{ccc|ccc} v_{Ca}^{\Sigma} & 0 & 0 & v_{Ca}^{\Delta} & 0 & 0 \\ 0 & v_{Cb}^{\Sigma} & 0 & 0 & v_{Cb}^{\Delta} & 0 \\ 0 & 0 & v_{Cc}^{\Sigma} & 0 & 0 & v_{Cc}^{\Delta} \\ \hline -v_{Ca}^{\Delta} & 0 & 0 & -v_{Ca}^{\Sigma} & 0 & 0 \\ 0 & -v_{Cb}^{\Delta} & 0 & 0 & -v_{Cb}^{\Sigma} & 0 \\ 0 & 0 & -v_{Cc}^{\Delta} & 0 & 0 & -v_{Cc}^{\Sigma} \end{array}\right]}_{\boldsymbol{V}_{\boldsymbol{Cmabc}}^{\boldsymbol{\Sigma\Delta}}} \underbrace{\left[\begin{array}{ccc|ccc} 1 & 0 & 0 & 1 & 0 & 0 \\ 0 & 1 & 0 & 0 & 1 & 0 \\ 0 & 0 & 1 & 0 & 0 & 1 \\ \hline 1 & 0 & 0 & -1 & 0 & 0 \\ 0 & 1 & 0 & 0 & -1 & 0 \\ 0 & 0 & 1 & 0 & 0 & -1 \end{array}\right]}_{\left[\boldsymbol{m}_{\boldsymbol{abc}}^{\boldsymbol{\Sigma}\top};\boldsymbol{m}_{\boldsymbol{abc}}^{\boldsymbol{\Delta}\top}\right]^{\top}} \left[\begin{array}{c} m_a^U \\ m_b^U \\ m_c^U \\ \hline m_a^L \\ m_b^L \\ m_c^L \end{array}\right] \tag{2.7}$$

For compactness, (2.7) is re-written in (2.8):

$$\left[\begin{array}{c} \boldsymbol{v}_{\boldsymbol{mabc}}^{\boldsymbol{\Sigma}} \\ \hline \boldsymbol{v}_{\boldsymbol{mabc}}^{\boldsymbol{\Delta}} \end{array}\right] = \frac{1}{2}\left[\begin{array}{c|c} diag(\boldsymbol{v}_{\boldsymbol{Cabc}}^{\boldsymbol{\Sigma}}) & diag(\boldsymbol{v}_{\boldsymbol{Cabc}}^{\boldsymbol{\Delta}}) \\ \hline -diag(\boldsymbol{v}_{\boldsymbol{Cabc}}^{\boldsymbol{\Delta}}) & -diag(\boldsymbol{v}_{\boldsymbol{Cabc}}^{\boldsymbol{\Sigma}}) \end{array}\right] \left[\begin{array}{c} \boldsymbol{m}_{\boldsymbol{abc}}^{\boldsymbol{\Sigma}} \\ \hline \boldsymbol{m}_{\boldsymbol{abc}}^{\boldsymbol{\Delta}} \end{array}\right] = \boldsymbol{V}_{\boldsymbol{Cmabc}}^{\boldsymbol{\Sigma\Delta}} \left[\begin{array}{c} \boldsymbol{m}_{\boldsymbol{abc}}^{\boldsymbol{\Sigma}} \\ \hline \boldsymbol{m}_{\boldsymbol{abc}}^{\boldsymbol{\Delta}} \end{array}\right] \tag{2.8}$$

where:

$$\boldsymbol{m}_{\boldsymbol{abc}}^{\boldsymbol{\Sigma}} = [m_a^{\Sigma}\ m_b^{\Sigma}\ m_c^{\Sigma}]^{\top} \quad \boldsymbol{v}_{\boldsymbol{mabc}}^{\boldsymbol{\Sigma}} = [v_{ma}^{\Sigma}\ v_{mb}^{\Sigma}\ v_{mc}^{\Sigma}]^{\top} \quad \boldsymbol{v}_{\boldsymbol{Cabc}}^{\boldsymbol{\Sigma}} = [v_{Ca}^{\Sigma}\ v_{Cb}^{\Sigma}\ v_{Cc}^{\Sigma}]^{\top}$$
$$\boldsymbol{m}_{\boldsymbol{abc}}^{\boldsymbol{\Delta}} = [m_a^{\Delta}\ m_b^{\Delta}\ m_c^{\Delta}]^{\top} \quad \boldsymbol{v}_{\boldsymbol{mabc}}^{\boldsymbol{\Delta}} = [v_{ma}^{\Delta}\ v_{mb}^{\Delta}\ v_{mc}^{\Delta}]^{\top} \quad \boldsymbol{v}_{\boldsymbol{Cabc}}^{\boldsymbol{\Delta}} = [v_{Ca}^{\Delta}\ v_{Cb}^{\Delta}\ v_{Cc}^{\Delta}]^{\top}$$

Note that the matrix $\boldsymbol{V}_{\boldsymbol{Cmabc}}^{\boldsymbol{\Sigma\Delta}}$ relates the modulation indices with the arm capacitor voltages in $\Sigma - \Delta$ and *abc* frame.

[2] To the author's knowledge, the term "difference current" was introduced in [113] since in the followed arm currents convention, upper and lower currents "arrive" to the AC node. In [116] (and others), the same current convention as this Thesis was maintained (opposite as [113]), while keeping the "difference current" nomenclature.

[3] The limits on the modulated voltages v_{mj}^{Σ} and v_{mj}^{Δ} are studied in Appendix E.

AC-grid current dynamics — "Δ"

Applying Kirchhoff's law to the circuit in Fig. 2.2, the following equations are derived for the phase j:

$$\frac{v_{dc}}{2} - v_{mj}^{U} - L_{arm}\frac{di_j^U}{dt} - R_{arm}i_j^U - L_f\frac{di_j^\Delta}{dt} - R_f i_j^\Delta - v_j^G = 0 \tag{2.9}$$

$$-\frac{v_{dc}}{2} + v_{mj}^{L} + L_{arm}\frac{di_j^L}{dt} + R_{arm}i_j^L - L_f\frac{di_j^\Delta}{dt} - R_f i_j^\Delta - v_j^G = 0 \tag{2.10}$$

With the addition of (2.9) and (2.10) and the consideration of (2.5), the three-phase AC-grid currents dynamics $\boldsymbol{i_{abc}^{\Delta}} = [i_a^\Delta \ i_b^\Delta \ i_c^\Delta]^\top$ are obtained, which are expressed using vector nomenclature in the stationary frame as in (2.11),

$$L_{eq}^{ac}\frac{d\boldsymbol{i_{abc}^{\Delta}}}{dt} = \boldsymbol{v_{mabc}^{\Delta}} - \boldsymbol{v_{abc}^{G}} - R_{eq}^{ac}\boldsymbol{i_{abc}^{\Delta}}, \tag{2.11}$$

where $\boldsymbol{v_{abc}^{G}}$ is the grid voltage vector defined as $[v_a^G \ v_b^G \ v_c^G]^\top$, whereas $\boldsymbol{v_{mabc}^{\Delta}}$ is the modulated voltage driving the AC-grid current defined as $[v_{ma}^\Delta \ v_{mb}^\Delta \ v_{mc}^\Delta]^\top$, or more precisely as:

$$\boldsymbol{v_{mabc}^{\Delta}} = -\frac{1}{2}\left(\boldsymbol{m_{abc}^{\Delta}}\circ\boldsymbol{v_{Cabc}^{\Sigma}} + \boldsymbol{m_{abc}^{\Sigma}}\circ\boldsymbol{v_{Cabc}^{\Delta}}\right) \tag{2.12}$$

where the *upper* and *lower* modulation indices (m_j^U, m_j^L) and modulated voltages (v_{mj}^U, v_{mj}^L) were replaced by their Σ-Δ equivalents for consistency. Equation (2.12) is obtained from a mathematical manipulation of (2.1) with (2.5) and (2.6). It is worth noticing that the operator "∘" will be used here to represent the element-wise multiplication of vectors (e.g. $\left[\begin{smallmatrix}a\\b\end{smallmatrix}\right]\circ\left[\begin{smallmatrix}c\\d\end{smallmatrix}\right] = \left[\begin{smallmatrix}ac\\bd\end{smallmatrix}\right]$). Furthermore, R_{eq}^{ac} and L_{eq}^{ac} are the equivalent AC resistance and inductance, respectively defined as $R_f + R_{arm}/2$ and $L_f + L_{arm}/2$ [114].

Common-mode currents — "Σ"

With the subtraction of (2.10) from (2.9), the three-phase common-mode currents dynamics in the stationary frame can be obtained, which are written by using vector notation as:

$$L_{arm}\frac{d\boldsymbol{i_{abc}^{\Sigma}}}{dt} = \frac{\boldsymbol{v_{dc}}}{2} - \boldsymbol{v_{mabc}^{\Sigma}} - R_{arm}\boldsymbol{i_{abc}^{\Sigma}}, \tag{2.13}$$

where $\boldsymbol{v_{dc}}$ is defined as $[v_{dc} \ v_{dc} \ v_{dc}]^\top$ and $\boldsymbol{v_{mabc}^{\Sigma}}$ is the modulated voltage driving the common-mode current defined as $[v_{ma}^\Sigma \ v_{mb}^\Sigma \ v_{mc}^\Sigma]^\top$, or more precisely as:

$$\boldsymbol{v_{mabc}^{\Sigma}} = \frac{1}{2}\left(\boldsymbol{m_{abc}^{\Sigma}}\circ\boldsymbol{v_{Cabc}^{\Sigma}} + \boldsymbol{m_{abc}^{\Delta}}\circ\boldsymbol{v_{Cabc}^{\Delta}}\right), \tag{2.14}$$

where the *upper* and *lower* modulation indices and voltage variables were replaced by their Σ-Δ equivalents for convenience here as well.

Arm capacitor voltage dynamics — "Σ" and "Δ"

Similarly, the dynamics of the voltage sum and difference between the equivalent capacitors of the AAM can be expressed respectively as in (2.15) and (2.16).

$$2C_{arm}\frac{d\boldsymbol{v_{Cabc}^{\Sigma}}}{dt} = \boldsymbol{m_{abc}^{\Delta}}\circ\frac{\boldsymbol{i_{abc}^{\Delta}}}{2} + \boldsymbol{m_{abc}^{\Sigma}}\circ\boldsymbol{i_{abc}^{\Sigma}} \tag{2.15}$$

$$2C_{arm}\frac{d\boldsymbol{v_{Cabc}^{\Delta}}}{dt} = \boldsymbol{m_{abc}^{\Sigma}}\circ\frac{\boldsymbol{i_{abc}^{\Delta}}}{2} + \boldsymbol{m_{abc}^{\Delta}}\circ\boldsymbol{i_{abc}^{\Sigma}} \tag{2.16}$$

2.3.3 Summary of MMC Model with SSTP Solution and frequency analysis in Steady-State of the $\Sigma - \Delta$ variables

The equations presented in this section can be represented in a block diagram as shown in Fig. 2.4. This figure highlights the functional relations between the different variables of the system.

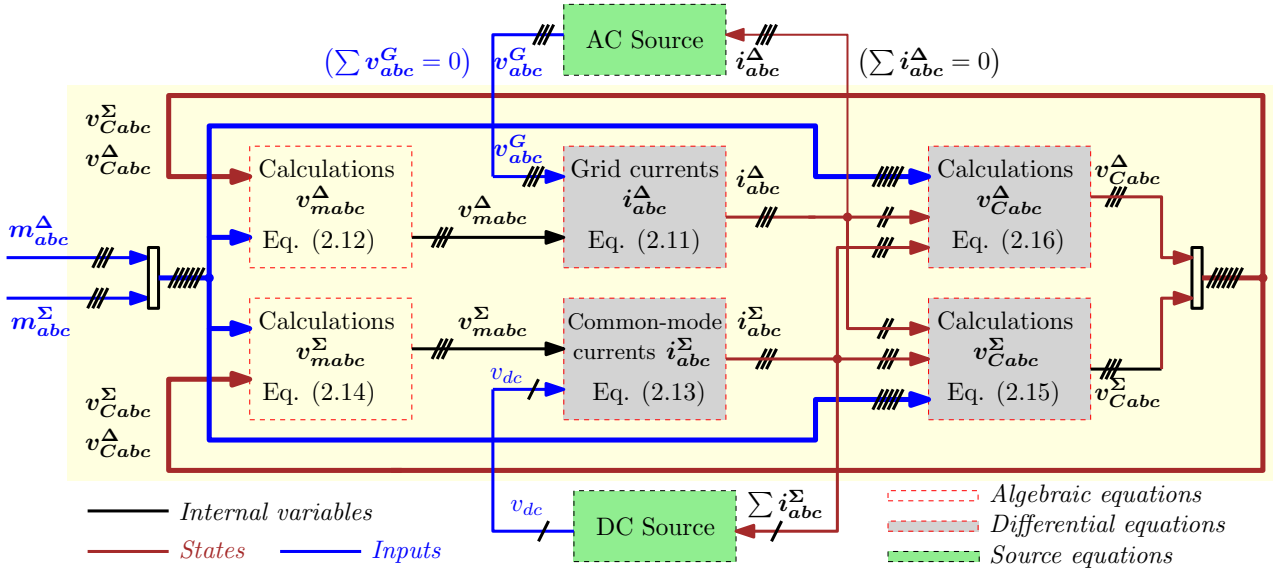

Figure 2.4 – MMC representation Σ-Δ in *abc* frame

In the following, a simplified frequency analysis for the MMC variables in steady-state is provided in order to evaluate their main harmonic content. For this task, a simple time domain simulation is performed of the MMC from Fig. 2.4. The AC and DC voltages are imposed, as well as the proper modulation indices from Fig. 2.5 which corresponds to an active power transit of 1 pu, while maintaining the reactive power to zero.

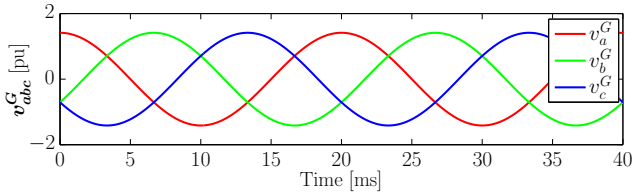

(a) AC voltages in *abc* frame

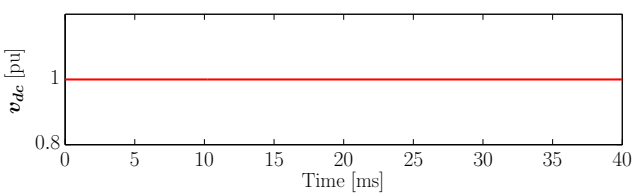

(b) DC Voltage

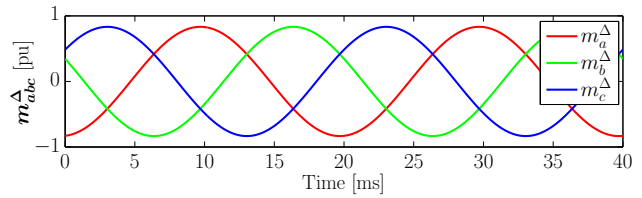

(c) $\boldsymbol{m}^{\boldsymbol{\Delta}}_{\boldsymbol{abc}} = [m^{\Delta}_{a}\ m^{\Delta}_{b}\ m^{\Delta}_{c}]^{\top}$

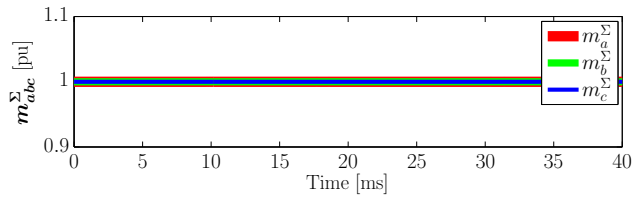

(d) $\boldsymbol{m}^{\boldsymbol{\Sigma}}_{\boldsymbol{abc}} = [m^{\Sigma}_{a}\ m^{\Sigma}_{b}\ m^{\Sigma}_{c}]^{\top}$

Figure 2.5 – MMC Steady-State Analysis - Inputs

The results of the MMC currents are shown in Fig. 2.6. In Fig. 2.6a, the AC grid currents $\boldsymbol{i}^{\boldsymbol{\Delta}}_{\boldsymbol{abc}}$ are shown. The Fast Fourier Transformation (FFT) is applied to $\boldsymbol{i}^{\boldsymbol{\Delta}}_{\boldsymbol{abc}}$ and results are

shown in Fig. 2.6b, where it can be observed that the main frequency component corresponds to the grids frequency ω as expected and also 3ω.

The common-mode current consists of a DC value, or a DC value in addition to oscillating signals at -2ω, depending on whether the second harmonic component of the common-mode current is eliminated by control or not [136, 137]. In this example, there is no control on these currents and the -2ω components are not eliminated for a better exemplification. Results are shown in Fig. 2.6c, where it can confirmed that they are pulsating with negative-sequence ("$a-c-b$" instead of "$a-b-c$" as the grid voltages) double grids angular frequency. The FFT of $\boldsymbol{i^{\Sigma}_{abc}}$ is shown in Fig. 2.6d without the DC component, and confirms that the 2ω component is preponderant and also that a small component of 4ω is present.

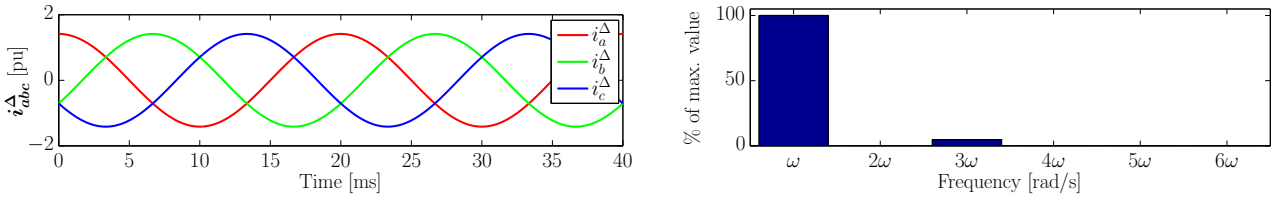

(a) $\boldsymbol{i^{\Delta}_{abc}} = [i^{\Delta}_a \; i^{\Delta}_b \; i^{\Delta}_c]^{\top}$ (b) FFT - i^{Δ}_j

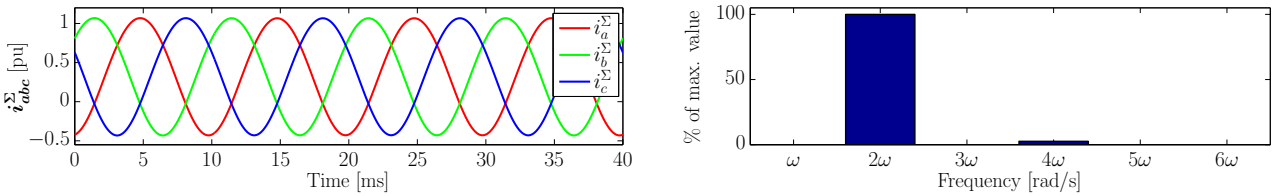

(c) $\boldsymbol{i^{\Sigma}_{abc}} = [i^{\Sigma}_a \; i^{\Sigma}_b \; i^{\Sigma}_c]^{\top}$ (d) FFT - i^{Σ}_j

Figure 2.6 – MMC Steady-State Analysis - Currents

Results of the arm capacitor voltages $\boldsymbol{v^{\Delta}_{Cabc}}$ are shown in Fig. 2.7a and the corresponding FFT in Fig. 2.7b, where it can be seen that the most important harmonic components are ω and 3ω. Furthermore, results from $\boldsymbol{v^{\Sigma}_{Cabc}}$ are given in Figs. 2.7c and 2.7d, showing that this variable is composed mainly by a 2ω component in addition to the DC value, which is more important than the amplitude of the oscillations.

These results can be explained regarding the modulated indices from Fig. 2.5d, where $m^{\Sigma}_j = 1$, and from Fig. 2.5c, where $m^{\Delta}_j \approx \hat{m}cos\,(\omega t)$ [108]. By inspecting the right-side of (2.15) (i.e. $m^{\Delta}_j i^{\Delta}_j/2 + m^{\Sigma}_j i^{\Sigma}_j$), it can be seen that in steady-state, the first product $m^{\Delta}_j i^{\Delta}_j/2$ gives a DC value in addition to an oscillatory signal at 2ω, while the second product $m^{\Sigma}_j i^{\Sigma}_j$ gives a DC value in case a constant value of i^{Σ}_j is imposed by control (e.g. by CCSC [109]), or a 2ω signal otherwise. Thus, both cases will result in a dominant oscillation frequency of 2ω in v^{Σ}_{Cj} [138]. Similarly for v^{Δ}_{Cj}, it is inspected the right-side of (2.16) (i.e. $m^{\Sigma}_j i^{\Delta}_j/2 + m^{\Delta}_j i^{\Sigma}_j$), where the first product, $m^{\Sigma}_j i^{\Delta}_j/2$, oscillates at ω, while the second product $m^{\Delta}_j i^{\Sigma}_j$ oscillates at ω in the case the CCSC is used or will result in a signal oscillating at ω superimposed to one at 3ω otherwise [136]. If the assumption $m^{\Sigma}_j = 1$ is no longer considered, but instead m^{Σ}_j is allowed to have a second harmonic component superimposed to its DC value, the first term of (2.16) will also produce an additional component at 3ω.

As will be shown in the remainder of this Chapter, this additional 3$^{\text{rd}}$ harmonic on the Δ variables don't affect significantly the initial frequency classification of the variables as it will be captured and isolated by the zero-sequence component after the application of Park transformation at ω without affecting its corresponding dq components.

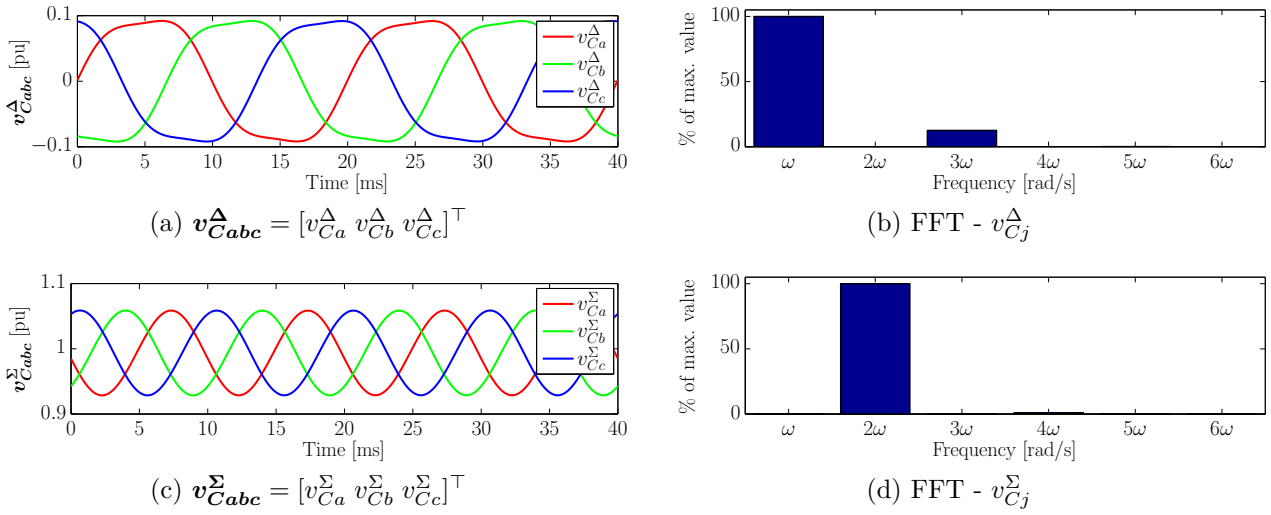

(a) $\boldsymbol{v}^{\boldsymbol{\Delta}}_{\boldsymbol{Cabc}} = [v^{\Delta}_{Ca}\ v^{\Delta}_{Cb}\ v^{\Delta}_{Cc}]^{\top}$ (b) FFT - v^{Δ}_{Cj}

(c) $\boldsymbol{v}^{\boldsymbol{\Sigma}}_{\boldsymbol{Cabc}} = [v^{\Sigma}_{Ca}\ v^{\Sigma}_{Cb}\ v^{\Sigma}_{Cc}]^{\top}$ (d) FFT - v^{Σ}_{Cj}

Figure 2.7 – MMC Steady-State Analysis - Arm capacitor voltages

The modulated voltages are shown in Fig. 2.8. Similar behavior in terms of frequency spectra as the MMC currents is observed, which is expected since these are the voltages that drive the currents.

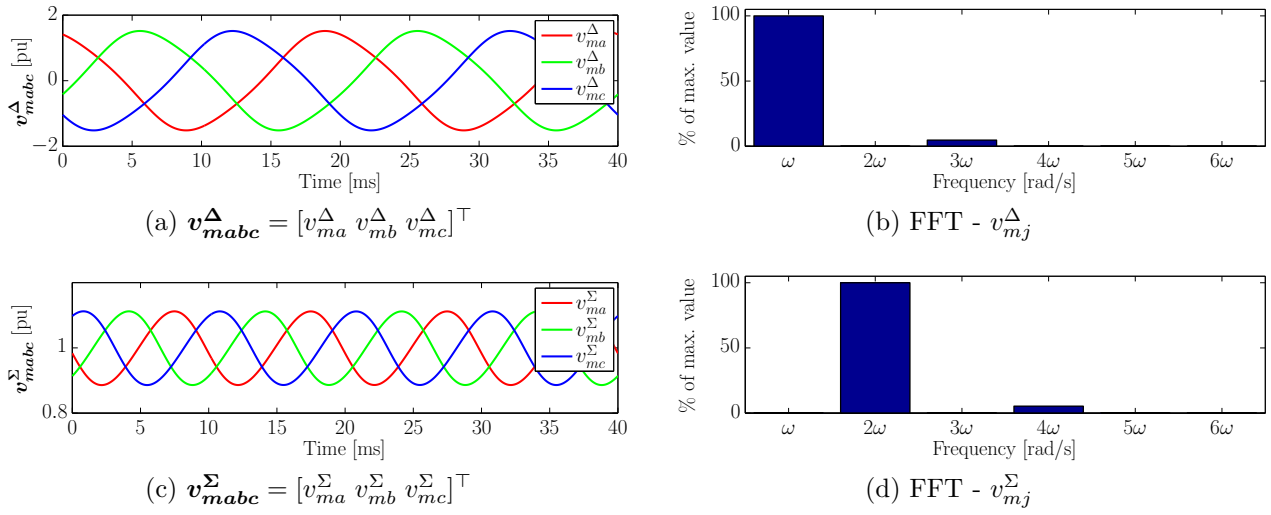

(a) $\boldsymbol{v}^{\boldsymbol{\Delta}}_{\boldsymbol{mabc}} = [v^{\Delta}_{ma}\ v^{\Delta}_{mb}\ v^{\Delta}_{mc}]^{\top}$ (b) FFT - v^{Δ}_{mj}

(c) $\boldsymbol{v}^{\boldsymbol{\Sigma}}_{\boldsymbol{mabc}} = [v^{\Sigma}_{ma}\ v^{\Sigma}_{mb}\ v^{\Sigma}_{mc}]^{\top}$ (d) FFT - v^{Σ}_{mj}

Figure 2.8 – MMC Steady-State Analysis - Internal modulated voltages

This initial classification of the state and control variables according to their main oscillatory frequency is summarized in Table 2.1 and is considered the base for the methodology presented in the following section.

Table 2.1 – MMC variables in Σ-Δ representation

Main frequency content: ω, 3ω	Main frequency content: -2ω, DC
$i^{\Delta}_{j} = i^{U}_{j} - i^{L}_{j}$	$i^{\Sigma}_{j} = (i^{U}_{j} + i^{L}_{j})/2$
$v^{\Delta}_{Cj} = (-v^{U}_{Cj} + v^{L}_{Cj})/2$	$v^{\Sigma}_{Cj} = (v^{U}_{Cj} + v^{L}_{Cj})/2$
$v^{\Delta}_{mj} = (-v^{U}_{mj} + v^{L}_{mj})/2$	$v^{\Sigma}_{mj} = (v^{U}_{mj} + v^{L}_{mj})/2$
$m^{\Delta}_{j} = m^{U}_{j} - m^{L}_{j}$	$m^{\Sigma}_{j} = m^{U}_{j} + m^{L}_{j}$

2.4 Non-linear MMC model with Steady-State Time-Invariant solution: $\Sigma-\Delta$ representation in *dqz* frame

In this section, the derivations needed for obtaining the state-space time-invariant representation of the MMC with voltage-based formulation is presented in detail on basis of the approach from [127]. This step is mandatory in order to be able to get a very accurate LTI model of MMC which can be used for small signal stability analysis as explained in Chapter 1. Moreover, thanks to the decomposition of the system, the root causes of internal phenomenon of MMC can be explained.

As shown in the frequency classifications from Table 2.1, the "Δ" variables are associated mainly with periodic oscillations of ω, and the "Σ" variables with -2ω. In the first attempt to obtain Steady-State Time Invariant variables of the MMC, the Δ-variables ($\boldsymbol{v}^{\boldsymbol{\Delta}}_{\boldsymbol{Cabc}}$, $\boldsymbol{i}^{\boldsymbol{\Delta}}_{\boldsymbol{abc}}$ and $\boldsymbol{m}^{\boldsymbol{\Delta}}_{\boldsymbol{abc}}$) are transformed into their *dqz* equivalents by means of a Park transformation $\boldsymbol{P}_{\boldsymbol{\omega}}$ at the grid fundamental frequency ω (see Appendix A). By contrast, the Σ-variables ($\boldsymbol{v}^{\boldsymbol{\Sigma}}_{\boldsymbol{Cabc}}$, $\boldsymbol{i}^{\boldsymbol{\Sigma}}_{\boldsymbol{abc}}$ and $\boldsymbol{m}^{\boldsymbol{\Sigma}}_{\boldsymbol{abc}}$) are transformed into their *dqz* equivalents by means of a Park transformation $\boldsymbol{P}_{\boldsymbol{-2\omega}}$ at twice the grid frequency in negative sequence, -2ω:

$$\boldsymbol{i}^{\boldsymbol{\Delta}}_{\boldsymbol{dqz}} \overset{\text{def}}{=} \boldsymbol{P}_{\boldsymbol{\omega}}\boldsymbol{i}^{\boldsymbol{\Delta}}_{\boldsymbol{abc}};\quad \boldsymbol{v}^{\boldsymbol{\Delta}}_{\boldsymbol{Cdqz}} \overset{\text{def}}{=} \boldsymbol{P}_{\boldsymbol{\omega}}\boldsymbol{v}^{\boldsymbol{\Delta}}_{\boldsymbol{Cabc}};\quad \boldsymbol{v}^{\boldsymbol{\Delta}}_{\boldsymbol{mdqz}} \overset{\text{def}}{=} \boldsymbol{P}_{\boldsymbol{\omega}}\boldsymbol{v}^{\boldsymbol{\Delta}}_{\boldsymbol{mabc}};\quad \boldsymbol{m}^{\boldsymbol{\Delta}}_{\boldsymbol{dqz}} \overset{\text{def}}{=} \boldsymbol{P}_{\boldsymbol{\omega}}\boldsymbol{m}^{\boldsymbol{\Delta}}_{\boldsymbol{abc}} \tag{2.17a}$$

$$\boldsymbol{i}^{\boldsymbol{\Sigma}}_{\boldsymbol{dqz}} \overset{\text{def}}{=} \boldsymbol{P}_{\boldsymbol{-2\omega}}\boldsymbol{i}^{\boldsymbol{\Sigma}}_{\boldsymbol{abc}};\quad \boldsymbol{v}^{\boldsymbol{\Sigma}}_{\boldsymbol{Cdqz}} \overset{\text{def}}{=} \boldsymbol{P}_{\boldsymbol{-2\omega}}\boldsymbol{v}^{\boldsymbol{\Sigma}}_{\boldsymbol{Cabc}};\quad \boldsymbol{v}^{\boldsymbol{\Sigma}}_{\boldsymbol{mdqz}} \overset{\text{def}}{=} \boldsymbol{P}_{\boldsymbol{-2\omega}}\boldsymbol{v}^{\boldsymbol{\Sigma}}_{\boldsymbol{mabc}};\quad \boldsymbol{m}^{\boldsymbol{\Sigma}}_{\boldsymbol{dqz}} \overset{\text{def}}{=} \boldsymbol{P}_{\boldsymbol{-2\omega}}\boldsymbol{m}^{\boldsymbol{\Sigma}}_{\boldsymbol{abc}} \tag{2.17b}$$

The Park transformations are applied to the time-domain results from Section 2.3.3. In Figs. 2.9a and 2.9c, results of the currents $\boldsymbol{i}^{\boldsymbol{\Delta}}_{\boldsymbol{dqz}}$ and modulated voltages $\boldsymbol{v}^{\boldsymbol{\Delta}}_{\boldsymbol{mdqz}}$ are respectively shown. Since the grid currents are oscillating at a single frequency ω, the results for $\boldsymbol{i}^{\boldsymbol{\Delta}}_{\boldsymbol{dqz}}$ are constant values after the Park transformation is applied. Note that the zero-sequence of v^{Δ}_{mz} is oscillating at 3ω, but since there is no zero-sequence current path, the current i^{Δ}_{z} is null.

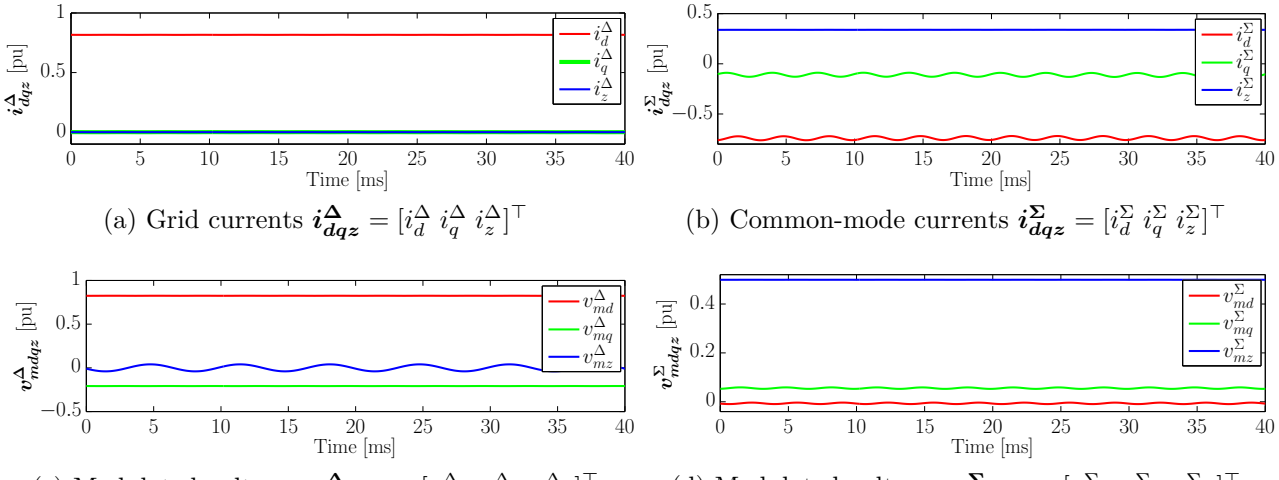

(a) Grid currents $\boldsymbol{i}^{\boldsymbol{\Delta}}_{\boldsymbol{dqz}} = [i^{\Delta}_{d}\ i^{\Delta}_{q}\ i^{\Delta}_{z}]^{\top}$

(b) Common-mode currents $\boldsymbol{i}^{\boldsymbol{\Sigma}}_{\boldsymbol{dqz}} = [i^{\Sigma}_{d}\ i^{\Sigma}_{q}\ i^{\Sigma}_{z}]^{\top}$

(c) Modulated voltages $\boldsymbol{v}^{\boldsymbol{\Delta}}_{\boldsymbol{mdqz}} = [v^{\Delta}_{md}\ v^{\Delta}_{mq}\ v^{\Delta}_{mz}]^{\top}$

(d) Modulated voltages $\boldsymbol{v}^{\boldsymbol{\Sigma}}_{\boldsymbol{mdqz}} = [v^{\Sigma}_{md}\ v^{\Sigma}_{mq}\ v^{\Sigma}_{mz}]^{\top}$

Figure 2.9 – MMC Steady-State Analysis in *dqz* frame - AC and common-mode currents

In Figs. 2.9b and 2.9d, results of the common-mode currents $\boldsymbol{i}^{\boldsymbol{\Sigma}}_{\boldsymbol{dqz}}$ and modulated voltages $\boldsymbol{v}^{\boldsymbol{\Sigma}}_{\boldsymbol{mdqz}}$ that drive those currents are respectively shown. Note that the zero-sequence of the modulated voltage v^{Σ}_{mz} as well as the current i^{Σ}_{z} are composed only by a constant component. The *dq* components of both variables present a constant value, but also oscillations at 6ω. This component is the same as the 4ω values found in the results from the Section 2.3.3 (in *abc* frame, the 4ω components with negative-sequence, are reflected as 6ω pulsations after

applying the Park transformation at -2ω [136]). However, note that the 6ω oscillations can be considered as negligible.

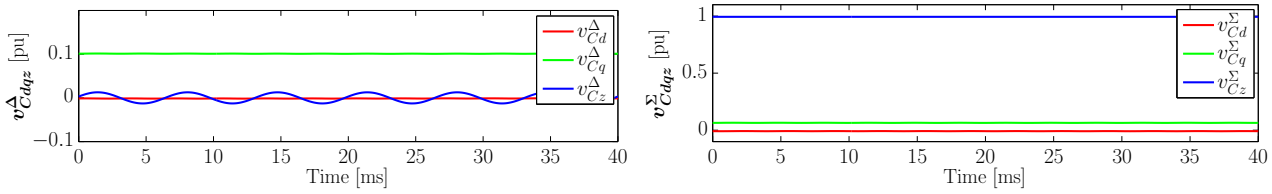

(a) Arm capacitors "Δ" $\boldsymbol{v}^{\boldsymbol{\Delta}}_{\boldsymbol{Cdqz}} = [v^{\Delta}_{Cd}\ v^{\Delta}_{Cq}\ v^{\Delta}_{Cz}]^{\top}$ (b) Arm capacitors "Σ" $\boldsymbol{v}^{\boldsymbol{\Sigma}}_{\boldsymbol{Cdqz}} = [v^{\Sigma}_{Cd}\ v^{\Sigma}_{Cq}\ v^{\Sigma}_{Cz}]^{\top}$

Figure 2.10 – MMC Steady-State Analysis in dqz frame - Arm capacitors

In Fig. 2.10a, the results of applying the Park transformations to $\boldsymbol{v}^{\boldsymbol{\Delta}}_{\boldsymbol{Cdqz}}$ are shown, where it can be seen that the dq components are constant, while the zero-sequence presents some 3ω oscillations [139]. Even though these oscillations may not be so important, it is detailed in the following of the Chapter how to model these dynamics with constant values. Finally, in Fig. 2.10b, the results for $\boldsymbol{v}^{\boldsymbol{\Sigma}}_{\boldsymbol{Cdqz}}$ are shown. At first sight, the three components dqz are almost constant after the applied transformation. However, if a zoom is applied on the dq results, some 6ω component can be found. These components will appear naturally during the development of the MMC model with SSTI solution, and further neglected due to the minimal contribution on the overall dynamics. It is also useful to observe in Fig. 2.10, that the most important value is v^{Σ}_{Cz}, which corresponds to the DC value of the arm capacitor voltages. The dq components of v^{Σ}_{C}, and the dqz components of v^{Δ}_{C} are related to the oscillations in steady-state presented in $\boldsymbol{v}^{\boldsymbol{U}}_{\boldsymbol{Cabc}}$ and $\boldsymbol{v}^{\boldsymbol{L}}_{\boldsymbol{Cabc}}$ (see Fig. 2.3).

The formulation of the MMC variables such that the initial separation of frequency components can be achieved constitutes the basis for the proposed modeling approach. In the remainder of this section, the mathematical derivation of dynamic equations with SSTI solution representing the dynamics of a three phase MMC will be expressed by using the approach from [127]. The mathematical reformulation consists in expressing the vector variables in the stationary abc frame as a function of their dqz equivalents at their respective rotating frequencies. The equations from this section can be obtained with the Matlab code from Appendix D.

2.4.1 Voltage difference Δ SSTI dynamics derivation

Initial formulation

The SSTI dynamics for the voltage difference v^{Δ}_{C} is derived as follows. The starting point is indeed the SSTP dynamics of the variables $\boldsymbol{v}^{\boldsymbol{\Delta}}_{\boldsymbol{Cabc}}$ given in (2.16), and recalled in (2.18a) for convenience. The first step consists in expressing the abc vectors in the stationary frame as function of their respective dqz equivalents. This can be seen in (2.18b), where $\boldsymbol{v}^{\boldsymbol{\Delta}}_{\boldsymbol{Cabc}}$, $\boldsymbol{m}^{\boldsymbol{\Sigma}}_{\boldsymbol{abc}}$, $\boldsymbol{i}^{\boldsymbol{\Delta}}_{\boldsymbol{abc}}$, $\boldsymbol{m}^{\boldsymbol{\Delta}}_{\boldsymbol{abc}}$ and $\boldsymbol{i}^{\boldsymbol{\Sigma}}_{\boldsymbol{abc}}$ have been respectively replaced by $\boldsymbol{P}^{\boldsymbol{-1}}_{\boldsymbol{\omega}}\boldsymbol{v}^{\boldsymbol{\Delta}}_{\boldsymbol{Cdqz}}$, $\boldsymbol{P}^{\boldsymbol{-1}}_{\boldsymbol{-2\omega}}\boldsymbol{m}^{\boldsymbol{\Sigma}}_{\boldsymbol{dqz}}$, $\boldsymbol{P}^{\boldsymbol{-1}}_{\boldsymbol{\omega}}\boldsymbol{i}^{\boldsymbol{\Delta}}_{\boldsymbol{dqz}}$, $\boldsymbol{P}^{\boldsymbol{-1}}_{\boldsymbol{\omega}}\boldsymbol{m}^{\boldsymbol{\Delta}}_{\boldsymbol{dqz}}$ and $\boldsymbol{P}^{\boldsymbol{-1}}_{\boldsymbol{-2\omega}}\boldsymbol{i}^{\boldsymbol{\Sigma}}_{\boldsymbol{dqz}}$ when considering (2.17).

$$2C_{arm}\frac{d\boldsymbol{v}^{\boldsymbol{\Delta}}_{\boldsymbol{Cabc}}}{dt} = \boldsymbol{m}^{\boldsymbol{\Sigma}}_{\boldsymbol{abc}} \circ \frac{\boldsymbol{i}^{\boldsymbol{\Delta}}_{\boldsymbol{abc}}}{2} + \boldsymbol{m}^{\boldsymbol{\Delta}}_{\boldsymbol{abc}} \circ \boldsymbol{i}^{\boldsymbol{\Sigma}}_{\boldsymbol{abc}} \tag{2.18a}$$

$$\underbrace{2C_{arm}\frac{d\boldsymbol{P}^{\boldsymbol{-1}}_{\boldsymbol{\omega}}}{dt}\boldsymbol{v}^{\boldsymbol{\Delta}}_{\boldsymbol{Cdqz}} + 2C_{arm}\boldsymbol{P}^{\boldsymbol{-1}}_{\boldsymbol{\omega}}\frac{d\boldsymbol{v}^{\boldsymbol{\Delta}}_{\boldsymbol{Cdqz}}}{dt}}_{\boldsymbol{\Phi}^{\boldsymbol{\Delta}}_{\boldsymbol{A}}} = \underbrace{\boldsymbol{P}^{\boldsymbol{-1}}_{\boldsymbol{-2\omega}}\boldsymbol{m}^{\boldsymbol{\Sigma}}_{\boldsymbol{dqz}} \circ \frac{\boldsymbol{P}^{\boldsymbol{-1}}_{\boldsymbol{\omega}}\boldsymbol{i}^{\boldsymbol{\Delta}}_{\boldsymbol{dqz}}}{2}}_{\boldsymbol{\Phi}^{\boldsymbol{\Delta}}_{\boldsymbol{B}}} + \underbrace{\boldsymbol{P}^{\boldsymbol{-1}}_{\boldsymbol{\omega}}\boldsymbol{m}^{\boldsymbol{\Delta}}_{\boldsymbol{dqz}} \circ \boldsymbol{P}^{\boldsymbol{-1}}_{\boldsymbol{-2\omega}}\boldsymbol{i}^{\boldsymbol{\Sigma}}_{\boldsymbol{dqz}}}_{\boldsymbol{\Phi}^{\boldsymbol{\Delta}}_{\boldsymbol{C}}} \tag{2.18b}$$

The equation expressed in (2.18b), must be multiplied by the Park transformation matrix at the angular frequency ω, so that it can be possible to solve for $d\boldsymbol{v}^{\boldsymbol{\Delta}}_{\boldsymbol{Cdqz}}/dt$.

Multiplying $\boldsymbol{\Phi}^{\boldsymbol{\Delta}}_{\boldsymbol{A}}$ by $\boldsymbol{P}_{\boldsymbol{\omega}}$, gives:

$$\boldsymbol{P}_{\boldsymbol{\omega}}\boldsymbol{\Phi}^{\boldsymbol{\Delta}}_{\boldsymbol{A}} = 2C_{arm}\boldsymbol{J}_{\boldsymbol{\omega}}\boldsymbol{v}^{\boldsymbol{\Delta}}_{\boldsymbol{Cdqz}} + 2C_{arm}\frac{d\boldsymbol{v}^{\boldsymbol{\Delta}}_{\boldsymbol{Cdqz}}}{dt} \tag{2.19}$$

where $\boldsymbol{J}_{\boldsymbol{\omega}}$ is defined as in (2.20):

$$\boldsymbol{J}_{\boldsymbol{\omega}} \overset{\text{def}}{=} \boldsymbol{P}_{\boldsymbol{\omega}}\frac{d\boldsymbol{P}^{\boldsymbol{-1}}_{\boldsymbol{\omega}}}{dt} = \begin{bmatrix} 0 & \omega & 0 \\ -\omega & 0 & 0 \\ 0 & 0 & 0 \end{bmatrix} \tag{2.20}$$

Furthermore, multiplying $\boldsymbol{\Phi}^{\boldsymbol{\Delta}}_{\boldsymbol{B}}$ by $\boldsymbol{P}_{\boldsymbol{\omega}}$ gives:

$$\boldsymbol{P}_{\boldsymbol{\omega}}\boldsymbol{\Phi}^{\boldsymbol{\Delta}}_{\boldsymbol{B}} = \boldsymbol{P}_{\boldsymbol{\omega}}\left(\boldsymbol{P}^{\boldsymbol{-1}}_{\boldsymbol{-2\omega}}\boldsymbol{m}^{\boldsymbol{\Sigma}}_{\boldsymbol{dqz}} \circ \frac{\boldsymbol{P}^{\boldsymbol{-1}}_{\boldsymbol{\omega}}\boldsymbol{i}^{\boldsymbol{\Delta}}_{\boldsymbol{dqz}}}{2}\right) = \boldsymbol{M}^{\boldsymbol{\Delta}}_{\boldsymbol{\Phi_B}}\begin{bmatrix} i^{\Delta}_d & i^{\Delta}_q & i^{\Delta}_z \end{bmatrix}^{\top} \tag{2.21}$$

where $\boldsymbol{M}^{\boldsymbol{\Delta}}_{\boldsymbol{\Phi_B}}$ is expressed in (2.22). For simplicity, it will be considered that the system under study does not allow for the existence of the zero-sequence grid current; i.e., $i^{\Delta}_z = 0$, highlighted in gray in (2.21). Under this assumption, only the dq component of (2.21) is time-invariant, as the 3ω oscillatory signals that appear in $\boldsymbol{M}^{\boldsymbol{\Delta}}_{\boldsymbol{\Phi_B}}$ are either multiplying i^{Δ}_z (third column of the matrix) or appear in the last row. However, it is possible to rewrite also the dynamics of v^{Δ}_{Cz} in SSTI form by means of additional mathematical manipulations, as will be shown further.

$$\boldsymbol{M}^{\boldsymbol{\Delta}}_{\boldsymbol{\Phi_B}} = \tfrac{1}{4}\left[\begin{array}{cc:c} m^{\Sigma}_d + 2m^{\Sigma}_z & -m^{\Sigma}_q & 2m^{\Sigma}_d\cos(3\omega t) - 2m^{\Sigma}_q\sin(3\omega t) \\ -m^{\Sigma}_q & -m^{\Sigma}_d + 2m^{\Sigma}_z & 2m^{\Sigma}_q\cos(3\omega t) + 2m^{\Sigma}_d\sin(3\omega t) \\ \hdashline m^{\Sigma}_d\cos(3\omega t) - m^{\Sigma}_q\sin(3\omega t) & m^{\Sigma}_q\cos(3\omega t) + m^{\Sigma}_d\sin(3\omega t) & 2m^{\Sigma}_z \end{array}\right] \tag{2.22}$$

Finally, multiplying $\boldsymbol{\Phi}^{\boldsymbol{\Delta}}_{\boldsymbol{C}}$ from (2.18b) by $\boldsymbol{P}_{\boldsymbol{\omega}}$ gives:

$$\boldsymbol{P}_{\boldsymbol{\omega}}\boldsymbol{\Phi}^{\boldsymbol{\Delta}}_{\boldsymbol{C}} = \boldsymbol{P}_{\boldsymbol{\omega}}\left(\boldsymbol{P}^{\boldsymbol{-1}}_{\boldsymbol{\omega}}\boldsymbol{m}^{\boldsymbol{\Delta}}_{\boldsymbol{dqz}} \circ \boldsymbol{P}^{\boldsymbol{-1}}_{\boldsymbol{-2\omega}}\boldsymbol{i}^{\boldsymbol{\Sigma}}_{\boldsymbol{dqz}}\right) = \boldsymbol{M}^{\boldsymbol{\Delta}}_{\boldsymbol{\Phi_C}}\begin{bmatrix} i^{\Sigma}_d & i^{\Sigma}_q & i^{\Sigma}_z \end{bmatrix}^{\top} \tag{2.23}$$

where $\boldsymbol{M}^{\boldsymbol{\Delta}}_{\boldsymbol{\Phi_C}}$ is expressed in (2.24).

$$\boldsymbol{M}^{\boldsymbol{\Delta}}_{\boldsymbol{\Phi_C}} = \frac{1}{2}\left[\begin{array}{cc:c} m^{\Delta}_d + 2m^{\Delta}_z\cos(3\omega t) & -m^{\Delta}_q - 2m^{\Delta}_z\sin(3\omega t) & 2m^{\Delta}_d \\ -m^{\Delta}_q + 2m^{\Delta}_z\sin(3\omega t) & -m^{\Delta}_d + 2m^{\Delta}_z\cos(3\omega t) & 2m^{\Delta}_q \\ \hdashline m^{\Delta}_d\cos(3\omega t) + m^{\Delta}_q\sin(3\omega t) & m^{\Delta}_q\cos(3\omega t) - m^{\Delta}_d\sin(3\omega t) & 2m^{\Delta}_z \end{array}\right] \tag{2.24}$$

Here, $\boldsymbol{M}^{\boldsymbol{\Delta}}_{\boldsymbol{\Phi_C}}$ requires further mathematical manipulation to achieve the desired SSTI performance, as the 3ω signals also appear. Moreover, they affect not only the zero-sequence as in the previous case, yet the dq components as well.

Replacing the definitions given in (2.19), (2.21) and (2.23) in $\boldsymbol{P}^{\boldsymbol{-1}}_{\boldsymbol{\omega}}\boldsymbol{\Phi}^{\boldsymbol{\Delta}}_{\boldsymbol{A}} = \boldsymbol{P}^{\boldsymbol{-1}}_{\boldsymbol{\omega}}\boldsymbol{\Phi}^{\boldsymbol{\Delta}}_{\boldsymbol{B}} + \boldsymbol{P}^{\boldsymbol{-1}}_{\boldsymbol{\omega}}\boldsymbol{\Phi}^{\boldsymbol{\Delta}}_{\boldsymbol{C}}$ and solving for the voltage difference dynamics in their dqz coordinates results in (2.25):

$$\frac{d\boldsymbol{v}^{\boldsymbol{\Delta}}_{\boldsymbol{Cdqz}}}{dt} = \frac{1}{2C_{arm}}\left(\boldsymbol{M}^{\boldsymbol{\Delta}}_{\boldsymbol{\Phi_B}}\begin{bmatrix} i^{\Delta}_d & i^{\Delta}_q & i^{\Delta}_z \end{bmatrix}^{\top} + \boldsymbol{M}^{\boldsymbol{\Delta}}_{\boldsymbol{\Phi_C}}\begin{bmatrix} i^{\Sigma}_d & i^{\Sigma}_q & i^{\Sigma}_z \end{bmatrix}^{\top}\right) - \boldsymbol{J}_{\boldsymbol{\omega}}\boldsymbol{v}^{\boldsymbol{\Delta}}_{\boldsymbol{Cdqz}} \tag{2.25}$$

Since neither $\boldsymbol{M}^{\boldsymbol{\Delta}}_{\boldsymbol{\Phi_B}}$ or $\boldsymbol{M}^{\boldsymbol{\Delta}}_{\boldsymbol{\Phi_C}}$ are SSTI, equation (2.25) is not directly providing a SSTI solution. This issue is treated in the remainder of this section.

Deriving the SSTI *dq* dynamics of (2.25)

First, the dq dynamics of (2.25) are addressed. As discussed earlier, since it is assumed that $i_z^{\Delta} = 0$, only $\boldsymbol{M}_{\boldsymbol{\Phi_C}}^{\boldsymbol{\Delta}}$ is hindering a SSTI representation for the dq dynamics due to the appearance of the $\cos(3\omega t)$ and $\sin(3\omega t)$ in the 2×2 sub-matrix at the upper left corner of $\boldsymbol{M}_{\boldsymbol{\Phi_C}}^{\boldsymbol{\Delta}}$ in (2.24), referred to as $\boldsymbol{M}_{\boldsymbol{\Phi_C}}^{\boldsymbol{\Delta 2\times 2}}$. One possible solution is to assume that the MMC control will always set m_z^{Δ} to zero, as was done in [127], as m_z^{Δ} is multiplying all of the 3ω oscillating signals. However, this lead to a restrictive model from a control perspective as it will be discussed in the following Chapter, and therefore such assumption is avoided here. Taking inspiration from common engineering practices to increase controllability in VSCs [131], the proposed solution is to redefine m_z^{Δ} as a third harmonic injection, as given in (2.26), where $m_{Z_d}^{\Delta}$ and $m_{Z_q}^{\Delta}$ are two SSTI variables which are linked to the amplitude and phase angle of third harmonic oscillations in m_z^{Δ}.

$$m_z^{\Delta} \stackrel{\text{def}}{=} m_{Z_d}^{\Delta} \cos(3\omega t) + m_{Z_q}^{\Delta} \sin(3\omega t) \tag{2.26}$$

Replacing the new definition (2.26) in (2.24) results in the sub-matrix $\boldsymbol{M}_{\boldsymbol{\Phi_C}}^{\boldsymbol{\Delta 2\times 2}}$ from (2.27a), which yields (2.27b) after developing.

$$\boldsymbol{M}_{\boldsymbol{\Phi_C}}^{\boldsymbol{\Delta 2\times 2}} = \tfrac{1}{2}\begin{bmatrix} m_d^{\Delta} + 2\left(m_{Z_d}^{\Delta}\cos(3\omega t) + m_{Z_q}^{\Delta}\sin(3\omega t)\right)\cos(3\omega t) & -m_q^{\Delta} - 2\left(m_{Z_d}^{\Delta}\cos(3\omega t) + m_{Z_q}^{\Delta}\sin(3\omega t)\right)\sin(3\omega t) \\ -m_q^{\Delta} + 2\left(m_{Z_d}^{\Delta}\cos(3\omega t) + m_{Z_q}^{\Delta}\sin(3\omega t)\right)\sin(3\omega t) & -m_d^{\Delta} + 2\left(m_{Z_d}^{\Delta}\cos(3\omega t) + m_{Z_q}^{\Delta}\sin(3\omega t)\right)\cos(3\omega t) \end{bmatrix} \tag{2.27a}$$

$$\boldsymbol{M}_{\boldsymbol{\Phi_C}}^{\boldsymbol{\Delta 2\times 2}} = \tfrac{1}{2}\begin{bmatrix} +\left(m_d^{\Delta} + m_{Z_d}^{\Delta}\right) & -\left(m_q^{\Delta} + m_{Z_q}^{\Delta}\right) \\ -\left(m_q^{\Delta} - m_{Z_q}^{\Delta}\right) & -\left(m_d^{\Delta} - m_{Z_d}^{\Delta}\right) \end{bmatrix} + \underbrace{\begin{bmatrix} +\cos(6\omega t) & +\sin(6\omega t) \\ +\sin(6\omega t) & -\cos(6\omega t) \end{bmatrix}\begin{bmatrix} +m_{Z_d}^{\Delta} & +m_{Z_q}^{\Delta} \\ +m_{Z_q}^{\Delta} & -m_{Z_d}^{\Delta} \end{bmatrix}}_{\approx 0} \tag{2.27b}$$

Furthermore, the multiplication of the oscillatory signals at 3ω induces some terms at 6ω, which can be neglected as will be confirmed via time-domain simulations.

Deriving SSTI expressions for the zero-sequence dynamics of (2.25)

The zero sequence dynamics equation of (2.25), is given again in (2.28) for convenience.

$$\begin{aligned} \frac{dv_{Cz}^{\Delta}}{dt} =& \frac{1}{C_{arm}}\left[\frac{1}{8}\left(m_d^{\Sigma}i_d^{\Delta} + m_q^{\Sigma}i_q^{\Delta} + 2m_d^{\Delta}i_d^{\Sigma} + 2m_q^{\Delta}i_q^{\Sigma}\right)\cos(3\omega t) + \dots \right. \\ & \left. \cdots + \frac{1}{8}\left(-m_q^{\Sigma}i_d^{\Delta} + m_d^{\Sigma}i_q^{\Delta} + 2m_q^{\Delta}i_d^{\Sigma} - 2m_d^{\Delta}i_q^{\Sigma}\right)\sin(3\omega t) + \frac{m_z^{\Delta}}{2}i_z^{\Sigma}\right] \end{aligned} \tag{2.28}$$

By replacing the new definition of m_z^{Δ} given in (2.26) into (2.28), the zero-sequence dynamics of v_{Cz}^{Δ} can be written as:

$$\frac{dv_{Cz}^{\Delta}}{dt} = \frac{1}{C_{arm}}\left[\Psi_d \cos(3\omega t) + \Psi_q \sin(3\omega t)\right] \tag{2.29}$$

where Ψ_d and Ψ_q are defined as below.

$$\begin{aligned} \Psi_d =& \frac{1}{8}\left(+m_d^{\Sigma}i_d^{\Delta} + m_q^{\Sigma}i_q^{\Delta} + 2m_d^{\Delta}i_d^{\Sigma} + 2m_q^{\Delta}i_q^{\Sigma} + 4m_{Z_d}^{\Delta}i_z^{\Sigma}\right) \\ \Psi_q =& \frac{1}{8}\left(-m_q^{\Sigma}i_d^{\Delta} + m_d^{\Sigma}i_q^{\Delta} + 2m_q^{\Delta}i_d^{\Sigma} - 2m_d^{\Delta}i_q^{\Sigma} + 4m_{Z_q}^{\Delta}i_z^{\Sigma}\right) \end{aligned}$$

Since the zero sequence dynamics in (2.29) are still time-varying in steady-state, further reformulation is necessary to obtain the desired model with SSTI solution. This can be obtained

by defining an auxiliary virtual state $v^{\Delta}_{CZ_\beta}$, shifted 90° with respect to the original "single-phase" time-periodic voltage difference signal v^{Δ}_{Cz} according to the approach from [127]. This approach is conceptually similar to the commonly applied strategy of generating a virtual two-phase system for representing single-phase systems in a SRRF [140] (also called Fictive Axis Emulator [141]).

The real and virtual voltage difference zero-sequence variables can be labeled as $v^{\Delta}_{CZ_\alpha}$ and $v^{\Delta}_{CZ_\beta}$, and together they define an orthogonal $\alpha\beta$-system. This $\alpha\beta$-system can be expressed by (2.30a)-(2.30b), where the first equation is exactly the same as (2.29), while the second equation replaces the $\cos(3\omega t)$ and $\sin(3\omega t)$ that appear in (2.29) by $\sin(3\omega t)$ and $-\cos(3\omega t)$, respectively.

$$\frac{dv^{\Delta}_{CZ_\alpha}}{dt} = \frac{1}{C_{arm}}\left[\Psi_d \cos(3\omega t) + \Psi_q \sin(3\omega t)\right] \tag{2.30a}$$

$$\frac{dv^{\Delta}_{CZ_\beta}}{dt} = \frac{1}{C_{arm}}\left[\Psi_d \sin(3\omega t) - \Psi_q \cos(3\omega t)\right] \tag{2.30b}$$

Defining $\boldsymbol{v^{\Delta}_{CZ_{\alpha\beta}}} \stackrel{\text{def}}{=} [v^{\Delta}_{CZ_\alpha} v^{\Delta}_{CZ_\beta}]^\top$, the equations (2.30a) and (2.30b) are written in a compact form as shown in (2.31).

$$\frac{d\boldsymbol{v^{\Delta}_{CZ_{\alpha\beta}}}}{dt} = \frac{1}{C_{arm}}\left\{\boldsymbol{T_{3\omega}}\begin{bmatrix}\Psi_d & \Psi_q\end{bmatrix}^\top\right\} \tag{2.31}$$

where $\boldsymbol{T_{3\omega}}$ is a rotation matrix at 3ω as defined in (2.32).

$$\boldsymbol{T_{3\omega}} \stackrel{\text{def}}{=} \begin{bmatrix}\cos(3\omega t) & \sin(3\omega t)\\ \sin(3\omega t) & -\cos(3\omega t)\end{bmatrix} \tag{2.32}$$

Furthermore, by defining $\boldsymbol{v^{\Delta}_{CZ}} \stackrel{\text{def}}{=} [v^{\Delta}_{CZ_d} v^{\Delta}_{CZ_q}]^\top$ which verifies:

$$\boldsymbol{v^{\Delta}_{CZ_{\alpha\beta}}} = \boldsymbol{T^{-1}_{3\omega}} \boldsymbol{v^{\Delta}_{CZ}}, \tag{2.33}$$

replacing (2.33) into (2.31), multiplying by $\boldsymbol{T_{3\omega}}$ and solving for the dynamics of $\boldsymbol{v^{\Delta}_{CZ}}$ gives:

$$\frac{d\boldsymbol{v^{\Delta}_{CZ}}}{dt} = \frac{1}{C_{arm}}\left\{\begin{bmatrix}\Psi_d & \Psi_q\end{bmatrix}^\top - C_{arm}\boldsymbol{J_{3\omega}}\boldsymbol{v^{\Delta}_{CZ}}\right\} \tag{2.34}$$

where $\boldsymbol{J_{3\omega}}$ is defined as in (2.35).

$$\boldsymbol{J_{3\omega}} \stackrel{\text{def}}{=} \begin{bmatrix}0 & -3\omega\\ 3\omega & 0\end{bmatrix}. \tag{2.35}$$

Equation (2.34) will produce now a SSTI solution. The original oscillating zero-sequence component v^{Δ}_{Cz} can always be re-created as a function of $v^{\Delta}_{CZ_d}$ and $v^{\Delta}_{CZ_q}$ by means of (2.33), as:

$$v^{\Delta}_{Cz} = v^{\Delta}_{CZ_d}\cos(3\omega t) + v^{\Delta}_{CZ_q}\sin(3\omega t) \tag{2.36}$$

Final formulation

It is useful to redefine a new augmented vector for the SSTI voltage difference states $\boldsymbol{v^{\Delta}_{CdqZ}}$ (with capital Z), as:

$$\boldsymbol{v^{\Delta}_{CdqZ}} \stackrel{\text{def}}{=} \begin{bmatrix}v^{\Delta}_{Cd} & v^{\Delta}_{Cq} & v^{\Delta}_{CZ_d} & v^{\Delta}_{CZ_q}\end{bmatrix}^\top, \tag{2.37}$$

as well as for the "Δ" modulation indices, as:

$$\boldsymbol{m}^{\boldsymbol{\Delta}}_{\boldsymbol{dqZ}} \stackrel{\text{def}}{=} \begin{bmatrix} m^{\Delta}_{d} & m^{\Delta}_{q} & m^{\Delta}_{Z_d} & m^{\Delta}_{Z_q} \end{bmatrix}^{\top}. \tag{2.38}$$

With the new definitions $v^{\Delta}_{CZ_d}$, $v^{\Delta}_{CZ_q}$ and their associated dynamics given (2.34) as well as taking into account the modified (sub-)matrix $\boldsymbol{M}^{\boldsymbol{\Delta 2\times 2}}_{\boldsymbol{\Phi_C}}$ given in (2.27b); the SSTP dynamics of $\boldsymbol{v}^{\boldsymbol{\Delta}}_{\boldsymbol{Cdqz}}$ from (2.25) may be now expressed in their SSTI equivalents, by means of the 4×1 state vector $\boldsymbol{v}^{\boldsymbol{\Delta}}_{\boldsymbol{CdqZ}}$ as shown in (2.39), with $\boldsymbol{J_G}$ defined in (2.40).

$$\begin{aligned} \frac{d\boldsymbol{v}^{\boldsymbol{\Delta}}_{\boldsymbol{CdqZ}}}{dt} = &- \boldsymbol{J_G}\boldsymbol{v}^{\boldsymbol{\Delta}}_{\boldsymbol{CdqZ}} + \frac{1}{C_{arm}} \left\{ \frac{1}{8} \begin{bmatrix} \left(m^{\Sigma}_{d} + 2m^{\Sigma}_{z}\right) & -m^{\Sigma}_{q} \\ -m^{\Sigma}_{q} & \left(-m^{\Sigma}_{d} + 2m^{\Sigma}_{z}\right) \\ +m^{\Sigma}_{d} & m^{\Sigma}_{q} \\ -m^{\Sigma}_{q} & m^{\Sigma}_{d} \end{bmatrix} \boldsymbol{i}^{\boldsymbol{\Delta}}_{\boldsymbol{dq}} + ... \right. \\ &\left. \cdots + \frac{1}{4} \begin{bmatrix} +\left(m^{\Delta}_{d} + m^{\Delta}_{Z_d}\right) & -\left(m^{\Delta}_{q} + m^{\Delta}_{Z_q}\right) & m^{\Delta}_{d} \\ -\left(m^{\Delta}_{q} - m^{\Delta}_{Z_q}\right) & -\left(m^{\Delta}_{d} - m^{\Delta}_{Z_d}\right) & m^{\Delta}_{q} \\ m^{\Delta}_{d} & m^{\Delta}_{q} & 2m^{\Delta}_{Z_d} \\ m^{\Delta}_{q} & -m^{\Delta}_{d} & 2m^{\Delta}_{Z_q} \end{bmatrix} \boldsymbol{i}^{\boldsymbol{\Sigma}}_{\boldsymbol{dqz}} \right\}. \end{aligned} \tag{2.39}$$

$$\boldsymbol{J_G} \stackrel{\text{def}}{=} \begin{bmatrix} 0 & \omega & \\ -\omega & 0 & \boldsymbol{0_{2\times 2}} \\ \boldsymbol{0_{2\times 2}} & & \boldsymbol{J_{3\omega}} \end{bmatrix} \tag{2.40}$$

2.4.2 Voltage sum Σ SSTI dynamics derivation

Initial formulation

The SSTI dynamics for the voltage sum can be derived in a similar way as for the voltage difference. The starting point is indeed the SSTP dynamics of the variable given in (2.15) and recalled in (2.41a) for convenience. The first step consist in expressing the stationary frame abc vectors present in (2.41a) as functions of their respective dqz equivalents. This is done in (2.41b), where $\boldsymbol{v}^{\boldsymbol{\Sigma}}_{\boldsymbol{Cabc}}$, $\boldsymbol{m}^{\boldsymbol{\Delta}}_{\boldsymbol{abc}}$, $\boldsymbol{i}^{\boldsymbol{\Delta}}_{\boldsymbol{abc}}$, $\boldsymbol{m}^{\boldsymbol{\Sigma}}_{\boldsymbol{abc}}$ and $\boldsymbol{i}^{\boldsymbol{\Sigma}}_{\boldsymbol{abc}}$ have been respectively replaced by $\boldsymbol{P}^{\boldsymbol{-1}}_{\boldsymbol{-2\omega}}\boldsymbol{v}^{\boldsymbol{\Sigma}}_{\boldsymbol{Cdqz}}$, $\boldsymbol{P}^{\boldsymbol{-1}}_{\boldsymbol{\omega}}\boldsymbol{m}^{\boldsymbol{\Delta}}_{\boldsymbol{dqz}}$, $\boldsymbol{P}^{\boldsymbol{-1}}_{\boldsymbol{\omega}}\boldsymbol{i}^{\boldsymbol{\Delta}}_{\boldsymbol{dqz}}$, $\boldsymbol{P}^{\boldsymbol{-1}}_{\boldsymbol{-2\omega}}\boldsymbol{m}^{\boldsymbol{\Sigma}}_{\boldsymbol{dqz}}$ and $\boldsymbol{P}^{\boldsymbol{-1}}_{\boldsymbol{-2\omega}}\boldsymbol{i}^{\boldsymbol{\Sigma}}_{\boldsymbol{dqz}}$. Notice that here also, the choice of the inverse Park transformation at ω ($\boldsymbol{P}^{\boldsymbol{-1}}_{\boldsymbol{\omega}}$) or at 2ω ($\boldsymbol{P}^{\boldsymbol{-1}}_{\boldsymbol{-2\omega}}$) is according to the frequency separation of the variables given in Table 2.1.

Equation (2.41b) can be divided in three parts: $\boldsymbol{\Phi}^{\boldsymbol{\Sigma}}_{\boldsymbol{A}}$, $\boldsymbol{\Phi}^{\boldsymbol{\Sigma}}_{\boldsymbol{B}}$ and $\boldsymbol{\Phi}^{\boldsymbol{\Sigma}}_{\boldsymbol{C}}$, as indicated in (2.41b). These three parts are treated consecutively in the following.

$$2C_{arm}\frac{d\boldsymbol{v}^{\boldsymbol{\Sigma}}_{\boldsymbol{Cabc}}}{dt} = \boldsymbol{m}^{\boldsymbol{\Delta}}_{\boldsymbol{abc}} \circ \frac{\boldsymbol{i}^{\boldsymbol{\Delta}}_{\boldsymbol{abc}}}{2} + \boldsymbol{m}^{\boldsymbol{\Sigma}}_{\boldsymbol{abc}} \circ \boldsymbol{i}^{\boldsymbol{\Sigma}}_{\boldsymbol{abc}} \tag{2.41a}$$

$$\underbrace{2C_{arm}\frac{d\boldsymbol{P}^{\boldsymbol{-1}}_{\boldsymbol{-2\omega}}}{dt}\boldsymbol{v}^{\boldsymbol{\Sigma}}_{\boldsymbol{Cdqz}} + 2C_{arm}\boldsymbol{P}^{\boldsymbol{-1}}_{\boldsymbol{-2\omega}}\frac{d\boldsymbol{v}^{\boldsymbol{\Sigma}}_{\boldsymbol{Cdqz}}}{dt}}_{\boldsymbol{\Phi}^{\boldsymbol{\Sigma}}_{\boldsymbol{A}}} = \underbrace{\boldsymbol{P}^{\boldsymbol{-1}}_{\boldsymbol{\omega}}\boldsymbol{m}^{\boldsymbol{\Delta}}_{\boldsymbol{dqz}} \circ \frac{\boldsymbol{P}^{\boldsymbol{-1}}_{\boldsymbol{\omega}}\boldsymbol{i}^{\boldsymbol{\Delta}}_{\boldsymbol{dqz}}}{2}}_{\boldsymbol{\Phi}^{\boldsymbol{\Sigma}}_{\boldsymbol{B}}} + \underbrace{\boldsymbol{P}^{\boldsymbol{-1}}_{\boldsymbol{-2\omega}}\boldsymbol{m}^{\boldsymbol{\Sigma}}_{\boldsymbol{dqz}} \circ \boldsymbol{P}^{\boldsymbol{-1}}_{\boldsymbol{-2\omega}}\boldsymbol{i}^{\boldsymbol{\Sigma}}_{\boldsymbol{dqz}}}_{\boldsymbol{\Phi}^{\boldsymbol{\Sigma}}_{\boldsymbol{C}}} \tag{2.41b}$$

The equation expressed in (2.41b), needs to be multiplied by Park transformation at -2ω, so that it can be solved for $d\boldsymbol{v}^{\boldsymbol{\Sigma}}_{\boldsymbol{Cdqz}}/dt$. Multiplying $\boldsymbol{\Phi}^{\boldsymbol{\Sigma}}_{\boldsymbol{A}}$ by $\boldsymbol{P}_{\boldsymbol{-2\omega}}$ gives (2.42), where $\boldsymbol{J}_{\boldsymbol{-2\omega}}$ is defined as $-2\boldsymbol{J}_{\boldsymbol{\omega}}$.

$$\boldsymbol{P}_{\boldsymbol{-2\omega}}\boldsymbol{\Phi}^{\boldsymbol{\Sigma}}_{\boldsymbol{A}} = 2C_{arm}\boldsymbol{J}_{\boldsymbol{-2\omega}}\boldsymbol{v}^{\boldsymbol{\Sigma}}_{\boldsymbol{Cdqz}} + 2C_{arm}\frac{d\boldsymbol{v}^{\boldsymbol{\Sigma}}_{\boldsymbol{Cdqz}}}{dt} \tag{2.42}$$

Furthermore, multiplying $\boldsymbol{\Phi}_{\boldsymbol{B}}^{\boldsymbol{\Sigma}}$ by $\boldsymbol{P}_{\boldsymbol{-2\omega}}$ gives (2.43), where $\boldsymbol{M}_{\boldsymbol{\Phi}_{\boldsymbol{B}}}^{\boldsymbol{\Sigma}}$ is expressed in (2.44).

$$\boldsymbol{P}_{\boldsymbol{-2\omega}}\boldsymbol{\Phi}_{\boldsymbol{B}}^{\boldsymbol{\Sigma}} = \boldsymbol{P}_{\boldsymbol{-2\omega}}\left(\boldsymbol{P}_{\boldsymbol{\omega}}^{\boldsymbol{-1}}\boldsymbol{m}_{\boldsymbol{dqz}}^{\boldsymbol{\Delta}} \circ \frac{\boldsymbol{P}_{\boldsymbol{\omega}}^{\boldsymbol{-1}}\boldsymbol{i}_{\boldsymbol{dqz}}^{\boldsymbol{\Delta}}}{2}\right) = \boldsymbol{M}_{\boldsymbol{\Phi}_{\boldsymbol{B}}}^{\boldsymbol{\Sigma}}\begin{bmatrix} i_d^{\Delta} & i_q^{\Delta} & i_z^{\Delta} \end{bmatrix}^{\top} \tag{2.43}$$

As mentioned earlier, it is assumed for simplicity in this work that there cannot be any zero-sequence grid current; i.e., $i_z^{\Delta} = 0$ (highlighted in gray).

$$\boldsymbol{M}_{\boldsymbol{\Phi}_{\boldsymbol{B}}}^{\boldsymbol{\Sigma}} = \frac{1}{4}\left[\begin{array}{cc:c} +m_d^{\Delta} + 2m_z^{\Delta}\cos(3\omega t) & -m_q^{\Delta} + 2m_z^{\Delta}\sin(3\omega t) & 2\left(m_d^{\Delta}\cos(3\omega t) + m_q^{\Delta}\sin(3\omega t)\right) \\ -m_q^{\Delta} - 2m_z^{\Delta}\sin(3\omega t) & -m_d^{\Delta} + 2m_z^{\Delta}\cos(3\omega t) & 2\left(m_q^{\Delta}\cos(3\omega t) - m_d^{\Delta}\sin(3\omega t)\right) \\ \hdashline m_d^{\Delta} & m_q^{\Delta} & 2m_z^{\Delta} \end{array}\right] \tag{2.44}$$

Equation (2.21) does not yet produce a SSTI solution, as the elements in the upper left 2×2 sub-matrix of $\boldsymbol{M}_{\boldsymbol{\Phi}_{\boldsymbol{B}}}^{\boldsymbol{\Sigma}}$ in (2.44), contain sine and cosine signals oscillating at 3ω. Note that this is also the case for the terms highlighted in gray, but since these are being multiplied by $i_z^{\Delta} = 0$, they are not considered in this work. To overcome this obstacle, the same solution used in the previous section is applied: as all the oscillating terms are being multiplied by m_z^{Δ}, it is convenient to redefine m_z^{Δ} by a third harmonic injection as in (2.26), as a function of the SSTI virtual variables $m_{Z_d}^{\Delta}$ and $m_{Z_q}^{\Delta}$. Replacing (2.26) into (2.44) allows for re-writing (2.43) as in (2.45).

$$\begin{aligned} \boldsymbol{P}_{\boldsymbol{-2\omega}}\boldsymbol{\Phi}_{\boldsymbol{B}}^{\boldsymbol{\Sigma}} = \frac{1}{4}&\begin{bmatrix} +\left(m_d^{\Delta} + m_{Z_d}^{\Delta}\right)i_d^{\Delta} - \left(m_q^{\Delta} - m_{Z_q}^{\Delta}\right)i_q^{\Delta} \\ -\left(m_q^{\Delta} + m_{Z_q}^{\Delta}\right)i_d^{\Delta} - \left(m_d^{\Delta} - m_{Z_d}^{\Delta}\right)i_q^{\Delta} \\ m_d^{\Delta}i_d^{\Delta} + m_q^{\Delta}i_q^{\Delta} \end{bmatrix} + ... \\ ... + \underbrace{\frac{1}{4}\begin{bmatrix} \cos(6\omega t) & -\sin(6\omega t) & 0 \\ -\sin(6\omega t) & -\cos(6\omega t) & 0 \\ 0 & 0 & 0 \end{bmatrix}\begin{bmatrix} +m_{Z_d}^{\Delta}i_d^{\Delta} - m_{Z_q}^{\Delta}i_q^{\Delta} \\ -m_{Z_q}^{\Delta}i_d^{\Delta} - m_{Z_d}^{\Delta}i_q^{\Delta} \\ 0 \end{bmatrix}}_{\approx 0} \end{aligned} \tag{2.45}$$

Equation (2.45) will become time-invariant only if it is assumed that the oscillatory signals at 6ω can be neglected, which has been confirmed via time-domain simulations.

In a similar fashion, $\boldsymbol{\Phi}_{\boldsymbol{C}}^{\boldsymbol{\Sigma}}$; i.e., the second component on the right side of (2.41b), is multiplied by $\boldsymbol{P}_{\boldsymbol{-2\omega}}$, resulting in (2.46), which can be considered SSTI if the sixth harmonic components are neglected. Here again, the validity of the approximation was confirmed via time-domain simulations.

$$\begin{aligned} \boldsymbol{P}_{\boldsymbol{-2\omega}}\boldsymbol{\Phi}_{\boldsymbol{C}}^{\boldsymbol{\Sigma}} = \frac{1}{2}&\begin{bmatrix} 2m_z^{\Sigma}i_d^{\Sigma} + 2m_d^{\Sigma}i_z^{\Sigma} \\ 2m_z^{\Sigma}i_q^{\Sigma} + 2m_q^{\Sigma}i_z^{\Sigma} \\ m_d^{\Sigma}i_d^{\Sigma} + m_q^{\Sigma}i_q^{\Sigma} + 2m_z^{\Sigma}i_z^{\Sigma} \end{bmatrix} + ... \\ ... + \underbrace{\frac{1}{2}\begin{bmatrix} \left(+m_d^{\Sigma}i_d^{\Sigma} - m_q^{\Sigma}i_q^{\Sigma}\right)\cos(6\omega t) - \left(m_q^{\Sigma}i_d^{\Sigma} + m_d^{\Sigma}i_q^{\Sigma}\right)\sin(6\omega t) \\ \left(-m_d^{\Sigma}i_d^{\Sigma} + m_q^{\Sigma}i_q^{\Sigma}\right)\sin(6\omega t) - \left(m_q^{\Sigma}i_d^{\Sigma} + m_d^{\Sigma}i_q^{\Sigma}\right)\cos(6\omega t) \\ 0 \end{bmatrix}}_{\approx 0} \end{aligned} \tag{2.46}$$

Final formulation

The SSTI dynamics of the voltage sum vector $\boldsymbol{v}^{\boldsymbol{\Sigma}}_{\boldsymbol{Cdqz}}$ are found by replacing the SSTI equations (2.42), (2.45) and (2.46) in (2.41b) and solving for $d\boldsymbol{v}^{\boldsymbol{\Sigma}}_{\boldsymbol{Cdqz}}/dt$, resulting in (2.47).

$$\frac{d\boldsymbol{v}^{\boldsymbol{\Sigma}}_{\boldsymbol{Cdqz}}}{dt} = -\boldsymbol{J}_{\boldsymbol{-2\omega}}\boldsymbol{v}^{\boldsymbol{\Sigma}}_{\boldsymbol{Cdqz}} + ... \tag{2.47}$$
$$... + \frac{1}{C_{arm}}\left\{\frac{1}{4}\begin{bmatrix}2m_z^\Sigma & 0 & 2m_d^\Sigma \\ 0 & 2m_z^\Sigma & 2m_q^\Sigma \\ m_d^\Sigma & m_q^\Sigma & 2m_z^\Sigma\end{bmatrix}\boldsymbol{i}^{\boldsymbol{\Sigma}}_{\boldsymbol{dqz}} + \frac{1}{8}\begin{bmatrix}+\left(m_d^\Delta + m_{Z_d}^\Delta\right) & -\left(m_q^\Delta - m_{Z_q}^\Delta\right) \\ -\left(m_q^\Delta + m_{Z_q}^\Delta\right) & -\left(m_d^\Delta - m_{Z_d}^\Delta\right) \\ m_d^\Delta & m_q^\Delta\end{bmatrix}\boldsymbol{i}^{\boldsymbol{\Delta}}_{\boldsymbol{dq}}\right\}$$

2.4.3 Common-mode currents Σ SSTI dynamics derivation

The SSTI dynamics for the common-mode currents are derived in the following. First, the equation of the dynamics for $\boldsymbol{i}^{\boldsymbol{\Sigma}}_{\boldsymbol{abc}}$ in stationary frame given in (2.13) and recalled in (2.48a), is rewritten by expressing the *abc* vectors in the equation as a function of their *dqz* equivalents, as indicated in (2.48b).

$$L_{arm}\frac{d\boldsymbol{i}^{\boldsymbol{\Sigma}}_{\boldsymbol{abc}}}{dt} = \frac{\boldsymbol{v_{dc}}}{2} - \boldsymbol{v}^{\boldsymbol{\Sigma}}_{\boldsymbol{mabc}} - R_{arm}\boldsymbol{i}^{\boldsymbol{\Sigma}}_{\boldsymbol{abc}} \tag{2.48a}$$

$$L_{arm}\frac{d\boldsymbol{P}^{\boldsymbol{-1}}_{\boldsymbol{-2\omega}}}{dt}\boldsymbol{i}^{\boldsymbol{\Sigma}}_{\boldsymbol{dqz}} + L_{arm}\boldsymbol{P}^{\boldsymbol{-1}}_{\boldsymbol{-2\omega}}\frac{d\boldsymbol{i}^{\boldsymbol{\Sigma}}_{\boldsymbol{dqz}}}{dt} = \frac{\boldsymbol{v_{dc}}}{2} - \boldsymbol{P}^{\boldsymbol{-1}}_{\boldsymbol{-2\omega}}\boldsymbol{v}^{\boldsymbol{\Sigma}}_{\boldsymbol{mdqz}} - R_{arm}\boldsymbol{P}^{\boldsymbol{-1}}_{\boldsymbol{-2\omega}}\boldsymbol{i}^{\boldsymbol{\Sigma}}_{\boldsymbol{dqz}} \tag{2.48b}$$

By further multiplying (2.48b) by $\boldsymbol{P}_{\boldsymbol{-2\omega}}$ and solving for $d\boldsymbol{i}^{\boldsymbol{\Sigma}}_{\boldsymbol{dqz}}/dt$ gives:

$$L_{arm}\frac{d\boldsymbol{i}^{\boldsymbol{\Sigma}}_{\boldsymbol{dqz}}}{dt} = \begin{bmatrix}0 & 0 & \frac{v_{dc}}{2}\end{bmatrix}^\top - \boldsymbol{v}^{\boldsymbol{\Sigma}}_{\boldsymbol{mdqz}} - R_{arm}\boldsymbol{i}^{\boldsymbol{\Sigma}}_{\boldsymbol{dqz}} - L_{arm}\boldsymbol{J}_{\boldsymbol{-2\omega}}\boldsymbol{i}^{\boldsymbol{\Sigma}}_{\boldsymbol{dqz}}, \tag{2.49}$$

where $\boldsymbol{v}^{\boldsymbol{\Sigma}}_{\boldsymbol{mdqz}} = \boldsymbol{P}^{\boldsymbol{-1}}_{\boldsymbol{-2\omega}}\boldsymbol{v}^{\boldsymbol{\Sigma}}_{\boldsymbol{mabc}}$, and $\boldsymbol{v}^{\boldsymbol{\Sigma}}_{\boldsymbol{mabc}}$ is defined in (2.14). Nonetheless, in order to assess if (2.49) is SSTI, $\boldsymbol{v}^{\boldsymbol{\Sigma}}_{\boldsymbol{mdqz}}$ needs to be rewritten by expressing the *abc* vectors in the equation as a function of their *dqz* equivalents, as indicated in (2.50).

$$\begin{aligned}\boldsymbol{v}^{\boldsymbol{\Sigma}}_{\boldsymbol{mdqz}} =& \frac{1}{2}\boldsymbol{P}_{\boldsymbol{-2\omega}}\left(\boldsymbol{P}^{\boldsymbol{-1}}_{\boldsymbol{-2\omega}}\boldsymbol{m}^{\boldsymbol{\Sigma}}_{\boldsymbol{dqz}} \circ \boldsymbol{P}^{\boldsymbol{-1}}_{\boldsymbol{-2\omega}}\boldsymbol{v}^{\boldsymbol{\Sigma}}_{\boldsymbol{Cdqz}} + \boldsymbol{P}^{\boldsymbol{-1}}_{\boldsymbol{\omega}}\boldsymbol{m}^{\boldsymbol{\Delta}}_{\boldsymbol{dqz}} \circ \boldsymbol{P}^{\boldsymbol{-1}}_{\boldsymbol{\omega}}\boldsymbol{v}^{\boldsymbol{\Delta}}_{\boldsymbol{Cdqz}}\right) \\ =& \boldsymbol{V}^{\boldsymbol{\Sigma}}_{\boldsymbol{A}}\begin{bmatrix}m_d^\Sigma & m_q^\Sigma & m_z^\Sigma\end{bmatrix}^\top + \boldsymbol{V}^{\boldsymbol{\Sigma}}_{\boldsymbol{B}}\begin{bmatrix}m_d^\Delta & m_q^\Delta & m_z^\Delta\end{bmatrix}^\top_,\end{aligned} \tag{2.50}$$

where $\boldsymbol{V}^{\boldsymbol{\Sigma}}_{\boldsymbol{A}}$ and $\boldsymbol{V}^{\boldsymbol{\Sigma}}_{\boldsymbol{B}}$ are expressed in (2.51) and (2.52), respectively.

$$\boldsymbol{V}^{\boldsymbol{\Sigma}}_{\boldsymbol{A}} = \frac{1}{4}\begin{bmatrix}2v_{Cz}^\Sigma & 0 & 2v_{Cd}^\Sigma \\ 0 & 2v_{Cz}^\Sigma & 2v_{Cq}^\Sigma \\ v_{Cd}^\Sigma & v_{Cq}^\Sigma & 2v_{Cz}^\Sigma\end{bmatrix} + ... \tag{2.51}$$
$$... + \frac{1}{4}\begin{bmatrix}\underbrace{\begin{matrix}v_{Cd}^\Sigma\cos(6\omega t) - v_{Cq}^\Sigma\sin(6\omega t) & -v_{Cq}^\Sigma\cos(6\omega t) + v_{Cd}^\Sigma\sin(6\omega t) & 0 \\ -v_{Cq}^\Sigma\cos(6\omega t) - v_{Cd}^\Sigma\sin(6\omega t) & -v_{Cd}^\Sigma\cos(6\omega t) + v_{Cq}^\Sigma\sin(6\omega t) & 0 \\ 0 & 0 & 0\end{matrix}}_{\approx 0}\end{bmatrix}$$

$$\boldsymbol{V}^{\boldsymbol{\Sigma}}_{\boldsymbol{B}} = \tfrac{1}{4}\begin{bmatrix}+v_{Cd}^\Delta + 2v_{Cz}^\Delta\cos(3\omega t) & -v_{Cq}^\Delta + 2v_{Cz}^\Delta\sin(3\omega t) & +2v_{Cd}^\Delta\cos(3\omega t) + 2v_{Cq}^\Delta\sin(3\omega t) \\ -v_{Cq}^\Delta - 2v_{Cz}^\Delta\sin(3\omega t) & -v_{Cd}^\Delta + 2v_{Cz}^\Delta\cos(3\omega t) & -2v_{Cd}^\Delta\sin(3\omega t) + 2v_{Cq}^\Delta\cos(3\omega t) \\ v_{Cd}^\Delta & v_{Cq}^\Delta & 2v_{Cz}^\Delta\end{bmatrix} \tag{2.52}$$

If the sixth harmonic components are neglected, $\boldsymbol{V_A^\Sigma}$ given in (2.51) can be considered as SSTI. This is confirmed via time-domain simulations. However, this is not the case for $\boldsymbol{V_B^\Sigma}$ given in (2.52), as it presents non-negligible third harmonic oscillations. To overcome this obstacle, it is necessary to replace into (2.51) and in (2.50) the new definitions of both m_z^Δ and v_{Cz}^Δ given in (2.26) and (2.36), respectively. Doing so, results in the SSTI definition of $\boldsymbol{v_{mdqz}^\Sigma}$ in (2.53), where $\boldsymbol{V_B^{\Sigma\star}}$ is given in (2.54) and is SSTI if the sixth harmonic components are neglected.

$$\boldsymbol{v_{mdqz}^\Sigma} = \boldsymbol{V_A^\Sigma}\begin{bmatrix} m_d^\Sigma & m_q^\Sigma & m_z^\Sigma \end{bmatrix}^\top + \boldsymbol{V_B^{\Sigma\star}}\begin{bmatrix} m_d^\Delta & m_q^\Delta & m_{Z_d}^\Delta & m_{Z_q}^\Delta \end{bmatrix}^\top, \tag{2.53}$$

$$\boldsymbol{V_B^{\Sigma\star}} = \frac{1}{4}\begin{bmatrix} +v_{Cd}^\Delta + v_{CZ_d}^\Delta & +v_{CZ_q}^\Delta - v_{Cq}^\Delta & v_{Cd}^\Delta & v_{Cq}^\Delta \\ -v_{Cq}^\Delta - v_{CZ_q}^\Delta & -v_{Cd}^\Delta + v_{CZ_d}^\Delta & v_{Cq}^\Delta & -v_{Cd}^\Delta \\ v_{Cd}^\Delta & v_{Cq}^\Delta & v_{CZ_d}^\Delta & v_{CZ_q}^\Delta \end{bmatrix} + \ldots \tag{2.54}$$

$$\underbrace{\begin{bmatrix} +v_{CZ_d}^\Delta\cos(6\omega t) + v_{CZ_q}^\Delta\sin(6\omega t) & +v_{CZ_d}^\Delta\sin(6\omega t) - v_{CZ_q}^\Delta\cos(6\omega t) & +v_{Cd}^\Delta\cos(6\omega t) + v_{Cq}^\Delta\sin(6\omega t) & -v_{Cq}^\Delta\cos(6\omega t) + v_{Cd}^\Delta\sin(6\omega t) \\ -v_{CZ_d}^\Delta\sin(6\omega t) + v_{CZ_q}^\Delta\cos(6\omega t) & +v_{CZ_d}^\Delta\cos(6\omega t) + v_{CZ_q}^\Delta\sin(6\omega t) & -v_{Cd}^\Delta\sin(6\omega t) + v_{Cq}^\Delta\cos(6\omega t) & +v_{Cd}^\Delta\cos(6\omega t) + v_{Cq}^\Delta\sin(6\omega t) \\ 0 & 0 & +v_{CZ_d}^\Delta\cos(6\omega t) + v_{CZ_q}^\Delta\sin(6\omega t) & +v_{CZ_d}^\Delta\sin(6\omega t) - v_{CZ_q}^\Delta\cos(6\omega t) \end{bmatrix}}_{\approx 0}$$

Replacing (2.51) and (2.54) in (2.53), gives:

$$\begin{bmatrix} v_{md}^\Sigma \\ v_{mq}^\Sigma \\ v_{mz}^\Sigma \end{bmatrix} = \frac{1}{4}\left[\begin{array}{ccc|cccc} 2v_{Cz}^\Sigma & 0 & 2v_{Cd}^\Sigma & v_{Cd}^\Delta + v_{CZ_d}^\Delta & v_{CZ_q}^\Delta - v_{Cq}^\Delta & v_{Cd}^\Delta & v_{Cq}^\Delta \\ 0 & 2v_{Cz}^\Sigma & 2v_{Cq}^\Sigma & -v_{Cq}^\Delta - v_{CZ_q}^\Delta & v_{CZ_d}^\Delta - v_{Cd}^\Delta & v_{Cq}^\Delta & -v_{Cd}^\Delta \\ v_{Cd}^\Sigma & v_{Cq}^\Sigma & 2v_{Cz}^\Sigma & v_{Cd}^\Delta & v_{Cq}^\Delta & v_{CZ_d}^\Delta & v_{CZ_q}^\Delta \end{array}\right] \left[\begin{array}{c} m_d^\Sigma \\ m_q^\Sigma \\ m_z^\Sigma \\ \hline m_d^\Delta \\ m_q^\Delta \\ m_{Z_d}^\Delta \\ m_{Z_q}^\Delta \end{array}\right] \tag{2.55}$$

Note that in (2.55) the terms v_{Cz}^Σ are highlighted in blue. The reason is that the numerical value of v_{Cz}^Σ is around the value of v_{dc}, while the remaining components in (2.55) are always lower than v_{dc}.

Finally, the SSTI dynamics of the common-mode currents are given in (2.56), where the sixth harmonic components are neglected.

$$\frac{d\boldsymbol{i_{dqz}^\Sigma}}{dt} = \frac{1}{L_{arm}}\left\{\begin{bmatrix} 0 \\ 0 \\ \frac{v_{dc}}{2} \end{bmatrix} - R_{arm}\boldsymbol{i_{dqz}^\Sigma} - \underbrace{\left(\boldsymbol{V_A^\Sigma m_{dqz}^\Sigma} + \boldsymbol{V_B^{\Sigma\star} m_{dqZ}^\Delta}\right)}_{\boldsymbol{v_{mdqz}^\Sigma}}\right\} - \boldsymbol{J_{\text{-}2\omega}}\boldsymbol{i_{dqz}^\Sigma} \tag{2.56}$$

The dynamic equation in (2.56) can be expressed as a circuit diagram as in Fig. 2.11. The dq components of $\boldsymbol{i_{dqz}^\Sigma}$ are represented with two coupled circuits. These currents don't flow to the AC- neither DC-side of the MMC; they *circulate* inside the converter. In fact, that is the reason why these components are called *circulating currents*. Also note that the zero-sequence component i_z^Σ is proportional to the DC current, in fact $i_{dc} = 3 \times i_z^\Sigma$. Moreover, in the circuit of i_z^Σ it is added an inductor L_{dc} (marked in red). This inductor may represent the DC smoothing reactor on the DC-side of the MMC as studied in [79], or the inductor from the DC breaker which can have an important value [142]. Nevertheless, for the rest of this Chapter, L_{dc} is not taken into account.

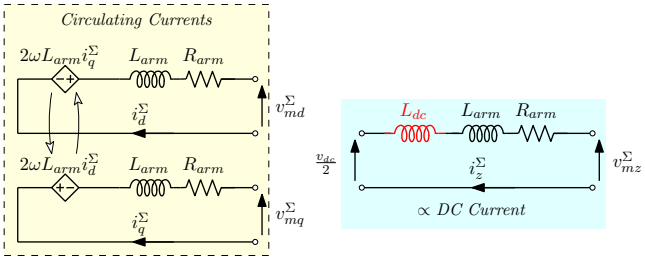

Figure 2.11 – Common-mode currents circuit diagram

Finally, note in Fig. 2.11 that each modulated voltage v_m^Σ are driving each one of the dqz currents. It may appear that the dq and z components are decoupled, but this is only achieved by a proper selection of the modulation indices. This is due to the relations in (2.55), which corresponds to a highly coupled matrix relating each component of v_m^Σ with all the modulation indices (even with the "Δ" variables in dqZ frame).

2.4.4 Grid currents Δ SSTI dynamics derivation

Finally, the derivation of SSTI expressions for the grid current dynamics are presented in the following. The beginning of the proof is the SSTP dynamics equation of the grid current in the stationary reference frame given in (2.11)-(2.12), and recalled in (2.57a) for convenience. As for the previous cases, the dynamics are rewritten by expressing the abc vectors present in (2.57a) as a function of their dqz equivalents, as indicated in (2.57b).

$$L_{eq}^{ac}\frac{d\boldsymbol{i}_{\boldsymbol{abc}}^{\boldsymbol{\Delta}}}{dt} = \boldsymbol{v}_{\boldsymbol{mabc}}^{\boldsymbol{\Delta}} - \boldsymbol{v}_{\boldsymbol{abc}}^{\boldsymbol{G}} - R_{eq}^{ac}\boldsymbol{i}_{\boldsymbol{abc}}^{\boldsymbol{\Delta}}, \tag{2.57a}$$

$$L_{eq}^{ac}\frac{d\boldsymbol{P}_{\boldsymbol{\omega}}^{\boldsymbol{-1}}}{dt}\boldsymbol{i}_{\boldsymbol{dqz}}^{\boldsymbol{\Delta}} + L_{eq}^{ac}\boldsymbol{P}_{\boldsymbol{\omega}}^{\boldsymbol{-1}}\frac{d\boldsymbol{i}_{\boldsymbol{dqz}}^{\boldsymbol{\Delta}}}{dt} = \boldsymbol{P}_{\boldsymbol{\omega}}^{\boldsymbol{-1}}\boldsymbol{v}_{\boldsymbol{mdqz}}^{\boldsymbol{\Delta}} - \boldsymbol{P}_{\boldsymbol{\omega}}^{\boldsymbol{-1}}\boldsymbol{v}_{\boldsymbol{dqz}}^{\boldsymbol{G}} - R_{eq}^{ac}\boldsymbol{P}_{\boldsymbol{\omega}}^{\boldsymbol{-1}}\boldsymbol{i}_{\boldsymbol{dqz}}^{\boldsymbol{\Delta}} \tag{2.57b}$$

By multiplying (2.57b) by $\boldsymbol{P}_{\boldsymbol{\omega}}$ and solving for $d\boldsymbol{i}_{\boldsymbol{dqz}}^{\boldsymbol{\Delta}}/dt$ gives (2.58).

$$L_{eq}^{ac}\frac{d\boldsymbol{i}_{\boldsymbol{dqz}}^{\boldsymbol{\Delta}}}{dt} = \boldsymbol{v}_{\boldsymbol{mdqz}}^{\boldsymbol{\Delta}} - \boldsymbol{v}_{\boldsymbol{dqz}}^{\boldsymbol{G}} - R_{eq}^{ac}\boldsymbol{i}_{\boldsymbol{dqz}}^{\boldsymbol{\Delta}} - L_{eq}^{ac}\boldsymbol{J}_{\boldsymbol{\omega}}\boldsymbol{i}_{\boldsymbol{dqz}}^{\boldsymbol{\Delta}} \tag{2.58}$$

where $\boldsymbol{v}_{\boldsymbol{dqz}}^{\boldsymbol{G}} = [v_d^G\ v_q^G\ 0]^\top$, $\boldsymbol{v}_{\boldsymbol{mdqz}}^{\boldsymbol{\Delta}} \overset{\text{def}}{=} \boldsymbol{P}_{\boldsymbol{\omega}}\boldsymbol{v}_{\boldsymbol{mabc}}^{\boldsymbol{\Delta}}$ and $\boldsymbol{v}_{\boldsymbol{mabc}}^{\boldsymbol{\Delta}}$ is defined in (2.12). Nonetheless, $\boldsymbol{v}_{\boldsymbol{mdqz}}^{\boldsymbol{\Delta}}$ needs to be assessed in order to verify if (2.58) produces a SSTI solution. For this purpuse, $\boldsymbol{v}_{\boldsymbol{mdqz}}^{\boldsymbol{\Delta}}$ is rewritten by expressing the abc vectors in its definition as a function of their dqz equivalents, as indicated in (2.59a).

$$\boldsymbol{v}_{\boldsymbol{mdqz}}^{\boldsymbol{\Delta}} = -\boldsymbol{P}_{\boldsymbol{\omega}}\frac{1}{2}\left(\boldsymbol{P}_{\boldsymbol{\omega}}^{\boldsymbol{-1}}\boldsymbol{m}_{\boldsymbol{dqz}}^{\boldsymbol{\Delta}} \circ \boldsymbol{P}_{\boldsymbol{-2\omega}}^{\boldsymbol{-1}}\boldsymbol{v}_{\boldsymbol{Cdqz}}^{\boldsymbol{\Sigma}} + \boldsymbol{P}_{\boldsymbol{-2\omega}}^{\boldsymbol{-1}}\boldsymbol{m}_{\boldsymbol{dqz}}^{\boldsymbol{\Sigma}} \circ \boldsymbol{P}_{\boldsymbol{\omega}}^{\boldsymbol{-1}}\boldsymbol{v}_{\boldsymbol{Cdqz}}^{\boldsymbol{\Delta}}\right) \tag{2.59a}$$

$$\boldsymbol{v}_{\boldsymbol{mdqz}}^{\boldsymbol{\Delta}} = \boldsymbol{V}_{\boldsymbol{A}}^{\boldsymbol{\Delta}}\begin{bmatrix} m_d^\Sigma & m_q^\Sigma & m_z^\Sigma \end{bmatrix}^\top + \boldsymbol{V}_{\boldsymbol{B}}^{\boldsymbol{\Delta}}\begin{bmatrix} m_d^\Delta & m_q^\Delta & m_z^\Delta \end{bmatrix}^\top \tag{2.59b}$$

where $\boldsymbol{V}_{\boldsymbol{A}}^{\boldsymbol{\Delta}}$ and $\boldsymbol{V}_{\boldsymbol{B}}^{\boldsymbol{\Delta}}$ are expressed in (2.60) and (2.61), respectively.

$$\boldsymbol{V}_{\boldsymbol{A}}^{\boldsymbol{\Delta}} = \frac{1}{4}\begin{bmatrix} -v_{Cd}^\Delta - 2v_{Cz}^\Delta\cos(3\omega t) & +v_{Cq}^\Delta + 2v_{Cz}^\Delta\sin(3\omega t) & -2v_{Cd}^\Delta \\ +v_{Cq}^\Delta - 2v_{Cz}^\Delta\sin(3\omega t) & +v_{Cd}^\Delta - 2v_{Cz}^\Delta\cos(3\omega t) & -2v_{Cq}^\Delta \\ -v_{Cd}^\Delta\cos(3\omega t) - v_{Cq}^\Delta\sin(3\omega t) & v_{Cd}^\Delta\sin(3\omega t) - v_{Cq}^\Delta\cos(3\omega t) & -2v_{Cz}^\Delta \end{bmatrix} \tag{2.60}$$

$$\boldsymbol{V}_{\boldsymbol{B}}^{\boldsymbol{\Delta}} = \tfrac{1}{4}\begin{bmatrix} -v_{Cd}^\Sigma - 2v_{Cz}^\Sigma & v_{Cq}^\Sigma & -2v_{Cd}^\Sigma\cos(3\omega t) + 2v_{Cq}^\Sigma\sin(3\omega t) \\ v_{Cq}^\Sigma & -2v_{Cz}^\Sigma + v_{Cd}^\Sigma & -2v_{Cq}^\Sigma\cos(3\omega t) - 2v_{Cd}^\Sigma\sin(3\omega t) \\ +v_{Cq}^\Sigma\sin(3\omega t) - v_{Cd}^\Sigma\cos(3\omega t) & -v_{Cq}^\Sigma\cos(3\omega t) - v_{Cd}^\Sigma\sin(3\omega t) & -2v_{Cz}^\Sigma \end{bmatrix} \tag{2.61}$$

Both matrices present non-negligible third order harmonic components preventing the possibility of considering SSTI solutions from (2.58). As performed in previous section, it is necessary to replace into (2.60) and (2.61), the new definitions of m_z^{Δ} and v_{Cz}^{Δ} given in given in (2.26) and (2.36), respectively. Moreover, the zero-sequence of the modulated voltage v_{mz}^{Δ} is defined following the same approach as for m_z^{Δ} and v_{Cz}^{Δ}:

$$v_{mz}^{\Delta} \stackrel{\text{def}}{=} v_{mZ_d}^{\Delta}\cos(3\omega t) + v_{mZ_q}^{\Delta}\sin(3\omega t) \tag{2.62}$$

By doing so, the definition of the modulation voltage $\boldsymbol{v}_{\boldsymbol{mdqZ}}^{\boldsymbol{\Delta}}$ can be expressed as in (2.63), where $\boldsymbol{V}_{\boldsymbol{A'}}^{\boldsymbol{\Delta}}$ and $\boldsymbol{V}_{\boldsymbol{B'}}^{\boldsymbol{\Delta}}$ are given in (2.64) and (2.65), and will result in SSTI solutions if the sixth harmonic are neglected.

$$\boldsymbol{v}_{\boldsymbol{mdqZ}}^{\boldsymbol{\Delta}} \stackrel{\text{def}}{=} [v_{md}^{\Delta}, v_{mq}^{\Delta}, v_{mZ_d}^{\Delta}, v_{mZ_q}^{\Delta}]^{\top} = \boldsymbol{V}_{\boldsymbol{A'}}^{\boldsymbol{\Delta}}\begin{bmatrix} m_d^{\Sigma} & m_q^{\Sigma} & m_z^{\Sigma}\end{bmatrix}^{\top} + \boldsymbol{V}_{\boldsymbol{B'}}^{\boldsymbol{\Delta}}\begin{bmatrix} m_d^{\Delta} & m_q^{\Delta} & m_{Z_d}^{\Delta} & m_{Z_q}^{\Delta}\end{bmatrix}^{\top} \tag{2.63}$$

$$\begin{aligned}\boldsymbol{V}_{\boldsymbol{A'}}^{\boldsymbol{\Delta}} =& \frac{1}{4}\begin{bmatrix} -v_{Cd}^{\Delta} - v_{CZ_d}^{\Delta} & +v_{Cq}^{\Delta} + v_{CZ_q}^{\Delta} & -2v_{Cd}^{\Delta} \\ +v_{Cq}^{\Delta} - v_{CZ_q}^{\Delta} & +v_{Cd}^{\Delta} - v_{CZ_d}^{\Delta} & -2v_{Cq}^{\Delta} \\ -v_{Cd}^{\Sigma} & -v_{Cq}^{\Delta} & -2v_{CZ_d}^{\Delta} \\ -v_{Cq}^{\Sigma} & +v_{Cd}^{\Delta} & -2v_{CZ_q}^{\Delta}\end{bmatrix} + \dots \\ \dots +& \underbrace{\begin{bmatrix} -v_{CZ_d}^{\Delta}\cos(6\omega t) - v_{CZ_q}^{\Delta}\sin(6\omega t) & +v_{CZ_d}^{\Delta}\sin(6\omega t) - v_{CZ_q}^{\Delta}\cos(6\omega t) & 0 \\ +v_{CZ_q}^{\Delta}\cos(6\omega t) - v_{CZ_d}^{\Delta}\sin(6\omega t) & -v_{CZ_q}^{\Delta}\sin(6\omega t) - v_{CZ_d}^{\Delta}\cos(6\omega t) & 0 \\ 0 & 0 & 0 \\ 0 & 0 & 0\end{bmatrix}}_{\approx 0}\end{aligned} \tag{2.64}$$

$$\begin{aligned}\boldsymbol{V}_{\boldsymbol{B'}}^{\boldsymbol{\Delta}} =& \frac{1}{4}\begin{bmatrix} -v_{Cd}^{\Sigma} - 2v_{Cz}^{\Sigma} & +v_{Cq}^{\Sigma} & -v_{Cd}^{\Sigma} & +v_{Cq}^{\Sigma} \\ +v_{Cq}^{\Sigma} & -2v_{Cz}^{\Sigma} + v_{Cd}^{\Sigma} & -v_{Cq}^{\Sigma} & -v_{Cd}^{\Sigma} \\ -v_{Cd}^{\Sigma} & -v_{Cq}^{\Sigma} & -2v_{Cz}^{\Sigma} & 0 \\ +v_{Cq}^{\Sigma} & -v_{Cd}^{\Sigma} & 0 & -2v_{Cz}^{\Sigma}\end{bmatrix} + \dots \\ \dots +& \underbrace{\begin{bmatrix} 0 & 0 & v_{Cq}^{\Sigma}\sin(6\omega t) - v_{Cd}^{\Sigma}\cos(6\omega t) & -v_{Cq}^{\Sigma}\cos(6\omega t) - v_{Cd}^{\Sigma}\sin(6\omega t) \\ 0 & 0 & -v_{Cq}^{\Sigma}\cos(6\omega t) - v_{Cd}^{\Sigma}\sin(6\omega t) & -v_{Cq}^{\Sigma}\sin(6\omega t) + v_{Cd}^{\Sigma}\cos(6\omega t) \\ 0 & 0 & 0 & 0 \\ 0 & 0 & 0 & 0\end{bmatrix}}_{\approx 0}\end{aligned} \tag{2.65}$$

Replacing (2.64) and (2.65) in (2.63), gives:

$$\begin{bmatrix} v_{md}^{\Delta} \\ v_{mq}^{\Delta} \\ v_{mZ_d}^{\Delta} \\ v_{mZ_q}^{\Delta}\end{bmatrix} = \frac{1}{4}\left[\begin{array}{ccc|ccc} -v_{Cd}^{\Delta} - v_{CZ_d}^{\Delta} & v_{Cq}^{\Delta} + v_{CZ_q}^{\Delta} & -2v_{Cd}^{\Delta} & -v_{Cd}^{\Sigma} - 2v_{Cz}^{\Sigma} & v_{Cq}^{\Sigma} & -v_{Cd}^{\Sigma} & v_{Cq}^{\Sigma} \\ v_{Cq}^{\Delta} - v_{CZ_q}^{\Delta} & v_{Cd}^{\Delta} - v_{CZ_d}^{\Delta} & -2v_{Cq}^{\Delta} & v_{Cq}^{\Sigma} & v_{Cd}^{\Sigma} - 2v_{Cz}^{\Sigma} & -v_{Cq}^{\Sigma} & -v_{Cd}^{\Sigma} \\ -v_{Cd}^{\Delta} & -v_{Cq}^{\Delta} & -2v_{CZ_d}^{\Delta} & -v_{Cd}^{\Sigma} & -v_{Cq}^{\Sigma} & -2v_{Cz}^{\Sigma} & 0 \\ -v_{Cq}^{\Delta} & v_{Cd}^{\Delta} & -2v_{CZ_q}^{\Delta} & v_{Cq}^{\Sigma} & -v_{Cd}^{\Sigma} & 0 & -2v_{Cz}^{\Sigma}\end{array}\right]\begin{bmatrix} m_d^{\Sigma} \\ m_q^{\Sigma} \\ m_z^{\Sigma} \\ \hline m_d^{\Delta} \\ m_q^{\Delta} \\ m_{Z_d}^{\Delta} \\ m_{Z_q}^{\Delta}\end{bmatrix} \tag{2.66}$$

The complete formulation of $\boldsymbol{v}_{\boldsymbol{mdqZ}}^{\boldsymbol{\Delta}}$ from (2.63) is useful for control purposes as it will be detailed in the following Chapter. As it was stated before, the zero-sequence current doesn't have a path to flow due to the AC-side connection, but it doesn't mean that the voltage v_{mz}^{Δ} should be equal to zero: this is a degree of freedom [143, 144].

Finally, the SSTI dynamics of the grid currents are given in (2.67), where $\boldsymbol{V_A^{\Delta\star}}$ and $\boldsymbol{V_V^{\Delta\star}}$ are the sub-matrices from $\boldsymbol{v^{\Delta}_{mdqZ}}$, expressed in (2.68) and (2.69), respectively.

$$\frac{d\boldsymbol{i^{\Delta}_{dq}}}{dt} = \frac{1}{L^{ac}_{eq}} \left\{ -\boldsymbol{v^{G}_{dq}} - R^{ac}_{eq}\boldsymbol{i^{\Delta}_{dq}} + \underbrace{\left(\boldsymbol{V_A^{\Delta\star}}\boldsymbol{m^{\Sigma}_{dqz}} + \boldsymbol{V_B^{\Delta\star}}\boldsymbol{m^{\Delta}_{dqZ}}\right)}_{\boldsymbol{v^{\Delta}_{mdq}}} \right\} - \boldsymbol{J_{\omega}}\boldsymbol{i^{\Delta}_{dq}} \tag{2.67}$$

$$\boldsymbol{V_A^{\Delta\star}} = \frac{1}{4}\begin{bmatrix} -v^{\Delta}_{Cd} - v^{\Delta}_{CZ_d} & +v^{\Delta}_{Cq} + v^{\Delta}_{CZ_q} & -2v^{\Delta}_{Cd} \\ +v^{\Delta}_{Cq} - v^{\Delta}_{CZ_q} & +v^{\Delta}_{Cd} - v^{\Delta}_{CZ_d} & -2v^{\Delta}_{Cq} \end{bmatrix} \tag{2.68}$$

$$\boldsymbol{V_B^{\Delta\star}} = \frac{1}{4}\begin{bmatrix} -v^{\Sigma}_{Cd} - 2v^{\Sigma}_{Cz} & +v^{\Sigma}_{Cq} & -v^{\Sigma}_{Cd} & +v^{\Sigma}_{Cq} \\ +v^{\Sigma}_{Cq} & -2v^{\Sigma}_{Cz} + v^{\Sigma}_{Cd} & -v^{\Sigma}_{Cq} & -v^{\Sigma}_{Cd} \end{bmatrix} \tag{2.69}$$

The dq components are naturally coupled due to the Park transformation, with the terms $\omega L^{ac}_{eq} i^{\Delta}_{d}$ and $\omega L^{ac}_{eq} i^{\Delta}_{q}$. Moreover, they are also coupled due to the relation of the voltages v^{Δ}_{m} and the modulation indices Δ and Σ in (2.66).

2.4.5 Modulated voltages in dq frame

The modulated voltages $\boldsymbol{v^{\Sigma}_{mdqz}}$ from (2.55) and $\boldsymbol{v^{\Delta}_{mdqZ}}$ from (2.66) can be expressed in a single equation as shown in (2.70). This equation shows the relations between the modulated voltages and the modulation indices (MMC inputs), with the arm capacitor voltages with the "Σ-Δ" representation in dqz frame. This expression is a key point for the MMC control in dqz frame.

$$\left[\begin{array}{c} v^{\Sigma}_{md} \\ v^{\Sigma}_{mq} \\ \hline v^{\Sigma}_{mz} \\ \hline v^{\Delta}_{md} \\ v^{\Delta}_{mq} \\ v^{\Delta}_{mZ_d} \\ v^{\Delta}_{mZ_q} \end{array}\right] = \underbrace{\frac{1}{4}\left[\begin{array}{ccc|ccc|c} 2v^{\Sigma}_{Cz} & 0 & 2v^{\Sigma}_{Cd} & v^{\Delta}_{Cd} + v^{\Delta}_{CZ_d} & v^{\Delta}_{CZ_q} - v^{\Delta}_{Cq} & v^{\Delta}_{Cd} & v^{\Delta}_{Cq} \\ 0 & 2v^{\Sigma}_{Cz} & 2v^{\Sigma}_{Cq} & -v^{\Delta}_{Cq} - v^{\Delta}_{CZ_q} & v^{\Delta}_{CZ_d} - v^{\Delta}_{Cd} & v^{\Delta}_{Cq} & -v^{\Delta}_{Cd} \\ v^{\Sigma}_{Cd} & v^{\Sigma}_{Cq} & 2v^{\Sigma}_{Cz} & v^{\Delta}_{Cd} & v^{\Delta}_{Cq} & v^{\Delta}_{CZ_d} & v^{\Delta}_{CZ_q} \\ \hline -v^{\Delta}_{Cd} - v^{\Delta}_{CZ_d} & v^{\Delta}_{Cq} + v^{\Delta}_{CZ_q} & -2v^{\Delta}_{Cd} & -v^{\Sigma}_{Cd} - 2v^{\Sigma}_{Cz} & v^{\Sigma}_{Cq} & -v^{\Sigma}_{Cd} & v^{\Sigma}_{Cq} \\ v^{\Delta}_{Cq} - v^{\Delta}_{CZ_q} & v^{\Delta}_{Cd} - v^{\Delta}_{CZ_d} & -2v^{\Delta}_{Cq} & v^{\Sigma}_{Cq} & v^{\Sigma}_{Cd} - 2v^{\Sigma}_{Cz} & -v^{\Sigma}_{Cq} & -v^{\Sigma}_{Cd} \\ -v^{\Delta}_{Cd} & -v^{\Delta}_{Cq} & -2v^{\Delta}_{CZ_d} & -v^{\Sigma}_{Cd} & -v^{\Sigma}_{Cq} & -2v^{\Sigma}_{Cz} & 0 \\ -v^{\Delta}_{Cq} & v^{\Delta}_{Cd} & -2v^{\Delta}_{CZ_q} & v^{\Sigma}_{Cq} & -v^{\Sigma}_{Cd} & 0 & -2v^{\Sigma}_{Cz} \end{array}\right]}_{\boldsymbol{V^{\Sigma\Delta}_{CmdqZ}}} \left[\begin{array}{c} m^{\Sigma}_{d} \\ m^{\Sigma}_{q} \\ \hline m^{\Sigma}_{z} \\ \hline m^{\Delta}_{d} \\ m^{\Delta}_{q} \\ m^{\Delta}_{Z_d} \\ m^{\Delta}_{Z_q} \end{array}\right] \tag{2.70}$$

Equation (2.70) may be written in a compact form as:

$$\left[\begin{array}{c} \boldsymbol{v^{\Sigma}_{mdqz}} \\ \hline \boldsymbol{v^{\Delta}_{mdqZ}} \end{array}\right] = \boldsymbol{V^{\Sigma\Delta}_{CmdqZ}} \left[\begin{array}{c} \boldsymbol{m^{\Sigma}_{dqz}} \\ \hline \boldsymbol{m^{\Delta}_{dqZ}} \end{array}\right] \tag{2.71}$$

2.4.6 Summary of MMC Model with SSTI Solution

To summarize, the proposed MMC model with SSTI solution is graphically represented in Fig. 2.12, where the SSTI dynamics can be represented by means of equations (2.39), (2.47), (2.56) and (2.67), corresponding to the 12 SSTI state variables of the arm voltages difference $\boldsymbol{v^{\Delta}_{CdqZ}}$, arm voltages sum $\boldsymbol{v^{\Sigma}_{Cdqz}}$, circulating currents $\boldsymbol{i^{\Sigma}_{dqz}}$ and grid currents $\boldsymbol{i^{\Delta}_{dq}}$, as expressed in (2.72). Moreover, this model accepts 7 SSTI control inputs represented by the sum and difference of the modulation indices $\boldsymbol{m^{\Sigma}_{dqz}}$ and $\boldsymbol{m^{\Delta}_{dqZ}}$. In addition, the model receives 3 physical SSTI inputs represented by the voltage at the DC terminals v_{dc} and the dq components of the grid voltage, $\boldsymbol{v^{G}_{dq}}$, as expressed in (2.73).

$$\boldsymbol{x_{MMC}} = \begin{bmatrix} i^{\Delta}_{d} & i^{\Delta}_{q} & i^{\Sigma}_{d} & i^{\Sigma}_{q} & i^{\Sigma}_{z} & v^{\Sigma}_{Cd} & v^{\Sigma}_{Cq} & v^{\Sigma}_{Cz} & v^{\Delta}_{Cd} & v^{\Delta}_{Cq} & v^{\Delta}_{Cz} & v^{\Delta}_{CZ_d} & v^{\Delta}_{CZ_q} \end{bmatrix}^{\top} \in \mathbb{R}^{12} \tag{2.72}$$

$$\boldsymbol{u}_{MMC} = \Big[\underbrace{m_d^{\Sigma}\ m_q^{\Sigma}\ m_z^{\Sigma}\ m_d^{\Delta}\ m_q^{\Delta}\ m_{Z_d}^{\Delta}\ m_{Z_q}^{\Delta}}_{\textbf{Control inputs}}\ \underbrace{v_{dc}\ v_d^G\ v_q^G}_{\textbf{Phys.}}\Big]^{\top} \in \mathbb{R}^{10} \tag{2.73}$$

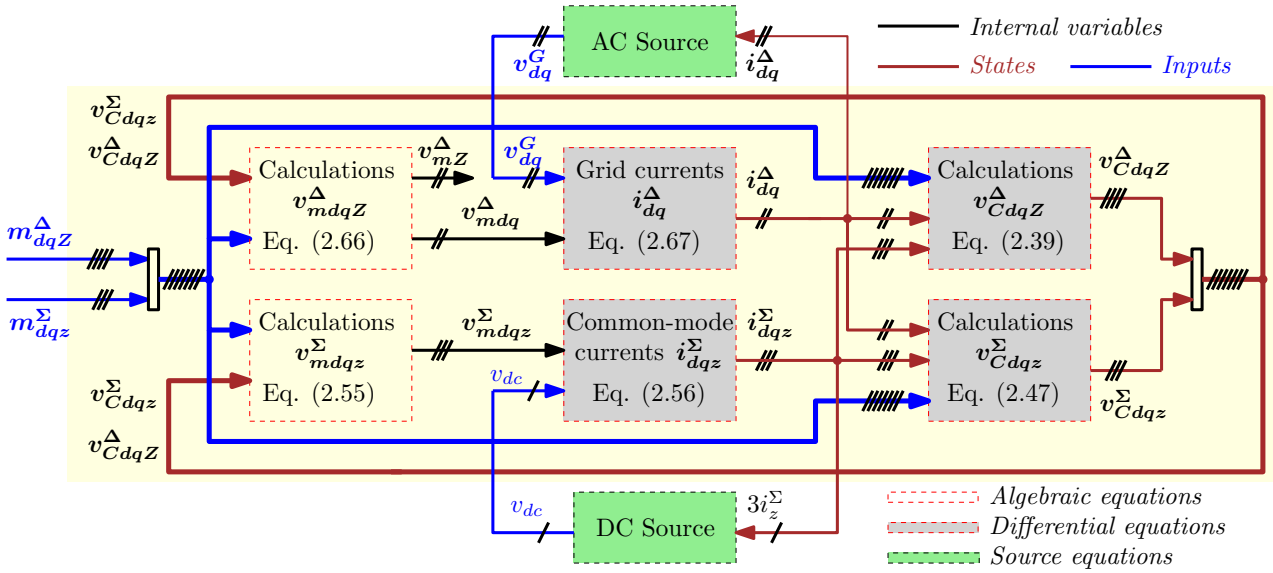

Figure 2.12 – Summary of the MMC equations with SSTI solution in dqz frame

The physical meaning of the variables in dqz frame are discussed in the following:

1. **Grid currents "Δ"** — $\boldsymbol{i_{dq}^{\Delta}} = [i_d^{\Delta}\ i_q^{\Delta}]^{\top}$ — (2.67): The classical AC currents in dq frame, with similar equation as for the *2-level* VSC. These currents are driven by the grid voltages $\boldsymbol{v_{dq}^{G}} = [v_d^G\ v_q^G]^{\top}$ and the AC-side modulated voltages $\boldsymbol{v_{mdq}^{\Delta}} = [v_{md}^{\Delta}\ v_{mq}^{\Delta}]^{\top}$.

2. **Modulated voltages "Δ"** — $\boldsymbol{v_{mdqZ}^{\Delta}} = [(\boldsymbol{v_{mdq}^{\Delta}})^{\top}\ v_{mZ_d}^{\Delta}\ v_{mZ_q}^{\Delta}]^{\top}$ — (2.66): The dq components of $\boldsymbol{v_{mdqZ}^{\Delta}}$ drive the AC-side currents $\boldsymbol{i_{dq}^{\Delta}}$; while the components $v_{mZ_d}^{\Delta}$ and $v_{mZ_q}^{\Delta}$ allows a SSTI representation of the amplitude and phase of the periodic third-harmonic component of the zero-sequence AC modulated voltage, which may be used explicitly for improving the limits of the MMC [145]. Contrary to the *2-level* VSC, where the modulated AC voltage is given by chopping the DC voltage; in the MMC the voltages $\boldsymbol{v_{mdqZ}^{\Delta}}$ are obtained by the modulation of the arm capacitor voltages. As shown in (2.66), all the modulated signals and capacitor voltages in dqz frame are involved in a highly coupled mechanism for the generation of $\boldsymbol{v_{mdqZ}^{\Delta}}$. With a proper modulation of these voltages, the grid currents can be controlled.

3. **Common-mode currents "Σ"** — $\boldsymbol{i_{dqz}^{\Sigma}} = [i_d^{\Sigma}\ i_q^{\Sigma}\ i_z^{\Sigma}]^{\top}$ — (2.56): The dq components corresponds to the internal circulating currents inside the converter. These currents are driven only by the internal modulated voltage v_{md}^{Σ} and v_{mq}^{Σ}. The z sequence component (which is the sum of all currents in abc) is proportional to the DC output current and hence, it is in charge of the active power transfer on the DC-side. This current is driven by the DC voltage and the internal modulated voltage v_{mz}^{Σ}.

4. **Modulated voltages "Σ"** — $\boldsymbol{v_{mdqz}^{\Sigma}} = [v_{md}^{\Sigma}\ v_{mq}^{\Sigma}\ v_{mz}^{\Sigma}]^{\top}$ — (2.55): For the generation of $\boldsymbol{v_{mdqz}^{\Sigma}}$, all the modulated signals and capacitor voltages in dqz frame are involved in a highly coupled mechanism similarly as for the modulated voltages "Δ". With these voltages, the three common mode currents can be regulated.

5. **Arm capacitor voltages "Σ" — $\boldsymbol{v^{\Sigma}_{Cdqz}} = [i^{\Sigma}_{d}\ i^{\Sigma}_{q}\ i^{\Sigma}_{z}]^{\top}$ — (2.47):** The dq variables corresponds to the amplitude and phase of the three-phase arm capacitors voltages sum, while the z component corresponds to the algebraic sum of the six arm capacitor voltages. The way that these variables can be controlled is detailed in the following Chapter.

6. **Arm capacitor voltages "Δ" — $\boldsymbol{v^{\Delta}_{CdqZ}}$ — (2.39):** As for the "Σ" variables, the dq components correspond to the amplitude and phase of the three-phase arm capacitors voltages difference. The z sequence, due to its natural time-periodic behavior, is modeled with two state variables ($v^{\Delta}_{CZ_d}$ and $v^{\Delta}_{CZ_q}$); representing the amplitude and phase of v^{Δ}_{Cz}.

It is important to recall that all the variables of the MMC model from Fig. 2.12 reach a constant equilibrium in steady-state operation. This characteristic presents several advantages such as the direct calculation of operating points by numerical resolution of the state-space equations; the application of Jacobian linearization for small-signal stability analysis based on eigenvalue analysis as presented in Chapter 1, application of mathematical tools for dynamic studies of linear models, among others.

2.5 Model validation by time-domain simulation

The objective of this section is to perform the validation of the obtained MMC model by time-domain simulations. However, a control system with SSTI solution should be first considered for this task. In the following section, the most basic MMC control is presented: The AC current controllers in dq frame and the "Un-Compensated Modulation" (UCM).

2.5.1 Modulation and Grid Current Controllers

The considered AC current controller for the MMC in this section is basically the same as for the classical *2-level* VSC from Section 1.2.2. The implementation of the controller is shown in Fig. 2.13a for the EMT model. In this figure, the angle θ_C is considered to be perfectly estimated by the PLL. Moreover, the boundary between the dq and abc frame is given by a green dashed vertical line, highlighting the Park transformations used to cross the boundary. The references for the modulated voltages $v^{\Sigma*}_{mj}$ is set to $v_{dc}/2$ [117].

For the EMT model, the modulation indices are calculated with the "Un-Compensated Modulation" (UCM) [146] (also called "direct modulation" in [137]). This modulation is based on the approximation that the arm capacitor voltages are near v_{dc} (i.e. $v^{\Sigma}_{C} \approx v_{dc}$) while considering that all the components from v^{Δ}_{C} are zero. With this assumption, the matrix $\boldsymbol{V^{\Sigma\Delta}_{Cmabc}}$ from (2.8) is approximated as shown in (2.74).

$$\boldsymbol{V^{\Sigma\Delta}_{Cmabc}} = \frac{1}{2}\left[\begin{array}{ccc|ccc} v^{\Sigma}_{Ca} & 0 & 0 & v^{\Delta}_{Ca} & 0 & 0 \\ 0 & v^{\Sigma}_{Cb} & 0 & 0 & v^{\Delta}_{Cb} & 0 \\ 0 & 0 & v^{\Sigma}_{Cc} & 0 & 0 & v^{\Delta}_{Cc} \\ \hline -v^{\Delta}_{Ca} & 0 & 0 & -v^{\Sigma}_{Ca} & 0 & 0 \\ 0 & -v^{\Delta}_{Cb} & 0 & 0 & -v^{\Sigma}_{Cb} & 0 \\ 0 & 0 & -v^{\Delta}_{Cc} & 0 & 0 & -v^{\Sigma}_{Cc} \end{array}\right] \approx \underbrace{\frac{1}{2}\left[\begin{array}{ccc|ccc} v_{dc} & 0 & 0 & 0 & 0 & 0 \\ 0 & v_{dc} & 0 & 0 & 0 & 0 \\ 0 & 0 & v_{dc} & 0 & 0 & 0 \\ \hline 0 & 0 & 0 & -v_{dc} & 0 & 0 \\ 0 & 0 & 0 & 0 & -v_{dc} & 0 \\ 0 & 0 & 0 & 0 & 0 & -v_{dc} \end{array}\right]}_{\boldsymbol{V^{UCM}_{Cmabc}}} \tag{2.74}$$

In this way, the modulation indices under the UCM method in abc frame are calculated as in (2.75). More details on the implementation of MMC controllers for the EMT simulation are

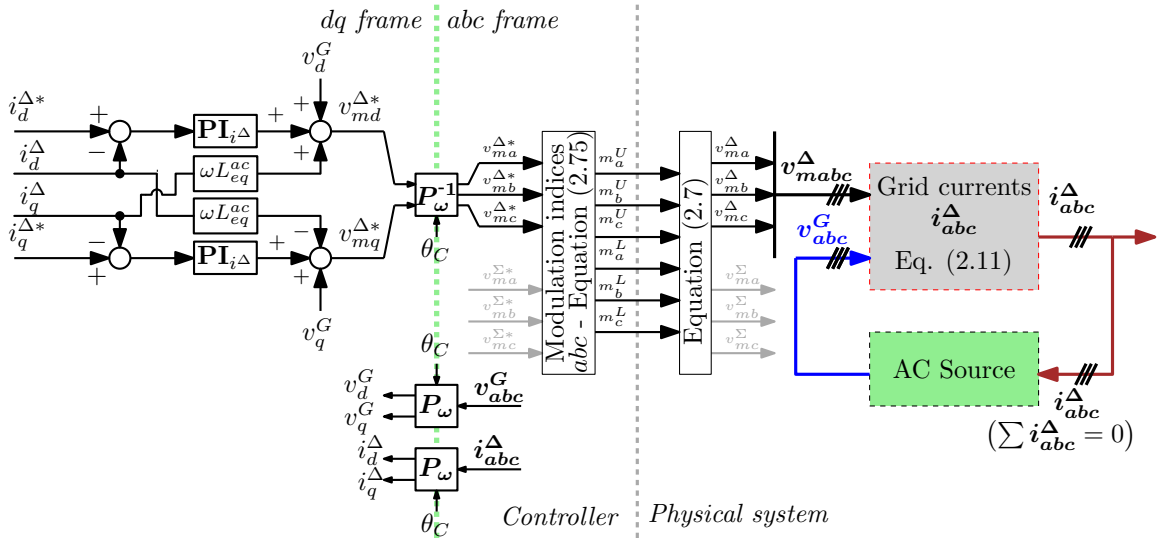

(a) Grid current controller for EMT model (b) Part of MMC-AAM model - Fig. 2.4

Figure 2.13 – Grid current controller for EMT model in mixed reference frames (*abc* for the MMC, and *dq* for the controller)

given in Appendix F.

$$\begin{bmatrix} \boldsymbol{m}^{U}_{\boldsymbol{abc}} \\ \boldsymbol{m}^{L}_{\boldsymbol{abc}} \end{bmatrix} = \underbrace{\frac{1}{2}\left[\begin{array}{ccc|ccc} 1 & 0 & 0 & 1 & 0 & 0 \\ 0 & 1 & 0 & 0 & 1 & 0 \\ 0 & 0 & 1 & 0 & 0 & 1 \\ \hline 1 & 0 & 0 & -1 & 0 & 0 \\ 0 & 1 & 0 & 0 & -1 & 0 \\ 0 & 0 & 1 & 0 & 0 & -1 \end{array}\right]}_{\textbf{From } \Sigma\Delta \textbf{ to U,L}} \underbrace{\frac{2}{v_{dc}}\left[\begin{array}{ccc|ccc} 1 & 0 & 0 & 0 & 0 & 0 \\ 0 & 1 & 0 & 0 & 0 & 0 \\ 0 & 0 & 1 & 0 & 0 & 0 \\ \hline 0 & 0 & 0 & -1 & 0 & 0 \\ 0 & 0 & 0 & 0 & -1 & 0 \\ 0 & 0 & 0 & 0 & 0 & -1 \end{array}\right]}_{\left[\boldsymbol{m}^{\Sigma}_{\boldsymbol{abc}}{}^{\top};\boldsymbol{m}^{\Delta}_{\boldsymbol{abc}}{}^{\top}\right]^{\top}} \begin{bmatrix} \boldsymbol{v}^{\boldsymbol{\Sigma *}}_{\boldsymbol{mabc}} \\ \boldsymbol{v}^{\boldsymbol{\Delta *}}_{\boldsymbol{mabc}} \end{bmatrix} \tag{2.75}$$

Full *dq* frame

The grid current controller for the MMC-SSTI is shown in Fig. 2.14a. In this figure, all the variables are in *dqz* frame. The references for the modulated voltages $v^{\Sigma *}_{mz}$ is set to $v_{dc}/2$, while all the others are set to zero.

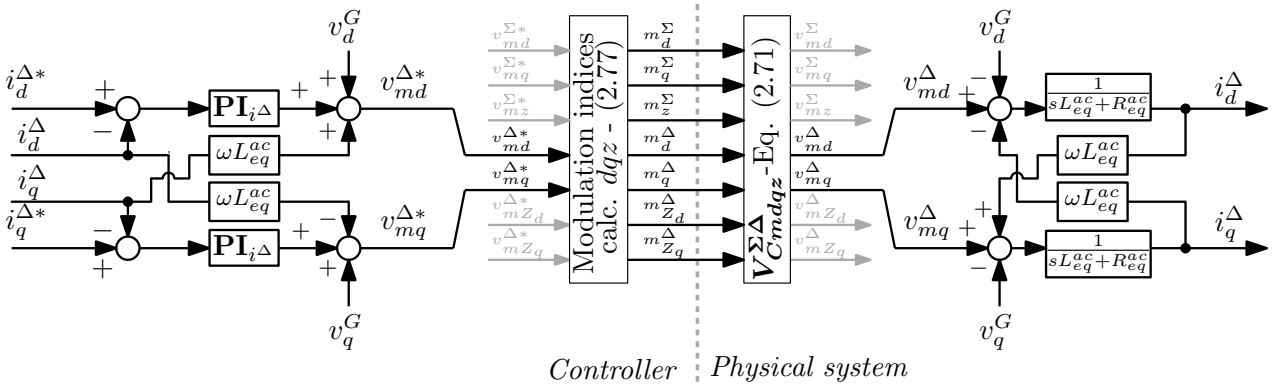

(a) Grid current controller for MMC-SSTI model (b) Part of MMC-SSTI model in *dq* frame

Figure 2.14 – Grid current controller for EMT model in full *dq* for the MMC-SSTI model

For considering the UCM for the dqz MMC model, it is approximated $v_{Cz}^{\Sigma} \approx v_{dc}$, while the rest of the arm capacitor voltages are neglected (the dq components from v_C^{Σ}, and all the components from v_C^{Δ}). With this assumption, the matrix $\boldsymbol{V}_{\boldsymbol{CmdqZ}}^{\boldsymbol{\Sigma\Delta}}$ from (2.71) is approximated as follows:

$$\boldsymbol{V}_{\boldsymbol{CmdqZ}}^{\boldsymbol{\Sigma\Delta}} \approx \underbrace{\frac{1}{2}\left[\begin{array}{ccc|cccc} v_{dc} & 0 & 0 & 0 & 0 & 0 & 0 \\ 0 & v_{dc} & 0 & 0 & 0 & 0 & 0 \\ 0 & 0 & v_{dc} & 0 & 0 & 0 & 0 \\ \hline 0 & 0 & 0 & -v_{dc} & 0 & 0 & 0 \\ 0 & 0 & 0 & 0 & -v_{dc} & 0 & 0 \\ 0 & 0 & 0 & 0 & 0 & -v_{dc} & 0 \\ 0 & 0 & 0 & 0 & 0 & 0 & -v_{dc} \end{array}\right]}_{\boldsymbol{V}_{\boldsymbol{CmdqZ}}^{\boldsymbol{UCM}}} \tag{2.76}$$

In this way, the modulation indices under the UCM method in dqz frame are calculated as:

$$\left[\begin{array}{c} \boldsymbol{m}_{\boldsymbol{dqz}}^{\boldsymbol{\Sigma}} \\ \hline \boldsymbol{m}_{\boldsymbol{dqZ}}^{\boldsymbol{\Delta}} \end{array}\right] = \left(\boldsymbol{V}_{\boldsymbol{CmdqZ}}^{\boldsymbol{UCM}}\right)^{-1} \left[\begin{array}{c} \boldsymbol{v}_{\boldsymbol{mdqz}}^{\boldsymbol{\Sigma *}} \\ \hline \boldsymbol{v}_{\boldsymbol{mdqZ}}^{\boldsymbol{\Delta *}} \end{array}\right] \tag{2.77}$$

2.5.2 Time domain results

To validate the developed modeling approach, results from time-domain simulation of the following three different models are shown and compared in this section.

1. The proposed time-invariant MMC model derived in Section 2.4 and represented by Fig. 2.12, corresponding to the SSTI dynamics in dqz of the arm voltages difference, arm voltages sum, common-mode currents and grid currents. The implemented AC current controller and modulation are given in Fig. 2.14. Simulations result obtained with this model are identified in the legend by "$SSTI$".

2. The AAM of a three-phase MMC (also called "Model # 3: *MMC Arm Switching Function*" in [111]). Each arm is represented by a controlled voltage source and where the internal arm voltage dynamics is represented by an equivalent arm capacitance as indicated in the lower right part of Fig. 2.2 [115, 147, 148]. The implemented AC current controller and modulation are given in Fig. 2.13. The model is simulated in EMTP-RV. Simulation results obtained with this model are identified in the legend by "AAM".

3. The system from Fig. 2.2 implemented in EMTP-RV for an MMC with 400 sub-modules per arm, with a capacitance of $0.01302F$ each. The MMC is modeled with the so-called "Model # 2: *Equivalent Circuit-Based Model*" from [111]. This model includes the switching operations and the dynamics of the sub-module capacitor voltage balancing algorithm from [109], as indicated in Fig. 2.1 [149]. The implemented AC current controller and modulation are given in Fig. 2.13. Simulation results obtained with this model are identified in the legend by "EMT".

It is worth mentioning that the verification of the scientific contribution represented by the proposed modeling approach should be done first and foremost with respect to the model it has been derived from; i.e., the AAM. This initial comparison, where the AAM is considered as the reference model, is enough to evaluate the accuracy of the modeling proposal and the simplifications it entails. Thus, the analysis of simulation results that will follow is mainly focused on these two modeling approaches. Nonetheless, for a more practical-oriented comparison, the

detailed switching model has been included as well, to provide an indication on the accuracy of both the well-established AAM and the proposed modeling approach with respect to a detailed switching model of the MMC. All simulations are based on the MMC HVDC single-terminal configuration shown in Fig. 2.15, with the parameters given in the Appendix A.

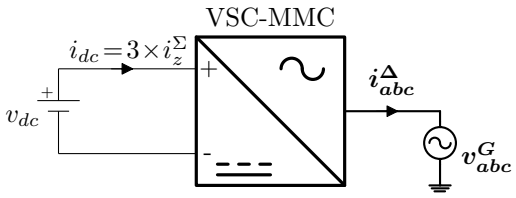

Figure 2.15 – MMC connected to AC and DC perfect sources

For comparing the models, the transient and steady-state responses are performed in dqz frame and in per-unit quantities. Thus, in most cases, the results obtained from the reference model are post-transformed into the appropriate SRRFs to ease the comparison. Starting the simulation with a power transfer of $P_{ac} = 1$ pu and $Q_{ac} = 0$ pu, the following scenario is chosen in order to excite the different dynamics existing in the models:

1. At $t = 0.1$ s: Reactive power reference (i.e. $i_q^{\Delta *}$) is set to -0.1 pu.

2. At $t = 0.4$ s: Active power reference (i.e. $i_d^{\Delta *}$) is reduced to 0.5 pu.

The dynamics of the dq components of the grid current are shown in Fig. 2.16. It is possible to see that for this variable the reference model and the proposed model with SSTI dynamics are practically overlapping.

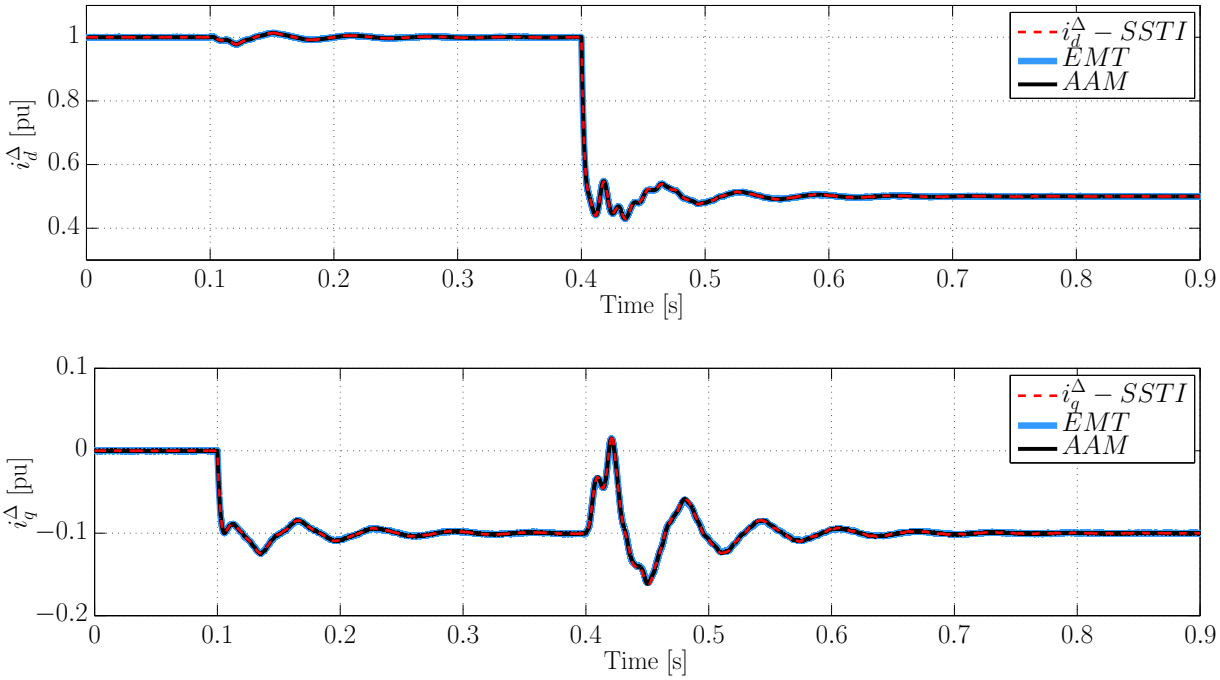

Figure 2.16 – Comparison of the proposed SSTI model with the AAM and EMT models: grid current dq components

In Fig. 2.17, the results of the common-mode currents $\boldsymbol{i}_{\boldsymbol{dqz}}^{\boldsymbol{\Sigma}}$ are shown. In the upper sub-figure it is depicted the currents in abc frame for the EMT model. The dynamics of the

circulating currents $\boldsymbol{i}_{\boldsymbol{dq}}^{\boldsymbol{\Sigma}}$ and zero-sequence current i_z^{Σ} are shown in the middle and lower sub-figures of Fig. 2.17. It can be noticed that the accuracy of the model is very good for the zero-sequence component i_z^{Σ}. The results of the dq components $\boldsymbol{i}_{\boldsymbol{dq}}^{\boldsymbol{\Sigma}}$ for the compared models are almost the same, only a large zoom (Fig. 2.18) enables to observe the 6^{th} harmonic in the reference models which is obviously not visible in the model obtained with SSTI solution. In light of the results, the assumption of neglecting the 6^{th} harmonic in the modeling with the SSTI solution is confirmed.

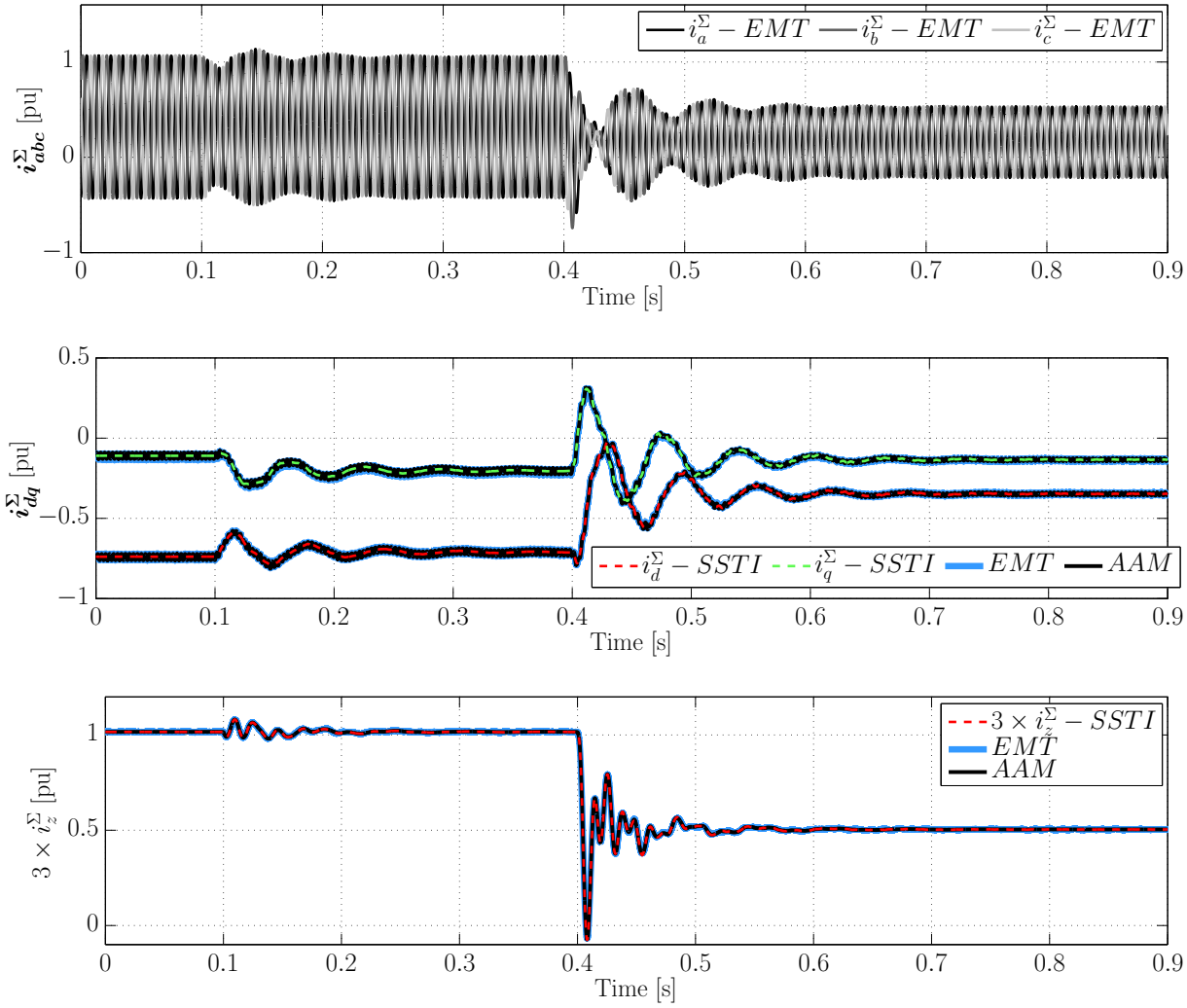

Figure 2.17 – Comparison of the derived SSTI model with the AAM and EMT models: common-mode currents $\boldsymbol{i}_{\boldsymbol{dqz}}^{\boldsymbol{\Sigma}}$ i) dq components and ii) zero-sequence

The dynamics of the voltage sum $\boldsymbol{v}_{\boldsymbol{Cdqz}}^{\boldsymbol{\Sigma}}$ are illustrated in Fig. 2.19, where it can be seen how the variables calculated with the AAM-MMC used as reference are overlapping those calculated with the model with SSTI solution derived in this Chapter. Notice that the steady-state value of v_{Cz}^{Σ} changes with respect to each of the reference steps, since there is no regulation of the energy stored in the MMC. Furthermore, the non-zero steady-state values of $\boldsymbol{v}_{\boldsymbol{Cdq}}^{\boldsymbol{\Sigma}}$ emphasizes the 2ω oscillations that this variable has in the stationary abc reference frame.

Similarly, the dynamics of the energy difference $\boldsymbol{v}_{\boldsymbol{Cdqz}}^{\boldsymbol{\Delta}}$ are depicted in Fig. 2.20. More precisely, the upper figure is illustrating the dq components behavior of this variable under the above described case scenario while the lower figure does the same for the zero-sequence. In terms of accuracy, both of the sub-figures show how the proposed model with SSTI solution ac-

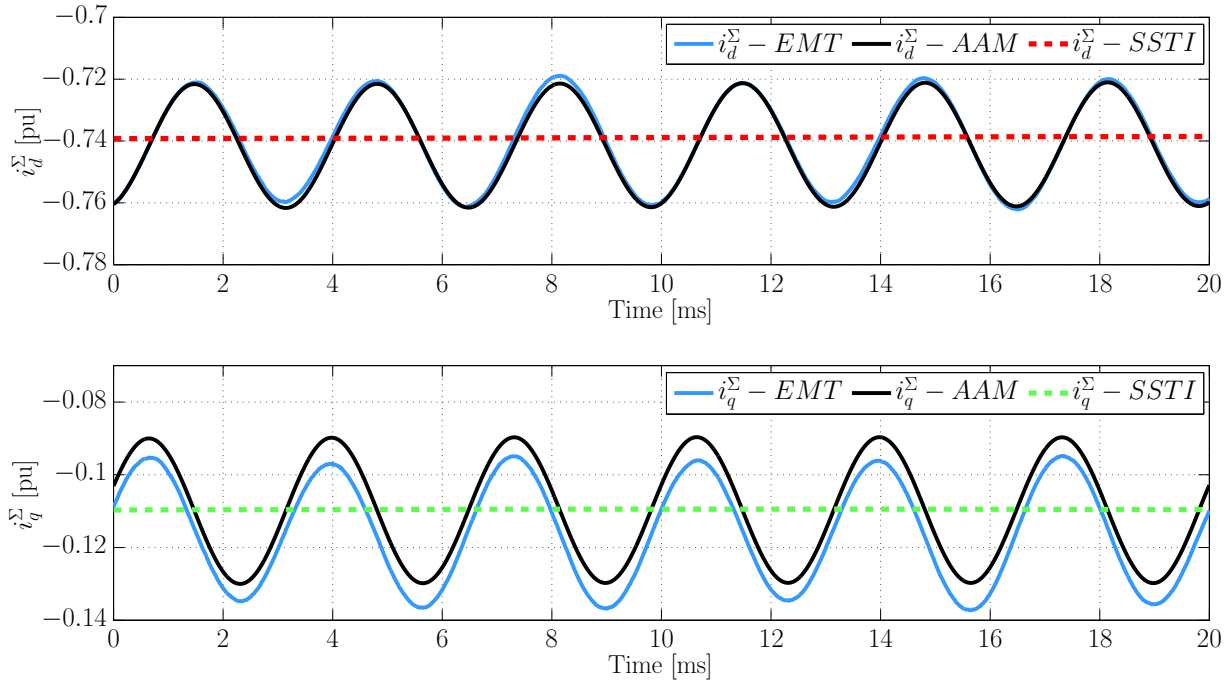

Figure 2.18 – Circulating currents $\boldsymbol{i}_{\boldsymbol{dq}}^{\boldsymbol{\Sigma}}$ zoom

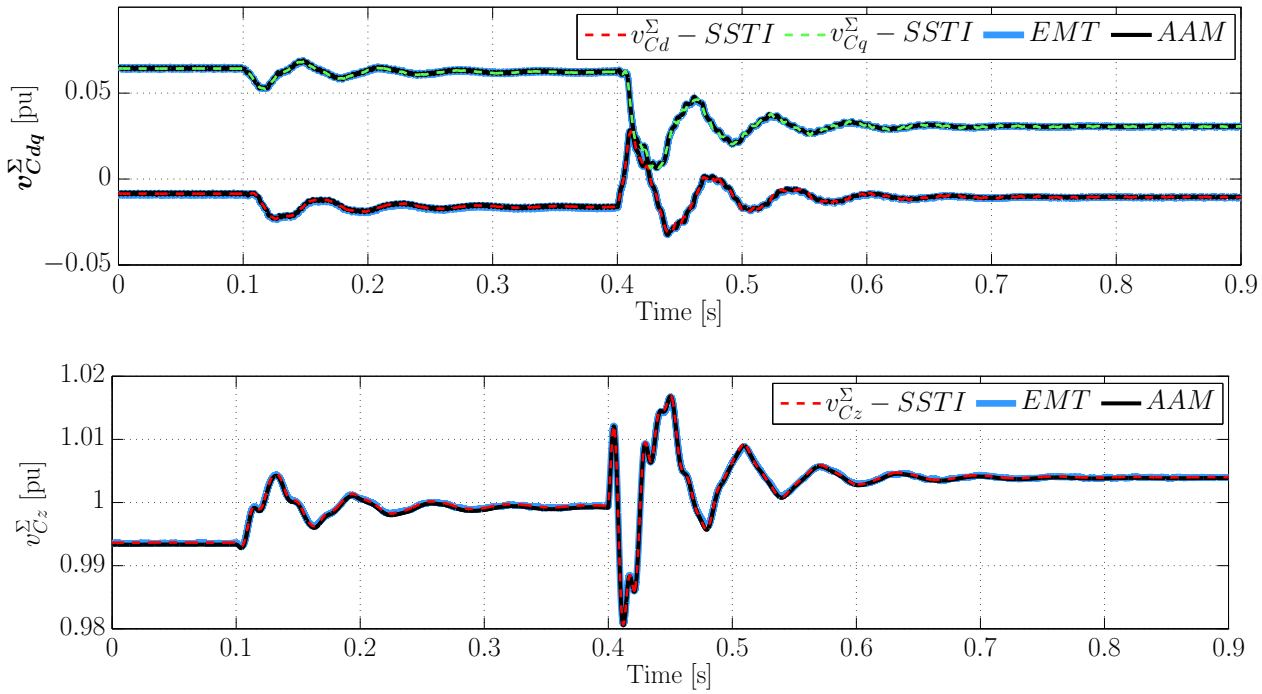

Figure 2.19 – Comparison of the derived SSTI model with the AAM and EMT models: arm capacitor voltage sum $\boldsymbol{v}_{\boldsymbol{Cdqz}}^{\boldsymbol{\Sigma}}$ i) dq components and ii) zero-sequence

curately captures the behavior of the AAM-MMC model used as reference. This is particularly true for the case of $\boldsymbol{v}_{\boldsymbol{Cdq}}^{\boldsymbol{\Delta}}$ as almost no distinction can be made between the voltage waveforms resulting from the two models. For v_{Cz}^{Δ} however, it is possible to notice a slight mismatch between the derived model and the AAM, particularly during the transient behavior between $t = 0.15$ s and $t = 0.2$ s. This is indeed associated to the neglected sixth harmonic components

in the mathematical derivation of the proposed model with SSTI solution. Nonetheless, the model accuracy is not compromised since it has a very little influence on the general dynamics.

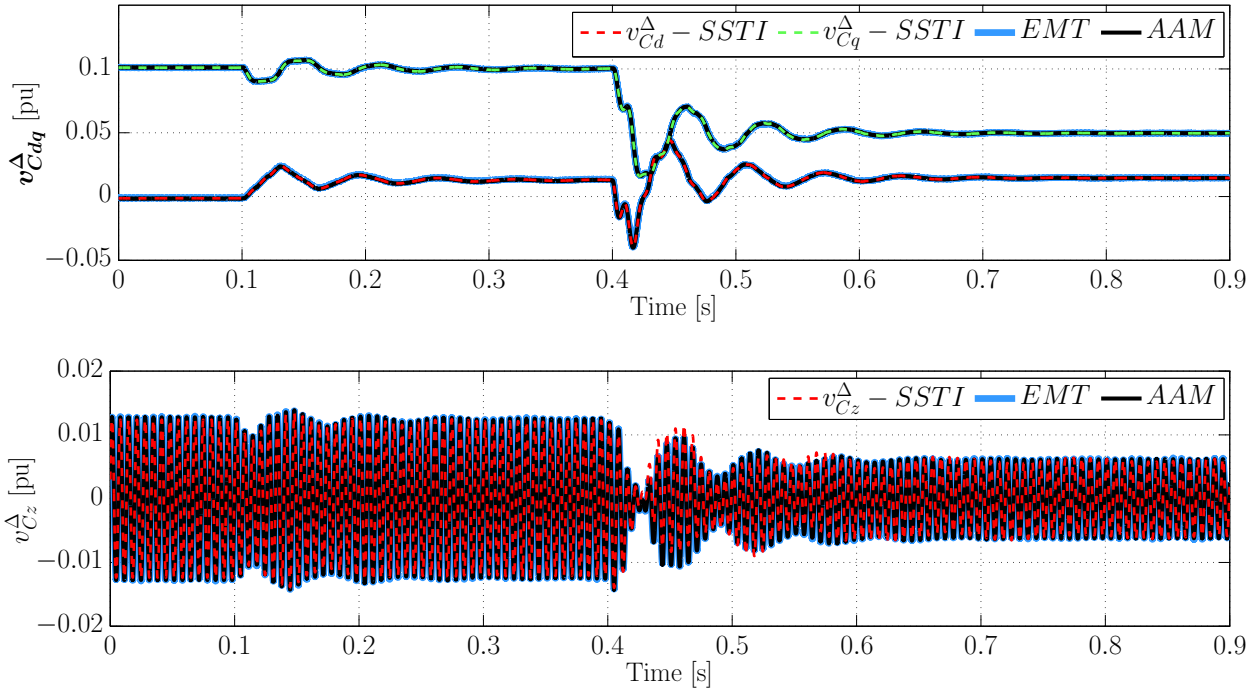

Figure 2.20 – Comparison of the derived SSTI model with the AAM and EMT models: arm capacitor voltage difference $\boldsymbol{v^{\Delta}_{Cdqz}}$ i) dq components and ii) zero-sequence component transformed to scalar, time-periodic, representation

Notice that the comparison between the reference and the proposed MMC model with SSTI solution has been done using the SSTP signal v^{Δ}_{Cz} instead of its equivalent SSTI version $\boldsymbol{v^{\Delta}_{CZ}}$ defined in Section 2.4. This is done for simplicity, as the dynamics of the virtual system used to create $\boldsymbol{v^{\Delta}_{CZ}}$ do not directly exist in the reference AAM-MMC model. However, for the sake of completeness, the dynamics of the SSTI $\boldsymbol{v^{\Delta}_{CZ}}$ obtained with the proposed model are depicted in Fig. 2.21, where it can be confirmed that both the $v^{\Delta}_{CZ_d}$ and $v^{\Delta}_{CZ_q}$ sub-variables reach a constant value in steady-state operation.

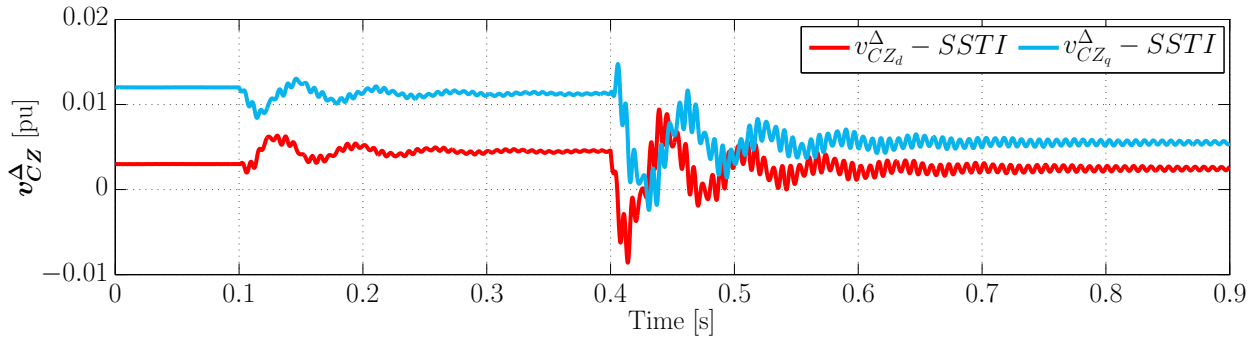

Figure 2.21 – SSTI representation of the voltage difference zero sequence

2.6 Chapter Conclusions

This Chapter presents a modeling approach for obtaining a state-space representation of an MMC with Steady-State Time-Invariant (SSTI) solution. The presented approach can be considered independent from the modulation and control strategy adopted, as only the physical equations of the MMC have been mathematically manipulated, gaining a more generalized model compared to previous works available in the literature. Results from time-domain simulation of a detailed MMC model with 400 sub-modules per arm are presented as point of reference to illustrate the validity of the derived model. These results demonstrate how the model with SSTI solution accurately captures the MMC internal dynamics while all variables settle to a constant equilibrium in steady-state operation.

The proposed model was achieved thanks to a voltage-current Σ-Δ formulation which enabled separation of the MMC variables according to their oscillation frequencies as part of the initial model formulation. A procedure for deriving equivalent SSTI dqz representation of all state variables by applying Park transformations at different frequencies was presented, referring the variables to three different rotating reference frames, rotating at once, twice and three times the grid fundamental frequency. The resulting model captures the internal dynamics of the MMC such as circulating currents and arm capacitor voltages.

Utilization of the proposed model can enable a wide range of studies related to MMC-based HVDC system analysis such as small-signal stability studies by eigenvalue analysis, considering an individual MMC HVDC terminal, or an HVDC terminal integrated in a larger power system configuration. Furthermore, this model can be used for developing appropriate controller architectures and fine tuning of their parameters, as it highlights one by one the dynamic modes present in an MMC.

The MMC models used in this Chapter are exploited in this Thesis for dynamic analysis of the converter and further integration in MTDC grids, which are referred as follows:

- **EMT:** The efficient MMC model for EMT studies from [112], and called "Model # 2: *Equivalent Circuit-Based Model*" in [111]. This model includes also the sub-modules balancing algorithm [109]. The MMC and its controller are implemented in EMTP-RV.
- **AAM:** The Arm Averaged Model (or "Model # 3: *MMC Arm Switching Function*") implemented in EMTP-RV.
- **SSTI:** The MMC model with Steady-State Time Invariant solution developed in Section 2.4 and represented by the Fig. 2.12. The considered SSTI representation of the MMC controller is detailed in the text and in the figure labels. This model is simulated in Matlab/Simulink.

Chapter 3

On MMC control for its integration in MTDC grids

3.1 Introduction

This Chapter deals with the control strategies of the MMC for its integration in MTDC grids. The objective is to make use of mathematical tools for linear model analysis in order to study the stability of a MMC station associated to different control strategies. In this way, the main characteristics of each configuration are highlighted thanks to the linear version of the MMC model with Steady-State Time Invariant solution from the previous Chapter.

In Chapter 2, a very basic MMC control strategy based on the grid current controllers was used to validate the MMC-SSTI model, where the Un-Compensated Modulation (UCM) method was implemented. The idea of this controller was to modulate the AC voltages to obtain the desired AC currents. However, as it was shown in the simulation results from Section 2.5, a large amount of circulating currents appear inside the MMC ($\boldsymbol{i}_{\boldsymbol{dq}}^{\boldsymbol{\Sigma}}$). For this reason, in [135] it was introduced the *Circulating Current Suppressing Controller* in dq frame (or simply CCSC). After the appearance of this strategy, it gained a lot of popularity as it was widely adopted in the literature due to its simplicity, and several publications were already focused on the dynamic analysis of the MMC with the CCSC as [125, 150, 151]. However, as stated in [152], the CCSC controller may fail to guarantee stable operation of the MMC. In this Chapter, it is further shown that the uncontrolled DC current may cause undesired interactions with the DC grid being the root cause of the unpropitious behavior. For this reason, the *Energy-based* controller strategy is introduced, where extra control loops in cascade are added to regulate the dynamics of interest: for instance, the previously un-controlled DC current and a stored energy regulator to balance the AC and DC powers explicitly [153, 154].

Since many *Energy-based* control strategies rely on stationary frame per-phase control loops [155,156], a similar mathematical methodology as in Chapter 2 is used to refer the MMC control equations from stationary (abc) to rotating (dq) frames. The developed controller is suitable for obtaining the MMC and its control in SSTI representation, which can be linearized to obtain a linear time invariant model where small-signal stability analysis can be performed [157].

The rest of the Chapter is organized as follows. After detailing the preliminaries on the MMC controllers, in Section 3.2, the *Classical CCSC* strategy is introduced and analyzed. Also, the issues with this basic strategy are highlighted. For improving the stability, the *Energy-based* control strategy is deduced in Section 3.3. This strategy adds only two controllers to the *Classical CCSC*. In Section 3.4, an advanced controller which specifically controls all the MMC state variables is introduced.

Preliminaries

Due to the complexity and flexibility of the MMC, several controllers can be found in the literature [137]. For the proper operation of the MMC, the controller must fulfill the following specifications [146, 158]:

1. **Match AC and DC power flows:** In Fig. 3.1a, it is shown that if an AC and DC power mismatch occurs, the average of the internal stored energy per phase $\overline{W}_j^{\Sigma}$ will grow continuously. When a proper energy regulation is set up, the energy can be maintained at a desired reference level $\overline{W}_j^{\Sigma*}$, as shown in Fig. 3.1b) [108].
2. **Horizontal balancing — Exchange energy phase to phase:** The control system must guarantee that the stored energy per-phase are maintained to a proper value, as exemplified in Fig. 3.1c [114].
3. **Vertical balancing — Exchange energy arm to arm:** Within each phase leg, the energy stored should be equally repartitioned within the upper and lower arms, as shown in Fig. 3.1ds **[159]**.
4. **Sub-module balancing — Exchange energy SM to SM:** This control level should guarantee that the capacitor voltages at each SM are maintained in a close range with respect to the SMs of their respective arms [110].

The last item (Sub-module balancing) is highly covered in the literature and it is not a matter of interest in this Thesis since the main focus is given to the High-level controllers. However, an implementation of the strategy from [109] is considered for the complete EMT model (See Appendix F).

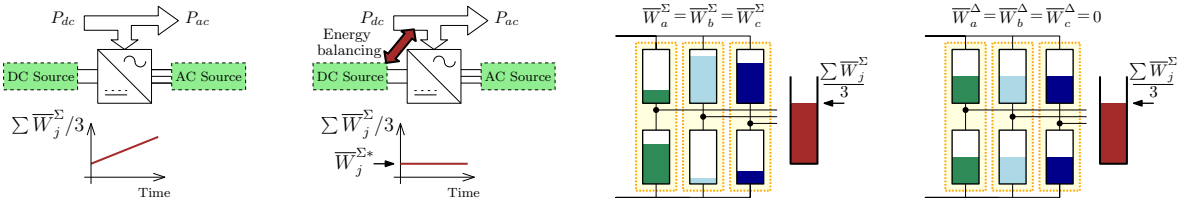

(a) Power mismatch (b) Power match (c) Horizontal balancing (d) Vertical balancing

Figure 3.1 – Control specifications of the MMC: graphical description

For anticipating the inclusion of the MMC directly into MTDC grids, a configuration of a single converter is used in this Chapter as shown in Fig. 3.2. A simplified model is assumed for the DC bus dynamics consisting of an equivalent capacitor C_{dc} which emulates the capacitance of the DC cables and other converter stations connected to the grid. This approach is similar to what was presented for a classical *2-level* VSC (see Section 1.2.3). Also, in parallel with C_{dc} there is a controlled current source i_l whose output power is P_l^* as an equivalent model of the power exchanged in the HVDC system. The equation of the DC bus used in this Chapter is given in (3.1). Since the DC voltage is given by a dynamic state, the droop controller presented in Section 1.4 is used.

$$C_{dc}\frac{dv_{dc}}{dt} = i_l - i_{dc} = \frac{P_l^*}{v_{dc}} - 3i_z^{\Sigma} \tag{3.1}$$

For the analysis of the system from Fig. 3.2 when considering different control strategies, the SSTI model from Chapter 2 is used, where (3.1) is taken into account for the DC side as shown in Fig. 3.3

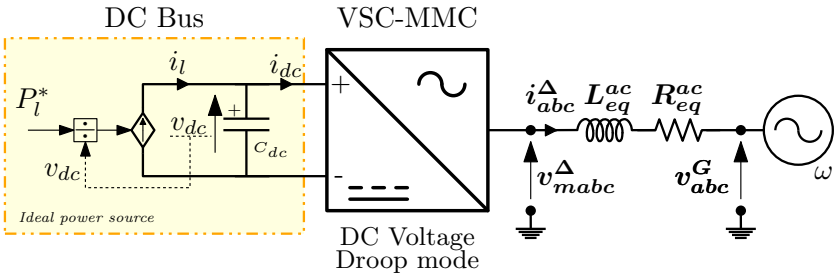

Figure 3.2 – Schematic of the reference configuration with MMC connected to a DC bus capacitor and a DC ideal power source

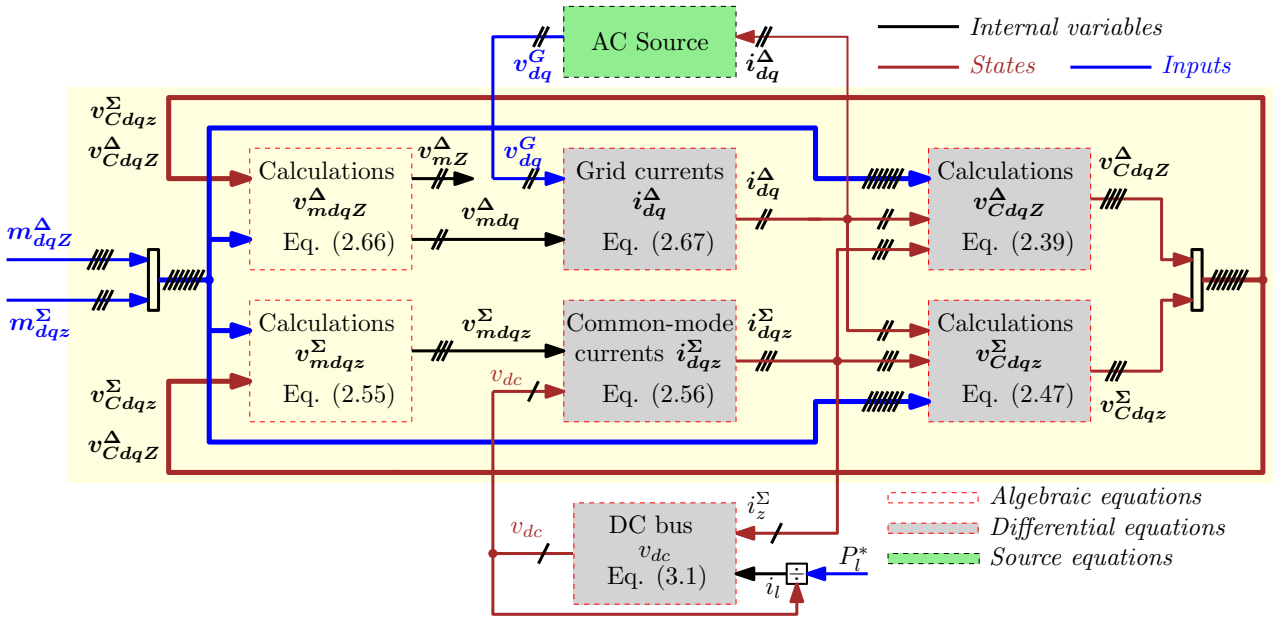

Figure 3.3 – MMC SSTI model of the reference configuration with MMC connected to a DC bus capacitor and a DC ideal power source

3.2 Classical Circulating Current Suppressing Controller Strategy

As it was shown in the simulation results from Section 2.5, when the MMC controller is only controlling the AC currents in combination with the Un-Compensated Modulation (UCM), a non-negligible amount of circulating currents $\boldsymbol{i}^{\boldsymbol{\Sigma}}_{\boldsymbol{dq}}$ exists inside the MMC. These currents augment the RMS value of the arm currents, increasing the internal losses in the converter. For eliminating these circulating currents, several options were already investigated in the literature [137]. The widely adopted method is called "Circulating Current Suppressing Controller", or simply "CCSC", which is shown in Fig. 3.4 [135]. This controller monitors the circulating currents $\boldsymbol{i}^{\boldsymbol{\Sigma}}_{\boldsymbol{dq}}$ and, with two PIs controllers in double SRRF, the currents are controlled to zero at every time. This means that in *abc* frame, the oscillations at double line frequency are canceled in steady-state. As it is highlighted in Fig. 3.5, there is no closed loop control for the third-current i^{Σ}_{z}. One peculiarity of this control strategy lies in the fact that the modulation index m^{Σ}_{z} is a constant value. This is due since $v^{\Sigma*}_{mz}$ is set to $v_{dc}/2$, and when obtaining m^{Σ}_{z} with UCM from (2.77), results in $m^{\Sigma}_{z} = (v_{dc}/2)/(2/v_{dc}) = 1$ [108].

For demonstrating the effectiveness of the controller proposed in [135], a similar simulation

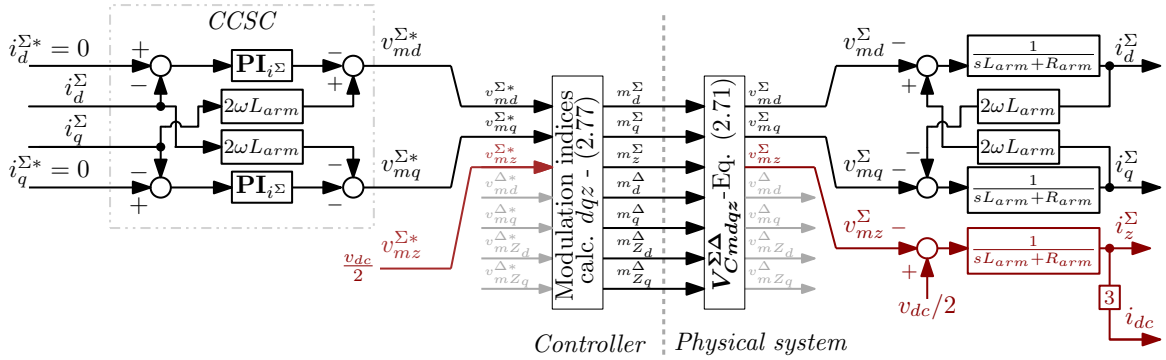

(a) CCSC for MMC-SSTI model (b) Part of MMC-SSTI model in dq frame

Figure 3.4 – Circulating Current Suppressing Controller structure

as in Section 2.5 is performed (i.e. an MMC connected to ideal AC and DC sources and also, the same models are compared: EMT, AAM and SSTI). With the same initial operating point as in Section 2.5, the CCSC is activated at $t = 0.1$ s. The controllers gains of the CCSC are calculated to achieve a theoretical response time τ_i^Σ of 5 ms and ζ_i^Σ of 0.7 (See Appendix C). The output DC current of the converter is left uncontrolled with this strategy, and it is naturally adjusted to balance the AC and DC power flow [115]. Results are shown in Fig. 3.5. In Fig. 3.5a, the common-mode currents in *abc* frame $\boldsymbol{i}_{\boldsymbol{abc}}^{\boldsymbol{\Sigma}}$ are shown (only the EMT model). Before the activation of the CCSC, it is noticeable the high amount of 2ω components in the currents $\boldsymbol{i}_{\boldsymbol{abc}}^{\boldsymbol{\Sigma}}$. When the CCSC is activated, the currents $\boldsymbol{i}_{\boldsymbol{dq}}^{\boldsymbol{\Sigma}}$ are controlled to zero (meaning no oscillations in *abc* frame) as shown in Fig. 3.5b.

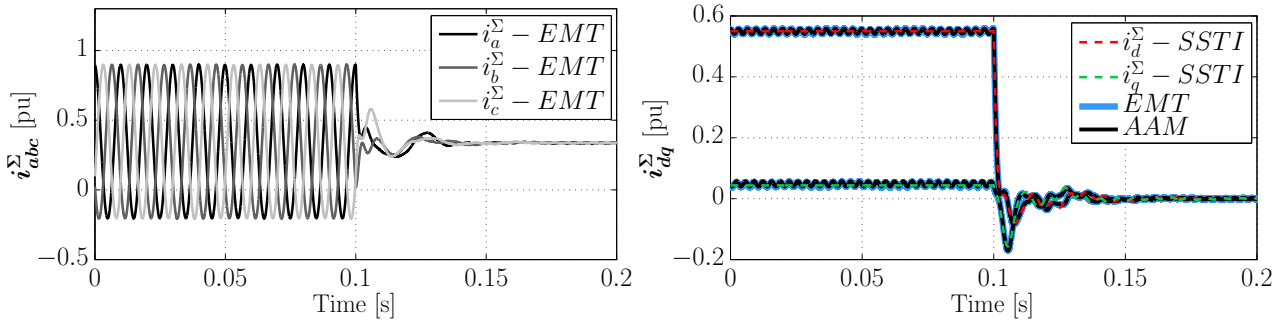

(a) $\boldsymbol{i}_{\boldsymbol{abc}}^{\boldsymbol{\Sigma}}$ (b) $\boldsymbol{i}_{\boldsymbol{dq}}^{\boldsymbol{\Sigma}}$

Figure 3.5 – CCSC Validation - Common-mode currents i^Σ - CCSC activated at $t = 0.1$s

The addition of the CCSC in conjunction with the already presented controller from Section 2.5.1 forms the first control strategy that is investigated in this Thesis, named as *Classical Circulating Current Suppressing Controller* (also named as "Global Control # 1" in [108] or "Non-energy based control" in [114]).

Since the strategy from Fig. 3.6 is based on the current control of the AC side and the internal circulating currents in rotating frame (dq), the mathematical expression of this controller is already in a "Steady-State Time Invariant" (SSTI) representation. This means that it is readily adapted to the MMC-SSTI model developed in Chapter 2. In the following sections, an analysis of the single terminal HVDC system from Fig. 3.2 is performed to highlight the main characteristics and limitations of this strategy.

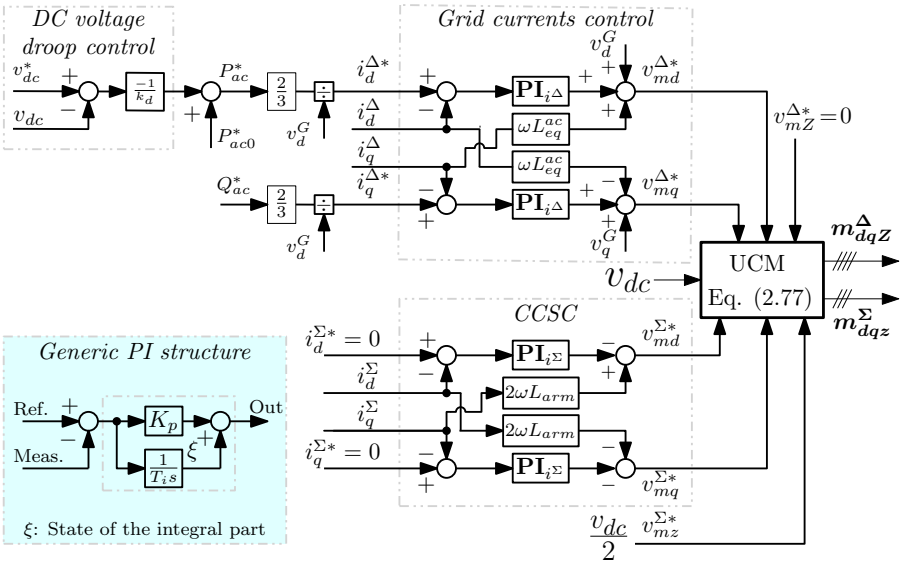

Figure 3.6 – *Classical CCSC* strategy with UCM associated with DC voltage droop controller — SSTI representation

3.2.1 Model linearization and time domain validation

For evaluating the *Classical CCSC* strategy, first an equivalent linear model (LTI) is obtained by direct linearization of the MMC-SSTI with the associated controller. The non-linear time-invariant model presented in Section 2.4 with the control from Fig. 3.6 are connected as shown in Fig. 3.7.

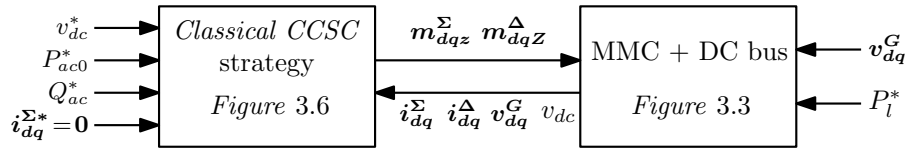

Figure 3.7 – SSTI model of MMC, DC bus and *Classical CCSC*

This interconnected model is represented by a subset of ordinary differential equation, with $\boldsymbol{x_{ccsc}}$ representing the states of the system as in (3.2) and $\boldsymbol{u_{ccsc}}$ the inputs as in (3.3).

$$\boldsymbol{x_{ccsc}} = [\underbrace{\boldsymbol{\xi_{i^{\Delta}_{dq}}}\ \boldsymbol{\xi_{i^{\Sigma}_{dq}}}}_{\text{Controllers}}\ \underbrace{\boldsymbol{i^{\Delta}_{dq}}\ \boldsymbol{i^{\Sigma}_{dqz}}\ \boldsymbol{v^{\Sigma}_{Cdqz}}\ \boldsymbol{v^{\Delta}_{CdqZ}}}_{\text{MMC}}\ \underbrace{v_{dc}}_{\text{DC bus}}\ ]^{\top} \in \mathbb{R}^{17} \tag{3.2}$$

$$\boldsymbol{u_{ccsc}} = [\underbrace{v^{*}_{dc}\ P^{*}_{ac0}\ Q^{*}_{ac}\ i^{\Sigma *}_{d}\ i^{\Sigma *}_{q}}_{\text{Controllers}}\ \underbrace{v^{G}_{d}\ v^{G}_{q}}_{\text{AC grid}}\ \underbrace{P^{*}_{l}}_{\text{DC grid}}\ ]^{\top} \in \mathbb{R}^{8} \tag{3.3}$$

The non-linear model resulting from Fig. 3.7 can be linearized around a steady-state operating point by means of the Jacobian linearization method, resulting in a LTI representation (See Section 1.2.4). The obtained LTI model is used for evaluating small-signal dynamics and stability by eigenvalue analysis.

Starting with a DC power transfer of 1 pu (from DC to AC), a step is applied on P^{*}_{l} of -0.1 pu at 0.05 s. The reactive power is controlled to zero during this scenario. Simulation results are gathered in Fig. 3.8. The dynamic response of the DC power P_{dc} is shown in Fig. 3.8a (i.e. measured power in the reference model and the calculated power for the linearized model as $P_{dc} = 3i^{\Sigma}_{z}v_{dc}$). The step applied on P^{*}_{l} produces a power imbalance in the DC bus, so the

MMC reacts with the droop controller and its internal energy to achieve the new equilibrium point. The DC voltage results are shown in Fig. 3.8b. Due to the DC voltage droop control (proportional controller with gain k_d), a steady-state error is obtained after the transient. The internal energy of the MMC participates in the dynamics of the DC voltage regulation by discharging its internal capacitors into the DC bus during the transients, as seen in the voltage v_{Cz}^{Σ}. The behavior of v_{Cz}^{Σ} is similar to v_{dc} as expected from the discussion in **[160]**.

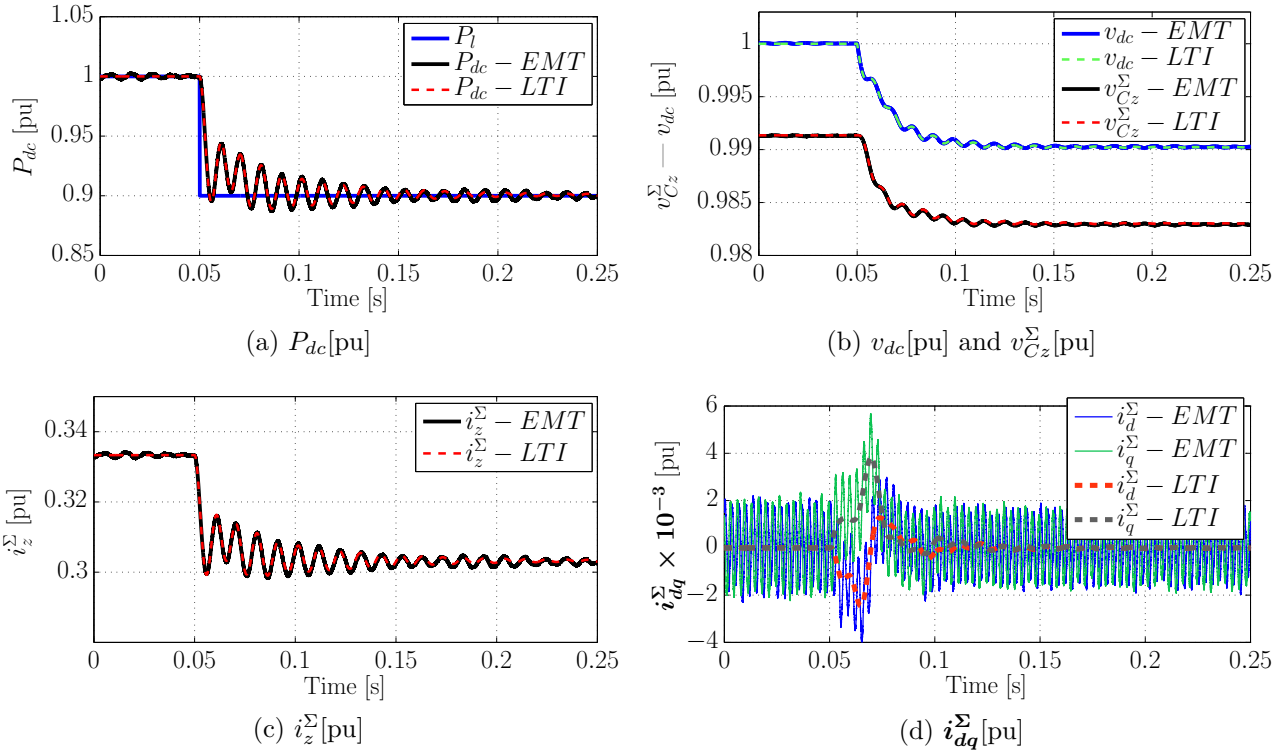

(a) P_{dc}[pu]

(b) v_{dc}[pu] and v_{Cz}^{Σ}[pu]

(c) i_z^{Σ}[pu]

(d) $\boldsymbol{i_{dq}^{\Sigma}}$[pu]

Figure 3.8 – Time domain validation *Classical CCSC* – Step applied on P_l of 0.1 pu – EMT: EMTP-RV simulation with detailed converter, LTI: Linear time-invariant state-space model in Simulink

The results of the common-mode currents are shown in Fig. 3.8c for the zero-sequence and in Fig. 3.8d for the dq components. The EMT model presents oscillations at 6ω in steady state in the dq components. These oscillations were neglected during the development of the time-invariant model (See Chapter 2). As seen in the comparisons from Fig. 3.8d, the model captures the average dynamics with reasonable accuracy even if the 6^{th} harmonic components are ignored (notice the scale). For all other variables, there are negligible differences between the different models.

3.2.2 Stability analysis

Since the linearized model from Fig. 3.7 has been validated, it can be used for small signal stability analysis and indirectly infer about the *reference system* (in this study, the complete *Simulatio model* in EMTP-RV). The impact of three main parameters influencing the DC voltage dynamics are evaluated: the DC capacitance, the droop gain k_d **[160]** and the response time of the current loops.

Influence of the DC capacitance

In MTDC systems, the value of the equivalent DC capacitance depends on the number of MMC stations connected to the grid as well as the cable lengths [**160**]. This value may vary because some converters could be disconnected or the grid topology reconfigured. For this reason, the MMC should be able to operate under different situations that can result from changes of the DC grid topology and parameters. For evaluating the impact of the DC side capacitance on the small-signal stability, a parametric sweep is performed on the electrostatic constant H_{dc} which is defined as,

$$H_{dc} = \frac{1}{2} C_{dc} \frac{v_{dcn}^2}{P_n}. \tag{3.4}$$

The value of H_{dc} is varied from 40 ms down to 5 ms. This last value represents a small capacitance of the DC bus ($24,4\mu F << (6 \times C_{arm})$), which could represent the DC capacitance of a short cable. The first results consider a power direction from DC to AC side of 1 GW (1 pu) of power transfer. Results are shown in Fig. 3.9a. In this case, for the selected values the system remains stable.

It is known that the converters dynamics depend on the operating point [**161**]. The same parametric sweep as the previous example is performed with the opposite power transfer direction (i.e. from AC to DC side). The results are shown in Fig. 3.9b, demonstrating that the system becomes unstable when the equivalent DC capacitor decreases.

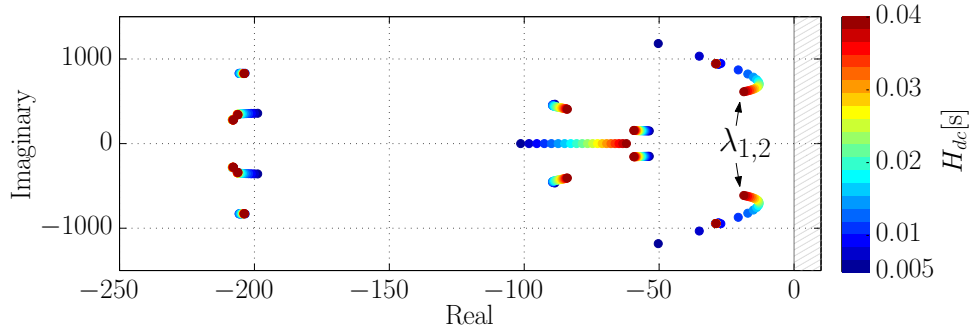

(a) $P_{dc0} = 1$ pu – Power flow: DC ⇒ AC

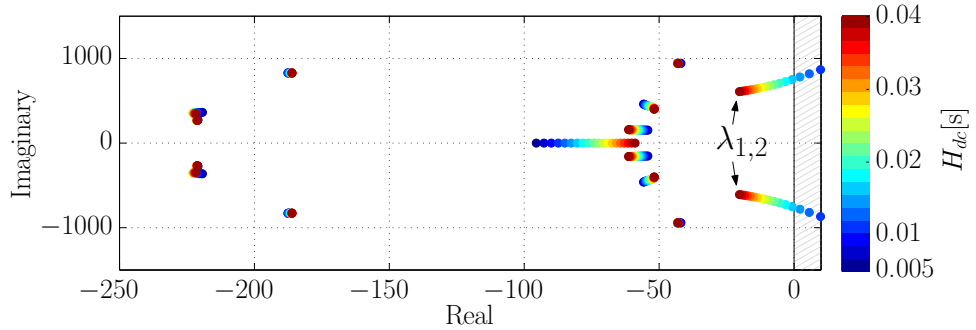

(b) $P_{dc0} = -1$ pu – Power flow: DC ⇐ AC

Figure 3.9 – Parametric sweep of DC capacitor H_{dc} — DC Operating point $v_{dc0} = 1$ pu — $k_d = 0.1$ pu — *Classical CCSC*

Influence of the droop parameter

In this case, the droop parameter k_d is varied from 0.2 pu down to 0.05 pu. The considered power direction is from AC to DC since it is the worst case from the previous section. Results

are shown in Fig. 3.10. When lower values of droop are used, the eigenvalues $\lambda_{1,2}$ shift to the right-hand plane (RHP) resulting in unstable behavior.

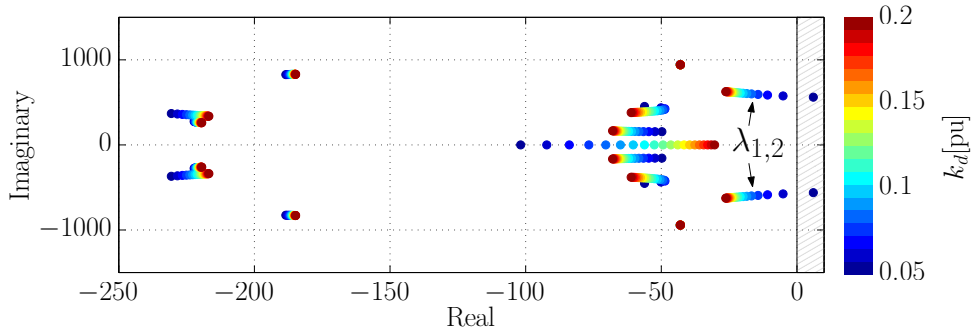

Figure 3.10 – Parametric sweep of Droop parameter k_d — DC Operating point $v_{dc0} = 1$ pu, $P_{dc0} = -1$ pu — *Classical CCSC*

Influence of current controllers

For evaluating the impact of the current controllers on the stability, the response times of the grid current control loops are varied as well as the circulating current control loops (CCSC). Results are shown in Fig. 3.11a for the variation of τ_i^{Δ} and Fig. 3.11b for τ_i^{Σ}. When faster controllers are used (lower values of response times), the eigenvalues $\lambda_{1,2}$ shift to the RHP.

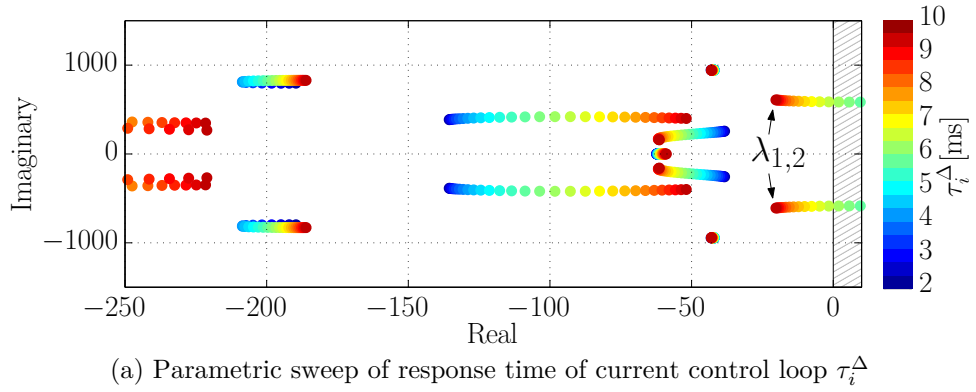

(a) Parametric sweep of response time of current control loop τ_i^{Δ}

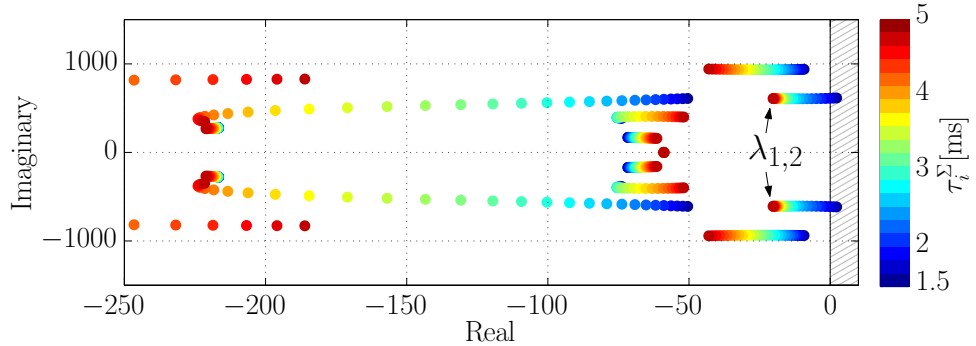

(b) Parametric sweep of response time of circulating current control loop (CCSC) τ_i^{Σ}

Figure 3.11 – Parametric sweep of response time of current controllers — DC Operating point $v_{dc0} = 1$ pu, $P_{dc0} = -1$ pu

3.2.3 Identification of unstable eigenvalues

As observed in the previous results (Figs. 3.9, 3.10 and 3.11), the system may become unstable due to the same pair of eigenvalues for all cases ($\lambda_{1,2}$). For understanding the origin of these eigenvalues, participation factor analysis is performed for the case from the previous sub-section and the results are shown in Fig. 3.12.

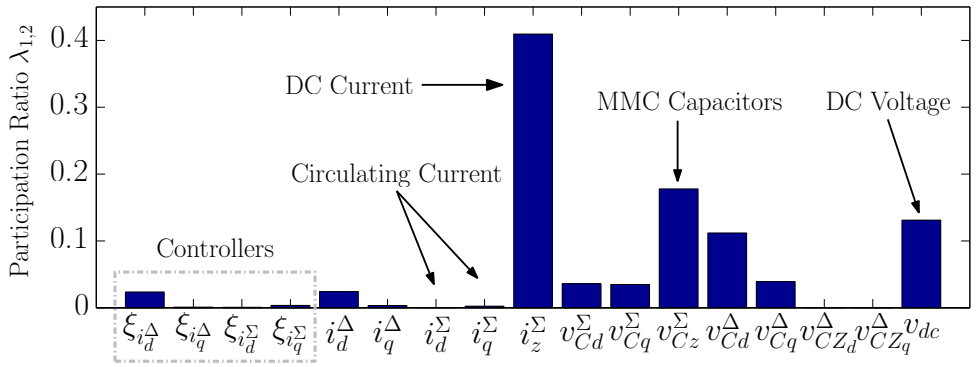

Figure 3.12 – Results from participation factor analysis - Eigenvalues $\lambda_{1,2}$ — $\tau_i^\Delta = 10$ ms; $\tau_i^\Sigma = 5$ ms; $k_d = 0.1$ pu; $H_{dc} = 40$ ms

Results from Fig. 3.12 indicate that the states with the highest participation in the critical modes are i_z^Σ (i.e. the DC current), v_{Cz}^Σ (the state of the MMC which represents the internally stored energy) and v_{dc} (DC voltage). It also shows that the internal circulating currents $\boldsymbol{i_{dq}^\Sigma}$ do not have significant influence on these eigenvalues and neither do the integral part of the controllers (with the chosen bandwidths).

The impact of the proportional gains of the controllers are evaluated by calculating the participation factors for each point from Figs. 3.11 and the results are shown in Fig. 3.13. In Fig. 3.13a, a similar pattern is observed for the participation factors as in Fig. 3.12. For fast response times of the CCSC, the dq components of v_C^Σ participate more on the studied eigenvalues, but the system is unstable as shown in Fig. 3.11b. Nevertheless, for realistic values of response times, the most important states are i_z^Σ, v_{Cz}^Σ and v_{dc}, which corresponds to the results in Fig. 3.12.

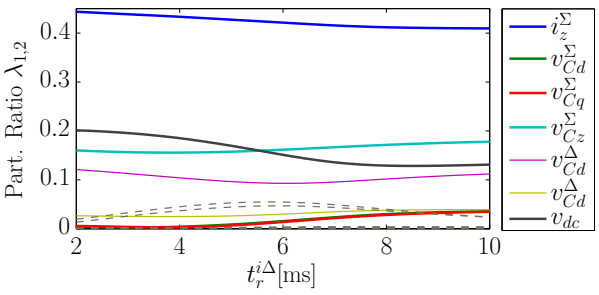

(a) Results from participation factor analysis - Eigenvalues $\lambda_{1,2}$

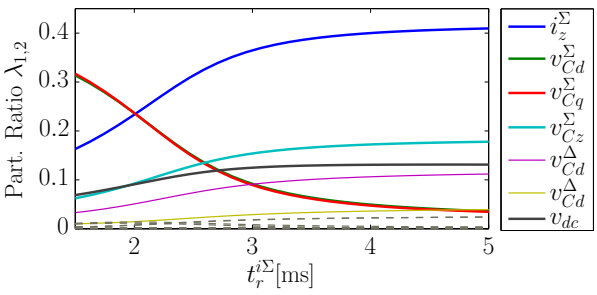

(b) Results from participation factor analysis - Eigenvalues $\lambda_{1,2}$

Figure 3.13 – Participation factors for different response times — Dashed lines correspond to the states that are not listed in the legends — DC Operating point $v_{dc0} = 1$ pu, $P_{dc0} = -1$ pu

3.3 Small signal stability improvement of an MMC with Energy-based controller

Since the instabilities identified in the studied cases are due mainly to the uncontrolled output current i_z^Σ, the next step is naturally the explicit control of this current for improving the behavior of the system.

3.3.1 Energy-based controller # 1

The considered control strategy from previous section controls two out of three common-mode currents i^Σ. The uncontrolled zero-sequence component of i^Σ may cause interactions with the DC bus and the internal capacitor voltages, and can potentially make the system unstable. To improve the stability of the studied system, it is proposed to add a DC current control loop (or what is the same, a controller for i_z^Σ).

In the *Classical CCSC* strategy from last section, the energy is naturally following the DC bus voltage. The DC current is adjusting itself to achieve an implicit balance of energy and between AC and DC power in steady state. When controlling the DC current, this natural balance is lost so the DC current has to be determined explicitly to regulate the internally stored energy and balance the AC and DC power flow.

Inner control loop — Z-sequence Σ current

The design of the controller for i_z^Σ is based on the z-component from equation of (2.56) which is re-written in (3.5) for convenience, and a simple PI can be deduced as shown in Fig. 3.14. For tuning purposes, v_{mz}^Σ is supposed to be equal to $v_{mz}^{\Sigma*}$.

$$\frac{di_z^\Sigma}{dt} = \frac{1}{L_{arm}}\left(\frac{v_{dc}}{2} - v_{mz}^\Sigma - R_{arm} i_z^\Sigma\right) \tag{3.5}$$

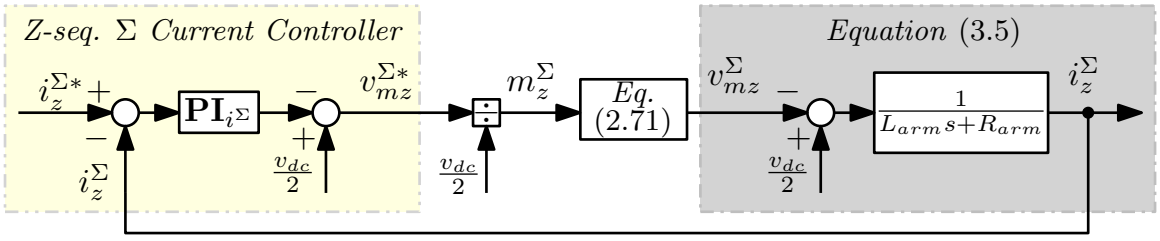

Figure 3.14 – Block diagram of the i_z^Σ current control

Outer control loop — Energy controller

For generating the current reference $i_z^{\Sigma*}$ an outer loop is needed. The proposed strategy is based on the explicit control of the the total stored energy W_z^Σ on the MMC capacitors C_{arm} given by the power balance between AC and DC sides [117]. For designing this controller, a model with the explicit relation between the DC current i_{dc} and the total stored energy W_z^Σ is needed. Assuming $P_{ac}^* \approx P_{ac}$, a simplified expression of the sum energy dynamics can be defined as [117]:

$$\frac{dW_z^\Sigma}{dt} \approx P_{dc} - P_{ac} \approx v_{dc} \underbrace{3i_z^\Sigma}_{i_{dc}} - P_{ac}^* \tag{3.6}$$

The deduced controller structure is shown in Fig. 3.15. For tuning purposes, the inner i_z^Σ current controller is considered as a unity gain.

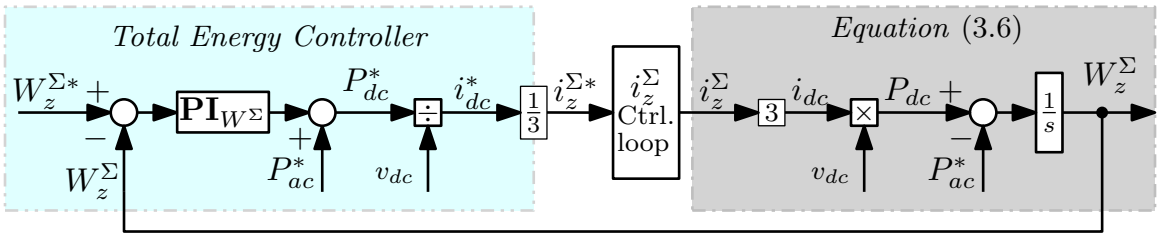

Figure 3.15 – Controller design for W_z^Σ

Finally, the complete control structure is shown in Fig. 3.16, where the response time for the total energy τ_W^Σ is set to 50 ms (i.e. 10 times slower than the inner Σ current loop). At this moment, the energy reference $W_z^{\Sigma*}$ is set to 1 pu in this Chapter, for maintaining a constant level of stored energy (corresponding to the rated capacitor voltages). As explained in the Appendix G [**162**], the energy W_z^Σ is calculated from the *dqz* components as in (3.7).

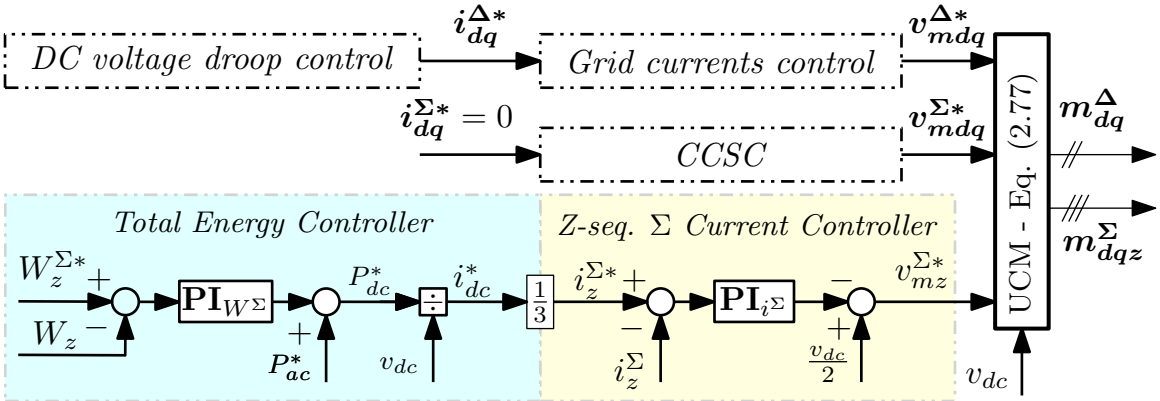

Figure 3.16 – Complete *Energy-based* control - Current and Energy controllers

$$W_z^\Sigma \approx C_{arm}\left(\frac{\left(v_{Cd}^\Sigma\right)^2}{2}+\frac{\left(v_{Cq}^\Sigma\right)^2}{2}+\left(v_{Cz}^\Sigma\right)^2\right)+C_{arm}\sum_{k=d,q,Z_d,Z_q}\frac{\left(v_{Ck}^\Delta\right)^2}{2} \tag{3.7}$$

In general, the additional set of cascaded controllers (for the energy W_z^Σ and the current i_z^Σ) could make the tuning of the controllers more complicated. If they are not properly tuned, the use of cascaded loops could also cause poorer dynamics or additional stability problems (or problems with windup etc. if there are saturation limits) in case of large signal transients. However, the tuning of the current control loop i_z^Σ can be based on the same approach as for the other current controllers. Thus, the added controller of the zero sequence current doesn't add much complication to the control system. The tuning of the energy controller W_z^Σ could be considered more challenging due to the coupling between the various states and controllers in the system. However, this issue can be addressed with the help of the energetic model from (3.6); the tuning can be done directly from this simple system. Selecting a time response of $\tau_W^\Sigma = 10 \times \tau_i^\Sigma$, as it is usually done, a proper decoupling between both loops can be achieved.

3.3.2 Model linearization and time domain validation

In a similar way as in Section 3.2.1, the system comprising the non-linear SSTI model from Fig. 3.3 and the controller from Fig. 3.16 are connected as shown in Fig. 3.17.

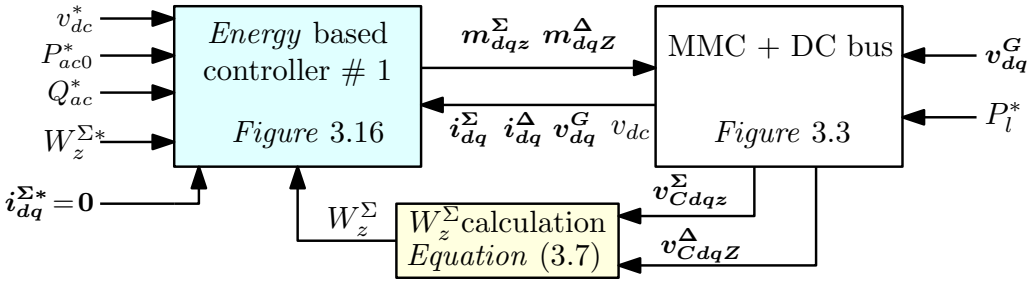

Figure 3.17 – SSTI model of MMC, DC bus and *Energy-based* controller # 1

In this case, the number of states is $n = 19$, since the additional ordinary differential equations from the added controllers (for the energy W_z and the current i_z^{Σ}) are also considered, resulting in a vector of states x_W as in (3.8) (the additional states with respect to the Classical CCSC are marked in blue). The vector of inputs $\boldsymbol{u_{W\#1}}$ for the *Energy-based* control, with $m = 9$ elements, is shown in (3.9) (the additional input with respect to the Classical CCSC is marked in blue).

$$\boldsymbol{x_{W\#1}} = [\underbrace{\xi_{i_z^{\Sigma}}\ \xi_{i_W^{\Sigma}}\ \boldsymbol{\xi_{i^{\Delta}_{dq}}}\ \boldsymbol{\xi_{i^{\Sigma}_{dq}}}}_{\text{Controllers}}\ \underbrace{\boldsymbol{i^{\Delta}_{dq}}\ \boldsymbol{i^{\Sigma}_{dqz}}\ \boldsymbol{v^{\Sigma}_{Cdqz}}\ \boldsymbol{v^{\Delta}_{CdqZ}}}_{\text{MMC}}\ \underbrace{v_{dc}}_{\text{DC bus}}\ ]^{\top} \in \mathbb{R}^{19} \tag{3.8}$$

$$\boldsymbol{u_{W\#1}} = [\underbrace{W_z^{\Sigma*}\ v^*_{dc}\ P^*_{ac0}\ Q^*_{ac}\ i_d^{\Sigma*}\ i_q^{\Sigma*}}_{\text{Controllers}}\ \underbrace{v_d^G\ v_q^G}_{\text{AC grid}}\ \underbrace{P^*_l}_{\text{DC grid}}\ ]^{\top} \in \mathbb{R}^{9} \tag{3.9}$$

To validate the developed small-signal model of the MMC with *Energy-based* control, results from time domain simulations are shown in Fig. 3.18. The event and parameters are the same as for Section 3.2.1, but it can be observed that the transient behavior of the DC power and voltage are well controlled contrary to the oscillatory behavior from the *Classical CCSC* strategy (Fig. 3.8).

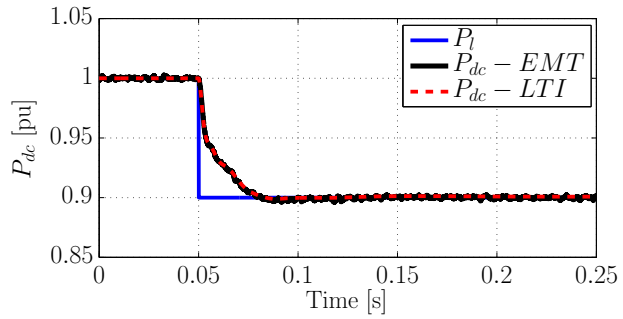

(a) P_{dc}[pu]

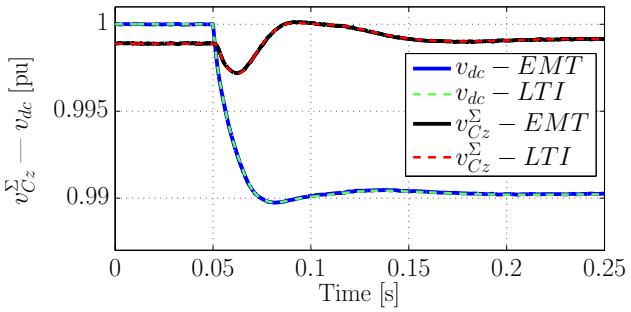

(b) v_{dc} and v^{Σ}_{Cz}[pu]

Figure 3.18 – Time domain validation *Energy-based # 1* controller – Step applied on P_l of 0.1 pu – *EMT*: EMTP-RV simulation with detailed converter, *LTI*: Linear time-invariant state-space model in Simulink

3.3.3 Stability analysis with Energy-based controller

As shown in Section 3.2.2, when the *Classical CCSC* from Fig. 3.6 was considered, some instabilities were observed with low values of droop gain k_d or low equivalent capacitance on the DC side (i.e. low values of H_{dc}). For demonstrating the stability improvement with the *Energy-based* controller from Fig. 3.16, the same parametric sweep is performed as for Fig. 3.9 and Fig. 3.10. The results are gathered in Fig. 3.19. For both situations, it is only shown the case where the power flow is from the DC side to the AC side since it was the case where the instabilities occurred in Section 3.2.2. However, with this controller, the system presents similar behavior from both power directions.

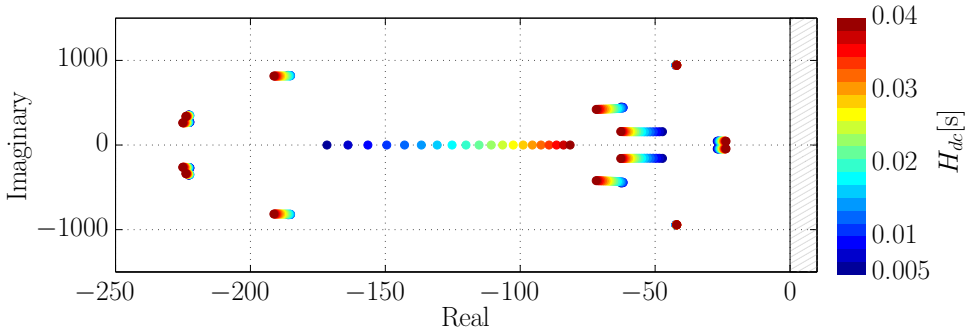

(a) Influence of DC capacitor H_{dc} — $k_d = 0.1$ pu

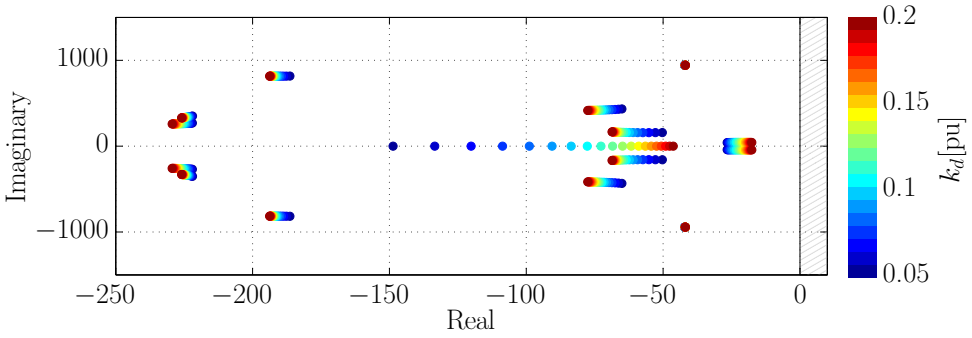

(b) Influence of droop gain k_d — $H_{dc} = 40$ ms

Figure 3.19 – Parametric sweeps for *Energy-based control # 1* — $v_{dc0} = 1$ pu, $P_{dc0} = -1$ pu, $k_d = 0.1$ pu — Power flow: DC ⇐ AC

For the case of the variation of H_{dc} in Fig. 3.19a, as well for the variation of k_d in Fig. 3.19b it can be clearly observed that stability is guaranteed for the studied cases.

3.3.4 Stability comparison with the Classical CCSC

For comparing the stability improvement, the eigenvalues from Fig. 3.9b and Fig. 3.19a with an electrostatic constant H_{dc} of 14.2 ms are shown in Fig. 3.20. The value of H_{dc} is chosen for highlighting the stability limits for the *Classical CCSC*. The unstable poles have a value of $2.81 \pm j781$, which corresponds to a frequency of 124 Hz approximately.

The stability improvements with the *Energy-based* controller are highlighted by a time domain simulation. The operating point is the same as for Fig. 3.20 and the simulated scenario considers an step of 0.1 pu applied on P_l. Simulation results are shown in Fig. 3.21. Since, for this set of parameters, the configuration of the MMC with *Classical CCSC* is unstable, the simulation is started with an extra capacitor connected in parallel with C_{dc} for stabilizing the

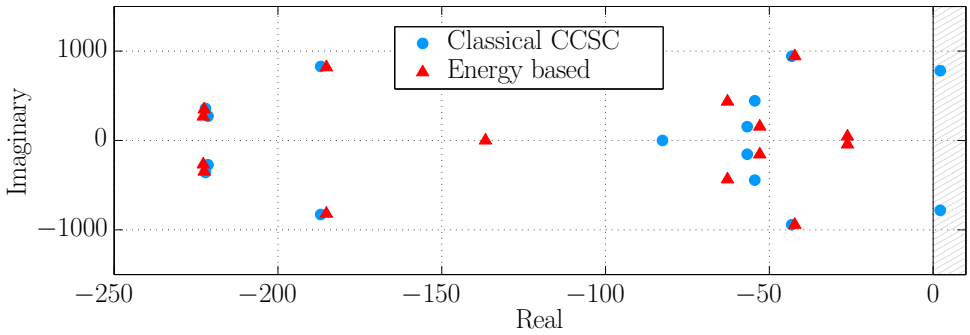

Figure 3.20 – Eigenvalues comparison *Energy-based # 1* and *Classical CCSC* control — DC Operating point $v_{dc0} = 1$ pu, $P_{dc0} = -1$ pu, Power flow: DC ⇐ AC — $k_d = 0.1$ pu

system, which is disconnected at $t = 0$ s. The frequency of the oscillations corresponds to the frequency of the unstable eigenvalues from Fig. 3.20.

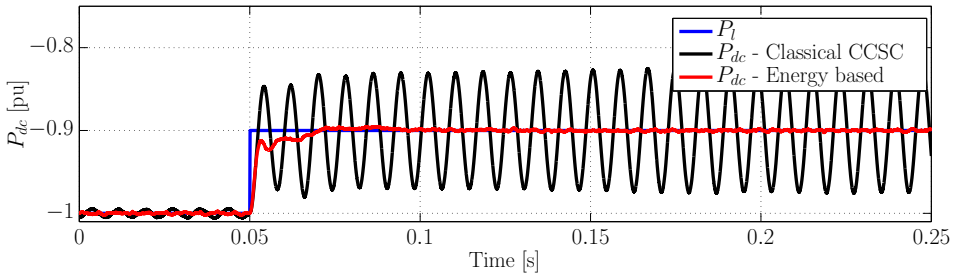

(a) P_{dc}[pu]

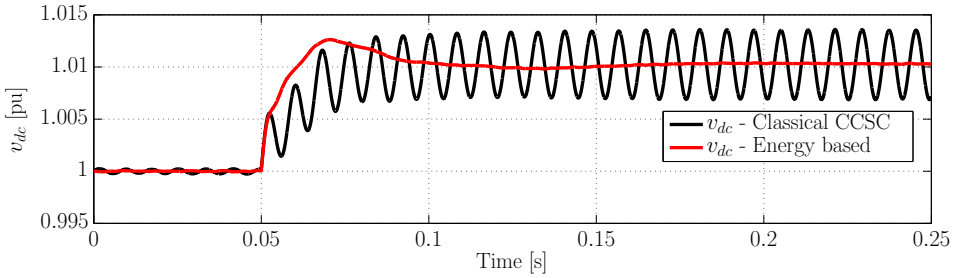

(b) v_{dc}[pu]

Figure 3.21 – Time domain comparison in EMTP-RV with detailed converters with *Classical CCSC* and *Energy-based # 1* strategies — Step applied on P_l of 0.1 pu — $H_{dc} = 14.2$ ms

The reader may refer to **[163]** for additional simulation results, such as the improvement of the system stability when considering the *Energy-based # 1* for fast active power reversals, where the *Classical CCSC* results unstable.

3.3.5 Issues with Energy-based controller # 1

The Energy-based controller # 1 described in this Section complies with all the specifications illustrated in Fig. 3.1. However, the current and voltage variables of the MMC are highly coupled as it is demonstrated in the following time-domain simulations. In this case, a step on the reactive current reference $i_q^{\Delta *}$ of 0.3 pu is applied at $t = 0.05$ s and the results are shown in Fig. 3.22.

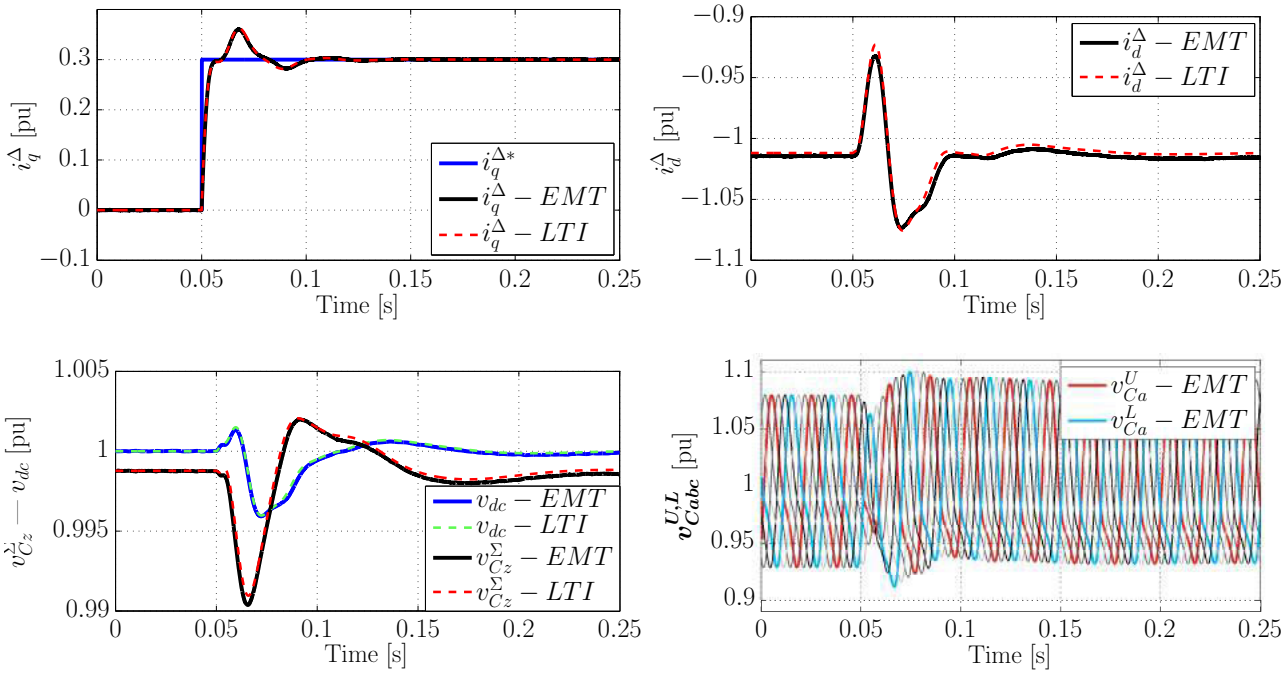

Figure 3.22 – Time domain results with *Energy-based # 1* strategy (with UCM) — Step applied on $i_q^{\Delta*}$ — $H_{dc} = 40$ ms — $k_d = 0.1$ pu

The dynamic response of i_q^{Δ} doesn't present a pure second-order response type as for the *2-level VSC* from Section 1.2 (See simulation results from Fig. 1.9). Also, as it can be observed in the grid current on the d axis, the dq currents are not decoupled, even if the decoupling terms are added to the grid current controller. Moreover, the change on the AC-side reactive current causes a small perturbation on the DC bus. In the presented simulation case, the coupling doesn't imply that the system behavior is not acceptable, but it may limit the system for designing advanced control strategies where fast current controllers are needed [164]. Finally, in the lower-right figure from Fig. 3.22 shows the results of the arm capacitor voltages in abc frame, where it can be observed that the voltages are balanced during the simulation.

Decoupling state variables with Compensated Modulation

As it was explained in Section 2.5.1, the modulation indices of the MMC for the EMT model or the SSTI were calculated until now with the Un-Compensated Modulation (UCM), and recalled in Fig. 3.23a for a generic phase j. As observed, the modulation index m_j^U (m_j^L) is calculated dividing the modulated voltage reference v_{mj}^{U*} (v_{mj}^{L*}) by v_{dc}, without assuring that the actual applied voltage is equal to its references, i.e. $v_{mj}^{U} \neq v_{mj}^{U*}$ ($v_{mj}^{L} \neq v_{mj}^{L*}$). This coupling is preventing to accurately control the d and q axis of the grid currents, among other drawbacks. However, this issue can be easily solved by compensating the arm capacitor fluctuations using the actual measure (or estimation) of v_{Cj}^{U} and v_{Cj}^{L} for obtaining the modulation indices by simply inverting the relation of the *Physical system* given in (2.1), and expressed in Fig. 3.23b [116]. This technique is referred as "Compensated Modulation" (CM), and it allows to assure that $v_{mj}^{U} = v_{mj}^{U*}$ and $v_{mj}^{L} = v_{mj}^{L*}$ simultaneously [114, 146].

The concept of the compensated modulation is easy to understand when it is approached in abc frame with "Upper-Lower" representation and considering each phase individually as it was done in Fig. 3.23. However, in dqz and "Σ-Δ" representation for a three-phase approach this

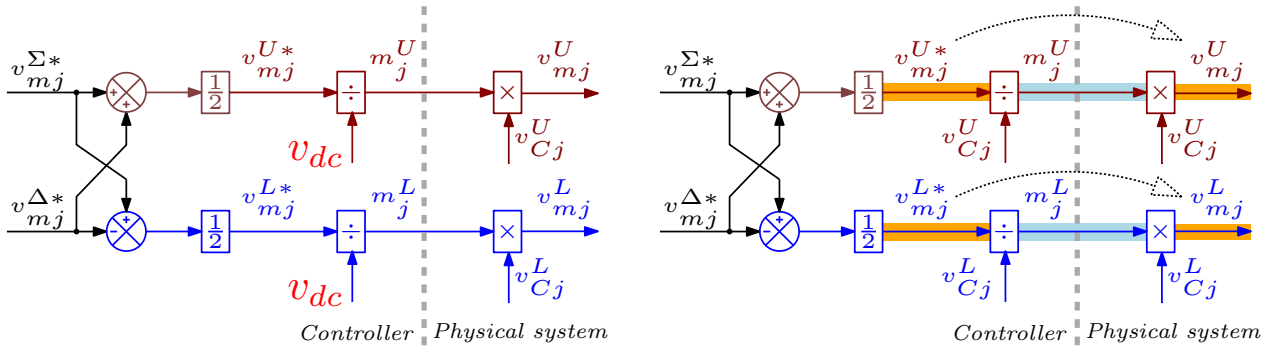

(a) Un-Compensated Modulation (UCM) (b) Compensated Modulation (CM)

Figure 3.23 – Un-Compensated and Compensated modulation for the Arm Averaged Model in *abc* frame with "Upper-Lower" representation for the phase j

task is more cumbersome since complicated matrix relations are needed. For the representation of the CM in dqz, let us develop mathematically the modulation process in a three-phase approach and *abc* frame using the appropriated matrices in "Σ-Δ" representation for ease of understanding. First, consider the relation given in (2.8), which is repeated in (3.10) in matrix form for convenience. This equation represents the *Physical system* similarly as in Fig. 3.23, but now it is relating the modulation indices with the modulated voltages in "Σ-Δ" representation by means of the 6×6 matrix $\boldsymbol{V}^{\boldsymbol{\Sigma\Delta}}_{\boldsymbol{Cmabc}}$.

$$\begin{bmatrix} v^{\Sigma}_{ma} \\ v^{\Sigma}_{mb} \\ v^{\Sigma}_{mc} \\ \hline v^{\Delta}_{ma} \\ v^{\Delta}_{mb} \\ v^{\Delta}_{mc} \end{bmatrix} = \underbrace{\frac{1}{2}\left[\begin{array}{ccc|ccc} v^{\Sigma}_{Ca} & 0 & 0 & v^{\Delta}_{Ca} & 0 & 0 \\ 0 & v^{\Sigma}_{Cb} & 0 & 0 & v^{\Delta}_{Cb} & 0 \\ 0 & 0 & v^{\Sigma}_{Cc} & 0 & 0 & v^{\Delta}_{Cc} \\ \hline -v^{\Delta}_{Ca} & 0 & 0 & -v^{\Sigma}_{Ca} & 0 & 0 \\ 0 & -v^{\Delta}_{Cb} & 0 & 0 & -v^{\Sigma}_{Cb} & 0 \\ 0 & 0 & -v^{\Delta}_{Cc} & 0 & 0 & -v^{\Sigma}_{Cc} \end{array}\right]}_{\boldsymbol{V}^{\boldsymbol{\Sigma\Delta}}_{\boldsymbol{Cmabc}}} \begin{bmatrix} m^{\Sigma}_{a} \\ m^{\Sigma}_{b} \\ m^{\Sigma}_{c} \\ \hline m^{\Delta}_{a} \\ m^{\Delta}_{b} \\ m^{\Delta}_{c} \end{bmatrix} \tag{3.10}$$

In the controller, the expression of the compensated modulation technique in matrix form is then given by (3.11), where the modulation indices are calculated with the reference modulated voltages multiplied by the inverse of the 6×6 matrix $\boldsymbol{V}^{\boldsymbol{\Sigma\Delta}}_{\boldsymbol{Cmabc}}$.

$$\begin{bmatrix} m^{\Sigma}_{a} \\ m^{\Sigma}_{b} \\ m^{\Sigma}_{c} \\ \hline m^{\Delta}_{a} \\ m^{\Delta}_{b} \\ m^{\Delta}_{c} \end{bmatrix} = \left(\boldsymbol{V}^{\boldsymbol{\Sigma\Delta}}_{\boldsymbol{Cmabc}}\right)^{-1} \begin{bmatrix} v^{\Sigma*}_{ma} \\ v^{\Sigma*}_{mb} \\ v^{\Sigma*}_{mc} \\ \hline v^{\Delta*}_{ma} \\ v^{\Delta*}_{mb} \\ v^{\Delta*}_{mc} \end{bmatrix} \tag{3.11}$$

By analogy, the same process in matrix form is performed for the MMC-SSTI controller to represent the compensated modulation technique in dqz frame. First, the relation between the MMC modulation indices with the modulated voltages in "Σ-Δ" representation and SRRF dqz

by means of the the 7×7 matrix $\boldsymbol{V}^{\boldsymbol{\Sigma\Delta}}_{\boldsymbol{CmdqZ}}$ developed in in Section 2.4 is recalled in (3.12)[1].

$$\begin{bmatrix} v^{\Sigma}_{md} \\ v^{\Sigma}_{mq} \\ v^{\Sigma}_{mz} \\ \hline v^{\Delta}_{md} \\ v^{\Delta}_{mq} \\ v^{\Delta}_{mZ_d} \\ v^{\Delta}_{mZ_q} \end{bmatrix} = \underbrace{\frac{1}{4}\left[\begin{array}{ccc|ccc|c} 2v^{\Sigma}_{Cz} & 0 & 2v^{\Sigma}_{Cd} & v^{\Delta}_{Cd}+v^{\Delta}_{CZ_d} & v^{\Delta}_{CZ_q}-v^{\Delta}_{Cq} & v^{\Delta}_{Cd} & v^{\Delta}_{Cq} \\ 0 & 2v^{\Sigma}_{Cz} & 2v^{\Sigma}_{Cq} & -v^{\Delta}_{Cq}-v^{\Delta}_{CZ_q} & v^{\Delta}_{CZ_d}-v^{\Delta}_{Cd} & v^{\Delta}_{Cq} & -v^{\Delta}_{Cd} \\ v^{\Sigma}_{Cd} & v^{\Sigma}_{Cq} & 2v^{\Sigma}_{Cz} & v^{\Delta}_{Cd} & v^{\Delta}_{Cq} & v^{\Delta}_{CZ_d} & v^{\Delta}_{CZ_q} \\ \hline -v^{\Delta}_{Cd}-v^{\Delta}_{CZ_d} & v^{\Delta}_{Cq}+v^{\Delta}_{CZ_q} & -2v^{\Delta}_{Cd} & -v^{\Sigma}_{Cd}-2v^{\Sigma}_{Cz} & v^{\Sigma}_{Cq} & -v^{\Sigma}_{Cd} & v^{\Sigma}_{Cq} \\ v^{\Delta}_{Cq}-v^{\Delta}_{CZ_q} & v^{\Delta}_{Cd}-v^{\Delta}_{CZ_d} & -2v^{\Delta}_{Cq} & v^{\Sigma}_{Cq} & v^{\Sigma}_{Cd}-2v^{\Sigma}_{Cz} & -v^{\Sigma}_{Cq} & -v^{\Sigma}_{Cd} \\ -v^{\Delta}_{Cd} & -v^{\Delta}_{Cq} & -2v^{\Delta}_{CZ_d} & -v^{\Sigma}_{Cd} & -v^{\Sigma}_{Cq} & -2v^{\Sigma}_{Cz} & 0 \\ -v^{\Delta}_{Cq} & v^{\Delta}_{Cd} & -2v^{\Delta}_{CZ_q} & v^{\Sigma}_{Cq} & -v^{\Sigma}_{Cd} & 0 & -2v^{\Sigma}_{Cz} \end{array}\right]}_{\boldsymbol{V}^{\boldsymbol{\Sigma\Delta}}_{\boldsymbol{CmdqZ}}} \begin{bmatrix} m^{\Sigma}_{d} \\ m^{\Sigma}_{q} \\ m^{\Sigma}_{z} \\ \hline m^{\Delta}_{d} \\ m^{\Delta}_{q} \\ m^{\Delta}_{Z_d} \\ m^{\Delta}_{Z_q} \end{bmatrix} \tag{3.12}$$

Finally, for the SSTI representation of the compensated modulation technique in dqz frame the inverse of the the 7×7 matrix $\boldsymbol{V}^{\boldsymbol{\Sigma\Delta}}_{\boldsymbol{CmdqZ}}$ is used, as expressed in (3.13).

$$\begin{bmatrix} m^{\Sigma}_{d} \\ m^{\Sigma}_{q} \\ m^{\Sigma}_{z} \\ \hline m^{\Delta}_{d} \\ m^{\Delta}_{q} \\ m^{\Delta}_{Z_d} \\ m^{\Delta}_{Z_q} \end{bmatrix} = \left(\boldsymbol{V}^{\boldsymbol{\Sigma\Delta}}_{\boldsymbol{CmdqZ}}\right)^{-1} \begin{bmatrix} v^{\Sigma*}_{md} \\ v^{\Sigma*}_{mq} \\ v^{\Sigma*}_{mz} \\ \hline v^{\Delta*}_{md} \\ v^{\Delta*}_{mq} \\ v^{\Delta*}_{mZ_d} \\ v^{\Delta*}_{mZ_q} \end{bmatrix} \tag{3.13}$$

The relation given in (3.13) can be solved symbolically obtaining (3.14). This may be performed with commercial software such as Matlab (with Symbolic toolbox) or Wolfram Mathematica, among others. However, the expressions given by $f_{CM,1}$ to $f_{CM,7}$ are highly complex to be written in this Thesis[2].

$$\begin{aligned} m^{\Sigma}_{d} &= f_{CM,1}\left(\boldsymbol{v}^{\boldsymbol{\Sigma*}}_{\boldsymbol{mdqz}},\ \boldsymbol{v}^{\boldsymbol{\Delta*}}_{\boldsymbol{mdqZ}},\ \boldsymbol{v}^{\boldsymbol{\Sigma}}_{\boldsymbol{Cdqz}},\ \boldsymbol{v}^{\boldsymbol{\Delta}}_{\boldsymbol{CdqZ}}\right) \\ m^{\Sigma}_{q} &= f_{CM,2}\left(\boldsymbol{v}^{\boldsymbol{\Sigma*}}_{\boldsymbol{mdqz}},\ \boldsymbol{v}^{\boldsymbol{\Delta*}}_{\boldsymbol{mdqZ}},\ \boldsymbol{v}^{\boldsymbol{\Sigma}}_{\boldsymbol{Cdqz}},\ \boldsymbol{v}^{\boldsymbol{\Delta}}_{\boldsymbol{CdqZ}}\right) \\ m^{\Sigma}_{z} &= f_{CM,3}\left(\boldsymbol{v}^{\boldsymbol{\Sigma*}}_{\boldsymbol{mdqz}},\ \boldsymbol{v}^{\boldsymbol{\Delta*}}_{\boldsymbol{mdqZ}},\ \boldsymbol{v}^{\boldsymbol{\Sigma}}_{\boldsymbol{Cdqz}},\ \boldsymbol{v}^{\boldsymbol{\Delta}}_{\boldsymbol{CdqZ}}\right) \\ m^{\Delta}_{d} &= f_{CM,4}\left(\boldsymbol{v}^{\boldsymbol{\Sigma*}}_{\boldsymbol{mdqz}},\ \boldsymbol{v}^{\boldsymbol{\Delta*}}_{\boldsymbol{mdqZ}},\ \boldsymbol{v}^{\boldsymbol{\Sigma}}_{\boldsymbol{Cdqz}},\ \boldsymbol{v}^{\boldsymbol{\Delta}}_{\boldsymbol{CdqZ}}\right) \\ m^{\Delta}_{q} &= f_{CM,5}\left(\boldsymbol{v}^{\boldsymbol{\Sigma*}}_{\boldsymbol{mdqz}},\ \boldsymbol{v}^{\boldsymbol{\Delta*}}_{\boldsymbol{mdqZ}},\ \boldsymbol{v}^{\boldsymbol{\Sigma}}_{\boldsymbol{Cdqz}},\ \boldsymbol{v}^{\boldsymbol{\Delta}}_{\boldsymbol{CdqZ}}\right) \\ m^{\Delta}_{Z_d} &= f_{CM,6}\left(\boldsymbol{v}^{\boldsymbol{\Sigma*}}_{\boldsymbol{mdqz}},\ \boldsymbol{v}^{\boldsymbol{\Delta*}}_{\boldsymbol{mdqZ}},\ \boldsymbol{v}^{\boldsymbol{\Sigma}}_{\boldsymbol{Cdqz}},\ \boldsymbol{v}^{\boldsymbol{\Delta}}_{\boldsymbol{CdqZ}}\right) \\ m^{\Delta}_{Z_q} &= f_{CM,7}\left(\boldsymbol{v}^{\boldsymbol{\Sigma*}}_{\boldsymbol{mdqz}},\ \boldsymbol{v}^{\boldsymbol{\Delta*}}_{\boldsymbol{mdqZ}},\ \boldsymbol{v}^{\boldsymbol{\Sigma}}_{\boldsymbol{Cdqz}},\ \boldsymbol{v}^{\boldsymbol{\Delta}}_{\boldsymbol{CdqZ}}\right) \end{aligned} \tag{3.14}$$

For summarizing, Fig. 3.24 shows the modulation indices calculation process for the three-phase system in *abc* (for the classical AAM model) and *dqz* (for the SSTI-MMC model).

It is important to highlight that at this point that, even if the zero-sequence voltages references $v^{\Delta*}_{mZ_d}$ and $v^{\Delta*}_{mZ_q}$ are set voluntarily to zero, it doesn't imply that the modulation indices $m^{\Delta}_{Z_d}$ and $m^{\Delta}_{Z_q}$ are zero as well. This was the case for the UCM, but not anymore for the CM. This is the main reason of the modeling efforts in Section 2.4.1 by not neglecting the modulation indices $m^{\Delta}_{Z_d}$ and $m^{\Delta}_{Z_q}$.

In Fig. 3.25 it is depicted the MMC-SSTI model considering *Energy-based* controller # 1 with CM. Since the algebraic equations have changed with respect to Fig. 3.17, a new LTI

[1]It is recalled that the matrix $\boldsymbol{V}^{\boldsymbol{\Sigma\Delta}}_{\boldsymbol{CmdqZ}}$ has now 7 columns and rows instead of 6, since the z-seq. of the Δ variables were split into 2 components Z_d and Z_q for achieving an SSTI representation.

[2]When assuming that CM is used, a different formulation for the SSTI-MMC model can be performed, as in [165]. In that case, the state variables of the MMC are the energies W^{Σ} and W^{Δ}, instead of capacitor voltages.

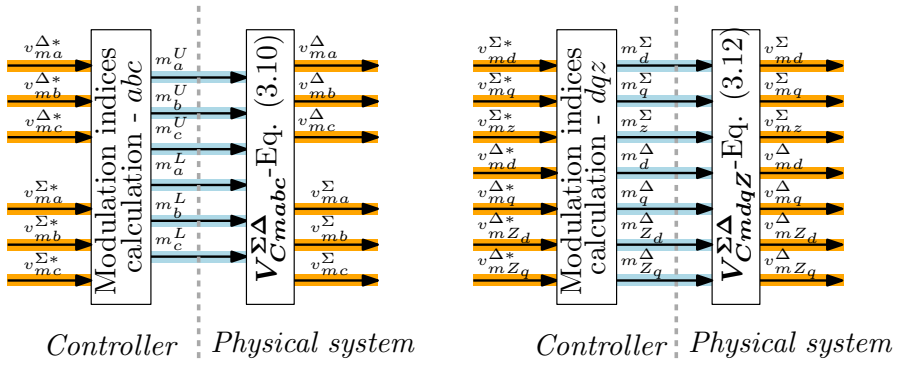

(a) Modulation for AAM model (b) Modulation for MMC-SSTI model

Figure 3.24 – Relating modulated voltage references with the actual modulated voltages - Modulation indices calculation

model should be considered by the linearization of the equations formed with Fig. 3.25 (note that the model order remains unchanged). Once the LTI model is obtained, the same simulation is performed as in the previous sub-section. A step on the reactive current reference $i_q^{\Delta *}$ of 0.3 pu is applied at $t = 0.05$ s and the results are shown in Fig. 3.26.

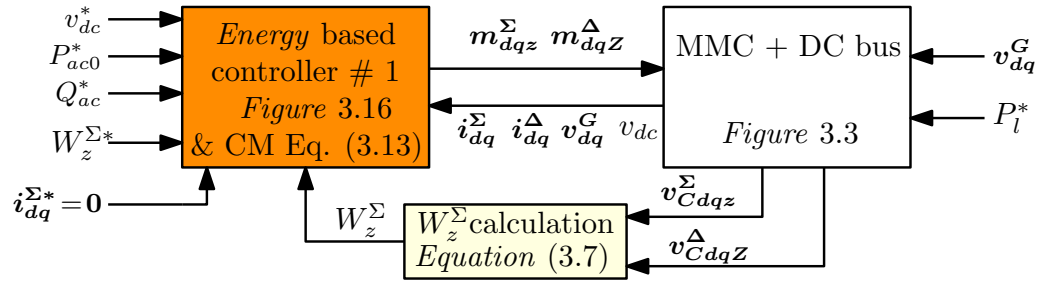

Figure 3.25 – SSTI model of MMC, DC bus and *Energy-based* controller # 1 with CM

When comparing the results of the grid currents i^{Δ} from Fig. 3.22 (with UCM) and in Fig. 3.26 (with CM), it can be noticed that when the CM is considered, an accurate decoupling between the currents in d and q axes can be achieved. However, as shown in Fig. 3.26, the arm voltages are not balanced and presenting undamped oscillations. On the one hand, a perfect decoupling between the grid currents are achieved, but on the other hand, results for other variables are deteriorated.

In Fig. 3.27 it is shown the results of the eigenvalues of the LTI model. As it can be seen, the real-part of two pairs of eigenvalues are near zero ($\lambda_{1,2}$, with a natural frequency of 100 Hz and $\lambda_{3,4}$ with 50 Hz). This proves that if the CM is considered with the *Energy-based* controller # 1, the stability is not ensured as it was observed with UCM [166].

For understanding the origin of the unstable eigenvalues, participation factors are calculated and the results are shown in Fig. 3.28. As it can be observed, the states that participate in the two pairs of critical eigenvalues are the arm capacitor voltages v^{Σ}_{Cd}, v^{Σ}_{Cq} for $\lambda_{1,2}$, and v^{Δ}_{Cd}, v^{Δ}_{Cq} for $\lambda_{3,4}$. In fact, the *Energy-based* controller # 1 only deals with the total energy on the MMC (Specification from Fig. 3.1b), but the energy "re-allocation" (i.e. horizontal and vertical energy balancing) is left uncontrolled (Specifications from Figs. 3.1c and 3.1d). When the UCM was considered, this energy balancing inside the MMC was obtained intrinsically [115, 166]. If the CM is considered, the energy inside the MMC should be explicitly controlled for assuring a correct dynamic behavior of the converter, as discussed in **[159]**.

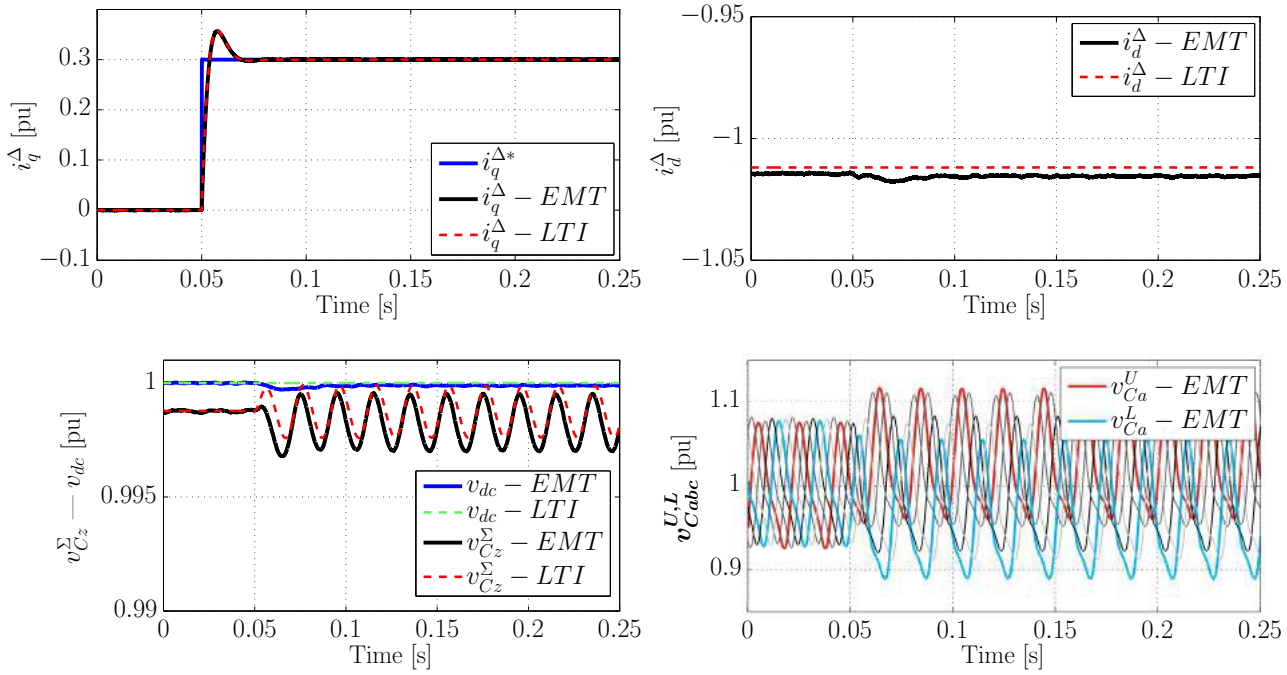

Figure 3.26 – Time domain results with *Energy-based # 1* strategy (with CM) — Step applied on $i_q^{\Delta*}$ — $H_{dc} = 40$ ms — $k_d = 0.1$ pu

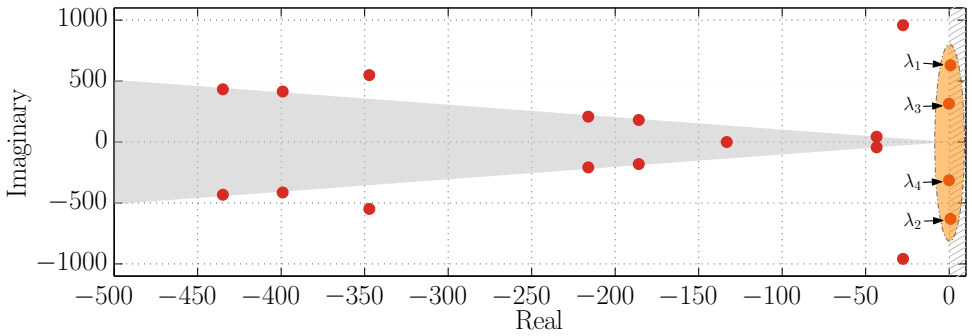

Figure 3.27 – Eigenvalues of *Energy-based # 1* with Compensated Modulation — DC Operating point $v_{dc0} = 1$ pu, $P_{dc0} = -1$ pu, Power flow: DC ⇐ AC — $k_d = 0.1$ pu

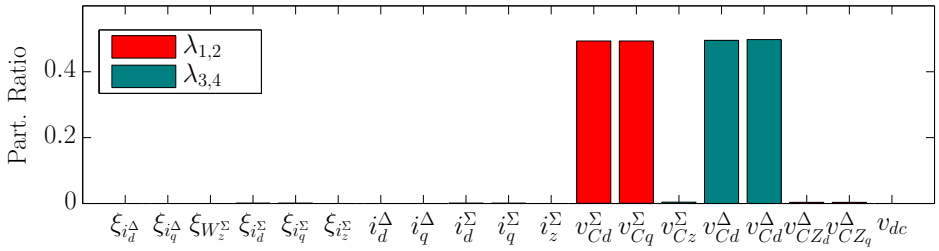

Figure 3.28 – Participation factor analysis of *Energy-based # 1* with Compensated Modulation — DC Operating point $v_{dc0} = 1$ pu, $P_{dc0} = -1$ pu, Power flow: DC ⇐ AC — $k_d = 0.1$ pu

For improving the dynamic behavior while guaranteeing the control specifications from Fig. 3.1, a complete *Energy-based* controller should be considered [114, 116].

3.4 Complete Energy-based controller # 2 with Compensated Modulation

The concept of *Energy-based* controllers is not new by itself. Several studies were already performed detailing the cascaded controller for the management of the stored energy in the MMC [108, 114, 146, 167]. Normally, these controllers are developed in the stationary reference frame *abc*, where an inversion-based technique from the energetic model of each leg of the MMC can be followed [116]. Also, several studies focus on the energy controllers in the stationary reference frame $\alpha\beta z$, which is particularly useful when considering unbalanced situations on the AC grid [79, 168, 169].

Due to the extreme complexity of the MMC-SSTI model in full *dqz* frame, it was preferred not to develop a new controller based on the new model in this Thesis. For this reason, the intention is to refer an already existing and well documented *abc* controller into *dqz* SRRF for evaluating the stability of the MMC with complete energy-based controllers. In the following, a resume of the findings in **[162]** is given.

3.4.1 Energy-based controller in mixed reference frames

An overview of the structure for a typical *Energy-based* control strategy which verifies the specifications is shown in Fig. 3.29 [117] (referred now as *Energy-based* control strategy # 2). The AC-side controller is similar to the one already presented in Fig. 3.6 and Fig. 3.16. More details on this controller can be found in the Appendix F.

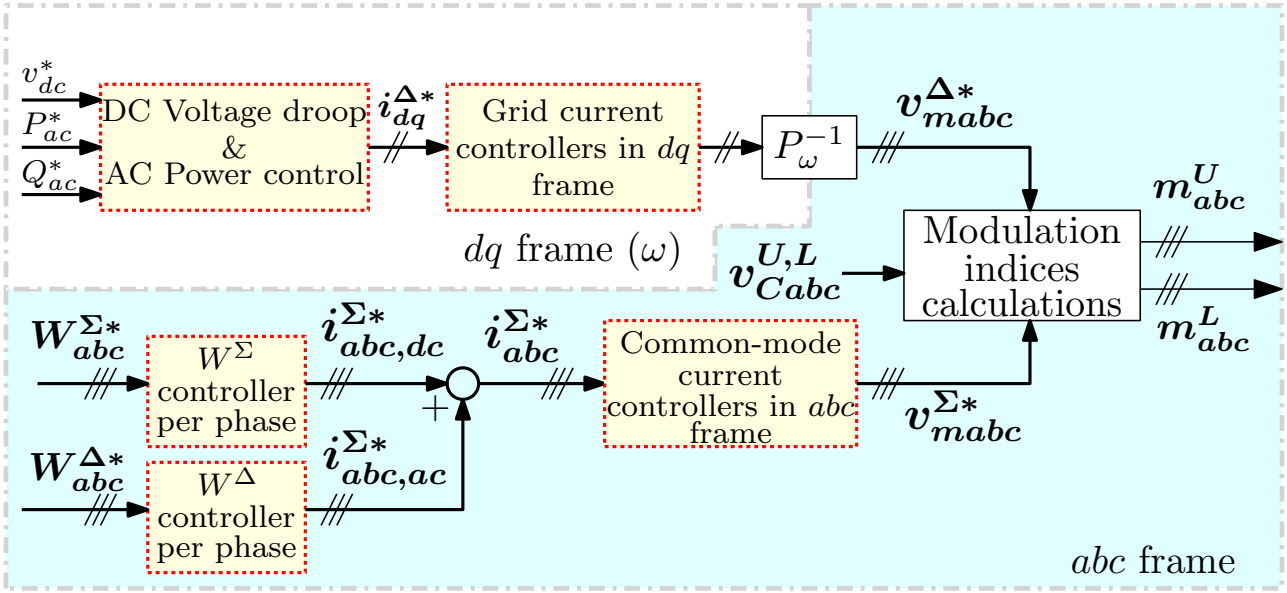

Figure 3.29 – General scheme *Energy-based* control # 2 in mixed reference frames (*abc* and *dq*)

For controlling the time-averaged[3] energy sum $\overline{W}_j^\Sigma$ for each phase, three independent PI controllers are implemented. The time-averaged value $\overline{W}_j^\Sigma$ is obtained with a second-order notch filter tuned at 2ω [170]. Setting the same energy reference for each phase (i.e. $\overline{W}_a^{\Sigma *} =$

[3]The term *time-averaged* is used to highlight that $\overline{W}_j^\Sigma$ is a DC value in steady state, and all the oscillations are filtered before sendind the signal to the controller.

$\overline{W}_b^{\Sigma*} = \overline{W}_c^{\Sigma*}$), the specification from Fig. 3.1c is assured. These controllers generate the DC component of the common-mode current references $i_{j,dc}^{\Sigma*}$ for the corresponding phase. The detail of the controller structure is shown in Fig. 3.30.

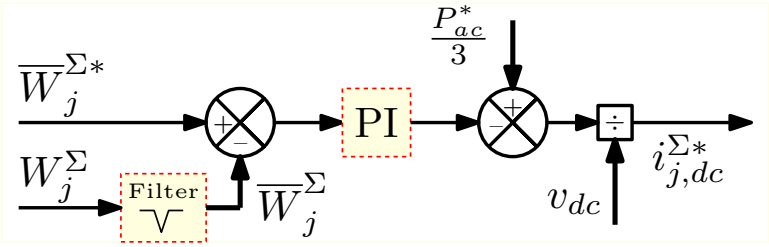

Figure 3.30 – Energy sum (Σ) controller (phase j)

The energy difference controller is depicted in Fig. 3.31, where V^G is the RMS value of the AC grid voltage, $\boldsymbol{R}$ is defined in (3.15) and $\boldsymbol{K}$ is defined in (3.16) . This controller guarantees specification 3 (i.e. vertical balancing). The control details can be found in [**159**].

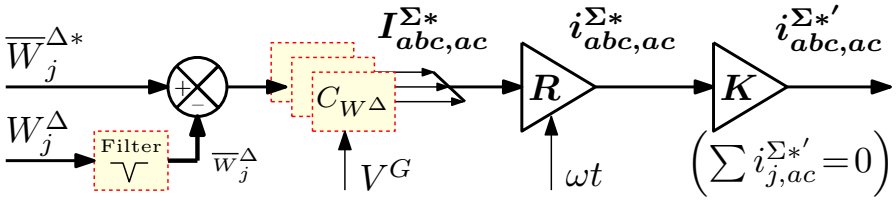

Figure 3.31 – Energy difference (Δ) controller (three-phase)

$$\boldsymbol{R} = \sqrt{2}\begin{bmatrix} \cos(\omega t) & 0 & 0 \\ 0 & \cos\left(\omega t - \frac{2\pi}{3}\right) & 0 \\ 0 & 0 & \cos\left(\omega t - \frac{2\pi}{3}\right) \end{bmatrix} \tag{3.15}$$

$$\boldsymbol{K} = \begin{bmatrix} 1 & -\frac{1}{2} & -\frac{1}{2} \\ -\frac{1}{2} & 1 & -\frac{1}{2} \\ -\frac{1}{2} & -\frac{1}{2} & 1 \end{bmatrix} \tag{3.16}$$

The three common-mode currents (for each phase j) are corrected to their references via three independent PI controllers as well [170]. Finally, the modulation signals m_j^U and m_j^L are obtained according to the CM from (3.11).

3.4.2 SSTI-SRRF representation of Stationary Frame Energy-based controllers

For obtaining the full representation of the system in SRRF frame, it is still needed to reformulate the controllers in stationary frame of the control structure from Fig. 3.29. The overall *Energy-based* controller in dqz frame is shown in Fig. 3.32. The expressions of the MMC energies W^Σ and W^Δ in dqz are related with the arm capacitor voltages $\boldsymbol{v}_{\boldsymbol{Cdqz}}^{\boldsymbol{\Sigma}}$ and $\boldsymbol{v}_{\boldsymbol{CdqZ}}^{\boldsymbol{\Delta}}$, and their deductions are found in Appendix G.1.

In the upcoming subsections, the equations of the controller in abc are referred to their corresponding SRRFs with a similar approach than used for the MMC modeling in Chapter 2 according to the following classification:

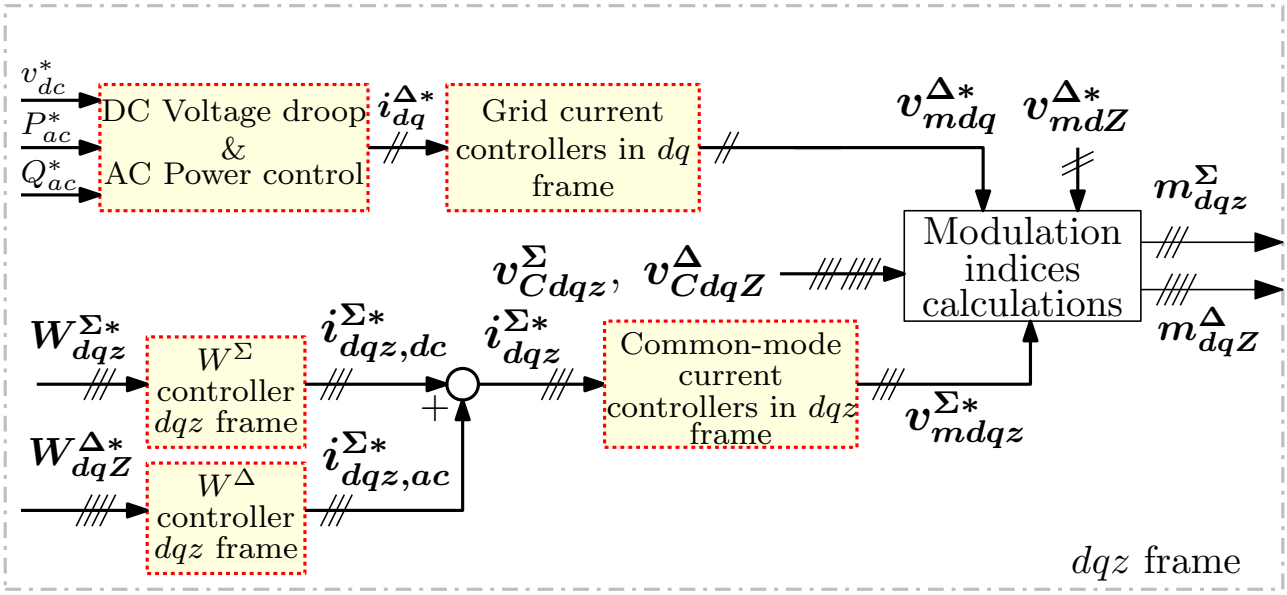

Figure 3.32 – General scheme *Energy-based* control # 2 in full dqz frame

- Common-mode "Σ" current controllers at -2ω: In Fig. 3.29, the common mode currents are regulated through three independent PI controllers (one per each abc phase). The details for referring the three-phase regulators from abc to dqz frame are given in Appendix G.2.1. It should be remarked that the resulting current controller is not the same as the CCSC structure from Fig. 3.4. As seen in Fig. 3.32, the current references $\boldsymbol{i^{\Sigma*}_{dqz}}$ are provided by the outer loops (i.e. energy controllers).
- Energy "W^{Σ}" controllers and averaging filters at 2ω: Similarly as for the current controllers, three independent PI regulators are used to control the energy stored in each phase-leg of the MMC. Moreover, notch filters tuned at 2ω are used on the measures to obtain the time-average value of the energies $\overline{W}^{\Sigma}_{j}$. The energy references in dqz frame are discussed later.
- Energy "W^{Δ}"controllers and averaging filters at ω: Again, three independent controllers are used for the energy differences. Similarly as for the arm capacitor voltage difference $\boldsymbol{v^{\Delta}_{Cdqz}}$, the energy W^{Δ}_{z} is not in a SSTI signal. For this reason, the same concept as or v^{Δ}_{Cz} is used: the energy W^{Δ}_{z} is represented by two state variables, $W^{\Delta}_{Z_d}$ and $W^{\Delta}_{Z_q}$ for modeling the dynamics of the amplitude and phase of W^{Δ}_{z}; both are SSTI variables then. For the measures, the notch-filters per-phase are referred to the SRRF as well.

3.4.3 Energy Σ controller reformulation

The PI controller and the notch filter used in W^{Σ} controllers from Fig. 3.30 are expressed in dqz frame with the methodology explained in section G.2.

Averaging filter for energy "Σ" measures

The energy sum $\boldsymbol{W^{\Sigma}_{abc}} = [W^{\Sigma}_{a}\ W^{\Sigma}_{b}\ W^{\Sigma}_{c}]^{\top}$ is filtered to obtain $\overline{\boldsymbol{W}}^{\boldsymbol{\Sigma}}_{\boldsymbol{abc}} = [\overline{W}^{\Sigma}_{a}\ \overline{W}^{\Sigma}_{b}\ \overline{W}^{\Sigma}_{c}]^{\top}$ before sending the signals to the PI controller in abc frame (Fig. 3.30) with a notch filter. In dqz frame, the variables $\boldsymbol{W^{\Sigma}_{dqz}} = [W^{\Sigma}_{d}\ W^{\Sigma}_{q}\ W^{\Sigma}_{z}]^{\top}$ are filtered to obtain $\overline{\boldsymbol{W}}^{\boldsymbol{\Sigma}}_{\boldsymbol{dqz}} = [\overline{W}^{\Sigma}_{d}\ \overline{W}^{\Sigma}_{q}\ \overline{W}^{\Sigma}_{z}]^{\top}$,

and the variables are obtained as in (3.17).

$$\boldsymbol{W}^{\boldsymbol{\Sigma}}_{\boldsymbol{abc}} = \boldsymbol{P}^{\boldsymbol{-1}}_{\boldsymbol{-2\omega}} \boldsymbol{W}^{\boldsymbol{\Sigma}}_{\boldsymbol{dqz}}; \quad \overline{\boldsymbol{W}}^{\boldsymbol{\Sigma}}_{\boldsymbol{abc}} = \boldsymbol{P}^{\boldsymbol{-1}}_{\boldsymbol{-2\omega}} \overline{\boldsymbol{W}}^{\boldsymbol{\Sigma}}_{\boldsymbol{dqz}} \tag{3.17}$$

Considering the SSTI representation of a generic notch-filter tuned to block the frequencies at ω_n (see (G.24)), the filter associated to the energy measures $\boldsymbol{W}^{\boldsymbol{\Sigma}}_{\boldsymbol{dqz}}$ can be expressed as in (3.18) with $\omega_n = 2\omega$ and a damping ratio given by ζ, which is set at 0.7 for all notch-filters in this Thesis.

$$\frac{d\boldsymbol{F}^{\boldsymbol{\Sigma}}_{\boldsymbol{1dqz}}}{dt} = \boldsymbol{F}^{\boldsymbol{\Sigma}}_{\boldsymbol{2dqz}} - 4\zeta\omega \boldsymbol{F}^{\boldsymbol{\Sigma}}_{\boldsymbol{1dqz}} - 4\zeta\omega \boldsymbol{W}^{\boldsymbol{\Sigma}}_{\boldsymbol{dqz}} - \boldsymbol{J}_{\boldsymbol{-2\omega}} \boldsymbol{F}^{\boldsymbol{\Sigma}}_{\boldsymbol{1dqz}} \tag{3.18a}$$

$$\frac{d\boldsymbol{F}^{\boldsymbol{\Sigma}}_{\boldsymbol{2dqz}}}{dt} = -4\omega^2 \boldsymbol{F}^{\boldsymbol{\Sigma}}_{\boldsymbol{1dqz}} - \boldsymbol{J}_{\boldsymbol{-2\omega}} \boldsymbol{F}^{\boldsymbol{\Sigma}}_{\boldsymbol{2dqz}} \tag{3.18b}$$

$$\overline{\boldsymbol{W}}^{\boldsymbol{\Sigma}}_{\boldsymbol{dqz}} = \boldsymbol{F}^{\boldsymbol{\Sigma}}_{\boldsymbol{1dqz}} + \boldsymbol{W}^{\boldsymbol{\Sigma}}_{\boldsymbol{dqz}} \tag{3.18c}$$

The state variables of the second-order filter in dqz frame are expressed in $\boldsymbol{F}^{\boldsymbol{\Sigma}}_{\boldsymbol{1dqz}} = [F^{\Sigma}_{1d}\ F^{\Sigma}_{1q}\ F^{\Sigma}_{1z}]^{\top}$ and $\boldsymbol{F}^{\boldsymbol{\Sigma}}_{\boldsymbol{2dqz}} = [F^{\Sigma}_{2d}\ F^{\Sigma}_{2q}\ F^{\Sigma}_{2z}]^{\top}$.

PI controller for energy "Σ"

The PI controller expressed in dqz frame is obtained with the methodology explained in G.2.1 for a generic three-phase independent PI regulators in abc referred to the SRRF at $n\omega$. In this case, $n\omega = -2\omega$ and the methodology is applied to the controller from Fig. 3.30. The result is shown in (3.19). The output of the controller is then the "DC" current reference $\boldsymbol{i}^{\boldsymbol{\Sigma *}}_{\boldsymbol{dqz,dc}}$ as expressed in (3.20) [114].

$$T_i^{W^{\Sigma}} \frac{d\boldsymbol{\xi}^{\boldsymbol{W^{\Sigma}}}_{\boldsymbol{dqz}}}{dt} = \overline{\boldsymbol{W}}^{\boldsymbol{\Sigma *}}_{\boldsymbol{dqz}} - \overline{\boldsymbol{W}}^{\boldsymbol{\Sigma}}_{\boldsymbol{dqz}} - T_i^{W^{\Sigma}} \boldsymbol{J}_{\boldsymbol{-2\omega}} \boldsymbol{\xi}^{\boldsymbol{W^{\Sigma}}}_{\boldsymbol{dqz}} \tag{3.19}$$

$$\boldsymbol{i}^{\boldsymbol{\Sigma *}}_{\boldsymbol{dqz,dc}} = \frac{1}{v_{dc}} \begin{bmatrix} 0 \\ 0 \\ \frac{P^*_{ac}}{3} \end{bmatrix} - \frac{1}{v_{dc}} \left(\boldsymbol{\xi}^{\boldsymbol{W^{\Sigma}}}_{\boldsymbol{dqz}} + K_p^{W^{\Sigma}} \left(\overline{\boldsymbol{W}}^{\boldsymbol{\Sigma *}}_{\boldsymbol{dqz}} - \overline{\boldsymbol{W}}^{\boldsymbol{\Sigma}}_{\boldsymbol{dqz}} \right) \right) \tag{3.20}$$

The three state variables for the PI controllers are given by $\boldsymbol{\xi}^{\boldsymbol{W^{\Sigma}}}_{\boldsymbol{dqz}} = [\xi_d^{W^{\Sigma}}\ \xi_q^{W^{\Sigma}}\ \xi_z^{W^{\Sigma}}]^{\top}$. The choice for the reference values $\overline{\boldsymbol{W}}^{\boldsymbol{\Sigma *}}_{\boldsymbol{dqz}} = [\overline{W}_d^{\Sigma *}\ \overline{W}_q^{\Sigma *}\ \overline{W}_z^{\Sigma *}]^{\top}$ is explained in the following section.

Energy "Σ" references in dqz frame

In abc frame it is a common practice to set equal energy references per-phase to ensure the horizontal balancing illustrated in Fig. 3.1c. However, in dqz frame the choice of the references may not be trivial. For clarifying this concept, a simple analysis is carried on. In Fig. 3.33, the three-phase measures of $\boldsymbol{W}^{\boldsymbol{\Sigma}}_{\boldsymbol{abc}}$ are filtered to obtain the variables $\overline{\boldsymbol{W}}^{\boldsymbol{\Sigma}}_{\boldsymbol{abc}}$. and the signals before, and after the filter are transformed into dqz variables with $\boldsymbol{P}_{\boldsymbol{-2\omega}}$.

For the sake of clarity, let us consider a generic three-phase signal $\boldsymbol{W}^{\boldsymbol{\Sigma}}_{\boldsymbol{abc}}$ oscillating at -2ω with negative sequence with amplitude $\hat{W}_j$ and phase α^{Σ}_W, and the DC component of each phase is equal to $W_{0,j}$. The expression of each component of $\boldsymbol{W}^{\boldsymbol{\Sigma}}_{\boldsymbol{abc}}$ can be expressed as in (3.21).

$$\begin{aligned} W^{\Sigma}_a &= W_{0,a} + \hat{W}_a \cos\left(-2\omega t + \alpha^{\Sigma}_W\right) \\ W^{\Sigma}_b &= W_{0,b} + \hat{W}_b \cos\left(-2\omega t - 2\pi/3 + \alpha^{\Sigma}_W\right) \\ W^{\Sigma}_c &= W_{0,c} + \hat{W}_c \cos\left(-2\omega t + 2\pi/3 + \alpha^{\Sigma}_W\right) \end{aligned} \tag{3.21}$$

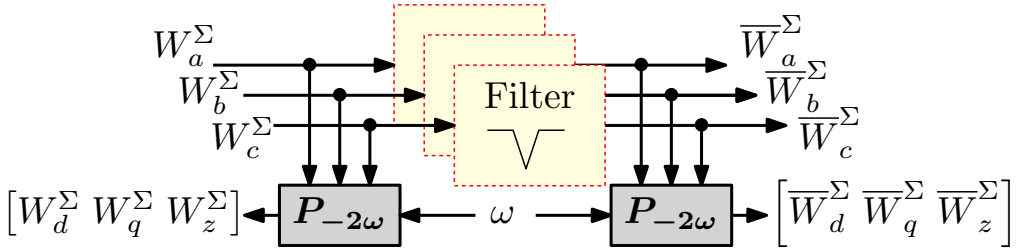

Figure 3.33 – Averaging filter on the measure of $\boldsymbol{W_{abc}^{\Sigma}}$

Assuming a perfect notch-filter, the filtered values of each W_j^Σ, namely $\overline{W}_j^\Sigma$, don't present any oscillations at the notch frequency (2ω for this case). The expressions of the energies post-filtered are then given by (3.22).

$$\begin{aligned}
\overline{W}_a^\Sigma &= W_{0,a} + \hat{W}_a \cancel{\cos\left(-2\omega t + \alpha_W^\Sigma\right)} = W_{0,a} \\
\overline{W}_b^\Sigma &= W_{0,b} + \hat{W}_b \cancel{\cos\left(-2\omega t - 2\pi/3 + \alpha_W^\Sigma\right)} = W_{0,b} \\
\overline{W}_c^\Sigma &= W_{0,c} + \hat{W}_c \cancel{\cos\left(-2\omega t + 2\pi/3 + \alpha_W^\Sigma\right)} = W_{0,c}
\end{aligned} \tag{3.22}$$

In fact, the energy controllers per-phase regulate the DC component of each energy by setting $\overline{W}_j^\Sigma$ to the DC reference value $W_{0,j}^*$. If equal level of energy is desired for each phase-leg, this is achieved by the selection of $W_{0,a}^* = W_{0,b}^* = W_{0,c}^* = W_0^*$.

Assuming equal amplitude of oscillations for the energy per-phase such that $\hat{W}_a = \hat{W}_a = \hat{W}_a = \hat{W}$, and also considering that the energy is equally split between the phase legs so $W_{0,a} = W_{0,b} = W_{0,c} = W_0^*$, after applying Park transformation at -2ω to $\boldsymbol{W_{abc}^{\Sigma}}$ from (3.21) yields:

$$\begin{aligned}
W_d^\Sigma &= +\hat{W}\cos\left(\alpha_W^\Sigma\right) \\
W_q^\Sigma &= -\hat{W}\sin\left(\alpha_W^\Sigma\right) \\
W_z^\Sigma &= W_0^*
\end{aligned} \tag{3.23}$$

As observed in (3.23), the dq components are constant values which depends on the amplitude $\hat{W}$ and phase α_W^Σ of the energy oscillating part. These variables are correlated to the operating point of the converter. Moreover, the z sequence is representing the energy level W_0^*. With the same assumptions, applying Park transformation at -2ω to $\overline{\boldsymbol{W}}_{\boldsymbol{abc}}^{\boldsymbol{\Sigma}}$ from (3.22) yields (3.24):

$$\begin{aligned}
\overline{W}_d^\Sigma &= 0 \\
\overline{W}_q^\Sigma &= 0 \\
\overline{W}_z^\Sigma &= W_0^*
\end{aligned} \tag{3.24}$$

As shown in (3.24), the dq components of the filtered energies "Σ" variables are zero. This means that the amplitude $\hat{W}$ and phase α_W^Σ are not being imposed by the controller: the information about the operating point of the converter has been filtered. For this reason, the energy references $\overline{W}_d^{\Sigma*}$ and $\overline{W}_q^{\Sigma*}$ are set to zero. The total stored energy is settled by the zero-sequence component $\overline{W}_z^\Sigma$. Finally, the structure of the energy Σ controller $\boldsymbol{W_{abc}^{\Sigma}}$ in SRRF is illustrated in Fig. 3.34.

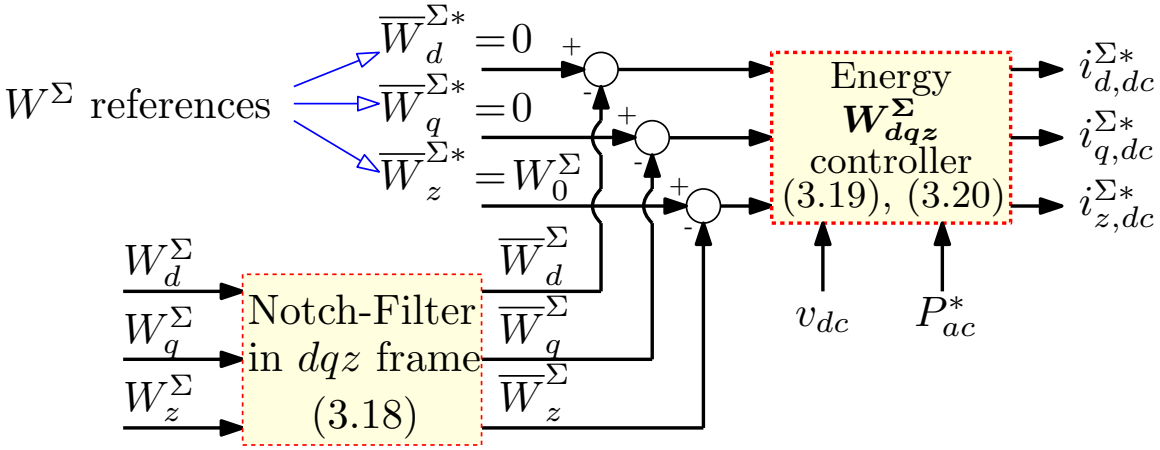

Figure 3.34 – Detail of the Energy Σ controller $\boldsymbol{W}_{\boldsymbol{dqz}}^{\boldsymbol{\Sigma}}$ in SRRF

3.4.4 Energy Δ controller reformulation

In this section, the controllers and the notch filter used in W^{Δ} controllers from Fig. 3.31 are expressed in dqZ frame (i.e. d, q, Z_d, Z_q) with the methodology explained in section G.2.

Averaging filter for energy "Δ" measures

The three-phase energy difference measures $\boldsymbol{W}_{\boldsymbol{abc}}^{\boldsymbol{\Delta}} = [W_a^{\Delta}\ W_b^{\Delta}\ W_c^{\Delta}]^{\top}$ are filtered with a notch filter tuned at ω, obtaining $\overline{\boldsymbol{W}}_{\boldsymbol{abc}}^{\boldsymbol{\Delta}} = [\overline{W}_a^{\Delta}\ \overline{W}_b^{\Delta}\ \overline{W}_c^{\Delta}]^{\top}$, before sending the signals to the PI controllers in abc frame as shown in Fig. 3.31 [**159**]. Prior to the transcription of the abc controller into the SRRF dqz, it is first needed to express the abc signals as a function of their dqz components by means of the inverse Park transformation. As for the other "Δ" variables studied in Chapter 2, the zero-sequence of the energy difference is not represented by a SSTI variable: it oscillates at 3ω [165]. For overcoming this issue, the same approach is followed as for the zero-sequence arm capacitor voltage difference, i.e. v_{Cz}^{Δ}, which was solved by the separation of the variable into two SSTI state variables in the axes Z_d and Z_q. Taking this into account, the zero-sequence of the energy difference is expressed similarly as used in (2.36), by means of the virtual variables $W_{Z_d}^{\Delta}$ and $W_{Z_q}^{\Delta}$. Finally, the expressions of the "Δ" energies as a function of their dqZ components is given by (3.25) and (3.26) for $\boldsymbol{W}_{\boldsymbol{abc}}^{\boldsymbol{\Delta}}$ and $\overline{\boldsymbol{W}}_{\boldsymbol{abc}}^{\boldsymbol{\Delta}}$ respectively.

$$\boldsymbol{W}_{\boldsymbol{abc}}^{\boldsymbol{\Delta}} = \boldsymbol{P}_{\boldsymbol{\omega}}^{-\mathbf{1}} \left[W_d^{\Delta}\ W_q^{\Delta}\ W_{Z_d}^{\Delta} \cos(3\omega t) + W_{Z_q}^{\Delta} \sin(3\omega t) \right]^{\top} \tag{3.25}$$

$$\overline{\boldsymbol{W}}_{\boldsymbol{abc}}^{\boldsymbol{\Delta}} = \boldsymbol{P}_{\boldsymbol{\omega}}^{-\mathbf{1}} \left[\overline{W}_d^{\Delta}\ \overline{W}_q^{\Delta}\ \overline{W}_{Z_d}^{\Delta} \cos(3\omega t) + \overline{W}_{Z_q}^{\Delta} \sin(3\omega t) \right]^{\top} \tag{3.26}$$

For referring the notch-filter from abc to dqZ frame, the methodology described in Appendix G.2.2 is followed. However, since in this case the zero-sequence is represented by 2 state variables, the same approach as used in Section 2.4.1 is followed. Then, the notch filter tuned at ω with damping ratio $\zeta = 0.7$ of $\boldsymbol{W}_{\boldsymbol{dqZ}}^{\boldsymbol{\Delta}}$ in dqZ frame is expressed as in (3.27).

$$\frac{d\boldsymbol{F}_{\mathbf{1}\boldsymbol{dqZ}}^{\boldsymbol{\Delta}}}{dt} = \boldsymbol{F}_{\mathbf{2}\boldsymbol{dqZ}}^{\boldsymbol{\Delta}} - \boldsymbol{J_G} \boldsymbol{F}_{\mathbf{1}\boldsymbol{dqZ}}^{\boldsymbol{\Delta}} - 2\zeta\omega \left(\boldsymbol{W}_{\boldsymbol{dqZ}}^{\boldsymbol{\Delta}} + \boldsymbol{F}_{\mathbf{1}\boldsymbol{dqZ}}^{\boldsymbol{\Delta}} \right) \tag{3.27a}$$

$$\frac{d\boldsymbol{F}_{\mathbf{2}\boldsymbol{dqZ}}^{\boldsymbol{\Delta}}}{dt} = -\omega^2 \boldsymbol{F}_{\mathbf{1}\boldsymbol{dqZ}}^{\boldsymbol{\Delta}} - \boldsymbol{J_G} \boldsymbol{F}_{\mathbf{2}\boldsymbol{dqZ}}^{\boldsymbol{\Delta}} \tag{3.27b}$$

$$\overline{\boldsymbol{W}}_{\boldsymbol{dqZ}}^{\boldsymbol{\Delta}} = \boldsymbol{W}_{\boldsymbol{dqZ}}^{\boldsymbol{\Delta}} + \boldsymbol{F}_{\mathbf{1}\boldsymbol{dqZ}}^{\boldsymbol{\Delta}} \tag{3.27c}$$

where $\boldsymbol{J_G}$ was defined in (2.40). The state variables of the second-order filter in dqZ frame are expressed in $\boldsymbol{F^{\Delta}_{1dqz}} = [F^{\Delta}_{1d}\ F^{\Delta}_{1q}\ F^{\Delta}_{1Z_d}\ F^{\Delta}_{1Z_q}]^{\top}$ and $\boldsymbol{F^{\Delta}_{2dqz}} = [F^{\Delta}_{2d}\ F^{\Delta}_{2q}\ F^{\Delta}_{2Z_d}\ F^{\Delta}_{2Z_q}]^{\top}$.

PI controller for energy "Δ"

Finally, the PI controller from Fig. 3.31 is now referred to the dqZ axes (i.e. d, q, Z_d, Z_q). The same procedure as before is used on the zero-sequence component, where the four states of the integral part of the PI controller are given by (3.28):

$$\boldsymbol{\xi^{W^{\Delta}}_{dqZ}} = \left[\xi^{W^{\Delta}}_{d}\ \xi^{W^{\Delta}}_{q}\ \xi^{W^{\Delta}}_{Z_d}\ \xi^{W^{\Delta}}_{Z_q}\right]^{\top} \tag{3.28}$$

The four differential equations of the integral part of the PI controller is given in (3.29).

$$T_i^{W^{\Delta}} \frac{d\boldsymbol{\xi^{W^{\Delta}}_{dqZ}}}{dt} = \overline{\boldsymbol{W}}^{\boldsymbol{\Delta *}}_{\boldsymbol{dqZ}} - \overline{\boldsymbol{W}}^{\boldsymbol{\Delta}}_{\boldsymbol{dqZ}} - T_i^{W^{\Delta}} \boldsymbol{J_G} \boldsymbol{\xi^{W^{\Delta}}_{dqZ}} \tag{3.29}$$

Then, the output of the PI controller is obtained applying the Park transformation at ω and 3ω to the control law from Fig. 3.31, which yields (3.30):

$$\boldsymbol{I^{\Sigma *}_{dqZ,ac}} = -\frac{1}{V^G}\left(\boldsymbol{\xi^{W^{\Delta}}_{dqZ}} + K_p^{W^{\Delta}}\left(\overline{\boldsymbol{W}}^{\boldsymbol{\Delta *}}_{\boldsymbol{dqZ}} - \overline{\boldsymbol{W}}^{\boldsymbol{\Delta}}_{\boldsymbol{dqZ}}\right)\right) \tag{3.30}$$

For multiplying the output of the energy-difference controller by the matrix $\boldsymbol{R}$ and $\boldsymbol{K}$ defined in (3.15) and (3.16) respectively, it is necessary to obtain the three-phase vector $\boldsymbol{I^{\Sigma *}_{abc,ac}}$ as a function of the components dqZ, which is obtained as:

$$\boldsymbol{I^{\Sigma *}_{abc,ac}} = \boldsymbol{P^{-1}_{\omega}} \begin{bmatrix} I^{\Sigma *}_{d,ac} \\ I^{\Sigma *}_{q,ac} \\ I^{\Sigma *}_{Zd,ac}\cos(3\omega t) + I^{\Sigma *}_{Zq,ac}\sin(3\omega t) \end{bmatrix} \tag{3.31}$$

Note that the inverse Park transformation in Fig. 3.31 has a frequency of ω and not 2ω as the other "Σ" variables. The reason is that the frequency of the "ac" component of the current i^{Σ} reference used for balancing the W^{Δ} is ω.

Finally, for obtaining the common-mode currents reference in dqz frame, the Park transformation at 2ω is applied to the controllers output from Fig. 3.31. The results are shown in (3.32) where the 6$^{\text{th}}$ harmonic has been neglected.

$$\boldsymbol{P_{-2\omega}} \boldsymbol{i^{\Sigma *'}_{abc,ac}} = \boldsymbol{P_{-2\omega}}\left(\boldsymbol{K R I^{\Sigma *}_{abc,ac}}\right) \tag{3.32a}$$

$$\boldsymbol{i^{\Sigma *'}_{dqz,ac}} = \frac{3}{2\sqrt{2}} \begin{bmatrix} I^{\Sigma *}_{d,ac} + I^{\Sigma *}_{Zd,ac} \\ I^{\Sigma *}_{q,ac} + I^{\Sigma *}_{Zq,ac} \\ 0 \end{bmatrix} \tag{3.32b}$$

Finally, the structure of the energy Δ controller $\boldsymbol{W^{\Delta}_{abc}}$ in SRRF is illustrated in Fig. 3.35, where it can be seen that the filtered energy references are set all to zero. This choice guarantees equal energy distribution between upper and lower arms per-phase of the MMC.

3.4.5 Complete control structure

The complete control structure represented in dqz coordinates is summarized in Fig. 3.36. The modulation indices calculation ($\boldsymbol{m^{\Delta}_{dq}}$ and $\boldsymbol{m^{\Sigma}_{dqz}}$) is performed with the CM from (3.13). The common-mode current controllers for $\boldsymbol{i^{\Sigma}_{dqz}}$ is obtained from Fig. G.3 with $n = -2\omega$. The

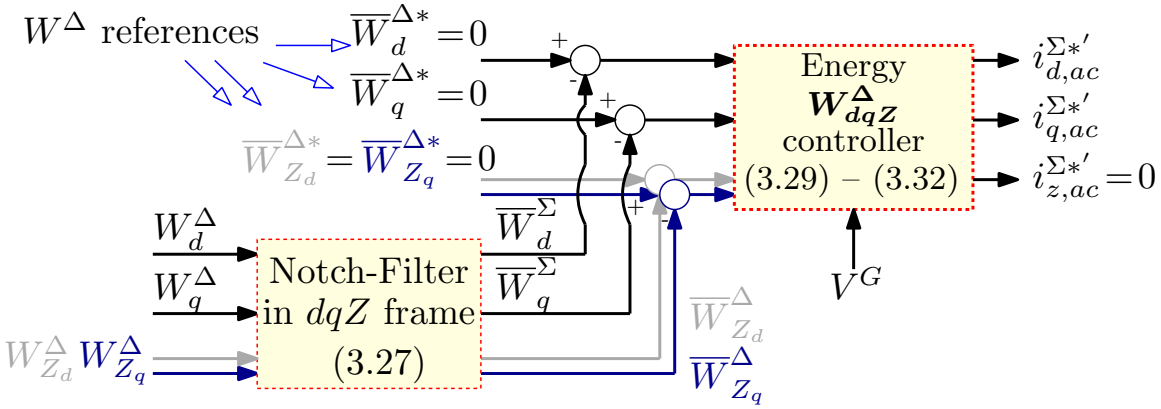

Figure 3.35 – Detail of the Energy Δ controller $\boldsymbol{W}_{\boldsymbol{dqZ}}^{\boldsymbol{\Delta}}$ in SRRF

current and energy control loops sum and difference are tuned for a response time of 5 ms, 50 ms and 100 ms respectively.

This controller resulted from the transcription of the scheme from Fig. 3.29 to dqz frame. It is important to note that this formulation highlights the decoupling of the z-sequence of the energy sum W_z^{Σ} (proportional to the total stored energy) and the common-mode current i_z^{Σ} (proportional to the DC current). This characteristic is explored in Chapter 4.

3.4.6 Model linearization and time domain validation

In a similar way as in Section 3.3.2, the system comprising the non-linear SSTI model from Fig. 3.3 and the controller from Fig. 3.36 are connected as shown in Fig. 3.37. The system states are gathered in (3.33), while the inputs in (3.34).

$$\boldsymbol{x_{W\#2}} = [\underbrace{\boldsymbol{i_{dq}^{\Delta}};\ \boldsymbol{i_{dqz}^{\Sigma}};\ \boldsymbol{v_{Cdqz}^{\Sigma}};\ \boldsymbol{v_{CdqZ}^{\Delta}};\ v_{dc};}_{\textbf{Phys.}}\ \ldots \tag{3.33}$$

$$\ldots \underbrace{\boldsymbol{F_{1dqz}^{\Sigma}};\ \boldsymbol{F_{2dqz}^{\Sigma}};\ \boldsymbol{\xi_{W_{dqz}^{\Sigma}}};\ \boldsymbol{\xi_{i_{dqz}^{\Sigma}}};\ \boldsymbol{\xi_{i_{dq}^{\Delta}}};\ \boldsymbol{F_{1dqZ}^{\Delta}};\ \boldsymbol{F_{2dqZ}^{\Delta}};\ \boldsymbol{\xi_{W_{dqZ}^{\Delta}}}}_{\textbf{Control}}]^{\top} \in \mathbb{R}^{39}$$

$$\boldsymbol{u_{W\#2}} = [\underbrace{v_{dc}^{*}\ P_{ac0}^{*}\ Q_{ac}^{*}\ \overline{\boldsymbol{W}}_{\boldsymbol{dqz}}^{\boldsymbol{\Sigma *}}\ \overline{\boldsymbol{W}}_{\boldsymbol{dqZ}}^{\boldsymbol{\Delta *}}}_{\text{Controllers}}\ \underbrace{v_d^G\ v_q^G}_{\text{AC grid}}\ \underbrace{P_l^{*}}_{\text{DC grid}}\ ]^{\top} \in \mathbb{R}^{13} \tag{3.34}$$

Once the SSTI model from Fig. 3.37 is linearized to obtain the LTI version of the model, a new time domain simulation is performed. For validating the controller, the linear model is not mandatory, but it is useful to perform stability analysis. Starting with a DC power transfer of 1 pu, an step of -0.1 pu is applied at $t = 0.05$ s. The simulation results are depicted in Fig. 3.38.

As shown in Figs. 3.38c and 3.38d, the energies related with the arm voltages oscillations are well controlled during the transient. This can be seen in the results in abc frame in Fig. 3.38h. The total stored energy W_z^{Σ} in Fig. 3.38e is maintained in the nominal value as well. The zero sequence W_z^{Δ} results is shown in Fig. 3.38f, which is post-processed with $W_z^{\Delta} = W_{Z_d}^{\Delta}\cos(3\omega t) + W_{Z_q}^{\Delta}\sin(3\omega t)$ for the LTI model. Finally, the modulation indices of the modulation indices $\boldsymbol{m_{dqz}^{\Delta}}$ are shown in Fig. 3.38g, where it can be seen that the zero-sequence m_z^{Δ} is not zero during the simulation due to the CM method.

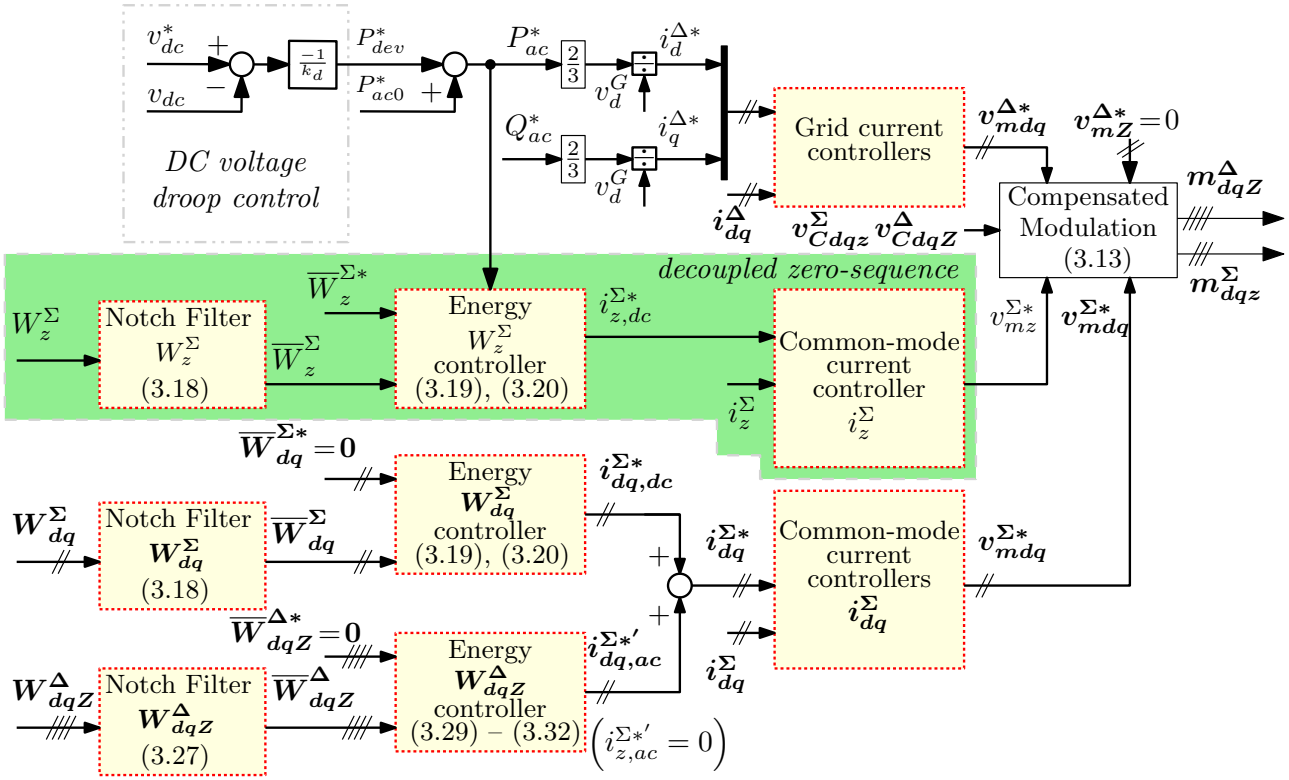

Figure 3.36 – Complete structure *Energy-based* control# 2 in SRRFs — Mathematical equivalence of Fig. 3.29.

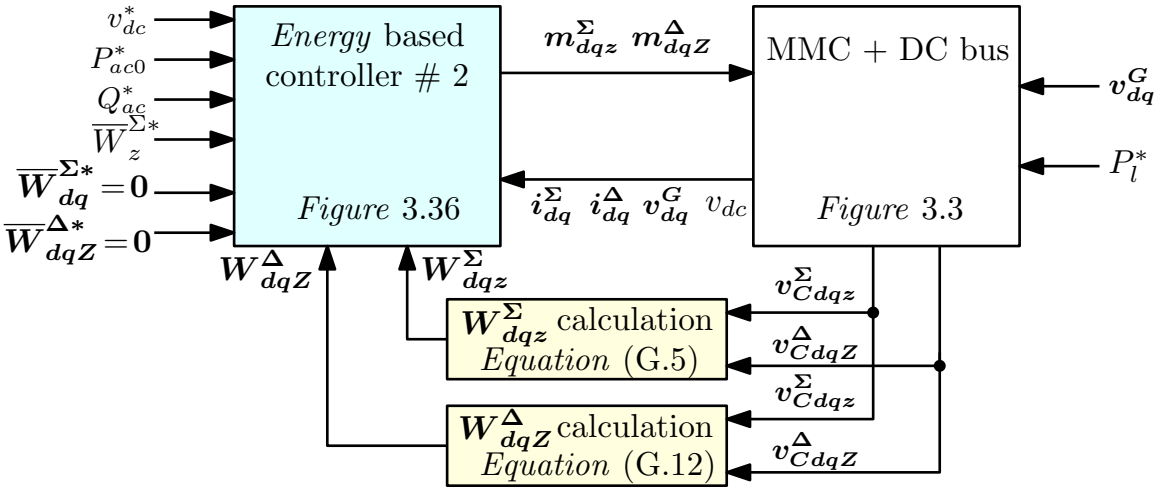

Figure 3.37 – SSTI model of MMC, DC bus and *Energy-based* controller # 2 — Energies calculations $\boldsymbol{W}^{\boldsymbol{\Sigma}}_{\boldsymbol{dqz}}$ and $\boldsymbol{W}^{\boldsymbol{\Delta}}_{\boldsymbol{dqZ}}$ are given in Appendix G.1

It is important to note that the LTI model clearly reproduced the dynamics of the complete system. For this reason, the eigenvalues can be calculated to study the full order EMT model. In Fig. 3.39 it is shown the results of a parametric sweep of the DC capacitor H_{dc} in Fig. 3.39a, and for the droop parameter k_d in Fig. 3.39b.

As seen in the eigenvalues results from Fig. 3.39, the system is stable for the considered parameters, while guaranteeing an accurate decoupling of AC active and reactive power is achieved thanks to the CM. These results validate the approach followed for the *Energy-based* controller # 2 from this Chapter.

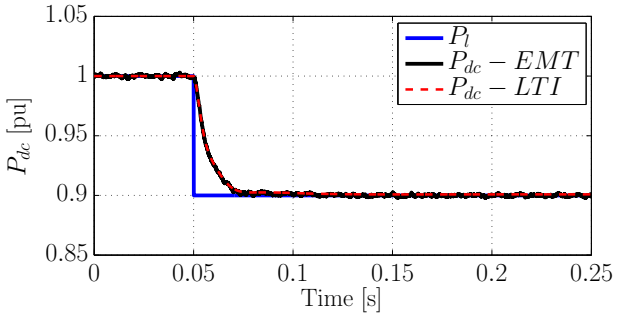

(a) P_{dc}[pu]

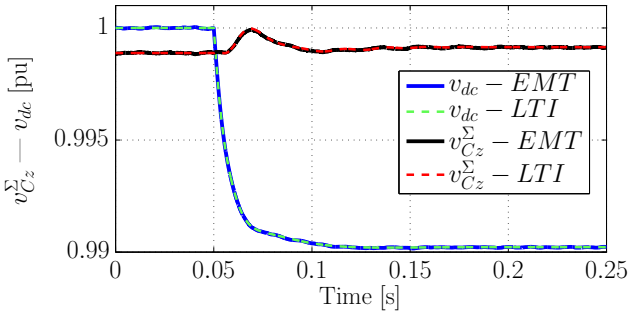

(b) v_{dc} and v_{Cz}^{Σ}[pu]

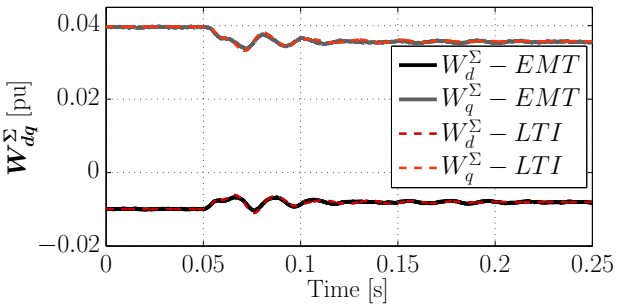

(c) $\boldsymbol{W_{dq}^{\Sigma}}$[pu]

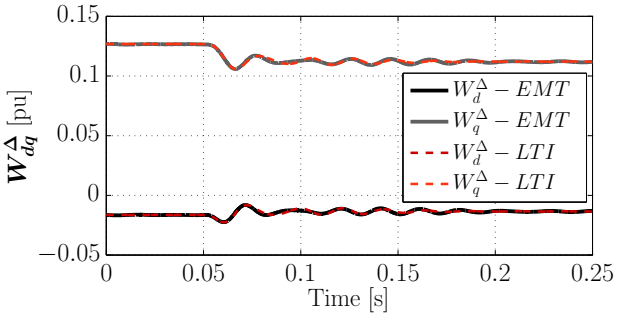

(d) $\boldsymbol{W_{dq}^{\Delta}}$[pu]

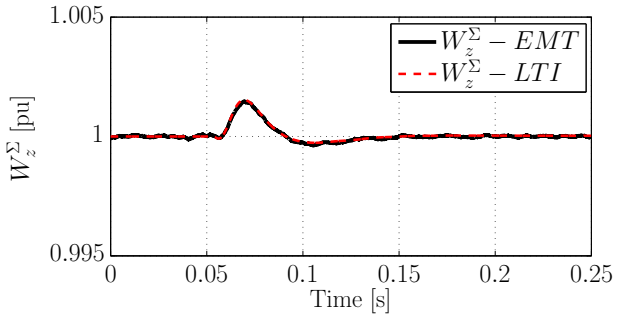

(e) W_z^{Σ}[pu]

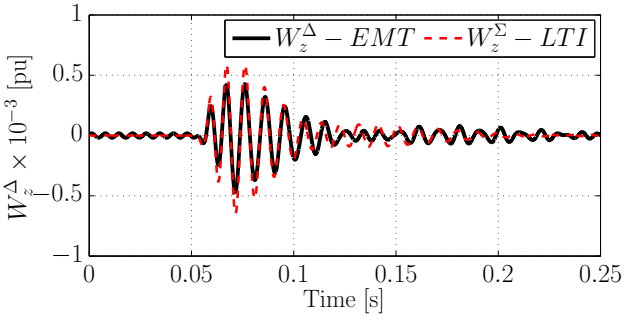

(f) W_z^{Δ}[pu]

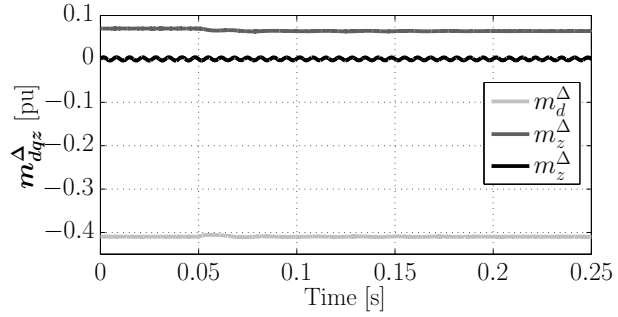

(g) $\boldsymbol{m_{dqz}^{\Delta}}$[pu] (EMT Only)

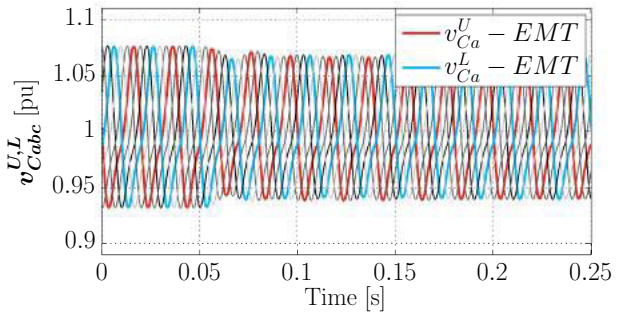

(h) $\boldsymbol{v_{Cabc}^{U,L}}$[pu] (EMT Only)

Figure 3.38 – Time domain validation *Energy-based # 2* controller – Step applied on P_l of 0.1 pu – *EMT*: EMTP-RV simulation with detailed converter, *LTI*: Linear time-invariant state-space model in Simulink

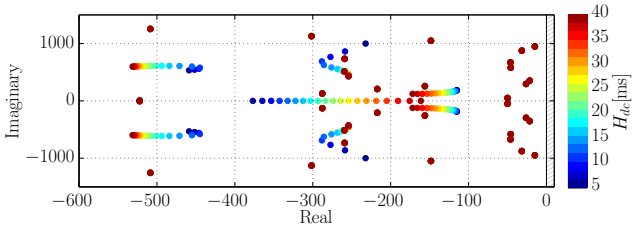

(a) Influence of DC capacitor H_{dc} — $k_d = 0.1$ pu

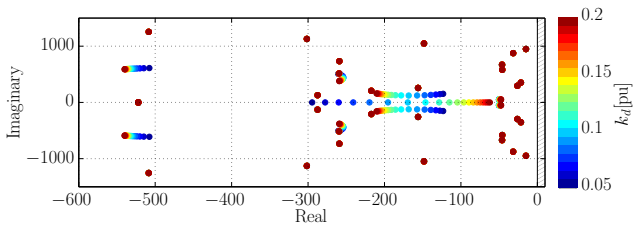

(b) Influence of droop gain k_d — $H_{dc} = 40$ ms

Figure 3.39 – Parametric sweeps for *Energy-based control # 2* — $v_{dc0} = 1$ pu, $P_{dc0} = -1$ pu, $k_d = 0.1$ pu — Power flow: DC $\Leftarrow$ AC

3.5 Chapter Conclusions

This Chapter dealt with the MMC control strategies for its integration in MTDC grids. For this reason, a variable DC bus voltage and the proportional droop-controller is considered. Two main control strategies of the MMC were detailed. First, the *Classical CCSC* controller was presented, which is widely adopted in the literature. This classical controller is interesting since its implementation is rather simple. However, by the analysis of the linearized model of the MMC and the *Classical CCSC* strategy, it is demonstrated that this method may fail to guarantee stable operation for several situations. The reason is that the DC current is left uncontrolled, so the risk of interactions with the DC grid could be problematic. Nevertheless, this strategy is still considered in the rest of this Thesis due to its popularity.

As an improvement of the *Classical CCSC* strategy, the *Energy-based* control approach is introduced. The first variant (*Energy-based* control # 1) results from a basic modification of the *Classical CCSC* approach by the addition of the DC current controller. For generating the reference for the DC current, an energy controller is designed. It is based on the possibility that the MMC provides to control the AC and DC powers independently. Even if this strategy showed good results, the existing coupling between the AC and DC sides does not allow a fully independent control for the AC active and reactive powers. For solving this issue, the Compensated Modulation is introduced. However, the *Energy-based* control # 1 with CM fails to guarantee the stability of the internal variables of the MMC. For this reason, the *Energy-based* control # 2 is introduced. The novelty from this Chapter is the mathematical transformation of the control equations from *abc* to *dqz* frame to adapt the controller for being used with the complete SSTI model from Chapter 2. Finally, this controller is validated in time domain simulations, and the eigenvalue analysis showed that the stability characteristics from *Energy-based* control # 1 are maintained, while guaranteeing an independent control of the AC active and reactive powers.

Since the MMC and the *Energy-based* control # 2 have 39 state variables, the high number of eigenvalues for one single converter results in difficult analysis of the LTI model. When considering an MTDC system, where several MMCs are connected to the same grid, the number of eigenvalues grows rapidly, making the analysis a very complex task. For this reason, the simplified models are mandatory for the study of large systems, as long as the simplified models reproduce accurately the AC and DC interactions of the converter and controller.

Chapter 4

On the application of SSTI-MMC reduced order models for interfacing AC and DC grids

4.1 Introduction

In the previous Chapter, a very detailed model of the MMC associated to different types of controllers have been developed. It allows carrying on very accurate studies but may be too complex to be integrated in large-scale systems like MTDC grids or large AC systems including HVDC links [171]. For this reason, the availability of open and generic models is important when performing system studies specially for operation and stability analysis [172]. Many techniques for model order reduction were already successfully applied on the AC systems, however the fast and coupled dynamics of DC grids complicates this task [173].

When considering the MMC, the development of reduced order models depends on the applied control system on the real converter. As it was stated in Chapter 3, there are many control techniques available in the literature [137]. Two main strategies arise between the vast options: the *Classical CCSC* and the *Energy-based* control. This Chapter focuses on the validity of the simplified reduced order models of the MMC when considering each of these two control strategies.

The methodology applied in this Chapter is depicted in Fig. 4.1. Starting with the complete Steady-State Time-Invariant (SSTI) MMC model interfacing simplified AC and DC grids (Full order model), some physical assumptions are made to derive the reduced order model presented in **[123]** (Reduced order model); this is performed in Section 4.2. Once the reduced model is obtained, the applied methodology deals with the comparison of the small-signal dynamics of the MMC model that results when considering the *Energy-based* control with Compensated Modulation (CM) from Section 3.4, or the *Classical CCSC* from Section 3.2. For the comparison tests between the linearized models, there are endless possibilities to consider but in this Chapter only some of the most representative examples are carried on.

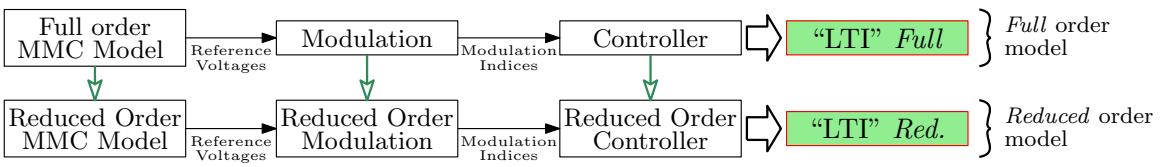

Figure 4.1 – Comparisons of SSTI-MMC models

The rest of this Chapter is organized as follows. In Section 4.2, the physical system used as a benchmark for comparing the full order and reduced models is presented. In Section 4.3, the *Energy-based* control is assumed for the complete model. The full and reduced order models are linearized and validated trough time domain simulations, comparing them against a detailed EMT *Simulation model*. Then, further analysis is carried on with the comparison of the resulting LTI models. In Section 4.4, a similar work is done but considering the *Classical CCSC* for the complete MMC. In Section 4.5 an analysis based on the frequency response of the obtained LTI models is performed. Finally, the Chapter conclusions are stated in Section 4.6.

4.2 MMC model with AC and DC side connections

4.2.1 System description

The comparison methodology is based on the small-signal analysis of the schematic shown in Fig. 4.2, where two different VSC-MMC models are considered. For this task, it is assumed that the MMC is connected to an equivalent AC grid modeled by a voltage source in series with an inductance. Contrary to the previous studies, the AC system is not considered as infinite anymore and the Short Circuit Ratio (SCR) will be taken into account in this Chapter. The DC side is the same as the one already introduced in Chapter 3, and the dynamics of v_{dc} were given in (3.1). The consideration of a simplified AC grid model allows to compare the interactions of the MMC with the AC and DC sides at the same time with the different reduced order models.

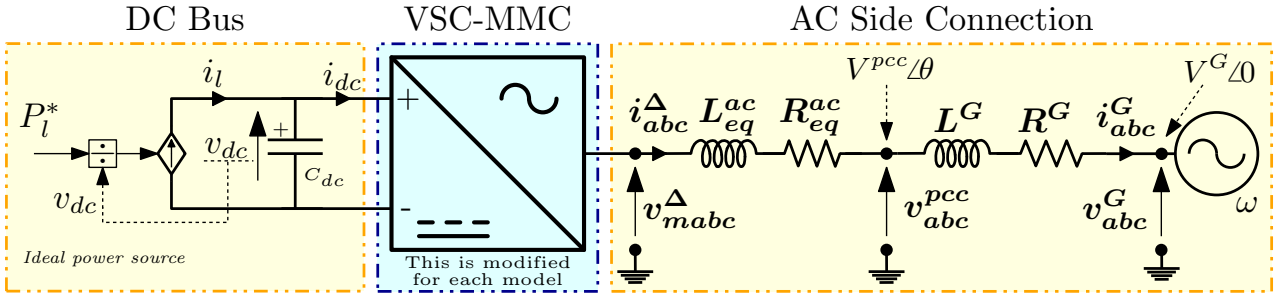

Figure 4.2 – MMC Connected to AC and DC equivalent grids

AC Side Connection

In case of classical *2-level* VSCs there is a bulky passive capacitive filter at the Point of Common Coupling in the AC side (PCC-AC), but in case of the MMC this filter is nonexistent due to the low harmonic content on the AC output voltage $\boldsymbol{v^{\Delta}_{mabc}}$, especially when a high number of levels is considered (more than 100) [174]. As it can be observed in the system from Fig. 4.2, the AC side connection is modeled with two "RL" circuits connected in series: $R^{ac}_{eq}L^{ac}_{eq}$ and R^GL^G, so the current is the same for both circuits (i.e. $\boldsymbol{i^{\Delta}_{abc}} = \boldsymbol{i^G_{abc}}$). The relation of the parameters R^G and L^G with the SCR is recalled in the Appendix A. The AC current dynamics are modeled as in (4.1):

$$\left(L^{ac}_{eq} + L^G\right)\frac{d\boldsymbol{i^{\Delta}_{dqz}}}{dt} = \boldsymbol{v^{\Delta}_{mdqz}} - \boldsymbol{v^G_{dqz}} - \left(R^{ac}_{eq} + R^G\right)\boldsymbol{i^{\Delta}_{dqz}} - \left(L^{ac}_{eq} + L^G\right)\boldsymbol{J_\omega i^{\Delta}_{dqz}} \tag{4.1}$$

where $\boldsymbol{v^G_{dqz}} = [v^G_d,\ v^G_q,\ 0]^\top$ and $\boldsymbol{v^{\Delta}_{mdqz}}$ is the AC-side modulated voltage of the MMC in dqz frame. Since there is no closed-loop circuit for the current i^{Δ}_z to flow, it is neglected.

The voltage at the PCC-AC is measured between the two "RL" circuits from Fig. 4.2, i.e. v_{pcc}. This voltage is not modeled as a dynamic state, so an algebraic equation is used instead [81, 175]. The expression of the voltage at the PCC-AC (i.e. $\boldsymbol{v}_{\boldsymbol{abc}}^{\boldsymbol{pcc}}$ transformed into $\boldsymbol{v}_{\boldsymbol{dq}}^{\boldsymbol{pcc}} \stackrel{\text{def}}{=} [v_d^{pcc} \; v_q^{pcc}]^\top$) is calculated as a function of the MMC output voltage $\boldsymbol{v}_{\boldsymbol{mdq}}^{\boldsymbol{\Delta}}$, the grid voltage $\boldsymbol{v}_{\boldsymbol{dq}}^{\boldsymbol{G}}$, and the current $\boldsymbol{i}_{\boldsymbol{dq}}^{\boldsymbol{\Delta}}$ as shown in (4.2):

$$v_d^{pcc} = \left(\frac{L_{eq}^{ac}}{L_{eq}^{ac}+L^G}\right) v_d^G + \left(\frac{R^G L_{eq}^{ac} - R_{eq}^{ac} L^G}{L_{eq}^{ac}+L^G}\right) i_d^{\Delta} + \left(\frac{L^G}{L_{eq}^{ac}+L^G}\right) v_{md}^{\Delta} \tag{4.2a}$$

$$v_q^{pcc} = \left(\frac{L_{eq}^{ac}}{L_{eq}^{ac}+L^G}\right) v_q^G + \left(\frac{R^G L_{eq}^{ac} - R_{eq}^{ac} L^G}{L_{eq}^{ac}+L^G}\right) i_q^{\Delta} + \left(\frac{L^G}{L_{eq}^{ac}+L^G}\right) v_{mq}^{\Delta} \tag{4.2b}$$

Reference SSTI-MMC model

Since this Chapter deals with the fidelity of the SSTI model order reduction, the model used as a reference is based on the model developed in Chapter 2. The block diagram of the reference SSTI-MMC model is shown in Fig. 4.3, where it can be seen that the AC side connection and DC bus are considered as "outside" the MMC model.

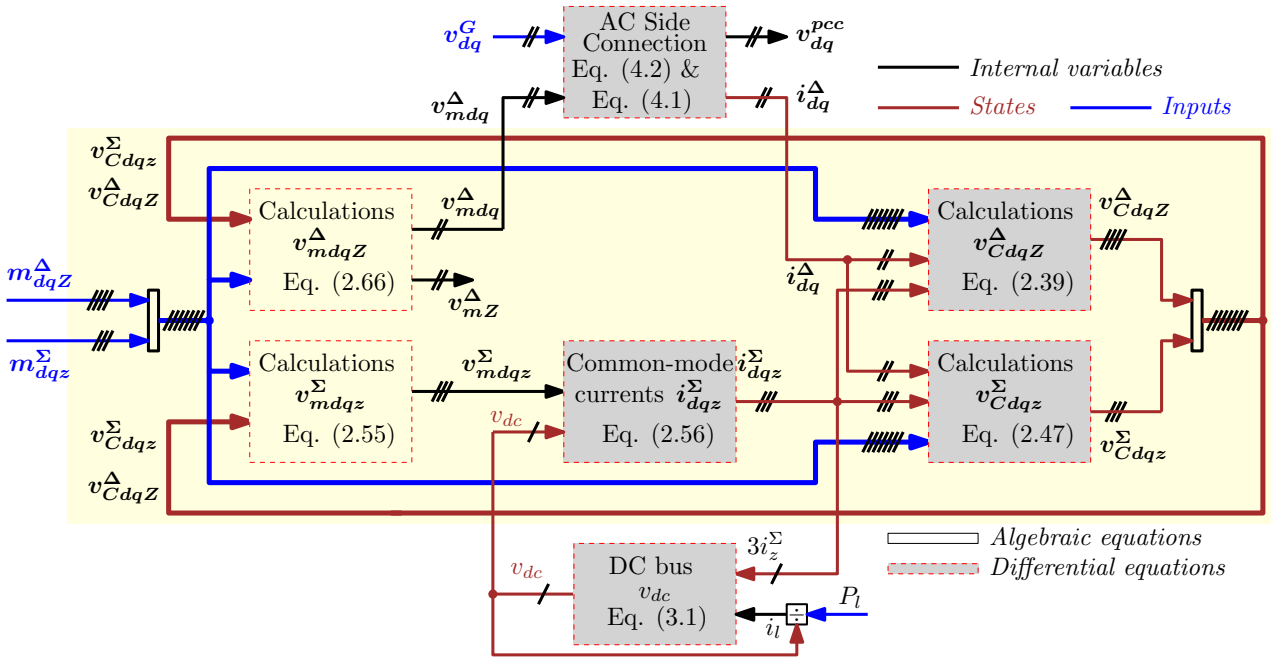

Figure 4.3 – MMC with SSTI Solution: Reference Model in this Chapter

The following subsection derives a reduced order model, using Fig. 4.3 as a starting point.

4.2.2 Reduced order model

A reduced order model can be obtained by performing some assumptions from a functional point of view [79]. In the following, results from the findings in **[123]** are summarized. In Fig. 4.4, the steady-state results in dqz of an EMT simulation considering the complete MMC with *Classical CCSC* transmitting 1 pu of active power are shown. The "Σ" currents are shown in Fig. 4.4a and, as expected, the circulating currents $\boldsymbol{i}_{\boldsymbol{dq}}^{\boldsymbol{\Sigma}}$ are almost zero during the steady-state due to the CCSC, while the DC current (which is proportional to z component) is near 1 pu. Even if the MMC equations in dqz frame developed in Chapter 2 showed that

there is a complex coupling between the circulating currents (mostly in the modulated voltages "Σ"), the MMC controller will always guarantee that the circulating currents are suppressed. This means that the currents $\boldsymbol{i}_{\boldsymbol{dq}}^{\boldsymbol{\Sigma}}$ may be omitted for the development of a reduced order model of the MMC. However, since the DC current is responsible for the exchange of active power with the DC side, this current must be taken into account (i.e. i_z^{Σ}).

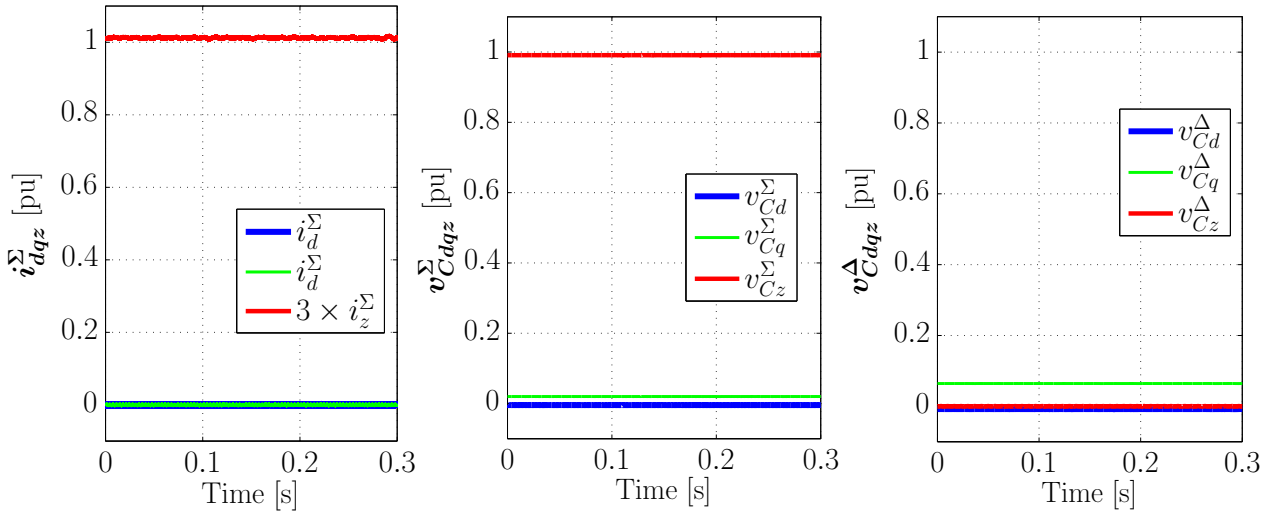

(a) $\boldsymbol{i}_{\boldsymbol{dq}}^{\boldsymbol{\Sigma}}$ and i_{dc} (b) $\boldsymbol{v}_{\boldsymbol{Cdq}}^{\boldsymbol{\Sigma}}$ and v_{Cz}^{Σ} (c) $\boldsymbol{v}_{\boldsymbol{Cdqz}}^{\boldsymbol{\Delta}}$

Figure 4.4 – Steady-State results of EMT model for justification on the selected variables for the reduced-order model

As discussed in Chapter 2, the arm capacitor voltages "Σ" in *abc* frame are composed by a DC component with superposed oscillations. The DC value corresponds to the average level of energy stored on phase leg of the converter station; this information is reflected[1] in the variable v_{Cz}^{Σ}. The oscillations around the DC value in *abc*, which are much lower in magnitude than the DC component, are transferred to the *dq* variables $\boldsymbol{v}_{\boldsymbol{Cdq}}^{\boldsymbol{\Sigma}}$. For this reason, the voltage v_{Cz}^{Σ} takes values around 1 pu while the *dq* components are near zero as shown in Fig. 4.4b. Since the z component takes much more important values than the *dq* components, $\boldsymbol{v}_{\boldsymbol{Cdq}}^{\boldsymbol{\Sigma}}$ may be neglected while keeping the state variable v_{Cz}^{Σ}.

In normal operation, the MMC controller guarantees that the energy stored in the upper and lower arms for each phase are equal in average (with or without an exclusive controller for this task). This is manifested in the arm capacitor voltages "Δ" in *abc* frame as oscillating variables around zero. Once they are reflected in *dqz* frame, the variables $\boldsymbol{v}_{\boldsymbol{Cdqz}}^{\boldsymbol{\Delta}}$ are not so important in terms of numerical value, as shown in Fig. 4.4c. For this reason, the voltages $\boldsymbol{v}_{\boldsymbol{Cdqz}}^{\boldsymbol{\Delta}}$ may be neglected for the development of a reduced order model.

Summarizing, the model simplification is performed by neglecting the *dq* components of v_C^{Σ} and i^{Σ}; and also neglecting the v_C^{Δ} variables, as described in Table 4.1 (i.e. from the internal variables, only the state variable v_{Cz}^{Σ} and i_z^{Σ} are kept).

If the MMC state variables $\boldsymbol{i}_{\boldsymbol{dq}}^{\boldsymbol{\Sigma}}$, $\boldsymbol{v}_{\boldsymbol{Cdq}}^{\boldsymbol{\Sigma}}$ and $\boldsymbol{v}_{\boldsymbol{Cdqz}}^{\boldsymbol{\Delta}}$ are neglected, the mathematical equations of the MMC in *dqz* from Chapter 2 are highly simplified. For instance, since the circulating currents $\boldsymbol{i}_{\boldsymbol{dq}}^{\boldsymbol{\Sigma}}$ are neglected, the zero-sequence component v_{Cz}^{Σ} can be re-written as in (4.3), where

[1]Partially, since the expression of the energies in *dqz* frame are also coupled between the three components, so it is not possible to affirm, a priori, that v_{Cz}^{Σ} includes all the information about the stored energy. See Appendix B.

Table 4.1 – MMC state variables in dqz frame to keep or neglect

State Variables	Description & Comment	Keep?
$\boldsymbol{i^{\Delta}_{dq}}$	AC grids currents in dqz frame	**YES**
$\boldsymbol{i^{\Sigma}_{dq}}$	Internal circulating currents	**NO**
i^{Σ}_{z}	Proportional to DC output current	**YES**
$\boldsymbol{v^{\Sigma}_{Cdq}}$	Information of the oscillations of v^{Σ}_{C}	**NO**
v^{Σ}_{Cz}	Sum of all arm capacitor voltages	**YES**
$\boldsymbol{v^{\Delta}_{Cdqz}}$	Arm capacitor voltage difference	**NO**

(4.3a) corresponds to the expression of (2.47) for the z axis.

$$C_{arm}\frac{dv^{\Sigma}_{Cz}}{dt} = \frac{1}{8}\left(m^{\Delta}_{d}i^{\Delta}_{d} + m^{\Delta}_{q}i^{\Delta}_{q}\right) + \frac{1}{4}\left(m^{\Sigma}_{d}\cancel{i^{\Sigma}_{d}} + m^{\Sigma}_{q}\cancel{i^{\Sigma}_{q}} + 2m^{\Sigma}_{z}i^{\Sigma}_{z}\right) \tag{4.3a}$$

$$C_{arm}\frac{dv^{\Sigma}_{Cz}}{dt} = \frac{1}{8}\left(m^{\Delta}_{d}i^{\Delta}_{d} + m^{\Delta}_{q}i^{\Delta}_{q}\right) + \frac{1}{2}m^{\Sigma}_{z}i^{\Sigma}_{z} \tag{4.3b}$$

The zero-sequence "Σ" current dynamics (i^{Σ}_{z}) are obtained from (2.56) as follows:

$$L_{arm}\frac{di^{\Sigma}_{z}}{dt} = \frac{1}{2}v_{dc} - v^{\Sigma}_{mz} - R_{arm}i^{\Sigma}_{z} \tag{4.4}$$

The AC current dynamics equations remain the same as for the complete model, i.e. as in (4.1). However, the expression for the modulated voltages "Σ" and "Δ" are simplified. The modulated voltages are obtained from (2.70), where only the components v^{Σ}_{mz}, v^{Δ}_{md} and v^{Δ}_{mq} are considered, and neglecting the variables from Table 4.1. The result is shown in (4.5).

$$\begin{bmatrix} v^{\Sigma}_{mz} \\ v^{\Delta}_{md} \\ v^{\Delta}_{mq} \end{bmatrix} = \frac{1}{4}\begin{bmatrix} 2v^{\Sigma}_{Cz} & 0 & 0 \\ 0 & -2v^{\Sigma}_{Cz} & 0 \\ 0 & 0 & -2v^{\Sigma}_{Cz} \end{bmatrix}\begin{bmatrix} m^{\Sigma}_{z} \\ m^{\Delta}_{d} \\ m^{\Delta}_{q} \end{bmatrix} \tag{4.5}$$

The states of the reduced order model corresponding to the physical variables are gathered in $\boldsymbol{x^{Red.}_{MMC}}$:

$$\boldsymbol{x^{Red.}_{MMC}} = \begin{bmatrix} i^{\Delta}_{d} & i^{\Delta}_{q} & i^{\Sigma}_{z} & v^{\Sigma}_{Cz} & v_{dc} \end{bmatrix}^{\top} \in \Re^{5} \tag{4.6}$$

The reduced order MMC model is then expressed by the dynamic equations (4.1), (4.4), (4.3) and the algebraic equation given in (4.5). This model accepts 3 control inputs: $\boldsymbol{m^{\Delta}_{dq}} = [m^{\Delta}_{d}\ m^{\Delta}_{q}]^{\top}$ and m^{Σ}_{z}. The block-diagram of the reduced order MMC model is shown in Fig. 4.5 where the physical inputs are the same as the complete model from Fig. 4.3.

It is recalled that both models (complete model from Fig. 4.3 and reduced from Fig. 4.5) are obtained with the amplitude invariant Park transformation (See Appendix A). At this stage, it is convenient to convert the reduced order model with the power invariant Park transformation, for allowing us to draw a comprehensive electrical circuit as it was already performed in **[123]**. For obtaining the mathematical scaling between the variables of the developed model from Fig. 4.5 and the one in **[123]**, (4.7) is used:

$$i_{gd} \overset{\text{def}}{=} \sqrt{\frac{3}{2}}i^{\Delta}_{d};\ i_{gq} \overset{\text{def}}{=} \sqrt{\frac{3}{2}}i^{\Delta}_{q};\ v_{md} \overset{\text{def}}{=} \sqrt{\frac{3}{2}}v^{\Delta}_{md};\ v_{mq} \overset{\text{def}}{=} \sqrt{\frac{3}{2}}v^{\Delta}_{mq};\ v_{gd} \overset{\text{def}}{=} \sqrt{\frac{3}{2}}v^{G}_{d};\ v_{gq} \overset{\text{def}}{=} \sqrt{\frac{3}{2}}v^{G}_{q} \tag{4.7}$$

Note that the grid currents are named as i_{gd} and i_{gq} for the power invariant version of the MMC model (the counterparts of $\boldsymbol{i^{\Delta}_{dq}}$), the grid voltages are v_{gd} and v_{gq} (for $\boldsymbol{v^{G}_{dq}}$), and the

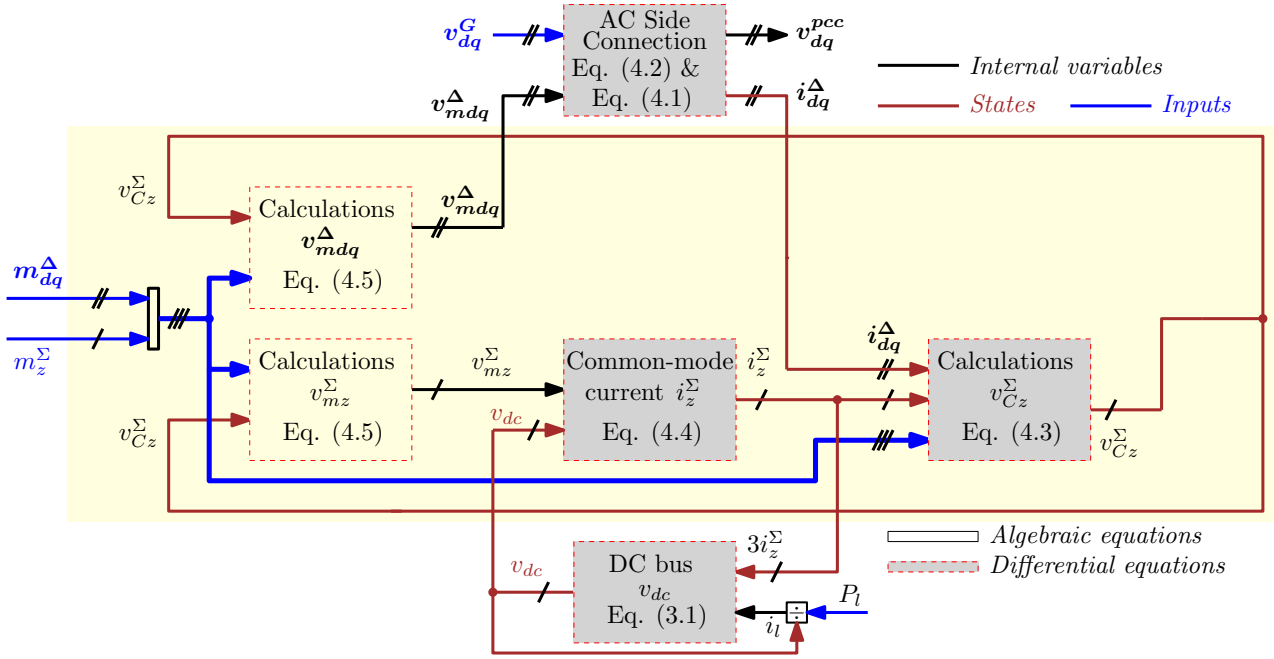

Figure 4.5 – Reduced order MMC model with SSTI Solution

modulated voltages for the AC side are v_{md} and v_{mq} for $\boldsymbol{v}^{\boldsymbol{\Delta}}_{\boldsymbol{mdq}}$. With (4.7), the grid current dynamics can be expressed as:

$$\left(L^{ac}_{eq}+L^{G}\right)\frac{di_{gd}}{dt}=v_{md}-v_{gd}-\left(R^{ac}_{eq}+R^{G}\right)i_{gd}-\left(L^{ac}_{eq}+L^{G}\right)\omega i_{gq} \tag{4.8}$$

$$\left(L^{ac}_{eq}+L^{G}\right)\frac{di_{gq}}{dt}=v_{mq}-v_{gq}-\left(R^{ac}_{eq}+R^{G}\right)i_{gq}+\left(L^{ac}_{eq}+L^{G}\right)\omega i_{gd} \tag{4.9}$$

Moreover, the arm capacitors v^{Σ}_{Cz} dynamics can be rewritten as[2]:

$$C_{mmc}\frac{dv^{\Sigma}_{Cz}}{dt}=-m_d i_{gd}-m_q i_{gq}+m_{dc}i_{dc} \tag{4.10}$$

where,

$$m_d \overset{\text{def}}{=} -\frac{3}{4}\sqrt{\frac{3}{2}}m^{\Delta}_d, \quad m_q \overset{\text{def}}{=} -\frac{3}{4}\sqrt{\frac{3}{2}}m^{\Delta}_q, \quad m_{dc} \overset{\text{def}}{=} m^{\Sigma}_z \tag{4.11}$$

and $C_{mmc}=6\times C_{arm}$. Taking into account that $i_{dc}=3i^{\Sigma}_z$, the DC current dynamics are expressed as:

$$L^{dc}_{eq}\frac{di_{dc}}{dt}=v_{dc}-v_{mdc}-R^{dc}_{eq}i_{dc} \tag{4.12}$$

where,

$$v_{mdc}=2v^{\Sigma}_{mz} \tag{4.13}$$

$$L^{dc}_{eq}\overset{\text{def}}{=}\frac{2}{3}L_{arm}, \quad R^{dc}_{eq}\overset{\text{def}}{=}\frac{2}{3}R_{arm} \tag{4.14}$$

Finally, the modulated voltages are expressed as in (4.15).

$$\begin{bmatrix} v_{mdc} \\ v_{md} \\ v_{mq} \end{bmatrix} = \begin{bmatrix} v^{\Sigma}_{Cz} & 0 & 0 \\ 0 & v^{\Sigma}_{Cz} & 0 \\ 0 & 0 & v^{\Sigma}_{Cz} \end{bmatrix} \begin{bmatrix} m_{dc} \\ m_d \\ m_q \end{bmatrix} \tag{4.15}$$

[2]Note that the signs of the modulated AC currents in (4.10) are in opposite direction with respect to (4.3).

With the differential equations from (4.8), (4.12) and (4.10); and the algebraic equation (4.15), the circuit diagram of the simplified MMC can be obtained as depicted in Fig. 4.6. With this circuit, *the double-stage nature of the MMC operation is clearly highlighted* [79], which is not evident when seeing the complete MMC structure as in Fig. 2.2. This implies that the DC bus capacitor C_{dc} is not coupled directly with C_{mmc}, as it was the case for the *2-level* VSC (See Section 1.3). As it will be detailed in further sections, this can be a disadvantage since the DC voltage v_{dc} is governed only by the capacitor C_{dc} [176].

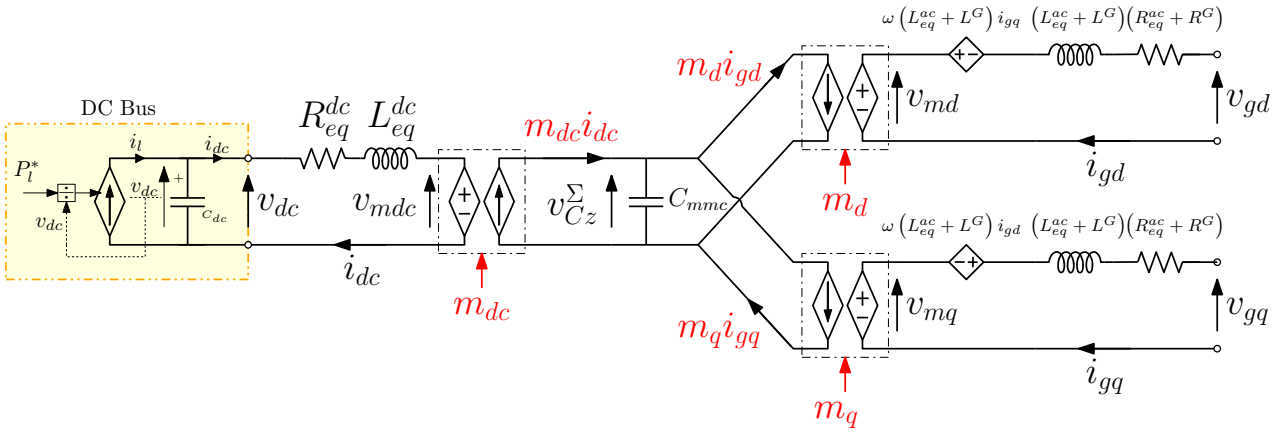

Figure 4.6 – Circuit diagram of SSTI-MMC simplified model from **[123]**

4.3 Comparison I: Considering Energy-based controller # 2 and Compensated Modulation

The aim of this section is to verify the accuracy of the reduced order model when the MMC is considered to be controlled with the *Energy-based* controller # 2 from Section 3.4 in conjunction with the Compensated Modulation (CM)[3]. As stated in the introduction of this Chapter, the comparison is performed based on the small-signal dynamics of both MMC models.

4.3.1 Controller for the reference model

First, the *Energy-based* controller # 2 strategy is slightly modified with respect to the control strategy detailed in Section 3.4. The modifications are necessary for taking into account the added AC simplified model.

It should be noted that the dq variables from the AC side of the MMC (currents $\boldsymbol{i}_{\boldsymbol{dq}}^{\boldsymbol{\Delta}}$) and the AC grid (voltages $\boldsymbol{v}_{\boldsymbol{dq}}^{\boldsymbol{pcc}}$) are referred to the SRRF which is rotating at the angular frequency ω imposed by the synchronous generators from the AC grid. In the MMC control system, the frequency ω is estimated typically by a Phase Locked Loop (PLL). The estimated frequency is noted as ω_C, and the angle between the phasors V^G (AC grid) and V^{pcc} (point of common coupling) is noted as θ_C.

In steady state, the frequencies ω and ω_C are equal, but during transients they can experience a deviation due to the non-infinite wideband of the PLL. This concept of two frequencies

[3]It is recalled that with CM, the relation $v_m = v_m^*$ for Σ and Δ variables is always valid.

involved in the modeling of the MMC and its controller (ω and ω_C) is illustrated in Fig. 4.7a where it is highlighted the new axes $\boldsymbol{dq^C}$ corresponding to the SRRF defined by the PLL.

In the control system, the voltages $\boldsymbol{v_{dq}^{pcc}}$ and grid currents $\boldsymbol{i_{dq}^{\Delta}}$ are referred to the axes $\boldsymbol{dq^C}$ defined by the PLL with the transformation matrix $\boldsymbol{T_C}(\theta_C)$, as shown in (4.16) [177]. In (4.16), a generic variable $\boldsymbol{x_{dq}} = [x_d\ x_q]$ is used to exemplify the projected variables into the $\boldsymbol{dq^C}$ axes, obtaining $\boldsymbol{x_{dq}^C} = [x_q^C\ x_q^C]$ [69, 119].

$$\begin{bmatrix} x_d^C \\ x_q^C \end{bmatrix} = \underbrace{\begin{bmatrix} \cos(\theta_C) & -\sin(\theta_C) \\ \sin(\theta_C) & \cos(\theta_C) \end{bmatrix}}_{\boldsymbol{T_C}(\theta_C)} \begin{bmatrix} x_d \\ x_q \end{bmatrix} \tag{4.16}$$

The structure of the PLL is shown in Fig. 4.7b, where it can be observed the transformations $\boldsymbol{T_C}(\theta_C)$ applied to $\boldsymbol{v_{dq}^{pcc}}$, $\boldsymbol{i_{dq}^{\Delta}}$ and $\boldsymbol{i_{dq}^{\Sigma}}$ only if they are controlled in dq frame (as for the *Classical CCSC*, as it will be used in Section 4.4).

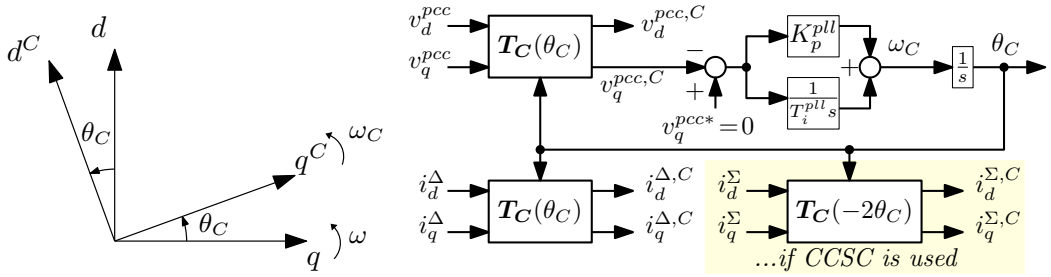

(a) dq reference frames (b) PLL structure and measures

Figure 4.7 – Phase Locked Loop

The controller in SRRF considered for the generalized MMC model with SSTI solution is shown in Fig. 4.8. Note that the grid current controller is referred to the axes given by the PLL, with an angular rotation of ω_C. For this reason, the transformation $\boldsymbol{T_C^{-1}}(\theta_C)$ is used to rotate the voltage references $\boldsymbol{v_{mdq}^{\Delta,C*}}$ back to the grid SRRF, obtaining $\boldsymbol{v_{mdq}^{\Delta*}}$.

In the EMT *Simulation model*, the control for the energy sum W^{Σ} and energy difference W^{Δ}, and the common-mode currents i^{Σ} are implemented in *abc* frame [178], i.e. it is almost independent from the PLL (the W^{Δ} uses the estimated angle for aligning the AC component of $i_{ac}^{\Sigma*}$ with the grid voltage). In the full-dqz model, this is equivalent to refer the controller equations of W^{Σ}, W^{Δ} and i^{Σ} to the SRRF of the AC grid, i.e. to ω. Only the grid current controllers i^{Δ} are referred to the SRRF defined by the PLL.

4.3.2 Controller for the reduced order model

Since there are less state variables of the physical system of the reduced order model (Fig. 4.5), the control structure is also simplified. The control model is obtained from the structure presented in Fig. 4.8, where the dq components of the energy "Σ" are neglected. Also, the energy difference controllers are not taken into account since the reduced order model considers that the vertical balancing (i.e. W^{Δ}) is perfectly controlled and decoupled from the rest of the system **[159]**. The Compensated Modulation for the reduced order model is obtained from (3.13), as expressed in (4.17). The resulting controller is shown in Fig. 4.9.

$$m_d^{\Delta} = -\frac{v_{md}^{\Delta*}}{v_{Cz}^{\Sigma}/2}; \quad m_q^{\Delta} = -\frac{v_{mq}^{\Delta*}}{v_{Cz}^{\Sigma}/2}; \quad m_z^{\Sigma} = \frac{v_{mz}^{\Sigma*}}{v_{Cz}^{\Sigma}/2} \tag{4.17}$$

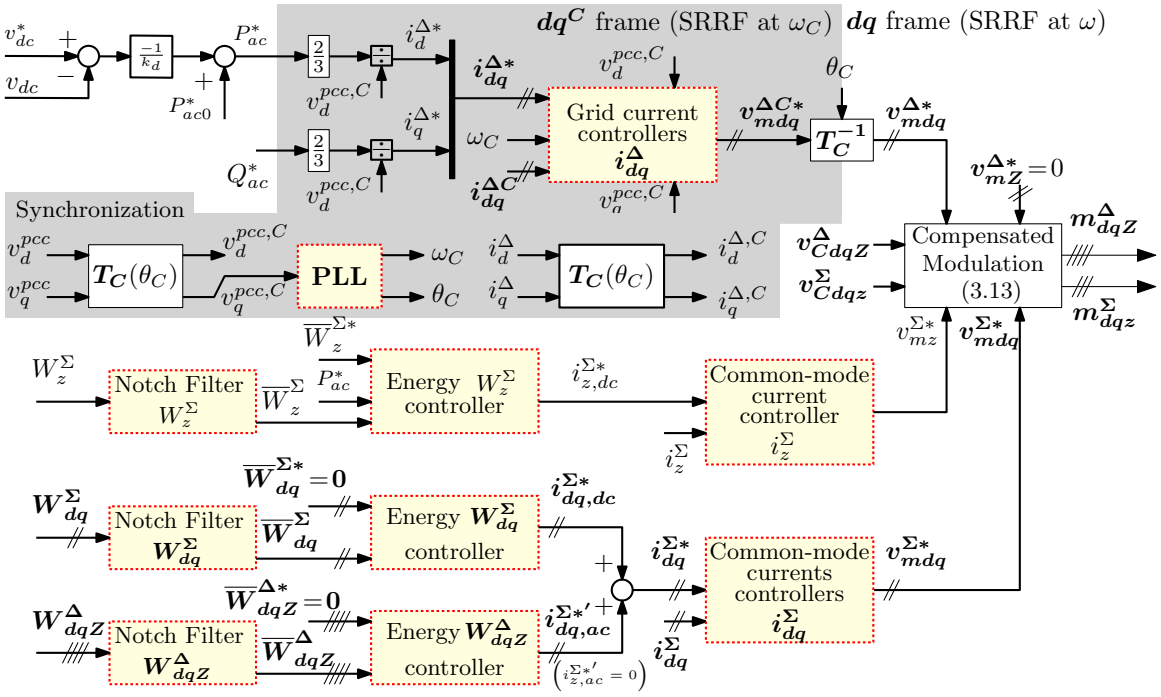

Figure 4.8 – Modified *Energy-based* controller # 2 for reference SSTI-MMC model from Fig. 4.3

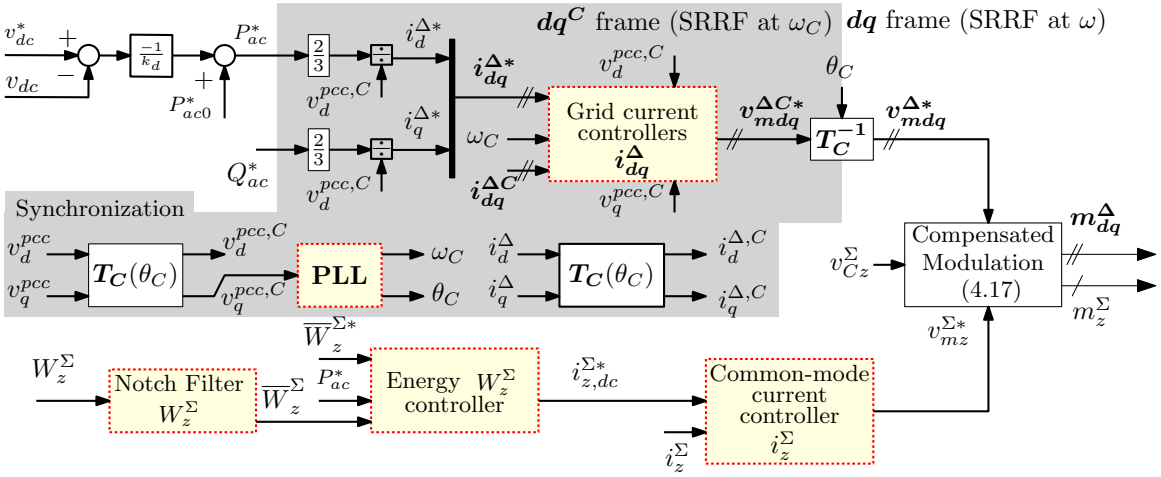

Figure 4.9 – Reduced *Energy-based* controller for simplified SSTI-MMC model from Fig. 4.5

Note that in Fig. 4.9, the notch filter for W_z^Σ is present, even if this variable is "pure DC". This is due to the fact that in the complete model, this filter exists for the three dqz variables (See Section 3.4.2). The states of the controllers for the reduced order model are listed in $\boldsymbol{x}_{\boldsymbol{Ctrl}}^{\boldsymbol{Red.}}$:

$$\boldsymbol{x}_{\boldsymbol{Ctrl}}^{\boldsymbol{Red.}} = \left[\theta_C \ \xi_{pll} \ F_{1z}^\Sigma \ F_{2z}^\Sigma \ \xi_{W_z^\Sigma} \ \xi_{i_z^\Sigma} \ \xi_{i_d^\Delta} \ \xi_{i_q^\Delta}\right]^\top \in \mathbb{R}^8 \tag{4.18}$$

4.3.3 Models Linearization: Time domain comparison

The MMC model in dqz frame with the AC and DC connections is summarized in Fig. 4.10 (Fig. 4.10a for the complete model and Fig. 4.10b for the reduced order model). The Linear Time Invariant (LTI) models for each configuration is obtained with the Jacobian linearization of the MMC and DC bus (*System I*) and the AC grid (*System II*) separately, with the

methodology explained in Section 1.2.4. Then, both systems are coupled with the methodology explained in the Appendix B.2 [9]. The reason of the separation in two different systems is due to the algebraic equation used in the calculation of $\boldsymbol{v}_{\boldsymbol{dq}}^{\boldsymbol{pcc}}$ in (4.2).

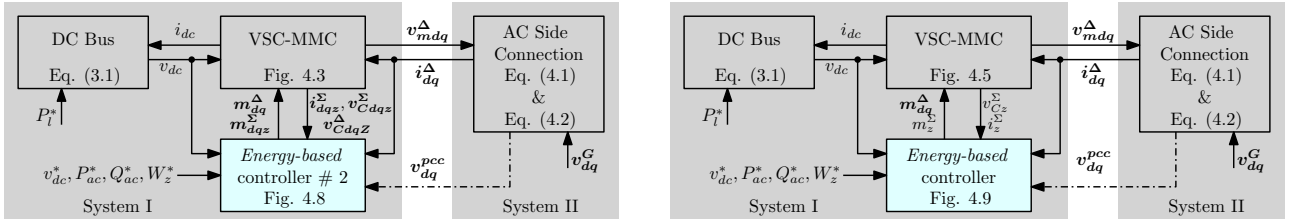

(a) SSTI-MMC Reference Model (*Full*)

(b) SSTI-MMC Reduced order Model (*Red.*)

Figure 4.10 – Reduced Order Model Validation of MMC with Energy-based controller

The states of the *Full*-order model are gathered in (4.19):

$$\boldsymbol{x}_{\boldsymbol{dqz}}^{\boldsymbol{Full}} = [F_{1d}^{\Sigma};\ F_{1q}^{\Sigma};\ F_{2d}^{\Sigma};\ F_{2q}^{\Sigma};\ \xi_{W_d^{\Sigma}};\ \xi_{W_q^{\Sigma}};\ \xi_{i_d^{\Sigma}};\ \xi_{i_q^{\Sigma}};\ i_d^{\Sigma};\ i_q^{\Sigma};\ v_{Cd}^{\Sigma};\ v_{Cq}^{\Sigma};\ldots \tag{4.19}$$
$$\ldots F_{1d}^{\Delta};\ F_{1q}^{\Delta};\ F_{1Z_d}^{\Delta};\ F_{1Z_q}^{\Delta};\ F_{2d}^{\Delta};\ F_{2q}^{\Delta};\ F_{2Z_d}^{\Delta};\ F_{2Z_q}^{\Delta};\ \xi_{W_d^{\Delta}};\ \xi_{W_q^{\Delta}};\ \xi_{W_{Z_d}^{\Delta}};\ \xi_{W_{Z_q}^{\Delta}};\ v_{Cd}^{\Delta};\ v_{Cq}^{\Delta};\ v_{CZ_d}^{\Delta};\ v_{CZ_q}^{\Delta};\ldots$$
$$\ldots \underbrace{\theta_C;\ \xi_{pll};\ F_{1z}^{\Sigma};\ F_{2z}^{\Sigma};\ \xi_{W_z^{\Sigma}};\ \xi_{i_z^{\Sigma}};\ i_z^{\Sigma};\ v_{Cz}^{\Sigma};\ v_{dc};\ \xi_{i_d^{\Delta}};\ \xi_{i_q^{\Delta}};\ i_d^{\Delta};\ i_q^{\Delta}}_{\text{Common states between the full and reduced order model}}]^{\top} \in \mathbb{R}^{41}$$

while the states of the reduced system are listed in $\boldsymbol{x}_{\boldsymbol{dqz}}^{\boldsymbol{Red.}}$:

$$\boldsymbol{x}_{\boldsymbol{dqz}}^{\boldsymbol{Red.}} = \left[\theta_C;\ \xi_{pll};\ F_{1z}^{\Sigma};\ F_{2z}^{\Sigma};\ \xi_{W_z^{\Sigma}};\ \xi_{i_z^{\Sigma}};\ i_z^{\Sigma};\ v_{Cz}^{\Sigma};\ v_{dc};\ \xi_{i_d^{\Delta}};\ \xi_{i_q^{\Delta}};\ i_d^{\Delta};\ i_q^{\Delta}\right]^{\top} \in \Re^{13} \tag{4.20}$$

Finally, in (4.21), the inputs for both LTI systems are gathered.

$$\boldsymbol{u}_{\boldsymbol{dqz}} = [\underbrace{P_l^*;\ v_d^G;\ v_q^G}_{\text{Physical inputs}};\ \underbrace{v_{dc}^*;\ P_{ac}^*;\ Q_{ac}^*;\ W_z^*}_{\text{Control inputs}}]^{\top} \in \mathbb{R}^8 \tag{4.21}$$

To validate the developed small-signal models of the MMC, results from a time-domain simulation of three different models are shown and discussed in the following:

1. *EMT*: The MMC *Simulation model* with the AC and DC simplified representations as in Fig. 4.2, implemented in EMTP-RV with 400 submodules (as used in Chapter 2 and Chapter 3).

2. *Full*: This model represents the linearized time-invariant model of the interconnected system from Fig. 4.10a, implemented in Matlab/Simulink.

3. *Red.*: This model represents the linearized time-invariant model of the interconnected system from Fig. 4.10b, implemented in Matlab/Simulink.

The operating point corresponds to the parameters given in Table 4.2.

Starting with a DC power transfer of 1 pu (from DC to AC), a step is applied on P_l^* of -0.1 pu at 0.05 s. The reactive power is controlled to zero during the whole simulation. Results are gathered in Fig. 4.11.

The dynamic response of the DC power P_{dc} and DC voltage v_{dc} are respectively shown in Figs. 4.11a and 4.11b, showing a perfect match between the compared models. The AC grid

Table 4.2 – Operating point of MMC for linearization

Variable	Value	Variable	Value
P_{dc0}	1 pu	k_d	0.1 pu
v_{dc0}	1 pu	C_{dc}	$4 \times C_{arm}$ F

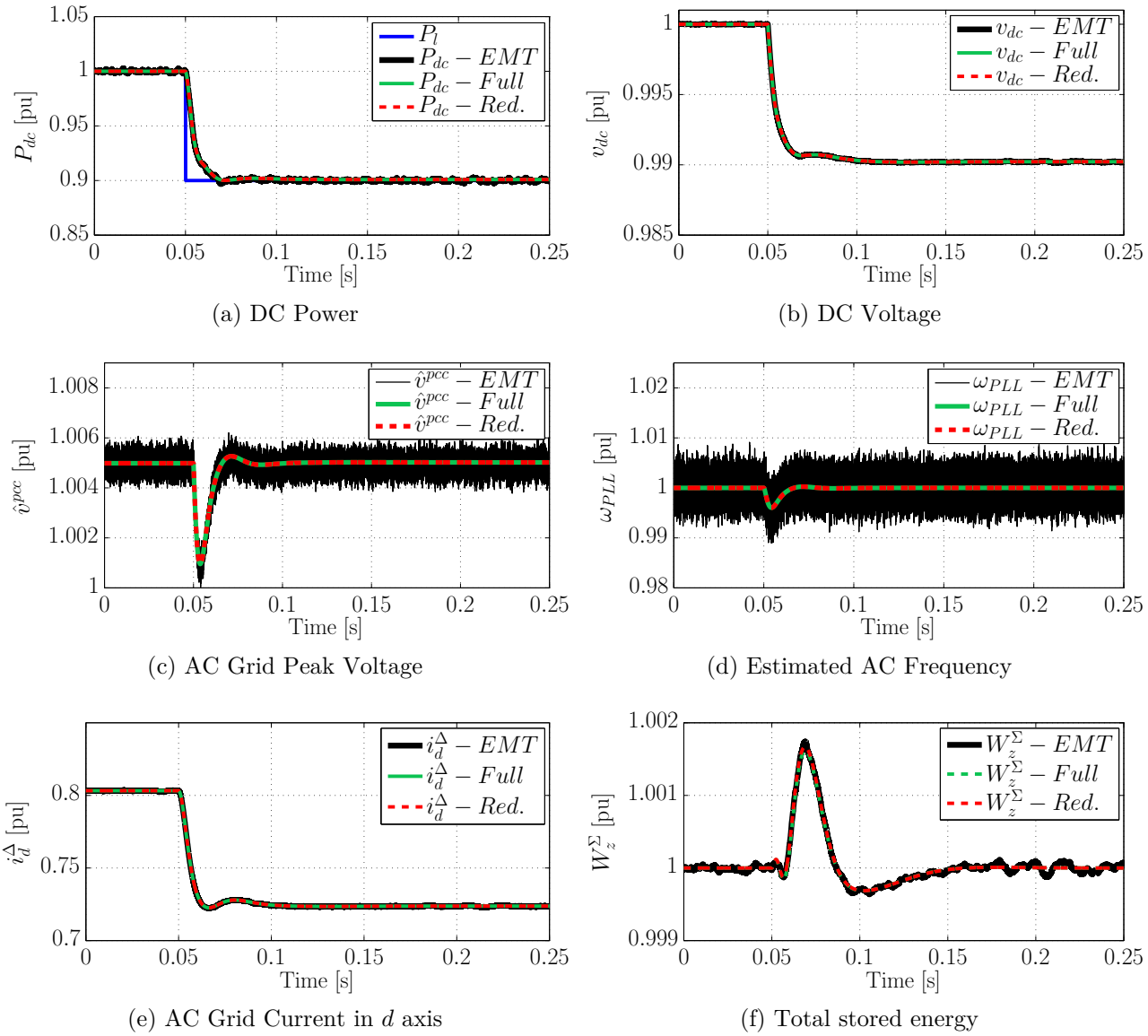

(a) DC Power

(b) DC Voltage

(c) AC Grid Peak Voltage

(d) Estimated AC Frequency

(e) AC Grid Current in d axis

(f) Total stored energy

Figure 4.11 – Reduced Order Model Validation of MMC with Energy-based controller. *EMT* : EMTP-RV simulation; *Full* : LTI model from Fig. 4.10a; *Red* : LTI model from Fig. 4.10b.

peak voltage $\hat{v}^{pcc}$ is shown in 4.11c (calculated as (4.22) for both LTI models). The estimated AC frequency by the PLL ω_C is given in Fig. 4.11d.

$$\hat{v}^{pcc} = \sqrt{(v_d^{pcc})^2 + (v_q^{pcc})^2} \tag{4.22}$$

As it can be seen, the EMT model presents high frequency oscillations in $\hat{v}^{pcc}$ and ω_C. This is due to the switching of the submodules which is transferred directly to the modulated voltage v_m^{Δ}, causing an AC current ripple. In turn, this originates the high frequency components in

the voltage $\hat{v}^{pcc}$. This phenomena is due to the physical behavior of the system, and it is always present when considering the MMC model with all the submodules. Since, in this case, there are no filters on the AC voltage measures before sending the signals to the PLL, the high-frequency components are transferred to the estimated frequency ω_C. For limiting the impact of the switching noise, more advanced PLL systems can be considered with appropriated filtering techniques. Nevertheless, this phenomena is proper to the EMT simulations (and in the "real" converters), and the LTI model only captures the time-averaged of these signals.

Finally, it is shown in Figs. 4.11e and 4.11f the results of the AC grid current i_d^{Δ}, and the total stored energy W_z^{Σ}. For these and the rest of variables, no noticeable difference is observed, validating the LTI models (*Full* and *Red.*) for the considered condition in terms of control tuning and physical parameters.

The time domain comparisons show that the reduced order model is very accurate for representing the MMC and the *Energy-based* controller with CM from the AC and DC standpoints. In the following section a more detailed comparison is performed with the modal analysis from both models.

4.3.4 Models comparisons with respect to their small-signal dynamics

In this section the complete and reduced model are compared in order to verify the validity of the simplified one. The first comparison is performed on the eigenvalues of the linear systems validated versus the EMT model previous section, which are shown in Fig. 4.12.

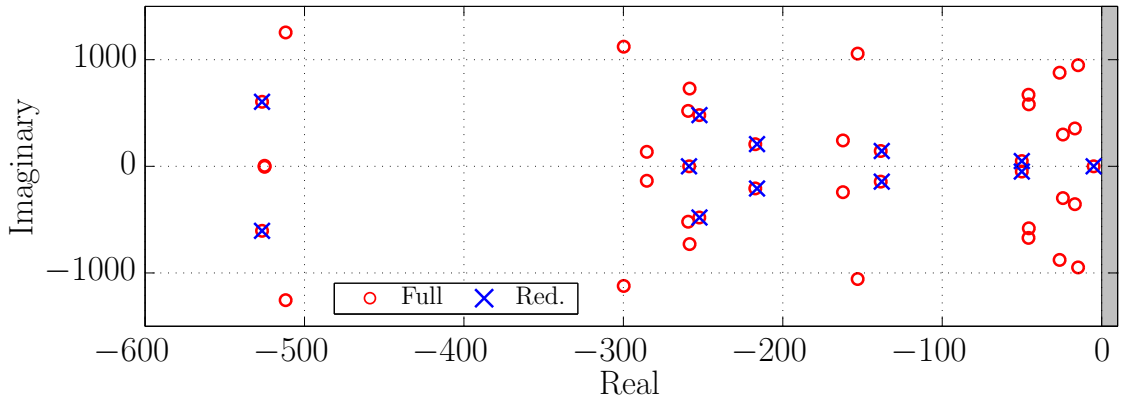

Figure 4.12 – Eigenvalues comparison of the complete and reduced MMC model with Energy-based control # 2 and CM

Results from Fig. 4.12 show that several eigenvalues from both models are virtually identical. The first hypothesis is that these eigenvalues are correlated to the similar state variables from both models. In the following, several tests are carried out to compare both models with more details.

Decoupling of the complete model

The eigenvalues of the full order LTI model are firstly studied, with special attention to the common eigenvalues found from Fig. 4.12. Second, the participation factor analysis are shown, where an important decoupling can be observed between a subset of MMC variables.

The eigenvalues of the *Full* order model plotted in Fig. 4.12 are shown in Table 4.3, where the common eigenvalues with the reduced order model are marked in blue. Note that these eigenvalues correspond only to the complete model, and not the reduced one.

	Eigenvalue	**Freq.**	**Damp.**
λ_1	-5	-	-
$\lambda_{2,3}$	$-16.2 \pm j958.3$	152.5	0.016944
$\lambda_{4,5}$	$-22.8 \pm j275.9$	43.9	0.082463
$\lambda_{6,7}$	$-25.4 \pm j332.2$	52.9	0.076328
$\lambda_{8,9}$	$-48.1 \pm j42.7$	6.8	0.74776
$\lambda_{10,11}$	$-51.2 \pm j586.1$	93.2	0.087033
$\lambda_{12,13}$	$-52.9 \pm j672.9$	107.1	0.078375
$\lambda_{14,15}$	$-62.5 \pm j893.7$	142.2	0.069791
$\lambda_{16,17}$	$-129.7 \pm j168.9$	26.9	0.60899
$\lambda_{18,19}$	$-137.2 \pm j962.6$	153.2	0.14112
$\lambda_{20,21}$	$-183.5 \pm j350.9$	55.9	0.46339
$\lambda_{22,23}$	$-215.5 \pm j207.9$	33.1	0.71965
$\lambda_{24,25}$	$-244.6 \pm j486.9$	77.5	0.44891
$\lambda_{26,27}$	$-248.6 \pm j759.2$	120.9	0.3112
λ_{28}	-256.9	-	-
$\lambda_{29,30}$	$-274.5 \pm j425.1$	67.7	0.54247
$\lambda_{31,32}$	$-276.1 \pm j105.7$	16.8	0.93394
$\lambda_{33,34}$	$-280.2 \pm j1151.5$	183.3	0.23641
$\lambda_{35,36}$	$-503.7 \pm j612.8$	97.5	0.63502
$\lambda_{37,38}$	$-521.2 \pm j1253.1$	199.4	0.38405
$\lambda_{39,40}$	$-529.2 \pm j7.7$	1.2	0.9999
λ_{41}	-2121.5	-	-

Table 4.3 – Eigenvalues of the complete model (common eigenvalues from *Full* and *Red* from Fig. 4.12 marked in blue)

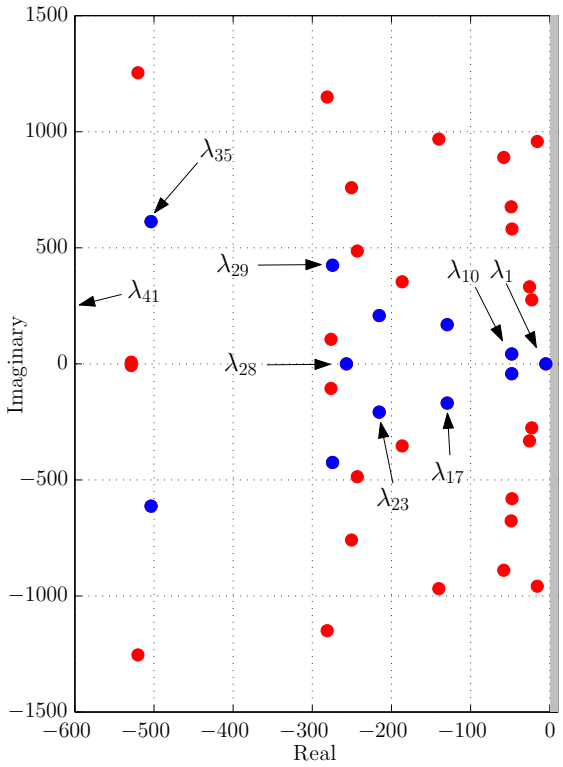

Figure 4.13 – Eigenvalues of the complete model (common eigenvalues from *Full* and *Red* from Fig. 4.12 marked in blue)

The information given in Table 4.3 is used to numerate and classify the eigenvalues for the following analysis. The participation factor analysis is used to verify if the 13 common state variables of the complete system with reduced order interact with the un-modeled state variables. The participation factor matrix is shown in Fig. 4.14, where the 13 common eigenvalues from Table 4.3 are grouped at the beginning of the "*x-axis*".

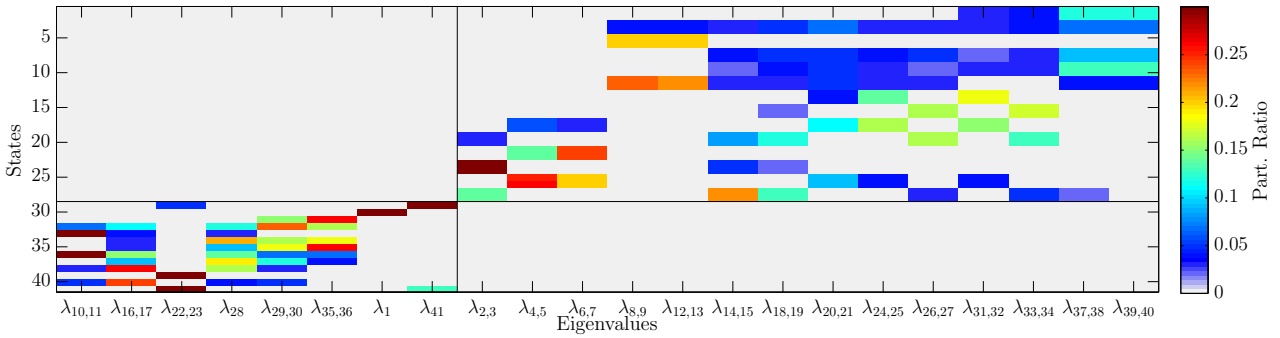

Figure 4.14 – Participation factor analysis of the complete LTI model

The results from Fig. 4.14 give some valuable information about the complete model. As it can be seen, the *lower-left* part (i.e. common state variables and eigenvalues) and *upper-right*

part (i.e. un-modeled variables of the reduced order model) of the participation factor matrix are decoupled: this means that the 13 state variables captured by the reduced order model are decoupled from the rest of the system. For this reason, the simplifications performed when developing the reduced order model are valid. Nevertheless, it should be recalled that the development of the MMC controller was performed in order to achieve a decoupled behavior.

Variation of operating point

Due to the non-linearities of the MMC, there is an impact of the choice of the operating point in terms of active power transfer for the linearization on the resulting eigenvalues [**161**]. For this reason, it is performed a parametric sweep in terms of DC power transmission P_{dc} from 1 pu to -1 pu. Results are shown in Fig. 4.15.

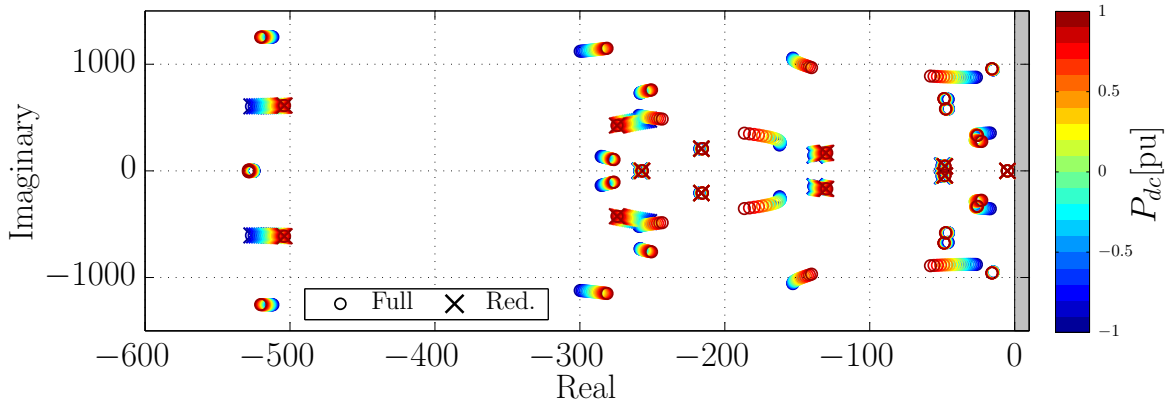

Figure 4.15 – Eigenvalues trajectories for P_{dc} variation ($k_d = 0.1$ pu) – Complete and reduced MMC model with Energy-based control and CM

As it can be seen from Fig. 4.15, several eigenvalues are shifted with respect to the different operating points. For both models, the 13 common eigenvalues are similar. Moreover, the stability is guaranteed for the considered variations.

Variation of DC capacitor

As it was shown in [**179**], the energy stored on the DC grid have an impact on the network stability. For this reason, the DC electrostatic constant H_{dc} is varied from 40 ms down to 5 ms. Results shown in Fig. 4.16.

For this kind of variations, the complete and reduced model gives similar results. It is also interesting to observe that the modes of the complete model which are not represented by the reduced model are not shifted by these variations: they remain at a fixed position. This confirms that the DC side is decoupled from the internal dynamics of the MMC for this *Energy-based* controller [**160**].

Variation of DC droop gain

In this case, the DC droop gain k_d is varied from 0.2 pu down to 0.05 pu, and the results are shown in Fig. 4.17. Similarly, as the previous case, the reduced order model replicates accurately the mode shifting of the complete model.

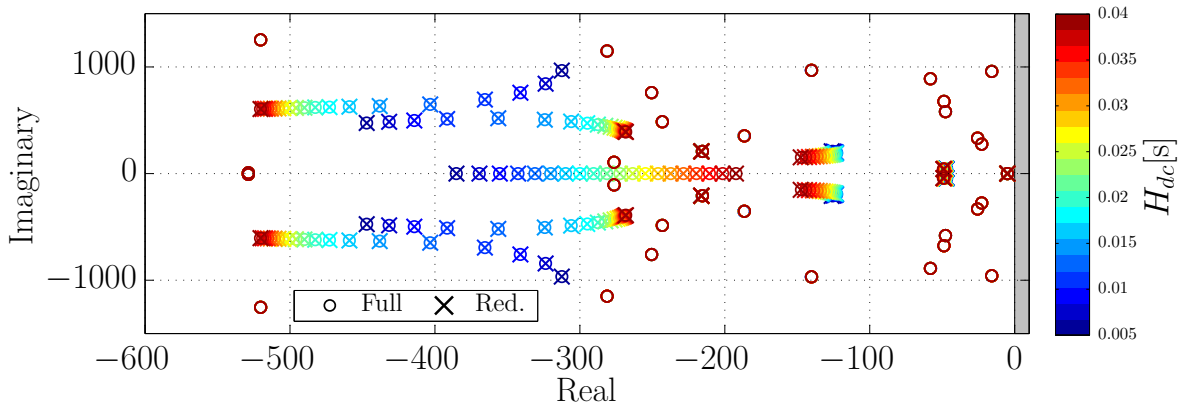

Figure 4.16 – Eigenvalues trajectories for H_{dc} variation ($P_{dc} = 1$ pu) – Complete and reduced MMC model with Energy-based control and CM

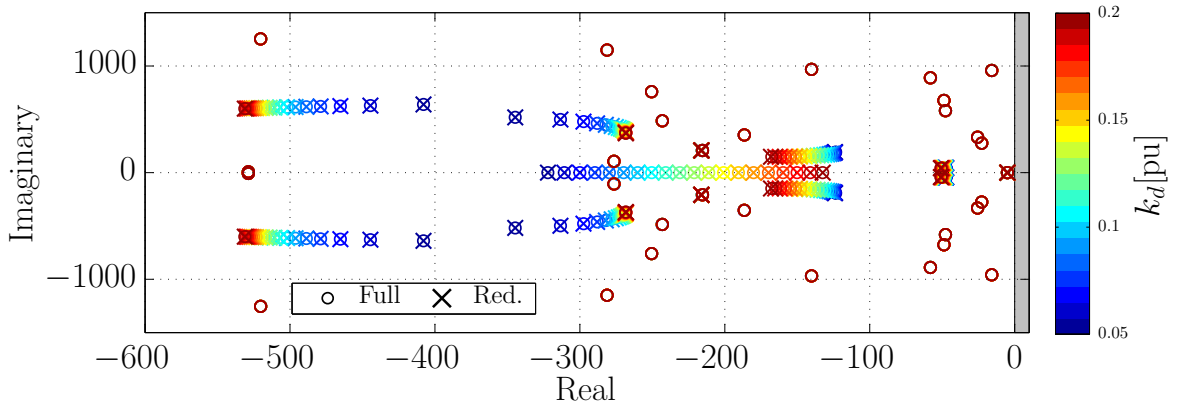

Figure 4.17 – Eigenvalues trajectories for k_d variation ($P_{dc} = 1$ pu) – Complete and reduced MMC model with Energy-based control and CM

Variation of common-mode current and energy sum controllers response times

The following tests are performed with a variation of the response times of the common-mode currents $t_r^{i\Sigma}$ and energy sum $t_r^{W\Sigma}$. Both response times are modified at the same time, keeping a time separation factor of 10, as expressed in (4.23), which is a common practice for avoiding interactions between the inner and outer control loops.

$$t_r^{W\Sigma} = 10 \times t_r^{i\Sigma} \tag{4.23}$$

The response time of $t_r^{i\Sigma}$ ($t_r^{W\Sigma}$) is varied from 5 ms (50 ms) down to 1 ms (10 ms). Results are shown in Fig. 4.18, where it can be observed that there are many eigenvalues sensitive to the performed variation.

Due to the extreme shifting of many modes in Fig. 4.18, the interpretation of the results is very complicated. But it can be observed that the complete model is unstable for a response time of $t_r^{i\Sigma}$ between 1.5 ms and 2 ms. The limit is found around $t_r^{i\Sigma} = 1.67$ ms and $t_r^{W\Sigma} = 16.7$ ms as shown in Fig. 4.19. Moreover, it can be seen that only the complete model is unstable, while the reduced order model is stable. This means that the instability is produced by the internal variables not modeled in the simplified model.

For validating the results, a new time-domain simulation is performed with the complete EMT *Simulation model*. The physical parameters considered for this simulation are the same

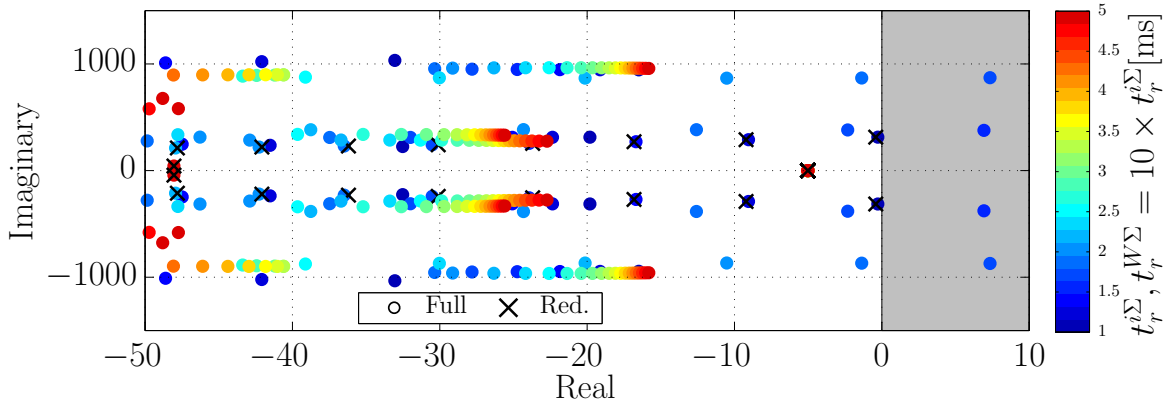

Figure 4.18 – Eigenvalues trajectories for $t_r^{i\Sigma}$ and $t_r^{W\Sigma}$ variation ($P_{dc} = 1$ pu) – Complete and reduced MMC model with Energy-based control and CM

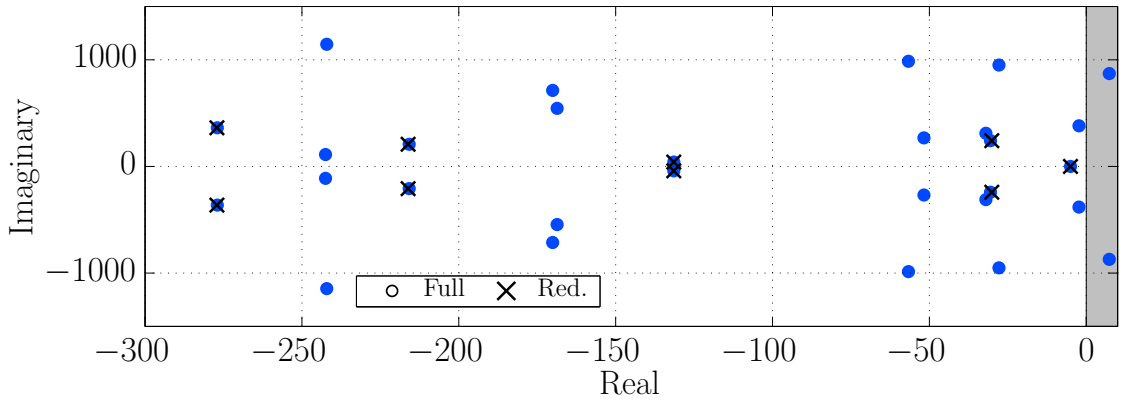

Figure 4.19 – Eigenvalues for $t_r^{i\Sigma} = 1.67$ ms and $t_r^{W\Sigma} = 16.7$ ms variation ($P_{dc} = 1$ pu) – Complete and reduced MMC model with Energy-based control and CM

as in Section 4.3.3, while the control parameters of i^{Σ} and W^{Σ} controllers are modified. The simulation events are listed as follows:

1. For $t < 0.15$ s, there is a power transfer of $P_{dc} = 1$ pu. The response times $t_r^{i\Sigma}$ and $t_r^{W\Sigma}$ are set to 1.83 ms and 18.3 ms, respectively.
2. At $t = 0.15$ s, the response times $t_r^{i\Sigma}$ and $t_r^{W\Sigma}$ are set to 1.67 ms and 16.7 ms, respectively (i.e. the unstable case from Fig. 4.19).
3. At $t = 0.2$ s, an step on P_l of -0.1 pu is applied.
4. At $t = 0.75$ s, the response times of $t_r^{i\Sigma}$ and $t_r^{W\Sigma}$ are set back to the initial values (i.e. 1.83 ms and 18.3 ms, respectively).

The simulation results are gathered in Fig. 4.20. The results of the DC power are shown in Fig. 4.20a where no noticeable change is perceived when the gains of the controllers are changed. The same statement stands for the DC voltage results in Fig. 4.20b. When the power step is applied, the transient results are more oscillatory for the DC power and voltages compared with the case in Section 4.3.3. This is normally due to an undesired interaction between the energy controllers and the DC voltage droop control.

In Fig. 4.20c it is shown the results for the common-mode currents $\boldsymbol{i}_{\boldsymbol{dqz}}^{\boldsymbol{\Sigma}}$. It can be observed that the current i_z^{Σ} is not affected by the change of the controllers parameters, while the

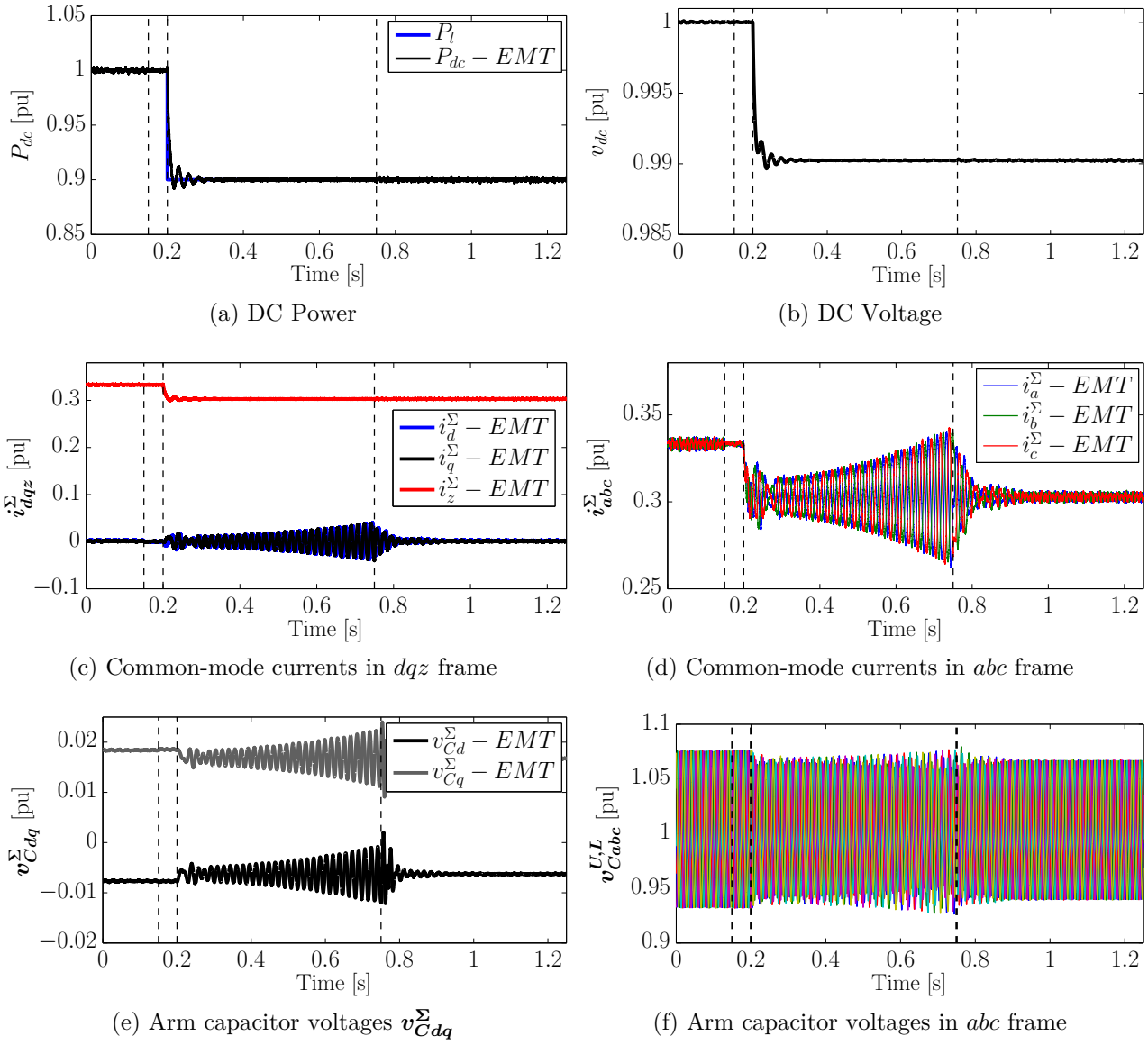

(a) DC Power

(b) DC Voltage

(c) Common-mode currents in dqz frame

(d) Common-mode currents in abc frame

(e) Arm capacitor voltages $\boldsymbol{v}_{\boldsymbol{Cdq}}^{\boldsymbol{\Sigma}}$

(f) Arm capacitor voltages in abc frame

Figure 4.20 – Unstable operation — Validation of MMC with complete Energy-based controller

currents $\boldsymbol{i}_{\boldsymbol{dq}}^{\boldsymbol{\Sigma}}$ clearly show the oscillatory instability. The same results, but in abc frame, are shown in Fig. 4.20d. When the controller gains are set back to their initial values, the system recovers the stability for $t > 0.75$ s. Finally, in Fig. 4.20e is shown the results for the arm capacitor voltage $\boldsymbol{v}_{\boldsymbol{Cdq}}^{\boldsymbol{\Sigma}}$, and Fig. 4.20f gathers the results of the arm capacitor voltages in abc frame. For both plots, the occurred instability and further clearance is observed as well.

It is recalled that this particular instability found and analyzed for the EMT *Simulation model* is observed only for the complete MMC model: the reduced order model is not capable to capture this behavior. More detailed studies should specify clearly the origin of the unstable behavior of the complete model for this condition, however this is out of the scope of this Chapter. As a partial hypothesis, this issue is originated by a strong interaction between the W^Σ and W^Δ controllers. The reason for this hypothesis is that the same simulation without W^Δ controller doesn't present the same behavior. Even if the control structure of W^Σ and W^Δ are designed in a decoupled way in abc frame, the internal variables are highly coupled at the inside of the MMC (more specifically, the variables $\boldsymbol{v}_{\boldsymbol{Cdqz}}^{\boldsymbol{\Sigma}}$ and $\boldsymbol{v}_{\boldsymbol{CdqZ}}^{\boldsymbol{\Delta}}$).

Variation of AC grid strength

The last comparison is based on the variation of the AC grid strength. This change is reflected in the modification of the SCR, where lower values of SCR correspond to a higher AC grid impedance. Since the AC grid vector current controllers as they were presented and used up to this point on this Thesis are not suitable for weak grids (SCR < 3 [180]), they are modified according to [181] and shown in Fig. 4.21. This modification introduces a first-order filter before sending the feed-forward signals of the AC voltage on the current controllers outputs, and their time constants are chosen to be $T_{mv}^{\Delta} = 20$ ms as in [182]. With the consideration of this modified controller, the LTI models for the *Full* and *Reduced* order model are re-generated prior to the eigenvalues comparisons. The controller gains are maintained during the parametric sweep.

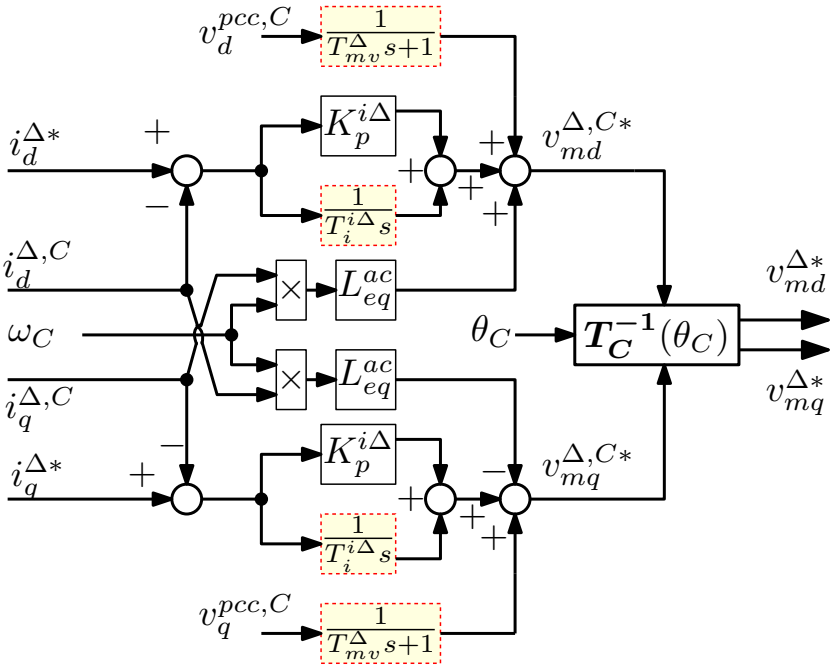

Figure 4.21 – AC Grid Current controller for weak grids

In Fig. 4.22 the eigenvalues from the linear models deduced from the complete SSTI-MMC model and the reduced order model are compared (lower figure corresponds to a zoom of upper figure). As it can be seen, the common eigenvalues from both systems presents a similar behavior when the SCR is varied. Both systems are unstable when the SCR is lower than approximately 2.8.

Results from this section reveals that, if the internal variables of the complete MMC are well controlled, the reduced order model replicates the main behavior from the AC and DC port characteristics. The complete model is useful for assuring that the internal variables are stable. However, for interfacing the MMC with *Energy-based* controller #2 with CM (i.e. full control of internal variables), it is recommended to use the reduced order model, since the accuracy from the AC and DC standpoints is not compromised. Also, the computational effort for linearizing and calculating the operating point when CM is considered in the *Full* order model is very high (more than 10 minutes[4] for only one operating point), while for the *Reduced* order model it is needed less than 30 s for a single point. This big difference in computing effort is due to the numerical resolution of the complex equations that are involved in the CM calculation (inversion of the 7×7 matrix from (3.13)).

[4]Using Matlab with Intel Core i7 2.7 GHz and 16 GB of RAM.

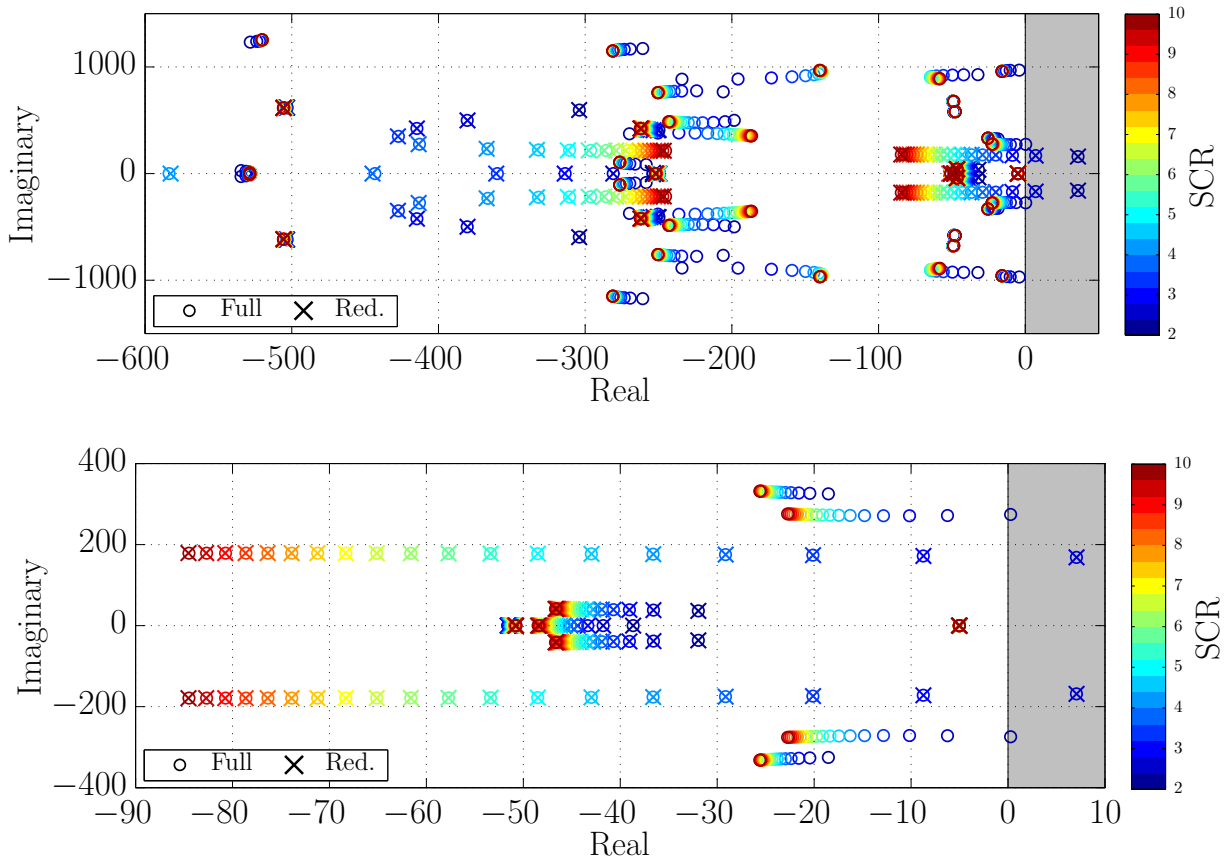

Figure 4.22 – Eigenvalues trajectories for SCR variation ($P_{dc} = 1$ pu) – Complete and reduced MMC model with Energy-based control and CM

In the following section, the same methodology is applied on the *Classical CCSC* with Un-Compensated Modulation.

4.4 Comparison II: Considering Classical CCSC and Un-Compensated Modulation

In this Section, it is studied if the reduced order model can reproduce in a macroscopic way the behavior of the MMC when it is controlled with the *Classical CCSC* strategy considering UCM. First, the modifications on the controllers for including the PLL are discussed.

From the discussion about the PLL and the two rotating frames (physical and controller), the *Classical CCSC* strategy used in the reference *Full* order SSTI-MMC model is the one shown in Fig. 4.23. Note that the transformation $\boldsymbol{T_C}(\theta_C)^{-1}$ is used to obtain the vector $\boldsymbol{v}^{\boldsymbol{\Delta}*}_{\boldsymbol{mdq}}$, but also the transformation $\boldsymbol{T_C}(\text{-}2\theta_C)^{-1}$ is used for $\boldsymbol{v}^{\boldsymbol{\Sigma}*}_{\boldsymbol{mdq}}$ since, in the EMT mode, the *Classical CCSC* is implemented in the SRRF defined by the axes $\boldsymbol{dq}^{\boldsymbol{C}}$ given by the PLL.

4.4.1 Reduced order model with Classical CCSC

For the reduced order SSTI-MMC model from Fig. 4.5, the adaptation of the *Classical CCSC* control strategy from Fig. 4.23 is needed. Since the simplified model doesn't consider the internal circulating currents $\boldsymbol{i}^{\boldsymbol{\Sigma}}_{\boldsymbol{dq}}$, the term "CCSC" may not be representative; however,

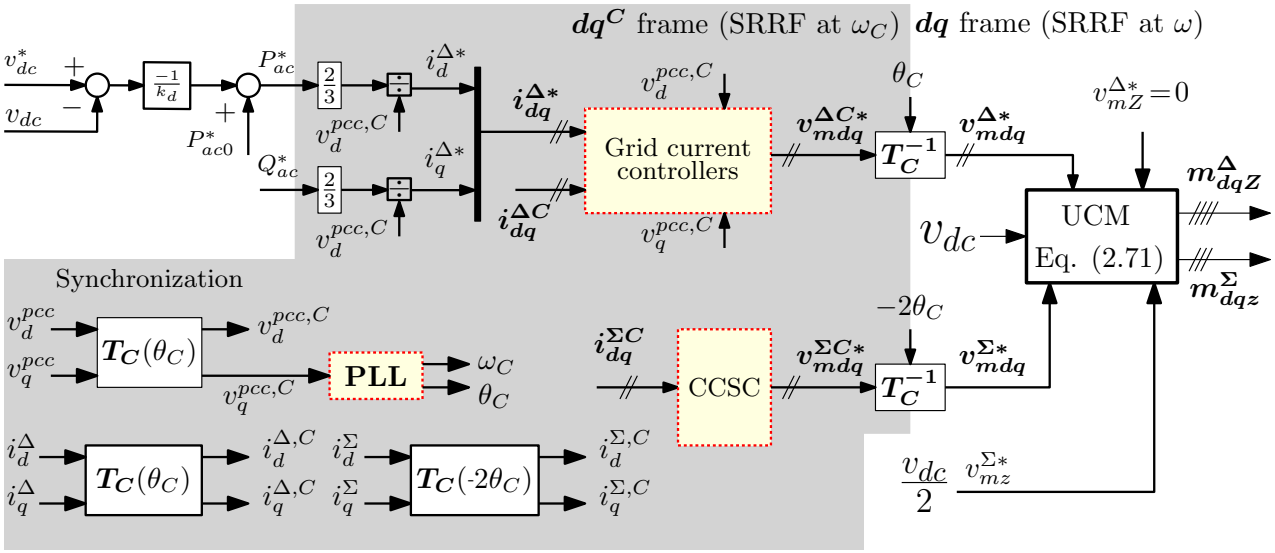

Figure 4.23 – *Classical CCSC* strategy with UCM considering PLL dynamics for SSTI-MMC

this nomenclature is kept for ease of understanding. For the representation of the UCM, (4.24) is used, which is directly obtained from (2.77). Finally, the control model is shown in Fig. 4.24.

$$m_d^{\Delta} = -\frac{v_{md}^{\Delta *}}{v_{dc}/2}; \quad m_q^{\Delta} = -\frac{v_{mq}^{\Delta *}}{v_{dc}/2}; \quad m_z^{\Sigma} = \frac{v_{mz}^{\Sigma *}}{v_{dc}/2} = \frac{v_{dc}}{2(v_{dc}/2)} = 1 \tag{4.24}$$

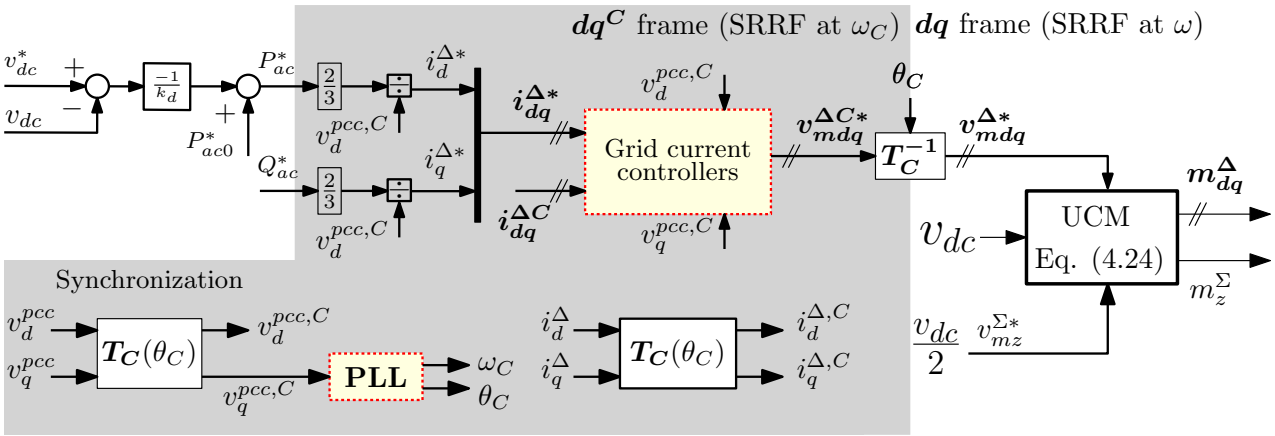

Figure 4.24 – *Classical CCSC* strategy with UCM considering PLL dynamics for Reduced order model

It is interesting to redraw the reduced order MMC model when considering UCM, specially by the fact that with this strategy the modulation index m_z^{Σ} is imposed by the control to 1, as expressed in (4.24). With this consideration, the circuit from Fig. 4.6 is modified as shown in Fig. 4.25, where the modification is impacted on the DC side.

This circuit helps to explain partially the oscillatory phenomena already shown in Section 3.2. It can be thought that there is a resonant "*RLC*" circuit formed by the DC capacitance, the internal capacitor C_{mmc} and $R_{eq}^{dc}L_{eq}^{dc}$. Since the current i_{dc} is left uncontrolled, it is clear that this current experiences several oscillations during transients. The resonance $f_{res,dc}$

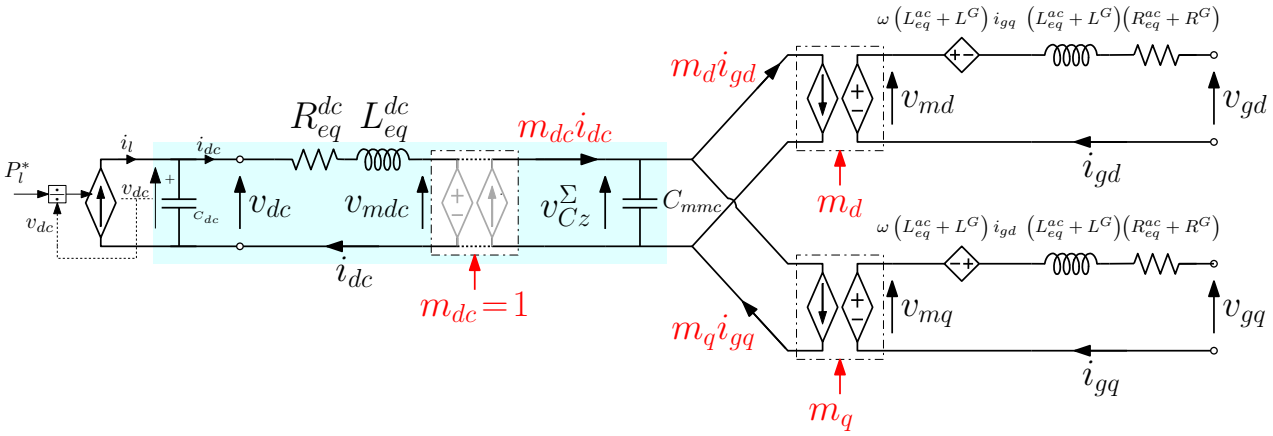

Figure 4.25 – Reduced order MMC model when considering *Classical CCSC* strategy with UCM

is calculated as [108]:

$$f_{res,dc} = \frac{1}{2\pi\sqrt{L_{eq}^{dc}\left(1/(1/C_{dc}+1/C_{mmc})\right)}} \tag{4.25}$$

With the parameters from the Appendix A, and considering that $C_{dc} = 4 \times C_{arm}$, the resonance $f_{res,dc}$ is approximately 99.7 Hz. The damping is provided by the resistance R_{eq}^{dc}.

Note that the obtained model from Fig. 4.25 is fundamentally the same as the "Model #4: *AVM of MMC*" from [111]. This model became very popular in the literature due to its simplicity [142, 183]. However, the aim of this section is to verify if it's safe to consider a simplified model without modeling explicitly the circulating currents (as the circuit in Fig. 4.25) for representing the complete SSTI-MMC model when considering the *Classical CCSC* with UCM; specifically if AC- and DC-side interactions are studied.

4.4.2 Models Linearization: Time domain comparison

The LTI models are obtained similarly as shown in Section 4.3.3, however, the complete model is represented as in Fig. 4.10a; while in Fig. 4.10b it is shown the summary of the connections for the reduced order model.

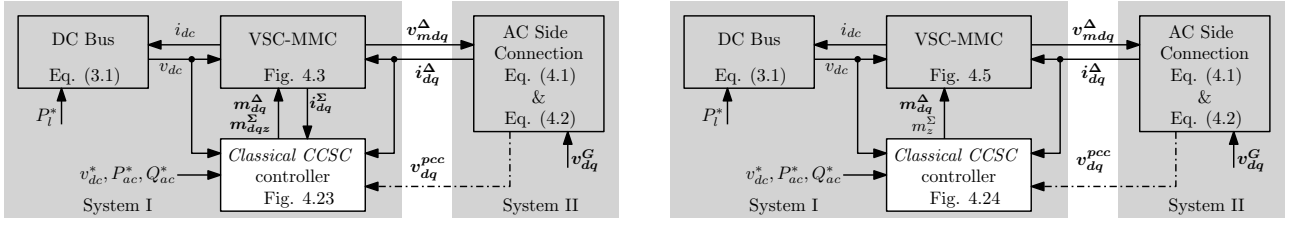

(a) SSTI-MMC Reference Model (*Full*) (b) SSTI-MMC Reduced order Model (*Red.*)

Figure 4.26 – Reduced Order Model Validation of MMC with *Classical CCSC*

The states of the *Full*-order model are gathered in (4.26):

$$\begin{aligned} \boldsymbol{x}_{\boldsymbol{dqz}}^{\boldsymbol{Full}} = [&\xi_{i_d^{\Sigma}};\ \xi_{i_q^{\Sigma}};\ i_d^{\Sigma};\ i_q^{\Sigma};\ v_{Cd}^{\Sigma};\ v_{Cq}^{\Sigma};\ v_{Cd}^{\Delta};\ v_{Cq}^{\Delta};\ v_{CZ_d}^{\Delta};\ v_{CZ_q}^{\Delta};\ \dots \\ \dots\ &\underbrace{\theta_C;\ \xi_{pll};\ i_z^{\Sigma};\ v_{Cz}^{\Sigma};\ v_{dc};\ \xi_{i_d^{\Delta}};\ \xi_{i_q^{\Delta}};\ i_d^{\Delta};\ i_q^{\Delta}}\ ]^{\top} \in \mathbb{R}^{19} \\ &\text{Common states between the full and reduced order model} \end{aligned} \tag{4.26}$$

while the states of the reduced system are listed in $\boldsymbol{x}_{\boldsymbol{dqz}}^{\boldsymbol{Red.}}$:

$$\boldsymbol{x}_{\boldsymbol{dqz}}^{\boldsymbol{Red.}} = \left[\theta_C;\ \xi_{pll};\ i_z^{\Sigma};\ v_{Cz}^{\Sigma};\ v_{dc};\ \xi_{i_d^{\Delta}};\ \xi_{i_q^{\Delta}};\ i_d^{\Delta};\ i_q^{\Delta}\right]^{\top} \in \Re^9 \tag{4.27}$$

Finally, in (4.21), the inputs for both LTI systems[5] are gathered.

$$\boldsymbol{u}_{\boldsymbol{dqz}} = [\underbrace{P_l^*;\ v_d^G;\ v_q^G}_{\text{Physical inputs}};\ \underbrace{v_{dc}^*;\ P_{ac}^*;\ Q_{ac}^*}_{\text{Control inputs}}]^{\top} \in \mathbb{R}^7 \tag{4.28}$$

The developed small-signal models of the MMC are compared with time domain simulations against the *EMT* model with *Classical CCSC*, the LTI models (whose parameters are given in Table 4.2) are discussed in the following:

1. *Full*: LTI model of the interconnected system from Fig. 4.26a, implemented in Simulink. The operating point corresponds to the nominal ratings.

2. *Red.*: LTI model of the interconnected system from Fig. 4.26b, implemented in Simulink. The operating point corresponds to the nominal ratings.

Starting with a DC power transfer of 1 pu (from DC to AC), a step is applied on P_l^* of -0.1 pu at 0.05 s. The reactive power is controlled to zero during the whole simulation. Simulation results are gathered in Fig. 4.27.

At first glance, it is evident that the simplified model doesn't reproduce accurately the behavior of the complete model. The oscillations on the electrical variables are poorly damped in the *Reduced* order model with respect to the *Full* order and EMT models. The frequency of the oscillations is around 100 Hz for both models, as it was expected by (4.25).

4.4.3 Models comparisons with respect to their small-signal dynamics

In this section the complete and reduced model are compared in order to verify the validity of the simplified one. The comparisons are performed by different parametric sweeps as it was done in Section 4.3.4.

Variation of operating point

The first comparison is performed via a parametric sweep in terms of DC power transmission P_{dc} from 1 pu to -1 pu. Results are shown in Fig. 4.28.

As it can be seen from Fig. 4.28, an interesting phenomenon is observed: when the power decreases from 1 pu to -1 pu, the eigenvalues that corresponds to the DC current (See Section 3.2.3) become more damped for the *Full* order model, while the eigenvalues of the *Reduced* order model become less damped. This phenomenon is verified with a similar time domain simulation as performed in Section 4.4.2, but in this time the initial DC power direction is given by $P_{dc} = -1$ pu, and the simulated event is a power step P_l of 0.1 pu. Results are gathered in Fig. 4.29, where it can be seen that the *Reduced* order model present more damping than the EMT and *Full* order model.

[5]The *Full* order model has also the circulating currents references $\boldsymbol{i}_{\boldsymbol{dq}}^{\boldsymbol{\Sigma *}}$ but since they are set to zero the whole time they are not added in (4.28).

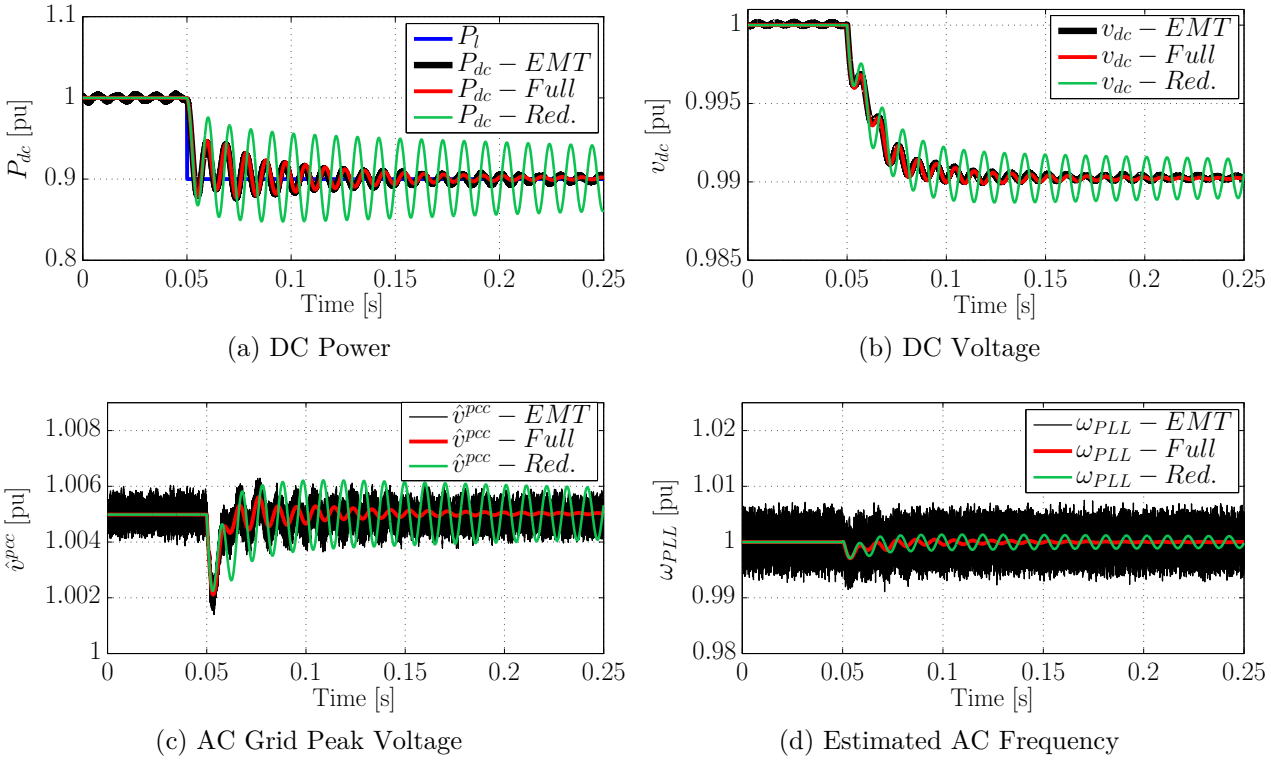

(a) DC Power

(b) DC Voltage

(c) AC Grid Peak Voltage

(d) Estimated AC Frequency

Figure 4.27 – Reduced Order Model Comparison of MMC with *Classical CCSC* - $P_{dc} = 1$ pu. *EMT* : EMTP-RV simulation; *Full* : LTI model from Fig. 4.26a; *Red* : LTI model from Fig. 4.26b.

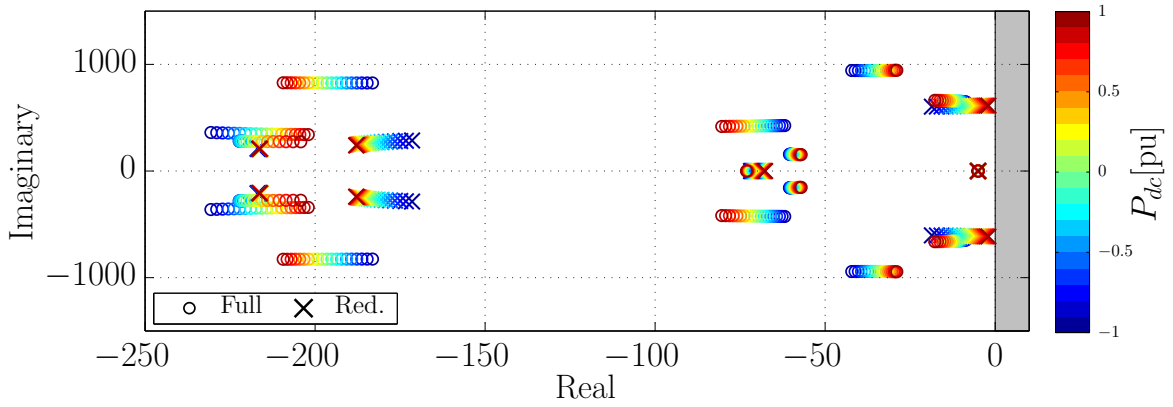

Figure 4.28 – Eigenvalues trajectories for P_{dc} variation ($k_d = 0.1$ pu) – Complete and reduced MMC model with *Classical CCSC* and UCM

Variation of DC droop gain

In this case, the droop parameter k_d is varied from 0.2 pu down to 0.05 pu. The considered power direction is from AC to DC since it is the worst case as seen in the previous section. Results are shown in Fig. 4.30. When lower values of droop are used, the pair of eigenvalues related to the DC current shifts to the right-hand plane (RHP) in both models. However, the *Reduced* model becomes unstable first.

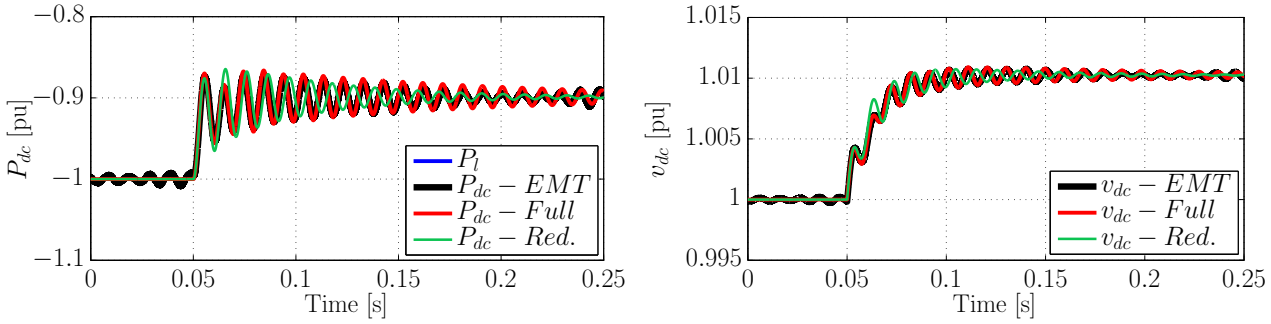

(a) DC Power (b) DC Voltage

Figure 4.29 – Reduced Order Model Comparison of MMC with *Classical CCSC* - $P_{dc} = -1$ pu. *EMT* : EMTP-RV simulation; *Full* : LTI model from Fig. 4.26a; *Red* : LTI model from Fig. 4.26b.

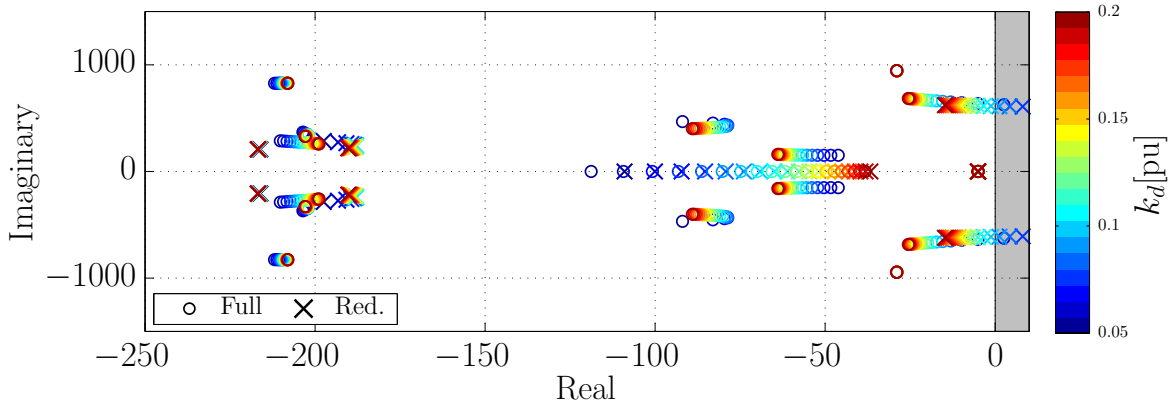

Figure 4.30 – Eigenvalues trajectories for k_d variation ($P_{dc} = 1$pu) – Complete and reduced MMC model with *Classical CCSC* and UCM

Variation of AC grid strength

For the last comparison, the AC grid strength is varied. In this case, the grid current controllers are modified as depicted in Fig. 4.21, by the addition of first order filters on the feed-forward AC voltage compensations. As already performed for the *Energy-based* controller, the SCR is decreased from 10 down to 3. Results are gathered in Fig. 4.31. Conversely, comparing to the droop gain variation, the *Full* order model is unstable for higher values of SCR than the *Reduced* order model. However, the difference is not highly noticeable.

As it is was shown in the eigenvalues comparisons from Figs. 4.28, 4.30 and 4.31, the *Reduced* order model cannot replicate with high accuracy the complete model when the MMC is considered to be controlled with the *Classical CCSC* and modulated with the UCM. When considering bigger systems, the noticeable difference in the behavior of both models from an AC and DC standpoints could potentially lead to false or biased results as a consequence of different couplings and interactions. However, it is recalled that the *Reduced* order model that results from these control considerations was already widely used in the bibliography [184]. In terms of computational time, the use of the *Full* order model doesn't necessarily correspond to big differences with respect to the *Reduced* order model. For this reason, when *Classical CCSC* and UCM is considered, it is recommended to consider the *Full* order model for not compromising the accuracy of the results.

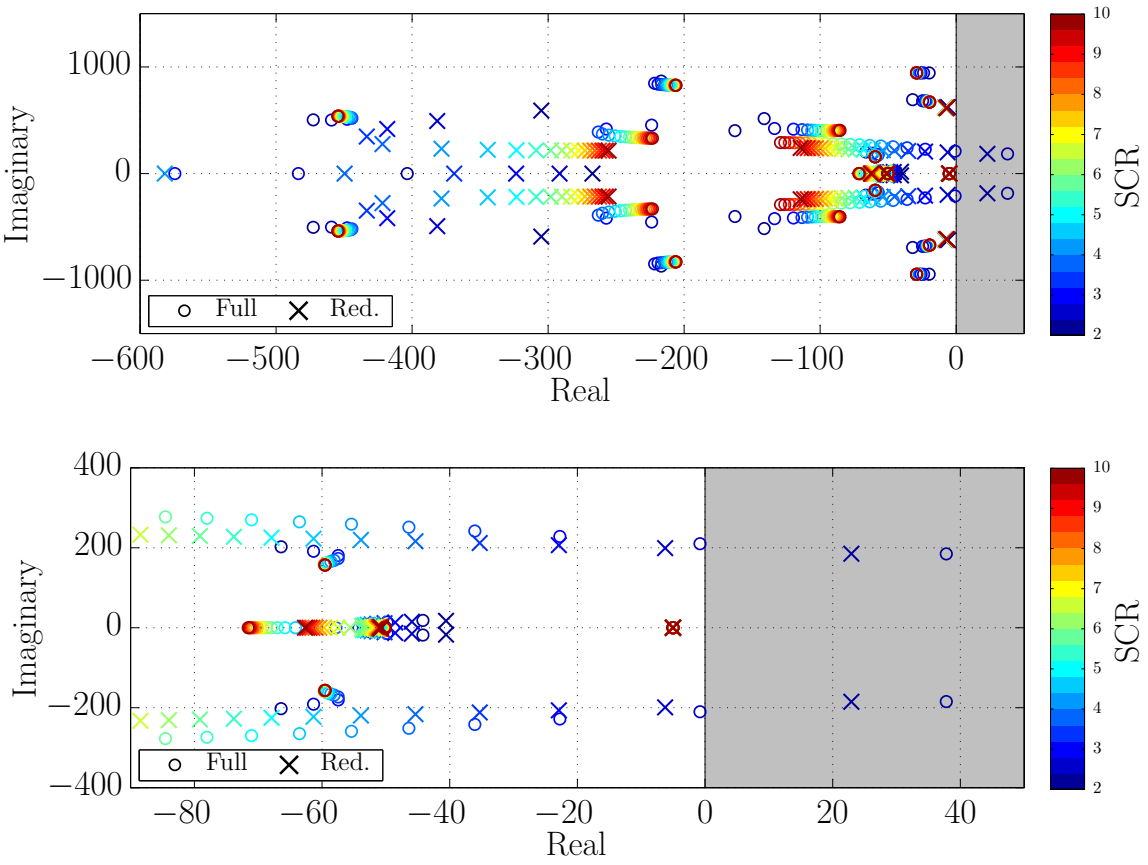

Figure 4.31 – Eigenvalues trajectories for SCR variation ($P_{dc} = 1$pu) – Complete and reduced MMC model with *Classical CCSC* and UCM

4.5 Frequency domain analysis

The impedance-based system stability studies gained a lot of popularity in the past years [185, 186]. Recent works already dealt with the impedance modeling with complete analytic formulations of the MMC AC and DC side impedances [187,188]. However, the control strategy adopted for the MMC was the *Classical CCSC*. The following comparison is carried out on the frequency domain characteristics of the *Full* and *Reduced* order models already compared via time-domain simulations and eigenvalues. It is important to note that this study is performed only to give a final conclusion on the utilization of the reduced order MMC model for linear analysis. In this section, it is proven that accurate representations can be obtained directly from the respective LTI models (for the full and reduced order model). Also, the comparison between the different control strategies highlighted in this Chapter allows to determine the validity of the reduced order model for representing the complete MMC from an AC or DC standpoint.

Firstly, it is recalled how to obtain the relation between one input and output (i.e. SISO) from the complete state-space LTI model (i.e. MIMO). Let us consider the MIMO system from (4.29) where s is the Laplace operator.

$$\begin{cases} s\,\boldsymbol{x_{sys}}(s) &= \boldsymbol{A_{sys}}\,\boldsymbol{x_{sys}}(s) + \boldsymbol{B_{sys}}\,u_{sys}(s) \\ y_{sys}(s) &= \boldsymbol{C_{sys}}\,\boldsymbol{x_{sys}}(s) + D_{sys}\,u_{sys}(s) \end{cases} \tag{4.29}$$

In (4.29), the vector $\boldsymbol{x_{sys}}$ represent the system states, and it is only considered one input u_{sys} and one output y_{sys}. The matrices $\boldsymbol{A_{sys}}$, $\boldsymbol{B_{sys}}$, $\boldsymbol{C_{sys}}$ and the constant D_{sys} are obtained from

the linearization of the SSTI models. Note that the operating point defined by $(\boldsymbol{x_{sys0}}, u_{sys0})$ used for the linearization is already embedded in the matrices from (4.29). The relation between the input u_{sys} and output y_{sys} is then obtained as:

$$\frac{y_{sys}(s)}{u_{sys}(s)} = \boldsymbol{C_{sys}} \left(s\boldsymbol{I} - \boldsymbol{A_{sys}}\right)^{-1} \boldsymbol{B_{sys}} + D_{sys} \tag{4.30}$$

From a physical perspective, if the input u_{sys} is the perturbation current i_l and the output y_{sys} is chosen as the DC bus voltage v_{dc}, the relation from (4.30) gives the DC impedance $Z_{dc}(s)$ as follows[6]:

$$Z_{dc}(s) = \frac{y_{sys}(s)}{u_{sys}(s)} = \frac{v_{dc}(s)}{i_l(s)} \tag{4.31}$$

Contrariwise, if the input u_{sys} is a perturbation around the input voltage v_d^G and the output y_{sys} is chosen as the grid current i_d^Δ, the relation from (4.32) gives the AC-side admittance $Y_{ac,d}(s)$ as follows:

$$Y_{ac,d}(s) = \frac{y_{sys}(s)}{u_{sys}(s)} = \frac{v_d^G(s)}{i_d^\Delta(s)} \tag{4.32}$$

The DC-side impedance and AC-side admittance for the LTI models (*Full* and *Red.*) are obtained from the direct application of (4.30) or (4.32) for each model. For obtaining the frequency responses of the EMT simulation model, the procedure detailed in [189] is used[7].

4.5.1 Energy-based controller with CM

The DC side impedance $Z_{dc}(s)$ is calculated for the *Full* and *Reduced* order model, and compared in the frequency domain in Fig. 4.32 for $P_{dc} = -1$ pu. As it can be seen, both results are the same for the considered operating point (nominal ratings) and chosen controllers. Moreover, both LTI models match very accurately with the EMT simulation, in which the 400 sub-modules per arm and associated balancing controllers are taken into account.

In Fig. 4.33, the comparison of the AC-side admittance $Y_{ac,d}$ is shown. In this case, a small offset can be observed for the EMT model with respect to both LTI models. This is due to the losses in the MMC which are not exactly the same as the LTI model. For frequencies higher than 1 kHz, a small but noticeable discrepancy is noticed on the magnitude and phase of the frequency response.

As it was previously discussed, the parametric sweep with respect to a variation of P_{dc} doesn't cause significant shift of the eigenvalues (See Fig. 4.15). In the frequency domain, this means that the DC-side and the AC-side admittances are not modified due to the DC operating point change. Most importantly, the use of the *Full* or *Reduced* order model for this particular control strategy is indistinct, i.e. same results can be obtained from both models for this type of linear studies.

4.5.2 Classical CCSC with UCM

In Fig. 4.34, the DC side $Z_{dc}(s)$ impedance that results from both LTI models for $P_{dc} = -1$ pu is shown. As it can be seen, the amplitude and phase of both models are very similar

[6]Strictly, a new current should be introduced on the DC bus independent from the DC power source to obtain $Z_{dc}(s)$. However, since the expression is linearized, perturbing the DC power source for small variations is equivalent to a current perturbation.

[7]The author acknowledge Dr. Hani Saad for helping with the simulation for obtaining the EMT results.

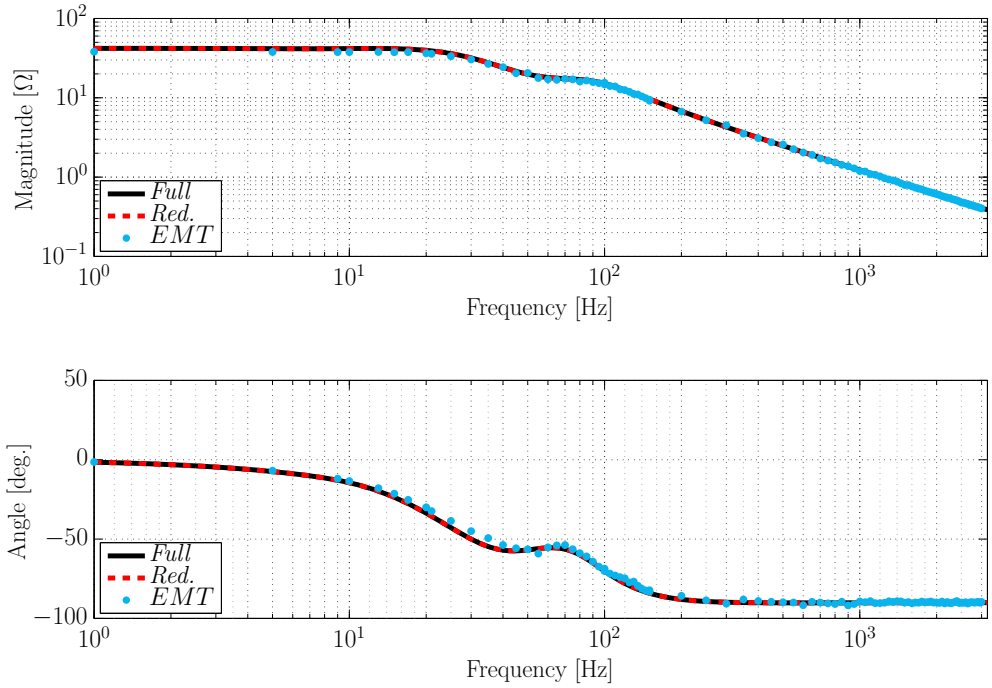

Figure 4.32 – DC side impedance $Z_{dc}(s)$ - EMT, *Full* order and *Reduced* order MMC model with *Energy-based* control and CM - $P_{dc} = -1$ pu

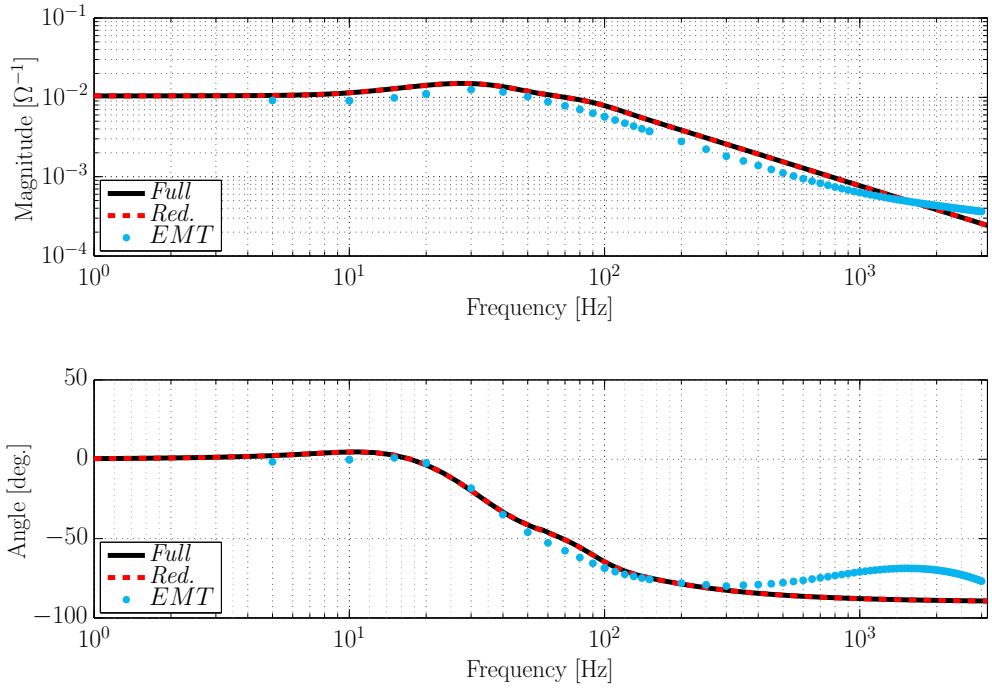

Figure 4.33 – AC side admittance $Y_{ac,d}$ - EMT, *Full* order and *Reduced* order MMC model with *Energy-based* control and CM - $P_{dc} = -1$ pu

for frequencies lower than 20 Hz, and higher than 200 Hz. Between 20 Hz and 200 Hz, the impedance is very different. There is a noticeable peak around 100 Hz (although, not exactly at the same frequency), which is the frequency of the oscillations seen in the time-domain results from Fig. 4.27 (for $P_{dc} = 1$ pu) and Fig. 4.29 (for $P_{dc} = -1$ pu). However, the magnitude of

the impedance at 100 Hz for the reduced order model is higher compared to for the full order model.

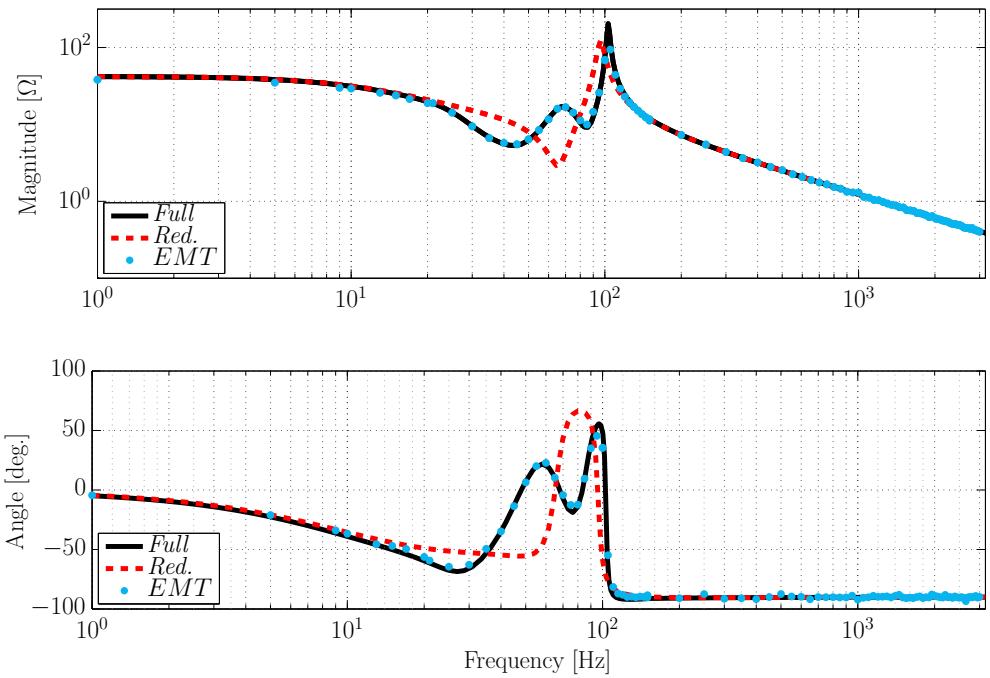

Figure 4.34 – DC side impedance $Z_{dc}(s)$ - EMT, Complete and reduced MMC model with *Classical CCSC* and UCM - $P_{dc} = -1$ pu

In Fig. 4.35, the comparison of the AC-side admittance $Y_{ac,d}$ is shown. For frequencies higher than 500 Hz the LTI models start diverging from the EMT simulation model. This is highly noticeable in the phase for the high frequency range (> 1 kHz).

When considering the *Classical CCSC* control strategy with UCM, the MMC dynamics depends highly on the active power direction, as discussed in Section 4.4. This means that for each active power operating point, the DC-side impedance and AC-side admittance varies considerably. Nevertheless, for a frequency range lower than 1 kHz, the MMC-SSTI model from Chapter 2 (i.e. *Full* order model) is able to reproduce the internal dynamics and AC- and DC- port behavior of the converter. However, the *Reduced* order model fails to reproduce the frequency response of the EMT model.

Once more, it is shown that it is not a good choice the use of the *Reduced* order model for representing the MMC when it is controlled with *Classical CCSC* with UCM.

4.6 Chapter Conclusions

The development of simplified MMC models for interfacing AC and DC grids is an important topic nowadays for the large-scale studies such as MTDC grids. However, to guarantee the validity of results for the DC grids, the fidelity of the reduced order model should not be compromised as little as possible. In this Chapter it was first introduced a simplified MMC reduced order model. Then, the small-signal dynamics of the resulting systems where studied. This task was performed for two different control strategies developed in Chapter 3.

For the analysis of MTDC grids in the following of this Thesis, two models will be adopted with respect to the control strategy adopted in the MMC:

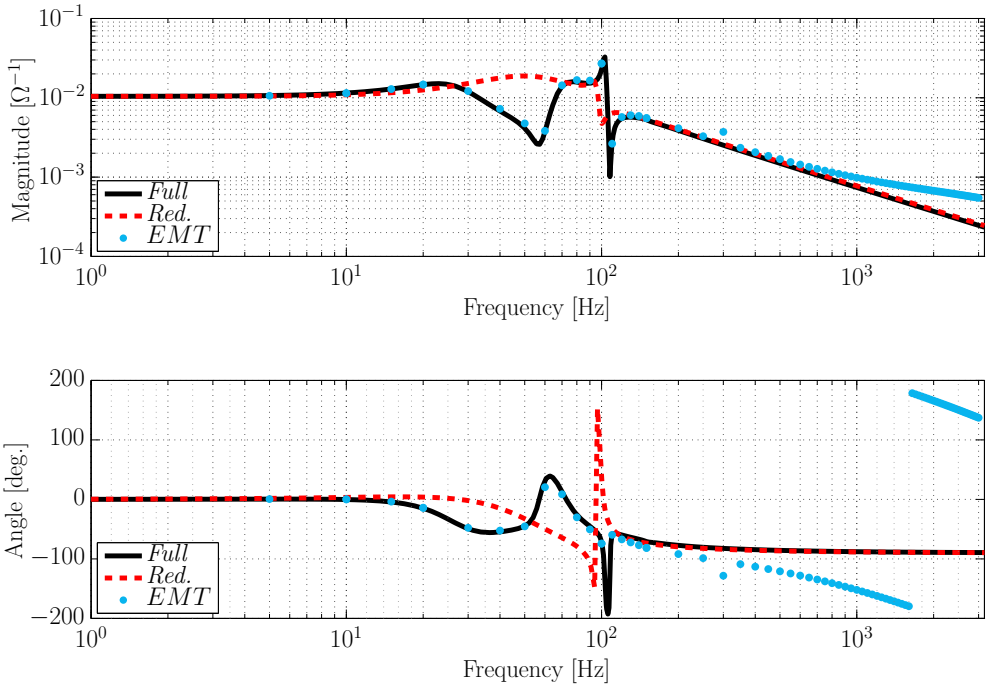

Figure 4.35 – AC side admittance $Y_{ac,d}$ - EMT, Complete and reduced MMC model with *Classical CCSC* and UCM - $P_{dc} = -1$ pu

- ***Energy-based* controllers with CM:** For this control strategy, the use of the *Reduced* order model is adapted for AC and DC grids without compromising the results. As it was introduced in Chapter 3 and formally demonstrated in this Chapter, the adoption of these control strategies allows a perfect decoupling between the internal MMC variables. For this reason, the *Reduced* order model reproduces accurately the MMC from a macroscopic way.

- ***Classical CCSC* with UCM:** In this case, the use of the *Reduced* order model will not be adopted in this Thesis. Instead, the *Full* order model is used. Thanks to the adopted modeling tools, the limitations of the usage of the *Reduced* order model were highlighted (also called called "Model #4: *AVM of MMC*").

Other control mixes, such as the utilization of *Energy-based* controllers with UCM, can be studied with the elements provided in this Chapter. However, due to the high number of control combinations, this Thesis will focus only on the aforementioned possibilities.

Chapter 5

Dynamic Analysis of MMC-Based MTDC grids for Interoperability Studies

5.1 Introduction

In multivendor MTDC grids, it is possible that the control strategies adopted on each converter station may differ. As it was studied in previous Chapters, different control techniques result in different DC voltage dynamics. Since, as discussed in Section 1.4, the analogous variable to the AC frequency on the DC grids is the DC voltage, the accurate control of this variable is fundamental for the proper functioning of the grid. For exemplification purposes, let us consider a generic four terminal MMC-based MTDC grid as depicted in Fig. 5.1. Comparing this scheme with the *2-level* VSC-based MTDC grid from Fig. 1.27, it can be observed that in Fig. 5.1, the DC capacitors are no longer part of the converters themselves, but from the equivalent capacitors from the cable models (marked in blue) [176]. The aforementioned capacitance may be more than 30 times smaller than for the case of *2-level* VSC, meaning that the voltage dynamics at each endpoint is highly volatile (see Appendix A and H).

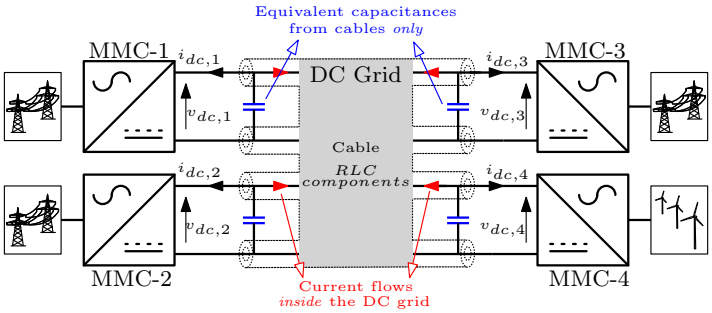

Figure 5.1 – Four terminal MMC-based MTDC grid: Available DC measures for each converter

In MTDC grids, the power flow is driven by the different DC values at each endpoint and the impedances of the DC grid, which depends on the DC grid scheme. If no communication is considered between the converters, when the DC voltage in a given station is perturbed (e.g. a change on the DC power setpoint), currents inside the grid are generated (marked in red). The propagation of the perturbation inside the grid is not instantaneous due to the DC grid impedances. Since the only available DC measure on the the other stations is their respective DC voltage, the MMC should react as fast as possible to clear the perturbation.

If the DC voltage dynamics at each endpoint are properly controlled, the risk of interactions between stations is highly diminished. Linear analysis tools can be used to study the MTDC dynamics but the generalization of findings and conclusions is a difficult task without taking into account each possible configuration [190]. In this Chapter it is intended to highlight the main key parameters of the DC grid dynamics with special focus on the DC voltage for MMC-based MTDC grids and how the MMC could be controlled to improve the DC voltage dynamics. Improving the behavior of the DC voltage reduces the interactions and enhances the interoperability of different converters.

This Chapter is focused on the DC dynamics in $N-1$ conditions, where heavy and abrupt changes on the DC power flows occur [191]. This case, which may be considered as a possible scenario, should be resolved by the converters with the measures that are available at each endpoint. In the considered MTDC, the converters connected to onshore terminals are equipped with droop controller to ensure a distributed control of the DC voltage at each endpoint without relying on external communications [192]. The rest of this Chapter is organized as follows: In Section 5.2, the modeling basis of the four-terminal MTDC grid are given: the EMT configuration as well as the linearized LTI model are detailed. In Section 5.3, the small-signal analysis tools used in the rest of the Chapter are described: eigenvalue analysis and Singular Value Decomposition (SVD). The influence of the MMC internal energy on the MTDC dynamics is studied in Section 5.4. Two different control options for the energy management in *Energy-based* controllers are presented in Section 5.5. In Section 5.6, a final time domain simulation is performed with detailed MTDC model in EMTP-RV, contrasting the results and validating the concepts discussed along the present Chapter.

5.2 MMC-Based MTDC modeling

5.2.1 EMT modeling of MMC-based MTDC grids

The four terminal MMC-based MTDC grid used as a benchmark for this Chapter is shown in Fig. 5.2. This configuration is similar to the one already introduced in Section 1.4. In the EMT *Simulation model* used as a reference, the MMCs are modeled with the so-called "Model # 2: *Equivalent Circuit-Based Model*" (ECBM) from [111] as already performed in the rest of this Thesis. However, the use of "Arm Averaged Models" is also a valid option for reducing the simulation time [193].

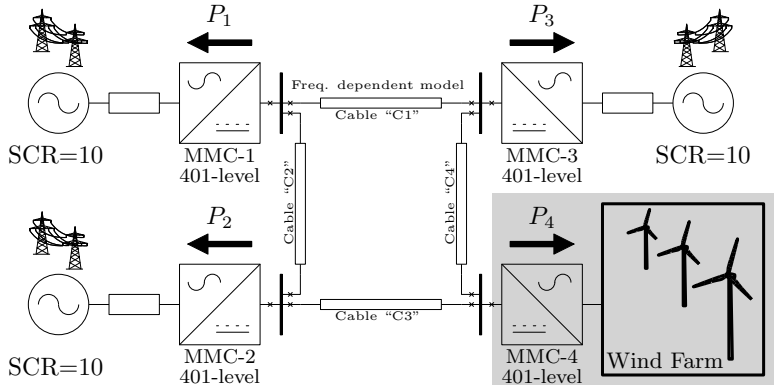

Figure 5.2 – Four terminal MMC-based MTDC grid used as a benchmark in this Chapter

Converters MMC-1, MMC-2 and MMC-3 are connected to onshore AC grids and they are equipped with DC voltage droop controllers. Even if many different droop techniques can be

found in the literature, the most common proportional droop control is taken into account as discussed in Section 1.4.1. For simplicity, each AC grid is considered to be equal, with a SCR of 10. In this Chapter, the focus is given to the DC-side interactions and not too much emphasis on the AC-side.

The model of the Wind Farm (WF) and its associated converter (MMC-4) is modeled[1] as shown in Fig. 5.3a. Note that the WF model and its power P_{wf} is modeled similarly as the "DC side connection" from Chapter 4 [95, 194]. The capacitor C_{wf} has a value of 10 μF (with the base parameters from Appendix A, corresponds to an electrostatic constant of $H_{cw} = 2.05$ ms). This value corresponds a very low level of DC energy storage, which allows to excite the dynamics of the complete MTDC grid when the power P_{wf} is varied.

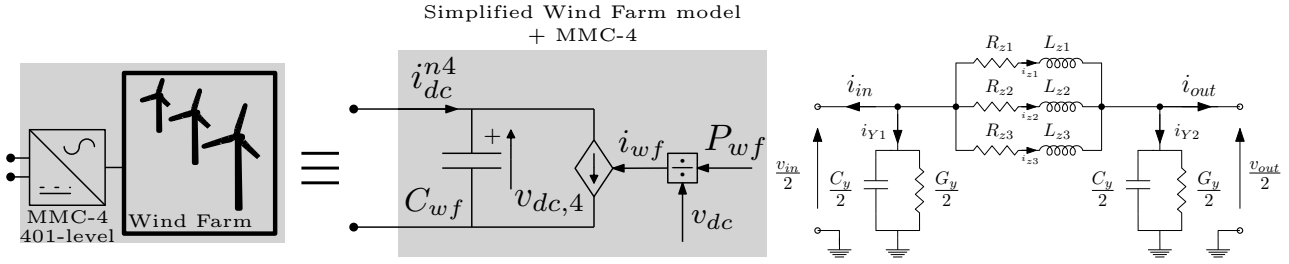

(a) Equivalent representation of Wind Farm and MMC-4 simplified model for DC grid analysis

(b) Equivalent circuit of "FD-Π model" with 3 parallel branches

Figure 5.3 – Wind farm and cable models for EMT simulation

The DC grid is composed by four sections of cables with equal length for simplicity (70 km), namely "$C1$", "$C2$", "$C3$" and "$C4$". Each cable is modeled with the *Frequency Dependant-PI model* (FD-Π) from [195, 196], which is shown in Fig. 5.3b. Modeling details and parameters of the FD-Π are detailed in Appendix H.

5.2.2 Small-Signal modeling of MMC-based MTDC grids

The small-signal model of the MTDC grid is performed following the methodology explained in Section 1.4, where several steps are carried out [197,198]. The most important concept is that the overall state-space representation of the MTDC system is obtained by the concatenation of different linear sub-systems (DC grids, AC grids, MMCs and their controllers) [9, 74]. The complete system is shown in Fig. 5.5 and the main steps for obtaining the state-space linear representation (LTI model) are discussed as follows:

1. **Creation of DC grid state-space representation:** The grid is formed with four FD-Π cable models detailed in Appendix H. This model is linear by nature (only RLC components). The capacitors of each node of connection with the MMCs are not considered in the state-space representation of the DC grid; instead, they are considered in the modeling of the MMCs. This way, the boundary of each converter results similar as the configurations already studied among this Thesis (e.g. in Chapter 3).

2. **Creation of LTI models of Converters with DC capacitor and controllers in linear state-space representation:** The considered structure is shown in Fig. 4.2, but in this case the DC input is a current resulting from the sum of all the currents arriving

[1]Strictly, the offshore MMC should be modeled similarly as the onshore MMC, and the WF model should be feeding the AC-power: this is adopted in **Journal II**, but the results of this Chapter don't lose generality.

to the node of Point of Common Coupling on the DC side (PCC-DC). Also, note that the considered capacitor for each MMC is the sum of all the DC cables capacitors of the cables being connected to the PCC-DC (See Fig. 5.4). It is recalled that the adopted MMC model depends on the control strategy considered: if the MMC is controlled with the *Classical CCSC* with UCM, the *full order* SSTI-MMC from Chapter 2 model is adopted. Contrariwise, if the MMC is controlled with the *Energy-based* controller with CM, the *reduced order* SSTI-MMC model is used instead, as concluded from Chapter 4.

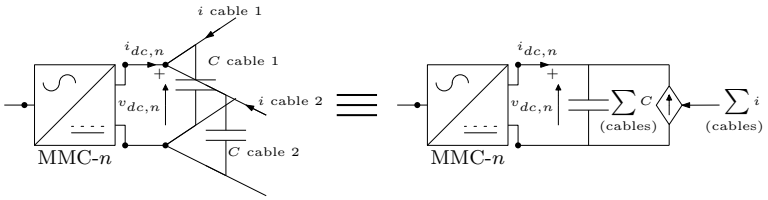

Figure 5.4 – Example of LTI MMCs with DC capacitor for small-signal MTDC model

3. **Calculation of Operating Point:** First, a DC load flow calculation is used to obtain all the DC voltages and currents at each PCC-DC [199]. This information is used as "known variables" for solving the non-linear equations of each MMC in a step-by-step process. This means that the process is sequential and it is not intended to solve all the system equations at once due to possible numerical convergence issues.

4. **Concatenation of linear subsystems:** Once the solutions of the operating point are obtained, it is possible to transform the matrices of the linear systems for each component and then combined into a single state-space global representation with the methodology explained in Appendix B [9].

5.2.3 Time Domain Validation

In order to validate the small-signal modeling approach, time-domain simulations are performed with the EMT model of the MTDC grid in EMTP-RV and the small-signal model with Matlab/Simulink. All DC cables are considered to have an equal length (70 km each one). The simulation case starts with a DC load flow provided in Table 5.1[2]. This DC operating point is independent from the control strategy adopted for the converters. At $t = 20$ ms, a sudden reduction of 0.1 pu of wind power production P_{wf} is simulated. In the following, the same case scenario is carried out considering *Classical CCSC*, or *Energy-based* control strategies.

Table 5.1 – DC Load Flow for time-domain simulations — Base values: 1000 MW; 640 kV

Station	Nominal power [MW]	P_{dc} [pu]	v_{dc} [pu]
MMC-1	1200	1.1930	1
MMC-2	1000	0.4	1.0017
MMC-3	1000	-0.6	1.0041
Wind Farm	1000	-1 (P_{wf})	1.0053

For setting the droop parameter k_d for each controller, the methodology explained in Section 1.4.2 is applied based on the steady-state deviation for a total loss of 1 pu of wind power

[2]Note that the Nominal Power of MMC-4 is 1200 MW, and the common base is chosen as 1000 MW.

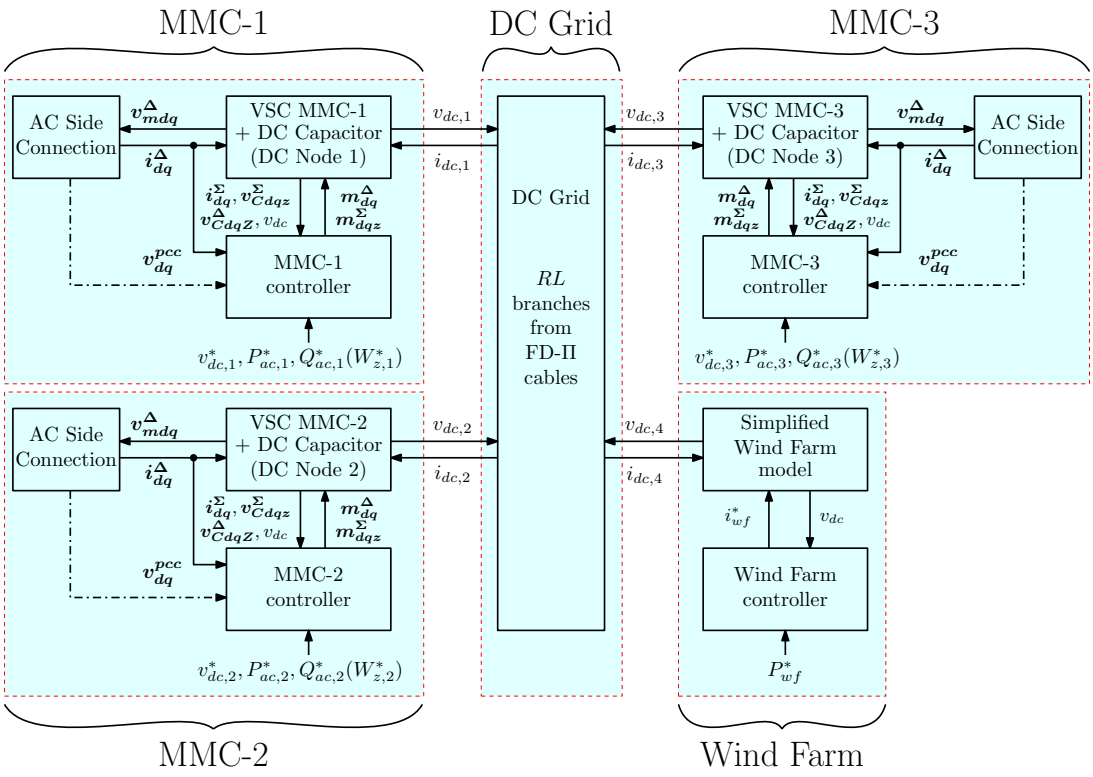

Figure 5.5 – SSTI model equations of MMC-based MTDC grid for linearization

production referred to as ΔP_{wf}, which is an $N-1$ condition. For an allowed ± 0.05 pu of DC voltage deviation around the operating point in $N-1$ conditions, the droop parameters k_d are set to 0.15 pu (see (1.57)).

Converters with Classical-CCSC

The first comparison considers that the control strategy for each MMCs is the *Classical CCSC* from Section 3.2 [135]. The simulation results of the DC powers are shown in Fig. 5.6a, which show that both modeling approach conduce to similar time-domain results. The DC power step on P_{wf} causes an imbalance in the DC power inflow, so the MMCs equipped with droop controller adjust their powers for achieving a new steady state condition.

Results of the DC voltage are gathered in Fig. 5.6b. As it can be seen, there is an offset on the final value for the DC voltages due to the voltage droop controllers. Results from Fig. 5.6a and 5.6b validate the small-signal model of the MTDC grid.

Converters with Energy-Based controllers

On this comparative study based on EMT simulation, the converters are equipped with the *Energy-based* controller described in Section 3.4. The EMT model takes into account the complete non-linear model and its controllers, while the LTI model is formed with the *Reduced order* model detailed in Chapter 4.

Simulation results of the DC powers at each endpoint are shown in Fig. 5.7a. In comparison with previous results where *Classical CCSC* was considered, the DC power transient results in less oscillations, and the steady-state condition is achieved faster. In Fig. 5.7b, the results of the DC voltages at each endpoint are shown. Comparing with Fig. 5.6b, the voltage transients present less oscillations, but a more pronounced peak after the simulated event is observed.

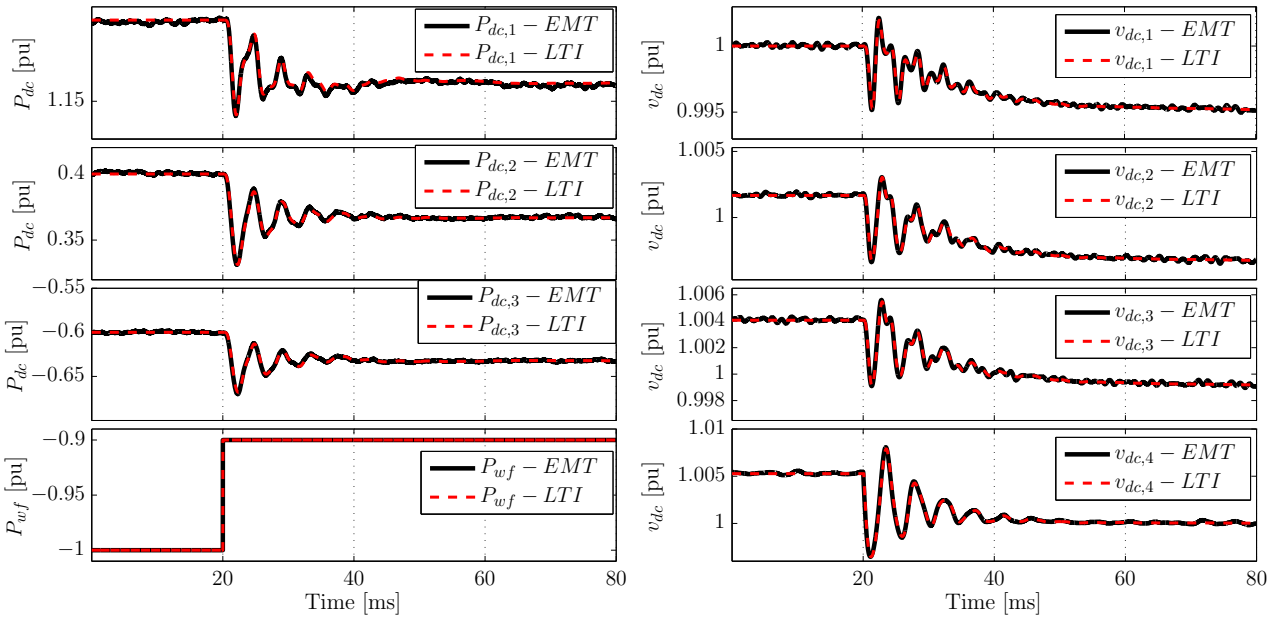

(a) DC Power

(b) DC Voltage

Figure 5.6 – Comparison of time-domain simulations of EMT and small-signal model (LTI) of a four terminal MTDC grid - Converters are equipped with *Classical CCSC*

Nevertheless, results from Fig. 5.7a and 5.7b validate the LTI model of the MTDC grid when considering *Energy-based* controllers for the converters.

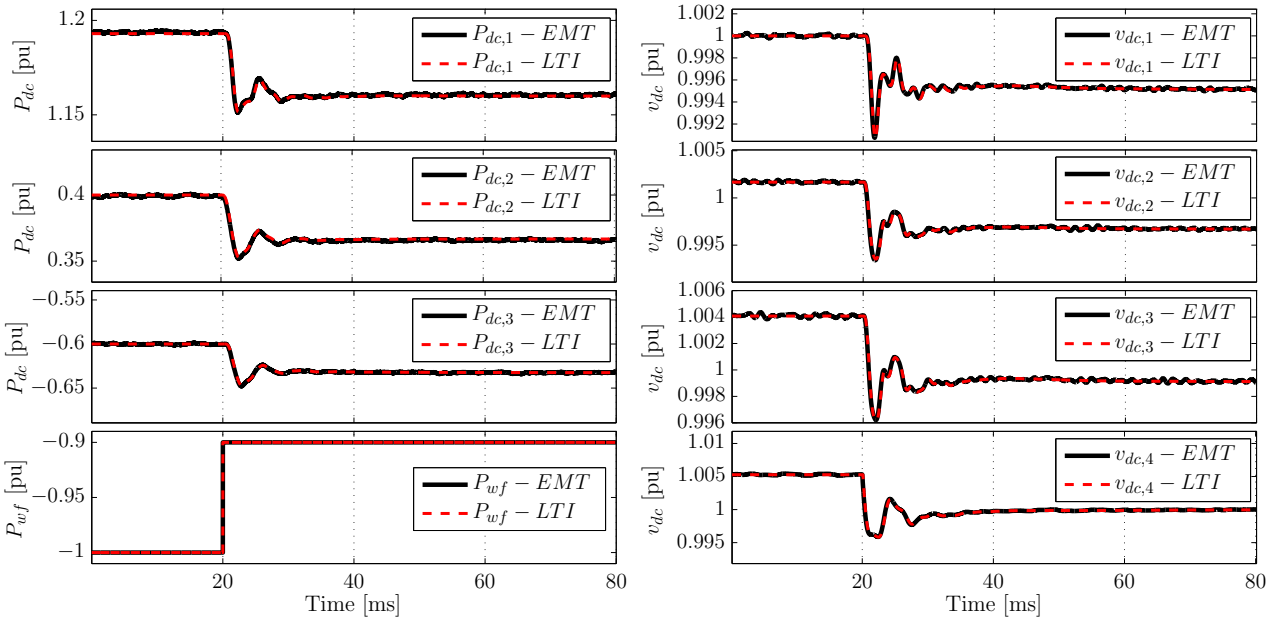

(a) DC Power

(b) DC Voltage

Figure 5.7 – Comparison of time-domain simulations of EMT and small-signal model (LTI) of a four terminal MTDC grid - Converters are equipped with *Energy-based* controllers

5.3 MTDC Linear analysis tools

In this section, analytic tools for the validated LTI system are applied. First, a brief analysis based on the eigenvalues of the MTDC is given. Then, the singular value decomposition method (SVD) is used for characterizing the system.

5.3.1 Eigenvalue analysis

Converters with Classical-CCSC

In this case, the complete LTI system is represented by 70 dynamic states (19 states from MMC-1, MMC-2 and MMC-3 and their controllers, as shown in (4.26), 1 state from MMC-4 and the Wind Farm and 3 states for each inductance of the cables). The eigenvalues of the LTI model when considering the converters with *Classical-CCSC* from Section 5.2.3 are shown in Fig. 5.8. This figure also shows the zone (marked in gray) where the damping of the eigenvalues laying inside the region have a damping ζ higher than 0.6 [72]. As it can be observed, many eigenvalues are placed outside this marked zone, meaning that many poles of the system are poorly damped. Also, several modes overlap due to the similar parameters of the converters.

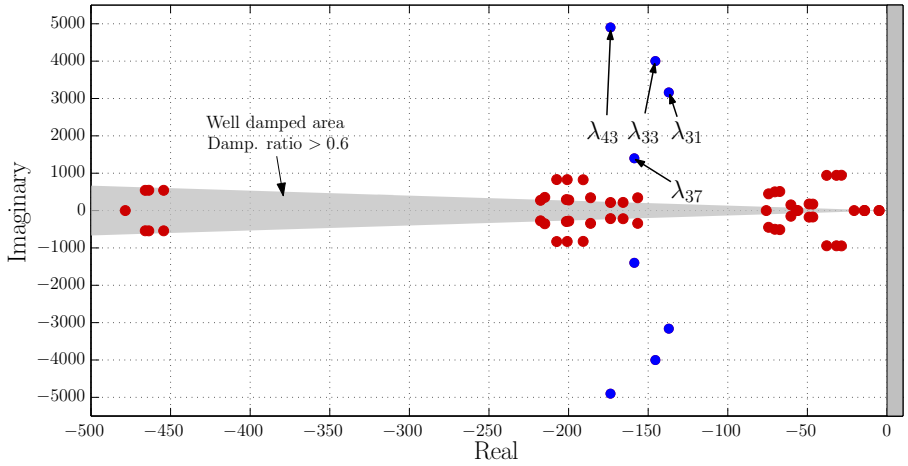

Figure 5.8 – LTI Eigenvalues - MMC equipped with *Classical-CCSC*

From the participation factor analysis (which is not shown since it doesn't provide additional information), it can be observed that many poles are related to many state variables from different converters. This coupling makes extremely difficult the proper analysis based only on the modes and they may even lead to uncertain conclusions [85]. From Fig. 5.8, special attention will be given to the eigenvalues $\lambda_{31,32}$, $\lambda_{33,34}$, $\lambda_{37,38}$ and $\lambda_{43,44}$, since they have participation from the DC voltage states. The selected eigenvalues are listed in Table 5.2.

Table 5.2 – DC Voltage related eigenvalues — MMCs with *Classical CCSC*

λ_i	**Eigenvalue**	**Freq. [Hz]**	**Damp. ratio**	**Dominant States** (From Participation Factor analysis)
$\lambda_{31,32}$	$-137 \pm j3162.1$	503.3	0.04	$i^{\Sigma}_{z,1}$; $v_{dc,1}$; $v_{dc,2}$; $v_{dc,3}$; $v_{dc,4}$; i^{C3}_{z1} ; i^{C4}_{z1}
$\lambda_{33,34}$	$-145.5 \pm j4001.3$	636.8	0.03	$i^{\Sigma}_{z,2}$; $v_{dc,2}$; $i^{\Sigma}_{z,3}$; $v_{dc,3}$; i^{C1}_{z1} ; i^{C2}_{z1} ; i^{C3}_{z1}; i^{C4}_{z1}
$\lambda_{37,38}$	$-158.7 \pm j1398.9$	222.7	0.1	$i^{\Sigma}_{z,2}$; $i^{\Sigma}_{z,3}$; $v_{dc,4}$; i^{C3}_{z1}; i^{C4}_{z1}
$\lambda_{43,44}$	$-173.7 \pm j4900.9$	780	0.03	$v_{dc,1}$; $v_{dc,2}$; $v_{dc,3}$; i^{C1}_{z1} ; i^{C2}_{z1}

Converters with Energy-based controllers

In this case, the analysis is carried out considering the *Energy-based* controllers, which was validated by time-domain simulations in Fig. 5.7. The complete LTI system has 52 states states (13 states from the reduced order models of MMC-1, MMC-2 and MMC-3 and their controllers, as shown in (4.20), 1 state from MMC-4 and the Wind Farm and 3 states for each inductance of the cables). Note that there are less eigenvalues than for the previous case, since now the *Reduced order* model is adopted; if the full order SSTI-MMC model had been used, the LTI would have had 136 states making difficult the linear analysis. The eigenvalues of the LTI system are plotted in Fig. 5.9. Also, as in previous case, several eigenvalues are overlapped due to the similar parameters used for the converters. After a participation factor analysis on each eigenvalues, the modes that have participation of the DC bus voltages are highlighted in blue, and listed in Table 5.3.

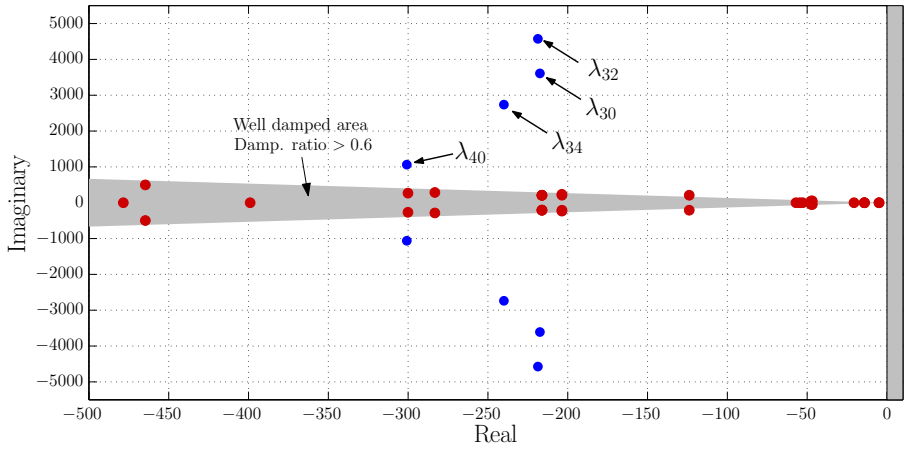

Figure 5.9 – LTI Eigenvalues - MMC equipped with *Energy-based* controller

Table 5.3 – DC Voltage related eigenvalues — MMCs with *Energy-based* controllers

λ_i	**Eigenvalue**	**Freq. [Hz]**	**Damp. ratio**	**Dominant States** (From Participation Factor analysis)
$\lambda_{30,31}$	$-217.5 \pm j3608.7$	574.3	0.06	$v_{dc,2}$; $v_{dc,3}$
$\lambda_{32,33}$	$-218.7 \pm j4572.9$	727.8	0.05	$v_{dc,1}$; $v_{dc,2}$; $v_{dc,3}$; i_{z1}^{C1} ; i_{z1}^{C2}
$\lambda_{34,35}$	$-240 \pm j2737.1$	435.6	0.08	$v_{dc,1}$; $v_{dc,4}$; i_{z1}^{C3} ; i_{z1}^{C4}
$\lambda_{40,41}$	$-300.8 \pm j1061.9$	169.02	0.27	$v_{dc,4}$; $i_{z,2}^{\Sigma}$; $i_{z,3}^{\Sigma}$

Comparing the eigenvalues from Tables 5.2 and 5.3, it can be seen that the eigenvalues related to the DC voltage at each converter are poorly damped, and the frequency range is between 400 Hz and 800 Hz for this particular configuration. This means that, a priori, the choice on the MMC controller as it was presented up to this point doesn't guarantee proper dynamics of the DC grid: the dynamics should be improved, and the issue of surpassing the allowed DC voltage deviation should be addressed. In the following, it is intended to explain the origin of this poorly damped modes of the system, and most importantly try to improve their locations for a better dynamic behavior of the MTDC grid.

The eigenvalue analysis is very powerful when the study is focused on the stability of the system. Nevertheless, when considering large MTDC schemes the number of dynamic states grows rapidly, and so the number of eigenvalues. For this reason, the utilization of

participation factors or sensitivity analysis are not easy to use and obtain general conclusions [27, 85]. Moreover, those techniques are only based on the $\boldsymbol{A}$ matrix of the linearized system, so the input-output relations of the system are not explicitly evaluated.

5.3.2 Singular Value Decomposition

For Multi-Inputs and Multi-Outputs (MIMO) systems, an useful tool is the Singular Value Decomposition (SVD), which is equivalent to the transfer function approach from Single-Input and Single-Output (SISO) systems [194, 200]. More information about the theory behind the SVD analysis can be found from [84]; in this Section it is only mentioned for a practical use.

SVD Theory recall

Once the linearized model is obtained, some inputs and outputs of interest are chosen. In this case, it is chosen the power reference from the Wind Farm as input ($\boldsymbol{u} = P_{wf}$). The considered outputs are the four DC voltages, so $\boldsymbol{y} = [v_{dc,1}\ v_{dc,2}\ v_{dc,3}\ v_{dc,4}]^\top$. Then, the matrix $\boldsymbol{G}(s)$ is created, which relates the chosen inputs and outputs [9], as shown in Fig. 5.10. Each element of the matrix $\boldsymbol{G}(s)$ is obtained as the SISO transfer functions as shown in Section 4.5. Of course, other options can be chosen at this step for the matrix $\boldsymbol{G}(s)$; this depends on the desired input-output relations of interest [201].

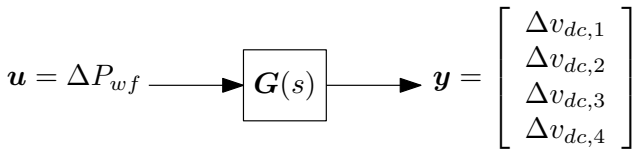

Figure 5.10 – SVD - Matrix $\boldsymbol{G(s)}$

The gain of the system $\boldsymbol{G}(s)$ between the input signal $\boldsymbol{u}(\omega)$ and the output $\boldsymbol{y}(\omega)$ is given by, in terms of the L^2 norm [9]:

$$\frac{\|\boldsymbol{y}(\omega)\|_2}{\|\boldsymbol{u}(\omega)\|_2} = \frac{\|\boldsymbol{G}(\omega)\boldsymbol{u}(\omega)\|_2}{\|\boldsymbol{u}(\omega)\|_2} = \frac{\sqrt{\Delta v_{dc,1}^2 + \Delta v_{dc,2}^2 + \Delta v_{dc,3}^2 + \Delta v_{dc,4}^2}}{\sqrt{\Delta P_{wf}^2}} \tag{5.1}$$

The singular values of the system transfer function $\boldsymbol{G}(j\omega)$ at the frequency ω are given by:

$$\sigma_i\left(\boldsymbol{G}(j\omega)\right) = \sqrt{\lambda_i\left(\boldsymbol{G}(j\omega)^\top \boldsymbol{G}(j\omega)\right)} \tag{5.2}$$

where $\lambda_i(\cdot)$ is the i-th eigenvalue of the matrix $\boldsymbol{G}^\top\boldsymbol{G}$. The maximum singular value $\bar{\sigma}\left(\boldsymbol{G}(j\omega)\right)$ is defined as the largest gain for the input $\boldsymbol{u}(\omega)$ at the pulsation ω:

$$\bar{\sigma}\left(\boldsymbol{G}(j\omega)\right) \stackrel{\text{def}}{=} \max_{u\neq 0} \frac{\|\boldsymbol{G}(\omega)\boldsymbol{u}(\omega)\|_2}{\|\boldsymbol{u}(\omega)\|_2} \tag{5.3}$$

The maximum allowable voltage deviation and the maximum possible power reference change of the converters can then be represented as a gain boundary in the multi-variable frequency response of the MTDC system. In fact, by ensuring that the maximum singular value does not bypass the gain boundaries corresponding to the DC voltage deviation, the linear MTDC system is assured to comply with the imposed constraint [9].

The boundary for a maximum allowed deviation of the DC voltage of any converter of 5% respect of a power variation of the wind farm of 1 pu (i.e. N-1 condition) is given by[3]:

$$20\log_{10}\left(\frac{\sqrt{\Delta v_{dc,1}^2+\Delta v_{dc,2}^2+\Delta v_{dc,3}^2+\Delta v_{dc,4}^2}}{\sqrt{\Delta P_{wf}^2}}\right)=20\log_{10}\left(\frac{\sqrt{4(0.05)^2}}{\sqrt{1^2}}\right)=-20\text{ db} \tag{5.4}$$

Application of SVD to the MTDC with Classical CCSC

In this section, the SVD tool is used to evaluate the MTDC grid with the MMCs controlled with *Classical CCSC* strategy. The first results illustrate a power variation of the WF P_{wf} from 0 pu to 1 pu, and results are shown in Fig. 5.11. Note that the boundary shifts for each value of P_{wf} calculated with (5.3). When P_{wf} is equal to 1 pu, the limit is defined by (5.4).

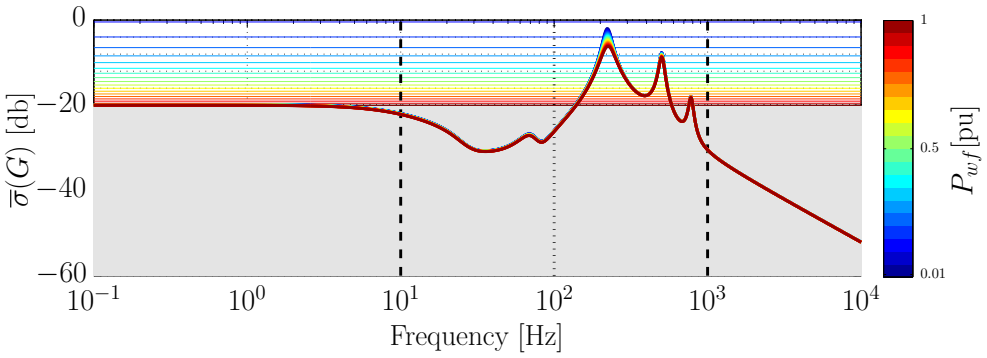

Figure 5.11 – SVD results for a sweep of the power from the Wind Farm – Onshore MMCs are controlled with *Classical CCSC* strategy

As seen on the SVD results from Fig. 5.11, it can be observed that the different values of P_{wf} don't affect considerably the frequency response. Four different frequency ranges may be distinguished:

1. *Low frequency range* — *Frequency* $< 10^1 Hz$: This range corresponds to the steady state deviation. Note that the droop constant used for this example is calculated for obtaining a DC voltage deviation of 5% for a variation of 1 pu of DC power (from any converter) with the theoretical calculation from Section 1.4.2. The SVD results for the low frequency ranges coincide with the value calculated in (5.4).
2. *Mid-low frequency range* — $10^1 Hz <$ *Frequency* $< 10^2 Hz$: In this frequency range it can be observed that the maximal gain of the system tends to become smaller. This means that for slow changes of P_{wf}, the MTDC grid will not have an important impact on the DC bus voltages and they will be easily maintained within the desired limits.
3. *Mid-high frequency range* — $10^2 Hz <$ *Frequency* $< 10^3 Hz$: In this range it can be clearly observed three resonant peaks around 220Hz, 500Hz and 780Hz correspond to the frequencies of the eigenvalues $\lambda_{37,38}$, $\lambda_{31,32}$ and $\lambda_{43,44}$ respectively (See Fig. 5.8 and Table 5.2).
4. *High-frequency range* — $10^3 Hz <$*Frequency* : For higher frequencies (more than 1kHz, the system attenuates all the high frequency perturbations.

Results from Fig. 5.11 show that the system gain is below the limits only when there is almost no power from the wind farm. For all the values of P_{wf} the limits are violated for the

[3]In fact, the 5% limit is applied on Δv_{dc} (i.e. $v_{dc} - v_{dc0}$) and not on the output variable v_{dc}, but in this Chapter it is considered that the operation point for all the DC voltages are set to 1 pu for simplicity

Mid-high frequency range. In [95] it is proposed to augment the boundary for this frequency range as it is stated that maintaining the gain below the limits is very complicated. In [9], and also in this report, it is chosen not to change the limit for the Mid-high frequency range.

The following test considers the variation of the droop gain for all the converters from 0.15 pu down to 0.05 pu. Results are shown in Fig. 5.12. As it can be seen, the most affected region is the low frequency range. When the droop gain is smaller, the system gain is decreased and that means that the voltage deviation is lower, as expected. Also, it can be seen that the Mid and High frequency range remains unaltered with respect to the first results in Fig. 5.11.

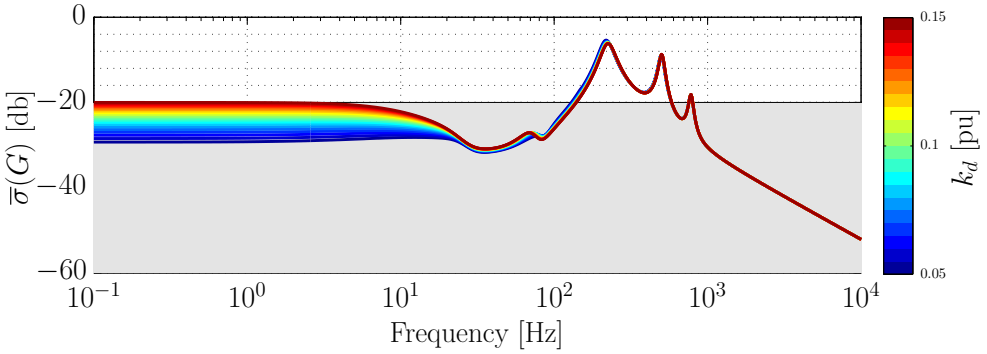

Figure 5.12 – SVD results for a sweep of the droop gain k_d of the MMCs – Onshore MMCs are controlled with *Classical CCSC* strategy

Finally, the last results are based on the variation of the DC cables length from 50 km up to 300 km. Results are shown in Fig. 5.13, while maintaining the droop constant to $k_d = 0.15$ pu. In this case, the SVD results is highly modified in Mid to High frequency range but almost no modification for the Low frequency range. When the DC cables are very long, the DC offset may be violated due to the voltage drops in the cables but this can be easily compensated with a slight modification of the droop gains k_d.

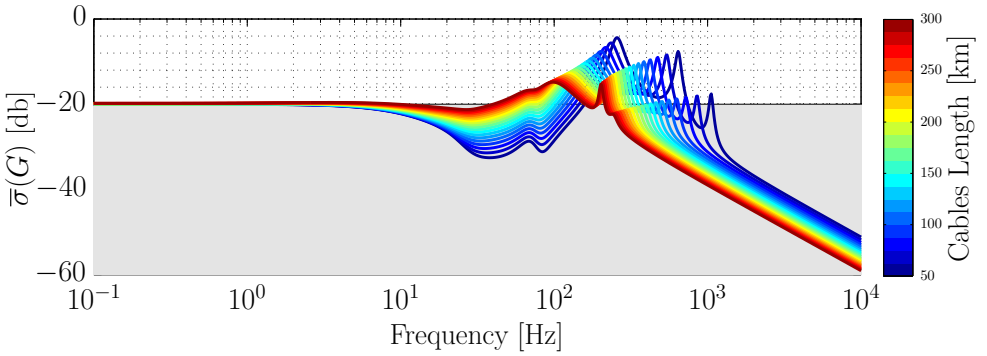

Figure 5.13 – SVD results for a sweep of the cables length – Onshore MMCs are controlled with *Classical CCSC* strategy

It is important to mention that the frequencies of the peaks of the SVD results from the Mid frequency range are modified for each different cable length. For longer cables, the peaks are reduced in amplitude and shifted to lower frequencies. The reason is that longer cables presents higher damping by their resistances (but increasing their inductance and capacitance as well, changing the place of the resonances). The resonances are not only due to the DC cables, but also on the MMC control strategy adopted as it will be shown in further sections.

Nevertheless, for all the combinations the SVD results show that the boundaries are easily violated for the Mid frequency range.

The obtained results for each of the variations of P_{wf}, k_d or the cable length results in different eigenvalues for each case. For each variation, it is mandatory to check if all the eigenvalues have a negative real part to ensure the global stability. This task is mandatory since the SVD does not give information about the system stability. This was verified for all the cases presented in this section, but not shown since they don't add any further information.

Application of SVD to the MTDC with Energy-based controllers

In the following, it is considered that the MMCs are equipped with *Energy-based* controller with constant energy reference. Only the SVD results for a variation on the wind power plant and the droop parameters are shown, which are gathered in Fig. 5.14.

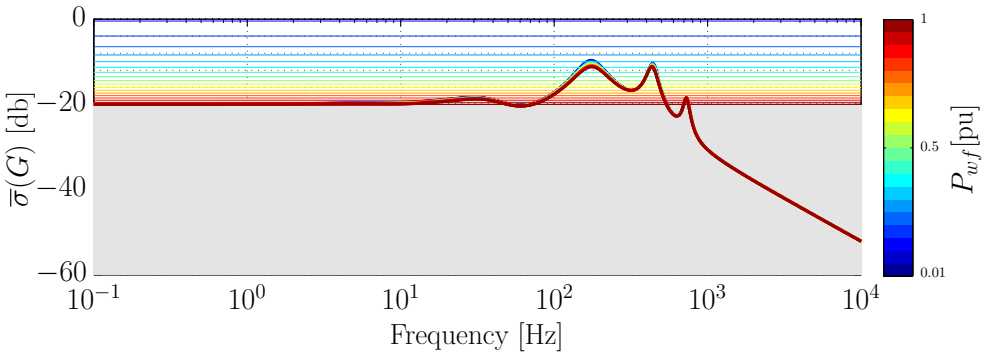

(a) Sweep of the wind farm power

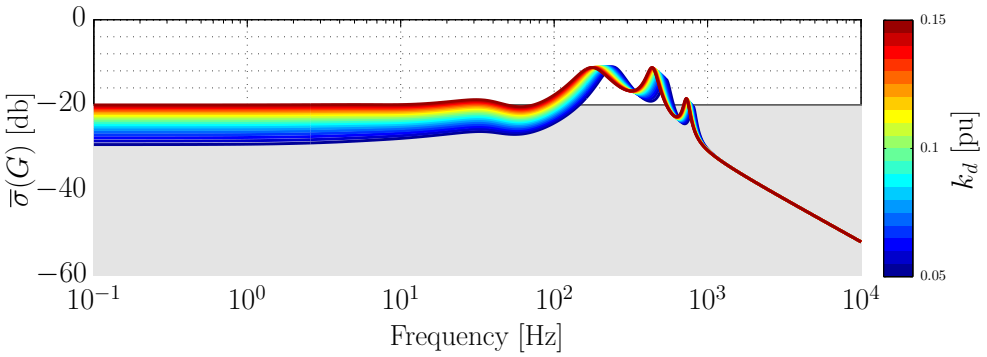

(b) Sweep of the droop parameter - $P_{wf} = -1$pu

Figure 5.14 – SVD results when the Onshore MMCs are controlled with *Energy-based* strategy — Constant energy reference for all the MMcs

In Fig. 5.14a it is shown the results for a wind power P_{wf} from 0 to 1pu. The Low- and High- frequency range responses are similar to the case where all MMCs are equipped with *Classical CCSC* (Fig. 5.11). Nevertheless, it can be seen that the Mid-low frequency range is not attenuated as in previous case. Moreover, the peak at 500Hz in the Mid-high range is slightly damped as well as the other peaks. For the droop variation in Fig. 5.14b, it can be seen that only the High-frequency range is not modified for the different gains, unlike the previous case in Fig. 5.12 where only the Low-frequency range was modified.

These results show that when all the MMCs are being controlled with *Energy-based* controllers with constant energy references, the dynamic behavior of the DC voltages of the MTDC

grid are not guaranteed to remain between the boundaries of a variation of ±5%. Nevertheless, the stability is assured for all the cases considered.

In the following sections, an in-depth analysis is carried out to improve the SVD results and hence, the dynamic behavior of the DC voltages in MMC-based MTDC grids.

5.4 Influence of MMC energy management on the dynamics of droop-controlled MTDC grids

As discussed in Section 1.4, the DC voltage dynamics are governed by the the energy stored under an electrostatic form since it corresponds mainly to the energy stored in converter station capacitors directly connected to the DC grid (as it is the case for *2-level* VSCs studied in Chapter 1). For the case of the MMC, since there is no capacitor connected directly to the DC bus, the internal energy can be shared or not with the MTDC grid depending on the applied control strategy. This has an important effect on the overall MTDC grid dynamics since the available energy on the DC bus is modified [**160**].

For analyzing the MTDC dynamics, the simplified DC dynamics formulation relating the stored energy of the MTDC grid and the droop constant from Section 1.4.2 is used. However, first it is needed to adapt the formula from (1.51) for considering the MMC instead of *2-level* VSC, which are very different in terms of dynamics [9, 202].

5.4.1 Participation of the internal stored energy on the DC bus voltage dynamics

For the adaptation of the simplified formula, let us first consider the *Reduced order* model developed in Chapter 4 as shown in Fig. 5.15, where the AC reactive power circuit (i.e. q axis) is neglected on purpose [203]. This circuit was already validated in Chapter 4 when using *Energy-based* controllers with CM, which is the main control structure for the rest of this Chapter.

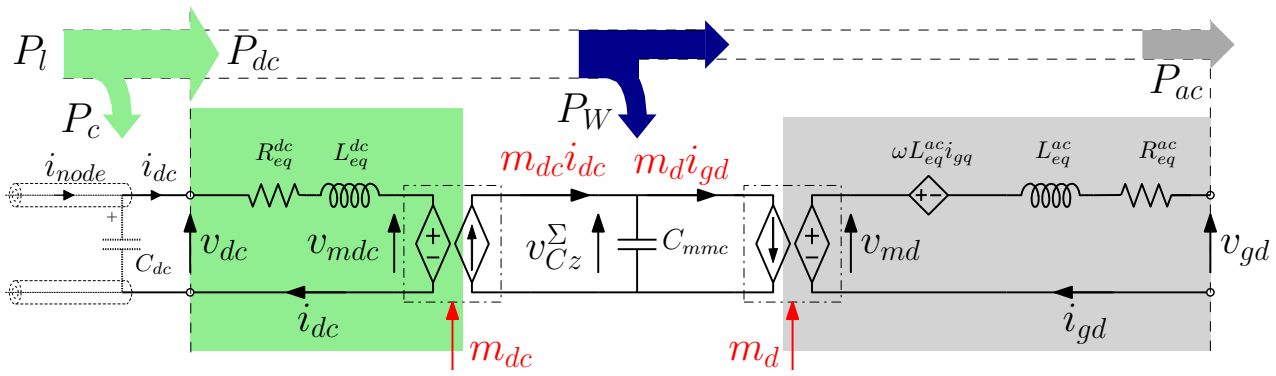

Figure 5.15 – Simplified MMC model — AC and DC powers distribution

The circuit in Fig. 5.15 helps to understand the power flow from DC to AC sides across one single converter. Suppose that there is a power P_l arriving at the node PCC-DC of the studied terminal. During transients, a fraction of this power, P_c, goes to the capacitor C_{dc}, which is the equivalent capacitor of the considered DC node. The DC power at the PCC-DC of the MMC is named as P_{dc}. A part of P_{dc}, namely P_W, is the responsible for charging the 6 equivalent arm capacitors of the MMC, i.e. modifying the internal energy W_z^{Σ}. The output

AC power is P_{ac}. For the following analysis, the instantaneous power on the inductors and the converter losses are neglected.

The energy stored on the DC cable (W_{dc}) depends on the power exchanged by the MMC (P_{dc}) with the DC bus and the power flowing from the current source (P_l) as expressed in (5.5).

$$\frac{dW_{dc}}{dt} = \frac{1}{2}C_{dc}\frac{dv_{dc}^2}{dt} = P_c = P_l - P_{dc} \tag{5.5}$$

The approximated dynamics of the energy stored on the MMC (W_z^{Σ}) was given in (3.6), and it is repeated in (5.6) for convenience (it is recalled that $C_{mmc} = 6 \times C_{arm}$). It is approximated since the *dq* components of the energy are neglected at this moment.

$$\frac{dW_z^{\Sigma}}{dt} \approx \frac{1}{2}C_{mmc}\frac{d(v_{Cz}^{\Sigma})^2}{dt} = P_W \approx P_{dc} - P_{ac} \tag{5.6}$$

Re-arranging (5.6), the DC power can be expressed as in

$$P_{dc} = \frac{1}{2}C_{mmc}\frac{d(v_{Cz}^{\Sigma})^2}{dt} + P_{ac} \tag{5.7}$$

Replacing (5.7) into (5.5) yields:

$$\frac{1}{2}C_{dc}\frac{dv_{dc}^2}{dt} + \frac{1}{2}C_{mmc}\frac{d(v_{Cz}^{\Sigma})^2}{dt} = P_l - P_{ac} \tag{5.8}$$

For the case when the MMC is controlled with *Classical CCSC*, the internal capacitors are charged or discharged accordingly in harmony with the DC bus (See results in Fig. 3.8b). For this reason, it can be assumed that $v_{Cz}^{\Sigma} \approx v_{dc}$ [115]; and hence, (5.8) results in (5.9).

$$\textit{Classical CCSC:}\ \frac{1}{2}\underbrace{(C_{dc} + C_{mmc})}_{C_{eff}}\frac{dv_{dc}^2}{dt} = P_l - P_{ac} \tag{5.9}$$

Equation (5.9) shows that the effective capacitance on the DC side C_{eff} is not only the one of the cables, but also the internal capacitor C_{mmc} **[160]**.

In case that the *Energy-based* controller with constant level of energy is considered, (5.9) is no longer valid since the value of v_{Cz}^{Σ} depends on the energy reference. For this strategy, the dedicated energy controller regulates the internal energy to a constant level (normally, 1 pu). Assuming a perfect energy controller, it can be written that[4] $\overline{W}_z^{\Sigma} = \overline{W}_z^{\Sigma *}$. This implies that $v_{Cz}^{\Sigma} = v_{Cz}^{\Sigma *}$, where $v_{Cz}^{\Sigma *} = \sqrt{2\overline{W}_z^{\Sigma *}/C_{mmc}}$, and consequently the term $d(v_{Cz}^{\Sigma})^2/dt$ is equal to zero. With this considerations, (5.8) results in (5.10).

$$\textit{Energy-based (constant energy):}\ \frac{1}{2}\underbrace{C_{dc}}_{C_{eff}}\frac{dv_{dc}^2}{dt} + \underbrace{\frac{1}{2}C_{mmc}\frac{d(v_{Cz}^{\Sigma *})^2}{dt}}_{=0} = P_l - P_{ac} \tag{5.10}$$

Equation (5.10) shows that the effective capacitance on the DC side C_{eff} is now only considering the cable capacitances.

Neglecting the inductances of the cables, the effective DC bus capacitance for the MMC-based MTDC grid may now be written as the sum of the M cables and the N_c MMCs (see Section 1.4.2):

$$C_{eff} = \sum_{i=1}^{M} C_{cable,i} + \sum_{j=1}^{N_c} \lambda C_{mmc,j} \tag{5.11}$$

[4]It is recalled that $\overline{W}_z^{\Sigma}$ corresponds to the time averaged value of W_z^{Σ}.

where λ is 1 if the MMC is sharing the internal energy with the DC bus, or 0 if the energy is decoupled. From (5.9) and (5.10), and taking into account (5.11), it can be written:

$$\frac{1}{2}C_{eff}\frac{dv_{dc}^2}{dt} = P_l - P_{ac} \tag{5.12}$$

Equation (5.12) is used for extending the simplified MTDC model already done for the *2-level* VSC in Section 1.4.2, for taking into account the distinct capacitance of the grid.

5.4.2 Dynamic behavior of a droop controlled MMC-based MTDC grid

Dividing (5.12) by v_{dc} and considering (5.11), (5.13) is obtained.

$$C_{eff}\frac{dv_{dc}}{dt} = -\frac{P_{ac}^*}{v_{dc}} - \frac{P_l}{v_{dc}} = -i_{mdc} - i_l \tag{5.13}$$

The MMC associated with the droop controller can be represented in a circuit diagram as shown in Fig. 5.16. The current i_{mdc} is the internal modulated current inside the MMC that charges or discharges the internal capacitors.

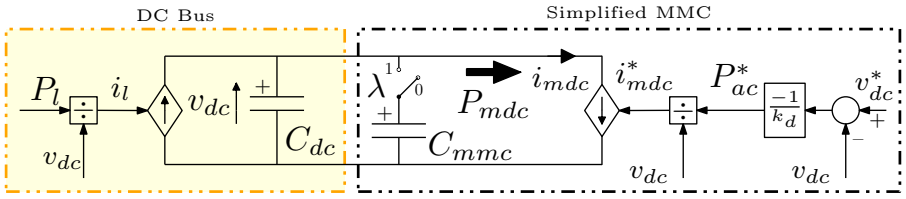

Figure 5.16 – Simplified droop-controlled MMC-VSC for analysis purposes

Note that the circuit from Fig. 5.16 is fundamentally the same as the *2-level* VSC [74]. The main difference is due to the effective capacitance on the DC side. In the case of the *2-level* VSC, this *physical* capacitance is directly connected to the DC bus. Contrariwise, in the MMC the effective capacitance depends on the control strategy adopted for the converter **[160]**. For this reason, the simplified formulation of the MTDC grid developed in Section 1.4.2 can be directly re-written, replacing only C_{mtdc} by the definition in (5.11), i.e. C_{eff}, as shown in (5.14):

$$\Delta v_{dc,pu} = -\frac{\frac{1}{\left(\sum_{j=1}^{N_d}\frac{P_{n,j}}{k_{d,j}}\right)}}{1 + \frac{v_{dc0}v_{dcn}C_{eff}}{\left(\sum_{j=1}^{N_d}\frac{P_{n,j}}{k_{d,j}}\right)}s}\frac{P_{n,j}}{v_{dcn}}\Delta P^*_{ac,j_{pu}} \tag{5.14}$$

where it is recalled that $\Delta v_{dc,pu}$ represents the voltage dynamics in per-unit of a single capacitor modeling the entire MTDC grid. Also, N_d is the amount of converters in droop control mode; $k_{d,j}$ is the droop constant of the converter j (in pu); v_{dc0} is the initial voltage value (in V); v_{dcn} is the nominal DC voltage (in V); $P_{n,j}$ the nominal power of the converter j and finally, $\Delta P^*_{ac,j_{pu}}$ is the power deviation (in pu).

As already performed in Section 1.4.2, it is assumed that all droop parameters are set to an equal value k_d, and the initial value of v_{dc} is equal to its nominal value (i.e. $v_{dc0} = v_{dcn}$) so (5.14) is simplified as follows:

$$\Delta v_{dc,pu} = -\frac{\frac{k_d}{N_d}}{1 + \frac{k_d}{N_d}\frac{C_{eff}v_{dcn}^2}{P_n}s}\Delta P^*_{ac,pu_j} \tag{5.15}$$

The voltage dynamics depends not only on the droop parameter k_d, but also on the equivalent capacitance of the DC grid (C_{eff}) which depends on the MMC control strategy. This capacitance does not affect the steady state voltage deviation.

Time Domain Comparison

For evaluating the effectiveness of the simplified formulation in (5.15), this equation is contrasted with the results from a large-signal simulation of a power step of the Wind Farm of 1 pu. The capacitances at stake are listed in Table 5.4.

Table 5.4 – Capacitor values of MMC and DC grid

Variable	Value
$C_{mmc,1} = C_{mmc,2} = C_{mmc,3}$	195.31 μF
$C_{mmc,4}$	10 μF
4× Cables (70 km each)	22.61 μF

Comparison results are shown in Fig. 5.17a for when considering that the MMCs are controlled with the *Classical CCSC*. From this comparison, it cannot be said that the simplified formulation reproduces the DC voltage dynamics. However, there is a similarity on the trend of the dynamics. Note that the voltage on the converter on the Wind Farm (in light gray) is the one that falls abruptly at the moment of the applied step, while the voltage on the other converters are maintained in between the limits of %5. For the *Energy-based* controllers, the comparisons are given in Fig. 5.17b. In this case, it is clearly seen that the voltage drop is produced abruptly for all converters due to the lower effective capacitance on the MTDC grid. Once again, the simplified model cannot reproduce very accurately the main dynamics.

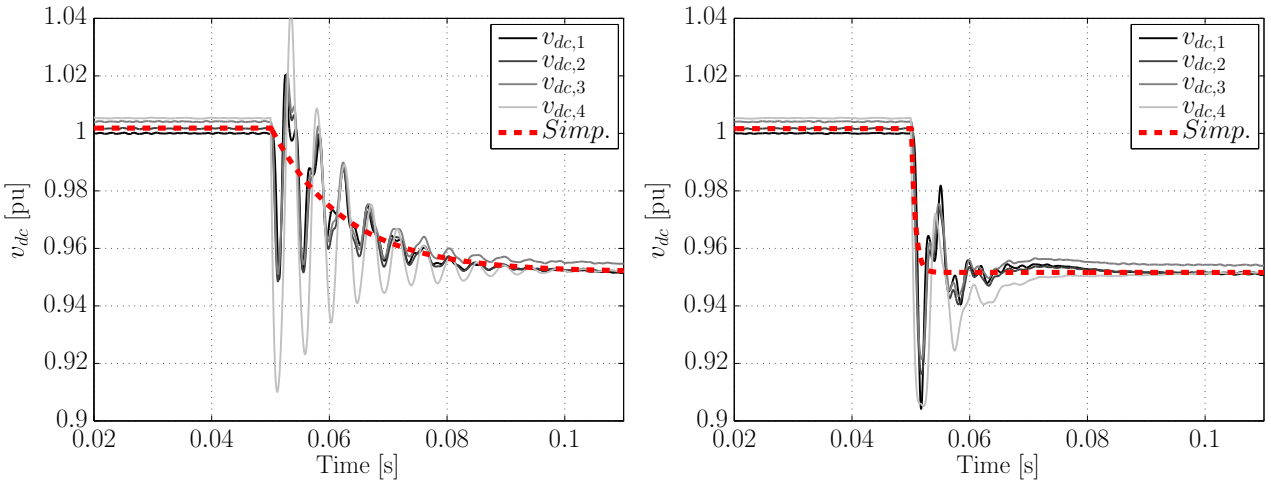

(a) *Classical CCSC* – $C_{eff} = 618.54$ μF (b) *Energy-based* controllers – $C_{eff} = 32.61$ μF

Figure 5.17 – Comparison of large-signal time-domain simulations of a four terminal MTDC grid with simplified MTDC dynamics formulation from (5.15)

Even though the simplified formulation failed to reproduce the voltage dynamics accurately for both cases, some important partial conclusions can be given. On the one hand, the *Classical CCSC* presents the advantage of natural sharing of its energy with the DC bus, so the effective

capacitance of the MTDC grid is enhanced. This "extra" stored energy on the DC side is necessary for a proper dynamic behavior of the MTDC grid. However, the fact that the DC-side dynamics of the MMC are not controlled causes extreme oscillations due to power variations in the grid (concept that was heavily covered in this Thesis). On the other hand, the *Energy-based* controller presents the advantage of an accurate control of the internal variables of the MMC, making it very robust to different situations. Nevertheless, if the energy management is considered to keep the internal energy level at a fixed value (and without any other actions), the effective DC capacitance of the MTDC grid is heavily diminished. For this reason, the changes on the power transfer on the DC grid will cause large variations on the DC bus voltage, which can be very dangerous for the proper operation of the cables.

From this discussion and from a DC-side point of view, converters should provide their internal energy to improve the DC voltage dynamics for augmenting the interoperability of the MMCs connected to MTDC grids. This functionality can be considered as analogous to the AC side frequency support; more synchronous machines with large inertia on their shafts collaborate in the improvement of the frequency regulation. The same concept is needed for the MMC-based MTDC grids.

5.5 MMC control variants for internal energy sharing with the MTDC grid

Up to this point, it is clear that the *Classical CCSC* presents several limitations for MTDC grids. Contrariwise, in the past section, the main drawback of the *Energy-based* controller as it was presented in this Thesis was clearly highlighted: the internal energy of the MMC is decoupled with the DC side. However, the fact that the internal variables can be accurately controlled is the main advantage that can be further explored. In this Section, *Energy-based* control variants are investigated to allow the internal energy of the MMC to participate in the improvement of the DC bus voltage dynamics. The main characteristic of the *Energy-based* controller is that the AC and DC powers can be controlled independently during the transients. This degree of freedom can be used for developing control solutions for taking advantage of the internal energy.

Let us consider again the *Reduced-order* model, as shown in Fig. 5.18 where now the *Energy-based* controller is adopted. In this figure, the independent control of the AC and DC powers are highlighted. The outer block, named as "Outer Loops - Energy Management" is in charge for generating the power references P^*_{ac} and P^*_{dc}. This section is focused on this block, where different variants are presented.

5.5.1 Coupled MMC energy with DC bus: Virtual Capacitor Control

In this strategy, the *Energy-based* controller is slightly modified for enabling the participation of the internal energy on the DC bus voltage dynamics. This is performed with an appropriated modification on the energy reference which is shown in (5.16) as proposed in [203, 204]. The parameter K is referred as "Capacitor Coefficient" and it is explained later on this Section [203].

$$\overline{W}_z^{\Sigma *} = \frac{1}{2} \underbrace{\mathrm{K}C_{mmc}}_{\text{Virtual Capacitor}} \left(v_{dc}^2 - v_{dc0}^2\right) + \overline{W}_{z0}^{\Sigma *} \tag{5.16}$$

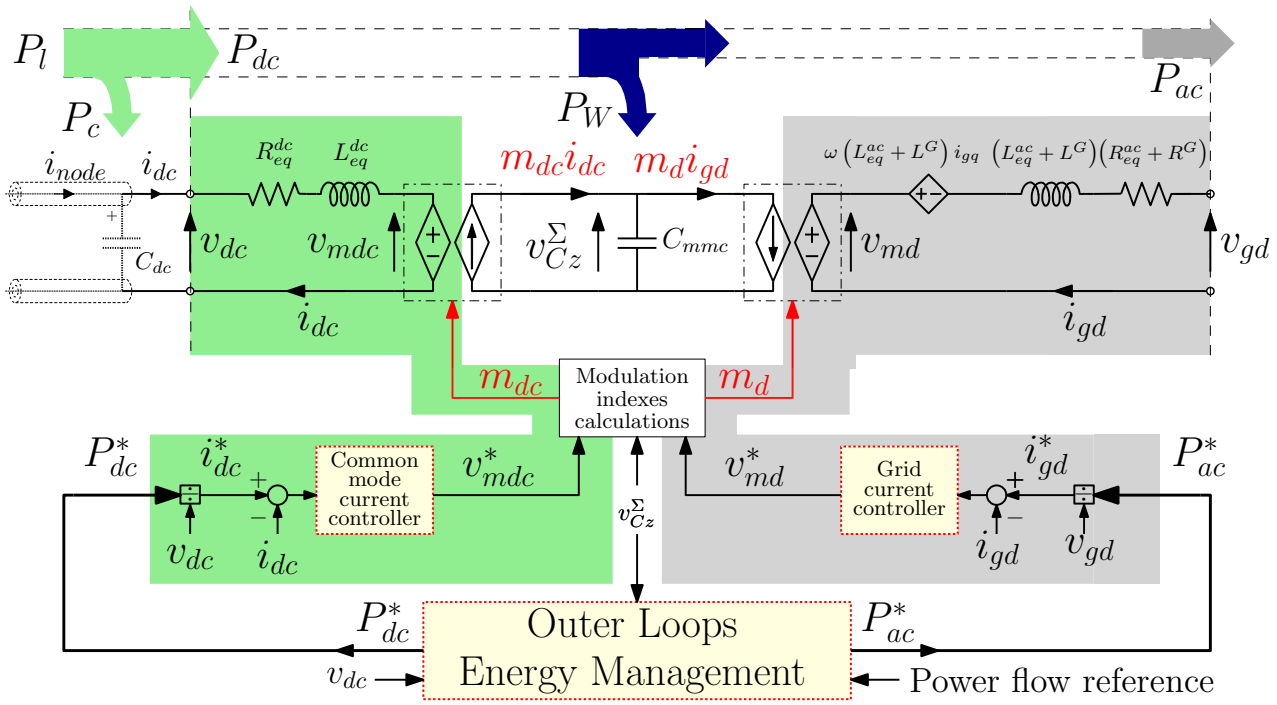

Figure 5.18 – Simplified MMC model with *Energy-based* control — AC and DC powers

In (5.16), v_{dc0} corresponds to the steady-state value of the DC voltage and $\overline{W}_{z0}^{\Sigma*}$ is the desired initial stored energy on the converter. The arm capacitors voltage reference $v_{Cz}^{\Sigma*}$ can be related to the energy reference in (5.16) as in (5.17).

$$v_{Cz}^{\Sigma*} = \sqrt{\frac{2\overline{W}_z^{\Sigma*}}{C_{mmc}}} = \sqrt{\mathrm{K}\left(v_{dc}^2 - v_{dc0}^2\right) + \overline{W}_{z0}^{\Sigma*}} \tag{5.17}$$

Replacing (5.17) into (5.8) and taking into account a perfect energy controller where it can be considered that $v_{Cz}^{\Sigma} = v_{Cz}^{\Sigma*}$, it yields (5.18). Note that the derivatives of v_{dc0}^2 and $\overline{W}_{z0}^{\Sigma*}$ are zero since they are set to constant values in normal operation.

$$\frac{1}{2}C_{dc}\frac{dv_{dc}^2}{dt} + \frac{1}{2}C_{mmc}\frac{d(\mathrm{K}\left(v_{dc}^2 - v_{dc0}^2\right) + \overline{W}_{z0}^{\Sigma*})}{dt} = P_l - P_{ac} \tag{5.18a}$$

$$\frac{1}{2}C_{dc}\frac{dv_{dc}^2}{dt} + \frac{1}{2}C_{mmc}\frac{d\mathrm{K}v_{dc}^2}{dt} = P_l - P_{ac} \tag{5.18b}$$

Re-organizing (5.18b), (5.19) is obtained.

$$\textit{Virtual Capacitor:}\ \frac{1}{2}\underbrace{\left(C_{dc} + \mathrm{K}C_{mmc}\right)}_{C_{eff}}\frac{dv_{dc}^2}{dt} = P_l - P_{ac} \tag{5.19}$$

For the particular case where the terms v_{dc0}^2 and $\overline{W}_{z0}^{\Sigma*}$ are neglected in (5.17), it is obtained the same energy reference as first proposed in [176]. However, the strategy from [176] may conduce to excessive over-voltages on the sub-modules capacitors when selecting high values of K. This is due to the fact that the steady-state value of the arm capacitor voltages would be $\sqrt{\mathrm{K}}$ times the DC voltage value when using the strategy from [176]. However, this drawback is solved in [203] with the introduction of the terms v_{dc0}^2 and $\overline{W}_{z0}^{\Sigma*}$ in (5.17).

The implementation of the *Virtual Capacitor* control in shown in Fig. 5.19. For improving the tracking performance of the energy controllers, two options are envisaged: The first one consists in the addition of a derivative term. The second option is the modification of the controller tuning for having a faster energy response time. For this task, faster current controllers are needed for avoiding interactions between the different cascaded control loops [164]. In the following examples, the derivative action is preferred to avoid modifying the controller gains to enable a clearer comparison with the previous strategies. The gains are selected with a *trial and error* methodology via time domain simulations and the values which present an acceptable response are $k_W = 0.01$ and $T_W = k_W/10$. More advanced methodologies based on the linear models can be deployed to a better tuning of this gains as proposed in [205], however this aspect is out of the scope of this Thesis.

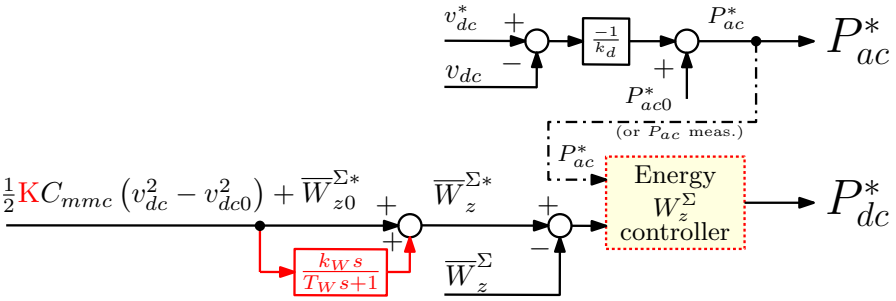

Figure 5.19 – *Energy-based* controllers with *Virtual Capacitor* control — See Section 3.4 for the details for the Energy W_z^{Σ} controller

In the following sub-sections the *Virtual Control* strategy is evaluated via time domain simulations, and the linear analysis tools.

Time domain simulations

For evaluating the developed strategy, the same large-signal time domain simulation as in Section 5.2.3 is performed. The energy references for converters MMC-1, MMC-2 and MMC-3 are given by (5.16), with $\mathrm{K} = 1.1$. The droop parameters are set to $k_d = 0.15$ pu for the three aforementioned converters. Starting with the DC power flow given in Table 5.1, the Wind farm is disconnected at $t = 20$ ms. The LTI model of the MTDC is re-generated taking into account the modification on the energy reference with (5.16). Simulation results for the DC power and voltages are gathered in Fig. 5.20. The first observation is that the LTI model reproduces accurately the MTDC behavior, even if some differences are observed in the transient (note that the applied step consist on a large-signal scenario). The DC voltages at the converters MMC-1, MMC-2 and MMC-3 are well maintained under the %5 limits, while the MMC-4 presents several oscillations.

In Fig. 5.20c a detail of the DC powers is depicted, where it can be seen that the DC power slope from 20 ms to 40 ms for MMC-1 is around 150 MW/ms, 340 MW/ms for MMC-2 and 335 MW/ms. This rate may be excessive for AC grids, where a maximum rate of 100 MW/ms may be specified; however the DC grid dynamics are much faster than the AC grids, so the rates observed in Fig. 5.20c are achievable.

Results from Fig. 5.21 gathers the time domain waveforms of the arm capacitor voltages for the MMC-1. Also, it is shown $\sqrt{W_z^{\Sigma}}$ and the DC voltage value $v_{dc,1}$. Note that the steady-state value at the beginning of the simulation are the same for all the shown signals. This is the main difference with the energy strategy from [176]; the energy reference from (5.16) allows that the

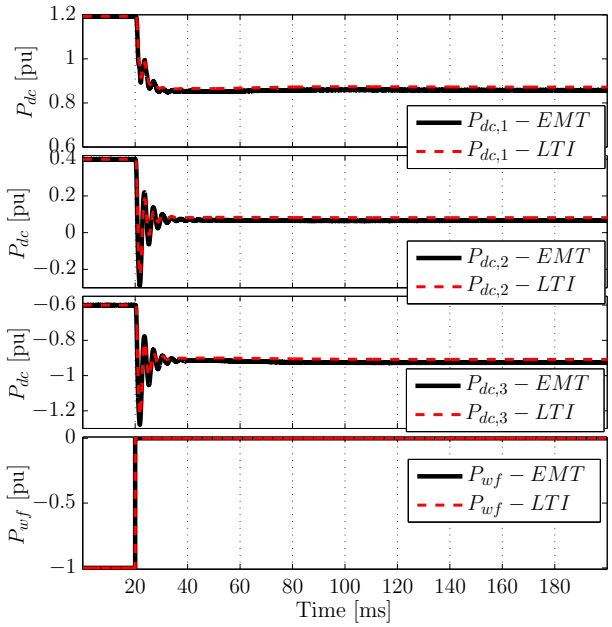

(a) DC Power

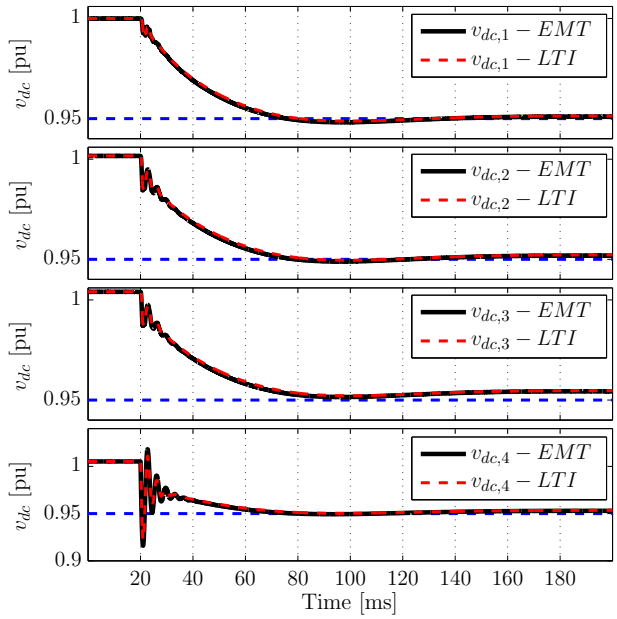

(b) DC Voltage

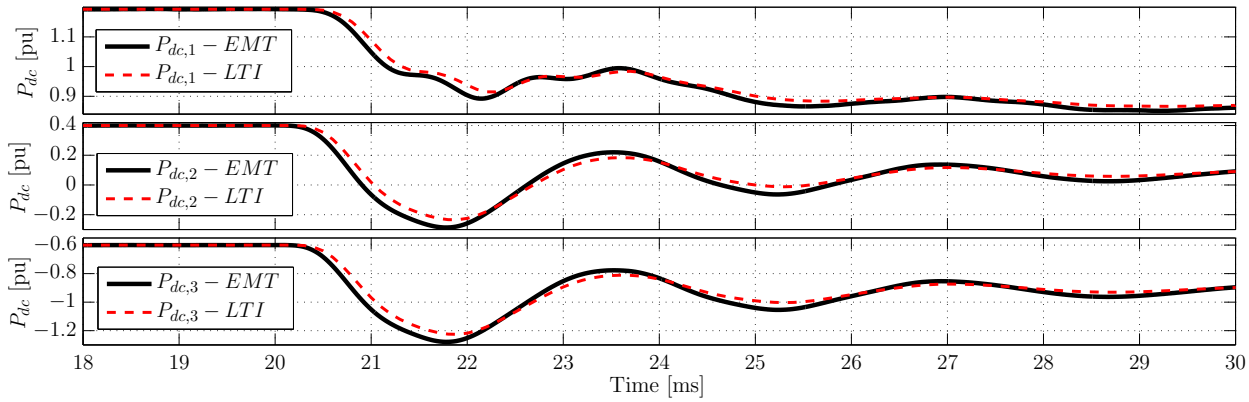

(c) DC Power — Detail

Figure 5.20 – Comparison of time-domain simulations of EMT and small-signal model (LTI) of a four terminal MTDC grid - Converters are equipped with *Energy-based* controllers with the *Virtual Capacitor* control (K = 1.1 for MMC-1, MMC-2 and MMC-3)

average value of the arm capacitor voltages remain at normal levels (e.g. 1 pu). However, after the transient, the difference between $\sqrt{W_z^{\Sigma}}$ and the DC voltage value $v_{dc,1}$ depends on the value of K and the voltage difference $v_{dc}^2 - v_{dc0}^2$. This characteristic is studied in a further sub-section.

Linear analysis

In Fig. 5.22, the eigenvalues of the validated LTI models for the MTDC grids with constant energy from Fig. 5.9 and with *Virtual Capacitor* control are shown. As observed, many eigenvalues shifted their positions. The eigenvalues marked in blue corresponds to the modes related to the DC voltages for each controls strategy from a participation factor analysis.

In Table 5.5 the eigenvalues related to the DC voltages of the converters are listed for the

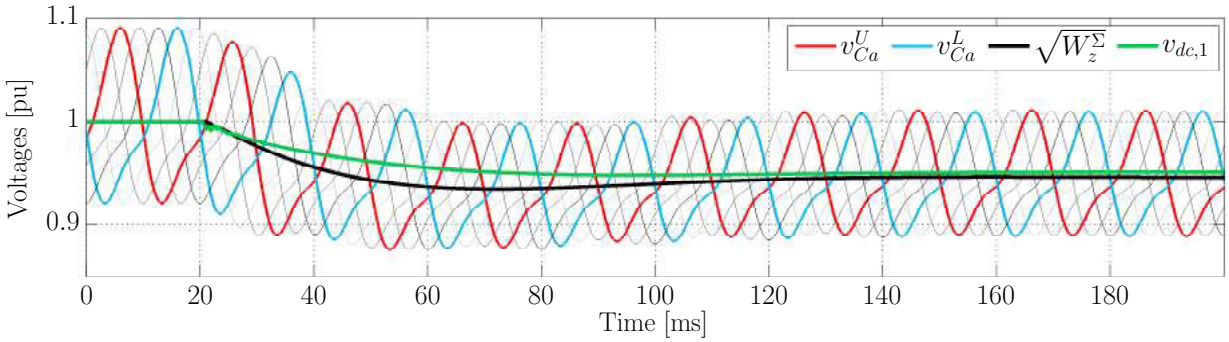

Figure 5.21 – Arm capacitor voltages, DC voltage and internal stored energy — MMC-1 — *Energy-based* controllers with *Virtual Capacitor* control

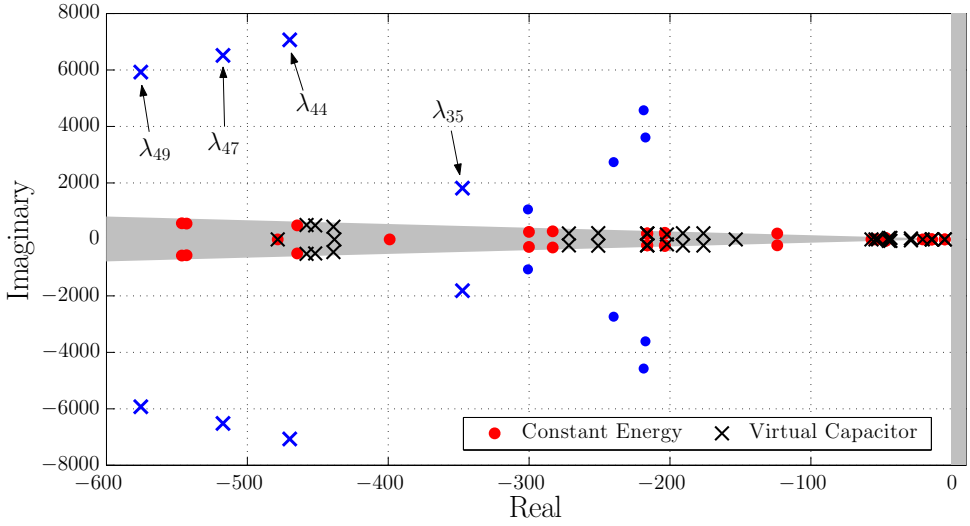

Figure 5.22 – LTI Eigenvalues - MMC equipped with *Energy-based* controllers with *Virtual Capacitor* control or constant energy level — Eigenvalues marked in blue correspond to DC voltage related modes

Virtual Capacitor control. As it can be noticed, these eigenvalues are not well damped as the rest of the eigenvalues of the system (see Fig. 5.22, where the rest of eigenvalues are located in the *well damped* gray zone). Comparing the DC voltage eigenvalues from Tables 5.3 and 5.5, it can be noticed that the DC voltage for MMC-4 is now related only to the currents in the cables. Moreover, the rest of eigenvalues are related to more than one DC voltage and always with the DC currents ($i_{dc} = 3i_z^{\Sigma}$) of the converters.

Table 5.5 – DC Voltage related eigenvalues — MMCs with *Virtual Capacitor* control

λ_i	**Eigenvalue**	**Freq. [Hz]**	**Damp. ratio**	**Dominant States** (From Participation Factor analysis)
$\lambda_{35,36}$	$-347.3 \pm j1815.6$	289	0.19	$v_{dc,4}$; i_{z1}^{C3} ; i_{z1}^{C4}
$\lambda_{44,45}$	$-469.9 \pm j7066.3$	1124.6	0.067	$i_{z,1}^{\Sigma}$; $v_{dc,1}$; $v_{dc,2}$; $v_{dc,3}$
$\lambda_{47,48}$	$-517.3 \pm j6516.6$	1037.2	0.08	$i_{z,2}^{\Sigma}$; $i_{z,3}^{\Sigma}$; $v_{dc,2}$; $v_{dc,3}$
$\lambda_{49,50}$	$-575.6 \pm j5924.8$	942.9	0.1	$i_{z,1}^{\Sigma}$; $v_{dc,1}$; $v_{dc,2}$

For evaluating the impact of different values for the "Capacitor Coefficient" K, in Fig. 5.23

it is shown the SVD results for the parametric sweep of K from 1 up to 2.4 for all converters. The impact is observed on the low-frequency range, since the virtually augmented capacitance of the MTDC grid behaves as a low-pass filter such as a single capacitor. The voltage spike around 290 Hz remains almost unaltered. This peak corresponds to the eigenvalue $\lambda_{35,36}$ from Table 5.5, which it was shown that it has no participation from the other converters (only from MMC-4, which doesn't participate on the DC voltage control).

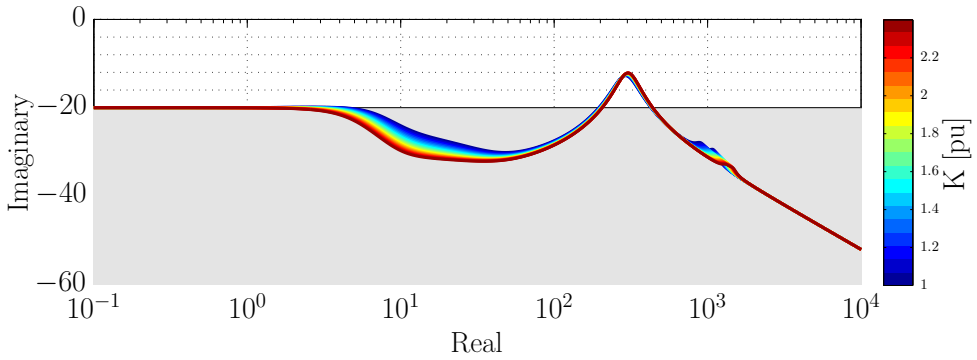

Figure 5.23 – SVD of MTDC with *Virtual Capacitor* strategy — Sweep of "Capacitor Coefficient" K for MMC-1, MMC-2 and MMC-3

It seems from Fig. 5.23, that augmenting indefinitely the "Capacitor Coefficient" K improves the MTDC dynamics. However, special attention should be given to the final value of the stored energy (or the arm capacitor voltages) since it is possible to hit the converter limits. This aspect is studied in the following sub-section.

Limitations of Virtual Capacitor strategy in droop-controlled MTDC grids

In [203], a theoretical analysis on the peak of the MMC internal energy W_z^{Σ} was given for the case of an HVDC point-to-point scheme. Moreover, since in that configuration there is one converter controlling exclusively the DC voltage v_{dc} to a fixed value (normally 1 pu), the steady state value for the stored energy after a perturbation, presents no challenge since the term $v_{dc}^2 - v_{dc0}^2$ from (5.16) is typically zero at the equilibrium.

In droop-controlled MTDC grids, the DC voltage is near the nominal value only when a dedicated master controller sets the proper references for regulating the DC power flow [**88**]. Right before a power imbalance, the DC voltage experiences a deviation due to the proportional droop controllers (see (1.51)). Consequently, for MTDC situations, and after an event, the term $v_{dc}^2 - v_{dc0}^2$ in (5.16) is not zero, so a deviation on the energy is expected for the steady state condition after an event. This difference on the energy level will exist until a dedicated master controller regulates again the stored energy.

The energy deviation W_{dev} after an event which causes a DC voltage change of Δv_{dc} is given in (5.20), where v_{dc0} is the DC voltage after the event and W_{z0}^{Σ} is the initial level of stored energy. Note that this equation is considering only the steady state values, and not during transients. As it can be seen, the total energy deviation is proportional to K, and depends also on Δv_{dc}, which is defined by the droop parameters of all the converters participating on the DC voltage regulation.

$$W_{dev}(\mathrm{K}) = \mathrm{K}((v_{dc0} - \Delta v_{dc})^2 - v_{dc0}^2) + W_{z0}^{\Sigma}) \text{ [pu]} \tag{5.20}$$

However, the information of (5.20) deals with the total stored energy of the converter, without taking into account the physical limits of the MMC. For exemplifying this phenomenon,

ten EMT parametric simulations are carried out where the "Capacitor Coefficient" K of the MMC-1 is varied from 1.5 up to 2.4. With the eigenvalue analysis (not shown since it doesn't add more information), the stability of the MTDC grid is verified for the considered values of K. For each simulation, the same scenario as for the large-signal simulations from Section 5.2.3 is considered: at $t = 20$ ms, the DC power from the Wind Farm is dropped abruptly to zero. Since the droop parameters for MMC-1, MMC-2 and MMC-3 are set to $k_d = 0.15$ pu, the final voltage deviation is around %5. Special attention is given to the steady-state condition after the simulated event.

In Fig. 5.24 it is shown the steady-state results for the 10 considered cases. In this figure, the final DC voltage is shown and its final value is 0.95 pu as expected. Also, the results for the arm capacitor voltage v_{Ca}^{U} from each simulation, and the modulated voltage v_{ma}^{U} are shown. As expected from (5.20), when higher values of K are used, the deviation of the average value of the energy is increased after the event, which is reflected in Fig. 5.24 as the diminution of the average value for the arm capacitor voltage. For this case scenario, when K is higher than 2.1 the arm capacitor voltages has such a low value, that it is not possible to form the desired arm voltage v_{ma}^{U} needed for the proper operation of the converter. This same phenomenon is shown in Fig. 5.25, where the maximum value of the modulation indexes are shown for MMC-1. As it can be seen, for higher values of K, the limit on $\boldsymbol{m}_{\boldsymbol{abc}}^{\boldsymbol{U}}$ is approached and further violated[5].

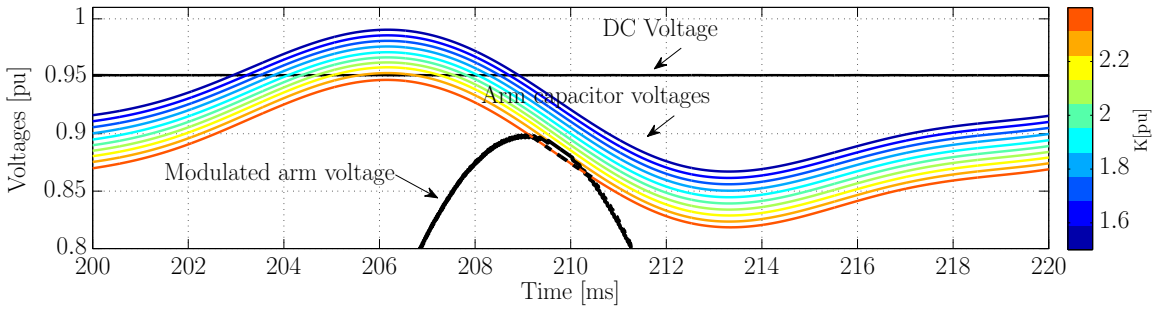

Figure 5.24 – DC Voltage v_{dc}, Arm capacitor voltage v_{Ca}^{U} and modulate voltage v_{ma}^{U} of MMC-1 (phase a, Upper arm) with *Virtual Capacitor* strategy for different values of K

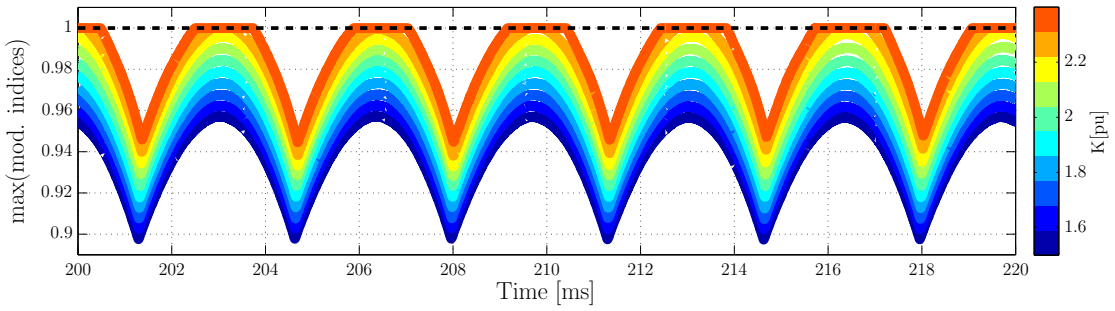

Figure 5.25 – Maximum value of the six modulation indices $\boldsymbol{m}_{\boldsymbol{abc}}^{\boldsymbol{U}}$ of MMC-1 with *Virtual Capacitor* strategy for different values of K

In this analysis, it was only taken into account the case where the DC voltage tends to decrease, and so does the internal stored energy. In the other way around, if v_{dc} increases, special attention should be given to the maximum limit on the voltage cells of the converter as studied in [203]. These characteristics of energy deviations, for the previous strategy and the

[5]More information about the HB-MMC limits is provided in Appendix E.

Virtual Capacitor control, make the choice of K a complicated task since several limitations should be taken into account. In the following section, a different approach for controlling the DC bus voltage while keeping the concept of energy sharing is given, which overcomes these limitations.

5.5.2 DC Power Derivative control

The last control option is inspired by the Virtual Synchronous Machine Inertia Emulation concept [206], where a dedicated control with derivative action is used to mimic the behavior of the converters such as a synchronous machine for regulating the AC frequency [207]. In this sub-section, a similar approach as the Inertia Emulation for the AC-side, is followed for the DC-side.

Since the *Energy-based* control strategy of the MMC has the ability to control independently the AC and DC powers (to a certain extent), a different choice for the roles of each power can be set. Up to this point, the droop controller was dedicated to act on the AC power reference P^*_{ac}, while P^*_{dc} was formed by the energy controller and the feed-forward action P^*_{ac}. However, an opposite strategy is also possible, as explored in [208, 209]: the energy controller may generate the AC power reference; while the droop controller generates directly the DC output power P^*_{dc}. If a derivative term with respect to "$(\mathrm{K}C_{mmc}/2)v_{dc}^2$" is also added to the DC power reference, (5.5) can be re-written as in (5.21):

$$\frac{1}{2}C_{dc}\frac{dv_{dc}^2}{dt} = P_l - P^*_{dc} \tag{5.21a}$$

$$\frac{1}{2}C_{dc}\frac{dv_{dc}^2}{dt} = P_l - \frac{\mathrm{K}C_{mmc}}{2}\frac{dv_{dc}^2}{dt} - P^*_{droop} - P^*_{dc0} \tag{5.21b}$$

Re-arranging (5.21b), it yields (5.22).

$$\textit{Derivative Control:}\ \frac{1}{2}\underbrace{(C_{dc} + \mathrm{K}C_{mmc})}_{C_{eff}}\frac{dv_{dc}^2}{dt} = P_l - P^*_{droop} - P^*_{dc0} \tag{5.22}$$

As shown in (5.22), the effective DC bus capacitance C_{eff} considers C_{dc} and also K times the total capacitance of the MMC. This results in the same value of C_{eff} as for the *Virtual Capacitor* control.

The studied energy management controller in this sub-section is given in Fig. 5.26, where the main characteristic for this case is that the generation of P^*_{ac} and P^*_{dc} are decoupled. Also, a derivative term for the squared value of v_{dc} is added to the DC power reference. Moreover, a washout filter (Low-Pass Filter (LPF)) is added for overcoming the fast changes of the derivative action.

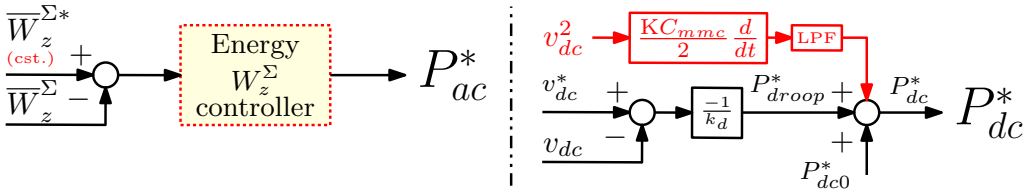

Figure 5.26 – Energy management controllers for droop-controlled MMC — Derivative control

Time domain simulations

The same time domain simulation is performed for the energy management strategy from Fig. 5.26, as in previous Section with the same simulation parameters. Results for the DC powers are shown in Fig. 5.27a, while in Fig. 5.27b they gather the results for the DC bus voltages. Comparing the results from Fig. 5.27 with the waveforms from previous strategy in Fig. 5.20, it can be noticed that the DC powers behave similarly.

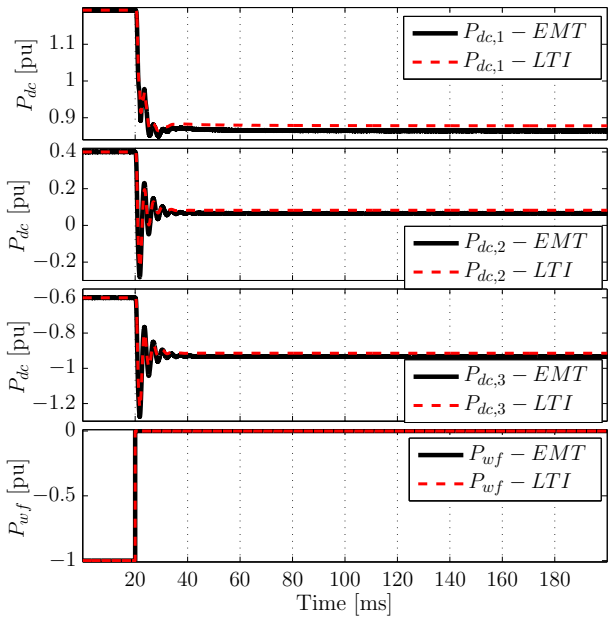

(a) DC Power

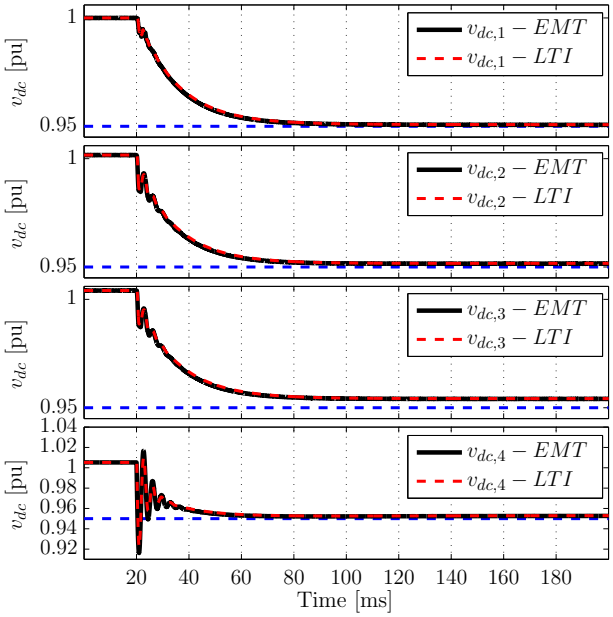

(b) DC Voltage

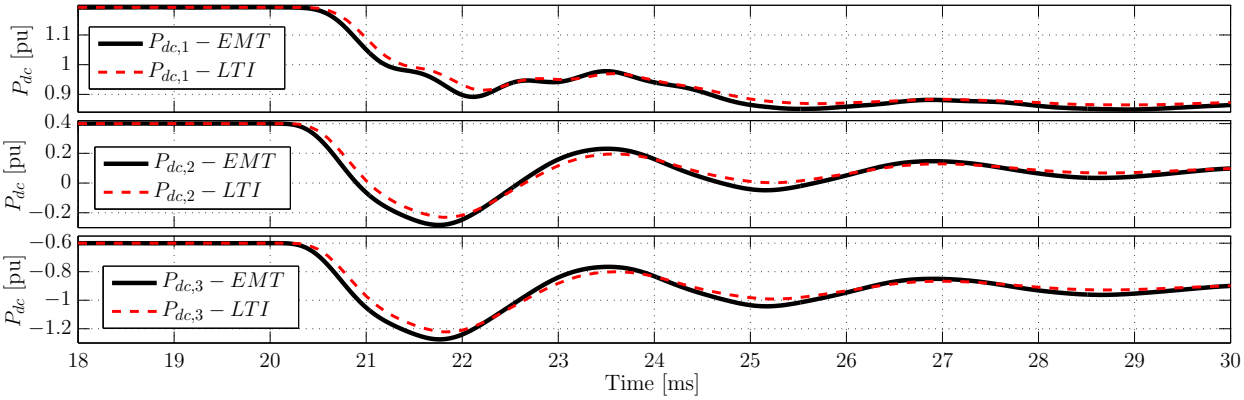

(c) DC Power (detail)

Figure 5.27 – Comparison of time-domain simulations of EMT and small-signal model (LTI) of a four terminal MTDC grid - Converters are equipped with *Energy-based* controllers with the derivative control from Fig. 5.26 (K = 1.1 for MMC-1, MMC-2 and MMC-3)

Similarly as in Fig. 5.21, results from Fig. 5.28a gathers the time domain waveforms of the arm capacitor voltages for the MMC-1. Also, it is shown $\sqrt{W_z^{\Sigma}}$ and the DC voltage value $v_{dc,1}$. In Fig. 5.28b, the AC and DC powers form MMC-1 are shown. At $t = 20$ ms, the wind farm power drops from 1 pu to zero abruptly; from the MMC-1 standpoint, the converter measures the DC voltage and reacts with the droop constant in conjunction with the derivative action

to damp the DC voltage oscillations. This is reflected in the fast action on the DC power. Once the DC voltage is stabilized, the DC power remains constant at the new operating point (around $t = 40$ ms). The energy used for supporting the DC voltage is obtained from the arm capacitor voltages, which are discharged. From the AC standpoint, the energy controller measures that the stored energy was perturbed, and reacts with the energy controller to restore the nominal arm voltages levels at 1 pu with a time response of 50 ms (from the W_z^{Σ} controller).

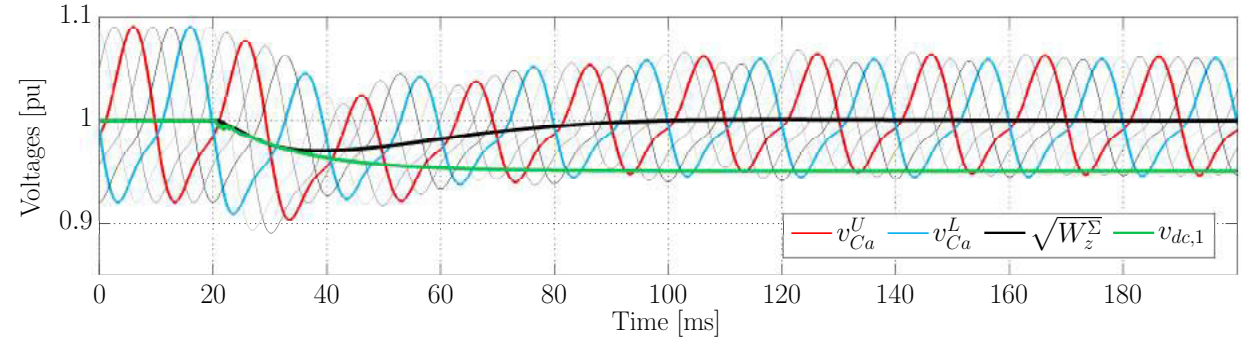

(a) Arm capacitor voltages, DC voltage and internal stored energy

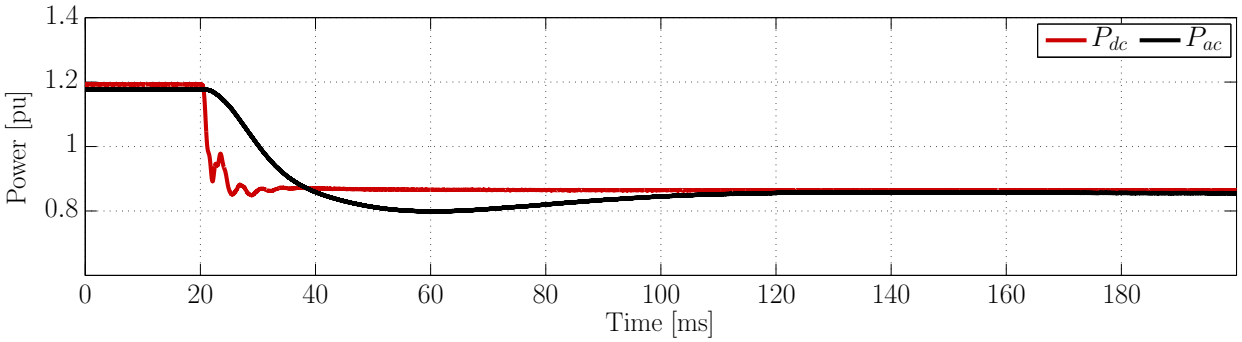

(b) AC and DC powers

Figure 5.28 – Electrical waveforms for MMC-1 — *Energy-based* controllers with Derivative control

Results from Fig. 5.28, shows that the derivative strategy from this sub-section overcomes the drawback of the steady-state deviation of the stored energy from the *Virtual Capacitor* control when used in droop-controlled MTDC grids.

Linear analysis and Comparisons with previous strategy

In Fig. 5.29, the eigenvalues from the derivative control and the *Virtual Capacitor* strategy are contrasted. As observed in the figure, the eigenvalues are not the same for both strategies. However, the same tendency is kept: the majority of modes are well damped, while four eigenvalues are poorly damped.

After a participation factor analysis, the four poorly damped eigenvalues are found to be related with the DC voltages. These eigenvalues are listed in Table 5.6. Comparing with the similar eigenvalues from Table 5.5, the modes from the derivative control are farther away from the RHP, while the natural frequencies are higher and the damping are slightly improved.

For comparing the frequency response for each strategy, in Fig. 5.30 they are contrasted the SVD results with the *Virtual Capacitor* control from Section 5.5.1. For the derivative

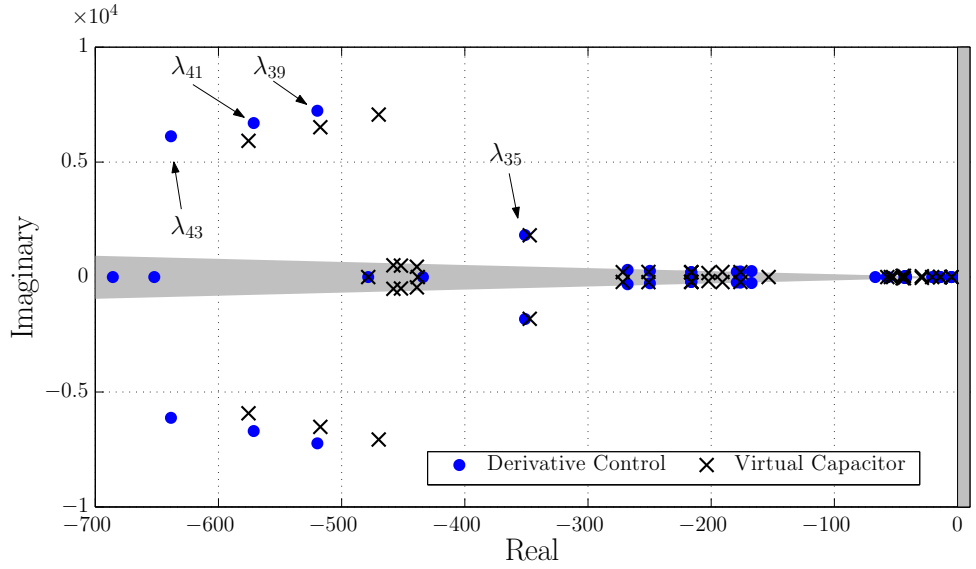

Figure 5.29 – LTI Eigenvalues - MMC equipped with *Energy-based* controllers with *Virtual Capacitor* control or Derivative control — K = 1.1

Table 5.6 – DC Voltage related eigenvalues — MMCs with Derivative control

λ_i	**Eigenvalue**	**Freq. [Hz]**	**Damp. ratio**	**Dominant States** (From Participation Factor analysis)
$\lambda_{35,36}$	$-351.1 \pm j1825.8$	290.6	0.19	$v_{dc,4}$; i_{z1}^{C3} ; i_{z1}^{C4}
$\lambda_{39,40}$	$-519.7 \pm j7232.7$	1151.1	0.07	$i_{z,1}^{\Sigma}$; $v_{dc,1}$; $v_{dc,2}$; $v_{dc,3}$
$\lambda_{41,42}$	$-571.4 \pm j6698.3$	1066.1	0.085	$i_{z,2}^{\Sigma}$; $i_{z,3}^{\Sigma}$; $v_{dc,2}$; $v_{dc,3}$
$\lambda_{43,44}$	$-638.6 \pm j6123.4$	974.6	0.12	$i_{z,1}^{\Sigma}$; $v_{dc,1}$; $v_{dc,2}$

control, the frequency response is slightly different in the Mid-low frequency range, but the rest of the response is highly similar with the other two strategies. This means that from a DC perspective, all the strategies discussed in this section present similar dynamics.

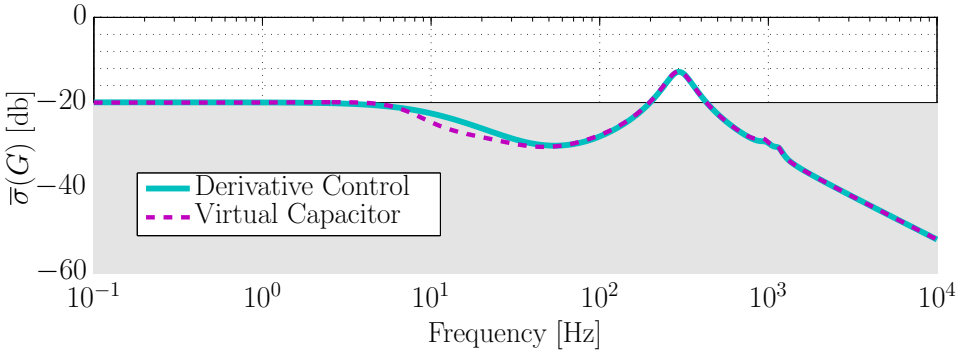

Figure 5.30 – SVD comparisons of MTDC with different energy management strategies: Derivative control (Section 5.5.2) and Virtual Capacitor control (Section 5.5.1) — K = 1.1

One potential drawback of the Derivative control explored in this section deals with the sensitivity of the derivative term on the controller respect to the noise on the measures. However, advanced filtering techniques may be applied to overcome this obstacle, which is out of the scope of this Thesis.

Improving DC voltage dynamics of MTDC grids with Wind Farms

For all studied cases, the DC voltage of the MMC-4 presents several oscillations. This is observed in the marked peak at the Mid-High frequency range in the SVD results from Fig. 5.30 around $\sim$ 290 Hz. This peak corresponds to the uncontrolled DC voltage of the capacitor of the wind farm (see Fig. 5.3a). Normally, if the wind farm is disconnected from the MMC-4, the power step appears on the AC power, but from the DC grid, the converter remains connected and the DC power cannot "disappear" (i.e. a step on P_{wf} is not realistic). The DC power results from the internal dynamics and controllers of the MMC connected to the wind farm. For this reason, the wind farm model and the MMC-4 are modified with the model from Fig. 5.31, where it is introduced the parameter $t_{r,wf}$, which represents the time constant between the AC and DC powers from the simplified representation of MMC-4.

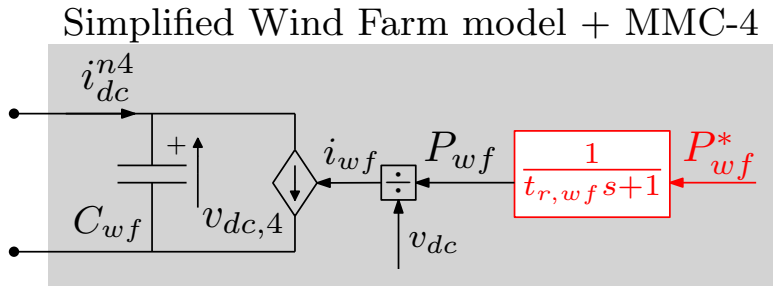

Figure 5.31 – Wind Farm and MMC-4 simplified model with $P_{wf} \neq P_{wf}^{*}$

For evaluating the impact of the time constant $t_{r,wf}$ on the SVD of the MTDC grid, a parametric sweep of $t_{r,wf}$ from 0 ms (pure step) to 2 ms is performed for the Derivative control considering K coefficient of 2.4 (value unreachable for the Virtual Capacitor control). The results are shown in Fig. 5.32. For both cases, the Low- and Mid-Low frequency range remains unaltered respect to the different values of $t_{r,wf}$. For the Mid-High to High frequency ranges, the systems gain is reduced when the time constant is slower as expected. The limits imposed by (5.4) is not violated only when the response time is higher than $t_{r,wf} \approx 1.1$ ms.

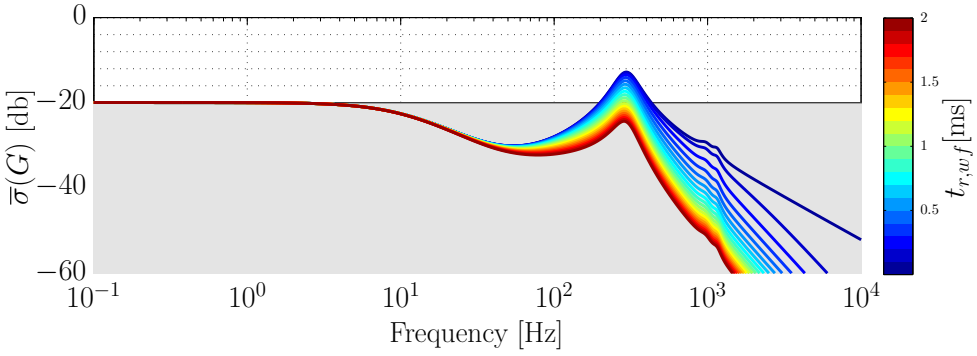

Figure 5.32 – SVD results for a sweep of $t_{r,wf}$ - $P_{wf} = -1$ pu with K = 2.4

For validating the results from Fig. 5.32, the same time domain simulation as in Section 5.5.2 is performed. In this case, it is considered the simplified wind farm model and MMC-4 with the model from Fig. 5.31 and it is considered that $t_{r,wf}$ is equal to 1.5 ms. Results are shown in Fig. 5.33a for the DC power and Fig. 5.33b for the DC bus voltage. As it can be observed, the voltages are maintained strictly within the acceptable limits.

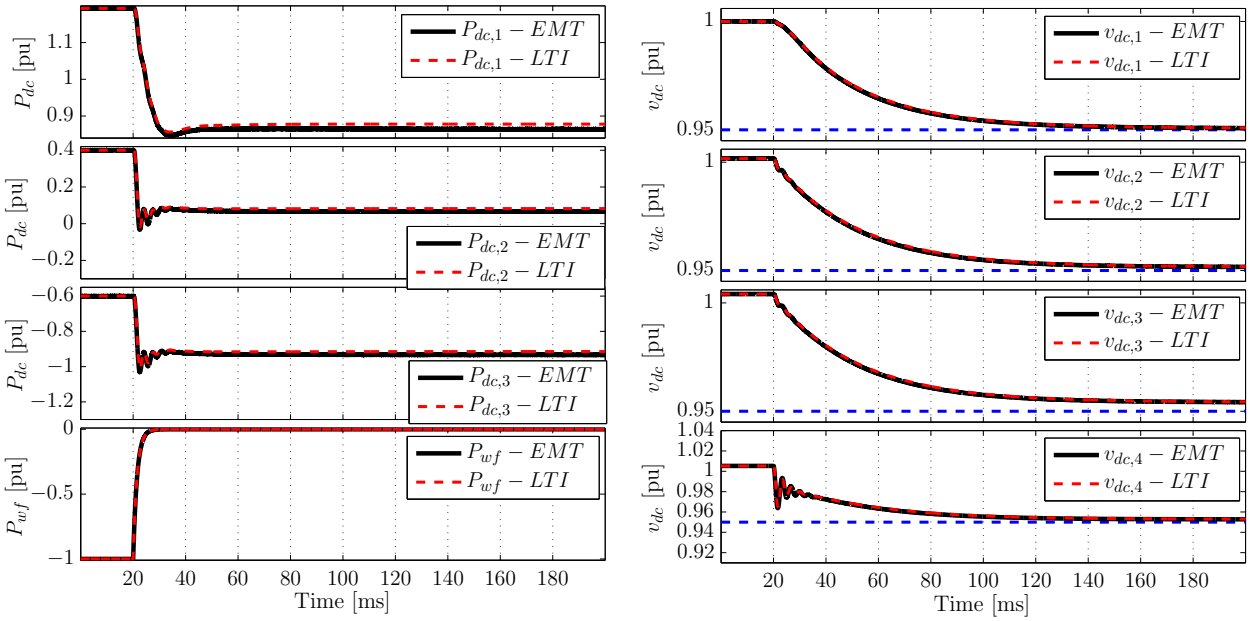

(a) DC Power

(b) DC Voltage

Figure 5.33 – Comparison of time-domain simulations of EMT and small-signal model (LTI) of a four terminal MTDC grid - Converters are equipped with *Energy-based* control with derivative action — K = 2.4 and $t_{r,wf} = 1.5$ms

Results from Figs. 5.32 and 5.33 suggests that avoiding the abrupt changes on the DC power in the wind farm side converter allows to maintain the DC bus voltage at the four terminals between the desired limits. This limit can be verified with the linear model of the complete system (MMCs and cables). This means that the converters associated to wind-farms may also collaborate to improve the power system stability [210,211]. In the following section, a detailed EMT simulation with realistic wind farm models and mixed controllers for the converters are analyzed in view of studying the interoperability.

5.6 EMT Simulation results with different control strategies: Interoperability analysis

For the last set of EMT simulations, it is considered that each MMC is controlled with different strategies, as if it was a realistic multivendor case. The wind farm is modeled with the aggregated model corresponding to full converter wind turbines (Type 4) [212]. Converter MMC-4 is represented by a detailed MMC imposing the AC voltage at its terminals (more details on this controller is found in Appendix F). Four different control strategies are mixed in the same MTDC grid:

- *Classical CCSC*: Control detailed in Section 3.2.
- *Constant energy*: *Energy-based* controller # 2 from Section 3.4.
- *Virtual capacitor* control: Strategy from Section 5.5.1.
- *Derivative* control: Strategy from Section 5.5.2.

Configuration I

The configuration for the first subset of simulations is given in Table 5.7, where different control strategies are adopted for each converter.

Table 5.7 – MTDC grid with different control strategies – Configuration II

Station	Control	K[pu]	C_{mmc} [μF]
MMC-1	*Virtual Capacitor*	1.1	195.3125
MMC-2	*Derivative* control	2.4	195.3125
MMC-3	*Constant energy*	Not applicable	195.3125
MMC-4	*Classical CCSC*	Not applicable	195.3125

From the MTDC standpoint, same converters are sharing their internal energy with the DC grid. For anticipating the results, (1.53) is used for the calculation of the DC voltage response time. With the information in Table 5.8, the effective DC bus capacitance for this example can be calculated as in (5.23) (note that the MMC-3 is not sharing the internal energy).

$$C_{eff} = \underbrace{(1.1 \times 195.3125\mu\text{F})}_{\text{MMC-1}} + \underbrace{(2.4 \times 195.3125\mu\text{F})}_{\text{MMC-2}} + \underbrace{195.3125\mu\text{F}}_{\text{MMC-4}} + \underbrace{22.6185\mu\text{F}}_{\text{DC cables}} \approx 902\mu\text{F} \quad (5.23)$$

Considering C_{eff} from (5.23), and taking into account that there are three converters with droop controller ($N_d = 3$) with gain $k_d = 0.15$, the theoretical first order response time is given in (5.24).

$$\tau_{v_{dc,mtdc}} = 3 \times \frac{k_d}{N_d} C_{eff} \frac{v_{dcn}^2}{P_n} = 3 \times \frac{0.15}{3} 902\mu\text{F} \frac{(640\text{kV})^2}{1\text{GW}} \approx 55\text{ms} \quad (5.24)$$

The initial power flow in the MTDC grid is the same as already used in this Chapter, and given in Table 5.1. The simulated event is the Wind Farm disconnection at $t = 20$ ms. Results of the AC and DC powers for each converter is shown in Fig. 5.34.

As it can be seen, the AC power $P_{ac,4}$ of MMC-4 drops abruptly to zero when the wind farm is disconnected. However, the DC power $P_{dc,4}$ does not follow a pure step (as considered in the simplified model from Fig. 5.3a); instead, the observed dynamics are due to the interactions between its internal energy, the uncontrolled DC current and the DC grid (see Section 3.2. For the DC power of MMC-1, MMC-2 and MMC-3 are more or less oscillatory, depending on the adopted strategy. The oscillations on $P_{dc,2}$ are important, due to the high coefficient K adopted (*Derivative* control). Also, $P_{ac,4}$ is also oscillatory which may be not convenient for its respective AC grid.

Results of the DC voltages are shown in Fig. 5.35, where it is also shown the *Simplified* first order dynamic model from (5.14). Results of $v_{dc,4}$ are more oscillatory since the associated converter is not actively controlling its DC power (note the oscillations on $P_{dc,4}$ from Fig. 5.34). Nevertheless, the DC voltage are well maintained between their limits. It is important to note also that the DC response time from (5.24) is verified in Fig. 5.35: Even if the simplified model presents several assumptions (neglecting all the controllers and assuming perfect energy controllers), the response time can be predicted accurately if the controllers are appropriately tuned.

In Fig. 5.36, results of the stored energy of each MMC are shown. The energy levels for MMC-2 and MMC-3 are stabilized to 1 pu since, while in MMC-3 and MMC-4 the energy levels are given by the DC voltage at their respective terminals and the constant K (for MMC-3).

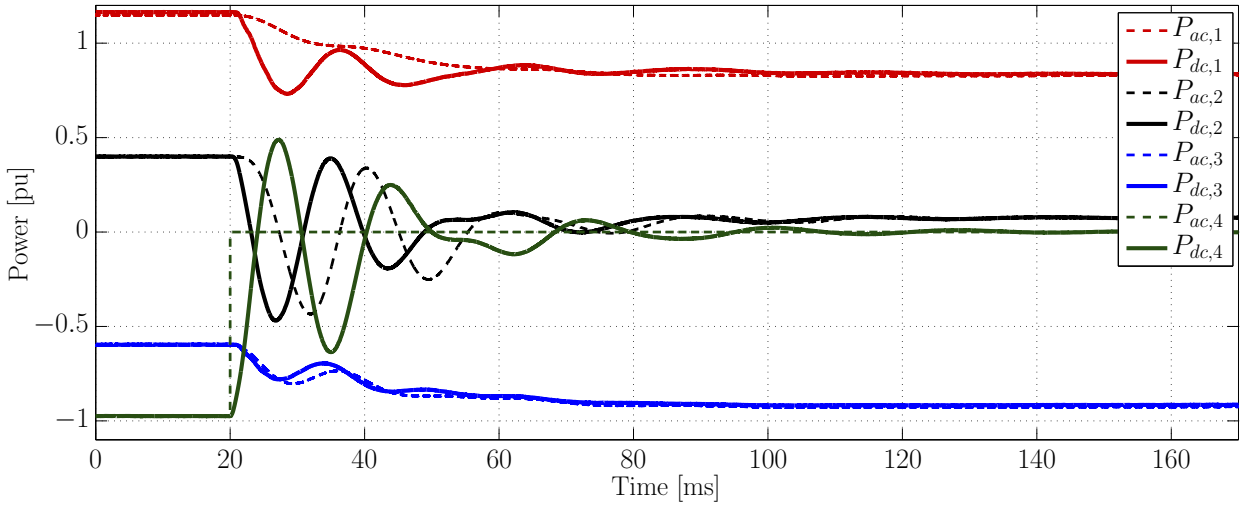

Figure 5.34 – Simulation for interoperability analysis – Configuration I – AC and DC powers

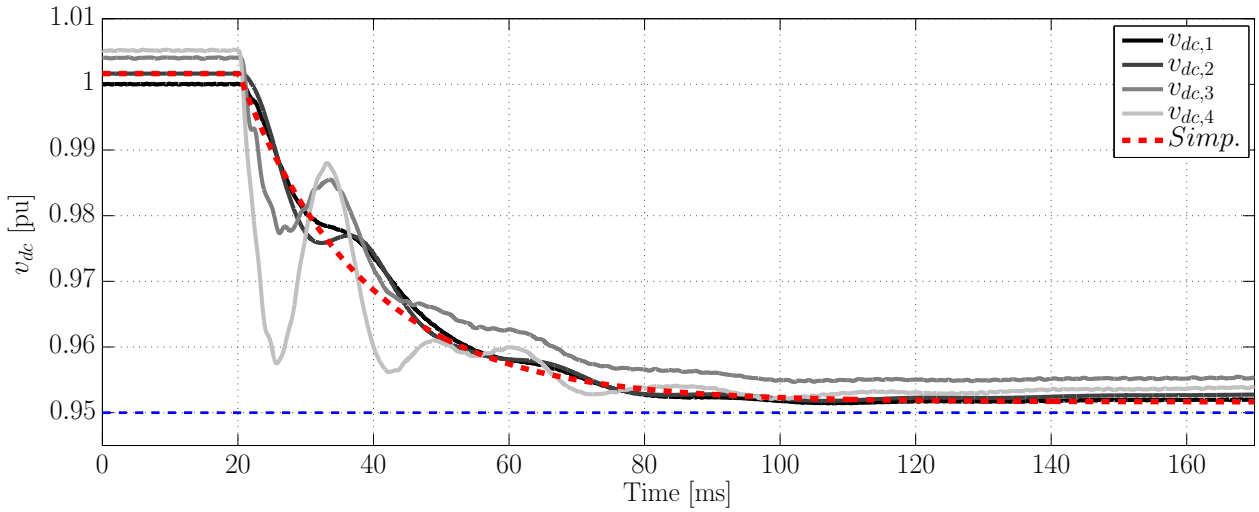

Figure 5.35 – Simulation for interoperability analysis – Configuration I – DC Voltages

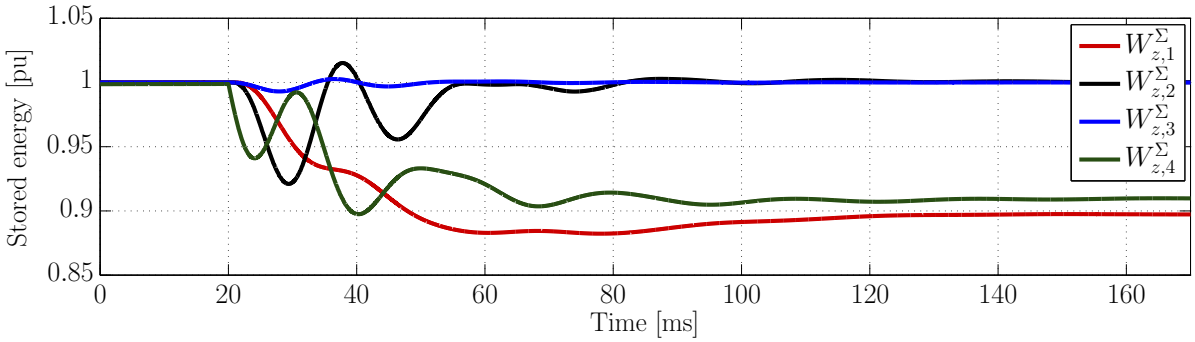

Figure 5.36 – Simulation for interoperability analysis – Configuration I – Stored energy

Configuration II

For the second and last interoperability analysis, the configuration given in Table 5.8 is adopted. Note that the only modification is the control swap of MMC-3 and MMC-4. In this example, the effective DC bus capacitance remains the same as in (5.23), so the theoretical

response time from the simplified model from (5.24) is unchanged.

Table 5.8 – MTDC grid with different control strategies – Configuration I

Station	Control	K[pu]	C_{mmc} [μF]
MMC-1	*Virtual Capacitor*	1.1	195.3125
MMC-2	*Derivative* control	2.4	195.3125
MMC-3	*Classical CCSC*	Not applicable	195.3125
MMC-4	*Constant energy*	Not applicable	195.3125

With the same simulated event as in **Configuration I**, results for the AC and DC powers for each converter are shown in Fig. 5.37. Note that the results of $P_{dc,4}$ are greatly improved with respect to $P_{dc,4}$ in Fig. 5.34 since now MMC-4 is actively controlling the DC power. When the wind-farm is disconnected, MMC-4 regulates its internal energy to 1 pu with the response time given by the energy controllers (around 50 ms). Since the perturbation seen from the DC side (given by $P_{dc,4}$) have smoother dynamics, the responses for the rest of the converters are improved as well.

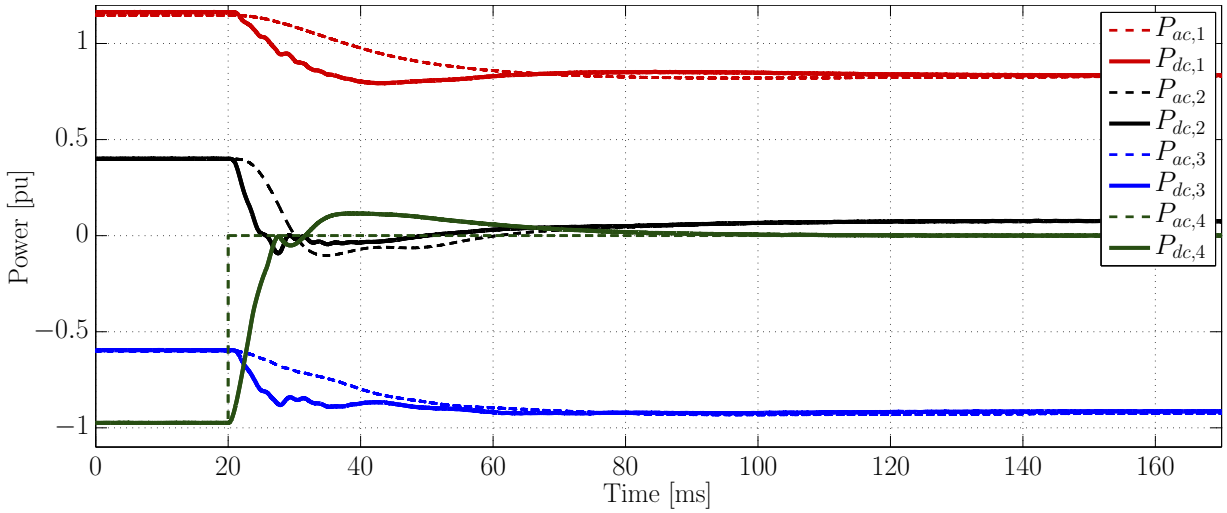

Figure 5.37 – Simulation for interoperability analysis – Configuration II – AC and DC powers

Results for the DC bus voltages are shown in Fig. 5.38, where it is also shown the *Simplified* first order dynamic model from (5.14). The response time is similar to the previous case, but since the DC power $P_{dc,4}$ is not a pure step, the voltage dynamics are clearly improved.

Finally, in Fig. 5.39, results of the stored energies are shown. In this case, MMC-2 and MMC-4 maintain their energies at 1 pu, while the others adapt their energy levels with respect to the DC voltage.

As a final discussion, simulation results suggests that the *Classical CCSC* may not be a suitable controls strategy for MTDC grids and most importantly, if a wind farm is associated to the converter. The MMC presents outstanding potential, and controllers which do not fully regulate their internal variables present the risk of hazardous oscillations which disturbs and increase the interactions between converters. However, even if a converter is controlled with the *Classical CCSC*, there are possibilities to improve the DC grid dynamics by the other converters if they are properly controlled.

The DC voltage dynamics in MMC-based MTDC grids are governed by many factors. Simulation results suggest that the droop parameter can be used effectively for setting the

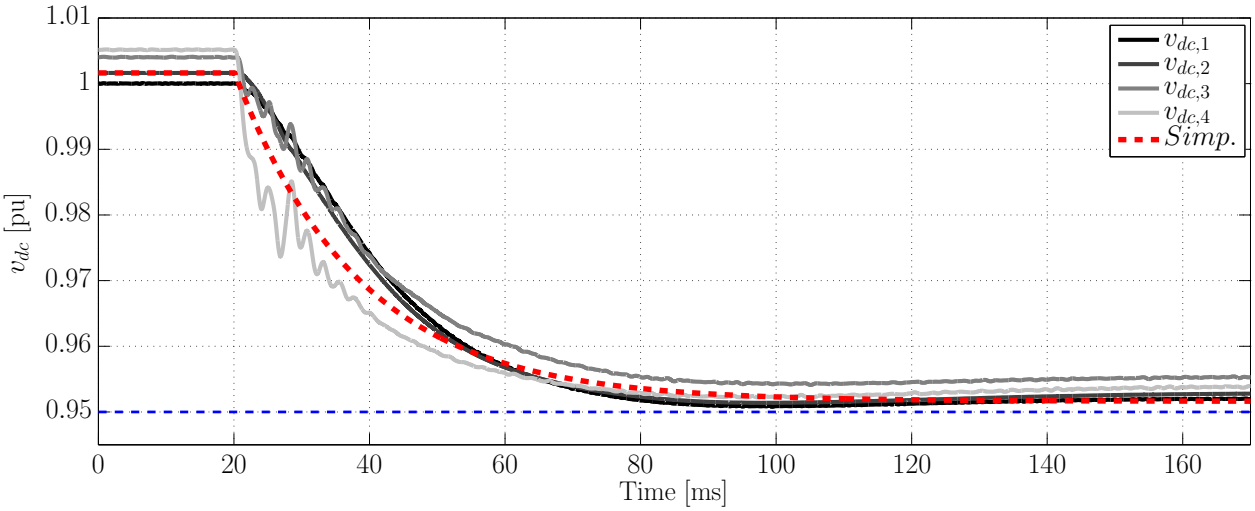

Figure 5.38 – Simulation for interoperability analysis – Configuration II – DC Voltages

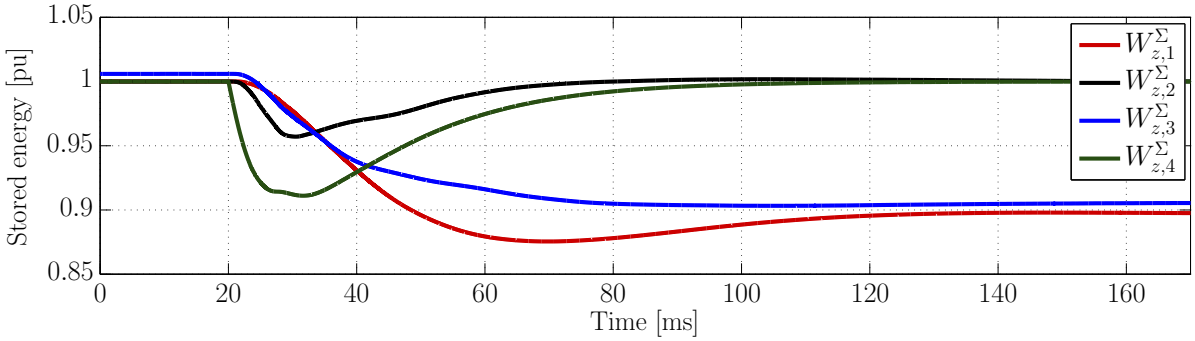

Figure 5.39 – Simulation for interoperability analysis – Configuration II – Stored energy

steady-state deviation and sharing the effort between converters, while energy management strategies can be involved in the overall response time (by virtually changing the effective DC grids capacitance). Only two methods for the energy management were presented, but more advanced strategies may be developed for improving even more the MTDC dynamics, and augmenting the interoperability between converters.

5.7 Chapter Conclusions

In this Chapter, a four-terminal MTDC based on droop-controlled MMCs was studied. This example helped to investigate the impact of different MMC control strategies on the overall MTDC dynamics. The objective was to identify the main key parameters that play an important role on the grid dynamics with the usage of linear analysis tools and EMT simulations for validating the studied concepts.

As discussed in the introduction, special attention is given to the DC voltage dynamics since the cables are one of the most critical parts of the grid. First, it was used the MMC controllers developed in previous Chapters: *Classical CCSC* and *Energy-based* controllers (with decoupled energy with the DC bus). Once more, the *Classical CCSC* strategy showed that the voltage limits are easily violated, and the grid dynamics are very poor. However, even if the consideration of *Energy-based* controllers improves partially the grid dynamics, the low energy storage level on the DC grid is not sufficient to guarantee acceptable dynamics.

In small MTDC grids, it may possibly be allowed to loosen the imposed limitation on the acceptable DC voltage deviation during transients. In this Chapter, it is proven that with appropriated MMC control strategies, the DC voltage deviations can be effectively limited if each MMC can use its own dedicated internal energy management control strategy. The development of different strategies are possible since the MMCs under *Energy-based* control strategy have the possibility to independently control their AC and DC powers (which was not possible with *2-level* VSC). Since the DC voltage is directly linked with the DC power at each terminal, different strategies can be employed. In this way, the internal energy of the MMCs can be used to support the DC voltage, as if the MMC behaved as a physical capacitor connected directly on the DC side. Most importantly, this capacitance can be even bigger than the internal MMC capacitance.

Two different variants for using the internal energy of the MMC to collaborate on the DC dynamics were considered: the first strategy is based on the coupling of the MMC internal energy with the DC bus setting the internal energy reference associated to the square of the DC voltage. Nevertheless, if a DC voltage deviation occurs (e.g. in droop-controlled MTDC grids after a severe change on the power flow), the arm capacitor voltages may be discharged abruptly, hitting the converter limits. The second option is based on a derivative control for improving the DC dynamics. Since with this strategy the internal energy and the DC bus are controlled in separated control paths, the internal energy is maintained at a nominal value at any time. However, the real implementation of derivative controllers should be studied in detail since they may be increase the sensitivity of the controllers (e.g. noise on the measures). It is important to mention that many other energy management techniques may arise for improving the DC voltage, however a main philosophy remain: the droop controller is in charge of the DC voltage and power deviation in steady state, while an extra energy management controller improves the DC voltage dynamics.

In terms of interoperability, this Chapter shows that the choice of the MMC controller have an important impact on the MTDC grid dynamics. The usage of *Energy-based* controllers may be preferred but smart management of the internal energy is needed. The MTDC grid is always a *weak grid* in terms of stored energy, so the converters which are feeding (e.g. with offshore wind farms) or taking power (e.g. onshore), should collaborate to strengthen the MTDC thanks to improved dynamics.

Chapter 6

Conclusions and Future Research

6.1 Conclusions

The integration of Multi-Terminal DC grids into the existing power networks has challenged many aspects of the electrical engineering field. On one hand, the technology is now fully available for HVDC projects with high power ratings. The Modular Multilevel Converter is the most suitable topology to cope with the ambitious objectives of HVDC integration and it is likely to be the most widely adopted topology for future projects. In the other hand, MTDC grids are likely to be multivendor schemes, where the development of control and protection algorithms for each converter station would be handled by each manufacturer involved in the project and they must guarantee interoperability for each converter within the DC and AC grids. As demonstrated in this Thesis, the possibilities for controlling the MMC are very wide, and the dynamics of DC grids are highly impacted with respect to the control chosen for each converter.

This Thesis aims at assessing some of the key elements for the dynamic analysis of MMC-based MTDC grids in order to study possible interoperability issues that may arise. In the following, the main Chapter conclusions are summarized:

1. A methodology for dynamic analysis of HVDC systems with power electronics converters was detailed in Chapter 1. The main aspects for modeling HVDC systems with *2-level* converters were detailed. First, the *simulation models* are distinguished from the *models for analysis*. The *simulation models* are detailed systems developed for Electro-Magnetic Transient simulations (typically used in the industry). These models represent, with high accuracy, the real behavior of the converters, but in many cases they are provided as black-box models (as in the *Best Paths* DEMO # 2 project) which make the study and categorization of the converters and controllers an impossible task (not to mention legal consequences). The *models for analysis*, which are typically non-linear continuous models represented by a subset of first order differential equations, are provided for the mathematical analysis of the converters and their integration in AC and DC grids. At this point, two mathematical families of models arise: The first one is referred to as "Steady-State Time-Periodical" model (SSTP), where the state variables in steady state have "sinus and cosines" terms in their equilibrium solution. This model is not suitable for classical linearization for eigenvalue analysis. In the second one, referred to as "Steady-State Time-Invariant" model (SSTI), all the state variables converge to a fixed value when the converter reaches a given operating point. This mathematical model can be linearized around an operating point so linear mathematical tools can be applied for stability and dynamic analysis of the complete systems. Furthermore, the

fundamentals of the operating principles and distributed control (droop) of MTDC grids are discussed.

2. To apply the aforementioned methodology with MMCs, a suitable non-linear continuous mathematical model is needed, able to represent all the internal dynamics with high accuracy, i.e. a *model for analysis* with SSTI representation. In Chapter 2, an in-depth analysis on the mathematical equations of the MMC in Synchronous Rotating Reference Frame is provided to deduce the complete SSTI MMC model. A detailed time-domain validation is provided, which proves an excellent matching with the detailed *simulation model* of the MMC.

3. Once the SSTI *model for analysis* of the MMC is obtained, the most common control strategies readily available are discussed in Chapter 3 for the integration of the converters in AC and DC grids. In this Chapter, two modulation strategies are discussed: Un-Compensated or Compensated Modulation, UCM or CM respectively. In addition, two main control strategies arise: *Classical CCSC* with UCM and *Energy-Based* controllers with CM. The first one is a typical control which relies on the elimination of the circulating currents inside the converter, while controlling the AC outputs. Since the DC current is left uncontrolled, it is shown that hazardous interactions of this current with the DC grid may occur and destabilize the entire system depending on several aspects (as DC grid capacitance, arm inductances or even controllers tuning). To improve the stability, the *Energy-Based* controllers are presented. This strategy is based on the control of all the internal variables of the MMC (currents and stored energies). However, it is first needed to adapt the controllers for their proper interface with the SSTI model previously developed. Some of the control loops are already developed in Synchronous Rotating Reference Frame (such as the AC grid current control loops in dq frame or the classical Circulating Current Suppressing Controller), while the others are expressed in Fixed Reference Frame (abc) as it is the case for the energy sum and energy controllers for internal balancing of the energies inside the converter. Mathematical manipulations are therefore exposed to fully express all the MMC control loops in SSTI form; finally, time-domain validations are also provided.

4. To study larger systems such as MTDC grids, the complexity of each converter and their controllers makes linear analysis difficult for interoperability studies. For this reason, Chapter 4 deals with the application of SSTI-MMC reduced order models to interface AC and DC grids. In this Chapter, a reduced order model that can potentially represent the terminal behavior of the MMC is developed. Several studies are performed to contrast the model validity when the MMC *simulation model* is controlled with the *Classical CCSC* and UCM on one hand, or by *Energy-Based* controllers and CM on the other hand. It is proven that the reduced order model can replicate accurately the behavior of the MMC when assuming an *Energy-Based* controllers with CM since the modulation technique decouples successfully the internal dynamics of the converter. This way, the un-modeled dynamics of the reduced-order model do not participate on the terminal behavior of the AC and DC sides under the studied cases (MMCs are under balanced AC grids and in normal operation mode). Furthermore, it is proven that the reduced-order model fails to represent accurately the MMC when considering the *Classical CCSC* with UCM. This conclusion is in counter-phase with several studies already published where the usage of the reduced order model was performed without a proper model validation. Consequently, the full order SSTI-MMC model from Chapter 2 is the recommended option when the

aforementioned control strategy is considered. For other control variants, such as the mixing of *Energy-based* controllers with UCM and CCSC, the use of the reduced-order model results in limited accuracy, since the UCM causes several internal couplings that should be represented to ensure the validity of the involved studies.

5. In Chapter 5, the study of MMC-based MTDC grids with offshore wind farms is performed in order to study the interoperability among various converters. Special focus is given to the dynamic behavior of the DC voltage at each converter DC point of connection. From the elements provided in previous Chapters, it was shown that the main characteristic of the MMC-based MTDC grids is the potential lack of stored energy on the DC grid which may cause hazardous oscillations on the DC voltages. For this reason, the studies are conducted to evaluate different energy management policies, in order to supply additional features for the DC grid and to improve the overall system dynamics. With the proper use of the MMC internal energy on each converter, the DC voltage behavior can be highly improved; in fact, even the response time of the entire grid can be adjusted by these control strategies. When taking advantage of these energy management strategies, the improvement of the DC voltage behavior at each terminal contributes to the reduction of possible interoperability issues between the converters.

As concluding remarks, it is important to highlight that the multivendor MTDC grids are very ambitious yet feasible layouts with respect to the control strategies. As exhibited in the *Best Paths* project, anticipating interoperability issues between MMCs provided by different HVDC suppliers is a modern concern. This Thesis is a first attempt to solve such issues from a technical perspective, mostly focusing on various converter controls. However, the *Best Paths* project also highlighted other kinds of difficulties related to the Intellectual Property, which make it almost impossible to use the methodologies and concepts developed in this Thesis without violating confidentiality requirement. For the development and study of future multivendor schemes, it may be convenient to disclose some fundamental information to be able to use at least generic models that can reproduce the behavior of the vendors' models. In the ideal case, the disclosure of the main control strategy applied in the MMC could maximize the impact and validity of research studies.

6.2 Future Research

From this Thesis, various tracks may be followed to extend the studies of MMC systems in order to interfacing AC and DC grids, as listed hereunder:

- As pointed out in the Introduction, VSCs can synthesize AC voltage waveforms, the quality of which is particularly outstanding with the MMC. In future grids, it may happen that HVDC converters are feeding AC loads without any synchronous machines. In that situation, VSCs are no longer feeding the AC grid ("grid feeding" mode), but creating by themselves the AC grid ("grid forming" mode). This means that the interoperability of multivendor schemes with power electronic converters operating in "grid forming" mode connected to the same AC grid should be assessed. Also, the synchronization between the involved VSCs in this particular control mode should be studied carefully.
- Un-balanced situations on the AC grid occur regularly. In these cases, the control design, as well as the grid synchronization techniques should be revisited. These cases were studied in the literature for *2-level* VSCs and some of them with MMCs; however the

MMC provides many options for control strategies as exposed in this Thesis so the most relevant solution is yet to be investigated.

- The study of AC and DC faults and how they are managed is crucial for the development of HVDC systems. Many converter topologies are readily available with inherent fault-blocking capabilities such as the full-bridge MMC, but also the late advances of fast DC breakers are showing that this evolving technology may cope with DC faults. The AC and DC faults handling with different options should be assessed to find a good compromise between performance and cost.
- If DC breakers are to be installed in HVDC systems, it obliges to check over the modeling and control systems to take into account the new devices into the HVDC grid (e.g. large inductances connected on the DC side are likely to impact on the DC current dynamics, for this reason, the DC current controllers should take into account this modification).
- In this Thesis it was shown that linear models can be used to represent MMCs, their controllers and the whole DC grid. The mathematical tools used among this document are quite popular, but sometimes it is difficult to obtain relevant conclusions from them. The linear models developed during this Thesis may have a large number of state-variables when considering large systems. This results in a high number of modes, making the eigen-analysis a complicated task. Improved model order reduction techniques should be developed for a better understanding of the interactions in HVDC grids.
- For obtaining the LTI model for classical linear analysis, an SSTI-MMC model was obtained. This SSTI model is mathematically complex as shown in Chapter 2. On the other hand, the MMC model for analysis with LTP theory is very well-known and relatively simple (i.e. the AAM). However, the LTP theory may be somehow complex to be applied in large systems. It is relevant to further investigate and compare analysis based on LTP models and LTI to complement each other.
- In Chapter 2, the 6^{th} harmonic components appearing in the "Σ" variables were constantly ignored. By time domain simulations, it was shown that the amplitude of these components are negligible with respect to their constant components. However, it should be of interest to study if there is a case where the aforementioned 6^{th} harmonic components may influence in the stability of the MMC.
- In the last months, impedance-based stability has become quite successful for HVDC studies, dealing mostly with *2-level* VSC converters [185]. In this Thesis, the MMC model and control were developed in a way that the impedance expression can be obtained in a straightforward manner. The use of impedance-based stability analysis using MMCs and considering different control strategies may be a relevant topic of further studies. In real projects, the specifications from the TSOs to the vendors are more likely to be expressed in time-domain requirements; however, it may be relevant to complement this information with detailed and determined frequency responses for the converter (i.e. imposing the "frequency response shapes" and boundaries that the converters must comply). Moreover, the impedance-based analysis techniques may be compatible for dealing with "black-box" converter models, and still being able to conclude on the system stability, as recently discussed in [213].
- The coordinated control of MTDC grids is a key stone on the proper functioning of the electrical systems. Several techniques were already developed in past years focusing on classical *2-level* VSC. The internal MMC energy management may be used for ancillary services on DC grids (as explored in this Thesis) but also on the AC grids. Dedicated master controllers for the alleviation of AC corridors in power systems can be achieved by a proper management with the fast responsive MMCs.

Nomenclature

Acronyms

Circulating Currents $\boldsymbol{i}_{\boldsymbol{dq}}^{\boldsymbol{\Sigma}}$ or $\boldsymbol{i}_{\boldsymbol{\alpha\beta}}^{\boldsymbol{\Sigma}}$

AAM Arm Averaged Model (Model #3 in [111])

CCSC Circulating Current Suppressing Controller

CM Compensated Modulation

ECBM Equivalent Circuit-Based Model (Model #2 in [111])

FD-Π Frequency Dependent Π cable model

HVDC High Voltage Direct Current

MIMO Multi Input Multi Output

MTDC Multi-Terminal DC Grid

PCC-AC Point of Common Coupling on AC side

PCC-DC Point of Common Coupling on DC side

PI Proportional-Integral controller

PID Proportional-Integral-Derivative controller

SCR Short-Circuit Ratio

SIMO Single Input Multi Output

SISO Single Input Single Output

SSTI Steady-State Time Invariant

SSTP Steady-State Time Periodic

TSO Transmission System Operator

UCM Un-Comensated modulation

MMC/VSC Parameters

$C_{eq} \quad = 6C_{arm}$

$L_{eq}^{ac} = L_f + L_{arm}/2$

$L_{eq}^{dc} = 2L_{arm}/3$

$R_{eq}^{ac} = R_f + R_{arm}/2$

$R_{eq}^{dc} = 2R_{arm}/3$

C Sub-modules capacitance

C_{eff} Equivalent capacitance of the MTDC grid (MMC)

C_{mtdc} Equivalent capacitance of the MTDC grid (*2-level VSC*)

C_S DC-side capacitance of a *2-level VSC*

H_S DC-side electrostatic constant of a *2-level VSC*

k_{dr} DC Voltage droop parameter in SI

k_d DC Voltage droop parameter in PU

L_{arm} Arm inductor

L_f AC filter inductor

N Number of submodules within an arm

R_{arm} Arm series equivalent resistance

R_f AC filter resistance

S_i Switch in a submodule, lower switch S_1; upper switch S_2

$C_{arm} = C/N$

Vectors

$\overline{\boldsymbol{W}}_{\boldsymbol{abc}}^{\boldsymbol{\Delta}} = [\overline{W}_a^{\Delta}, \overline{W}_b^{\Delta}, \overline{W}_c^{\Delta}]^{\top}$ - Filtered value of the energy "Δ" in *abc* frame

$\overline{\boldsymbol{W}}_{\boldsymbol{dqz}}^{\boldsymbol{\Delta}} = [\overline{W}_d^{\Delta}, \overline{W}_q^{\Delta}, \overline{W}_z^{\Delta}]^{\top}$ - Filtered value of the energy "Σ" in *dqz* frame

$\overline{\boldsymbol{W}}_{\boldsymbol{dqZ}}^{\boldsymbol{\Delta}} = [\overline{W}_d^{\Delta}, \overline{W}_q^{\Delta}, \overline{W}_{Z_d}^{\Delta}, \overline{W}_{Z_q}^{\Delta}]^{\top}$ - Filtered value of the energy "Δ" in *dqZ* frame

$\overline{\boldsymbol{W}}_{\boldsymbol{abc}}^{\boldsymbol{\Sigma}} = [\overline{W}_a^{\Sigma}, \overline{W}_b^{\Sigma}, \overline{W}_c^{\Sigma}]^{\top}$ - Filtered value of the energy "Σ" in *abc* frame

$\overline{\boldsymbol{W}}_{\boldsymbol{dqz}}^{\boldsymbol{\Sigma}} = [\overline{W}_d^{\Sigma}, \overline{W}_q^{\Sigma}, \overline{W}_z^{\Sigma}]^{\top}$ - Filtered value of the energy "Σ" in *dqz* frame

$\boldsymbol{i}_{\boldsymbol{abc}}^{\boldsymbol{\Delta}} = [i_a^{\Delta}, i_b^{\Delta}, i_c^{\Delta}]^{\top}$ - Grid currents "Δ" in *abc* frame

$\boldsymbol{i}_{\boldsymbol{dqz}}^{\boldsymbol{\Delta}} = [i_d^{\Delta}, i_q^{\Delta}, i_z^{\Delta}]^{\top}$ - Grid currents "Δ" in *dqz* frame

$\boldsymbol{i}_{\boldsymbol{abc}}^{\boldsymbol{\Sigma}} = [i_a^{\Sigma}, i_c^{\Sigma}, i_c^{\Sigma}]^{\top}$ - Common mode currents in the MMC in *abc* frame

$\boldsymbol{i}_{\boldsymbol{dqz}}^{\boldsymbol{\Sigma}} = [i_d^{\Sigma}, i_q^{\Sigma}, i_z^{\Sigma}]^{\top}$ - Common mode currents in the MMC in *dqz* frame

$\boldsymbol{m}^{\boldsymbol{\Delta}}_{\boldsymbol{abc}} = [m^{\Delta}_a, m^{\Delta}_b, m^{\Delta}_c]^{\top}$ - Modulation indexes "Δ" in *abc* frame

$\boldsymbol{m}^{\boldsymbol{\Delta}}_{\boldsymbol{dqz}} = [m^{\Delta}_d, m^{\Delta}_q, m^{\Delta}_z]^{\top}$ - Modulation indexes "Δ" in *dqz* frame

$\boldsymbol{m}^{\boldsymbol{\Delta}}_{\boldsymbol{dqZ}} = [m^{\Delta}_d, m^{\Delta}_q, m^{\Delta}_{Z_d}, m^{\Delta}_{Z_q}]^{\top}$ - Modulation indexes "Δ" in *dqZ* frame

$\boldsymbol{m}^{\boldsymbol{\Sigma}}_{\boldsymbol{abc}} = [m^{\Sigma}_a, m^{\Sigma}_b, m^{\Sigma}_c]^{\top}$ - Modulation indexes "Σ" in *abc* frame

$\boldsymbol{m}^{\boldsymbol{\Sigma}}_{\boldsymbol{dqz}} = [m^{\Sigma}_d, m^{\Sigma}_q, m^{\Sigma}_z]^{\top}$ - Modulation indexes "Σ" in *dqz* frame

$\boldsymbol{v}^{\boldsymbol{\Delta}}_{\boldsymbol{Cabc}} = [v^{\Delta}_{Ca}, v^{\Delta}_{Cb}, v^{\Delta}_{Cc}]^{\top}$ - Arm capacitor voltages "Δ" in *abc* frame

$\boldsymbol{v}^{\boldsymbol{\Delta}}_{\boldsymbol{Cdqz}} = [v^{\Delta}_{Cd}, v^{\Delta}_{Cq}, v^{\Delta}_{Cz}]^{\top}$ - Arm capacitor voltages "Δ" in *dqz* frame

$\boldsymbol{v}^{\boldsymbol{\Delta}}_{\boldsymbol{CdqZ}} = [v^{\Delta}_{Cd}, v^{\Delta}_{Cq}, v^{\Delta}_{CZ_d}, v^{\Delta}_{CZ_q}]^{\top}$ - Arm capacitor voltages "Δ" in *dqZ* frame

$\boldsymbol{v}^{\boldsymbol{\Sigma}}_{\boldsymbol{Cabc}} = [v^{\Sigma}_{Ca}, v^{\Sigma}_{Cb}, v^{\Sigma}_{Cc}]^{\top}$ - Arm capacitor voltages "Σ" in *abc* frame

$\boldsymbol{v}^{\boldsymbol{\Sigma}}_{\boldsymbol{Cdqz}} = [v^{\Sigma}_{Cd}, v^{\Sigma}_{Cq}, v^{\Sigma}_{Cz}]^{\top}$ - Arm capacitor voltages "Σ" in *dqz* frame

$\boldsymbol{v}^{\boldsymbol{G}}_{\boldsymbol{dqz}} = [v^{G}_d, v^{G}_q, v^{G}_z]^{\top}$ - AC grid voltages in *dqz* frame

$\boldsymbol{v}^{\boldsymbol{\Delta}}_{\boldsymbol{mdqz}} = [v^{\Delta}_{md}, v^{\Delta}_{mq}, v^{\Delta}_{mz}]^{\top}$ - Modulated voltages driving "Δ" in *dqz* frame

$\boldsymbol{v}^{\boldsymbol{\Delta}}_{\boldsymbol{mdqZ}} = [v^{\Delta}_{md}, v^{\Delta}_{mq}, v^{\Delta}_{mZ_d}, v^{\Delta}_{mZ_q}]^{\top}$ - Modulated voltages "Δ" in *dqZ* frame

$\boldsymbol{v}^{\boldsymbol{\Sigma}}_{\boldsymbol{mabc}} = [v^{\Sigma}_{ma}, v^{\Sigma}_{mb}, v^{\Sigma}_{mc}]^{\top}$ - Modulated voltages driving "Σ" currents in *abc* frame

$\boldsymbol{v}^{\boldsymbol{\Sigma}}_{\boldsymbol{mdqz}} = [v^{\Sigma}_{md}, v^{\Sigma}_{mq}, v^{\Sigma}_{mz}]^{\top}$ - Modulated voltages "Σ" in *dqZ* frame

$\boldsymbol{W}^{\boldsymbol{\Delta}}_{\boldsymbol{abc}} = [W^{\Delta}_a, W^{\Delta}_b, W^{\Delta}_c]^{\top}$ - Energy "Δ" in *abc* frame

$\boldsymbol{W}^{\boldsymbol{\Delta}}_{\boldsymbol{dqz}} = [W^{\Delta}_d, W^{\Delta}_q, W^{\Delta}_z]^{\top}$ - Energy "Δ" in *dqz* frame

$\boldsymbol{W}^{\boldsymbol{\Delta}}_{\boldsymbol{dqZ}} = [W^{\Delta}_d, W^{\Delta}_q, W^{\Delta}_{Z_d}, W^{\Delta}_{Z_q}]^{\top}$ - Energy "Δ" in *dqZ* frame

$\boldsymbol{W}^{\boldsymbol{\Sigma}}_{\boldsymbol{abc}} = [W^{\Sigma}_a, W^{\Sigma}_b, W^{\Sigma}_c]^{\top}$ - Energy "Σ" in *abc* frame

$\boldsymbol{W}^{\boldsymbol{\Sigma}}_{\boldsymbol{dqz}} = [W^{\Sigma}_d, W^{\Sigma}_q, W^{\Sigma}_z]^{\top}$ - Energy "Σ" in *dqz* frame

Variables

$\overline{W}^{\Delta}_z = \overline{W}^{\Delta}_{Z_d}\cos(3\omega) + \overline{W}^{\Delta}_{Z_q}\sin(3\omega)$ - Zero-sequence filtered energy "Δ"

$i_{dc} = i^{\Sigma}_a + i^{\Sigma}_b + i^{\Sigma}_c = 3i^{\Sigma}_z$ - DC current

$i^{\Delta}_j = i^{U}_j - i^{L}_j$ - AC line current of the phase j

$i^{\Sigma}_j = (i^{U}_j + i^{L}_j)/2$ - Common-mode current of the phase j

λ_i Eigenvalue i

$m^{\Delta}_z = m^{\Delta}_{Z_d}\cos(3\omega) + m^{\Delta}_{Z_q}\sin(3\omega)$ - Zero-sequence modulation index "Δ"

ω AC grid angular frequency

v_{Cj}^{Δ} $= (v_{Cj}^{U} - v_{Cj}^{L})/2$

v_{Cz}^{Δ} $= v_{CZ_d}^{\Delta}\cos(3\omega) + v_{CZ_q}^{\Delta}\sin(3\omega)$ - Zero-sequence arm capacitors "Δ"

v_{Cj}^{Σ} $= (v_{Cj}^{U} + v_{Cj}^{L})/2$

v_{mj}^{Δ} $= (-v_{mj}^{U} + v_{mj}^{L})/2$ - Modulated voltage of the phase j driving i_j^{Δ}

v_{mz}^{Δ} $= v_{mZ_d}^{\Delta}\cos(3\omega) + v_{mZ_q}^{\Delta}\sin(3\omega)$ - Zero-sequence modulated voltage"Δ"

v_{mj}^{Σ} $= (v_{mj}^{U} + v_{mj}^{L})/2$ - Modulated voltage of the phase j driving i_j^{Σ}

W_j^{Δ} $= C_{arm}((v_{Cj}^{U})^2 - (v_{Cj}^{L})^2)/2$

W_z^{Δ} $= W_{Z_d}^{\Delta}\cos(3\omega) + W_{Z_q}^{\Delta}\sin(3\omega)$ - Zero-sequence energy"Δ"

W_j^{Σ} $= C_{arm}((v_{Cj}^{U})^2 + (v_{Cj}^{L})^2)/2$

i_{mj}^{L} Modulated current of the lower arm of the phase j

i_{mj}^{U} Modulated current of the upper arm of the phase j

i_j^{L} Arm current of the upper arm of the phase j

i_j^{U} Arm current of the upper arm of the phase j

I_{bdc} Nominal DC current

I_{bdq} Nominal AC current in dq frame

j $= 1, 2, 3, 4$ - VSC index (Chapter 1)

j $= a, b, c$ - Phase name

m_j^{L} Modulation index of the upper arm of the phase j (between 0 and 1)

m_j^{U} Modulation index of the upper arm of the phase j (between 0 and 1)

P_b Nominal AC and DC power

v_{mj}^{L} Modulated voltage of the lower arm of the phase j

v_{mj}^{U} Modulated voltage of the upper arm of the phase j

V_{bdc} Nominal DC bus voltage

V_{bdq} Nominal AC voltage in dq frame

v_{Ci} Capacitor voltage of the submodule i

v_{dc} DC bus voltage

v_j^{G} AC phase voltage of the phase j

Bibliography

[1] S. Solomon, G.-K. Plattner, R. Knutti, and P. Friedlingstein, "Irreversible climate change due to carbon dioxide emissions," *Proceedings of the National Academy of Sciences*, vol. 106, no. 6, pp. 1704–1709, 2009.

[2] P. M. Cox, R. A. Betts, C. D. Jones, S. A. Spall, and I. J. Totterdell, "Acceleration of global warming due to carbon-cycle feedbacks in a coupled climate model," *Nature*, vol. 408, no. 6809, p. 184, 2000.

[3] W. Obergassel, C. Arens, L. Hermwille, N. Kreibich, F. Mersmann, H. E. Ott, and H. Wang-Helmreich, *Phoenix from the Ashes: An Analysis of the Paris Agreement to the United Nations Framework Convention on Climate Change*. Wuppertal Institut für Klima, Umwelt, Energie, 2016.

[4] ETSO, "European wind integration study (EWIS) — towards a successful integration of wind power into european electricity grids," project report, ETSO, January 2007.

[5] P. Buijs, D. Bekaert, D. Van Hertem, and R. Belmans, "Needed investments in the power system to bring wind energy to shore in belgium," in *PowerTech, 2009 IEEE Bucharest*, pp. 1–6, June 2009.

[6] N. Ahmed, A. Haider, D. Van Hertem, L. Zhang, and H.-P. Nee, "Prospects and challenges of future hvdc supergrids with modular multilevel converters," in *Power Electronics and Applications (EPE 2011), Proceedings of the 2011-14th European Conference on*, pp. 1–10, Aug 2011.

[7] P. Buijs, D. Bekaert, S. Cole, D. V. Hertem, and R. Belmans, "Transmission investment problems in europe: Going beyond standard solutions," *Energy Policy*, vol. 39, no. 3, pp. 1794 – 1801, 2011.

[8] T. M. Haileselassie, *Control, Dynamics and Operation of Multi-terminal VSC-HVDC Transmission Systems*. PhD thesis, Norwegian University of Science and Technology (NTNU), 2012.

[9] S. Akkari, *Control of a multi-terminal HVDC (MTDC) system and study of the interactions between the MTDC and the AC grids*. PhD thesis, Université Paris-Saclay, 2016.

[10] J. Descloux, *Protection contre les courts-circuits des réseaux à courant continu de forte puissance*. PhD thesis, École Doctorale Électronique, Électrotechnique, Automatique et Traitement du Signal de Grenoble - Laboratoire de Génie Électrique de Grenoble (G2Elab), 2013.

[11] D. V. Hertem and M. Ghandhari, "Multi-terminal VSC HVDC for the european supergrid: Obstacles," *Renewable and Sustainable Energy Reviews*, vol. 14, pp. 3156–3163, December 2010.

[12] B. Andersen, L. Xu, and K. Wong, "Topologies for VSC transmission," in *Seventh International Conference on AC-DC Power Transmission*, pp. 298–304, Nov 2001.

[13] M. Bahrman and B. Johnson, "The abcs of HVDC transmission technologies," *Power and Energy Magazine, IEEE*, vol. 5, pp. 32–44, March 2007.

[14] F. Wang, L. Bertling, T. Le, A. Mannikoff, and A. Bergman, "An overview introduction of vsc-hvdc: State-of-art and potential applications in electric power systems," in *Cigrè International Symposium, Bologna, Italy, Sept. 2011.*, 2011.

[15] P. Jones and C. Davidson, "Calculation of power losses for MMC-based VSC HVDC stations," in *15th European Conference on Power Electronics and Applications (EPE)*, 2013. Conference Location : Lille.

[16] A. Lesnicar and R. Marquardt, "An innovative modular multilevel converter topology suitable for a wide power range," in *Power Tech Conference Proceedings, 2003 IEEE Bologna*, vol. 3, pp. 6 pp. Vol.3–, June 2003.

[17] C. Oates and C. Davidson, "A comparison of two methods of estimating losses in the modular multi-level converter," in *Proceedings of the 2011-14th European Conference on Power Electronics and Applications (EPE 2011)*, pp. 1–10, Aug 2011.

[18] Q. Tu and Z. Xu, "Power losses evaluation for modular multilevel converter with junction temperature feedback," in *Power and Energy Society General Meeting, 2011 IEEE*, pp. 1–7, July 2011.

[19] K. Sharifabadi, L. Harnefors, H.-P. Nee, S. Norrga, and R. Teodorescu, *Design, Control, and Application of Modular Multilevel Converters for HVDC Transmission Systems*. John Wiley & Sons, 2016.

[20] M. Supponen, "Ten-year network development plan 2010-2020." ENTSO-E, 2010.

[21] Wind Europe (ex EWEA), "Oceans of opportunity: Harnessing europe's largest domestic energy resource," tech. rep.

[22] A. Egea-Àlvarez, *Multiterminal HVDC transmission systems for offshore wind*. PhD thesis, Universitat Politècnica de Catalunya, 2014.

[23] R. T. Pinto, *Multi-Terminal DC Networks: System Integration, Dynamics and Control*. PhD thesis, TU Delft, 2014.

[24] D. V. Hertem, M. Ghandhari, and M. Delimar, "Technical limitations towards a supergrid — a european prospective," in *2010 IEEE International Energy Conference*, pp. 302–309, Dec 2010.

[25] G. P. Adam, S. J. Finney, and B. Williams, "Interoperability of voltage source converters in dc grids," *IET Generation, Transmission Distribution*, vol. 7, pp. 1310–1317, November 2013.

[26] T. K. Vrana and S. Energi, "Review of HVDC component ratings: Xlpe cables and VSC converters," in *2016 IEEE International Energy Conference (ENERGYCON)*, pp. 1–6, April 2016.

[27] G. Stamatiou, *Analysis of VSC-based HVDC systems*. PhD thesis, Chalmers University of Technology, 2016.

[28] "BestPaths official site." Online: `http://www.bestpaths-project.eu/`.

[29] V. Akhmatov, M. Callavik, C. Franck, S. Rye, T. Ahndorf, M. Bucher, H. Muller, F. Schettler, and R. Wiget, "Technical guidelines and prestandardization work for first HVDC grids," *Power Delivery, IEEE Transactions on*, vol. 29, pp. 327–335, Feb 2014.

[30] O. Despouys, A. Petit, P. Rault, T. Larsson, K. Hämynen, M. Zeller, A. Rentschler, S. Finney, D. Vozikis, J. Freytes, X. Guillaud, S. Gao, J. Rimez, A. Burgos, L. Coronado, and C. Longás, "First recommendations to enhance interoperability in HVDC-VSC multi-vendor schemes," tech. rep., Deliverable D4.3, Best Paths project, October 2016.

[31] Wikipedia, "Definition of interoperability." Online: `https://en.wikipedia.org/wiki/Interoperability`.

[32] X. Xiang, M. M. C. Merlin, and T. C. Green, "Cost analysis and comparison of hvac, lfac and hvdc for offshore wind power connection," in *12th IET International Conference on AC and DC Power Transmission (ACDC 2016)*, pp. 1–6, May 2016.

[33] N. Flourentzou, V. Agelidis, and G. Demetriades, "VSC-based HVDC power transmission systems: An overview," *IEEE Transactions on Power Electronics*, vol. 24, pp. 592–602, March 2009.

[34] D. Jovcic and K. Ahmed, *High voltage direct current transmission: converters, systems and DC grids*. John Wiley & Sons, 2015.

[35] Wikipedia, "List of HVDC projects." Online: `https://en.wikipedia.org/wiki/List_of_HVDC_projects`.

[36] ABB, "Borwin1." Online: `http://new.abb.com/systems/hvdc/references/borwin1`.

[37] Wikipedia, "BorWin1." Online: `https://fr.wikipedia.org/wiki/BorWin1`.

[38] Siemens, "Living energy - issue 5." Online: `https://www.energy.siemens.com/ru/pool/hq/energy-topics/publications/living-energy/pdf/issue-05/Living-Energy-5-HVDC-San-Francisco-Trans-Bay-Cable.pdf`, July 2011.

[39] Wikipedia, "Trans bay cable." Online: `https://fr.wikipedia.org/wiki/Trans_Bay_Cable`.

[40] G. Bathurst and P. Bordignan, "Delivery of the nan'ao multi-terminal vsc-hvdc system," in *11th IET International Conference on AC and DC Power Transmission*, pp. 1–6, Feb 2015.

[41] Inelfe, "Energy for a better future." Online: `https://www.inelfe.eu/`.

[42] Europacable, "An introduction to high voltage direct current (HVDC) underground cables," tech. rep., Europacable, 2011.

[43] R. Adapa, "High-wire act: HVDC technology: The state of the art," *IEEE Power and Energy Magazine*, vol. 10, pp. 18–29, Nov 2012.

[44] C. C. Davidson and G. de Preville, "The future of high power electronics in transmission and distribution power systems," in *2009 13th European Conference on Power Electronics and Applications*, pp. 1–14, Sept 2009.

[45] A. Dekka, B. Wu, R. L. Fuentes, M. Perez, and N. R. Zargari, "Evolution of topologies, modeling, control schemes, and applications of modular multilevel converters," *IEEE Journal of Emerging and Selected Topics in Power Electronics*, vol. PP, no. 99, pp. 1–1, 2017.

[46] K. Ilves, *Modeling and Design of Modular Multilevel Converters for Grid Applications*. PhD thesis, KTH Royal Institute of Technology, 2012.

[47] J. P. Rodriguez, *Dynamic Averaged Models of VSC-Based HVDC Systems for Electromagnetic Transient Programs*. PhD thesis, École Polytechnique de Montréal, 2013.

[48] S. Dennetière, H. Saad, B. Clerc, E. Ghahremani, W. Li, and J. Bélanger, "Validation of a mmc model in a real-time simulation platform for industrial hil tests," in *2015 IEEE Power Energy Society General Meeting*, pp. 1–5, July 2015.

[49] S. Dennetière, *Contributions à la modélisation et à la validation des modèles de liasons HVDC de type VSC-MMC dans les outils de simulation temps réel*. PhD thesis, École Polytechnique de Montréal, February 2017.

[50] C.-C. e. a. Liu, "Preliminary analysis of HVDC networks for off-shore wind farms and their coordinated protection," tech. rep., Status report for European Commission, Deliverable D5.1. FP7 Twenties project EC-GA nº 249812, November 2011.

[51] O. Despouys, "Offshore dc grids: Impact of topology on power flow control," in *AC and DC Power Transmission (ACDC 2012), 10th IET International Conference on*, pp. 1–6, Dec 2012.

[52] B. Silva, C. Moreira, L. Seca, Y. Phulpin, and J. Peas Lopes, "Provision of inertial and primary frequency control services using offshore multiterminal hvdc networks," *Sustainable Energy, IEEE Transactions on*, vol. 3, pp. 800–808, Oct 2012.

[53] A. E. Leon, "Short-term frequency regulation and inertia emulation using an MMC-based MTDC system," *IEEE Transactions on Power Systems*, vol. PP, no. 99, pp. 1–1, 2017.

[54] Z. Hafizhah, "Reliability modelling of a multi-terminal high voltage direct current (HVDC) system based on half-bridge modular multilevel converter (MMC)," Master's thesis, TU Delft, July 2017.

[55] A. Egea-Àlvarez, J. Beerten, D. V. Hertem, and O. Gomis-Bellmunt, "Primary and secondary power control of multiterminal HVDC grids," in *10th IET International Conference on AC and DC Power Transmission (ACDC 2012)*, pp. 1–6, Dec 2012.

[56] T. Haileselassie and K. Uhlen, "Precise control of power flow in multiterminal vsc-hvdcs using dc voltage droop control," in *Power and Energy Society General Meeting, 2012 IEEE*, pp. 1–9, July 2012.

[57] C. Barker and R. Whitehouse, "Autonomous converter control in a multi-terminal HVDC system," in *9th IET International Conference on AC and DC Power Transmission*, pp. 1–5, Oct 2010.

[58] J. Beerten, *Modeling and Control of DC Grids*. PhD thesis, KU Leuven - Science, Engineering and Technologies, 2013.

[59] G. Tang, Z. He, and H. Pang, "R&d and application of voltage sourced converter based high voltage direct current engineering technology in china," *Journal of Modern Power Systems and Clean Energy*, vol. 2, no. 1, pp. 1–15, 2014.

[60] H. Rao, "Architecture of nan'ao multi-terminal VSC-HVDC system and its multi-functional control," *Power and Energy Systems, CSEE Journal of*, vol. 1, pp. 9–18, March 2015.

[61] X. Li, Z. Yuan, J. Fu, Y. Wang, T. Liu, and Z. Zhu, "Nanao multi-terminal vsc-hvdc project for integrating large-scale wind generation," in *2014 IEEE PES General Meeting / Conference Exposition*, pp. 1–5, July 2014.

[62] G. Tang, Z. He, H. Pang, X. Huang, and X. p. Zhang, "Basic topology and key devices of the five-terminal dc grid," *CSEE Journal of Power and Energy Systems*, vol. 1, pp. 22–35, June 2015.

[63] P. Rodriguez and K. Rouzbehi, "Multi-terminal dc grids: challenges and prospects," *Journal of Modern Power Systems and Clean Energy*, vol. 5, pp. 515–523, Jul 2017.

[64] P. Kundur, N. J. Balu, and M. G. Lauby, *Power system stability and control*. McGraw-hill New York, 1994.

[65] P. M. Anderson and A. A. Fouad, *Power system control and stability*. John Wiley & Sons, 2008.

[66] X.-F. Wang, Y. Song, and M. Irving, *Modern power systems analysis*. Springer Science & Business Media, 2010.

[67] J. Beerten, O. Gomis-Bellmunt, X. Guillaud, J. Rimez, A. van der Meer, and D. Van Hertem, "Modeling and control of HVDC grids: A key challenge for the future power system," in *Power Systems Computation Conference (PSCC), 2014*, pp. 1–21, Aug 2014.

[68] J. Mahseredjian, S. Dennetiére, L. Dubé, B. Khodabakhchian, and L. Gérin-Lajoie, "On a new approach for the simulation of transients in power systems," *Electric Power Systems Research*, vol. 77, no. 11, pp. 1514 – 1520, 2007. Selected Topics in Power System Transients - Part {II6th} International Conference on Power System Transients.

[69] N. R. Chaudhuri, R. Majumder, B. Chaudhuri, and J. Pan, "Stability analysis of VSC MTDC grids connected to multimachine ac systems," *IEEE Transactions on Power Delivery*, vol. 26, pp. 2774–2784, Oct 2011.

[70] G. O. Kalcon, G. P. Adam, O. Anaya-Lara, S. Lo, and K. Uhlen, "Small-signal stability analysis of multi-terminal VSC-based dc transmission systems," *IEEE Transactions on Power Systems*, vol. 27, pp. 1818–1830, Nov 2012.

[71] J. Beerten, S. D'Arco, and J. A. Suul, "Identification and small-signal analysis of interaction modes in VSC mtdc systems," *IEEE Transactions on Power Delivery*, vol. 31, pp. 888–897, April 2016.

[72] G. Pinares, *Analysis of dc-network stability of VSC-based HVDC grids*. PhD thesis, Chalmers University of Technology, 2016.

[73] J. Kwon, X. Wang, F. Blaabjerg, and C. L. Bak, "Comparison of lti and ltp models for stability analysis of grid converters," in *2016 IEEE 17th Workshop on Control and Modeling for Power Electronics (COMPEL)*, pp. 1–8, June 2016.

[74] P. Rault, *Dynamic Modeling and Control of Multi-Terminal HVDC Grids*. PhD thesis, Ecole Centrale de Lille - L2EP, March 2014.

[75] R. W. Erickson and D. Maksimović, *Fundamentals of power electronics*. Springer Science & Business Media, 2007.

[76] J. Slotine and W. Li, *Applied Nonlinear Control*. Prentice Hall, 1991.

[77] B. A. Francis, "ECE311S - Dynamic Systems and Control Linearization of Nonlinear Systems." Course Notes, Online: `http://www.control.utoronto.ca/~broucke/ece311s/Handouts/linearization.pdf`, 2007.

[78] Wikipedia, "Periodic point." Online: `https://en.wikipedia.org/wiki/Periodic_point`.

[79] N. Cherix, *Functional Description and Control Design of Modular Multilevel Converters*. PhD thesis, École Polytechnique Fédérale De Lausanne (EPFL), 2015.

[80] B. Jacobson, P. Karlsson, G. Asplund, L. Harnefors, and T. Jonsson, "VSC-HVDC transmission with cascaded two-level converters," *CIGRE Sessions*, pp. B4–B110, 2010.

[81] W. Wang, A. Beddard, M. Barnes, and O. Marjanovic, "Analysis of active power control for VSC-HVDC," *IEEE Transactions on Power Delivery*, vol. 29, pp. 1978–1988, Aug 2014.

[82] X. Guillaud, *Sur la modélisation et la commande des redresseurs de courant à interrupteurs bi-commandables*. PhD thesis, Université Lille 1, December 1992.

[83] A. Packard, K. Poolla, and R. Horowitz, "ME 132 - Dynamic Systems and Feedback." Course Notes, Online: `https://jagger.berkeley.edu/~pack/me132/AllNotes.pdf`, 2005.

[84] S. Skogestad and I. Postlethwaite, *Multivariable Feedback Control: Analysis and design*. John Wiley & Sons, 2007.

[85] N. B. Gallegos, *Sensibilité Paramétrique pour l'Analyse Dynamique des Réseaux à Courant Continu*. PhD thesis, Ecole Centrale de Lille - L2EP, December 2016.

[86] S. D'Arco, J. Beerten, and J. A. Suul, "Classification and analysis of impact on small-signal dynamics and stability from expansion of vsc-hvdc systems to multi-terminal hvdc grids," in *13th IET International Conference on AC and DC Power Transmission (ACDC 2017)*, pp. 1–8, Feb 2017.

[87] K. Rouzbehi, J. I. Candela, G. B. Gharehpetian, L. Harnefors, A. Luna, and P. Rodriguez, "Multiterminal DC grids: Operating analogies to AC power systems," *Renewable and Sustainable Energy Reviews*, vol. 70, pp. 886 – 895, 2017.

[88] P. Rault, J. Freytes, X. Guillaud, F. Colas, H. Saad, O. Despouys, and S. Nguefeu, "Coordinated control for multi terminal DC grids connected to offshore wind farms," in *2016 IEEE 17th Workshop on Control and Modeling for Power Electronics (COMPEL)*, pp. 1–8, June 2016.

[89] S. A. Amamra, F. Colas, X. Guillaud, P. Rault, and S. Nguefeu, "Laboratory demonstration of a multiterminal vsc-hvdc power grid," *IEEE Transactions on Power Delivery*, vol. 32, pp. 2339–2349, Oct 2017.

[90] K. Rouzbehi, A. Miranian, J. Candela, A. Luna, and P. Rodriguez, "A generalized voltage droop strategy for control of multiterminal dc grids," *Industry Applications, IEEE Transactions on*, vol. 51, pp. 607–618, Jan 2015.

[91] M. Avendano-Mora, M. Barnes, and J. Y. Chan, "Comparison of control strategies for multiterminal vsc-hvdc systems for offshore wind farm integration," in *Power Electronics, Machines and Drives (PEMD 2014), 7th IET International Conference on*, pp. 1–6, April 2014.

[92] L. Xu, B. Williams, and L. Yao, "Multi-terminal dc transmission systems for connecting large offshore wind farms," in *Power and Energy Society General Meeting - Conversion and Delivery of Electrical Energy in the 21st Century, 2008 IEEE*, pp. 1–7, July 2008.

[93] J. Beerten, S. Cole, and R. Belmans, "Modeling of multi-terminal VSC HVDC systems with distributed dc voltage control," *IEEE Transactions on Power Systems*, vol. 29, pp. 34–42, Jan 2014.

[94] C. Barker, R. Whitehouse, J. Lang, and S. Wang, "Risk of multiple cross-over of control characteristics in multi-terminal HVDC," *IET Generation, Transmission Distribution*, vol. 10, no. 6, pp. 1353–1360, 2016.

[95] E. Prieto-Araujo, F. Bianchi, A. Junyent-Ferré, and O. Gomis-Bellmunt, "Methodology for droop control dynamic analysis of multiterminal VSC-HVDC grids for offshore wind farms," *IEEE Transactions on Power Delivery*, vol. 26, pp. 2476–2485, Oct 2011.

[96] F. Thams, R. Eriksson, and M. Molinas, "Interaction of droop control structures and its inherent effect on the power transfer limits in multiterminal VSC-HVDC," *IEEE Transactions on Power Delivery*, vol. 32, pp. 182–192, Feb 2017.

[97] T. Nakajima and S. Irokawa, "A control system for hvdc transmission by voltage sourced converters," in *Power Engineering Society Summer Meeting, 1999. IEEE*, vol. 2, pp. 1113–1119 vol.2, 1999.

[98] C. Dierckxsens, K. Srivastava, M. Reza, S. Cole, J. Beerten, and R. Belmans, "A distributed dc voltage control method for VSC mtdc systems," *Electric Power Systems Research*, vol. 82, no. 1, pp. 54 – 58, 2012.

[99] H. Li, C. Liu, G. Li, and R. Iravani, "An enhanced dc voltage droop-control for the VSC–HVDC grid," *IEEE Transactions on Power Systems*, vol. 32, pp. 1520–1527, March 2017.

[100] S. Wenig, F. Rojas, K. Schönleber, M. Suriyah, and T. Leibfried, "Simulation framework for dc grid control and acdc interaction studies based on modular multilevel converters," *IEEE Transactions on Power Delivery*, vol. 31, pp. 780–788, April 2016.

[101] T. Vrana, L. Zeni, and O. Fosso, "Active power control with undead-band voltage and frequency droop applied to a meshed dc grid test system," in *Energy Conference and Exhibition (ENERGYCON), 2012 IEEE International*, pp. 612–616, Sept 2012.

[102] S. D'Arco and J. Suul, "Generalized implementations of piecewise linear control characteristics for multiterminal HVDC," in *Power Electronics, Electrical Drives, Automation and Motion (SPEEDAM), 2014 International Symposium on*, pp. 66–72, June 2014.

[103] G. Stamatiou and M. Bongiorno, "Power-dependent droop-based control strategy for multi-terminal HVDC transmission grids," *IET Generation, Transmission Distribution*, vol. 11, no. 2, pp. 383–391, 2017.

[104] W. Wang, M. Barnes, and O. Marjanovic, "Frequency-response analysis and compensator enhancement of droop control for VSC-HVDC," in *11th IET International Conference on AC and DC Power Transmission*, pp. 1–8, Feb 2015.

[105] N. R. Chaudhuri and B. Chaudhuri, "Adaptive droop control for effective power sharing in multi-terminal dc (mtdc) grids," *IEEE Transactions on Power Systems*, vol. 28, pp. 21–29, Feb 2013.

[106] A. K. Marten, F. Sass, and D. Westermann, "Continuous p-v-characteristic parameterization for multi-terminal HVDC systems," *IEEE Transactions on Power Delivery*, vol. 32, pp. 1665–1673, Aug 2017.

[107] T. Haileselassie and K. Uhlen, "Impact of dc line voltage drops on power flow of mtdc using droop control," *IEEE Transactions on Power Systems*, vol. 27, pp. 1441–1449, Aug 2012.

[108] H. Saad, *Modélisation et simulation d'un liason HVDC de type VSC-MMC*. PhD thesis, École Polytechnique de Montréal, March 2015.

[109] Q. Tu, Z. Xu, and L. Xu, "Reduced switching-frequency modulation and circulating current suppression for modular multilevel converters," in *Transmission and Distribution Conference and Exposition (T D), 2012 IEEE PES*, pp. 1–1, May 2012.

[110] A. Zama, S. A. Mansour, D. Frey, A. Benchaib, S. Bacha, and B. Luscan, "A comparative assessment of different balancing control algorithms for modular multilevel converter (MMC)," in *2016 18th European Conference on Power Electronics and Applications (EPE'16 ECCE Europe)*, pp. 1–10, Sept 2016.

[111] H. Saad, S. Dennetière, J. Mahseredjian, P. Delarue, X. Guillaud, J. Peralta, and S. Nguefeu, "Modular multilevel converter models for electromagnetic transients," *IEEE Transactions on Power Delivery*, vol. 29, pp. 1481–1489, June 2014.

[112] U. Gnanarathna, A. Gole, and R. Jayasinghe, "Efficient modeling of modular multilevel HVDC converters (MMC) on electromagnetic transient simulation programs," *IEEE Transactions on Power Delivery*, vol. 26, pp. 316–324, Jan 2011.

[113] A. Antonopoulos, L. Angquist, and H.-P. Nee, "On dynamics and voltage control of the modular multilevel converter," in *13th European Conference on Power Electronics and Applications, EPE '09*, pp. 1–10, Sept 2009.

[114] S. Samimi, *Modélisation et Commande des Convertisseurs MMC en vue de leur Intégration dans le Réseau Electrique*. PhD thesis, Ecole Centrale de Lille - L2EP, November 2016.

[115] L. Harnefors, A. Antonopoulos, S. Norrga, L. Angquist, and H. P. Nee, "Dynamic analysis of modular multilevel converters," *IEEE Transactions on Industrial Electronics*, vol. 60, pp. 2526–2537, July 2013.

[116] P. Delarue, F. Gruson, and X. Guillaud, "Energetic macroscopic representation and inversion based control of a modular multilevel converter," in *15th European Conference on Power Electronics and Applications (EPE 2013)*, pp. 1–10, Sept 2013.

[117] H. Saad, X. Guillaud, J. Mahseredjian, S. Dennetière, and S. Nguefeu, "MMC capacitor voltage decoupling and balancing controls," *IEEE Transactions on Power Delivery*, vol. 30, pp. 704–712, April 2015.

[118] K. Ilves, A. Antonopoulos, S. Norrga, and H.-P. Nee, "Steady-state analysis of interaction between harmonic components of arm and line quantities of modular multilevel converters," *IEEE Transactions on Power Electronics*, vol. 27, pp. 57–68, January 2012.

[119] S. Liu, Z. Xu, W. Hua, G. Tang, and Y. Xue, "Electromechanical transient modeling of modular multilevel converter based multi-terminal HVDC systems," *IEEE Transactions on Power Systems*, vol. 29, pp. 72–83, Jan 2014.

[120] D. C. Ludois and G. Venkataramanan, "Simplified terminal behavioral model for a modular multilevel converter," *IEEE Transactions on Power Electronics*, vol. 29, pp. 1622–1631, April 2014.

[121] N. T. Trinh, M. Zeller, K. Wuerflinger, and I. Erlich, "Generic model of MMC-VSC-HVDC for interaction study with ac power system," *IEEE Transactions on Power Systems*, vol. 31, pp. 27–34, Jan 2016.

[122] G. B. Diaz, J. A. Suul, and S. D'Arco, "Small-signal state-space modeling of modular multilevel converters for system stability analysis," in *2015 IEEE Energy Conversion Congress and Exposition (ECCE)*, pp. 5822–5829, Sept 2015.

[123] J. Freytes, L. Papangelis, H. Saad, P. Rault, T. V. Cutsem, and X. Guillaud, "On the modeling of MMC for use in large scale dynamic simulations," in *2016 Power Systems Computation Conference (PSCC)*, pp. 1–7, June 2016.

[124] A. Jamshidifar and D. Jovcic, "Circulating current suppression control dynamics and impact on MMC converter dynamics," in *2015 IEEE Eindhoven PowerTech*, pp. 1–6, June 2015.

[125] A. Jamshidifar and D. Jovcic, "Small-signal dynamic dq model of modular multilevel converter for system studies," *IEEE Transactions on Power Delivery*, vol. 31, pp. 191–199, Feb 2016.

[126] V. Najmi, M. N. Nazir, and R. Burgos, "A new modeling approach for modular multilevel converter (MMC) in d-q frame," in *2015 IEEE Applied Power Electronics Conference and Exposition (APEC)*, pp. 2710–2717, March 2015.

[127] G. Bergna, J. A. Suul, and S. D'Arco, "State-space modelling of modular multilevel converters for constant variables in steady-state," in *2016 IEEE 17th Workshop on Control and Modeling for Power Electronics (COMPEL)*, pp. 1–9, June 2016.

[128] T. Li, A. M. Gole, and C. Zhao, "Harmonic instability in MMC-HVDC converters resulting from internal dynamics," *IEEE Transactions on Power Delivery*, vol. 31, pp. 1738–1747, Aug 2016.

[129] Y. Sinha and A. Nampally, "Averaged model of modular multilevel converter in rotating dq frame," in *2016 IEEE International Conference on Renewable Energy Research and Applications (ICRERA)*, pp. 319–324, Nov 2016.

[130] Y. Sinha and A. Nampally, "Linearized dq averaged model of modular multilevel converter," in *2016 IEEE International Conference on Renewable Energy Research and Applications (ICRERA)*, pp. 861–866, Nov 2016.

[131] J. A. Houldsworth and D. A. Grant, "The use of harmonic distortion to increase the output voltage of a three-phase pwm inverter," *IEEE Transactions on Industry Applications*, vol. IA-20, pp. 1224–1228, Sept 1984.

[132] S. Norrga, L. Ängquist, and K. Ilves, "Operating region extension for multilevel converters in HVDC applications by optimisation methods," in *10th IET International Conference on AC and DC Power Transmission (ACDC 2012)*, pp. 1–6, Dec 2012.

[133] H. Saad, J. Peralta, S. Dennetière, J. Mahseredjian, J. Jatskevich, J. Martinez, A. Davoudi, M. Saeedifard, V. Sood, X. Wang, J. Cano, and A. Mehrizi-Sani, "Dynamic averaged and simplified models for MMC-based HVDC transmission systems," *IEEE Transactions on Power Delivery*, vol. 28, pp. 1723–1730, July 2013.

[134] T. Soong, *Modular Multilevel Converters with Integrated Energy Storage*. PhD thesis, University of Toronto, 2015.

[135] Q. Tu, Z. Xu, and J. Zhang, "Circulating current suppressing controller in modular multilevel converter," in *IECON 2010 - 36th Annual Conference on IEEE Industrial Electronics Society*, pp. 3198–3202, Nov 2010.

[136] F. Zhao, G. Xiao, M. Liu, S. Su, D. Yang, and F. Li, "Accurate mathematical steady-state models of arm and line harmonic characteristics for modular multilevel converter," in *2017 IEEE Applied Power Electronics Conference and Exposition (APEC)*, pp. 3479–3485, March 2017.

[137] S. Debnath, J. Qin, B. Bahrani, M. Saeedifard, and P. Barbosa, "Operation, control, and applications of the modular multilevel converter: A review," *IEEE Transactions on Power Electronics*, vol. 30, pp. 37–53, Jan 2015.

[138] R. Oliveira and A. Yazdani, "An enhanced steady-state model and capacitor sizing method for modular multilevel converters for HVDC applications," *IEEE Transactions on Power Electronics*, vol. PP, no. 99, pp. 1–1, 2017.

[139] Q. Song, W. Liu, X. Li, H. Rao, S. Xu, and L. Li, "A steady-state analysis method for a modular multilevel converter," *IEEE Transactions on Power Electronics*, vol. 28, pp. 3702–3713, Aug 2013.

[140] R. Teodorescu, M. Liserre, and P. Rodríguez, *Grid converters for photovoltaic and wind power systems*, vol. 29. IEEE/John Wiley & Sons, 2011.

[141] M. Vasiladiotis and A. Rufer, "Fictive axis emulator-based state feedback vector current control for single-phase voltage source converters," in *IECON 2013 - 39th Annual Conference of the IEEE Industrial Electronics Society*, pp. 773–778, Nov 2013.

[142] W. Wang, M. Barnes, O. Marjanovic, and O. Cwikowski, "Impact of dc breaker systems on multiterminal VSC-HVDC stability," *IEEE Transactions on Power Delivery*, vol. 31, pp. 769–779, April 2016.

[143] R. Picas, S. Ceballos, J. Pou, J. Zaragoza, G. Konstantinou, and V. Agelidis, "Closed-loop discontinuous modulation technique for capacitor voltage ripples and switching losses reduction in modular multilevel converters," *IEEE Transactions on Power Electronics*, vol. 30, pp. 4714–4725, Sept 2015.

[144] A. Dekka, B. Wu, V. Yaramasu, and N. R. Zargari, "Integrated model predictive control with reduced switching frequency for modular multilevel converters," *IET Electric Power Applications*, vol. 11, no. 5, pp. 857–863, 2017.

[145] G. Guo, Q. Song, W. Yang, Y. Wang, W. Liu, H. Rao, and S. Xu, "Application of third order harmonic voltage injection in a modular multilevel converter," *IEEE Transactions on Industrial Electronics*, vol. PP, no. 99, pp. 1–1, 2017.

[146] G. Bergna-Díaz, *Modular Multilevel Converter Control for HVDC Operation*. PhD thesis, École Centrale Supélec & Norwegian University of Science and Technology (NTNU), July 2015.

[147] S. Rohner, J. Weber, and S. Bernet, "Continuous model of modular multilevel converter with experimental verification," in *2011 IEEE Energy Conversion Congress and Exposition*, pp. 4021–4028, Sept 2011.

[148] A. Christe and D. Dujić, "State-space modeling of modular multilevel converters including line frequency transformer," in *17th European Conference on Power Electronics and Applications (EPE'15 ECCE-Europe)*, pp. 1–10, Sept 2015.

[149] S. S. Khan and E. Tedeschi, "Modeling of MMC for fast and accurate simulation of electromagnetic transients: A review," *Energies*, vol. 10, no. 8, 2017.

[150] T. Li, A. Gole, and C. Zhao, "Stability of a modular multilevel converter based HVDC system considering dc side connection," in *IET Conference Proceedings*, pp. 21 (6 .)–21 (6 .)(1), Institution of Engineering and Technology, January 2016.

[151] H. R. Wickramasinghe, G. Konstantinou, J. Pou, and V. G. Agelidis, "Interactions between indirect dc-voltage estimation and circulating current controllers of MMC-based HVDC transmission systems," *IEEE Transactions on Power Systems*, vol. PP, no. 99, pp. 1–1, 2017.

[152] N. R. Chaudhuri, R. Oliveira, and A. Yazdani, "Stability analysis of vector-controlled modular multilevel converters in linear time-periodic framework," *IEEE Transactions on Power Electronics*, vol. 31, pp. 5255–5269, July 2016.

[153] J. Böcker, B. Freudenberg, A. The, and S. Dieckerhoff, "Experimental comparison of model predictive control and cascaded control of the modular multilevel converter," *IEEE Transactions on Power Electronics*, vol. 30, pp. 422–430, Jan 2015.

[154] A. The, B. Freudenberg, S. Dieckerhoff, V. Vahrenholt, W. Fischer, R. Stornowski, and M. Wildmann, "Operation range of hvdc-mmc with circulating current suppression and energy balancing control," in *2015 17th European Conference on Power Electronics and Applications (EPE'15 ECCE-Europe)*, pp. 1–9, Sept 2015.

[155] G. Bergna, A. Garces, E. Berne, P. Egrot, A. Arzande, J.-C. Vannier, and M. Molinas, "A generalized power control approach in ABC frame for modular multilevel converter HVDC links based on mathematical optimization," *IEEE Transactions on Power Delivery*, vol. 29, pp. 386–394, Feb 2014.

[156] G. Bergna, E. Berne, P. Egrot, P. Lefranc, A. Arzande, J.-C. Vannier, and M. Molinas, "An energy-based controller for HVDC modular multilevel converter in decoupled double synchronous reference frame for voltage oscillation reduction," *Industrial Electronics, IEEE Transactions on*, vol. 60, pp. 2360–2371, June 2013.

[157] O. Sakinci, "Small-signal stability modelling and analysis of modular multilevel converter and its closed-loop controllers," Master's thesis, TU Delft, August 2017.

[158] B. Li, R. Li, B. W. Williams, and D. Xu, "Energy transfer analysis for capacitor voltage balancing of modular multilevel converters," in *2016 IEEE Transportation Electrification Conference and Expo (ITEC)*, pp. 1–6, June 2016.

[159] K. Shinoda, J. Freytes, A. Benchaib, J. Dai, H. Saad, and X. Guillaud, "Energy difference controllers for MMC without DC current perturbations," in *2nd International Conference on HVDC (HVDC2016 - CIGRE)*, Oct 2016.

[160] J. Freytes, P. Rault, F. Gruson, F. Colas, and X. Guillaud, "Dynamic impact of MMC controllers on DC voltage droop controlled MTDC grids," in *2016 18th European Conference on Power Electronics and Applications (EPE'16 ECCE Europe)*, pp. 1–10, Sept 2016.

[161] J. Freytes, S. Akkari, J. Dai, F. Gruson, P. Rault, and X. Guillaud, "Small-signal state-space modeling of an HVDC link with modular multilevel converters," in *2016 IEEE 17th Workshop on Control and Modeling for Power Electronics (COMPEL)*, pp. 1–8, June 2016.

[162] J. Freytes, G. Bergna, J. A. Suul, S. D'Arco, H. Saad, and X. Guillaud, "State-space modelling with steady-state time invariant representation of energy based controllers for modular multilevel converters," in *2017 IEEE Manchester PowerTech*, pp. 1–7, June 2017.

[163] J. Freytes, G. Bergna, J. A. Suul, S. D'Arco, F. Gruson, F. Colas, H. Saad, and X. Guillaud, "Improving small-signal stability of an MMC with CCSC by control of the internally stored energy," *IEEE Transactions on Power Delivery*, vol. PP, no. 99, pp. 1–1, 2017.

[164] A. Zama, A. Benchaib, S. Bacha, D. Frey, and S. Silvant, "High dynamics control for MMC based on exact discrete-time model with experimental validation," *IEEE Transactions on Power Delivery*, vol. PP, no. 99, pp. 1–1, 2017.

[165] G. Bergna-Diaz, J. A. Suul, and S. D'Arco, "Energy-based state-space representation of modular multilevel converters with a constant equilibrium point in steady-state operation," *IEEE Transactions on Power Electronics*, vol. PP, no. 99, pp. 1–1, 2017.

[166] W. h. Huang, Y. Huang, M. Li, and W. m. Gong, "Stability analysis of modular multilevel converter using nearest level modulation," in *IECON 2016 - 42nd Annual Conference of the IEEE Industrial Electronics Society*, pp. 2582–2587, Oct 2016.

[167] P. Munch, D. Gorges, M. Izak, and S. Liu, "Integrated current control, energy control and energy balancing of modular multilevel converters," in *IECON 2010 - 36th Annual Conference on IEEE Industrial Electronics Society*, pp. 150–155, Nov 2010.

[168] A. E. Leon and S. J. Amodeo, "Energy balancing improvement of modular multilevel converters under unbalanced grid conditions," *IEEE Transactions on Power Electronics*, vol. 32, pp. 6628–6637, Aug 2017.

[169] E. Prieto-Araujo, A. Junyent-Ferré, G. Clariana-Colet, and O. Gomis-Bellmunt, "Control of modular multilevel converters under singular unbalanced voltage conditions with equal positive and negative sequence components," *IEEE Transactions on Power Systems*, vol. 32, pp. 2131–2141, May 2017.

[170] A. Ferreira, C. Collados, O. Gomis-Bellmunt, and M. Teixido, "Modular multilevel converter electrical circuit model for HVDC applications," in *17th European Conference on Power Electronics and Applications (EPE'15 ECCE-Europe)*, pp. 1–10, Sept 2015.

[171] S. Teeuwsen, "Simplified dynamic model of a voltage-sourced converter with modular multilevel converter design," in *Power Systems Conference and Exposition, 2009. PSCE '09. IEEE/PES*, pp. 1–6, March 2009.

[172] M. Imhof, E. Iggland, and G. Andersson, "A simplified second-order model of a VSC-HVDC link for dynamic studies," in *Cigré International Symposium, Across Borders – HVDC Systems and Market Integration*, May 27-28, 2015.

[173] Y. Gu, N. Bottrell, and T. C. Green, "Reduced-order models for representing converters in power system studies," *IEEE Transactions on Power Electronics*, vol. PP, no. 99, pp. 1–1, 2017.

[174] S. Allebrod, R. Hamerski, and R. Marquardt, "New transformerless, scalable modular multilevel converters for HVDC-transmission," in *Power Electronics Specialists Conference, 2008. PESC 2008. IEEE*, pp. 174–179, June 2008.

[175] G. Pinares and M. Bongiorno, "Modeling and analysis of VSC-based HVDC systems for dc network stability studies," *IEEE Transactions on Power Delivery*, vol. 31, pp. 848–856, April 2016.

[176] S. Samimi, F. Gruson, P. Delarue, F. Colas, M. M. Belhaouane, and X. Guillaud, "MMC stored energy participation to the dc bus voltage control in an HVDC link," *IEEE Transactions on Power Delivery*, vol. 31, pp. 1710–1718, Aug 2016.

[177] B. Wen, D. Boroyevich, R. Burgos, P. Mattavelli, and Z. Shen, "Analysis of d-q small-signal impedance of grid-tied inverters," *IEEE Transactions on Power Electronics*, vol. 31, pp. 675–687, Jan 2016.

[178] W. Yang, Q. Song, and W. Liu, "Decoupled control of modular multilevel converter based on intermediate controllable voltages," *IEEE Transactions on Industrial Electronics*, vol. 63, pp. 4695–4706, Aug 2016.

[179] J. Freytes, G. Bergna, J. Suul, S. D'Arco, H. Saad, and X. Guillaud, "Small-signal model analysis of droop-controlled modular multilevel converters with circulating current suppressing controller," in *13th IET International Conference on AC and DC Power Transmission (ACDC 2017)*, pp. 16 (8 .)–16 (8 .)(1), Institution of Engineering and Technology, 2017.

[180] A. Egea-Àlvarez, S. Fekriasl, F. Hassan, and O. Gomis-Bellmunt, "Advanced vector control for voltage source converters connected to weak grids," *IEEE Transactions on Power Systems*, vol. 30, pp. 3072–3081, Nov 2015.

[181] L. Harnefors, M. Bongiorno, and S. Lundberg, "Input-admittance calculation and shaping for controlled voltage-source converters," *IEEE Transactions on Industrial Electronics*, vol. 54, pp. 3323–3334, Dec 2007.

[182] J. Z. Zhou, H. Ding, S. Fan, Y. Zhang, and A. M. Gole, "Impact of short-circuit ratio and phase-locked-loop parameters on the small-signal behavior of a VSC-HVDC converter," *IEEE Transactions on Power Delivery*, vol. 29, pp. 2287–2296, Oct 2014.

[183] Y. Li, G. Tang, J. Ge, Z. He, H. Pang, J. Yang, and Y. Wu, "Modeling and damping control of modular multilevel converter based dc grid," *IEEE Transactions on Power Systems*, vol. PP, no. 99, pp. 1–1, 2017.

[184] H. Saad, J. Peralta, S. Dennetière, J. Mahseredjian, J. Jatskevich, J. Martinez, A. Davoudi, M. Saeedifard, V. Sood, X. Wang, J. Cano, and A. Mehrizi-Sani, "Dynamic averaged and simplified models for MMC-based HVDC transmission systems," *IEEE Transactions on Power Delivery*, vol. 28, pp. 1723–1730, July 2013.

[185] M. Amin and M. Molinas, "Small-signal stability assessment of power electronics based power systems: A discussion of impedance- and eigenvalue-based methods," *IEEE Transactions on Industry Applications*, vol. PP, no. 99, pp. 1–1, 2017.

[186] A. Rygg, M. Molinas, C. Zhang, and X. Cai, "On the equivalence and impact on stability of impedance modelling of power electronic converters in different domains," *IEEE Journal of Emerging and Selected Topics in Power Electronics*, vol. PP, no. 99, pp. 1–1, 2017.

[187] M. Beza, M. Bongiorno, and G. Stamatiou, "Analytical derivation of the ac-side input admittance of a modular multilevel converter with open- and closed-loop control strategies," *IEEE Transactions on Power Delivery*, vol. PP, no. 99, pp. 1–1, 2017.

[188] G. Stamatiou, M. Beza, M. Bongiorno, and L. Harnefors, "Analytical derivation of the dc-side input admittance of the direct-voltage controlled modular multilevel converter," *IET Generation, Transmission & Distribution*, July 2017.

[189] H. Saad, Y. Fillion, S. Deschanvres, Y. Vernay, and S. Dennetière, "On resonances and harmonics in HVDC-MMC station connected to AC grid," *IEEE Transactions on Power Delivery*, vol. 32, pp. 1565–1573, June 2017.

[190] G. Grdenić and M. Delimar, "Small-signal stability analysis of interaction modes in VSC mtdc systems with voltage margin control," *Energies*, vol. 10, no. 7, p. 873, 2017.

[191] R. Eriksson, J. Beerten, M. Ghandhari, and R. Belmans, "Optimizing dc voltage droop settings for ac/dc system interactions," *IEEE Transactions on Power Delivery*, vol. 29, pp. 362–369, Feb 2014.

[192] J. Beerten and R. Belmans, "Analysis of power sharing and voltage deviations in droop-controlled dc grids," *IEEE Transactions on Power Systems*, vol. 28, pp. 4588–4597, Nov 2013.

[193] J. Xu, A. Gole, and C. Zhao, "The use of averaged-value model of modular multilevel converter in dc grid," *IEEE Transactions on Power Delivery*, vol. 30, pp. 519–528, April 2015.

[194] E. Prieto-Araujo, *Power converter control for offshore wind energy generation and transmission*. PhD thesis, Universitat Politècnica de Catalunya, 2016.

[195] J. Beerten, S. D'Arco, and J. Suul, "Cable model order reduction for HVDC systems interoperability analysis," in *11th IET International Conference on AC and DC Power Transmission*, pp. 1–10, Feb 2015.

[196] J. Beerten, S. D'Arco, and J. A. Suul, "Frequency-dependent cable modelling for small-signal stability analysis of VSC-HVDC systems," *IET Generation, Transmission & Distribution*, vol. 10, pp. 1370–1381(11), April 2016.

[197] X. Lu, W. Lin, T. An, J. Wen, and Y. Li, "State-space modelling of dc grid based on MMC," in *2nd International Conference on HVDC (HVDC2016 - CIGRE)*, Oct 2016.

[198] A. G. Endegnanew, K. Uhlen, G. Bergna-Diaz, and J. Beerten, "Small-signal modelling of an mmc-based hvdc link interfacing large ac systems," in *2016 IEEE 17th Workshop on Control and Modeling for Power Electronics (COMPEL)*, pp. 1–9, June 2016.

[199] A. Garcés, S. Sanchez, G. Bergna, and E. Tedeschi, "HVDC meshed multi-terminal networks for offshore wind farms: Dynamic model, load flow and equilibrium," in *2017 IEEE 18th Workshop on Control and Modeling for Power Electronics (COMPEL)*, pp. 1–6, July 2017.

[200] E. Prieto-Araujo, A. Egea-Alvarez, S. Fekriasl, and O. Gomis-Bellmunt, "Dc voltage droop control design for multiterminal hvdc systems considering ac and dc grid dynamics," *IEEE Transactions on Power Delivery*, vol. 31, pp. 575–585, April 2016.

[201] F. Thams, S. Chatzivasileiadis, E. Prieto-Araujo, and R. Eriksson, "Disturbance attenuation of dc voltage droop control structures in a multi-terminal HVDC grid," in *2017 IEEE Manchester PowerTech*, pp. 1–6, June 2017.

[202] J. Beerten, G. B. Diaz, S. D'Arco, and J. A. Suul, "Comparison of small-signal dynamics in mmc and two-level vsc hvdc transmission schemes," in *2016 IEEE International Energy Conference (ENERGYCON)*, pp. 1–6, April 2016.

[203] K. Shinoda, A. Benchaib, J. Dai, and X. Guillaud, "Virtual capacitor control: Mitigation of dc voltage fluctuations in mmc-based hvdc systems," *IEEE Transactions on Power Delivery*, vol. PP, no. 99, pp. 1–1, 2017.

[204] K. Shinoda, A. Benchaib, X. Guillaud, and J. Dai, "Virtual Capacitances," Aug. 2015. W0 Patent Application 2 017 021 642, August 3, 2015.

[205] S. Arunprasanth, U. D. Annakkage, C. Karawita, and R. Kuffel, "Generalized frequency-domain controller tuning procedure for VSC systems," *IEEE Transactions on Power Delivery*, vol. 31, pp. 732–742, April 2016.

[206] S. D'Arco, J. A. Suul, and O. B. Fosso, "Small-signal modelling and parametric sensitivity of a virtual synchronous machine," in *Power Systems Computation Conference (PSCC), 2014*, pp. 1–9, Aug 2014.

[207] E. Rakhshani, D. Remon, A. M. Cantarellas, and P. Rodriguez, "Analysis of derivative control based virtual inertia in multi-area high-voltage direct current interconnected power systems," *IET Generation, Transmission Distribution*, vol. 10, no. 6, pp. 1458–1469, 2016.

[208] S. Samimi, F. Gruson, P. Delarue, and X. Guillaud, "Synthesis of different types of energy based controllers for a modular multilevel converter integrated in an HVDC link," in *11th IET International Conference on AC and DC Power Transmission*, pp. 1–7, Feb 2015.

[209] G. Bergna, J. A. Suul, and S. D'Arco, "Impact on small-signal dynamics of using circulating currents instead of ac-currents to control the dc voltage in MMC HVDC terminals," in *2016 IEEE Energy Conversion Congress and Exposition (ECCE)*, pp. 1–8, Sept 2016.

[210] A. E. Leon, G. Revel, D. M. Alonso, and G. E. Alonso, "Wind power converters improving the power system stability," *IET Generation, Transmission Distribution*, vol. 10, no. 7, pp. 1622–1633, 2016.

[211] R. H. Renner and D. V. Hertem, "Potential of wind farms connected to HVDC grid to provide DC ancillary services," *IEEE Transactions on Sustainable Energy*, vol. PP, no. 99, pp. 1–1, 2017.

[212] U. Karaagac, J. Mahseredjian, L. Cai, and H. Saad, "Offshore wind farm modeling accuracy and efficiency in mmc-based multiterminal hvdc connection," *IEEE Transactions on Power Delivery*, vol. 32, pp. 617–627, April 2017.

[213] V. Salis, A. Costabeber, S. M. Cox, and P. Zanchetta, "Stability assessment of power-converter-based ac systems by ltp theory: Eigenvalue analysis and harmonic impedance estimation," *IEEE Journal of Emerging and Selected Topics in Power Electronics*, vol. PP, no. 99, pp. 1–1, 2017.

[214] IEC 60909-0:2016, "Short-circuit currents in three-phase a.c. systems - Part 0: Calculation of currents," standard, IEC, Jan. 2016.

[215] Wikipedia, "Direct-quadrature-zero transformation." Online: `https://en.wikipedia.org/wiki/Direct-quadrature-zero_transformation`.

[216] Wikipedia, "Alpha–beta transformation." Online: `https://en.wikipedia.org/wiki/Alpha-beta_transformation`.

[217] S. Sanchez, G. Bergna, and E. Tedeschi, "Tuning of control loops for grid-connected modular multilevel converters under a simplified port representation for large system studies," in *2017 Twelfth International Conference on Ecological Vehicles and Renewable Energies (EVER)*, pp. 1–8, April 2017.

[218] S. D'Arco, J. A. Suul, and O. B. Fosso, "Automatic tuning of cascaded controllers for power converters using eigenvalue parametric sensitivities," *IEEE Transactions on Industry Applications*, vol. 51, pp. 1743–1753, March 2015.

[219] M. Vasiladiotis, N. Cherix, and A. Rufer, "Accurate capacitor voltage ripple estimation and current control considerations for grid-connected modular multilevel converters," *IEEE Transactions on Power Electronics*, vol. 29, pp. 4568–4579, Sept 2014.

[220] K. Shinoda, A. Benchaib, J. Dai, and X. Guillaud, "Analysis of the lower limit of allowable energy in modular multilevel converters," in *2018 20th European Conference on Power Electronics and Applications (EPE'18 ECCE Europe) - Submitted*, 2018.

[221] K. Ilves, S. Norrga, L. Harnefors, and H.-P. Nee, "On energy storage requirements in modular multilevel converters," *IEEE Transactions on Power Electronics*, vol. 29, pp. 77–88, Jan 2014.

[222] H. Saad, J. Mahseredjian, and S. Dennetière, "VSC-MMC station models: Modular multilevel converter in EMTP-RV — user's manual," tech. rep., EMTP-RV, 2014.

[223] A. Beddard, M. Barnes, and R. Preece, "Comparison of detailed modeling techniques for MMC employed on VSC-HVDC schemes," *IEEE Transactions on Power Delivery*, vol. 30, pp. 579–589, April 2015.

[224] Q. Tu and Z. Xu, "Impact of sampling frequency on harmonic distortion for modular multilevel converter," *IEEE Transactions on Power Delivery*, vol. 26, pp. 298–306, Jan 2011.

[225] G. Bergna, J. Suul, E. Berne, P. Egrot, P. Lefranc, J. Vannier, and M. Molinas, "Mitigating dc-side power oscillations and negative sequence load currents in modular multilevel converters under unbalanced faults- first approach using resonant pi," in *IECON 2012 - 38th Annual Conference on IEEE Industrial Electronics Society*, pp. 537–542, Oct 2012.

[226] Z. OU and G. Wang, "Modular multilevel converter control strategy based on arm current control under unbalanced grid condition," *IEEE Transactions on Power Electronics*, vol. PP, no. 99, pp. 1–1, 2017.

[227] Y. Liang, J. Liu, T. Zhang, and Q. Yang, "Arm current control strategy for mmc-hvdc under unbalanced conditions," *IEEE Transactions on Power Delivery*, vol. 32, pp. 125–134, Feb 2017.

[228] L. Harnefors, S. Norrga, A. Antonopoulos, and H.-P. Nee, "Dynamic modeling of modular multilevel converters," in *PProceedings of the 2011-14th European Conference on Power Electronics and Applications (EPE 2011)*, pp. 1–10, Aug 2011.

[229] C. Oates, "Modular multilevel converter design for vsc hvdc applications," *Emerging and Selected Topics in Power Electronics, IEEE Journal of*, vol. 3, pp. 505–515, June 2015.

[230] J. W. Moon, C. S. Kim, J. W. Park, D. W. Kang, and J. M. Kim, "Circulating current control in mmc under the unbalanced voltage," *IEEE Transactions on Power Delivery*, vol. 28, pp. 1952–1959, July 2013.

[231] A. Morched, B. Gustavsen, and M. Tartibi, "A universal model for accurate calculation of electromagnetic transients on overhead lines and underground cables," *IEEE Transactions on Power Delivery*, vol. 14, pp. 1032–1038, Jul 1999.

[232] A. Beddard and M. Barnes, "Modelling of MMC-HVDC systems - an overview," *Energy Procedia*, vol. 80, pp. 201 – 212, 2015. 12th Deep Sea Offshore Wind R&D Conference, {EERA} DeepWind'2015.

[233] W. Leterme, N. Ahmed, J. Beerten, L. Angquist, D. Van Hertem, and S. Norrga, "A new HVDC grid test system for HVDC grid dynamics and protection studies in emt-type software," in *11th IET International Conference on AC and DC Power Transmission*, pp. 1–7, Feb 2015.

[234] S. D'Arco, J. A. Suul, and J. Beerten, "Analysis of accuracy versus model order for frequency-dependent pi-model of HVDC cables," in *2016 IEEE 17th Workshop on Control and Modeling for Power Electronics (COMPEL)*, pp. 1–8, June 2016.

[235] B. Gustavsen and A. Semlyen, "Rational approximation of frequency domain responses by vector fitting," *IEEE Transactions on Power Delivery*, vol. 14, pp. 1052–1061, Jul 1999.

[236] B. Gustavsen, "The vector fitting web site." Online: `https://www.sintef.no/projectweb/vectfit/`.

Appendices

Appendix A

Parameters and Transformations

A.1 Parameters of 2-level Voltage Source Converters

The main parameters used for the *2-level VSC* are shown in Tables A.1 and A.2.

Table A.1 – VSC Base values

S_b	1×10^9 VA
$\cos(\phi_n)$	1
P_b	1×10^9 W
U_{1n}	320×10^3 V
V_b	$\frac{U_{1n}}{\sqrt{3}}$ V
f_b	50 Hz
Ω_b	$2\pi f_b$ rad/s
V_{dcb}	640×10^3 V

Table A.2 – VSC Parameters

U_{1n}	320 kV	R_{eq}^{ac}	1.02 Ω
f_n	50 Hz	L_{eq}^{ac}	83.12 mH

A.2 Parameters of Modular Multilevel Converters

The main parameters used for the MMCs are shown in Tables A.3 and A.4.

Table A.3 – MMC Base values

S_b	1×10^9 VA
$\cos(\phi_n)$	1
P_b	1×10^9 W
U_{1n}	320×10^3 V
V_b	$\frac{U_{1n}}{\sqrt{3}}$ V
f_b	50 Hz
Ω_b	$2\pi f_b$ rad/s
V_{dcb}	640×10^3 V

Table A.4 – MMC Parameters

U_{1n}	320 kV	R_f	0.521 Ω
f_n	50 Hz	L_f	58.7 mH
N	400	R_{arm}	1.024 Ω
C_{arm}	32.55 μF	L_{arm}	48 mH

Note that the parameters R_{eq}^{ac} and L_{eq}^{ac} used for the MMC are the same to their homologous parameters from Table A.2, which are calculated as $R_{eq}^{ac} = R_f + R_{arm}/2$ and $L_{eq}^{ac} = L_f + L_{arm}/2$).

A.3 Parameters for AC grid

The Short-Circuit Ratio is defined as the ratio of the fault level at the Point of Common Coupling on the AC side (PCC-AC), S_{sc}, and the nominal power of the VSC S_b:

$$SCR = \frac{S_{sc}}{S_b} \tag{A.1}$$

Given the approximate fault level of the network feeder at the connection point (or point of common coupling), the impedance, resistance and reactance of the network feeder is calculated as follows [214]:

$$Z_g = \frac{cU_n}{S_{sc}} \tag{A.2a}$$

$$R^G = \frac{Z_g}{\sqrt{1+k^2}} \tag{A.2b}$$

$$X_g = kR^G; L^G = \frac{X_g}{2\pi f_n} \tag{A.2c}$$

where Z_g is the impedance of the network feeder (in Ω); R^G is the resistance of the network feeder (in Ω); X_g is the reactance of the network feeder (in Ω); L^G the inductance (in H); U_n is the nominal line-to-line voltage at the point of common-coupling (PCC) (in V); S_{sc} is the fault level of the network feeder (VA); c is a voltage factor which accounts for the maximum system voltage (1.05 for voltages < 1 kV, and 1.1 for voltages > 1 kV; in this thesis $c = 1$) and k is the ratio of X_g/R^G (in pu).

A.4 Park Transformation — *abc* to *dqz*

The Park transformation consists in using a new coordinates to express the three-phase variables in the static reference frame *abc* with angular frequency defined by $n\omega$ into the rotating frame defined by the axes *dqz* [215]. The *d* axis forms an angle $\theta = n\omega t$ with respect to the fixed vector *a* and the quadrature axis *q* is delayed by 90°. The *dq* axes rotate at an angular speed $n\omega$. This is shown in a graphical description in Fig. A.1.

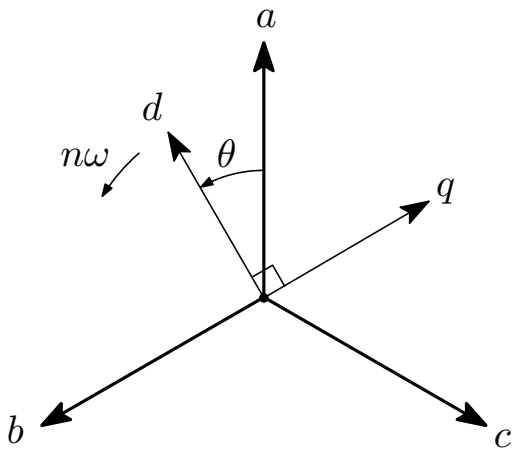

Figure A.1 – Transformation from *abc* to *dqz* in a graphical way

The mathematical transformation $\boldsymbol{P}_{n\omega}$ is defined in (A.3). The constant p will take the value 2/3 if it's desired to maintain the amplitude of the vectors after the transformation

(the so-called "Amplitude Invariant Park Transformation"). If the constant p takes the value $\sqrt{2/3}$, the power is maintained in abc and dqz frame (the so-called "Power Invariant Park Transformation").

$$\boldsymbol{P}_{n\omega} = p \begin{bmatrix} \cos(n\omega t) & \cos(n\omega t - \frac{2\pi}{3}) & \cos(n\omega t - \frac{4\pi}{3}) \\ \sin(n\omega t) & \sin(n\omega t - \frac{2\pi}{3}) & \sin(n\omega t - \frac{4\pi}{3}) \\ \frac{1}{2} & \frac{1}{2} & \frac{1}{2} \end{bmatrix} \tag{A.3}$$

A.5 Clarke Transformation — abc to $\alpha\beta z$

Another useful transformation widely used in electrical systems is the Clarke transformation [216]. This mathematical transformation projects the three-phase vectors in abc frame displaced 120° from each other, onto two stationary axes namely $\alpha\beta$, which are displaced by 90° from each other. The third axis, namely z, is the same as for the Park transformation. This transformation shown in a graphical description in Fig. A.2.

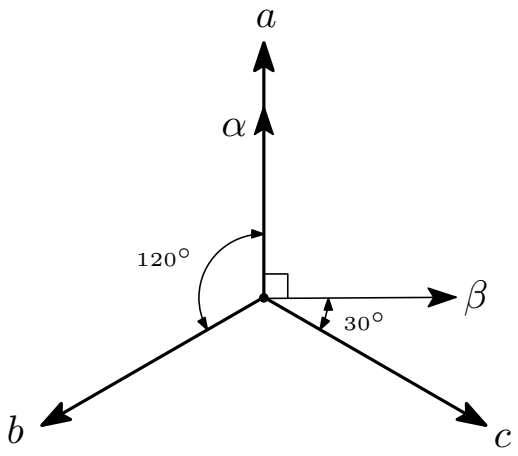

Figure A.2 – Transformation from abc to $\alpha\beta z$ in a graphical way

The mathematical transformation $\boldsymbol{C}_{\alpha\beta z}$ is defined in (A.4). Similarly as for the Park transformation, the constant p will take the value 2/3 if it's desired to maintain the amplitude of the vectors after the transformation (the so-called "Amplitude Invariant Clarke Transformation"). If the constant p takes the value $\sqrt{2/3}$, the power is maintained in abc and $\alpha\beta z$ frame (the so-called "Power Invariant Clarke Transformation").

$$\boldsymbol{C}_{\alpha\beta z} = p \begin{bmatrix} 1 & -\frac{1}{2} & -\frac{1}{2} \\ 0 & -\frac{\sqrt{3}}{2} & \frac{\sqrt{3}}{2} \\ \frac{1}{2} & \frac{1}{2} & \frac{1}{2} \end{bmatrix} \tag{A.4}$$

Appendix B

Mathematical Proofs and Tools

B.1 Open-loop control for *2-level* VSC

In this section it is demonstrated the Open-loop relations from (B.5) in Chapter 1. Considering an AC balanced grid, the dqz components of the voltages are given as:

$$\boldsymbol{v}_{\boldsymbol{dqz}}^{\boldsymbol{G}} = \begin{bmatrix} v_d^G \\ v_q^G \\ v_z^G (=0) \end{bmatrix} = \boldsymbol{P}_{\boldsymbol{\omega}} \begin{bmatrix} v_a^G \\ v_b^G \\ v_c^G \end{bmatrix} = \boldsymbol{P}_{\boldsymbol{\omega}} \begin{bmatrix} \hat{v}^G \cos(\omega t) \\ \hat{v}^G \cos(\omega t - 2\pi/3) \\ -v_a^G - v_b^G \end{bmatrix} = \begin{bmatrix} \hat{v}^G \\ 0 \\ 0 \end{bmatrix} \tag{B.1}$$

Assuming a perfect synchronization with the grid (i.e. ω is constant, or perfectly estimated), the current references i_d^{G*} and i_q^{G*} are related to the the active and reactive power references P_{ac}^* and Q_{ac}^* as shown in (B.2).

$$i_d^{G*} = \frac{2}{3}\frac{P_{ac}^*}{v_d^G}; \quad i_q^{G*} = \frac{2}{3}\frac{Q_{ac}^*}{v_d^G} \tag{B.2}$$

Taking into account the current references from (B.2) in dq frame, the abc components are obtained by the multiplication of the inverse of the Park's transformation $\boldsymbol{P}_{\boldsymbol{\omega}}^{\boldsymbol{-1}}$ to the vector $\boldsymbol{i}_{\boldsymbol{dqz}}^{\boldsymbol{G*}} = [i_d^{G*}, i_q^{G*}, 0]^\top$ as shown in (B.3).

$$\boldsymbol{i}_{\boldsymbol{abc}}^{\boldsymbol{G*}} = \boldsymbol{P}_{\boldsymbol{\omega}}^{\boldsymbol{-1}} \boldsymbol{i}_{\boldsymbol{dqz}}^{\boldsymbol{G*}} \tag{B.3}$$

Finally, the voltages $\boldsymbol{v}_{\boldsymbol{mabc}}^{\boldsymbol{*}}$ are given by the resolution of the equations (1.4) as follows:

$$v_{ma}^* = v_a^G + L_{eq}^{ac}\frac{di_a^{G*}}{dt} + R_{eq}^{ac}\, i_a^{G*} \tag{B.4a}$$

$$v_{mb}^* = v_b^G + L_{eq}^{ac}\frac{di_b^{G*}}{dt} + R_{eq}^{ac}\, i_b^{G*} \tag{B.4b}$$

$$v_{mc}^* = -v_{ma}^* - v_{mb}^* \tag{B.4c}$$

The results of (B.4) are given in (B.5).

$$v_{ma}^* = \hat{v}^G \cos(\omega t) + \frac{2}{3\hat{v}^G}\left(\omega L_{eq}^{ac}\left(Q^* \cos(\omega t) - P^* \sin(\omega t)\right)\right) + ... \tag{B.5a}$$

$$... + \frac{2}{3\hat{v}^G}\left(R_{eq}^{ac}\left(P^* \cos(\omega t) + Q^* \sin(\omega t)\right)\right)$$

$$v_{mb}^* = \hat{v}^G \cos(\omega t - 2\pi/3) + \frac{2}{3\hat{v}^G}\left(\omega L_{eq}^{ac}\left(Q^* \cos(\omega t - 2\pi/3) - P^* \sin(\omega t - 2\pi/3)\right)\right) + ... \tag{B.5b}$$

$$... + \frac{2}{3\hat{v}^G}\left(R_{eq}^{ac}\left(P^* \cos(\omega t - 2\pi/3) + Q^* \sin(\omega t - 2\pi/3)\right)\right)$$

$$v_{mc}^* = -v_{ma}^* - v_{mb}^* \tag{B.5c}$$

B.2 Concatenation of LTI models: State-Space Association Theoretical Principle

In this section, the theoretical principle for the association of two LTI models is provided. Through this Thesis, the concatenation of bigger systems is always performed first between two LTI models, and the resulting coupled model is then associated with a third one, and so on. The contents of this section were developed in [9].

Let us consider two independent LTI models expressed in (B.6) and (B.7) which may be linked by a certain input and output relationship:

$$\begin{cases} \dfrac{d}{dt}\boldsymbol{x_1} = \boldsymbol{A_1 x_1} + \boldsymbol{B_1 u_1} \\ \quad \boldsymbol{y_1} = \boldsymbol{C_1 x_1} + \boldsymbol{D_1 u_1} \end{cases} \tag{B.6}$$

$$\begin{cases} \dfrac{d}{dt}\boldsymbol{x_2} = \boldsymbol{A_2 x_2} + \boldsymbol{B_2 u_2} \\ \quad \boldsymbol{y_2} = \boldsymbol{C_2 x_2} + \boldsymbol{D_2 u_2} \end{cases} \tag{B.7}$$

The LTI model "1" ("2") have n_1 (n_2) states forming the vector $\boldsymbol{x_1}$ ($\boldsymbol{x_2}$), m_1 (m_2) inputs gathered in the vector $\boldsymbol{u_1}$ ($\boldsymbol{u_2}$) and p_1 (p_2) outputs on the vector $\boldsymbol{y_1}$ ($\boldsymbol{y_2}$). The LTI model is then completed with the $n_1 \times n_1$ matrix $\boldsymbol{A_1}$ ($n_2 \times n_2$ matrix $\boldsymbol{A_2}$), $n_1 \times m_1$ matrix $\boldsymbol{B_1}$ ($n_2 \times m_2$ matrix $\boldsymbol{B_2}$); $p_1 \times n_1$ matrix $\boldsymbol{C_1}$ ($p_2 \times n_2$ matrix $\boldsymbol{C_2}$) and $p_1 \times m_1$ matrix $\boldsymbol{D_1}$ ($p_2 \times m_2$ matrix $\boldsymbol{D_2}$).

The Step # 1 is to consider the "stack" of both sub-systems represented by their state-space models without taking into account any possible feedback between the inputs and the outputs between them, i.e. a sort of *open-loop* (ol):

$$\begin{cases} \dfrac{d}{dt}\boldsymbol{X_{ol}} = \boldsymbol{A_{ol} X_{ol}} + \boldsymbol{B_{ol} U_{ol}} \\ \quad \boldsymbol{Y_{ol}} = \boldsymbol{C_{ol} X_{ol}} + \boldsymbol{D_{ol} U_{ol}} \end{cases} \tag{B.8}$$

where

$$\boldsymbol{X_{ol}} = \begin{bmatrix} \boldsymbol{x_1} \\ \boldsymbol{x_2} \end{bmatrix} \in \mathbb{R}^{(n_1+n_2)\times 1};\ \boldsymbol{U_{ol}} = \begin{bmatrix} \boldsymbol{u_1} \\ \boldsymbol{u_2} \end{bmatrix} \in \mathbb{R}^{(m_1+m_2)\times 1};\ \boldsymbol{Y_{ol}} = \begin{bmatrix} \boldsymbol{y_1} \\ \boldsymbol{y_2} \end{bmatrix} \in \mathbb{R}^{(p_1+p_2)\times 1};$$

and,

$$\boldsymbol{A_{ol}} = \begin{bmatrix} \boldsymbol{A_1} & \boldsymbol{0} \\ \boldsymbol{0} & \boldsymbol{A_2} \end{bmatrix} \in \mathbb{R}^{(n_1+n_2)\times(n_1+n_2)};\ \boldsymbol{B_{ol}} = \begin{bmatrix} \boldsymbol{B_1} & \boldsymbol{0} \\ \boldsymbol{0} & \boldsymbol{B_2} \end{bmatrix} \in \mathbb{R}^{(n_1+n_2)\times(m_1+m_2)};$$
$$\boldsymbol{C_{ol}} = \begin{bmatrix} \boldsymbol{C_1} & \boldsymbol{0} \\ \boldsymbol{0} & \boldsymbol{C_2} \end{bmatrix} \in \mathbb{R}^{(p_1+p_2)\times(n_1+n_2)};\ \boldsymbol{D_{ol}} = \begin{bmatrix} \boldsymbol{D_1} & \boldsymbol{0} \\ \boldsymbol{0} & \boldsymbol{D_2} \end{bmatrix} \in \mathbb{R}^{(p_1+p_2)\times(m_1+m_2)}$$

The Step # 1 is exemplified in Fig. B.1

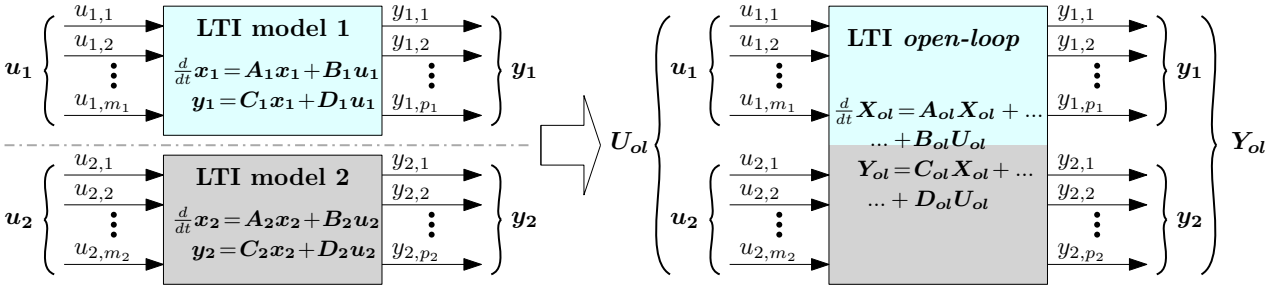

Figure B.1 – Concatenation of LTI models: Step # 1

The Step # 2 is to assume that some inputs of the system are connected to some of the outputs (closed-loop, cl). Those inputs are considered as *internal inputs* denoted by $\boldsymbol{U_{int}}$ while the inputs that are not connected to any output are considered as *external inputs*, denoted by $\boldsymbol{U_{ext}}$. In this way, the inputs of the "stacked" LTI model are re-ordered as shown in (B.9). This step is shown in Fig. B.2.

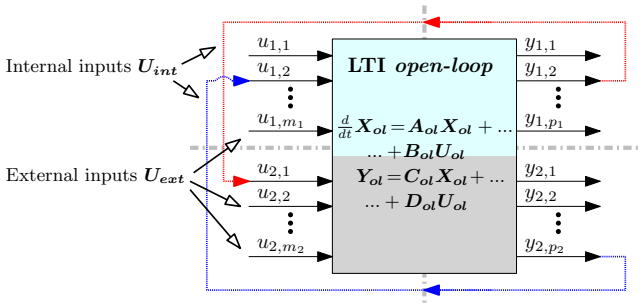

Figure B.2 – Concatenation of LTI models: Step # 2

$$\boldsymbol{U'_{ol}} = \boldsymbol{U_{int}} + \boldsymbol{U_{ext}} \tag{B.9}$$

The expressions of $\boldsymbol{U_{int}}$ and $\boldsymbol{U_{ext}}$ are given by:

$$\boldsymbol{U_{int}} = \boldsymbol{M_{int}}\ \boldsymbol{Y_{ol}};\ \ \boldsymbol{U_{ext}} = \boldsymbol{M_{ext}}\ \boldsymbol{U_{ol}}$$

The matrix $\boldsymbol{M_{int}}$, also called *interconnection matrix*, relates certain outputs of the *open-loop* LTI model $\boldsymbol{Y_{ol}}$ which are linked internally with certain inputs. On the contrary, the matrix $\boldsymbol{M_{ext}}$ relates the inputs of the *open-loop* LTI model $\boldsymbol{U_{ol}}$ which are not looped back into the "stacked" LTI model, i.e. they are external inputs. The creation of the matrices $\boldsymbol{M_{int}}$ and $\boldsymbol{M_{ext}}$ can be performed with a Matlab routine based on the identification of the output names of looped back variables as in [9].

The relationship between the inputs $\boldsymbol{U_{ol}}$ and the outputs $\boldsymbol{Y_{ol}}$ can then be expressed by:

$$\boldsymbol{U'_{ol}} = \boldsymbol{M_{int}}\ \boldsymbol{Y_{ol}} + \boldsymbol{M_{ext}}\ \boldsymbol{U_{ol}} \tag{B.10}$$

Replacing the new expression of $\boldsymbol{U'_{ol}}$ given in (B.10) into $\boldsymbol{U_{ol}}$ from (B.8) yields:

$$\begin{cases} \dfrac{d}{dt}\boldsymbol{X_{ol}} = \boldsymbol{A_{ol}}\ \boldsymbol{X_{ol}} + \boldsymbol{B_{ol}}\left(\boldsymbol{M_{int}}\ \boldsymbol{Y_{ol}} + \boldsymbol{M_{ext}}\ \boldsymbol{U_{ol}}\right) \\ \quad \boldsymbol{Y_{ol}} = \boldsymbol{C_{ol}}\boldsymbol{X_{ol}} + \boldsymbol{D_{ol}}\left(\boldsymbol{M_{int}}\ \boldsymbol{Y_{ol}} + \boldsymbol{M_{ext}}\ \boldsymbol{U_{ol}}\right) \end{cases} \tag{B.11}$$

The expression from (B.2) can be further developed. The term $\boldsymbol{B_{ol}}\left(\boldsymbol{M_{int}}\ \boldsymbol{Y_{ol}} + \boldsymbol{M_{ext}}\ \boldsymbol{U_{ol}}\right)$ from the first line (i.e. $d\boldsymbol{X_{ol}}/dt$) is expanded. For the second line, it can be noticed that $\boldsymbol{Y_{ol}}$ appears on both sides of the equation in the second line, so the outputs are grouped to obtain:

$$\begin{cases} \dfrac{d}{dt}\boldsymbol{X_{ol}} = \boldsymbol{A_{ol}}\ \boldsymbol{X_{ol}} + \boldsymbol{B_{ol}}\ \boldsymbol{M_{int}}\ \boldsymbol{Y_{ol}} + \boldsymbol{B_{ol}}\ \boldsymbol{M_{ext}}\ \boldsymbol{U_{ol}} \\ \quad \boldsymbol{Y_{ol}} = \left(\boldsymbol{I} - \boldsymbol{D_{ol}}\ \boldsymbol{M_{int}}\right)^{-1}\left(\boldsymbol{C_{ol}}\ \boldsymbol{X_{ol}} + \boldsymbol{D_{ol}}\ \boldsymbol{M_{ext}}\ \boldsymbol{U_{ol}}\right) \end{cases} \tag{B.12}$$

Defining the matrix $\boldsymbol{E_{ol}} \stackrel{\text{def}}{=} \left(\boldsymbol{I} - \boldsymbol{D_{ol}}\ \boldsymbol{M_{int}}\right)^{-1}$, the output is then expressed as $\boldsymbol{Y_{ol}} = \boldsymbol{E_{ol}}\boldsymbol{C_{ol}}\boldsymbol{X_{ol}} + \boldsymbol{E_{ol}}\boldsymbol{D_{ol}}\boldsymbol{M_{ext}}\boldsymbol{U_{ol}}$; so replacing the new expression of $\boldsymbol{Y_{ol}}$ into the first line of (B.12), it yields:

$$\begin{cases} \dfrac{d}{dt}\boldsymbol{X_{ol}} = \left(\boldsymbol{A_{ol}} + \boldsymbol{B_{ol}}\ \boldsymbol{M_{int}}\ \boldsymbol{E_{ol}}\ \boldsymbol{C_{ol}}\right)\ \boldsymbol{X_{ol}} + \left(\boldsymbol{B_{ol}} + \boldsymbol{B_{ol}}\ \boldsymbol{M_{int}}\ \boldsymbol{E_{ol}}\ \boldsymbol{D_{ol}}\right)\ \boldsymbol{M_{ext}}\ \boldsymbol{U_{ol}} \\ \quad \boldsymbol{Y_{ol}} = \boldsymbol{E_{ol}}\ \boldsymbol{C_{ol}}\ \boldsymbol{X_{ol}} + \boldsymbol{E_{ol}}\ \boldsymbol{D_{ol}}\ \boldsymbol{M_{ext}}\ \boldsymbol{U_{ol}} \end{cases} \tag{B.13}$$

The Step # 3 consist in creating the *closed-loop* state-space LTI model from (B.13) expressed as:

$$\begin{cases} \dfrac{d}{dt}\boldsymbol{X_{cl}} = \boldsymbol{A_{cl}}.\boldsymbol{X_{cl}} + \boldsymbol{B_{cl}}.\boldsymbol{U_{cl}} \\ \quad \boldsymbol{Y_{cl}} = \boldsymbol{C_{cl}}.\boldsymbol{X_{cl}} + \boldsymbol{D_{cl}}.\boldsymbol{U_{cl}} \end{cases} \tag{B.14}$$

Hence, by identification, and according to (B.14), the matrices of the closed-loop state-space representation are given by:

$$\begin{aligned} \boldsymbol{X_{cl}} &= \boldsymbol{X_{ol}} \\ \boldsymbol{U_{cl}} &= \boldsymbol{U_{ext}} = \boldsymbol{M_{ext}}\, \boldsymbol{U_{ol}} \\ \boldsymbol{Y_{cl}} &= \boldsymbol{Y_{ol}} \end{aligned} \tag{B.15}$$

and

$$\begin{aligned} \boldsymbol{A_{cl}} &= (\boldsymbol{A_{ol}} + \boldsymbol{B_{ol}}\, \boldsymbol{M_{int}}\, \boldsymbol{E_{ol}}\, \boldsymbol{C_{ol}}) \\ \boldsymbol{B_{cl}} &= (\boldsymbol{B_{ol}} + \boldsymbol{B_{ol}}\, \boldsymbol{M_{int}}\, \boldsymbol{E_{ol}}\, \boldsymbol{D_{ol}}) \\ \boldsymbol{C_{cl}} &= \boldsymbol{E_{ol}}\, \boldsymbol{C_{ol}} \\ \boldsymbol{D_{cl}} &= \boldsymbol{E_{ol}}\, \boldsymbol{D_{ol}} \end{aligned} \tag{B.16}$$

The Step # 3 is shown in Fig. B.3. Note that the states of the concatenated LTI model $\boldsymbol{X_{cl}}$ are the sum of the states of the individual models and the same stands for the outputs $\boldsymbol{Y_{ol}}$. Moreover, the inputs of the new system are only the "external" ones, i.e. the inputs that are not internally fed back.

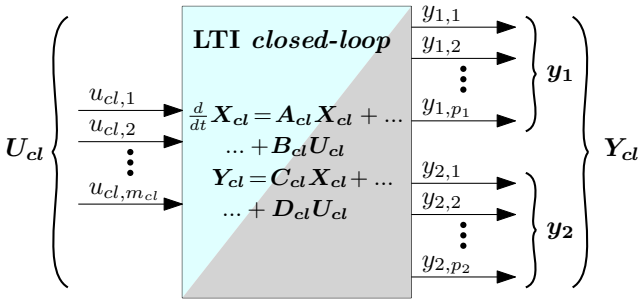

Figure B.3 – Concatenation of LTI models: Step # 3

Appendix C

Controller Tuning

There are many ways for the tuning of PI controllers [205, 217, 218]. In this Thesis, the classical pole-placement method is used, and explained in the following. Let us consider a first-order transfer function given by (C.1):

$$\frac{x}{u}(s) = \frac{1}{\kappa s} \tag{C.1}$$

where x corresponds to the dynamic state of the equation and u the input, which are assumed to be both SSTI variables. Moreover, κ represents the main parameter of the system (not tunable). For controlling the state variable x to a desired reference value x^*, a PI or IP controller may be used, as shown in Fig. C.1.

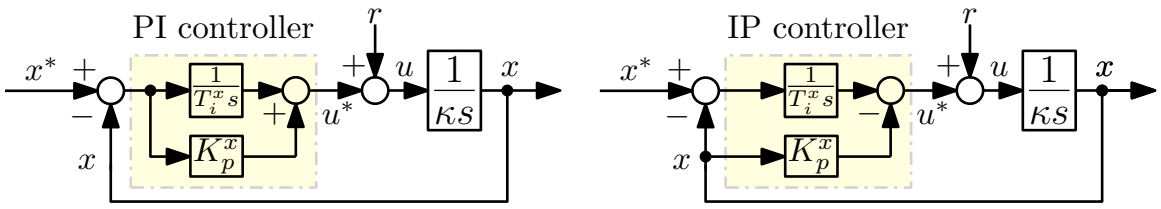

Figure C.1 – Generic PI/IP controller and first order plant

Note that the output of the controllers is noted as u^*, and the actual input for the plant is $u^* + r$, where r represents an external perturbation. For tuning purposes, it is considered that $u = u^*$.

The closed loop transfer function respect to the reference x^* for the PI controller and the plant (i.e. $x^*/x(s)$) is given in (C.2), while in (C.3) it is considered the IP controller.

$$\frac{x^*}{x}(s) = \frac{1 + K_p^x T_i^x s}{\kappa T_i^x s^2 + K_p^x T_i^x s + 1} \tag{C.2}$$

$$\frac{x^*}{x}(s) = \frac{1}{\kappa T_i^x s^2 + K_p^x T_i^x s + 1} \tag{C.3}$$

Note that the denominator of (C.2) and (C.3) are the same, the only difference is that the PI controller induces a zero on the numerator, which is not present when using IP controllers.

The gains K_p^x and T_i^x are calculated based on pole-placement method, where the denominators of (C.2) and (C.3) are compared to the well-known second-order transfer function characteristics given as follows:

$$T_f^{2^{\text{nd}}\text{order}} = \frac{1}{\omega_n^2} s^2 + \frac{2\zeta}{\omega_n} s + 1 \tag{C.4}$$

where ζ is the damping ratio and ω_n is the undamped natural frequency (in rad/s) of the system response. The controller gains are then chosen as follows:

$$\begin{cases} K_p^x = 2\zeta\omega_n\kappa \\ T_i^x = 1/\left(\omega_n^2\kappa\right) \end{cases} \tag{C.5}$$

The poles of (C.4) are given by:

$$\lambda_{1,2} = \omega_n\left(-\zeta \pm \sqrt{\zeta^2 - 1}\right) \tag{C.6}$$

For a damping ratio $\zeta = 0.7$, the response time τ_x is related with the frequency ω_n as in (C.7) [9].

$$\omega_n \approx \frac{3}{\tau_x} \tag{C.7}$$

As an example, let us consider the plant from (C.2) with $\kappa = 1$ pu for a time domain simulation, where the response of the closed-loops from Fig. C.1 are evaluated. The rest of the parameters are given in Table C.1. At $t = 0.1$ s, an unity step on x^* is applied. Then, a step on the perturbation r is applied at $t = 0.14$ s. The time-domain simulation results are depicted in Fig. C.2.

Table C.1 – Example on controller tuning for the transfer function in (C.2) with $\kappa = 1$ pu

Variable	Value	Variable	Value
τ_x	10 ms	K_p^x	420 pu
ω_n	300 rad/s	T_i^x	1.11×10^{-5} s

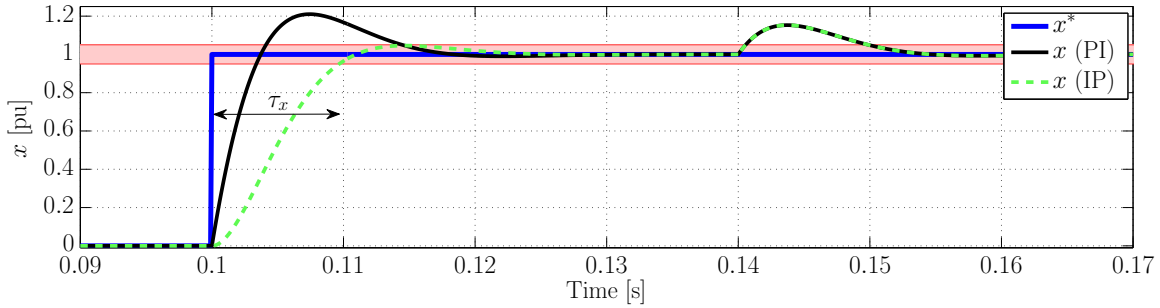

Figure C.2 – Dynamic response of the closed-loop system with PI or IP controllers (red band delimits the ±5 % of the applied step value)

As seen in the results, the response for the PI presents a large overshoot due to the zero in (C.2). Since this zero is filtered when using the IP (see (C.3)) this overshoot is limited. The theoretical response time τ_x is the time that the variable x takes to arrive at 95 % of its final value as denoted in Fig. C.2. Note that the response time τ_x is only respected when considering the IP controller for a reference step. When the perturbation r occurs at $t = 0.14$ s, both closed loops systems present the same dynamic response. This is due to the fact that the denominators in (C.2) and (C.3) are the same. From a practical point of view, the PI controllers are preferred [140]. The overshoot for the reference steps are easily avoided by filtering the reference x^*.

Finally, note that the methodology is similar for all control loops: it is only needed to take into account the variable κ from (C.1). For example, κ is replaced by the inductance L, capacitance C or electrostatic constant H, depending on the nature of the state variable x.

Appendix D

Matlab code for SSTI-MMC model

This Appendix summarizes the Matlab code used for obtaining the MMC model with Steady-State Time Invariant solution detailed in Chapter 2. In order to execute this code, the Symbolic toolbox from Matlab is needed.

Symbolic parameters definitions

```
%% Parameters

w = sym('w','real'); % AC Grid frequency in [rad/s] (ω)
t = sym('t','real'); % Time in [s] (t)

%% MMC Physical parameters

Carm = sym('Carm','real');   % Equivalent Arm capacitor voltages (C_arm)
Larm = sym('Larm','real');   % Arm inductance (L_arm)
Rarm = sym('Rarm','real');   % Arm equivalent resistance (R_arm)
Leqac = sym('Leqac','real'); % AC equivalent inductance (L_eq^ac)
Reqac = sym('Reqac','real'); % AC equivalent resistance (R_eq^ac)
```

Symbolic transformations definitions

```
%% Park Transformations
cte_Park =  (2/3); % Park constant

Parkw = ... % Park transformation at w (P_ω)
 (cte_Park*[ cos(w*t) cos(w*t-2*pi/3) cos(w*t-4*pi/3);
             sin(w*t) sin(w*t-2*pi/3) sin(w*t-4*pi/3);
                1/2         1/2          1/2       ]);

ParkInvw = simplify(inv(Parkw),10); % Inverse Park transformation at w (P_ω^-1)
Jw = simplify(Parkw*(diff(ParkInvw, t))); % Coupling J (J_ω)

Park2w = ... % Park transformation at -2w (P_-2ω)
 (cte_Park*[ cos(-2*w*t) cos(-2*w*t-2*pi/3) cos(-2*w*t-4*pi/3);
             sin(-2*w*t) sin(-2*w*t-2*pi/3) sin(-2*w*t-4*pi/3);
                  1/2             1/2              1/2       ]);

ParkInv2w = simplify(inv(Park2w),10); % Inverse Park transformation (P_-2ω^-1)
J2w = simplify(Park2w*(diff(ParkInv2w, t))); % Coupling (J_-2ω)

```

```
% Transformation 3w
T3w =  [  cos(3*w*t)  sin(3*w*t);
          sin(3*w*t) -cos(3*w*t)]; % Rotation matrix at 3w (T_3ω)

TInv3w = simplify(inv(T3w),10); % Inverse rotation matrix at 3w (T_3ω^-1)
J3w = simplify(T3w*(diff(TInv3w, t))); % Coupling J3w (J_3ω)
```

MMC symbolic variables definitions

```
%% Variable definitions: MMC Control Inputs

mSigmad = sym('mSigmad','real'); % (m_d^Σ)
mSigmaq = sym('mSigmaq','real'); % (m_q^Σ)
mSigmaz = sym('mSigmaz','real'); % (m_z^Σ)

mSigmadqz = [mSigmad mSigmaq mSigmaz]'; % (m_dqz^Σ)

mDeltad = sym('mDeltad','real'); %  (m_d^Δ)
mDeltaq = sym('mDeltaq','real'); %  (m_q^Δ)
mDeltaz = sym('mDeltaz','real'); %  (m_z^Δ)
mDeltaZd = sym('mDeltaZd','real'); % (m_Zd^Δ)
mDeltaZq = sym('mDeltaZq','real'); % (m_Zq^Δ)

mDeltadqz = [mDeltad mDeltaq mDeltaZd*cos(3*w*t)+mDeltaZq*sin(3*w*t)]'; % ...
    (m_dqz^Δ)
mDeltadqZdZq = [mDeltad mDeltaq mDeltaZd mDeltaZq]'; % (m_dqZ^Δ)

%% Variable definitions: MMC Currents

% Grid currents
iDeltad = sym('iDeltad','real'); % (i_d^Δ)
iDeltaq = sym('iDeltaq','real'); % (i_q^Δ)
iDeltaz = sym('iDeltaz','real'); % (i_z^Δ)

iDeltadqz = [iDeltad iDeltaq iDeltaz]'; % (i_dqz^Δ)

% Common-mode currents (or circulating currents)
iSigmad = sym('iSigmad','real'); % (i_d^Σ)
iSigmaq = sym('iSigmaq','real'); % (i_q^Σ)
iSigmaz = sym('iSigmaz','real'); % (i_z^Σ)

iSigmadqz = [iSigmad iSigmaq iSigmaz]'; % (i_dqz^Σ)

%% Variable definitions: MMC Capacitor voltages

% vC SUM
vCSigmad = sym('vCSigmad','real'); % (v_Cd^Σ)
vCSigmaq = sym('vCSigmaq','real'); % (v_Cq^Σ)
vCSigmaz = sym('vCSigmaz','real'); % (v_Cz^Σ)

vCSigmadqz = [vCSigmad vCSigmaq vCSigmaz]'; % (v_Cdqz^Σ)

% vC DELTA
vCDeltad = sym('vCDeltad','real'); % (v_Cd^Δ)
vCDeltaq = sym('vCDeltaq','real'); % (v_Cq^Δ)
vCDeltaz = sym('vCDeltaz','real'); % (v_Cz^Δ)
```

```
vCDeltaZd = sym('vCDeltaZd','real'); % (v^Δ_{CZ_d})
vCDeltaZq = sym('vCDeltaZq','real'); % (v^Δ_{CZ_q})

vCDeltadqz = [vCDeltad vCDeltaq vCDeltaz]'; % (v^Δ_{Cdqz})
vCDeltadqZdZq = [vCDeltad vCDeltaq vCDeltaZd vCDeltaZq]'; % (v^Δ_{CdqZ})
```

Voltage sum SSTI dynamics derivation from Section 2.4.2

```
%% Arm capacitor voltages SUM (v^Σ_C)

%Part B  (Φ^Σ_B)
PartSigmaB =  ...
    simplify(Park2w*((ParkInvw*mDeltadqz).*(ParkInvw*((1/2)*iDeltadqz))), 10);
EqsPartSigmaB = collect(PartSigmaB, iDeltadqz);
MatPartSigmaB = jacobian(EqsPartSigmaB, iDeltadqz);
MatPartSigmaBSimp = subs(simplify(expand(MatPartSigmaB)),[cos(6*t*w) ...
    sin(6*t*w)], [0 0]); % Neglect 6w terms

% Part C (Φ^Σ_C)
PartSigmaC =  ...
    simplify(Park2w*((ParkInv2w*mSigmadqz).*(ParkInv2w*iSigmadqz)), 10);
EqsPartSigmaC = collect(PartSigmaC, iSigmadqz);
MatPartSigmaC = jacobian(EqsPartSigmaC, iSigmadqz);
MatPartSigmaCSimp = subs(simplify(expand(MatPartSigmaC)), [cos(6*t*w) ...
    sin(6*t*w)], [0 0]); % Neglect 6w terms

% Part A = B + C (Φ^Σ_A = Φ^Σ_B + Φ^Σ_C)

dvCSigmadqz_dt = simplify((1/(2*Carm))*(MatPartSigmaBSimp*[iDeltad ...
    iDeltaq 0]' + MatPartSigmaCSimp*iSigmadqz - 2*Carm*J2w*vCSigmadqz)); % ...
    (dv^Σ_{Cdqz}/dt from (2.47))
```

Voltage difference SSTI dynamics derivation from Section 2.4.1

```
%% Arm capacitor voltages DELTA (v^Δ_C)

%Part B (Φ^Δ_B)
PartDeltaB =  simplify( ...
    Parkw*((ParkInv2w*mSigmadqz).*(ParkInvw*((1/2)*iDeltadqz))), 10);
EqsPartDeltaB = collect(PartDeltaB, iDeltadqz);
MatPartDeltaB = jacobian(EqsPartDeltaB, iDeltadqz);
MatPartDeltaBSimp = subs(simplify(MatPartDeltaB), [cos(6*t*w) ...
    sin(6*t*w)], [0 0]);

%Part C (Φ^Δ_C)
PartDeltaC =  simplify( ...
    Parkw*((ParkInvw*mDeltadqz).*(ParkInv2w*iSigmadqz)), 10);
EqsPartDeltaC = collect(PartDeltaC, iSigmadqz);
MatPartDeltaC = jacobian(EqsPartDeltaC, iSigmadqz);
MatPartDeltaCSimp = subs(simplify(MatPartDeltaC), [cos(6*t*w) ...
    sin(6*t*w)], [0 0]);

% Part A = B + C (Φ^Δ_A = Φ^Δ_B + Φ^Δ_C)

```

```
dvCDeltadqz_dt = simplify((1/(2*Carm))*(MatPartDeltaBSimp*[iDeltad ...
    iDeltaq 0]' + MatPartDeltaCSimp*iSigmadqz - 2*Carm*Jw*vCDeltadqz)); % ...
    (dq components from (2.25))

% ZERO SEQUENCE: vCDeltaZdZq  ([v^Δ_CZd v^Δ_CZq]^⊤)

dvCDeltaz_dt = dvCDeltadqz_dt(3); % (dv^Δ_Cz/dt not SSTI; from (2.25))

COS_part = subs(dvCDeltaz_dt, [sin(3*t*w) cos(3*t*w)], [0 1]); % (Ψ_d)
SIN_part = subs(dvCDeltaz_dt, [sin(3*t*w) cos(3*t*w)], [1 0]); % (Ψ_q)

dvCDeltaZalpha_dt = COS_part*cos(3*t*w) + SIN_part*sin(3*t*w); % (2.30a)
dvCDeltaZbeta_dt =  COS_part*sin(3*t*w) - SIN_part*cos(3*t*w); % (2.30b)

dvCDeltaZalphabeta_dt = [dvCDeltaZalpha_dt dvCDeltaZbeta_dt]';
vCDeltaZdZq = [vCDeltaZd vCDeltaZq]';

dvCDeltaZdZq_dt = simplify(simplify(expand(T3w*dvCDeltaZalphabeta_dt)) - ...
    J3w*vCDeltaZdZq); % ([dv^Δ_CZd/dt dv^Δ_CZq/dt]^⊤ SSTI)
```

Grid currents SSTI dynamics derivation from Section 2.4.4

```
%% AC-side Curents  (i^Δ_dqz)

vMDeltad = sym('vMDeltad','real'); %  (v^Δ_md)
vMDeltaq = sym('vMDeltaq','real'); %  (v^Δ_mq)
vMDeltaz = sym('vMDeltaz','real'); %  (v^Δ_mz)

diDeltadqz_dt = simplify((1/(Leqac))*([vMDeltad vMDeltaq vMDeltaz]' - ...
    [Vgd Vgq 0]' - Reqac*iDeltadqz - Leqac*Jw*iDeltadqz)); % (2.58)

% Modulated voltages

vCDeltadqz = [vCDeltad vCDeltaq ...
    vCDeltaZd*cos(3*t*w)+vCDeltaZq*sin(3*t*w)]'; % (v^Δ_Cdqz)
mDeltadqz = [mDeltad mDeltaq mDeltaZd*cos(3*t*w)+mDeltaZq*sin(3*t*w)]'; % ...
    (m^Δ_dqz)

vMDeltaabc = (-1/2).*((ParkInvw*mDeltadqz).*(ParkInv2w*vCSigmadqz) + ...
    (ParkInv2w*mSigmadqz).*(ParkInvw*vCDeltadqz));
vMDeltadqz = simplify(Parkw*vMDeltaabc);
vMDeltadqzSimp = subs(vMDeltadqz, [cos(6*t*w) sin(6*t*w)], [0 0]);  % ...
    (v^Δ_mdqz from (2.66))

% VMDeltaZd y Zq

vMDeltaZ = vMDeltadqz(3); % (v^Δ_mz from (2.62))

COS_part = simplify(subs(vMDeltaZ, [sin(3*t*w) cos(3*t*w)], [0 1]),10);
SIN_part = simplify(subs(vMDeltaZ, [sin(3*t*w) cos(3*t*w)], [1 0]),10);

vMDeltaZalpha = COS_part*cos(3*t*w) + SIN_part*sin(3*t*w);
vMDeltaZbeta =  COS_part*sin(3*t*w) - SIN_part*cos(3*t*w);

vMDeltaZalphabeta = [vMDeltaZalpha vMDeltaZbeta]';
vMDeltaZdq = simplify(T3w*vMDeltaZalphabeta);

```

```
vMDeltadqZdq = [vMDeltadqz(1) vMDeltadqz(2) vMDeltaZdq(1) vMDeltaZdq(2)]';
vMDeltadqZSimp = subs(vMDeltadqZdq, [cos(6*t*w) sin(6*t*w)], [0 0]); % ...
    (v^Δ_mdqZ from (2.66))
```

Common-mode SSTI dynamics derivation from Section 2.4.3

```
%% Common mode-currents (i^Σ_dqz)

vMSigmad = sym('vMSigmad','real'); % (v^Σ_md)
vMSigmaq = sym('vMSigmaq','real'); % (v^Σ_mq)
vMSigmaz = sym('vMSigmaz','real'); % (v^Σ_mz)

diSigmadqz_dt = simplify((1/(Larm))*([0 0 Vdc/2]' - [vMSigmad vMSigmaq ...
    vMSigmaz]' - Rarm*iSigmadqz - Larm*J2w*iSigmadqz)); % (2.49)

% Modulated voltages

vCDeltadqz = [vCDeltad vCDeltaq ...
    vCDeltaZd*cos(3*t*w)+vCDeltaZq*sin(3*t*w)]'; % (v^Δ_Cdqz)

vMSigmaabc = (1/2).*((ParkInv2w*mSigmadqz).*(ParkInv2w*vCSigmadqz) + ...
    (ParkInvw*mDeltadqz).*(ParkInvw*vCDeltadqz));
vMSigmadqz = simplify(Park2w*vMSigmaabc);
vMSigmadqzSimp = subs(vMSigmadqz,  [cos(6*t*w) sin(6*t*w)], [0 0]); % ...
    (v^Δ_mdqz from (2.55))
```

Equations summary

```
diary(strcat('MMC_NonLinear_VoltageBased_',datestr(clock, 30),'.txt'))
disp('%% %%%%%%%%%%%%%%%%%%%%%%%%%%%%%')
disp('%      STATE VARIABLES       %')
disp('%%%%%%%%%%%%%%%%%%%%%%%%%%%%%%%')
disp(' ')
disp([char(iDeltad), ', ',char(iDeltaq)])
disp([char(iSigmad), ', ',char(iSigmaq), ', ',char(iSigmaz)])
disp([char(vCSigmad), ', ',char(vCSigmaq), ', ',char(vCSigmaz)])
disp([char(vCDeltad), ', ',char(vCDeltaq), ', ',char(vCDeltaZd), ', ...
    ',char(vCDeltaZq)])
disp(' ')
disp('%% %%%%%%%%%%%%%%%%%%%%%%%%%%%%%')
disp('%            INPUTS           %')
disp('%%%%%%%%%%%%%%%%%%%%%%%%%%%%%%%')
disp(' ')
disp([char(mSigmad), ', ',char(mSigmaq), ', ',char(mSigmaz)])
disp([char(mDeltad), ', ',char(mDeltaq), ', ',char(mDeltaZd), ', ...
    ',char(mDeltaZq)])
disp(' ')
disp([char(Vgd), ', ',char(Vgq), ', ',char(w), ', ',char(Vdc)])
disp(' ')
disp('%% %%%%%%%%%%%%%%%%%%%%%%%%%%%%%')
disp('%        Parameters           %')
disp('%%%%%%%%%%%%%%%%%%%%%%%%%%%%%%%')
disp(' ')
disp('% Physical Parameters')
disp(' ')
disp(char(Carm))
```

```
disp(char(Rarm))
disp(char(Larm))
disp(strcat(char(Reqac),' % = Rf + Rarm/2'))
disp(strcat(char(Leqac),' % = Lf + Larm/2'))
disp(' ')
disp('%% %%%%%%%%%%%%%%%%%%%%%%%%%%%%')
disp('%     Grid currents in SI    %')
disp('%%%%%%%%%%%%%%%%%%%%%%%%%%%%%%%')
disp(' ')
disp('% Voltage vMDeltadqz')
disp(' ')
disp(strcat('vMDeltad',' = ', char(vMDeltadqZSimp(1)),';'))
disp(strcat('vMDeltaq',' = ', char(vMDeltadqZSimp(2)),';'))
disp(strcat('vMDeltaZd',' = ', char(vMDeltadqZSimp(3)),';'))
disp(strcat('vMDeltaZq',' = ', char(vMDeltadqZSimp(4)),';'))
disp(' ')
disp('% AC Current dynamics')
disp(' ')
disp(strcat('diDeltad_dt',' = ', char(diDeltadqz_dt(1)),';'))
disp(strcat('diDeltaq_dt',' = ', char(diDeltadqz_dt(2)),';'))
disp(' ')
disp('%% %%%%%%%%%%%%%%%%%%%%%%%%%%%%')
disp('% Common-mode currents in SI %')
disp('%%%%%%%%%%%%%%%%%%%%%%%%%%%%%%%')
disp(' ')
disp('% Modulated Voltage vMSigmadqz')
disp(' ')
disp(strcat('vMSigmad',' = ', char(vMSigmadqzSimp(1)),';'))
disp(strcat('vMSigmaq',' = ', char(vMSigmadqzSimp(2)),';'))
disp(strcat('vMSigmaz',' = ', char(vMSigmadqzSimp(3)),';'))
disp(' ')
disp('% Common-mode Current dynamics')
disp(' ')
disp(strcat('diSigmad_dt',' = ', char(diSigmadqz_dt(1)),';'))
disp(strcat('diSigmaq_dt',' = ', char(diSigmadqz_dt(2)),';'))
disp(strcat('diSigmaz_dt',' = ', char(diSigmadqz_dt(3)),';'))
disp(' ')
disp('%% %%%%%%%%%%%%%%%%%%%%%%%%%%%%')
disp('%        vC SIGMA in SI      %')
disp('%%%%%%%%%%%%%%%%%%%%%%%%%%%%%%%')
disp(' ')
disp(strcat('dvCSigmad_dt',' = ', char(dvCSigmadqz_dt(1)),';'))
disp(strcat('dvCSigmaq_dt',' = ', char(dvCSigmadqz_dt(2)),';'))
disp(strcat('dvCSigmaz_dt',' = ', char(dvCSigmadqz_dt(3)),';'))
disp(' ')
disp('%% %%%%%%%%%%%%%%%%%%%%%%%%%%%%')
disp('%        vC DELTA in SI      %')
disp('%%%%%%%%%%%%%%%%%%%%%%%%%%%%%%%')
disp(' ')
disp(strcat('dvCDeltad_dt',' = ', char(dvCDeltadqz_dt(1)),';'))
disp(strcat('dvCDeltaq_dt',' = ', char(dvCDeltadqz_dt(2)),';'))
disp(strcat('dvCDeltaZd_dt',' = ', char(dvCDeltaZdZq_dt(1)),';'))
disp(strcat('dvCDeltaZq_dt',' = ', char(dvCDeltaZdZq_dt(2)),';'))
disp(' ')
diary off
```

Appendix E

Steady-State Analysis and Limitations of MMC with Half-Bridge submodules

The objective of this Appendix is to provide a steady-state analysis of the MMC with Half-Bridge submodules for gaining insight on the converter operation and limits. First, the analytic expressions of the MMC voltages and currents are obtained. With this information, the physical limits of the considered MMC in this Thesis can be studied. The followed methodology can be further extended to other submodule topologies, but this is out of the scope of this Thesis.

E.1 MMC voltages and currents in steady-state

In the following of this section, the mathematical expressions of the steady-state variables of the MMC currents are voltages are obtained. The starting point for the methodology is the mathematical expressions of the MMC dynamic equations in dqz frame and Σ-Δ representation from Chapter 2, and then solving the equations by setting the time derivatives to zero. Then, the Σ-Δ variables in dqz frame are transformed to abc by means of the inverse Park transformation. Finally, after some mathematical manipulations, the expressions of the Upper and Lower variables are obtained. The provided steady-state formulations are useful for the steady-state analysis of the MMC and furthermore, for the complete initialization for time-domain simulations starting at any operating point.

For the ease of following the transformations from Σ-Δ to Upper-Lower, (E.1) summarizes the relations between both representations.

$$\left\{\begin{array}{ll} m_j^{\Sigma} & \stackrel{\text{def}}{=} m_j^U + m_j^L \\ m_j^{\Delta} & \stackrel{\text{def}}{=} m_j^U - m_j^L \\ i_j^{\Sigma} & \stackrel{\text{def}}{=} (i_j^U + i_j^L)/2 \\ i_j^{\Delta} & \stackrel{\text{def}}{=} i_j^U - i_j^L \\ v_{mj}^{\Sigma} & \stackrel{\text{def}}{=} (v_{mj}^U + v_{mj}^L)/2 \\ v_{mj}^{\Delta} & \stackrel{\text{def}}{=} (-v_{mj}^U + v_{mj}^L)/2 \\ v_{Cj}^{\Sigma} & \stackrel{\text{def}}{=} (v_{Cj}^U + v_{Cj}^L)/2 \\ v_{Cj}^{\Delta} & \stackrel{\text{def}}{=} (v_{Cj}^U - v_{Cj}^L)/2 \end{array}\right. \Leftrightarrow \left\{\begin{array}{ll} m_j^U & = (m_j^{\Sigma} + m_j^{\Delta})/2 \\ m_j^L & = (m_j^{\Sigma} - m_j^{\Delta})/2 \\ i_j^U & = i_j^{\Sigma} + i_j^{\Delta}/2 \\ i_j^L & = i_j^{\Sigma} - i_j^{\Delta}/2 \\ v_{mj}^U & = v_{mj}^{\Sigma} - v_{mj}^{\Delta} \\ v_{mj}^L & = v_{mj}^{\Sigma} + v_{mj}^{\Delta} \\ v_{Cj}^U & = v_{Cj}^{\Sigma} + v_{Cj}^{\Delta} \\ v_{Cj}^L & = v_{Cj}^{\Sigma} - v_{Cj}^{\Delta} \end{array}\right. \tag{E.1}$$

Modulated voltages and currents in dqz frame and Σ-Δ representation

First, some initial variables are assumed to be known, which are given in (E.2).

$$P_{ac}; \quad Q_{ac}; \quad i_d^{\Sigma}; \quad i_d^{\Sigma}; \quad W_{z0}^{\Sigma}; \quad v_{mz}^{\Delta}; \quad v_{dc}; \quad v_d^G; \quad v_q^G = 0; \quad \omega \tag{E.2}$$

From the active and reactive power expressions in dq frame, the grid currents can be calculated as (E.3) (assuming $v_q^G = 0$):

$$i_d^{\Delta} = \frac{2}{3}\frac{P_{ac}}{v_d^G}; \quad i_q^{\Delta} = \frac{2}{3}\frac{Q_{ac}}{v_d^G} \tag{E.3}$$

where P_{ac}, Q_{ac} and v_d^G are known variables according to (E.2). The AC-side modulated voltages v_{md}^{Δ} and v_{mq}^{Δ} are obtained from the AC currents dynamics given in (2.58) by setting the current derivative terms to zero (i.e. $d\boldsymbol{i}_{\boldsymbol{dq}}^{\boldsymbol{\Delta}}/dt = 0$), yielding:

$$v_{md}^{\Delta} = v_d^G + R_{eq}^{ac} i_d^{\Delta} + \omega L_{eq}^{ac} i_q^{\Delta} \tag{E.4a}$$
$$v_{mq}^{\Delta} = v_q^G + R_{eq}^{ac} i_q^{\Delta} - \omega L_{eq}^{ac} i_d^{\Delta} \tag{E.4b}$$

With (E.3) and (E.4), the voltages and currents for the AC-side (Δ variables) are obtained analytically. For calculating the voltages and currents for the Σ variables, a power balance between AC and DC sides is needed as expressed in (E.5): the DC power is equal to the AC power plus the internal MMC losses, where P_{loss}^{Δ} represent the losses generated by the AC-side currents, and P_{loss}^{Σ} are the losses generated inside the MMC by the Σ currents.

$$\underbrace{P_{dc}}_{3i_z^{\Sigma}v_{dc}} = P_{ac} + P_{loss}^{\Delta} + P_{loss}^{\Sigma} \tag{E.5}$$

Since the AC-side variables were already obtained, the AC-side losses P_{loss}^{Δ} are expressed as a function of *known* variables as follows:

$$P_{loss}^{\Delta} = R_{eq}^{ac}\left[\left(\sqrt{\frac{3}{2}} i_d^{\Delta}\right)^2 + \left(\sqrt{\frac{3}{2}} i_q^{\Delta}\right)^2\right] \tag{E.6}$$

where the constant $\sqrt{3/2}$ is due to the applied amplitude-invariant Park transformation (see Appendix A). The internal losses, generated by $\boldsymbol{i}_{\boldsymbol{dqz}}^{\boldsymbol{\Sigma}}$ are calculated as in (E.7), where P_{cc} indicates the losses generated by the circulating currents $\boldsymbol{i}_{\boldsymbol{dq}}^{\boldsymbol{\Sigma}}$:

$$P_{loss}^{\Sigma} = R_{arm}\left[\left(\sqrt{\tfrac{3}{2}} i_d^{\Sigma}\right)^2 + \left(\sqrt{\tfrac{3}{2}} i_q^{\Sigma}\right)^2 + \left(\sqrt{\tfrac{3}{2}} i_z^{\Sigma}\right)^2\right] = \underbrace{\frac{3R_{arm}}{2}\left(\left(i_d^{\Sigma}\right)^2 + \left(i_q^{\Sigma}\right)^2\right)}_{P_{cc}} + \tfrac{3R_{arm}}{2}\left(i_z^{\Sigma}\right)^2 \tag{E.7}$$

Replacing (E.6) and (E.7) into (E.5) yields:

$$P_{dc} = 3i_z^{\Sigma} v_{dc} = P_{ac} + P_{cc} + P_{loss}^{\Delta} + \frac{3R_{arm}}{2}\left(i_z^{\Sigma}\right)^2 \tag{E.8}$$

For obtaining the expression of i_z^{Σ}, the following second-order equation is needed to be solved:

$$\frac{3R_{arm}}{2}(i_z^{\Sigma})^2 - 3v_{dc} i_z^{\Sigma} + \left(P_{ac} + P_{loss}^{\Delta} + P_{cc}\right) = 0 \tag{E.9}$$

The current i_z^{Σ} is then calculated as:

$$i_z^{\Sigma} = \frac{v_{dc} \pm \sqrt{(v_{dc})^2 - (2R_{arm}/3)\left(P_{ac} + P_{loss}^{\Delta} + P_{cc}\right)}}{R_{arm}} \tag{E.10}$$

where two values are mathematically possible. However, by inspection, it can be noticed that the root of the second-order equation which has a *physical* meaning is obtained as follows:

$$i_z^{\Sigma} = \left[\frac{v_{dc} - \sqrt{(v_{dc})^2 - (2R_{arm}/3)\left(P_{ac} + P_{loss}^{\Delta} + P_{cc}\right)}}{R_{arm}} \right] \tag{E.11}$$

The modulated voltages v_{md}^{Σ}, v_{md}^{Σ} and v_{mz}^{Σ} are obtained from the dynamic equation for the common-mode currents given in (2.49) by setting the current derivative terms to zero (i.e. $d\boldsymbol{i}_{\boldsymbol{dqz}}^{\boldsymbol{\Sigma}}/dt = 0$):

$$v_{md}^{\Sigma} = -R_{arm} i_d^{\Sigma} + 2\omega L_{arm} i_q^{\Sigma} \tag{E.12a}$$
$$v_{mq}^{\Sigma} = -R_{arm} i_q^{\Sigma} - 2\omega L_{arm} i_d^{\Sigma} \tag{E.12b}$$
$$v_{mz}^{\Sigma} = \frac{v_{dc}}{2} - R_{arm} i_z^{\Sigma} \tag{E.12c}$$

Note that the modulated voltage v_{mz}^{Σ} driving i_z^{Σ} is almost equal to $v_{dc}/2$, since the term "$R_{arm} i_z^{\Sigma}$" is negligible due to the low value of R_{arm}. Finally, the summary of the expressions for the modulated voltages and currents of the MMC are listed in (E.13) and (E.14), respectively.

$$\boldsymbol{v}_{\boldsymbol{mdqz}}^{\boldsymbol{\Delta}} = [\underbrace{v_{md}^{\Delta}\ v_{mq}^{\Delta}}_{\text{(E.4)}}\ \underbrace{v_{mz}^{\Delta}}_{\text{Known}}]^{\top} \tag{E.13a}$$
$$\boldsymbol{v}_{\boldsymbol{mdqz}}^{\boldsymbol{\Sigma}} = [\underbrace{v_{md}^{\Sigma}\ v_{mq}^{\Sigma}\ v_{mz}^{\Sigma}}_{\text{(E.12)}}]^{\top} \tag{E.13b}$$

$$\boldsymbol{i}_{\boldsymbol{dqz}}^{\boldsymbol{\Delta}} = [\underbrace{i_d^{\Delta}\ i_q^{\Delta}}_{\text{(E.3)}}\ 0]^{\top} \tag{E.14a}$$
$$\boldsymbol{i}_{\boldsymbol{dqz}}^{\boldsymbol{\Sigma}} = [\underbrace{i_d^{\Sigma}\ i_q^{\Sigma}}_{\text{Known}}\ \underbrace{i_z^{\Sigma}}_{\text{(E.11)}}]^{\top} \tag{E.14b}$$

Note that v_{mz}^{Δ} is added in (E.13), since the control system may introduce this modulated voltage for improving the limits of the MMC, as studied in [145].

Modulated voltages and currents in *abc* frame and Upper-Lower representation

For expressing the modulated voltages in *abc* frame, the inverse Park transformation at ω for the Δ variables and at -2ω for the Σ variables is applied to the expression in (E.13) as:

$$\begin{bmatrix} v_{ma}^{\Delta}(t) \\ v_{mb}^{\Delta}(t) \\ v_{mc}^{\Delta}(t) \end{bmatrix} = \boldsymbol{P}_{\boldsymbol{\omega}}^{\boldsymbol{-1}}(t) \begin{bmatrix} v_{md}^{\Delta} \\ v_{mq}^{\Delta} \\ v_{mz}^{\Delta} \end{bmatrix} = \begin{bmatrix} v_{md}^{\Delta}\cos(\omega t) + v_{mq}^{\Delta}\sin(\omega t) + v_{mz}^{\Delta} \\ v_{md}^{\Delta}\cos(\omega t - \frac{2\pi}{3}) + v_{mq}^{\Delta}\sin(\omega t - \frac{2\pi}{3}) + v_{mz}^{\Delta} \\ v_{md}^{\Delta}\cos(\omega t - \frac{4\pi}{3}) + v_{mq}^{\Delta}\sin(\omega t - \frac{4\pi}{3}) + v_{mz}^{\Delta} \end{bmatrix} \tag{E.15a}$$

$$\begin{bmatrix} v_{ma}^{\Sigma}(t) \\ v_{mb}^{\Sigma}(t) \\ v_{mc}^{\Sigma}(t) \end{bmatrix} = \boldsymbol{P}_{\boldsymbol{-2\omega}}^{\boldsymbol{-1}}(t) \begin{bmatrix} v_{md}^{\Sigma} \\ v_{mq}^{\Sigma} \\ v_{mz}^{\Sigma} \end{bmatrix} = \begin{bmatrix} v_{md}^{\Sigma}\cos(-2\omega t) + v_{mq}^{\Sigma}\sin(-2\omega t) + v_{mz}^{\Sigma} \\ v_{md}^{\Sigma}\cos(-2\omega t - \frac{2\pi}{3}) + v_{mq}^{\Sigma}\sin(-2\omega t - \frac{2\pi}{3}) + v_{mz}^{\Sigma} \\ v_{md}^{\Sigma}\cos(-2\omega t - \frac{4\pi}{3}) + v_{mq}^{\Sigma}\sin(-2\omega t - \frac{4\pi}{3}) + v_{mz}^{\Sigma} \end{bmatrix} \tag{E.15b}$$

At this moment, the expressions of the Upper-Lower variables can be obtained following the definitions given in (E.1): (E.16) shows the results for the upper arm variables, and (E.17) for the lower arm quantities.

$$v_{ma}^{U}(t) = v_{ma}^{\Sigma}(t) - v_{ma}^{\Delta}(t) \tag{E.16a}$$
$$v_{mb}^{U}(t) = v_{mb}^{\Sigma}(t) - v_{mb}^{\Delta}(t) \tag{E.16b}$$
$$v_{mc}^{U}(t) = v_{mc}^{\Sigma}(t) - v_{mc}^{\Delta}(t) \tag{E.16c}$$

$$v_{ma}^{L}(t) = v_{ma}^{\Sigma}(t) + v_{ma}^{\Delta}(t) \tag{E.17a}$$
$$v_{mb}^{L}(t) = v_{mb}^{\Sigma}(t) + v_{mb}^{\Delta}(t) \tag{E.17b}$$
$$v_{mc}^{L}(t) = v_{mc}^{\Sigma}(t) + v_{mc}^{\Delta}(t) \tag{E.17c}$$

For obtaining the current expressions in Upper-Lower representation, the inverse Park transformation is applied to (E.14), as shown in (E.18).

$$\begin{bmatrix} i_a^{\Delta}(t) \\ i_b^{\Delta}(t) \\ i_c^{\Delta}(t) \end{bmatrix} = \boldsymbol{P}_{\boldsymbol{\omega}}^{\mathbf{-1}}(t) \begin{bmatrix} i_d^{\Delta} \\ i_q^{\Delta} \\ i_z^{\Delta} \end{bmatrix} = \begin{bmatrix} i_d^{\Delta}\cos(\omega t) + i_q^{\Delta}\sin(\omega t) \\ i_d^{\Delta}\cos(\omega t - \frac{2\pi}{3}) + i_q^{\Delta}\sin(\omega t - \frac{2\pi}{3}) \\ i_d^{\Delta}\cos(\omega t - \frac{4\pi}{3}) + i_q^{\Delta}\sin(\omega t - \frac{4\pi}{3}) \end{bmatrix} \tag{E.18a}$$

$$\begin{bmatrix} i_a^{\Sigma}(t) \\ i_b^{\Sigma}(t) \\ i_c^{\Sigma}(t) \end{bmatrix} = \boldsymbol{P}_{\boldsymbol{-2\omega}}^{\mathbf{-1}}(t) \begin{bmatrix} i_d^{\Sigma} \\ i_q^{\Sigma} \\ i_z^{\Sigma} \end{bmatrix} = \begin{bmatrix} i_d^{\Sigma}\cos(-2\omega t) + i_q^{\Sigma}\sin(-2\omega t) + i_z^{\Sigma} \\ i_d^{\Sigma}\cos(-2\omega t - \frac{2\pi}{3}) + i_q^{\Sigma}\sin(-2\omega t - \frac{2\pi}{3}) + i_z^{\Sigma} \\ i_d^{\Sigma}\cos(-2\omega t - \frac{4\pi}{3}) + i_q^{\Sigma}\sin(-2\omega t - \frac{4\pi}{3}) + i_z^{\Sigma} \end{bmatrix} \tag{E.18b}$$

Finally, the expressions of the upper and lower arm variables can be obtained as in (E.19) for the upper arm variables, and in (E.20) for the lower arm variables with the definitions given in (E.1).

$$i_a^U(t) = i_a^{\Sigma}(t) - \frac{i_a^{\Delta}(t)}{2} \tag{E.19a}$$

$$i_b^U(t) = i_b^{\Sigma}(t) - \frac{i_b^{\Delta}(t)}{2} \tag{E.19b}$$

$$i_c^U(t) = i_c^{\Sigma}(t) - \frac{i_c^{\Delta}(t)}{2} \tag{E.19c}$$

$$i_a^L(t) = i_a^{\Sigma}(t) + \frac{i_a^{\Delta}(t)}{2} \tag{E.20a}$$

$$i_b^L(t) = i_b^{\Sigma}(t) + \frac{i_b^{\Delta}(t)}{2} \tag{E.20b}$$

$$i_c^L(t) = i_c^{\Sigma}(t) + \frac{i_c^{\Delta}(t)}{2} \tag{E.20c}$$

Arm capacitor voltages in steady-state with Upper-Lower representation

For obtaining the mathematical expression of the arm capacitor voltages, the evolution of the stored energy $W_j^U(t)$ and $W_j^L(t)$ on each arm capacitor C_{arm} is used. This is expressed as shown in (E.21), which is based on the integral of the instantaneous power for each arm.

$$W_j^U(t) = \int v_{mj}^U(t)\; i_j^U(t)\; dt + W_{z0}^{\Sigma} \tag{E.21a}$$

$$W_j^L(t) = \int v_{mj}^L(t)\; i_j^L(t)\; dt + W_{z0}^{\Sigma} \tag{E.21b}$$

In this equation, W_{z0}^{Σ} corresponds to the average value of the stored energy of the selected arm which may be imposed by the energy-based control (in normal operation, the same amount of average energy is expected on each arm). It is possible to write the complete analytic expression of $W_j^U(t)$ and $W_j^L(t)$ taking into account the expressions of $v_{mj}^U(t)$ and $v_{mj}^L(t)$ given in (E.16) and (E.17), and the expressions of $i_j^U(t)$ and $i_j^L(t)$ given in (E.19) and (E.20), however, given the complexity of the resultant equations, only the upper arm of phase a is developed in the following:

$$W_a^U(t) = \underbrace{W_{cte}}_{\text{(E.23)}} + \underbrace{\widetilde{W}_{(\omega t)}}_{\text{(E.24)}} + \underbrace{\widetilde{W}_{(2\omega t)}}_{\text{(E.25)}} + \underbrace{\widetilde{W}_{(3\omega t)}}_{\text{(E.26)}} + \underbrace{\widetilde{W}_{(4\omega t)}}_{\text{(E.27)}} \tag{E.22}$$

In the following, each component of $W_a^U(t)$ is developed:

$$W_{cte} = W_{z0}^{\Sigma} + \frac{1}{8\omega}\left[\left(-v_{mq}^{\Delta} + \frac{8v_{mq}^{\Sigma}}{3}\right) i_d^{\Delta} + \left(-v_{md}^{\Delta} + 4v_{mz}^{\Delta} + \frac{4v_{md}^{\Sigma}}{3} - 4v_{mz}^{\Sigma}\right) i_q^{\Delta} + ... \right. \tag{E.23}$$

$$... + \left(-\frac{8v_{mq}^{\Delta}}{3} - v_{mq}^{\Sigma}\right) i_d^{\Sigma} + \left(-\frac{16v_{md}^{\Delta}}{3} + 4v_{mz}^{\Delta} - v_{md}^{\Sigma} - 4v_{mz}^{\Sigma}\right) i_q^{\Sigma} + \left(8v_{mq}^{\Delta} - 4v_{mq}^{\Sigma}\right) i_z^{\Sigma} + ...$$

$$\left. ... + \omega t\left(-2v_{md}^{\Delta} i_d^{\Delta} - 2v_{mq}^{\Delta} i_q^{\Delta} + 4v_{md}^{\Sigma} i_d^{\Sigma} + 4v_{mq}^{\Sigma} i_q^{\Sigma} - 8\left(v_{mz}^{\Delta} - v_{mz}^{\Sigma}\right) i_z^{\Sigma}\right)\right]$$

$$\widetilde{W}_{(\omega t)} = \frac{\cos(\omega t)}{\omega}\left(\frac{v_{mq}^{\Sigma}}{4}i_d^{\Delta} + \left(\frac{v_{md}^{\Sigma}}{4} + \frac{v_{mz}^{\Delta}}{2} - \frac{v_{mz}^{\Sigma}}{2}\right)i_q^{\Delta} - \frac{v_{mq}^{\Delta}}{2}i_d^{\Sigma} - \frac{v_{md}^{\Delta}}{2}i_q^{\Sigma} + v_{mq}^{\Delta}i_z^{\Sigma}\right) + ... \quad \text{(E.24)}$$
$$... + \frac{\sin(\omega t)}{\omega}\left(\left(\frac{v_{md}^{\Sigma}}{4} - \frac{v_{mz}^{\Delta}}{2} + \frac{v_{mz}^{\Sigma}}{2}\right)i_d^{\Delta} - \frac{v_{mq}^{\Sigma}}{4}i_q^{\Delta} - \frac{v_{md}^{\Delta}}{2}i_d^{\Sigma} + \frac{v_{mq}^{\Delta}}{2}i_q^{\Sigma} - v_{md}^{\Delta}i_z^{\Sigma}\right)$$

$$\widetilde{W}_{(2\omega t)} = \frac{\cos(2\omega t)}{2\omega}\left(\frac{v_{mq}^{\Delta}}{4}i_d^{\Delta} + \frac{v_{md}^{\Delta}}{4}i_q^{\Delta} + \left(-v_{mz}^{\Delta} + v_{mz}^{\Sigma}\right)i_q^{\Sigma} + v_{mq}^{\Sigma}i_z^{\Sigma}\right) + ... \quad \text{(E.25)}$$
$$... + \frac{\sin(2\omega t)}{2\omega}\left(-\frac{v_{md}^{\Delta}}{4}i_d^{\Delta} + \frac{v_{mq}^{\Delta}}{4}i_q^{\Delta} + \left(-v_{mz}^{\Delta} + v_{mz}^{\Sigma}\right)i_d^{\Sigma} + v_{md}^{\Sigma}i_z^{\Sigma}\right)$$

$$\widetilde{W}_{(3\omega t)} = \frac{\cos(3\omega t)}{3\omega}\left(\frac{v_{mq}^{\Sigma}}{4}i_d^{\Delta} - \frac{v_{md}^{\Sigma}}{4}i_q^{\Delta} + \frac{v_{mq}^{\Delta}}{2}i_d^{\Sigma} - \frac{v_{md}^{\Delta}}{2}i_q^{\Sigma}\right) + ... \quad \text{(E.26)}$$
$$... + \frac{\sin(3\omega t)}{3\omega}\left(\frac{v_{md}^{\Sigma}}{4}i_d^{\Delta} + \frac{v_{mq}^{\Sigma}}{4}i_q^{\Delta} - \frac{v_{md}^{\Delta}}{2}i_d^{\Sigma} - \frac{v_{mq}^{\Delta}}{2}i_q^{\Sigma}\right)$$

$$\widetilde{W}_{(4\omega t)} = \frac{\cos(4\omega t)}{4\omega}\left(\frac{v_{mq}^{\Sigma}}{2}i_d^{\Sigma} + \frac{v_{md}^{\Sigma}}{2}i_q^{\Sigma}\right) + \frac{\sin(4\omega t)}{4\omega}\left(\frac{v_{md}^{\Sigma}}{2}i_d^{\Sigma} - \frac{v_{mq}^{\Sigma}}{2}i_q^{\Sigma}\right) \quad \text{(E.27)}$$

It should be noted that $\widetilde{W}_{(\omega t)}$, $\widetilde{W}_{(2\omega t)}$, $\widetilde{W}_{(3\omega t)}$ and $\widetilde{W}_{(4\omega t)}$ are oscillating terms with average value equal to zero. The term W_{cte} is composed by W_{z0}^{Σ} and several other terms, which have to sum up to zero; if not, it means that the average value of the stored energy per-arm is being deviated. The equations (E.23) to (E.27) can be much simplified if, for instance, the circulating currents are assumed to be eliminated (i.e. $i_d^{\Sigma} = i_q^{\Sigma} = 0$), and v_{mz}^{Δ} is omitted. However, in the following, the most general formulation is kept.

The arm capacitor voltages $v_{Cj}^{U}(t)$ and $v_{Cj}^{L}(t)$ can be obtained directly with the expressions of the stored energy per-arm $W_j^U(t)$ and $W_j^L(t)$ as follows:

$$v_{Cj}^{U}(t) = \sqrt{\frac{2}{C_{arm}}W_j^U(t)} \quad \text{(E.28a)}$$

$$v_{Cj}^{L}(t) = \sqrt{\frac{2}{C_{arm}}W_j^L(t)} \quad \text{(E.28b)}$$

As discussed in Chapter 2, the arm capacitor voltages $v_{Cj}^{U}(t)$ and $v_{Cj}^{L}(t)$ have a constant DC value superimposed with oscillations at mainly ω, 2ω (negative sequence), 3ω and some content of 4ω. This is coherent with the frequency content found for (E.22). Furthermore, the DC component of $v_{Cj}^{U}(t)$ and $v_{Cj}^{L}(t)$ is related to the average value of the stored energy, W_{z0}^{Σ}.

Time-domain validation of analytic expressions

For validating the analytic formulations provided in this Section, a time-domain comparison is performed against the detailed EMT simulation considering the Equivalent Circuit-Based Model in EMTP-RV with 400 SMs per arm model used throughout this Thesis (see Appendix F). The adopted configuration is given in Fig. E.1, where the MMC is interfaced between ideal AC and DC sources for simplicity. The considered operating point is given in Table E.1.

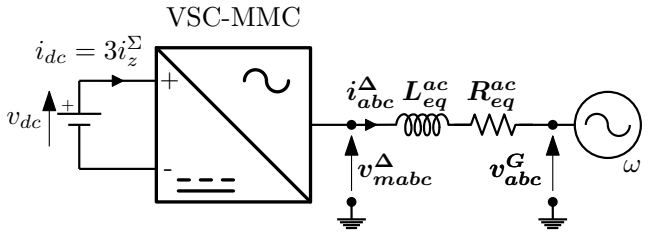

Figure E.1 – MMC connected to ideal AC and DC sources for time-domain validation of analytic expressions of voltages and currents

Table E.1 – MMC variables in Σ-Δ representation

Variable	Value	Variable	Value
P_{ac}	1000 MW	v_{dc}	640 kV
Q_{ac}	200 MVAr	v_d^G	$\sqrt{2}V_b$ V
i_d^{Σ}	0.156 kA (0.1 pu)	v_q^G	0 kV
i_q^{Σ}	0.312 kA (0.2 pu)	W_{z0}^{Σ}	1 pu

The comparison results are given in Fig. E.2. The arm capacitor voltage for the upper arm of phase a are shown in Fig. E.2a, where the analytic expression given in (E.28) is contrasted with the EMT simulation results. Also, the modulated voltages for the same arm (upper arm, phase a) is given on the same figure, where the expression given in (E.16) is used for the analytic results. For both variables, it can be noticed that the analytic expressions provide with high accuracy the steady-state waveforms of the EMT model, validating the equations provided in this Section.

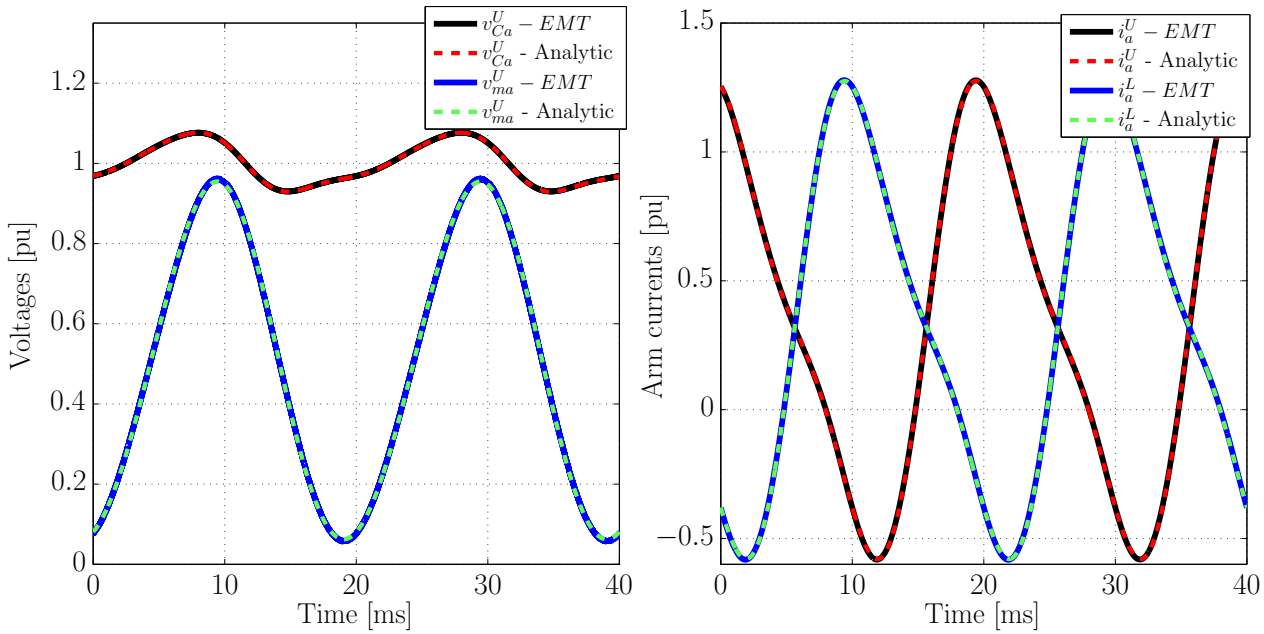

(a) Arm capacitor voltage and modulated voltage for phase a (upper only)

(b) Upper and Lower arm currents for phase a

Figure E.2 – Time domain validation of steady-state analytic formulation of voltages and currents — *EMT*: Detailed MMC model with 400 SMs per arm; *Analytic:* Calculations with the expressions provided in this Section

Finally, in Fig. E.2b, the results of the upper and lower arm currents for the phase a are contrasted. The arm currents for the analytic results are obtained with (E.19) and (E.20). Again, the steady-state waveform obtained with the mathematical expressions reproduce accurately the EMT currents. Results for the rest of the variables (other arms, and phases) provide similar results in terms of accuracy.

E.2 Physical limitations of MMC with Half-Bridge submodules

For exploiting the capabilities of the MMC, it is of high importance the knowledge of the physical limitations of the converter itself. Not only at the stage of the converter design (for instance, for sizing the MMC components such as inductances or capacitors), but also for taking advantage of the possibilities in the controller design.

E.2.1 Modulated voltages limitations with Upper-Lower representation

In Fig. E.3 the upper and lower arms of the MMC-AAM is depicted for the phase j. The voltages and currents shown in the figure were obtained analytically in the previous Section, which are used in the following for determining the MMC limitations. The main physical limitation is given by the fact that the modulated arm voltages can be varied as shown in (E.29), which is the main characteristic of the Half-Bridge submodules.

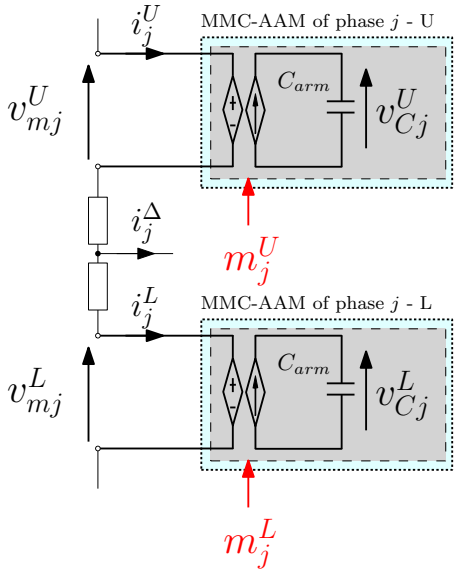

Figure E.3 – MMC single Arm Averaged Model of phase j for Upper and Lower arm

$$\underbrace{0 \leqslant}_{\text{Lower limit of } v_{mj}^U} \quad v_{mj}^U(t) \quad \underbrace{\leqslant v_{Cj}^U(t)}_{\text{Upper limit of } v_{mj}^U} \tag{E.29a}$$

$$\underbrace{0 \leqslant}_{\text{Lower limit of } v_{mj}^L} \quad v_{mj}^L(t) \quad \underbrace{\leqslant v_{Cj}^L(t)}_{\text{Upper limit of } v_{mj}^L} \tag{E.29b}$$

The lower limit for the arm modulated voltages is reached when all the sub-modules in the arm are bypassed: the modulated voltage takes the value equal to zero (or, which is the same, the modulation index is equal to zero). On the contrary, the maximum of the arm modulated voltage is obtained when all the sub-modules in the arm are inserted; in this case, the applied arm voltage is equal to the sum of all the voltages of the individual sub-modules capacitors. This voltage is essentially equal to $v_{Cj}^{U}(t)$ or $v_{Cj}^{L}(t)$ for the upper or lower arms, respectively, assuming a perfect sub-module balancing. In this case, the modulation index is equal to one.

Dividing (E.29a) by $v_{Cj}^{U}(t)$ and (E.29b) by $v_{Cj}^{L}(t)$, it yields:

$$0 \leqslant m_{j}^{U}(t) \leqslant 1 \tag{E.30a}$$

$$0 \leqslant m_{j}^{L}(t) \leqslant 1 \tag{E.30b}$$

which corresponds to the classical limitation on the modulation indices for the Half-Bridge MMC in Upper-Lower representation.

Lower limit of the modulated voltages

For exemplifying the lower limit of the modulated voltage (i.e. when $v_{mj}^{U}(t)$ or $v_{mj}^{L}(t)$ reach zero), a similar time-domain simulation as in previous Section is used. In this example, the same operating point as in Table E.1 is considered, however, the circulating currents are assumed to be zero (i.e. $i_{d}^{\Sigma} = i_{q}^{\Sigma} = 0$). Moreover, the DC voltage is considered to be 0.85 pu, which is a critically low value. Results for the arm modulated voltage $v_{mj}^{U}(t)$ and arm capacitor voltage $v_{Cj}^{U}(t)$ are shown in Fig. E.4, where the detailed EMT simulation is contrasted with the analytic calculation of $v_{mj}^{U}(t)$ from (E.16). Obviously, the analytic results of the modulated voltage cannot reproduce this physical limitation.

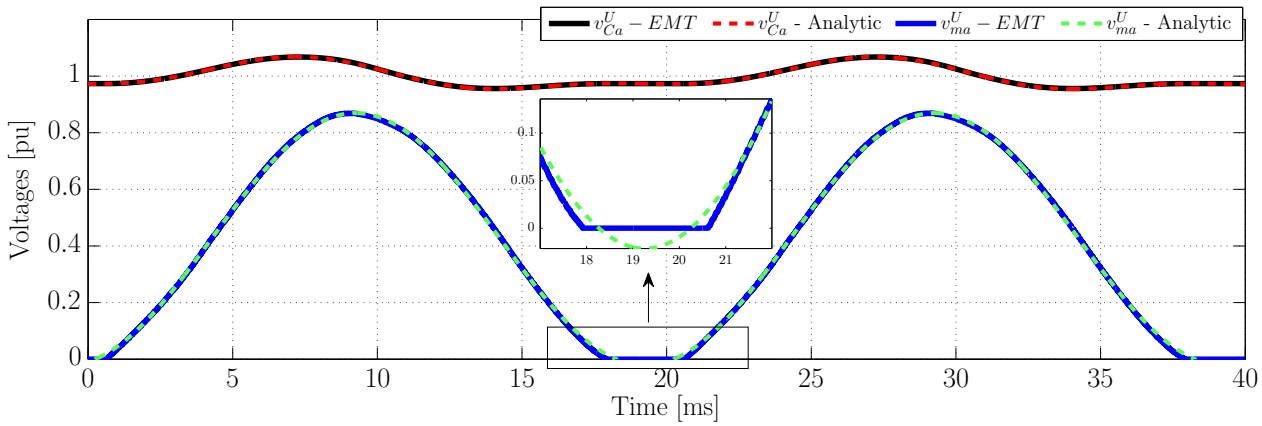

Figure E.4 – Time-domain simulation for exemplifying the lower limit of the modulated voltage - DC voltage $v_{dc} = 0.85$ pu (upper-arm of phase a only)

For calculating the lower limits of the modulated voltages, namely $v_{mj,min}^{U}(t)$ and $v_{mj,min}^{L}(t)$, the left-hand side of the inequality from (E.29a) is transformed into an equality:

$$v_{mj,min}^{U}(t) \rightarrow v_{mj}^{U}(t) = 0 \tag{E.31a}$$

$$v_{mj,min}^{L}(t) \rightarrow v_{mj}^{L}(t) = 0 \tag{E.31b}$$

The analytic limit can be calculated by replacing the expressions of $v_{mj}^{U}(t)$ and $v_{mj}^{U}(t)$ from (E.16) and (E.17) into (E.31). As an example, let us consider the lower limit for the upper

arm of phase a analytically:

$$v^{U}_{ma,min}(t) \rightarrow v^{\Sigma}_{md}\cos(-2\omega t)+v^{\Sigma}_{mq}\sin(-2\omega t)+v^{\Sigma}_{mz}-v^{\Delta}_{md}\cos(\omega t)-v^{\Delta}_{mq}\sin(\omega t)-v^{\Delta}_{mz}=0 \quad \text{(E.32)}$$

At this stage, the formulation given in (E.32) corresponds to a transcendental equation, and its analytic solution is not trivial. However, the solution can be found numerically for several operating points and system parameters [219]. For a fixed operating point, when the DC voltage decreases, the risk of hitting the lower limitation is increased. The same happens for high values of AC-voltage.

Upper limit of the modulated voltages

Similarly as for the exemplification of the lower limit, a time-domain simulation is used for the upper limit of the modulated voltage. The DC voltage is considered to be 1 pu again, but the average value of the stored energy per-arm is set to $W^{\Sigma}_{z0} = 0.78$ pu. This value may be generated by the use of the Virtual Capacitor Control as detailed in Section 5.5.1, or other Energy-based controllers techniques were the energy reference $W^{\Sigma *}_{z0}$ is being manipulated. Results are shown in Fig. E.5.

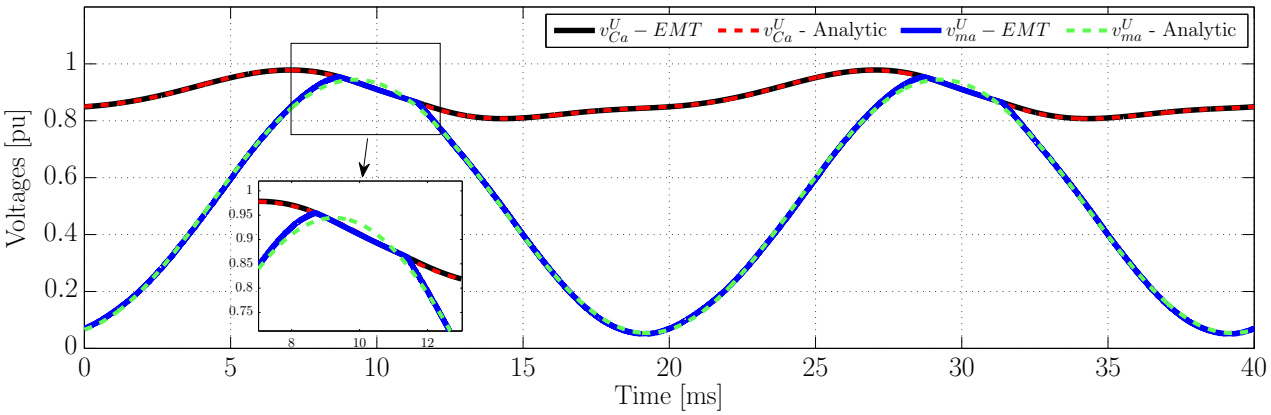

Figure E.5 – Time-domain simulation for exemplifying the upper limit of the modulated voltage - Arm average stored energy $W^{\Sigma}_{z0} = 0.78$ pu (upper-arm of phase a only)

As observed in the results in Fig. E.5 (zoomed part), the arm voltage is equal to the arm capacitor voltages near $t \approx 10$ ms.

For calculating the upper limits of the modulated voltages, namely $v^{U}_{mj,max}$ and $v^{L}_{mj,max}$, the right-hand side of the inequality from (E.29a) is transformed into an equality:

$$v^{U}_{mj,max}(t) \rightarrow v^{U}_{mj}(t) = v^{U}_{Cj}(t) \quad \text{(E.33a)}$$

$$v^{L}_{mj,max}(t) \rightarrow v^{L}_{mj}(t) = v^{L}_{Cj}(t) \quad \text{(E.33b)}$$

The analytic limit can be calculated by replacing the expressions of $v^{U}_{mj}(t)$ and $v^{U}_{mj}(t)$ given in (E.16) and (E.17), and the expressions of $v^{U}_{Cj}(t)$ and $v^{U}_{Cj}(t)$ given in (E.28a) and (E.28b) into (E.33). It is clear that after those replacements, the equations to be solved are transcendental (since there are many cosines and sines involved in the equations), and the analytic expression of this limit is not straightforward.

For avoiding the limitation exposed in Fig. E.5, some options can be considered: first, the insertion of third-harmonic on the arm modulated voltage can be used. This modifies the waveform of the arm modulated voltage, reducing and displacing its peak value, as explored

in [145]. This provides a wider margin between v_{mj} and v_{Cj}. Second, and the most obvious, is to increase the average value of the arm capacitor voltage $v_{Cj}^{U}(t)$ and $v_{Cj}^{U}(t)$. This value can be modified with the use of Energy-based controllers, as those presented in Section 3.3 and 3.4, where the average value of the stored energy is determined by $W_{z0}^{\Sigma *}$, and hence, the DC value of the arm capacitor voltages. Nevertheless, the minimum amount of stored energy varies with respect to the possible operating points and system parameters, so a determination of this limit should be further studied. This is explored in Section E.2.3.

E.2.2 Modulated voltages limitations with Σ-Δ representation

In previous Section, the explanation of the physical limits on the modulated voltages in Upper-Lower representation was given. In this Section it is intended to show how these limits translate to the Σ-Δ formulation.

Using the definitions given in (E.1) into (E.29), the inequalities for the modulated voltages limitations as a function of the Σ-Δ variables are obtained as follows:

$$0 \leqslant v_{mj}^{\Sigma} - v_{mj}^{\Delta} \leqslant v_{Cj}^{\Sigma} + v_{Cj}^{\Delta} \tag{E.34a}$$

$$0 \leqslant v_{mj}^{\Sigma} + v_{mj}^{\Delta} \leqslant v_{Cj}^{\Sigma} - v_{Cj}^{\Delta} \tag{E.34b}$$

As observed in these equations, the interpretation of the voltage limits in Σ-Δ is not straightforward. Considering the left side of (E.34) and after some mathematical manipulations, the expression in (E.35) can be obtained:

$$\left| v_{mj}^{\Delta} \right| \leqslant v_{mj}^{\Sigma} \tag{E.35}$$

This equation highlights that the AC-side modulated v_{mj}^{Δ} voltage should always be lower than the common-mode modulated voltage v_{mj}^{Σ}. This limit can be observed considering the lower limit of the modulated voltages provided in Fig. E.4: the same simulation is shown in Fig. E.6, where the modulated voltages are shown with their Σ-Δ representation.

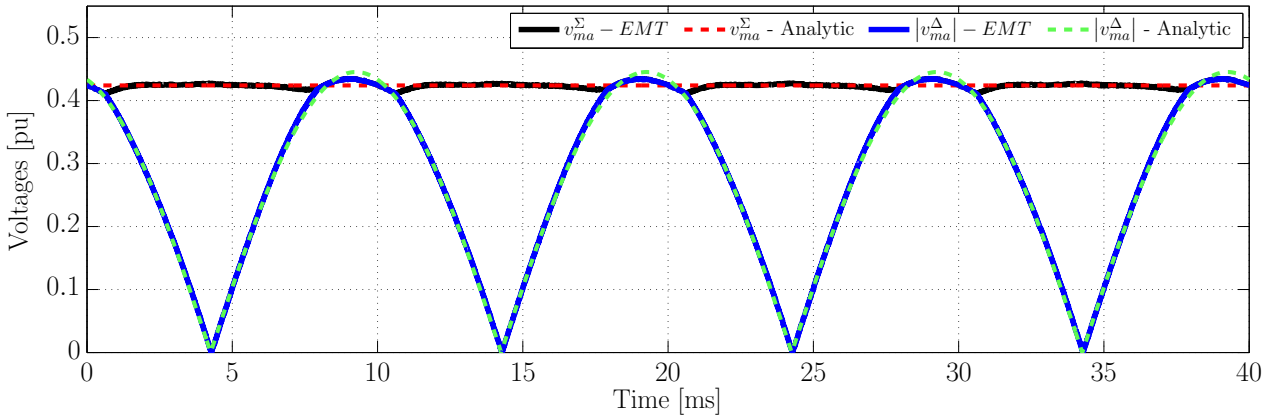

Figure E.6 – Time-domain simulation for exemplifying the limit of the modulated voltage in Σ-Δ representation given in (E.35) - DC voltage $v_{dc} = 0.85$ pu (phase a only) — Same simulation as given in Fig. E.4

Finally, considering the right side of (E.34) and after some mathematical manipulations, the expression in (E.36) can be obtained:

$$v_{mj}^{\Sigma} - v_{mj}^{\Delta} - v_{Cj}^{\Delta} \leqslant v_{Cj}^{\Sigma} \tag{E.36a}$$

$$v_{mj}^{\Sigma} + v_{mj}^{\Delta} + v_{Cj}^{\Delta} \leqslant v_{Cj}^{\Sigma} \tag{E.36b}$$

This limit can be observed considering the upper limit of the modulated voltages provided in Fig. E.5: the same simulation is shown in Fig. E.7, where the expression given (E.36) is highlighted.

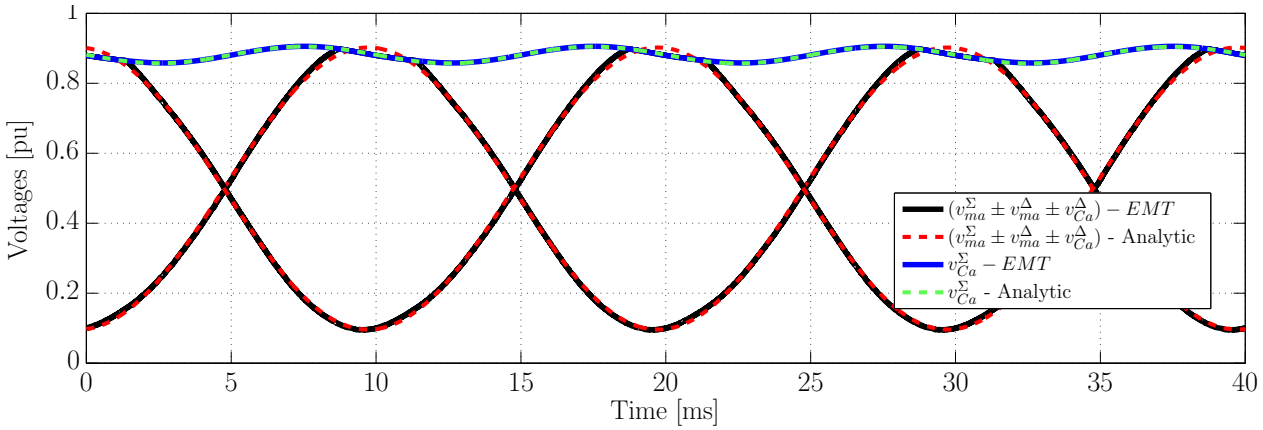

Figure E.7 – Time-domain simulation for exemplifying the limit of the modulated voltage in Σ-Δ representation given in (E.36) - Arm average stored energy $W^{\Sigma}_{z0} = 0.78$ pu (phase a only) — Same simulation as given in Fig. E.5

It should be noted in Fig. E.6 and E.7, that the analytic expressions were also plotted. In both cases, it can be observed that these expressions cannot reproduce the modulated voltages limitations similarly as in previous Section.

E.2.3 Impact of the stored energy on the modulated voltage limits

As stated before, the upper limit of the modulated voltages can be avoided by storing the sufficient amount of energy on each arm so the waveform of the arm capacitor voltages is always above the waveform of the modulated voltage. The minimum amount of stored energy for each operating point can be calculated numerically by iterations as in [219], or analytically as in [220].

For simplicity, the numerical iterative method is used. The initial variables for the procedure are: i^{Σ}_{d}, i^{Σ}_{d}, v^{Δ}_{mz}, v_{dc}, v^{G}_{d}, v^{G}_{q}, and ω. Then, the main steps are listed as follows, focusing on the upper-arm of phase a for simplicity:

1. Select active and reactive power P_{ac}, Q_{ac}.
2. Obtain the arm modulated voltage waveform as a function of time t, i.e. $v^{U}_{ma}(t)$, with (E.16), and arm capacitor voltage waveform as a function of time t, i.e. $v^{U}_{Ca}(t)$, with (E.28a) for one power cycle.
3. Iterate until it is found the minimum value of W^{Σ}_{z0} for such it is verified that $v_{ma}(t) = v^{U}_{Ca}(t)$ for any t comprised the power cycle.

Results are shown in Fig. E.8, considering that the AC and DC voltages are at nominal values, $v^{\Delta}_{mz} = 0$, and there are no circulating currents in the MMC (i.e. $i^{\Sigma}_{d} = i^{\Sigma}_{q} = 0$).

As it can be seen in Fig. E.8, the reactive power direction influences directly the amount of required stored energy, which is coherent with the findings in [221]. Note that the used value $W^{\Sigma}_{z0} = 0.78$ pu for obtaining the results in Fig. E.5 falls below the lower limit for $P_{ac} = 1$ pu and $Q_{ac} = 0.2$ pu (as expected).

The knowledge of the limitation of W^{Σ}_{z0} is of high importance for designing the Energy-based controllers with shared energy capabilities with the DC side, as presented in Section 5.5.

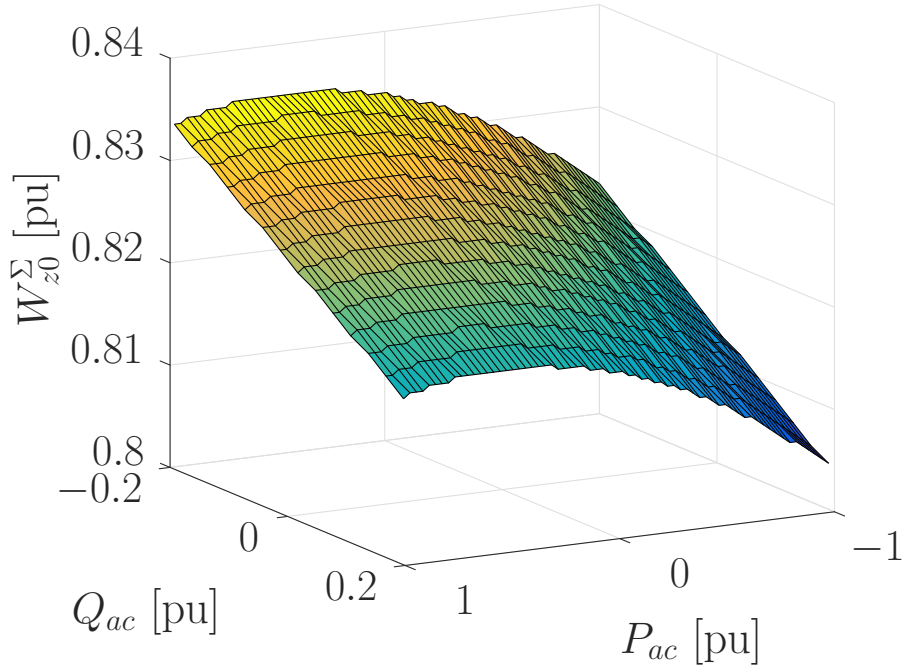

Figure E.8 – Minimum required average stored energy per-arm W_{z0}^{Σ} for different values of AC active and reactive powers — AC and DC voltages at nominal values, $v_{mz}^{\Delta} = 0$, and no circulating currents (i.e. $i_d^{\Sigma} = i_q^{\Sigma} = 0$)

Moreover, the limitations of the Virtual Capacitor strategy in droop-controlled MTDC grids can be directly assessed with the steady-state analysis provided in this Section.

E.2.4 MMC limitations in Small-Signal Stability analysis

It should be stated that all the linearized models used through this Thesis are not able to cope with the discontinuities produced by the modulated voltage limitations. For this reason, when performing small-signal stability analyses, it is of crucial importance to consider operating points within the acceptable range of normal operation to avoid hitting the converter limits. If the considered operating point falls beyond the converter limits, the linear analysis study losses its validity.

The analytic expressions of the MMC steady-state variables provided in this Appendix can be used to verify the inequalities to be satisfied on the modulated voltages. This verification is mandatory to carry on the linear studies for maintaining the validity of the derived models.

Appendix F

On the implementation of MMC controllers for EMT simulations

In this Appendix, the modeling and control details of the EMT model used as a reference throughout this Thesis are presented. First, the Equivalent Circuit-Based Model from [111] implemented in EMTP-RV is recalled. Then, the different parts of the control structure are detailed. Finally, the complete control structures used in the different sections of this Thesis are shown. A simulation case study is used to highlight the main characteristics of each controller.

F.1 Equivalent Circuit-Based Model in EMTP-RV

The reference EMT-MMC model used in this Thesis is the so-called "Equivalent-Circuit Based Model" (ECBM) detailed in [111] and implemented in the EMT simulation software "EMTP-RV". This MMC model is available in the software library. Originally, this model was developed mainly within the framework of the PhD Thesis from Dr. Hani Saad in [108]. This model is based on [112], where each switch of every sub-module is replaced by a resistance whose value depends on the status of the SM.

The ECBM implemented in EMTP-RV is depicted in Fig. F.1. In Fig. F.1a, the mask of the converter is provided, which was developed by Dr. Pierre Rault within the framework of the *Bestpaths* project. In this figure, the AC- and DC-side connections are clearly observed. For the example in this Appendix, the AC and DC grids are considered to be stiff voltage sources for simplicity. Inside the mask, the MMC model from Fig. F.1b can be found. This figure highlights, on the top, the electrical connections: on the AC side, the Y-D transformer is presented with internal parameters R_f, L_f, and the DC side by the positive and negative poles connections. Moreover, all the internal measures of the MMC are provided: the individual sub-module voltages v_{Ci} (400×6 signals, grouped in 6 vectors); the arm equivalent capacitor voltages $\boldsymbol{v^U_{Cabc}}$ and $\boldsymbol{v^L_{Cabc}}$ (which are the algebraic sum of the 400 sub-modules within each arm); the "Upper" and "Lower" arm currents $\boldsymbol{i^U_{abc}}$ and $\boldsymbol{i^L_{abc}}$ and the applied arm modulated voltages $\boldsymbol{v^U_{mabc}}$ and $\boldsymbol{v^L_{mabc}}$. It should be noted that the nomenclature used in the mask may not be the same as used in this Thesis, for this reason, both notations are shown in the figures.

In Fig. F.2, the implementation of the converter is shown (model inside the mask given in Fig. F.1b), where the aforementioned inputs and outputs can be observed. Moreover, the arm inductances L_{arm} and equivalent resistance R_{arm} are highlighted. More details on the implementation of MMC converters in EMTP-RV can be found in [222].

The MMC model provided in the EMTP-RV library have a fully functional controller similar as the *Classical CCSC* presented in Section 3.2. However, in this Thesis, all the control

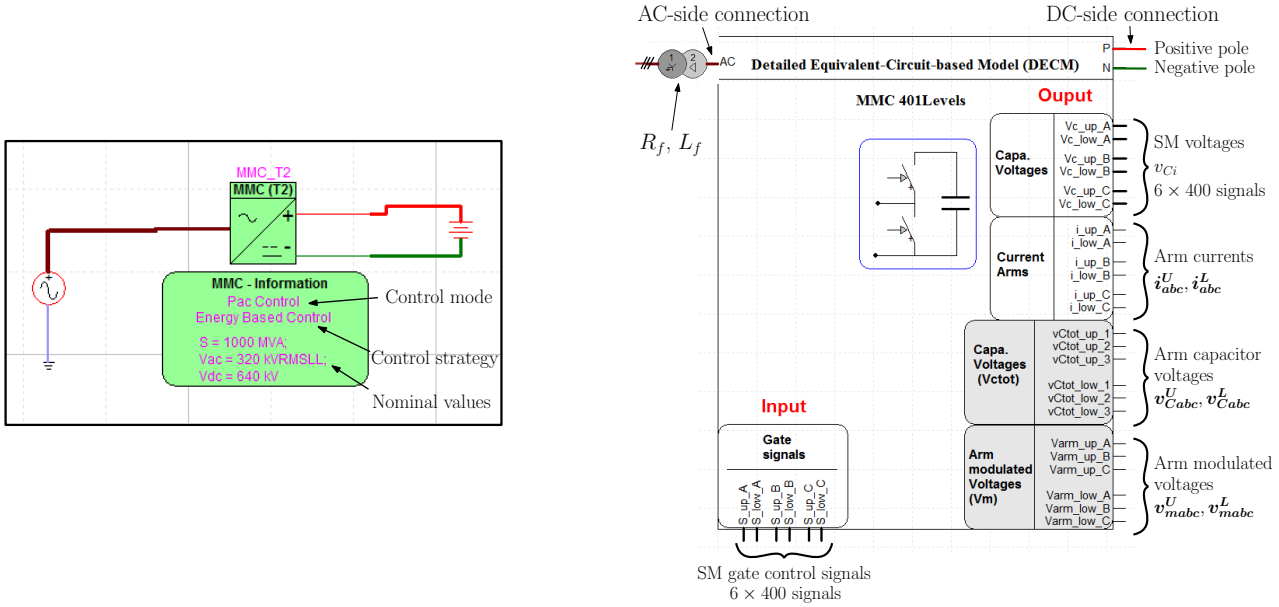

(a) MMC Mask (b) MMC Connections

Figure F.1 – Equivalent Circuit-Based Model in EMTP-RV: Mask and connections

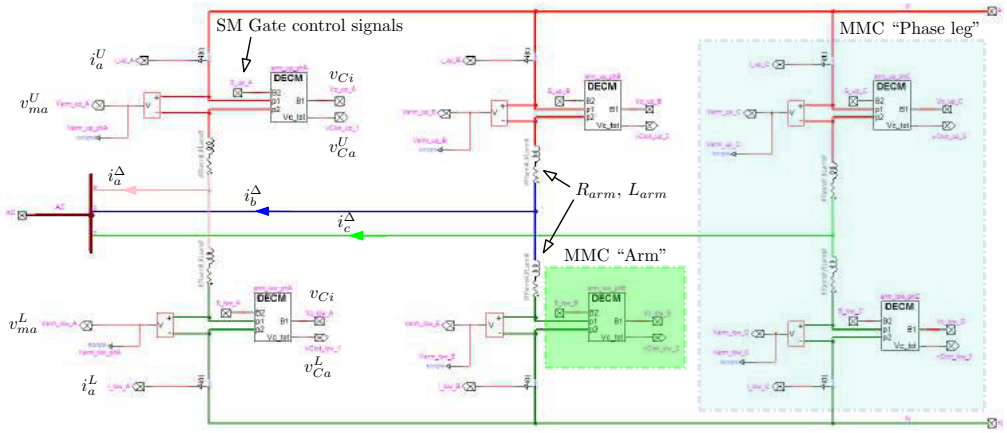

Figure F.2 – Equivalent Circuit-Based Model in EMTP-RV from Fig. F.1b

structures were re-developed. In the following, the details on the controllers implementation for the Equivalent Circuit-Based model in EMTP-RV are detailed.

F.2 MMC Control Structure

The MMC control structure can be split into two main parts: the "High-level" and "Low-level" control[1]. This separation is highlighted in Fig. F.3. The High-Level control is in charge of regulating the energy, power, currents and voltages on the converter, while the Low-Level control is in charge of the modulation voltages and the balancing of the sub-modules capacitor voltages. Note that the boundary between both control layers is given by the modulation indices in *abc* frame, i.e. $\boldsymbol{m^U_{abc}}$ and $\boldsymbol{m^L_{abc}}$. Also, in Fig. F.3b, the control structure for the "Arm-

[1]Note that this classification is not strictly the same as the one provided in [222]

Averaged Model" described in Chapter 2 is given. Comparing both figures, it can be seen that the High-Level controls structures for both models are strictly the same [223]. However, the Low-level control of the AAM is represented only by the modulation indices generated by the High-Level control. In the following, only the Equivalent Circuit-Based model is considered.

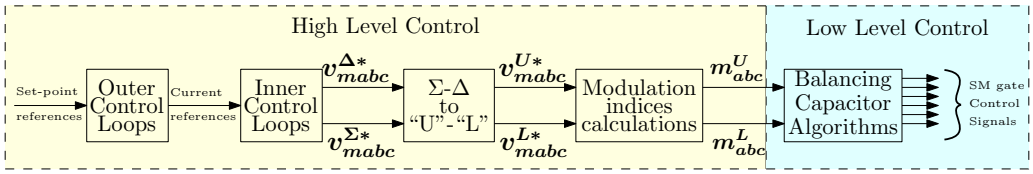

(a) Equivalent Circuit-Based Model

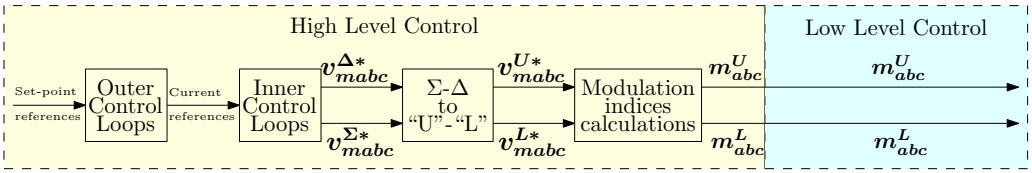

(b) Arm Averaged Model (AAM)

Figure F.3 – MMC Control structure

Low level control

The MMC Low-level control in EMTP-RV is shown in Fig. F.4. The inputs for this controller are: the modulation indices generated by the High-level control, the individual submodules capacitor voltages, the arm currents, and a new parameter ΔV_{tol} which is further described.

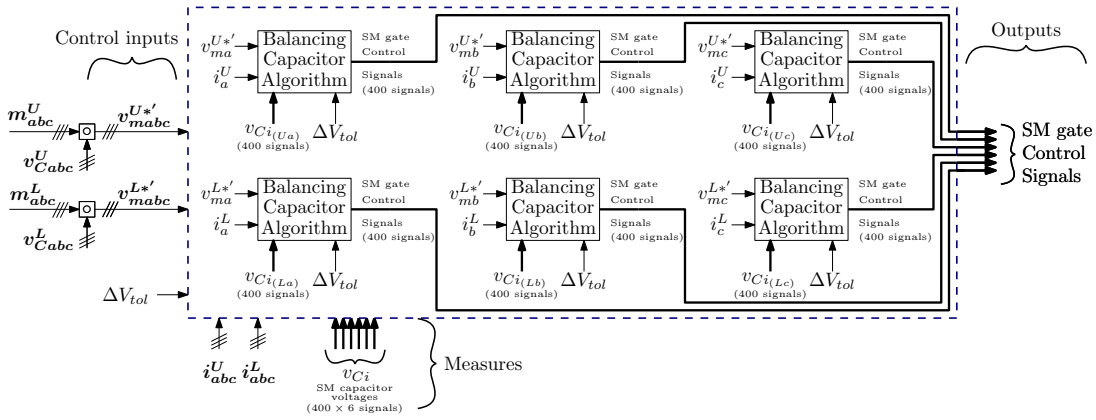

Figure F.4 – MMC Low level control for Equivalent Circuit-Based Model

As seen in Fig. F.4, the control inputs for the Low-level control are given by the arm modulated voltages reference, instead of directly the modulation indices, as given in (F.1):

$$v^{U*'}_{ma} = m^U_a v^U_{Ca}; \quad v^{U*'}_{mb} = m^U_b v^U_{Cb}; \quad v^{U*'}_{mc} = m^U_c v^U_{Cc} \tag{F.1a}$$

$$v^{L*'}_{ma} = m^L_a v^L_{Ca}; \quad v^{L*'}_{mb} = m^L_b v^L_{Cb}; \quad v^{L*'}_{mc} = m^L_c v^L_{Cc} \tag{F.1b}$$

Each of the modulated voltage reference $v^{U,L*'}_{m,j}$ is sent to the "Balancing Capacitor Algorithm" of the respective arm. These blocks were developed by Dr. Riad Kadri for a 20 SMs MMC

prototype and latter adapted by Thomas Pidancier, MSc (Eng), for 400 SMs. Inside these blocks, the sub-modules voltages are sorted with respect to their voltages, and the classical selection based on the reduced switching-frequency modulation from [109] is performed. The selection of the amount of submodules to be inserted in the circuit is calculated typically with the *Nearest Level Control* (NLC) [224]. However, in the strategy from Fig. F.4, the intention is to select the right amount of SMs taking into account their contribution to the applied modulated voltage in the arm. For having the modulated voltages as close as possible to the demanded reference, an extra SM can be inserted or bypassed to correct it. At the same time, the difference between the most and less charged SMs must be maintained within the specific limit defined by ΔV_{tol}.

For demonstrating the working principle, let us consider the simulation results of the MMC from Fig. F.1 with a power transmission of 1 GW of active power. Results from Fig. F.5a shows the 400 SMs voltages v_{Ci} in per-unit of the upper arm of phase a (similar results can be found for the others 5 arms). Also, the algebraic sum of all the SMs voltages within this arm is shown, i.e. v_{Ca}^{U}. In Fig. F.5b, the difference between the most and less charged SMs and the 5 % limit imposed on ΔV_{tol} are shown. As it can be seen, the SMs are maintained in a close range within the imposed limit.

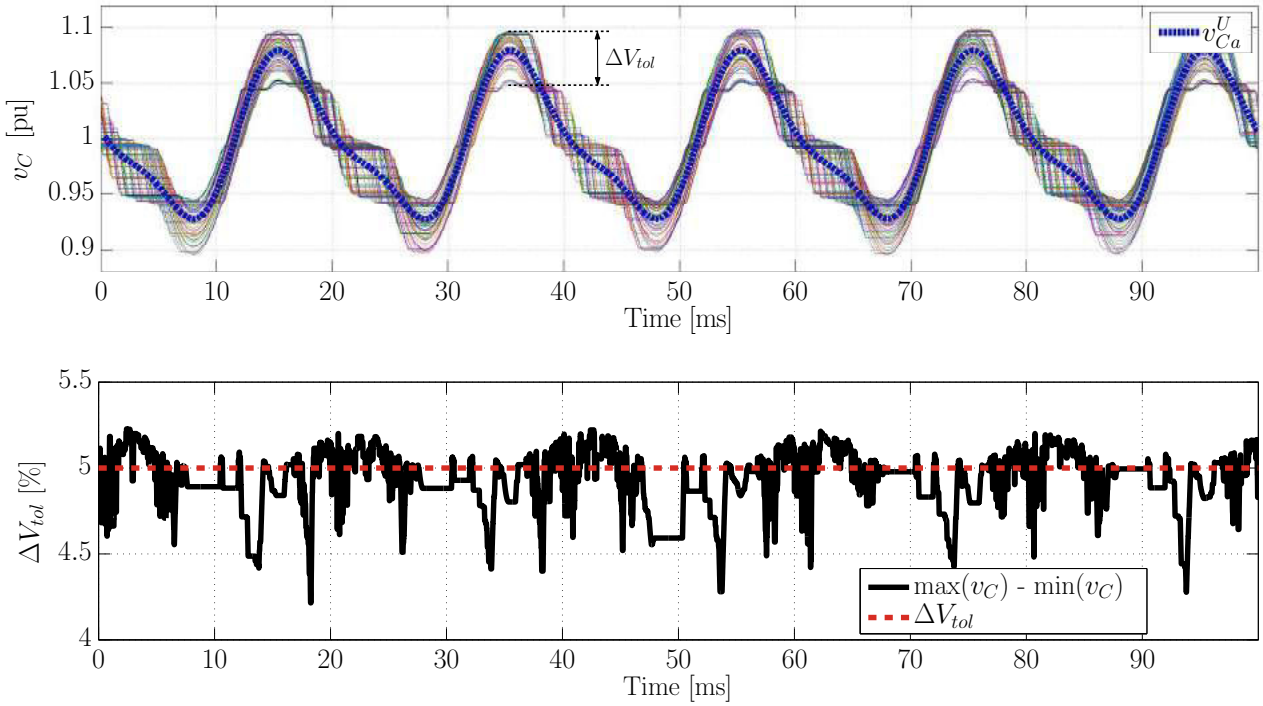

Figure F.5 – Simulation results for Low-level control: Sub-modules voltages

F.3 MMC High level controllers

In this section, the different High-level control structures used in this Thesis are detailed: first, the two main modulation indices calculations used in this Thesis are described (Uncompensated and Compensated modulation). Then, the different strategies defined by the "Inner Control Loops" and "Outer Control Loops" from Fig. F.3 are shown. For the sake of simplicity, the AC-side outer loops, the direct control of active and reactive powers from Fig. 1.8 are adopted for all strategies.

For the evaluation and discussion of each High level control, a simulation case study is proposed. Starting with no power transfer, and assuming a constant DC voltage fixed at 1 pu, the following events are considered:

1. At $t = 0.05$ s: Ramp applied on P^*_{ac} from 0 pu up to 1 pu in 100 ms.
2. At $t = 0.35$ s: Amplitude AC voltage from phase a, i.e. v^G_a, drops 20 %, generating an unbalance AC grid condition during 100 ms.
3. At $t = 0.55$ s: Step applied on P^*_{ac} from 1 pu down to 0.5 pu.
4. At $t = 0.8$ s: Step applied on Q^*_{ac} from 0 pu up to 0.2 pu.

The simulation scenario is described graphically in Fig. F.6, where Fig. F.6a shows the active and reactive power references, and Fig. F.6b the AC voltage. It is recalled that the presented controllers are not designed exclusively for dealing with an AC unbalanced scenario. However, several improvements are readily available in the literature for this cases, such as the ones proposed in [225–227].

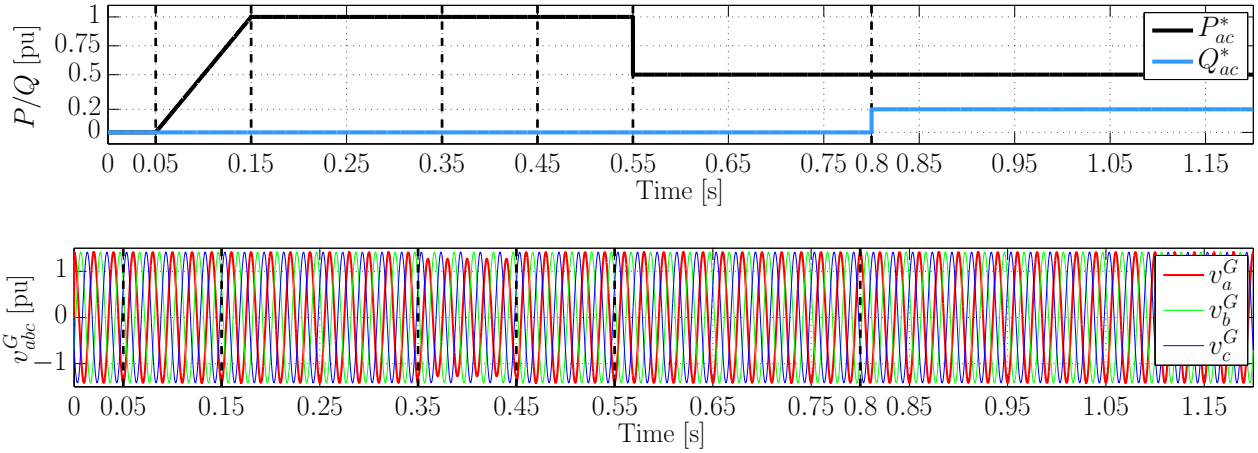

Figure F.6 – Scenario for the evaluation of different MMC High level controllers

F.3.1 Implementation of different modulation techniques: UCM and CM

Throughout this Thesis, two main modulation indices calculation techniques were widely used, namely "Uncompensated Modulation" (UCM) and "Compensated Modulation", which are shown in Fig. F.7. In this Figure, it is also shown the implementation of the block "Σ-Δ to "U"-"L"" from Fig. F.3, where the decoupling actions are shown [117].

The UCM strategy is depicted in Fig. F.7a, and as it can be seen, the 6 modulation indices signals are generated from the division of the 6 modulated arm voltages references by the DC voltage v_{dc}. This last signal may be obtained by the actual measure of the DC voltage or a fixed nominal value; however, the first option is preferred since the stability is slightly improved as studied in **[179]**. It is important to note that the modulation indices signals are later on multiplied by the respective equivalent arm capacitor voltages in the Low-level control, as given in (F.1). The difference between the arm modulated voltages v^*_m in Fig. F.7a and the variables $v^{*'}_m$ from Fig. F.4 creates an *error* which is the responsible of the natural power balance between the AC and DC sides, as shown in Section 2.5 and studied in [115]. However, the main drawback of this modulation technique is the appearance of circulating currents (or $\boldsymbol{i^{\Sigma}_{dq}}$), which are later suppressed by the CCSC [135].

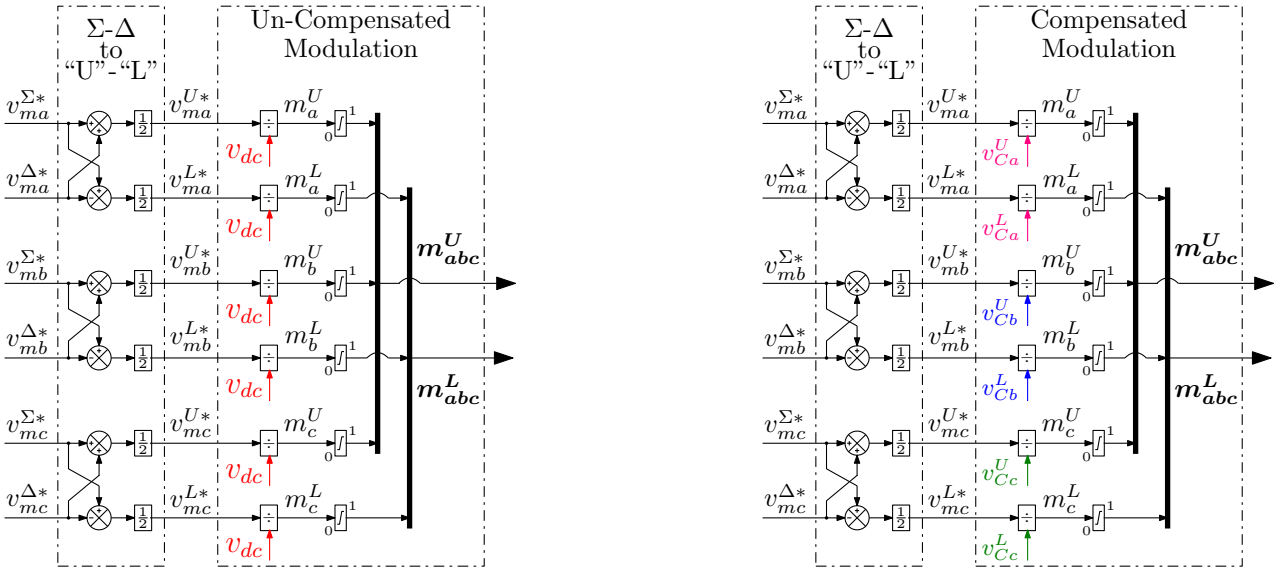

(a) Un-compensated modulation (UCM)

(b) Compensated modulation (CM)

Figure F.7 – Modulation strategies (in SI)

The CM strategy is depicted in Fig. F.7b, where it can be seen that the modulation indices are obtained by the division of the arm voltages references by their respective equivalent arm capacitor voltages. This corresponds to an exact inversion of the fundamental equation of the AAM as given in (2.1) and described later in Fig. 3.23. It is important to note that the modulation indices signals are later on multiplied back again by the respective equivalent arm capacitor voltages in the Low-level control, as given in (F.1), providing $v_m^{*'} = v_m^*$. For this reason, the natural balance of the AC and DC powers is lost and explicit control of the MMC internal variables is mandatory at this point [228]. However, the advantage of this strategy is that there is no circulating currents naturally induced as it was the case for UCM [137].

Naturally, the modulation indices signals are limited between 0 and 1 since, in this work, the Half-Bridge SM topology is considered. The basic limits are given by the bypassing of all sub-modules (corresponding to a modulation index equal to $m = 0$) or the insertion of all sub-modules (corresponding to $m = 1$). The rest of the control limitations are not explicitly implemented, since this Thesis deals with normal scenarios where the converters are maintained within their nominal values [229].

F.3.2 Measurements and per-unitation

The control structures in this Thesis are implemented with a per-unit approach. In this section, the measures and further per-unitation from Fig. F.8 are described.

In Fig. F.8a, the adopted Synchronization structure for aligning the AC voltage phasor with the d axis is shown. It consists in the classical Phase Locked Loop control loop widely used in the literature [64]. The outputs of this controller are the AC voltages at the Point of Common Coupling (PCC-AC) in dq frame and in per-unit, $v^{pcc}_{d,pu}$ and $v^{pcc}_{q,pu}$ (note that from now on, the sub-script "pu" is used to denote per-unit variables). Moreover, the estimated angular frequency $\omega_{C,pu}$ and angle θ_C are also obtained.

In Fig. F.8c, the calculations of the "Σ" and "Δ" currents are shown. Also, the Park transformations at -2ω and ω are used to obtain the dqz components of the aforementioned currents. Note that the "Δ" currents corresponds to the grid currents. In Fig. F.8b, the DC

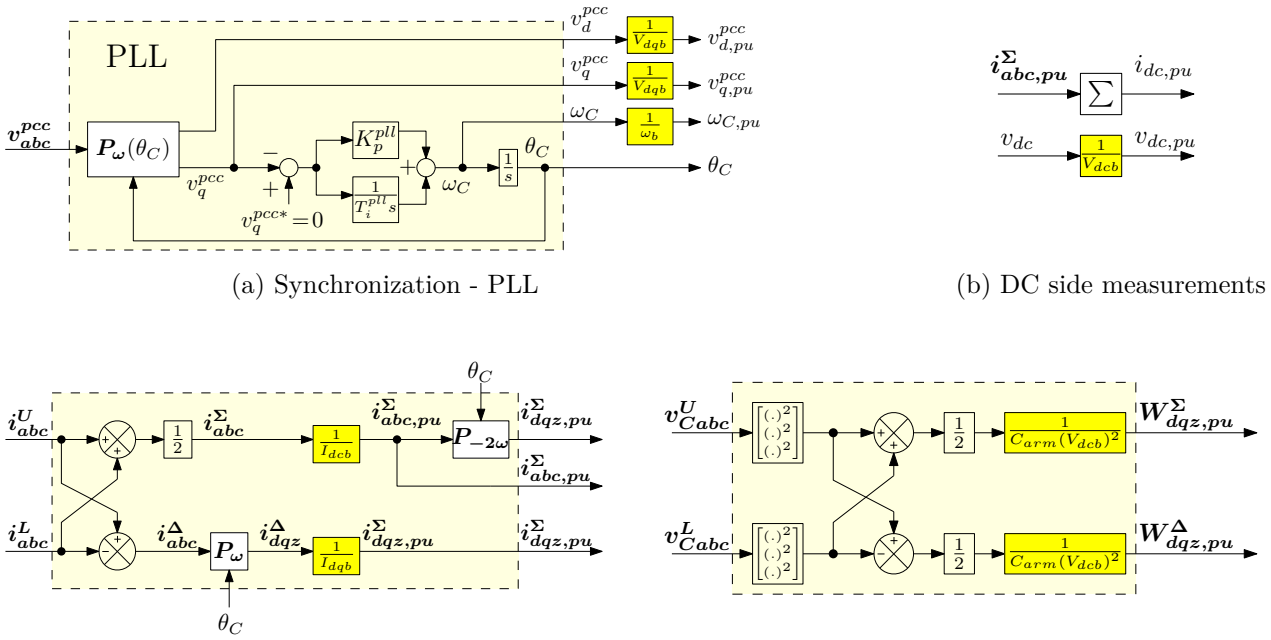

(a) Synchronization - PLL

(b) DC side measurements

(c) Current measurements

(d) Energies measurements

Figure F.8 – Synchronization, Measures and per-unitation

side measurements are shown, where the DC current $i_{dc,pu}$ is calculated as the sum of the "Σ" currents $\boldsymbol{i}_{\boldsymbol{abc,pu}}^{\boldsymbol{\Sigma}}$.

Finally, the energies "Σ" and "Δ" are calculated as depicted in Fig. F.8d based on the equivalent arm capacitor voltages.

F.3.3 Classical CCSC

The *Classical CCSC* control strategy from Section 3.2 is shown in Fig. F.9. For this strategy, the UCM technique from Fig. F.7a is adopted. Note that the obtained modulated reference voltages are transformed to *abc* frame and SI before sending the signals to the "Modulation Indices Calculation".

Simulation results with Classical CCSC

In Fig. F.10, the simulation results of the single MMC with *Classical CCSC* in the described scenario in Fig. F.6 are gathered. Results for the grid currents $\boldsymbol{i}_{\boldsymbol{dq}}^{\boldsymbol{\Delta}}$ shows a slight coupling during the simulation, particularly for the steps applied on P_{ac}^* and Q_{ac}^*. This coupling is mainly due to the UCM technique from Fig. F.7a. During the AC unbalance event, the grid currents oscillate at 2ω, which is the main limitation of the SRRF controllers (dq) when dealing with these events [140]. This oscillations are transferred to the DC side as seen in the results from the middle figure [230]. From the results of the currents $\boldsymbol{i}_{\boldsymbol{abc}}^{\boldsymbol{\Sigma}}$, it can be observed that the circulating currents are eliminated. However, several oscillations on the DC current are observed due to the lack of dedicated controller on this current as explored in Section 3.2. Nevertheless, the arm capacitor voltages $\boldsymbol{v}_{\boldsymbol{Cabc}}^{\boldsymbol{U}}$ and $\boldsymbol{v}_{\boldsymbol{Cabc}}^{\boldsymbol{L}}$ are well balanced during the simulation.

In Fig. F.11, results for the modulated voltages v_m^{Σ} for the period of time from 0.30 s up to 0.65 s are shown. Also, results of the currents $\boldsymbol{i}_{\boldsymbol{abc}}^{\boldsymbol{\Sigma}}$ for the same period are plotted. As seen

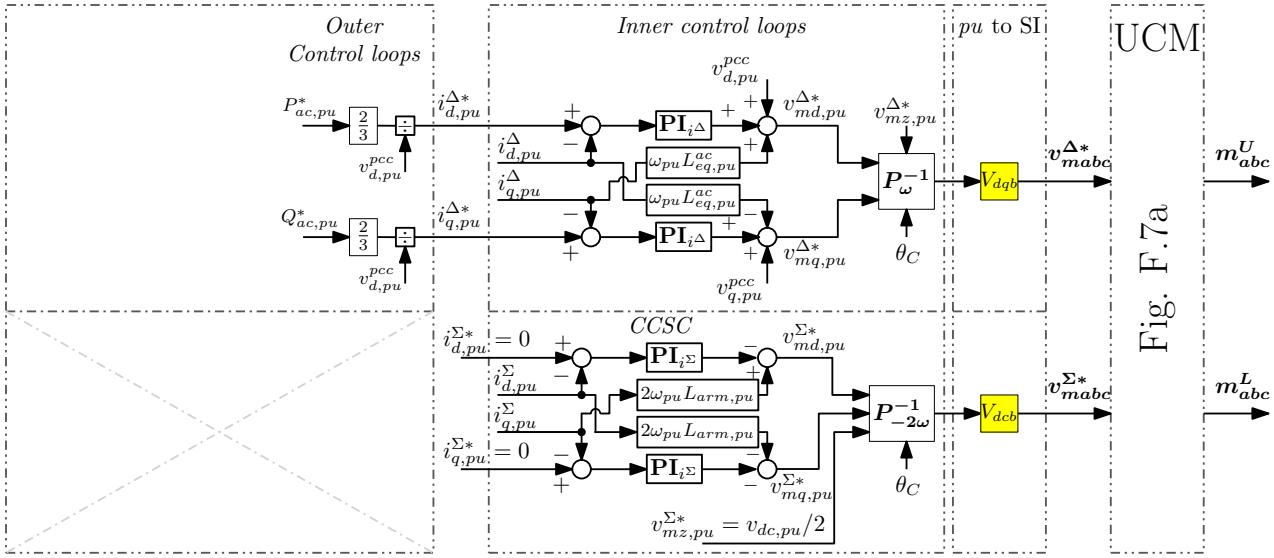

Figure F.9 – EMT implementation of *Classical CCSC* from Section 3.2

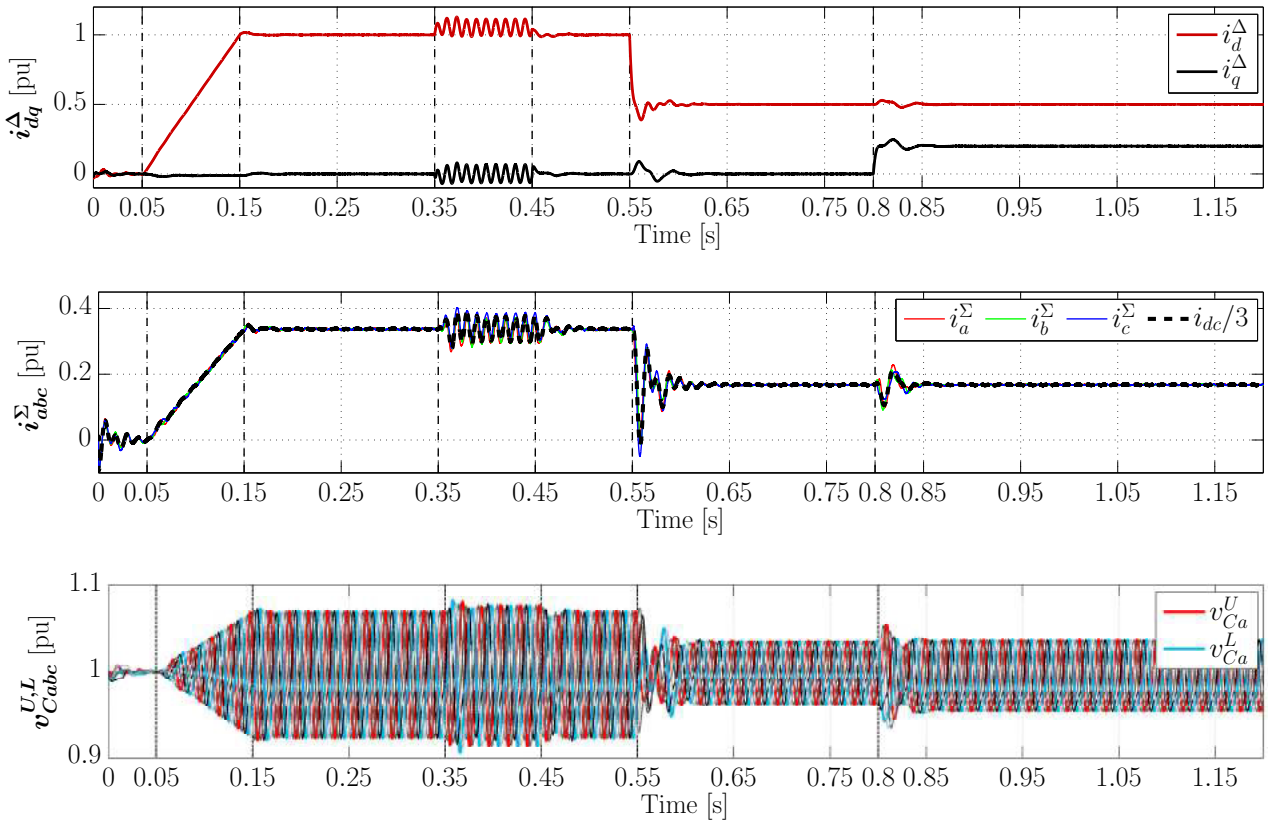

Figure F.10 – EMT simulation results for *Classical CCSC*

from Fig. F.9, the modulated voltage reference $v_{mz}^{\Sigma*}$ generated by the High level control is fixed to $v_{dc}/2$, however, the actual modulated voltage v_{mz}^{Σ} created by the MMC is naturally adapted for the induction of the current i_{dc} for balancing the AC and DC powers (it is recalled that $i_z^{\Sigma} = i_{dc}/3$). When the AC unbalance occurs, the coupling originated from the UCM generates the 2ω oscillations on i_{dc}. Finally, when the AC power step is applied at $t = 0.55$ s, the voltage v_{mz}^{Σ} experiments an uncontrolled transient, causing the high excursion on the DC current. It is recalled that, for this reason, the *Energy-based* controllers were introduced in Chapter 3.

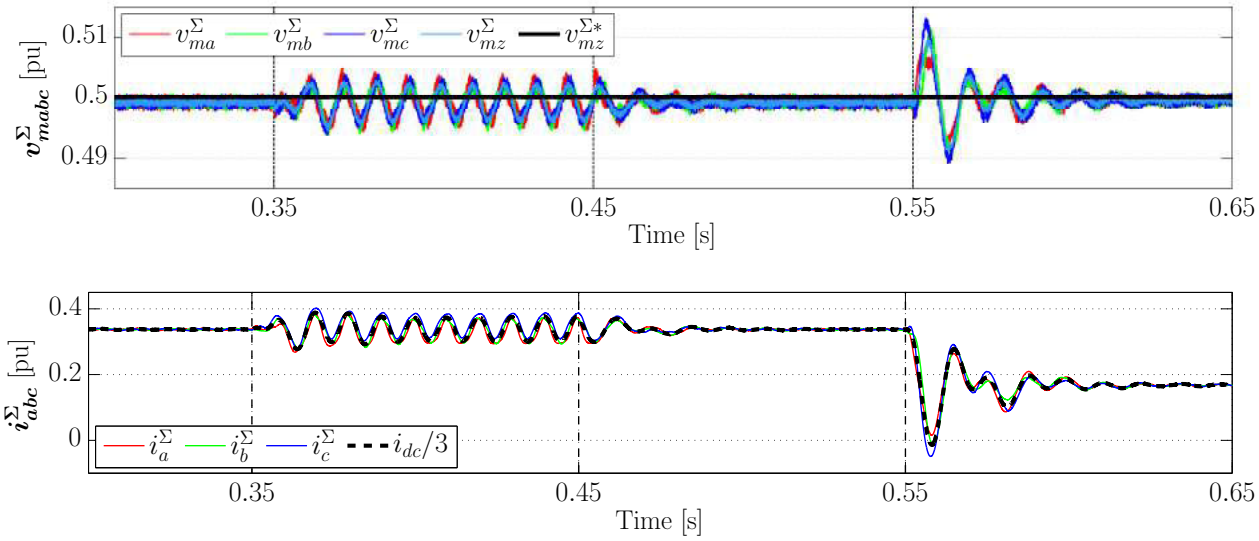

Figure F.11 – Results from "Σ" voltages and currents for *Classical CCSC*

F.3.4 Energy-based controller # 1

The first *Energy-based* control strategy used in this Thesis was presented in Section 3.3 which was based on the results from **[163]**, and its implementation is shown in Fig. F.12. This control structure is similar to the one in Fig. F.9 with the inclusion of two extra control loops: for the DC current and total energy (highlighted in light yellow).

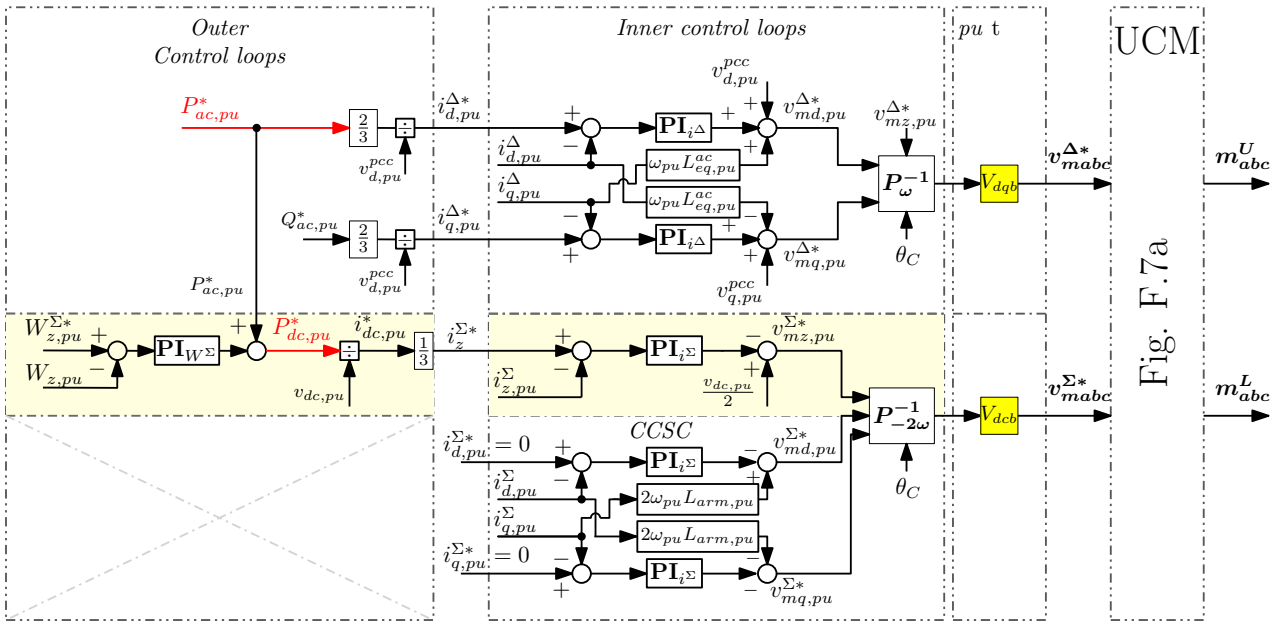

Figure F.12 – *Energy-based* controller # 1 from Section 3.3 **[163]**

The AC and DC power references are marked in red, i.e. $P^{*}_{ac,pu}$ and $P^{*}_{dc,pu}$ for highlighting the fact that the *Energy-based* control strategies are based on the explicit control of both powers independently. This strategy was used in Section 3.3 in conjunction with the UCM technique. When considering CM with this strategy, the un-controlled energies compromises the systems stability.

Simulation results with Energy-based controller # 1

Simulation results are gathered in Fig. F.13. The dynamics of the AC currents and arm capacitor voltages are similar as for the *Classical CCSC*. However, the transient of the DC current is improved.

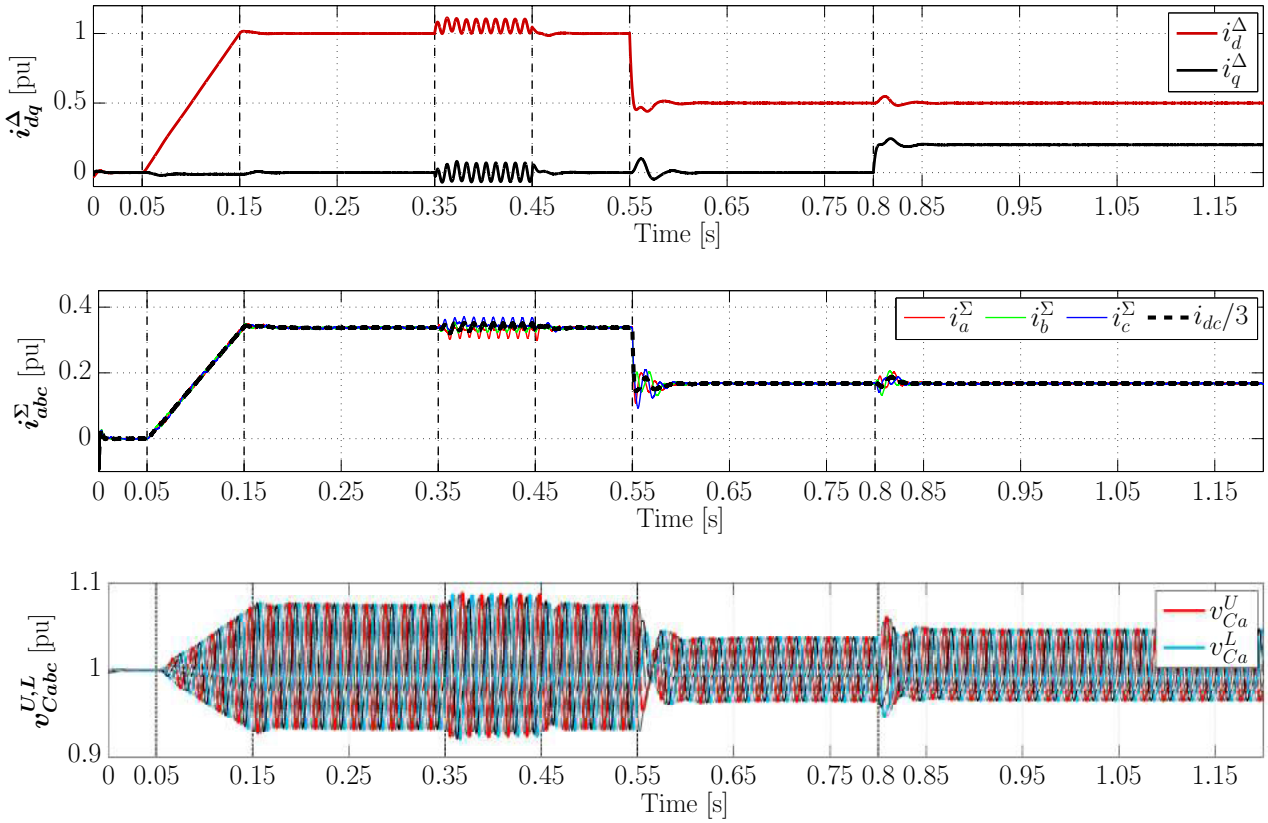

Figure F.13 – EMT simulation results for *Energy-based* controller # 1

In Fig. F.14, results for the modulated voltages $\boldsymbol{v}_{\boldsymbol{mabc}}^{\boldsymbol{\Sigma}}$ and currents $\boldsymbol{i}_{\boldsymbol{abc}}^{\boldsymbol{\Sigma}}$ are shown, similarly as in Fig. F.11. Even if the DC current is controlled, $v_{mz}^{\Sigma} \neq v_{mz}^{\Sigma *}$ due to the using of UCM.

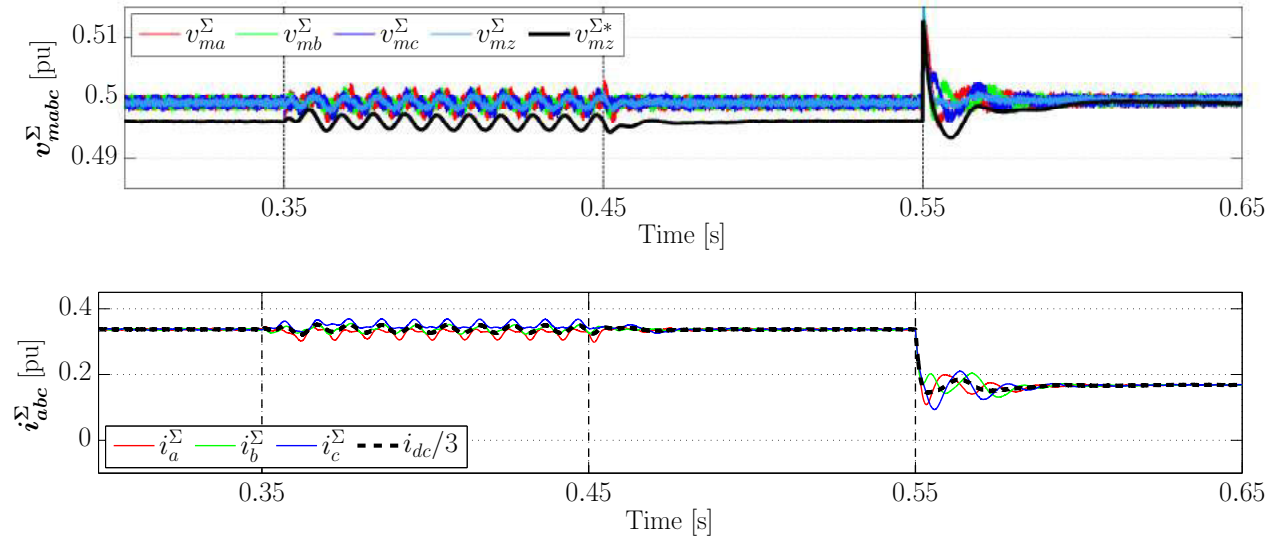

Figure F.14 – Results from "Σ" voltages and currents for *Energy-based* controller # 1

F.3.5 Energy-based controller # 2

The *Energy-based* control strategy # 2 was presented in Section 3.4, and it is based on the main findings from [114] and [116], and its implementation is shown in Fig. F.15. In this case, the energy controllers *per-phase* is clearly highlighted [170].

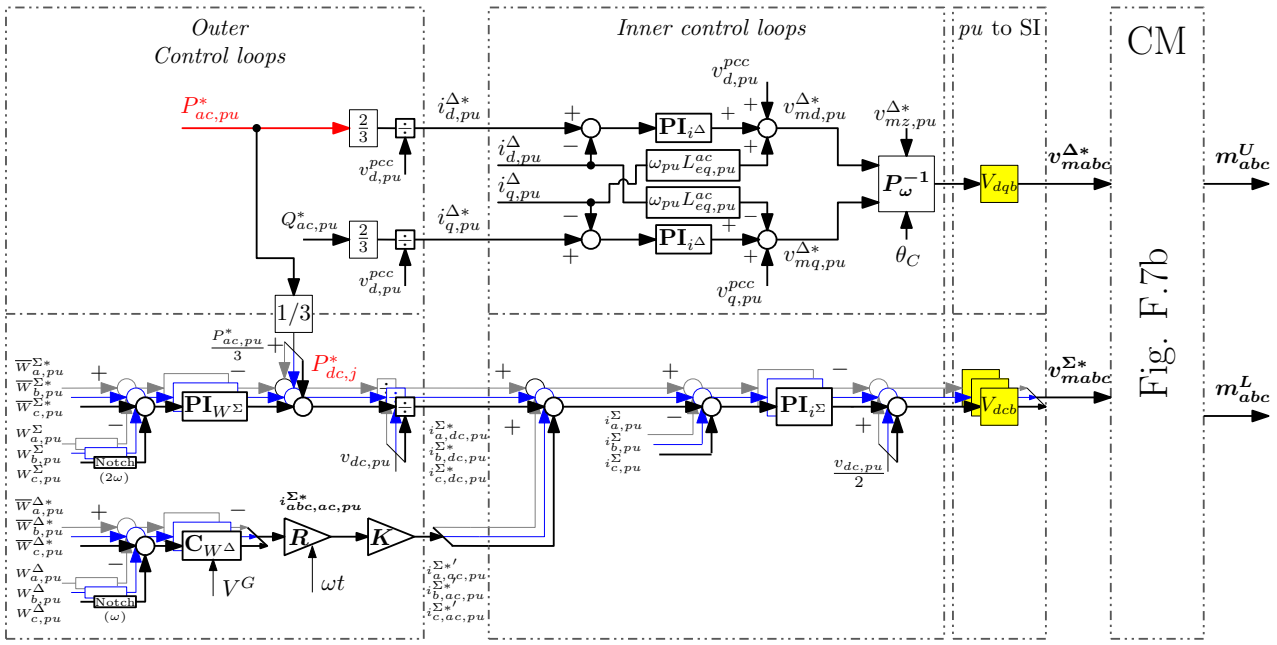

Figure F.15 – *Energy-based* controller # 2 from Section 3.4

In this Thesis, this controller is implemented with the CM modulation. However, the use of UCM is also possible as performed in **[162]**, but the presence of circulating currents $\boldsymbol{i}^{\boldsymbol{\Sigma}}_{\boldsymbol{dq}}$ obliges the use of an extra CCSC, as in [117]. All the control details from this strategy are well documented in [114] and [116].

Energy-based controller # 2 for Wind Farm Connection

In Fig. F.16, the AC side controller for Wind Farm connection as used in MMC-4 from Section 5.6 is shown. This controller is not based on the PLL synchronization loop: the AC angle is generated by this controller. Since there is no closed-loop control for the AC voltage, this strategy may be referred as *open-loop* control for WF connections.

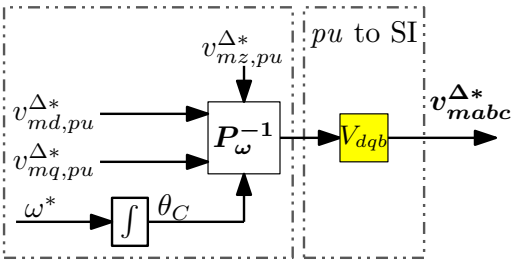

Figure F.16 – AC side controller for Wind Farm connection as used in MMC-4 from Section 5.6

For the rest of the controller, the lower part from Fig. F.15 was used, where the AC power compensation used for the DC power reference generation is now the measured AC power instead of $P^*_{ac,pu}$.

Simulation results with Energy-based controller # 1

Simulation results are gathered in Fig. F.17. The dynamics of the AC currents improved with respect to the previous control strategies, while simultaneously maintaining a good regulation of the DC current. The arm capacitor voltages presents different dynamics as in previous cases; however the arms are correctly equilibrated.

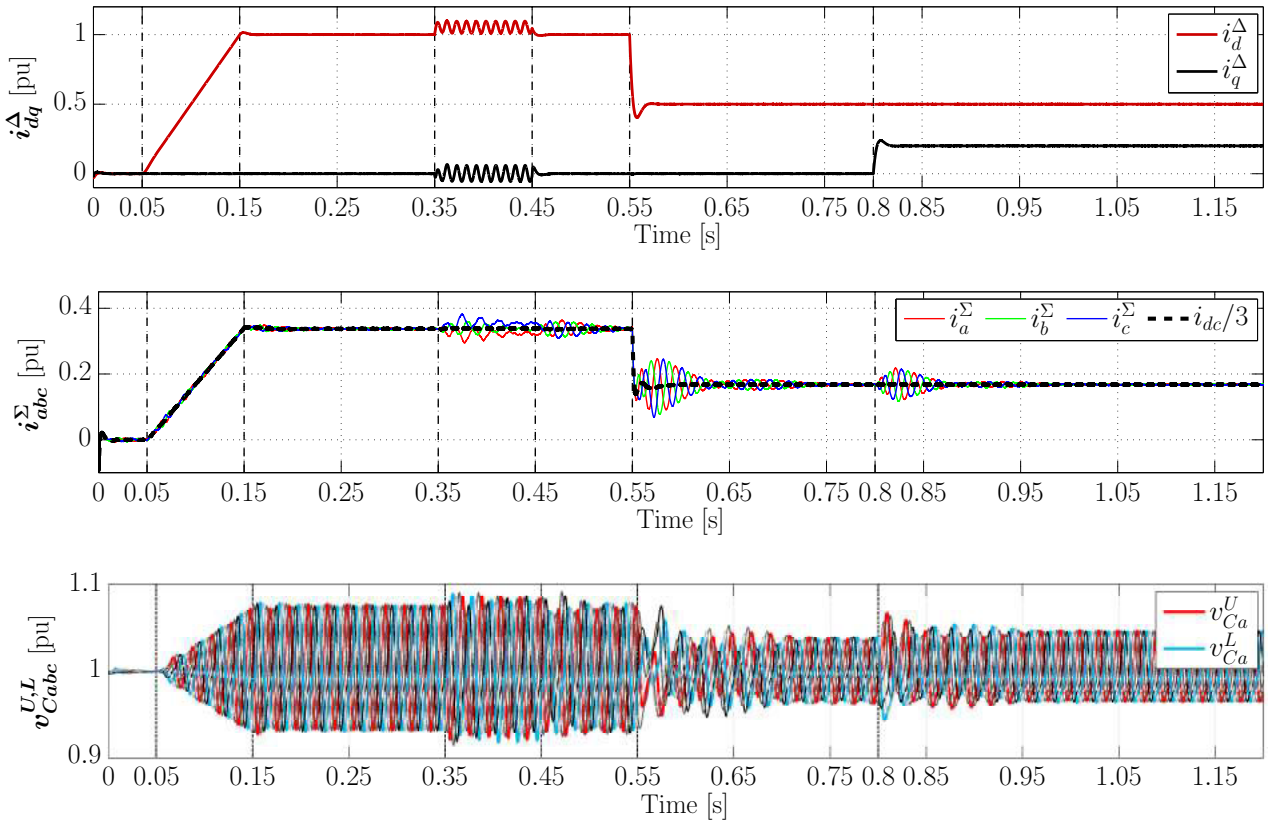

Figure F.17 – EMT simulation results for *Energy-based* controller # 2

In Fig. F.18, results for the modulated voltages $\boldsymbol{v}^{\boldsymbol{\Sigma}}_{\boldsymbol{mabc}}$ and currents $\boldsymbol{i}^{\boldsymbol{\Sigma}}_{\boldsymbol{abc}}$ are shown, similarly as in Fig. F.11. Note that v^{Σ}_{mz} is now equal to $v^{\Sigma*}_{mz}$ due to the using of CM. This choice allows an accurate control of all the MMC currents, i.e. i^{Δ} and i^{Σ}. During the unbalanced event, the DC current results unmodified, meaning that the 2ω perturbation is accurately isolated from the DC side.

F.3.6 Energy-based controller for energy "Σ" in $\alpha\beta z$ frame

Finally, the *Energy-based* controller for the energy "Σ" in $\alpha\beta z$ frame is presented. This control approach presents several advantages when dealing with unbalanced AC systems, since advanced modifications can be added to cope with this scenarios as studied in [168, 169]. The energy measures are first referred to the $\alpha\beta z$ axes as shown in (F.2), where the Clarke transformation $\boldsymbol{C}_{\alpha\beta z}$ from Appendix A is used.

$$\boldsymbol{i}^{\boldsymbol{\Sigma}}_{\boldsymbol{\alpha\beta z,pu}} = \boldsymbol{C}_{\boldsymbol{\alpha\beta z}} \boldsymbol{i}^{\boldsymbol{\Sigma}}_{\boldsymbol{abc,pu}} \tag{F.2a}$$

$$\boldsymbol{W}^{\boldsymbol{\Sigma}}_{\boldsymbol{\alpha\beta z,pu}} = \boldsymbol{C}_{\boldsymbol{\alpha\beta z}} \boldsymbol{W}^{\boldsymbol{\Sigma}}_{\boldsymbol{abc,pu}} \tag{F.2b}$$

The control structure is shown in Fig. F.19. As it can be seen, the energy "Δ" is still implemented in *abc* frame and it is the same as in Fig. F.16. However, this controller may

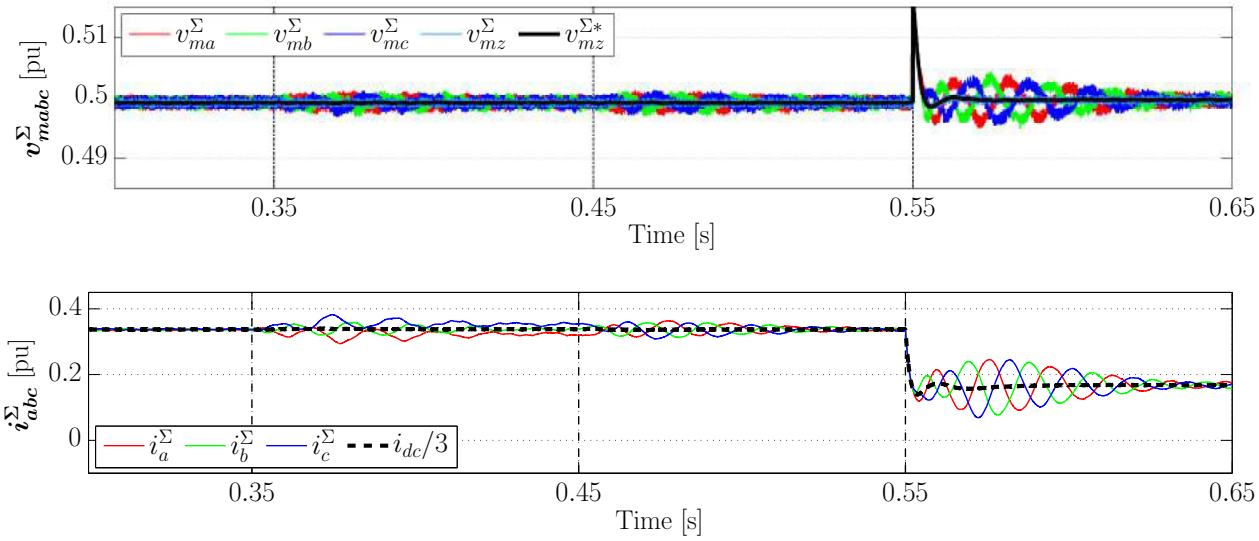

Figure F.18 – Results from "Σ" voltages and currents for *Energy-based* controller # 2

be also referred to the $\alpha\beta z$ frame if desired, as explored in [79, 167, 168], to name a few. The energy references $\overline{W}^{\Sigma*}_{\alpha,pu}$ and $\overline{W}^{\Sigma*}_{\beta,pu}$ are set to zero, similarly as for the dq references described in Section 3.4.2.

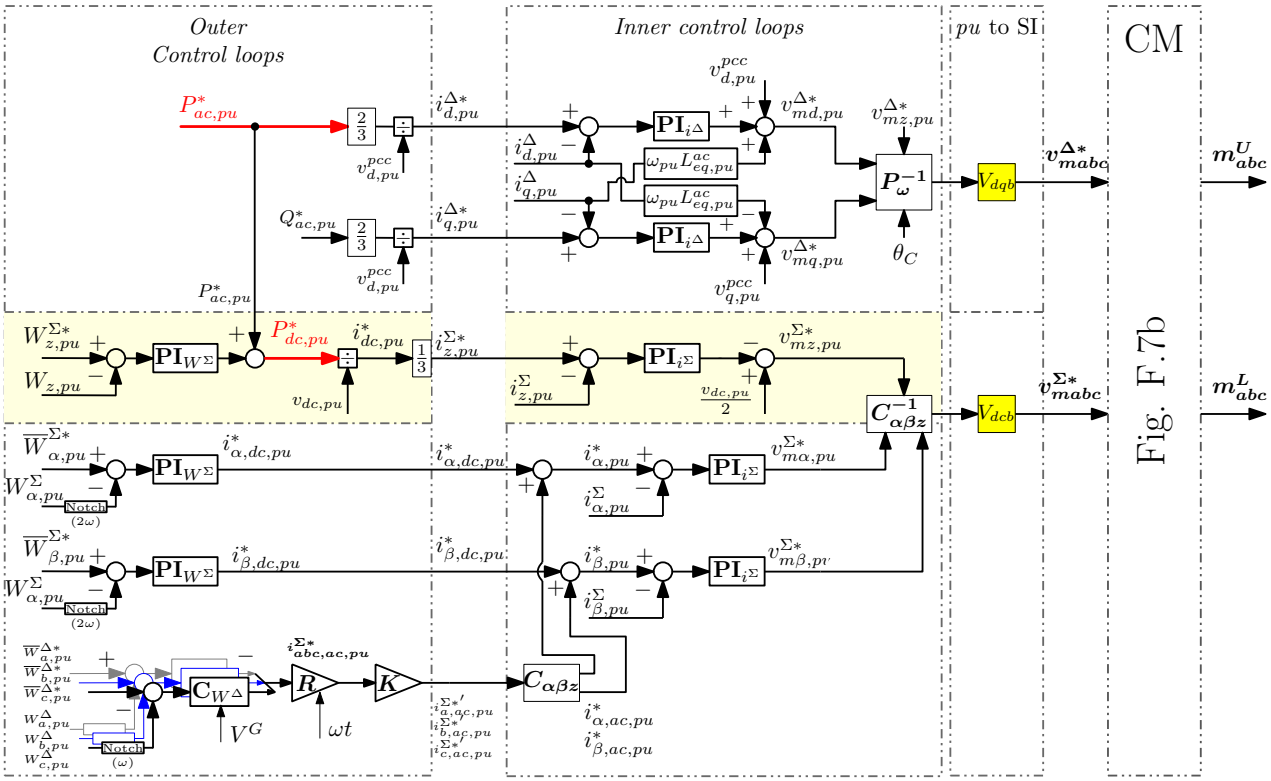

Figure F.19 – *Energy-based* controller in $\alpha\beta z$ frame for energy "Σ" suitable for energy-management strategy from Section 5.5.2

As it can be seen from Fig. F.19, the DC current (i.e. i^{Σ}_{z}) and total energy control loops are the same as for the *Energy-based* control # 1 from Fig. F.12 (highlighted in light yellow). Once again, the explicit control of $P^{*}_{ac,pu}$ and $P^{*}_{dc,pu}$ are highlighted.

Simulation results with Energy-based controller in $\alpha\beta z$ frame for energy "Σ"

Simulation results are gathered in Figs. F.20 and F.21. As observed in the results, a similar behavior is obtained as with the *Energy-based* controller # 2.

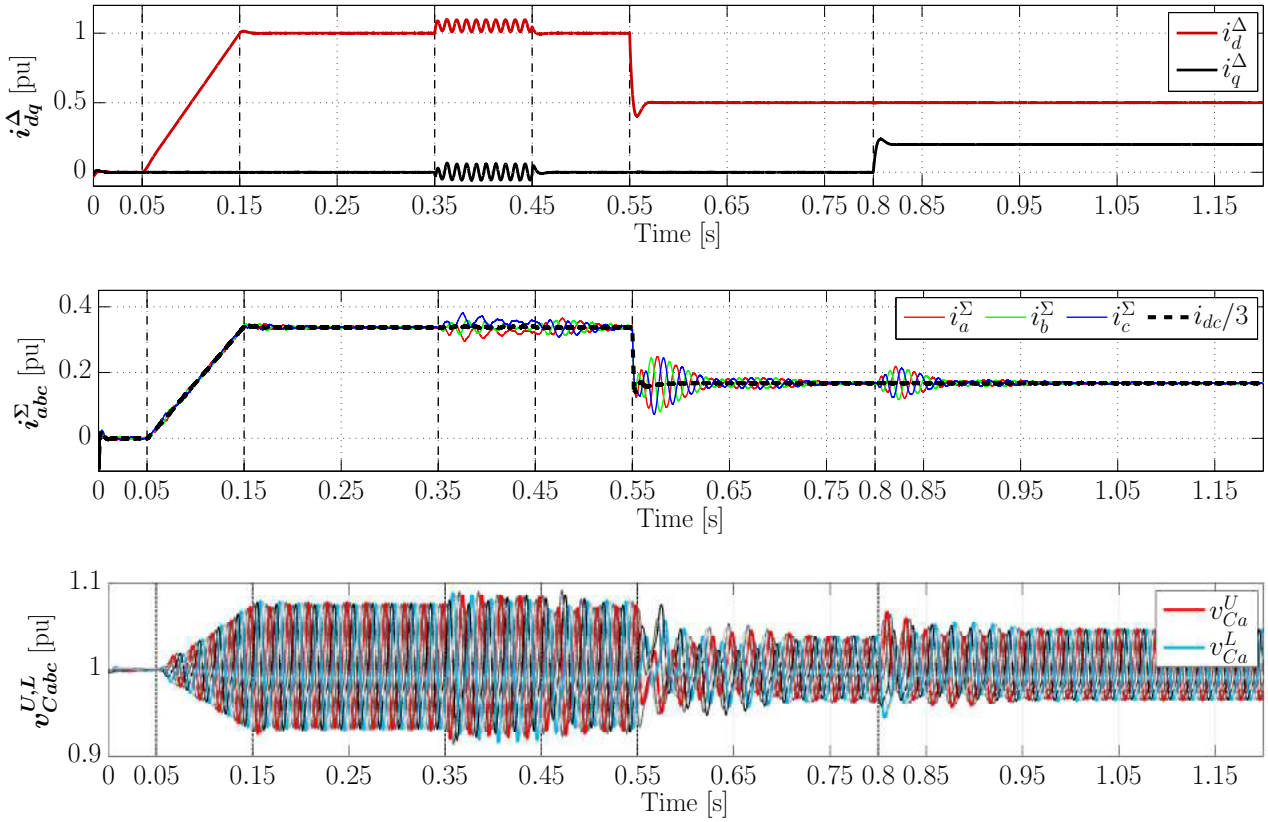

Figure F.20 – EMT simulation results for *Energy-based* controller in $\alpha\beta z$ frame for energy "Σ"

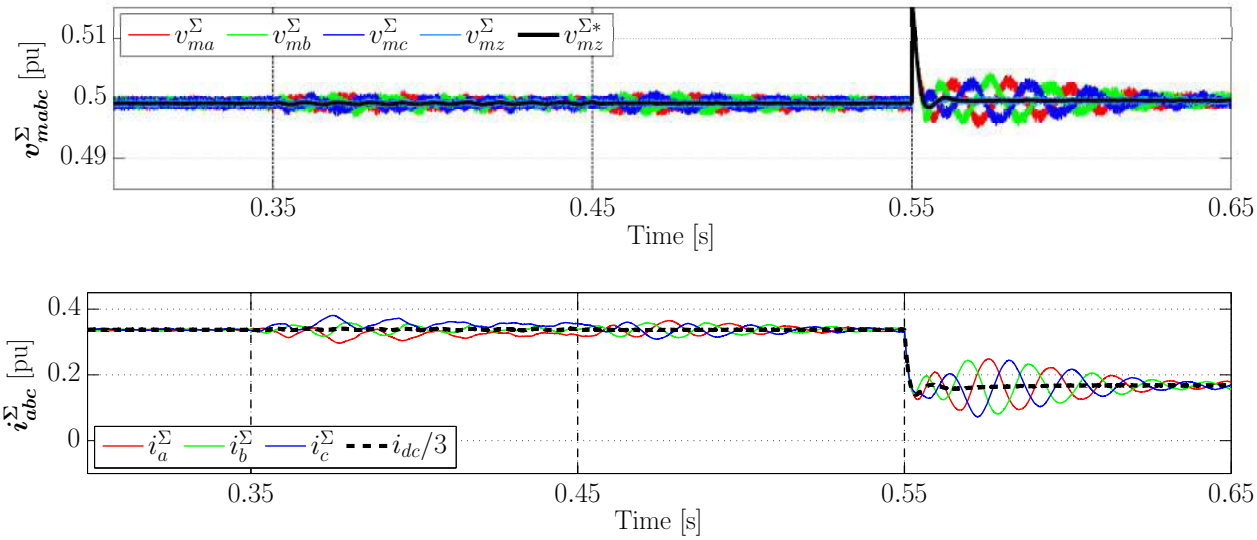

Figure F.21 – Results from "Σ" voltages and currents for *Energy-based* controller in $\alpha\beta z$ frame for energy "Σ"

Appendix G

Energy Based controllers representation in SRRF

In this Appendix, the mathematical demonstrations and developments of the *Energy-based* controller representation in SRRF are given, based on the main findings of **[162]**.

G.1 MMC Energy calculations

G.1.1 Energy expressions in *abc* frame

The energy sum W_j^{Σ} and difference W_j^{Δ} are calculated as expressed in (G.1) and (G.2) respectively **[162]**. In Fig. G.1, results of the energies from the simulation discussed in Section 2.3.3 are provided.

$$W_j^{\Sigma} = \frac{1}{2} C_{arm} \left(\left(v_{Cj}^{\Sigma} \right)^2 + \left(v_{Cj}^{\Delta} \right)^2 \right) \tag{G.1}$$

$$W_j^{\Delta} = \frac{1}{2} C_{arm} \left(2 v_{Cj}^{\Sigma} v_{Cj}^{\Delta} \right) \tag{G.2}$$

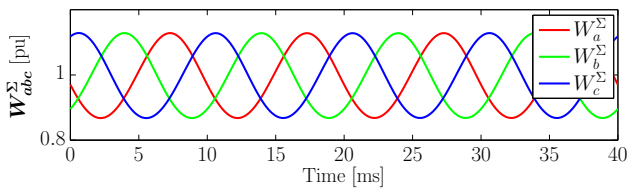

(a) $\boldsymbol{W_{abc}^{\Sigma}} = [W_a^{\Sigma}\ W_b^{\Sigma}\ W_c^{\Sigma}]^{\top}$

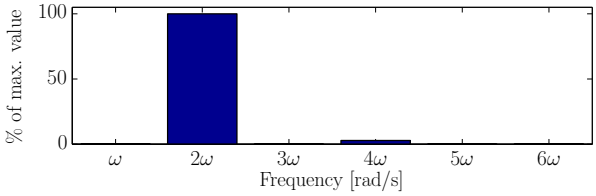

(b) FFT - W_j^{Σ}

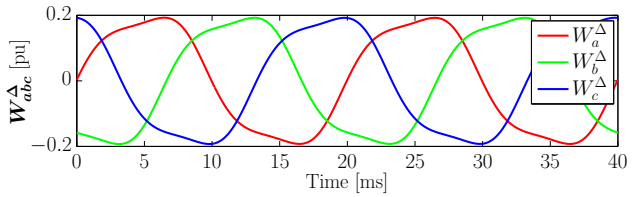

(c) $\boldsymbol{W_{abc}^{\Delta}} = [W_a^{\Delta}\ W_b^{\Delta}\ W_c^{\Delta}]^{\top}$

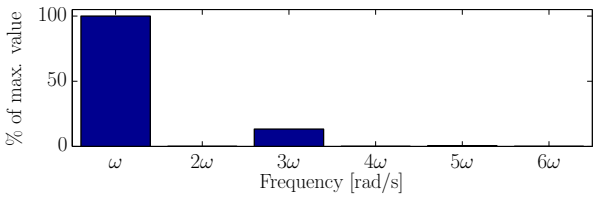

(d) FFT - W_j^{Δ}

Figure G.1 – MMC Steady State Analysis - Energies

As observed in Fig. G.1a, the variables $\boldsymbol{W}^{\boldsymbol{\Sigma}}_{\boldsymbol{abc}}$ are oscillating at 2ω with negative sequence. The main frequencies for are $\boldsymbol{W}^{\boldsymbol{\Sigma}}_{\boldsymbol{abc}}$ shown in the FFT from Fig. G.1b, which reveals that some components of 4ω are also present. Moreover, results for the variables $\boldsymbol{W}^{\boldsymbol{\Delta}}_{\boldsymbol{abc}}$ given in Figs. G.1c and G.1d, show that the main oscillations are ω and 3ω. Naturally, the "Σ-Δ" variables of the MMC energies also follows the frequency classification given in Table 2.1.

G.1.2 Energy expressions in dqz frame

The expressions of the MMC energies in dqz frame are obtained as shown in (G.3), where the Park transformation at -2ω is used for $\boldsymbol{W}^{\boldsymbol{\Sigma}}_{\boldsymbol{abc}}$, and the Park transformation at ω is used for $\boldsymbol{W}^{\boldsymbol{\Delta}}_{\boldsymbol{abc}}$, as suggested by the results from Fig. G.1.

$$\boldsymbol{W}^{\boldsymbol{\Sigma}}_{\boldsymbol{dqz}} \stackrel{\text{def}}{=} \boldsymbol{P}_{\boldsymbol{-2\omega}} \boldsymbol{W}^{\boldsymbol{\Sigma}}_{\boldsymbol{abc}} \tag{G.3a}$$

$$\boldsymbol{W}^{\boldsymbol{\Delta}}_{\boldsymbol{dqz}} \stackrel{\text{def}}{=} \boldsymbol{P}_{\boldsymbol{\omega}} \boldsymbol{W}^{\boldsymbol{\Delta}}_{\boldsymbol{abc}} \tag{G.3b}$$

Energy sum calculation in dqz frame

Taking into account (G.1), the three-phase energy sum $\boldsymbol{W}^{\boldsymbol{\Sigma}}_{\boldsymbol{abc}} = [W^{\Sigma}_{a},\ W^{\Sigma}_{b},\ W^{\Sigma}_{c}]^{\top}$ is calculated as a function of the arm capacitor voltages in dqz frame as follows (see (2.17)):

$$\boldsymbol{W}^{\boldsymbol{\Sigma}}_{\boldsymbol{abc}} = \frac{1}{2} C_{arm} \boldsymbol{P}^{\boldsymbol{-1}}_{\boldsymbol{-2\omega}} \boldsymbol{v}^{\boldsymbol{\Sigma}}_{\boldsymbol{Cdqz}} \circ \boldsymbol{P}^{\boldsymbol{-1}}_{\boldsymbol{-2\omega}} \boldsymbol{v}^{\boldsymbol{\Sigma}}_{\boldsymbol{Cdqz}} + \frac{1}{2} C_{arm} \boldsymbol{P}^{\boldsymbol{-1}}_{\boldsymbol{\omega}} \boldsymbol{v}^{\boldsymbol{\Delta}}_{\boldsymbol{Cdqz}} \circ \boldsymbol{P}^{\boldsymbol{-1}}_{\boldsymbol{\omega}} \boldsymbol{v}^{\boldsymbol{\Delta}}_{\boldsymbol{Cdqz}} \tag{G.4}$$

where it is recalled that $\boldsymbol{v}^{\boldsymbol{\Sigma}}_{\boldsymbol{Cdqz}} = [v^{\Sigma}_{Cd}\ v^{\Sigma}_{Cq}\ v^{\Sigma}_{Cz}]^{\top}$ and $\boldsymbol{v}^{\boldsymbol{\Delta}}_{\boldsymbol{Cdqz}} = \left[v^{\Delta}_{Cd}\ v^{\Delta}_{Cq}\ v^{\Delta}_{Cz}\right]^{\top}$. It is worth noticing that the operator "$\circ$" represents the element-wise multiplication of vectors (e.g. $\left[\begin{smallmatrix} a \\ b \end{smallmatrix}\right] \circ \left[\begin{smallmatrix} c \\ d \end{smallmatrix}\right] = \left[\begin{smallmatrix} ac \\ bd \end{smallmatrix}\right]$). Moreover, it is recalled that the zero-sequence of the arm capacitor voltages "Δ" is expressed as $v^{\Delta}_{Cz} = v^{\Delta}_{CZ_d} \cos(3\omega t) + v^{\Delta}_{CZ_q} \sin(3\omega t)$.

Multiplying (G.4) by $\boldsymbol{P}_{\boldsymbol{-2\omega}}$, taking into account (G.3a), and neglecting the 6^{th} harmonic component (G.5) is obtained.

$$\boldsymbol{W}^{\boldsymbol{\Sigma}}_{\boldsymbol{dqz}} = \begin{bmatrix} W^{\Sigma}_{d} \\ W^{\Sigma}_{q} \\ W^{\Sigma}_{z} \end{bmatrix} = \tfrac{1}{2} C_{arm} \begin{bmatrix} \left(v^{\Delta}_{Cd}\right)^2 - \left(v^{\Delta}_{Cq}\right)^2 + 2 v^{\Delta}_{CZ_d} v^{\Delta}_{Cd} + 2 v^{\Delta}_{CZ_q} v^{\Delta}_{Cq} + 4 v^{\Sigma}_{Cd} v^{\Sigma}_{Cz} \\ 2 v^{\Delta}_{Cq} v^{\Delta}_{CZ_d} - 2 v^{\Delta}_{Cd} v^{\Delta}_{CZ_q} - 2 v^{\Delta}_{Cd} v^{\Delta}_{Cq} + 4 v^{\Sigma}_{Cq} v^{\Sigma}_{Cz} \\ \left(v^{\Delta}_{Cd}\right)^2 + \left(v^{\Delta}_{Cq}\right)^2 + \left(v^{\Delta}_{CZ_d}\right)^2 + \left(v^{\Delta}_{CZ_q}\right)^2 + \left(v^{\Sigma}_{Cd}\right)^2 + \left(v^{\Sigma}_{Cq}\right)^2 + 2\left(v^{\Sigma}_{Cz}\right)^2 \end{bmatrix} \tag{G.5}$$

The expression from (G.5) relates the energies $\boldsymbol{W}^{\boldsymbol{\Sigma}}_{\boldsymbol{dqz}}$ with the arm capacitor voltages in dqz, i.e. $\boldsymbol{v}^{\boldsymbol{\Sigma}}_{\boldsymbol{Cdqz}}$ and $\boldsymbol{v}^{\boldsymbol{\Delta}}_{\boldsymbol{CdqZ}}$.

Energy difference calculation in dqz frame

Taking into account (G.2), the three-phase energy difference vector $\boldsymbol{W}^{\boldsymbol{\Delta}}_{\boldsymbol{abc}} = [W^{\Delta}_{a}\ W^{\Delta}_{b}\ W^{\Delta}_{c}]^{\top}$ is calculated as a function of the arm capacitor voltages in dqz frame as follows:

$$\boldsymbol{W}^{\boldsymbol{\Delta}}_{\boldsymbol{abc}} = C_{arm} \left(\boldsymbol{P}^{\boldsymbol{-1}}_{\boldsymbol{-2\omega}} \boldsymbol{v}^{\boldsymbol{\Sigma}}_{\boldsymbol{Cdqz}} \circ \boldsymbol{P}^{\boldsymbol{-1}}_{\boldsymbol{\omega}} \boldsymbol{v}^{\boldsymbol{\Delta}}_{\boldsymbol{Cdqz}} \right) \tag{G.6}$$

Multiplying (G.6) by $\boldsymbol{P}_{\boldsymbol{\omega}}$ and taking into account (G.3b), the expression of $\boldsymbol{W}^{\boldsymbol{\Delta}}_{\boldsymbol{dqz}}$ is obtained as in (G.7).

$$\boldsymbol{W}^{\boldsymbol{\Delta}}_{\boldsymbol{dqz}} = C_{arm} \boldsymbol{P}_{\boldsymbol{\omega}} \left(\boldsymbol{P}^{\boldsymbol{-1}}_{\boldsymbol{-2\omega}} \boldsymbol{v}^{\boldsymbol{\Sigma}}_{\boldsymbol{Cdqz}} \circ \boldsymbol{P}^{\boldsymbol{-1}}_{\boldsymbol{\omega}} \boldsymbol{v}^{\boldsymbol{\Delta}}_{\boldsymbol{Cdqz}} \right) \tag{G.7}$$

The results for the dq components from (G.7) are time-invariant after neglecting the 6$^{\text{th}}$ harmonic component. However, the zero-sequence W_z^{Δ} is pulsating at 3ω, as shown in (G.8). The same technique as for the zero-sequence component of v_{Cz}^{Δ} may be applied as explained in Section 2.4.1, i.e., an auxiliary virtual variable $W_{Z\beta}^{\Delta}$ which is 90° phase-shifted from W_z^{Δ} (renamed $W_{Z\alpha}^{\Delta}$ for convenience) is created. This is done by respectively replacing the $\sin(3\omega t)$ and $\cos(3\omega t)$ that appear in (G.8) by $\sin(3\omega t)$ and $-\cos(3\omega t)$, as given in (G.9).

$$W_z^{\Delta} = \underbrace{C_{arm}\left(v_{Cd}^{\Delta}v_{Cd}^{\Sigma} + v_{Cq}^{\Delta}v_{Cq}^{\Sigma} + 2v_{CZ_d}^{\Delta}v_{Cz}^{\Sigma}\right)}_{W_{Z_d}^{\Delta}}\cos(3\omega t) + ... \tag{G.8}$$
$$... + \underbrace{C_{arm}\left(v_{Cq}^{\Delta}v_{Cd}^{\Sigma} - v_{Cd}^{\Delta}v_{Cq}^{\Sigma} + 2v_{CZ_q}^{\Delta}v_{Cz}^{\Sigma}\right)}_{W_{Z_q}^{\Delta}}\sin(3\omega t)$$

$$W_{Z_\alpha}^{\Delta} = W_{Z_d}^{\Delta}\cos(3\omega t) + W_{Z_q}^{\Delta}\sin(3\omega t) \tag{G.9a}$$
$$W_{Z_\beta}^{\Delta} = W_{Z_d}^{\Delta}\sin(3\omega t) - W_{Z_q}^{\Delta}\cos(3\omega t) \tag{G.9b}$$

Furthermore, the expression from (G.9) is written in vector form as in (G.10), with the definitions given in (G.11) and $\boldsymbol{T_{3\omega}^{-1}} = \boldsymbol{T_{3\omega}}$ the rotational transformation defined in (2.32).

$$\boldsymbol{W_{Z_{\alpha\beta}}^{\Delta}} = \boldsymbol{T_{3\omega}^{-1}}\boldsymbol{W_Z^{\Delta}}, \tag{G.10}$$

$$\boldsymbol{W_{Z_{\alpha\beta}}^{\Delta}} \stackrel{\text{def}}{=} [W_{Z_\alpha}^{\Delta}\ W_{Z_\beta}^{\Delta}]^{\top};\quad \boldsymbol{W_Z^{\Delta}} \stackrel{\text{def}}{=} [W_{Z_d}^{\Delta}\ W_{Z_q}^{\Delta}]^{\top} \tag{G.11}$$

Finally, an extended definition of the modulated voltage difference is introduced as $\boldsymbol{W_{dqZ}^{\Delta}} \stackrel{\text{def}}{=} [W_d^{\Delta}\ W_q^{\Delta}\ W_{Z_d}^{\Delta}\ W_{Z_q}^{\Delta}]^{\top}$ and is expressed in (G.12).

$$\boldsymbol{W_{dqZ}^{\Delta}} = \begin{bmatrix} W_d^{\Delta} \\ W_q^{\Delta} \\ W_{Z_d}^{\Delta} \\ W_{Z_q}^{\Delta} \end{bmatrix} = C_{arm}\begin{bmatrix} v_{Cd}^{\Delta}v_{Cd}^{\Sigma} + 2v_{Cd}^{\Delta}v_{Cz}^{\Sigma} - v_{Cq}^{\Delta}v_{Cq}^{\Sigma} + v_{CZ_d}^{\Delta}v_{Cd}^{\Sigma} - v_{CZ_q}^{\Delta}v_{Cq}^{\Sigma} \\ 2v_{Cq}^{\Delta}v_{Cz}^{\Sigma} - v_{Cq}^{\Delta}v_{Cd}^{\Sigma} - v_{Cd}^{\Delta}v_{Cq}^{\Sigma} + v_{CZ_d}^{\Delta}v_{Cq}^{\Sigma} + v_{CZ_q}^{\Delta}v_{Cd}^{\Sigma} \\ v_{Cd}^{\Delta}v_{Cd}^{\Sigma} + v_{Cq}^{\Delta}v_{Cq}^{\Sigma} + 2v_{CZ_d}^{\Delta}v_{Cz}^{\Sigma} \\ v_{Cq}^{\Delta}v_{Cd}^{\Sigma} - v_{Cd}^{\Delta}v_{Cq}^{\Sigma} + 2v_{CZ_q}^{\Delta}v_{Cz}^{\Sigma} \end{bmatrix} \tag{G.12}$$

G.2 Methodology for expressing Energy based controllers in abc to dqz frame

In order to illustrate the methodology, the following subsections explains the reformulation of a generic set of three-phase PI controllers in the abc frame, and a second-order notch filter used to extract the average value of the per-phase energy components.

G.2.1 Generic PI controller

As an example, let us consider the generic three-phase PI controller in abc frame from Fig. G.2. It is controlling the variables $\boldsymbol{X_{abc}} = [X_a\ X_b\ X_c]^{\top}$ to their references $\boldsymbol{X_{abc}^*} = [X_a^*\ X_b^*\ X_c^*]^{\top}$. The outputs of the controllers are $\boldsymbol{Y_{abc}} = [Y_a\ Y_b\ Y_c]^{\top}$, and the states of the integral parts are $\boldsymbol{\xi_{abc}} = [\xi_a\ \xi_b\ \xi_c]^{\top}$. It is considered that the variables $\boldsymbol{X_{abc}}$ are pulsating at an angular frequency $n\omega$.

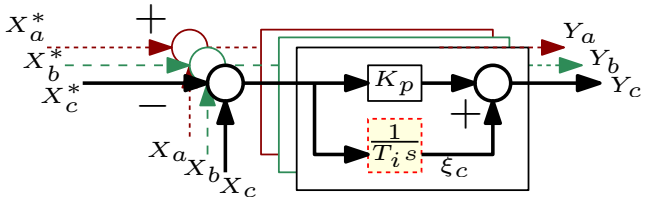

Figure G.2 – Generic three-phase PI independent controllers in *abc* frame

The reformulation of the generic PI from Fig. G.2 to the SRRF frame at $n\omega$ is performed in two steps. First, the integral part of the controller is obtained and second, the controllers output.

The differential equation of the integral part is:

$$T_i \frac{d\boldsymbol{\xi}_{\boldsymbol{abc}}}{dt} = \boldsymbol{X}^*_{\boldsymbol{abc}} - \boldsymbol{X}_{\boldsymbol{abc}} \tag{G.13}$$

This equation can be related to the dqz components at $n\omega$ as,

$$T_i \frac{d\boldsymbol{P}^{\boldsymbol{-1}}_{\boldsymbol{n\omega}} \boldsymbol{\xi}^{\boldsymbol{n\omega}}_{\boldsymbol{dqz}}}{dt} = \boldsymbol{P}^{\boldsymbol{-1}}_{\boldsymbol{n\omega}} \boldsymbol{X}^{\boldsymbol{n\omega *}}_{\boldsymbol{dqz}} - \boldsymbol{P}^{\boldsymbol{-1}}_{\boldsymbol{n\omega}} \boldsymbol{X}^{\boldsymbol{n\omega}}_{\boldsymbol{dqz}} \tag{G.14}$$

where

$$\boldsymbol{\xi}^{\boldsymbol{n\omega}}_{\boldsymbol{dqz}} = \boldsymbol{P}_{\boldsymbol{n\omega}} \boldsymbol{\xi}_{\boldsymbol{abc}}; \boldsymbol{X}^{\boldsymbol{n\omega}}_{\boldsymbol{dqz}} = \boldsymbol{P}_{\boldsymbol{n\omega}} \boldsymbol{X}_{\boldsymbol{abc}}; \boldsymbol{X}^{\boldsymbol{n\omega *}}_{\boldsymbol{dqz}} = \boldsymbol{P}_{\boldsymbol{n\omega}} \boldsymbol{X}^*_{\boldsymbol{abc}} \tag{G.15}$$

Expanding (G.14) and multiplying by $\boldsymbol{P}_{\boldsymbol{n\omega}}$ results in (G.16).

$$T_i \frac{d\boldsymbol{\xi}^{\boldsymbol{n\omega}}_{\boldsymbol{dqz}}}{dt} = \boldsymbol{X}^{\boldsymbol{n\omega *}}_{\boldsymbol{dqz}} - \boldsymbol{X}^{\boldsymbol{n\omega}}_{\boldsymbol{dqz}} - T_i \underbrace{\boldsymbol{P}_{\boldsymbol{n\omega}} \frac{d\boldsymbol{P}^{\boldsymbol{-1}}_{\boldsymbol{n\omega}}}{dt}}_{n\boldsymbol{J}_\omega} \boldsymbol{\xi}^{\boldsymbol{n\omega}}_{\boldsymbol{dqz}} \tag{G.16}$$

where the coupling matrix $n\boldsymbol{J}_{\boldsymbol{\omega}}$ was introduced in (2.20).

The output of the controller in *abc* frame is expressed as,

$$\boldsymbol{Y}_{\boldsymbol{abc}} = \boldsymbol{\xi}_{\boldsymbol{abc}} + K_p \left(\boldsymbol{X}^*_{\boldsymbol{abc}} - \boldsymbol{X}_{\boldsymbol{abc}} \right). \tag{G.17}$$

With the definitions given in (G.15), (G.17) may be written as,

$$\boldsymbol{Y}_{\boldsymbol{abc}} = \boldsymbol{P}^{\boldsymbol{-1}}_{\boldsymbol{n\omega}} \boldsymbol{\xi}^{\boldsymbol{n\omega}}_{\boldsymbol{dqz}} + K_p \left(\boldsymbol{P}^{\boldsymbol{-1}}_{\boldsymbol{n\omega}} \boldsymbol{X}^{\boldsymbol{n\omega *}}_{\boldsymbol{dqz}} - \boldsymbol{P}^{\boldsymbol{-1}}_{\boldsymbol{n\omega}} \boldsymbol{X}^{\boldsymbol{n\omega}}_{\boldsymbol{dqz}} \right) \tag{G.18}$$

Multiplying (G.18) by $\boldsymbol{P}_{\boldsymbol{n\omega}}$ yields,

$$\boldsymbol{Y}^{\boldsymbol{n\omega}}_{\boldsymbol{dqz}} = \boldsymbol{\xi}^{\boldsymbol{n\omega}}_{\boldsymbol{dqz}} + K_p \left(\boldsymbol{X}^{\boldsymbol{n\omega *}}_{\boldsymbol{dqz}} - \boldsymbol{X}^{\boldsymbol{n\omega}}_{\boldsymbol{dqz}} \right) \tag{G.19}$$

The complete PI structure in dqz frame at $n\omega$ is determined by (G.16) and (G.19). These results are expressed in block-diagram form in Fig. G.3. This model is the result of applying the Park transformation to the three-phase PI controllers from Fig. G.2. It can be noted that the cross-couplings in the model represents the phase-shift resulting from the application of PI controllers for tracking sinusoidal signals, and should not be confused with decoupling terms in a *classical dq* current controller.

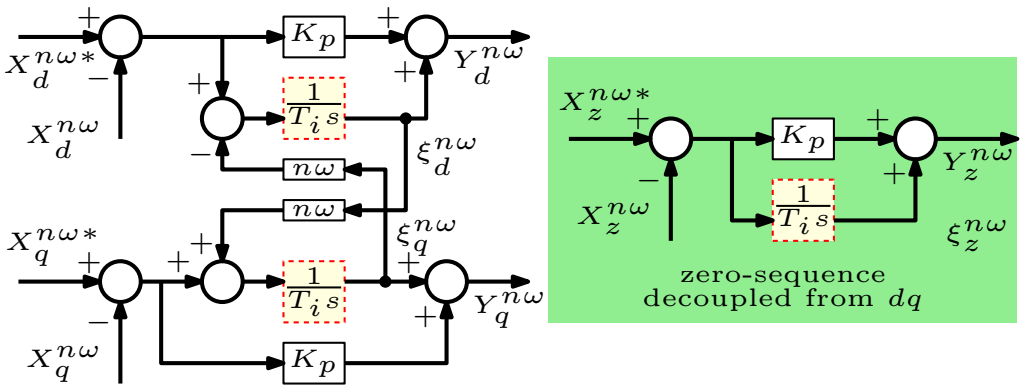

Figure G.3 – Generic three-phase PI controllers from Fig. G.2 in dqz frame

G.2.2 Second order notch filter

The filters used for the energies $\boldsymbol{W}^{\boldsymbol{\Sigma}}_{\boldsymbol{abc}}$ and $\boldsymbol{W}^{\boldsymbol{\Delta}}_{\boldsymbol{abc}}$ are second order notch filters tuned at their corresponding frequencies. As an example, let us consider the three phase signals $\boldsymbol{U}_{\boldsymbol{abc}} = [U_a\ U_b\ U_c]^\top$ and the filtered values $\overline{\boldsymbol{Y}}_{\boldsymbol{abc}} = [\overline{Y}_a\ \overline{Y}_b\ \overline{Y}_c]^\top$. The second order transfer function of the notch filter for the phase j is:

$$\frac{\overline{Y}_j}{U_j} = \frac{s^2 + \omega_n^2}{s^2 + 2\zeta\omega_n s + \omega_n^2} \tag{G.20}$$

where ω_n is the natural frequency and ζ is the damping coefficient. Equation (G.20) may be written as a second order differential function as:

$$\frac{d^2\overline{Y}_j}{dt^2} + 2\zeta\omega_n\frac{d\overline{Y}_j}{dt} + \omega_n^2\overline{Y}_j = \frac{d^2U_j}{dt^2} + \omega_n^2 U_j \tag{G.21}$$

Choosing the following state variables:

$$F_{1j} \stackrel{\text{def}}{=} \overline{Y}_j - U_j \tag{G.22a}$$

$$F_{2j} \stackrel{\text{def}}{=} \frac{d\overline{Y}_j}{dt} - \frac{dU_j}{dt} + 2\zeta\omega_n F_{1j} + 2\zeta\omega_n U_j \tag{G.22b}$$

The output of the notch filter can be obtained directly from (G.22a). Derivating the states from (G.22) and generalizing for a three-phase system it is obtained:

$$\frac{d\boldsymbol{F}_{\boldsymbol{1abc}}}{dt} = \boldsymbol{F}_{\boldsymbol{2abc}} - 2\zeta\omega_n\boldsymbol{F}_{\boldsymbol{1abc}} - 2\zeta\omega_n\boldsymbol{U}_{\boldsymbol{abc}} \tag{G.23a}$$

$$\frac{d\boldsymbol{F}_{\boldsymbol{2abc}}}{dt} = -\omega_n^2\boldsymbol{F}_{\boldsymbol{1abc}} \tag{G.23b}$$

$$\overline{\boldsymbol{Y}}_{\boldsymbol{abc}} = \boldsymbol{F}_{\boldsymbol{1abc}} + \boldsymbol{U}_{\boldsymbol{abc}} \tag{G.23c}$$

where $\boldsymbol{F}_{\boldsymbol{1abc}} = [F_{1a}\ F_{1b}\ F_{1c}]^\top$ and $\boldsymbol{F}_{\boldsymbol{2abc}} = [F_{2a}\ F_{2b}\ F_{2c}]^\top$.

Equation (G.23) can be transformed into the SRRF as:

$$\frac{d\boldsymbol{F}_{\boldsymbol{1dqz}}}{dt} = \boldsymbol{F}_{\boldsymbol{2dqz}} - 2\zeta\omega_n\boldsymbol{F}_{\boldsymbol{1dqz}} - 2\zeta\omega_n\boldsymbol{U}_{\boldsymbol{dqz}} - \boldsymbol{J}_{\boldsymbol{n\omega}}\boldsymbol{F}_{\boldsymbol{1dqz}} \tag{G.24a}$$

$$\frac{d\boldsymbol{F}_{\boldsymbol{2dqz}}}{dt} = -\omega_n^2\boldsymbol{F}_{\boldsymbol{1dqz}} - \boldsymbol{J}_{\boldsymbol{n\omega}}\boldsymbol{F}_{\boldsymbol{2dqz}} \tag{G.24b}$$

$$\overline{\boldsymbol{Y}}_{\boldsymbol{dqz}} = \boldsymbol{F}_{\boldsymbol{1dqz}} + \boldsymbol{U}_{\boldsymbol{dqz}} \tag{G.24c}$$

where $\boldsymbol{F}_{\boldsymbol{1dqz}} = [F_{1d}\ F_{1q}\ F_{1z}]^\top$, $\boldsymbol{F}_{\boldsymbol{2dqz}} = [F_{2d}\ F_{2q}\ F_{2z}]^\top$, $\boldsymbol{U}_{\boldsymbol{dqz}} = [U_d\ U_q\ U_z]^\top$ and $\overline{\boldsymbol{Y}}_{\boldsymbol{dqz}} = [\overline{Y}_d\ \overline{Y}_q\ \overline{Y}_z]^\top$. Equation (G.24) summarizes the three-phase notch filter in dqz frame.

Appendix H

DC Cable Modeling For Small-Signal Stability Analysis

One of the main components (and expensive indeed) of HVDC systems are the underground cables [42]. As for the converters, several models of the "real cables" are available for different kind of studies, as briefly summarized in Fig. H.1. The study of the DC cables exceeds the scope of this report: only the methodology for obtaining a cable model for interoperability studies is detailed.

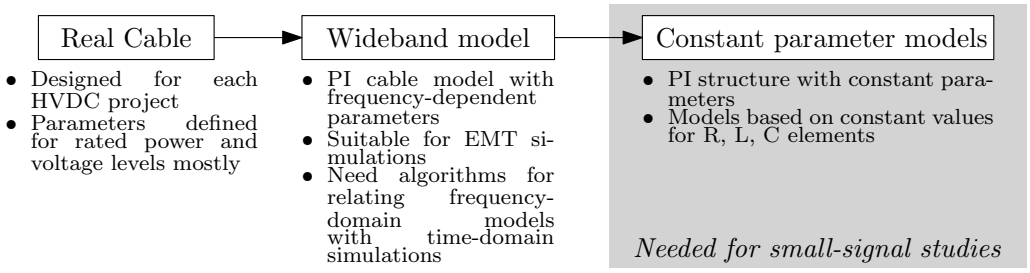

Figure H.1 – Modeling of DC cables for system studies

The most used cable model is the universal line model which is presented in [231], and implemented in the main EMT simulation software as EMTP-RV or PSCAD with the name of *Wideband* model (Fig. H.1). The particularity of the *Wideband* model is the detailed frequency-dependent behavior which is inherent of each cable and depends on its physical characteristics [232]. The difficulty of expressing this model with a state-space representation makes impossible its utilization for small-signal stability studies.

In many publications and studies, it is usual to represent the cable with a *Classical-PI* equivalent circuit, composed with R, L and C (constant parameters). However, this representation presents many limitations as already studied in [9, 74]. The main issue is the presence of unreal resonances which can conduct to false conclusions regarding the HVDC system.

Once the limitations of the *Classical-PI* cable model were pointed out, the author from [74] proposed a modification of the model for improving the accuracy with a new one called *Coupled-PI*. It is based on a physical comprehension of the DC cable and it modifies the typical PI structure for taken into account the coupling between the core and the screen. This is done with the insertion of a series inductance coupled with the screen circuit. Nevertheless, the *Coupled-PI* model fails to represent accurately the frequency dependence of the model parameters [9].

From the discussion in [74], the authors from [195] were motivated for improving the cable modeling for stability studies. The intention is to capture the frequency dependence of the

parameters with a modified PI model with constant parameters [196], resulting in the so-called *Frequency Dependant-PI model* (FD-Π) [195]. This model is the scope of this Appendix.

The rest of this Appendix is organized as follows: the cable models *Wideband* and FD-Π are first discussed and then the parameters and main assumptions are stated. Also, the methodology for obtaining the fitted parameters is explained. Finally, frequency and time domain simulations are carried on for validating the obtained model.

H.1 Wideband model

For EMT simulations, the *Wideband* model is the preferred one because of its high accuracy without compromising the simulation times. As it was stated before, the information needed for obtaining this model are the physical parameters of the cable. The considered parameters for the *Wideband* model are shown in Tables H.1 and H.2 which were provided by Dr. Salvatore D'Arco and Dr. Andrzej Holdyk[1]. The main assumption is that the armour and sheath are considered to be perfectly grounded, hence they can be eliminated by Kron reduction [195]. This implies that the voltages in armour and sheath remain limited, which is a realistic assumption for submarine HVDC power cables [233].

Table H.1 – EMT Cable Data - Single core - Number of cables: 1

Number of Conductors	Vertical Distance [m]	Horizontal Distance [m]	Outer Insulation Radius [m]
3	1	0	0.0637

Table H.2 – EMT Cable Data - Conductor/Insulator

Conductor Number	Inside Radius R_{in} [m]	Outside Radius R_{out} [m]	Resistivity ρ [Ω-m]	Relative Permeability MUE	Insulator Relative Permeability MUE-IN	Insulator Relative Permittivity EPS-IN	Insulator Loss Factor LFCT-IN	Phase Number KPH
1	0	0.0195	1.68E-08	1	1	2.658	0.001	1
2	0.0487	0.0517	2.20E-07	1	1	2.3	0.001	0
3	0.0547	0.0587	1.80E-07	10	1	2.3	0.001	0

The parameters from Tables H.1 and H.2 are loaded into the EMTP block "*Cable DATA*", creating the frequency-dependence parameters of the cable. Then, the block "*WB Fitter*" generates a model data file to be used by the cable model "*WB m - phase*". This process is shown in Fig. H.2.

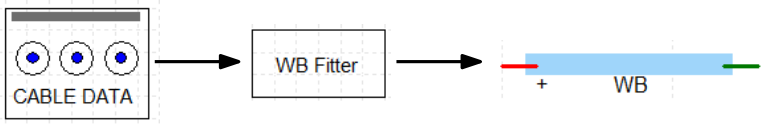

Figure H.2 – EMTP Wideband cable implementation

The resultant *Wideband* cable model can be represented as a PI model where their parameters vary with respect to the frequency f of the inputs as shown in Fig. H.3. The series

[1]The author acknowledge Dr. Salvatore D'Arco and Dr. Andrzej Holdyk for providing the cable model in EMTP-RV.

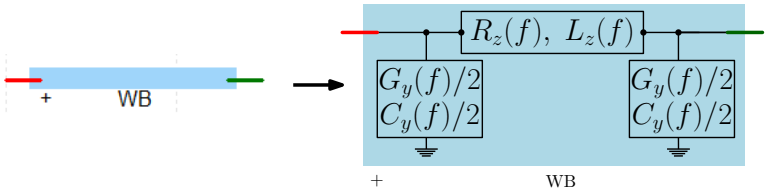

Figure H.3 – EMTP Wideband cable interpretation

resistance and inductance are noted as $R_z(f)$ and $L_z(f)$, respectively. The shunt parameters are noted as $G_z(f)$ and $C_z(f)$ for the conductance and capacitance. The parameters are obtained by their respective value per kilometer as:

$$R_z = r_z \times d; \quad L_z = l_z \times d; \quad G_z = g_z \times d; \quad C_z = c_z \times d \tag{H.1}$$

where r_z, l_z, g_z and c_z are the parameters per kilometer and d is the length of the cable in kilometers.

The frequency dependence of the parameters are plotted in Fig. H.4 per km. The series resistance r_z augment with higher frequencies and the inductance l_z tends to be smaller. For being able to represent the dynamics of the cable when studying the stability, the considered cable should be able to represent this characteristic to a certain extent.

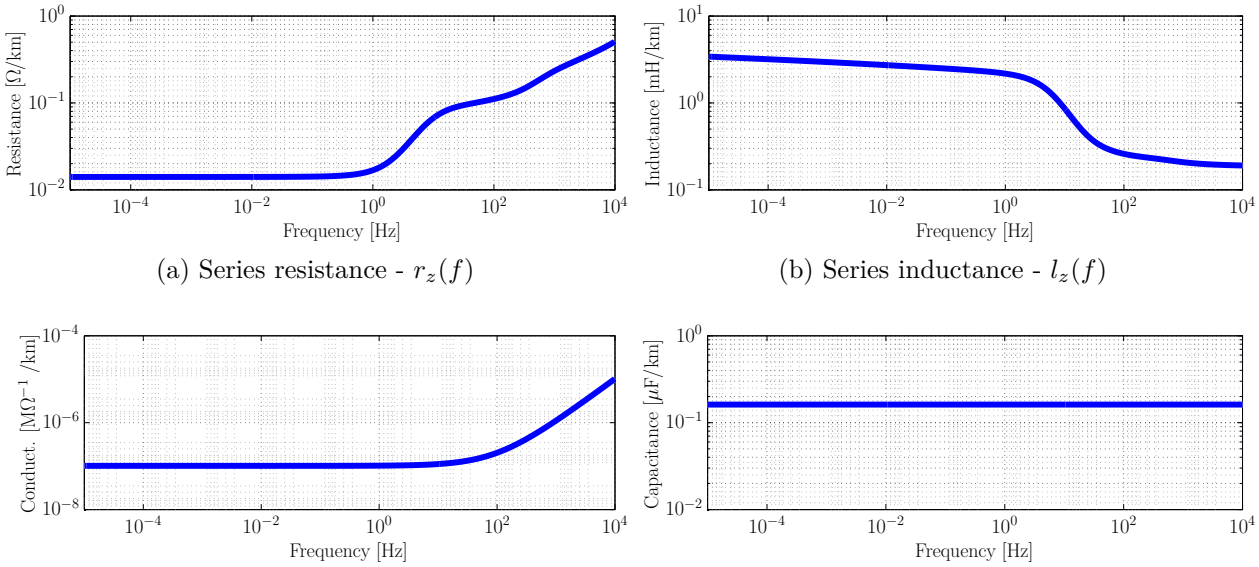

(a) Series resistance - $r_z(f)$

(b) Series inductance - $l_z(f)$

(c) Shunt conductance - $g_y(f)$

(d) Shunt capacitance - $c_y(f)$

Figure H.4 – Frequency dependence parameters of wideband cable

Figure H.4c shows the variation of the conductance $g_y(f)$ with the frequency. Even if the conductance presents a variation for high frequencies, the order of magnitude is very low (meaning that the shunt resistance is in fact extremely large, so little current will flow in this element). For this reason, it is safe to consider this parameter as a constant, or even neglect it. Finally, the capacitance $c_y(f)$ is shown in Fig. H.4d. As it is observed, $c_y(f)$ is modeled as a constant value for all frequencies. This is proper to the EMT software [195].

The following section explains how to obtain a PI model with constant parameters that replicates the frequency characteristic of the cable.

H.2 Frequency Dependent-PI cable model

This section describes the methodology used for modeling the DC cable as described in [195]. The key idea is to propose a "PI cell" structure with parallel branches in the series circuit as shown in Fig. H.5. The N parallel branches on each cell are meant to reproduce the frequency dependence of $r_z(f)$ and $l_z(f)$ from Fig. H.3. The M cells in series are aimed to approximate the hyperbolic correction factors [195].

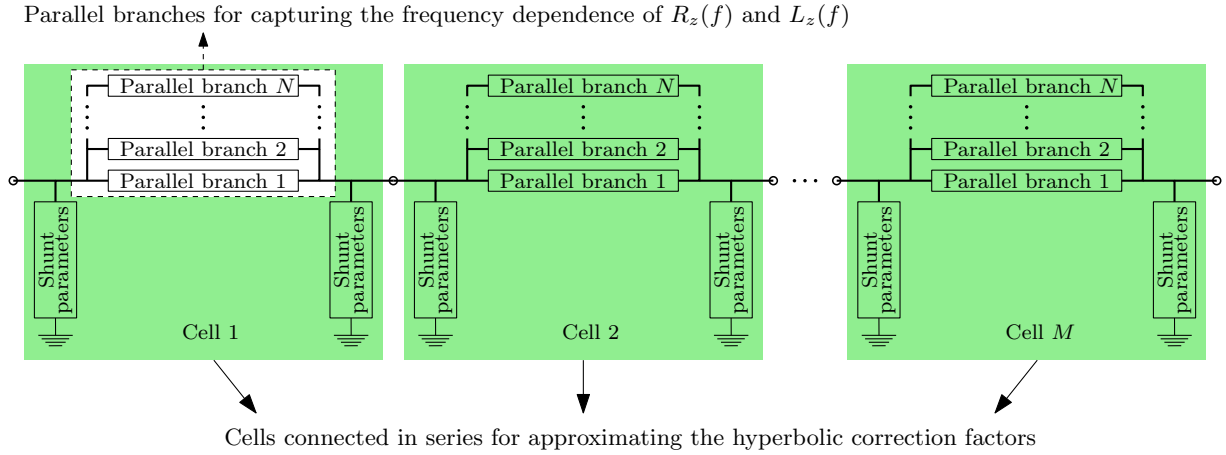

Figure H.5 – PI model with parallel branches - "FD-Π"

Equivalent circuit

If infinite numbers of N and M are considered, the *Wideband* model and the FD-Π should virtually present the same impedance variation with respect to the frequency. Nevertheless, if large number of cells and parallel branches are used, the order of the system increase exponentially [234], making the modeling of DC grids cumbersome and difficult to analyze. For this reason, only one cell with three parallel branches are considered as shown in Fig. H.6. The parameters are obtained with (H.1).

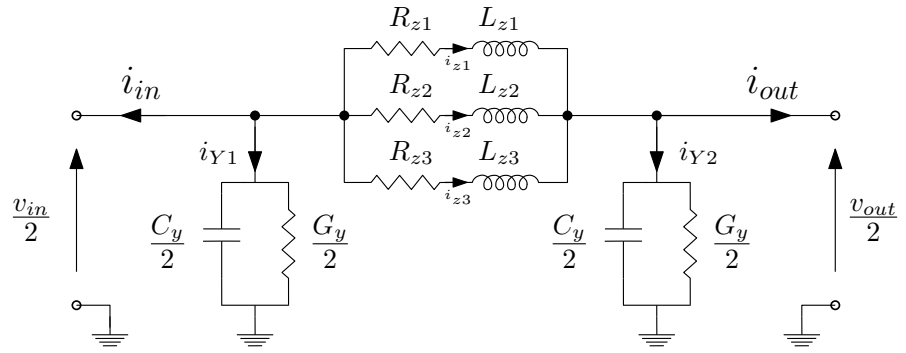

Figure H.6 – Equivalent circuit of "FD-Π model" for $N = 3$ and $M = 1$.

As discussed previously, the value of g_y will be considered as a constant value (or even neglected) since its value and variation respect to the frequency are rather low as seen in Fig. H.4c. In case of c_y, its value is taken directly from Fig. H.4d.

The following section describes the methodology for obtaining the values of r_{z1}, r_{z2}, r_{z3}, l_{z1}, l_{z2} and l_{z3}.

Methodology for obtaining the fitted parameters

The methodology is based on the rational approximation of frequency domain responses by vector fitting as presented in [235]. The general problem formulation is based in the rational function approximation given as:

$$F_{est}(s) = \sum_{n=1}^{N} \frac{c_n}{s - a_n} + e + sh \tag{H.2}$$

Given the frequency response of the "real" system $F_{real}(s)$, the vector fitting technique estimates all the coefficients in (H.2) so the frequency response of $F_{est}(s)$ approximates the frequency response of $F_{real}(s)$. The theory behind this technique exceeds the topic of this report and the vector fitting technique is used just as a tool, which can be downloaded from [236].

Considering only the parallel branches from Fig. H.6, as in Fig. H.7, the admittance of the equivalent branch is expressed as in (H.3).

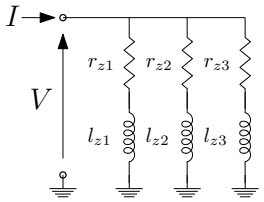

Figure H.7 – Parallel branches from Fig. H.6

$$Y_{est}(s) = \frac{I(s)}{V(s)} = \sum_{n=1}^{N=3} \frac{1}{l_{zn}s - (-r_{zn})} \tag{H.3}$$

Note that the expression of $Y_{est}(s)$ in (H.3) is similar to the general formulation in (H.2) if it is considered $c_n = 1$ and $e = h = 0$. The "$-$" sign in the denominator of (H.3) is added for having a similar formulation than (H.2).

From the output data of $r_z(f)$ and $l_z(f)$ from the *Wideband* cable (Figs. H.4a and H.4b), it is possible to obtain the "real" admittance $Y_{real}(s)$ of the series parameters as a function of the frequency as:

$$Y_{real}(2\pi f) = \frac{1}{conj(Z_{real}(2\pi f))} \tag{H.4}$$

Once the "real" admittance $Y_{real}(s)$ is obtained, the vector fitting tool is used for placing the poles of (H.3) automatically in a proper position to fit the frequency response ("*vectfit3*" function from [236]). The vector fitting tool presents many options for this tasks, as iterative placement, initial position of the poles, etc. These options may result in different final positions of the pole placement, but the exploration of all the possibilities exceed the scope of this work. The results of the fitted admittance is shown in Fig. H.8.

The difference on the magnitude and the angles are calculated as the absolute value of the difference of the admittance of the real and fitted response. The maximum difference in the magnitude is around 0.8 Ω^{-1} and it occurs near 0.35 Hz. This error hasn't a big impact on the overall frequency response of the complete FD-Π model since, at this low frequency, the cable behaves more likely a pure capacitor since the series inductance are almost not solicited. The biggest error on the angle is around 6.5° and it visible around a frequency of 815Hz. For improving the fitted response, the number of parallel branches (N) can be

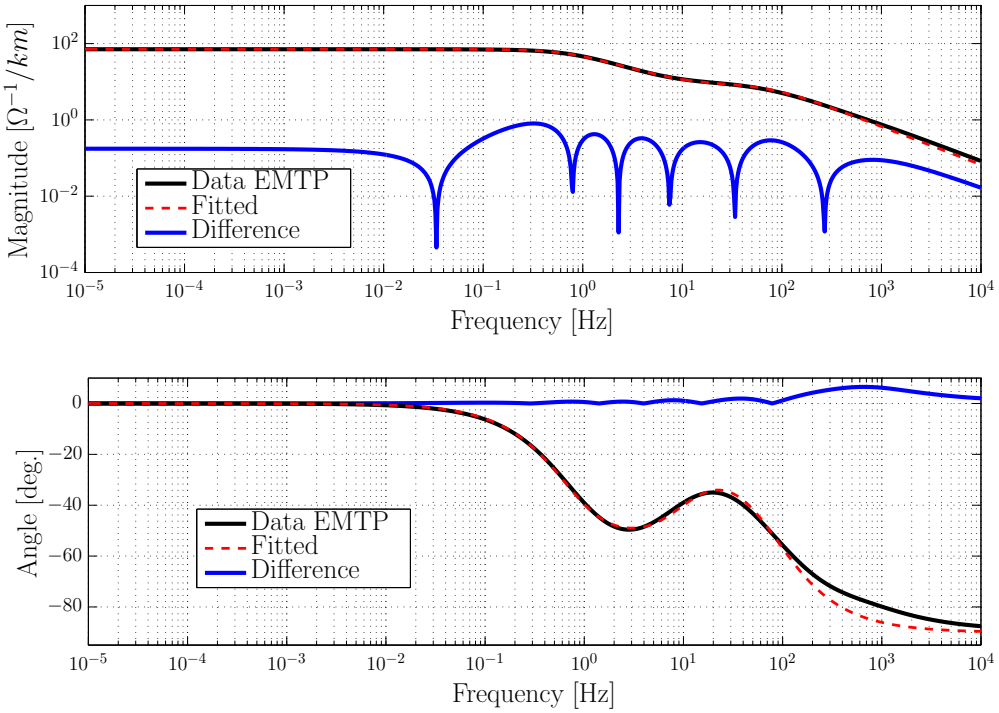

Figure H.8 – Comparison of the fitted admittance $Y_{est}(s)$ from the vector fitting tool and the reference $Y_{real}(s)$

augmented. Nevertheless, the order of the cable will grow rapidly making the further analysis more complicated.

The output from the function "*vectfit3*" are the poles of $Y_{est}(s)$ and the associated state-space function, so another step is needed for obtaining the values of r_{z1}, r_{z2}, r_{z3}, l_{z1}, l_{z2} and l_{z3}. This is obtained by converting the state-space model having common pole set into pole-residue model (this is done with the function "*ss2pr*" from [236]).

$$l_{zn} = \frac{1}{Res_{zn}}; \quad r_{zn} = -\lambda_{zn} l_{zn} \tag{H.5}$$

where l_{zn} and r_{zn} are the inductance and resistance of the parallel branch n; λ_{zn} and Res_{zn} are the pole and residue associated to the branch n. The "$-$" sign for r_{zn} is associated with the sign introduced in (H.3). Finally, the obtained numerical parameters with the described methodology are listed in Table H.3.

Table H.3 – Cable parameters for the Frequency-Dependent Π model

Parameter	Value	Parameter	Value
r_{z1}	0.1265 Ω/km	l_{z1}	0.2644 mH/km
r_{z2}	0.1504 Ω/km	l_{z2}	7.2865 mH/km
r_{z3}	0.0178 Ω/km	l_{z3}	3.6198 mH/km
g_y	0.1015 $\mu\Omega^{-1}/km$	c_y	0.16156 μF/km

H.3 Models comparison

The previous section shown how to obtain the parameters of the FD-Π cable model with $N = 3$ and $M = 1$. In this section, the resultant model is compared with the reference *Wideband*

model in frequency and time domain in EMTP-RV. For both comparison, the FD-Π model is developed in EMTP-RV with R, L, C elements implementing the same circuit from Fig. H.6. The considered parameters are the ones from Table H.3 and the cable length is 300 km (d).

H.3.1 Frequency domain comparison

The frequency domain comparison is done with the scheme from Fig. H.9, using the "*Input Impedance*" block from EMTP-RV. The results are gathered in Fig. H.10.

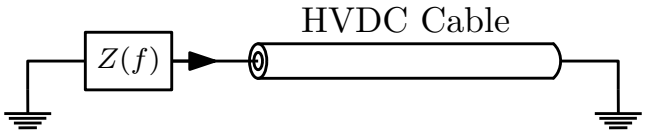

Figure H.9 – EMTP Scheme for frequency domain comparison

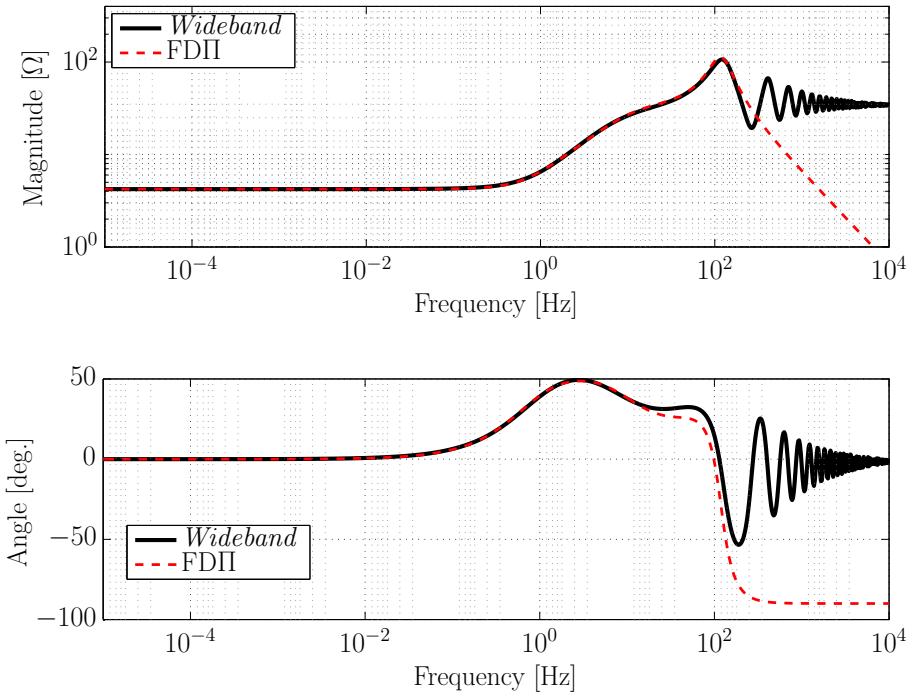

Figure H.10 – Complete frequency response comparison of the *Wideband* model and the Frequency-Dependent Π model with one cell and three parallel branches – Cable length 300 km

As seen in the results comparison of the cable impedance, the FD-Π cable model shows an acceptable accuracy up to the first resonance of the *Wideband* cable model (around 100 Hz). For higher frequencies, the *Wideband* model have many resonances that the FD-Π model is not capturing. For obtaining better results at these high frequencies, more cells connected in series are needed (increasing the model order) [234]. Nevertheless, it should be studied what is the range of resonances that will be excited in normal operation of the cable, i.e. if the model is modeled with extremely high accuracy for all frequencies, but the converters don't excite those frequencies, the enormous order of the cable model is not justified.

H.3.2 Time domain comparison

In this section the dynamic behavior of the *Wideband* model and the FD-Π model is compared based on EMT time-domain simulation. As for the previous comparison, one end of the cable is short-circuited, and in the other end, a current perturbation is injected while measuring the DC voltage at the same endpoint, as shown in Fig. H.11. A DC current step of 10 pu is injected for a duration of 200 ms, as shown in Fig. H.12a. The results of the obtained voltage are shown in Fig. H.12b.

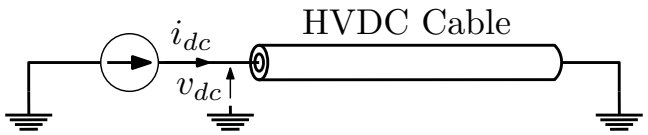

Figure H.11 – EMTP Scheme for time domain comparison

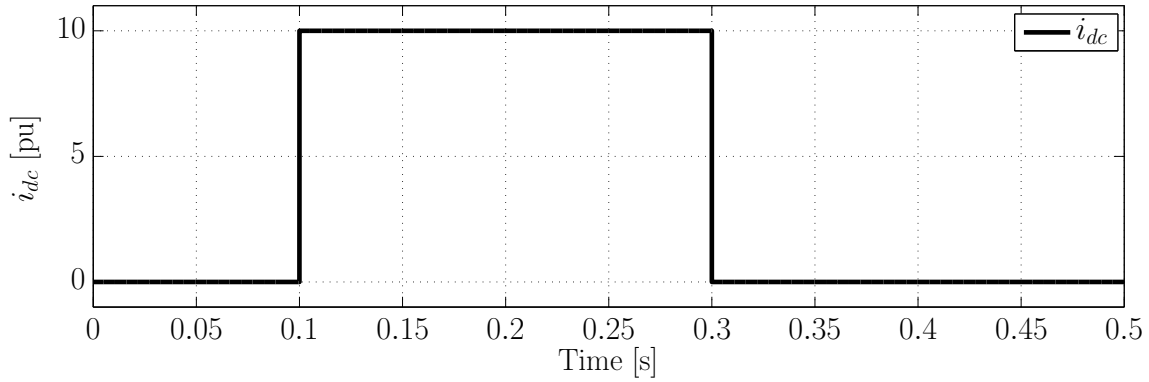

(a) DC Current Perturbation i_{dc}

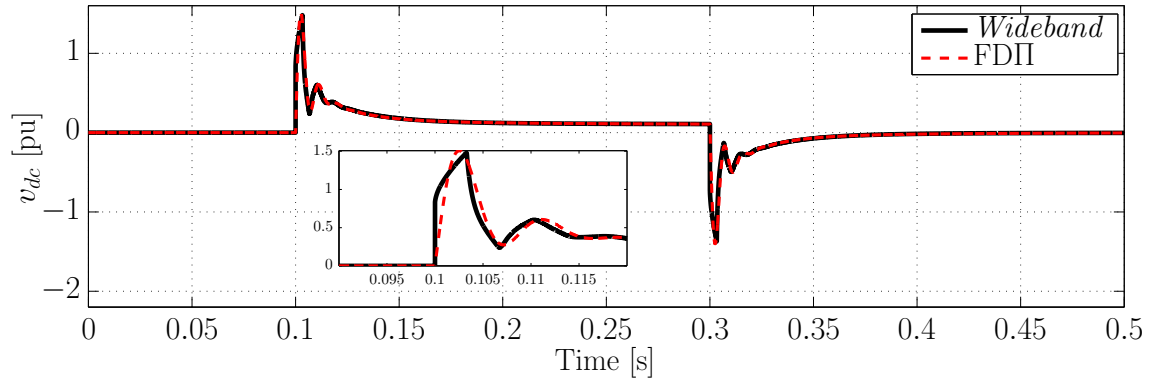

(b) DC Voltage v_{dc}

Figure H.12 – Time domain comparison of *Wideband* cable model and Frequency Dependent Π model – Cable length 300 km (d)

In Fig. H.12b a detail of the step at $t = 0.1$ s is also shown, where some slight differences can be observed. Nevertheless, the Frequency Dependent Π model replicates with acceptable accuracy the overall dynamic response of the *Wideband* model.

Analyse de stabilité en petit signaux des Convertisseurs Modulaires Multiniveaux et application à l'étude des MMC dans des Réseaux HVDC

Ces travaux de thèse portent essentiellement sur la modélisation, l'analyse et la commande des convertisseurs de type MMC intégrés dans un contexte MTDC. Le premier objectif de ce travail est d'aboutir à un modèle dynamique du convertisseur MMC, exprimé dans le repère *dq*, permettant d'une part, de reproduire avec précision les interactions AC-DC, et d'exprimer, d'autre part, la dynamique interne du convertisseur qui peut interagir également avec le reste du système. Le modèle développé peut être linéarisé facilement dans le but de l'exploiter pour l'étude de stabilité en se basant sur les techniques pour les systèmes linéaires à temps invariant. Ensuite, selon le modèle développé dans le repère *dq*, différentes stratégies de contrôle sont proposées en fonction de systèmes de contrôle-commande existantes dans la littérature mis en places pour le convertisseur MMC. Étant donné que l'ordre du système est un paramètre important pour l'étude des réseaux MTDC en présence de plusieurs stations de conversion de type MMC, l'approche de réduction de modèles à émerger comme une solution pour faciliter l'étude. En conséquence, différents modèles à ordre réduit sont développés, et qui sont validés par la suite, par rapport au modèle détaillé, exprimé dans le repère *dq*. Finalement, les modèles MMC développés ainsi que les systèmes de commande qui y ont associés sont exploités, pour l'analyse de stabilité en petits signaux des réseaux MMC-MTDC. Dans ce sens, la stratégie de commande associée à chaque MMC est largement évaluée dans le but d'investiguer les problèmes majeurs qui peuvent surgir au sein d'une configuration MTDC multi-constructeurs.

Mots clés

«Réseaux à courant continu multi-terminaux», «Convertisseur modulaire multiniveaux», «Modélisation dans l'espace d'états», «Stabilité en pétits signaux».

Small-signal stability analysis of Modular Multilevel Converters and application to MMC-based Multi-Terminal DC grids

This thesis deals with the modeling and control of MMCs in the context of MTDC. The first objective is to obtain an MMC model in *dq* frame which can reproduce accurately the AC- and DC- interactions, while representing at the same time the internal dynamics which may interact with the rest of the system. This model is suitable for linearization and stability studies, among other linear techniques. Then, based on the developed *dq* model, different control strategies are developed based on state-of-the-art MMC controllers. Since the dimension of the system is a limiting factor for studying MTDC grids with many MMCs, different reduced-order models are presented and compared with the detailed *dq* model. Finally, the developed MMC models with different controllers are used for the MTDC studies. The impact of the selected controllers for each MMC is evaluated to highlight the potential issues that may occur in multivendor schemes.

Keywords

«HVDC transmission», «Modular multilevel converter», «State-Space modeling», «Small-Signal stability analysis», «Interoperability in MTDC grids».